Proceedings of

Second International Conference on Multiscale Materials Modeling

Nasr M. Ghoniem
Editor

October 11-15, 2004
Los Angeles, California

Hosted by
University of California Los Angeles

Contents

C. Denoual , F. Bellencontre, Y. P. Pellegrini, CEA-DAM IdF (France)

Numerical Analysis of Nanotube Based NEMS Devices
C. H. Ke, H. D. Espinosa, N. Pugno, Northwestern University Evanston (USA)

A Multiscale Simulation for Electro-Mechanical Coupling of Ferroelectric Materials
J. Fan, Y. He, Alfred University (USA)

A Generalized Particle Dynamics Method for Atom-Continuum
J. Fan, Y. Yang, Z. Gao, Alfred University (USA)

Multi-Scale Model for Damage Analysis in Fiber-Reinforced Composites With Debonding
S. Ghosh, P. Raghavan, The Ohio State University (USA)

Void Hardening in BCC-Iron Studied by Atomic-Scale Modeling
S. I. Golubov, Y. Osetsky, R. Stoller, Oak Ridge National Laboratory (USA)

Modeling of flux-induced morphology evolution – from nano to mesoscale
A. Gusak, K. N. Tu, M. Pasichnyy, I. Sobchenko, T. Zaporozhets, Cherkasy National University (Cherkasy)

Molecular dynamics simulations of mechanical properties of boron-nitride nanotubes embedded in Si-B-N ceramics
M. Griebel, J. Hamaekers, University of Bonn (Garmany)

First-principles equation of state for energetic intermetallic and metal-metal oxide mixtures
X. Lu, S. V. Hanagud, Georgia Institute of Technology (USA)

Considerations in the formulation of a dislocation distribution function
C. S. Hartley, Air Force Office of Scientific Research (USA)

Field Theoretical Multiscale Polycrystal Plasticity and Its Applications to UFG, Nano-Crystalline and Amorphous Material
T. Hasebe, Kobe University (Japan)

Prediction of Initial Dislocation Nucleation in Metallic Systems via the Orbital-Free Density Functional Theory Local Quasicontinuum Method
R. L. Hayes, E. A. Carter, University of California, Los Angeles (USA); M. Fago, M. Ortiz, California Institute of Technology (USA)

Interphase and size effect in nanocomposites. Elastic and Viscoelastic behavior
E. Herve, V. Marcadon, A. Zaoui, Ecole polytechnique (France)

Comparison of mean field homogenisation methods: Elasto-plastic composite materials with random microstructure
P. Kanoute and J.L.Chaboche, ONERA (France)

Dislocation properties of Ni-Cu nanolaminates
A. Coho, N. Kioussis, California State University Northridge (USA); N. M. Ghoniem, University of California Los Angeles (USA)

Molecular dynamics simulation of scandium-stabilized zirconia
V. I. Barbashov, Yu. A. Komysa, Donetsk, Phys. Tech. Institut (Ukraine)

The long march to strain hardening in fcc single crystals
L. Kubin, B. Devincre, LEM, CNRS-ONERA (France); T. Hoc, Ecole Centrale Paris (France)

A Density-Functional Theory for Dislocation Structures
R. LeSar, Los Alamos National Laboratory (USA); J. M. Rickman, Lehigh University (USA)

Molecular dynamics simulation of healing of an ellipsoid crack in copper under compressive stress
M. Li, W. Y. Chu, K. W. Gao, L. J. Qiao, University of Science and Technology (China)

Nanovoid Cavitation by Dislocation Emission in Metals.
J. Marian, J. Knap and M. Ortiz, California Institute of Technology (USA)

Modeling of microstructural effects on the local mechanical fields in tempered martensite and bainite microstructures.
S. Sekfali, C. Rey, Ecole Centrale Paris (France); B. Marini, Commissariat à l'Energie Atomique (France)

Study of Mecanical Properties of Nanoscale Materials by Density Functional Molecular Dynamics and Lattice Green's Function
K. Masuda-Jindo, Tokyo Institute of Technology (Japan); Vu Van Hung, Hanoi National Pedagogic University (Vietnam)

Modelling modulus mismatch strengthening for dislocation dynamics simulations
V. Mohles, RWTH-Aachen (Germany); C. Kohler, University of Stuttgart (Germany)

Density functional theory study of intrinsic ductility of solids
S. Ogata, Osaka University (Japan); J. Li, N. Hirosaki, Ohio State University (USA); Y. Shibutani, National Institute for Materials Science (Japan); S. Yip, Massachusetts Institute of Technology (USA)

Thermoelasticity at High Temperatures and Pressures for Tantalum
D. Orlikowski, P. Soderlind, J. A. Moriarty, Lawrence Livermore National Laboratory (USA)

Explicit Expression for Stress in Multi-level Line Structures and in Connecting Vertical Vias
A. J. Rosakis, T.-S. Park, California Institute of Technology (USA); Subra Suresh, Massachusetts Institute of Technology (USA)

Strain localization: Effects of non-glide stresses on dislocation mobility
V. Racherla, J. L. Bassani, University of Pennsylvania (USA)

Grain-scale surface roughening simulation using large scale direct numerical simulation
Z. Zhao, R. Radovitzky, Massachusetts Institute of Technology (USA); A. Cuitino, Rutgers University (USA)

A continuum model to describe inverse size dependency in nanocrystals
A. Jerusalem, R. Radovitzky, Massachusetts Institute of Technology (USA)

Effect of Shape and Size Distribution of Precipitation Hardening in Superalloys
S. I. Rao, T. A. Parthasarathy, UES Inc.(USA); D. M. Dimiduk, P. M. Hazzledine, Air Force Reserach Laboratory (USA)

Multiscale modeling of elasticity and dissipation in NEMS resonators
R. E. Rudd, Lawrence Livermore National Laboratory (USA)

Dynamics Simulation of Material Interface using Molecular Dynamics and SPH methods
K. Saitoh, Y.Tateoka, N.Shinke, Kansai University (Japan)

Ideal interfacial strength between vanadium and oxide ceramics
M. Satou, K. Abe, Tohoku Univeristy (Japan); N. Kioussis, California State University Northridge (USA); N. M. Ghoniem, University of California Los Angeles (USA)

Growth of Dislocations in Nonuniform Fields - A Microelectronics Perspective
K.W. Schwarz, IBM Research Division (USA); D. Chidambarrao, IBM Systems and Technology Group (USA)

Continuum-level cohesive properties informed by quantum-mechanics for the simulation of hydrogen embrittlement

S. A. Serebrinsky, M. Ortiz, California Institute of Technology (USA); E. A. Carter, University of California Los Angeles (USA)

Crack Propagation of Silicon by Hybrid Tight-binding Molecular Dynamics
Y. Shibutani, N. Hori, S. Ogata, Osaka University (Japan); P. Gumbsch, Fraunhofer Inst. for Mechanics of Materials IWM (Germany)

Atomistic and mesoscale modeling of mechanical and chemical processes in molecular crystals
A. Strachan, B. L. Holian, Los Alamos National Laboratory (USA); A. C. T. van Duin, W. A. Goddard, III, California Institute of Technology (USA)

Dislocation growth in epitaxial thin film heterostructures
E. Tan, L. Sun, University of Iowa (USA)

Scalable Molecular Dynamics Methods for Reactive Force Fields
Aidan P. Thompson, John B. Aidun, Sandia National Laboratories (USA)

Modeling of the elastic behaviour of pearlitic microstructures
J. Toribio, R. Guzmán de Villoria, University of Salamanca (Spain)

Size effects in thin films: discrete dislocations and strain gradients
E. Van der Giessen, L. Nicola, University of Groningen (The Netherlands)

Bridging between QM and mesoscale: development and application of ReaxFF reactive potentials for Ru/Pt surface chemistry
A. C. T. van Duin, T. Jacob, Y. Jang, W. A. Goddard, III, California Institute of Technology (USA)

First Principles Simulation of Dislocation Cores
C. Woodward, Air Force Research Laboratory (USA) & Northwestern University (USA)

The Complexity of Dislocation Nucleation under Large Compressive Stress
G. Xu, D. Segall, C. Li, University of California Riverside (USA)

MD / DDD Study on Dislocation Behaviors at Matrix-Precipitate Interface in Nickel-Based Superalloys
K. Yashiro, F. Kurose, Y. Tabata, Y. Tomita, Kobe University (Japan); H. M. Zbib, Washington State University (USA)

Structure of Ferroelectric Domain Walls in the Nanoscale
A. Yavari, M. Ortiz and K. Bhattacharya, California Institute of Technology (USA)

Constitutive modeling of $L1_2$ crystals based on evolution of the superkink distribution
Y. Yuan, D.M. Parks, Massachusetts Institute of Technology (USA)

Voids under electromigration – from Monte Carlo to phenomenology
T. Zaporozhets, A. Gusak, I. Sobchenko, Yu. Lyashenko, Cherkasy National University (Cherkasy)

Formation of nanostructure under pulse loading and the problem of anomalous mass-transfer
T. Zaporozhets, Cherkasy National University (Cherkasy)

Meta-material physics and applications: towards to nano-scale plasmonics
X. Zhang, University of California Los Angeles (USA)

Grain-scale surface roughening simulation using large scale direct numerical simulation
Z. Zhao, R. Radovitzky, Massachusetts Institute of Technology (USA)

Activation Pathways for Crack Tip Plasticity and Environmental Attack
T. Zhu, S. Yip, Massachusetts Institute of Technology (USA); J. Li, Ohio State University (USA)

Hierarchical Modeling of Failure Mechanisms and Grain-Boundary Effects in Nanocrystalline Aggregates
T. Kameda, University of Tsukuba (Japan); M. A. Zikry, A. M. Rajendran, D. Brenner, North Carolina State University Raleigh (USA)

Symposium 2 Statistical Mechanics of Plasticity

An elastic manifold in glassy, time-dependent disorder:dislocation in a solute cloud
M. Alava,V. Vuorinen, S. Zapperi, Helsinki University of Technology (Italy)

A Model for the Spatio- temporal Dynamics of the Portevin- Le Chatiler effect: Chaos, Turbulence and Band Propagation
G. Ananthakrishna, Indian Institute of Science (India)

Effects of Non-Glide Stresses on Plastic Flow: from Atomistic Studies of Dislocations to Macroscopic Failure Mechanisms
J. L. Bassani, V. Vitek, University of Pennsylvania (USA)

Solute Effect in Shock Loaded Single Crystal Vanadium
J. Belak, J. U. Cazamias, R. Chau, J.H. Kinney, M. Kumar, R. Minich, Lawrence Livermore National Laboratory (USA)

Anomalous Hall-Petch Behavior of Ni_3Al: a Model Based on the Statistics of Weak-Links
D. C. Chrzan, Priam Pillai, University of California Berkeley & Lawrence Berkeley National Laboratory (USA)

The similitude principle in plasticity: long vs. short-range interactions
B. Devincre, L. P. Kubin, CNRS-ONERA (France); D. Gomez-Garcia, Universidad de Sevilla (Spain)

Mathematical and Numerical Modeling of Large Dislocation Systems
A. El-Azab, Florida State University (USA); B. Larson, Oak Ridge National Laboratory (USA); H. Weiland, Alcoa Technical Center (USA); Xuelin Han, D. Field, Washington State University (USA)

A new stochastic model for prediction of fatigue crack propagation
Kh. Farhangdoost, E. Pooladi, B. Ferdowsi, University of Mashhad (Iran)

Analytical estimation of forces of interaction is tesselated of charged planes depending on their relative arrangement
V. A. Feodorov, T.N. Plushnikova, A.V. Chivanov, M.V. Chemerkina, Tambov State University (Russia)

Characterization of Dislocation Structures in the Presence of Precipitates in Aluminum Alloys
D. P. Field, R.S. Yassar, P. Trivedi, Washington State Univ. (USA)

Solute - dislocation interaction and spatial coupling in the modeling of jerky flow
S. Varadhan, A. J. Beaudoin University of Illinois at Urbana-Champaign (USA); C. Fressengeas, Universit'e de Metz-CNRS (France)

Modelling in-plane torsion: a case of particular interest relating gnd and plastic strain gradients
A. Luque, J. Aldazabal, J. M. Martine-Esnaola, J. Gil Sevillano, University of Navarra M. de Lardizabal (Spain)

Theoretical and numerical modeling of plastic instabilities of the strain-rate softening type
P. Hähner, European Commission-Institute for Energy (The Netherlands)

3D Simulation of Dislocation Cell Structures based on Field Theory of Plasticity
T. Hasebe, Kobe University (Japan)

A continuum theory of dislocation motion
T. Hochrainer, Universitaet Karlsruhe (Germany)

Deformation-induced microstructures from 10,000 to 10nm in scale
D. A. Hughes, Sandia National Laboratories (USA); Niels Hansen, Risø National Laboratory (Denmark)

Dislocation Dynamics versus Kinetics
U. F. Kocks, Los Alamos National Laboratory (USA)

Avalanches and scaling in creep phenomena
M. Koslowski, R. LeSar, Robb Thomson, Los Alamos National Laboratory (USA)

Mechanisms controlling the size of misoriented dislocation cells
J. Kratochvil, Czech Technical University (Czech Republic); R. Sedlacek, Technische Universitat Munchen (Germany)

Application of Statistical Continuum Theory in Simulating Texture Evolution
D. S. Li, H. Garmestani, Georgia Institute of Technology (USA)

Studies of PLC deformation bands in strain-rate and stress-rate controlled tensile tests
H. Neuhäuser, F. B. Klose, F. Hagemann, H. Dierke, Technical University Carolo-Wilhelmina at Braunschweig (Germany)

Mechanisms of Solute-Dislocation Interaction in Al-Mg alloys: Experiments and Modeling of Dynamic Strain Ageing
R. C. Picu, Rensselaer Polytechnic Institute (USA); F. Barlat, H. Weiland, Alcoa Technical Center (USA)

Mesoscale Modeling of Dislocation Energetics and Dynamics
J. M. Rickman, Lehigh University (USA); R. LeSar, Los Alamos National Laboratory (USA)

Bending and torsion of thin samples in continuum dislocation-based approach
R. Sedlacek, Technische Universitat Munchen (Germany); J. Kratochvil, Czech Technical University (Czech Republic)

Atomistic Simulation of Dislocation Patterning in a Strain Gradient
R. L. B. Selinger, N. S. Weingarten, Catholic University (USA)

A large scale dislocation dynamics simulation of single crystal plasticity
M. Tang, W. Cai, V. Bulatov, T. Pierce, M. Rhee, M. Hiratani, T. Arsenlis, Lawrence Livermore National Laboratory (USA)

Multiple slip in a statistical-mechanics based strain-gradient
S. Yefimov, E. van der Giessen, University of Groningen (The Netherlands)

Role of Microchemistry in Deformation of Aluminum Alloys
H. Weiland, Alcoa Technical Center (USA)

Dislocation avalanches and strain hardening
T. Richeton, J. Weiss, F. Louchet, Laboratoire de Glaciologie et Géophysique de l′Environnement (France)

The continuum representation of dislocation dynamics
M. Zaiser, The University of Edinburgh (UK); A. El-Azab, Pacific Northwest National Laboratory (USA); I. Groma, Eotvos University Budapest (Hungary)

Depinning transition in dislocation assemblies
P. Moretti, , M. Zaiser, University of Edinburgh (UK); M. C. Miguel, Universitat de Barcelona (Spain); S. Zapperi, Università "La Sapienza" (Italy)

Modeling Dislocation Density-Grain Boundary Interactions with a Continuum Field Approach
A. Arsenlis, R. Becker ,V. V. Bulatov, Lawrence Livermore National Laboratory (USA)

The effects of grain size on the strengthening behavior of polycrystals: the dislocation density tensor approach
S. B. Biner, J. R. Morris, Iowa State University (USA)

Massively Parallel Dislocation Dynamics and Crystal Plasticity
W. Cai, V. V. Bulatov, T. Pierce, M. Hiratani, M. Rhee, M. Bartelt, M. Tang, Lawrence Livermore National Laboratory (USA)

Macroscopic behavior and field fluctuations in random viscoplastic polycrystals
R. Lebensohn, Los Alamos National Laboratory (USA); P. Ponte Castañeda, University of Pennsylvania (USA)

Connection of Hierarchical Multiscale Models in Simulating Phase Transformation of Ferroelectric Polymer
S. Zheng, A. M. Cuitiño, Rutgers University (USA); H. Su, W. A. Goddard, III (California Institute of Technology (USA); A. Strachan, Los Alamos National Laboratory (USA)

Mesoscale Simulation of Grain-Boundary Diffusion Creep
R. Ding, D. Wolf, Argonne National Laboratory (USA); D. Moldovan, Louisiana State University (USA); V. Yamakov, National Institute of Aerospace; S. R. Phillpot, University of Florida Gainesville (USA)

A Multi-Scale Modeling Scheme for Size Effects on Cyclic Plasticity
J. Fan, Z. Gao, X. Zeng, Alfred University (USA)

Multi-scale Modelling of Neutron Irradiation Effects at Grain Boundaries in Ferritic Alloys
R. G. Faulkner, Zheng Lu, Loughborough University (UK); R. B. Jones, Baznutec Ltd (UK); A. Crocker, University of Surrey (UK), P.E.J. Flewitt, BNFL Magnox Generation (UK)

Intense slip band formation and crack initiation in fatigued 316L explained by discrete dislocation simulations
C. Depres, M. C. Fivel, GPM2 (France); C.F. Robertson, CEA/Saclay (France)

Multiscale Modeling in Particle-Solidification Front Interactions
J. W. Garvin, Y Yang, H.S. Udaykumar, University of Iowa (USA)

Mechanical behavior of zirconia fully stabilized with high yttria content: An overview
D. Gómez, A. Gallardo, A. Domínguez, Universidad de Sevilla (Spain); L, Kubin, CNRS-ONERA (France)

Modeling by cluster dynamics of the homogeneous precipitation of ordered phases in Al(Zr,Sc) alloys
P. Guyot, L. Lae, Domaine Universitaire (France)

Direct computation of the Hall-Petch coefficient in fcc metals from dislocation-grain boundary simulations
C. H. Henager, Jr., R. J Kurtz, Pacific Northwest National Laboratory (USA); R. G. Hoagland, Los Alamos National Laboratory (USA)

Interaction between grain and specimen size: measurements of strain and orientation gradients in single grains as a function of the applied load
M. Henning, H. Vehoff, University of Saarland (Germany)

Deformation mechanisms in metallic, nanolayered composites
R. G. Hoagland, A. Misra, Los Alamos National Laboratory (USA)

A Creep-demormed lamellar structure
L. K. Hsiung, Lawrence Livermore National Laboratory (USA)

Modelling low temperature brittle fracture of polycrystalline zinc
G. Smith, A. G. Crocker. University of Surrey (UK); G. M. Hughes, P. E. J. Flewitt, University of Bristol (UK)

Simulation of Microstructure Evolution in Technical Materials: Parallel Algorithms for an Irregular Cellular Automaton
K. G. F. Janssens, Sandia National Laboratories (USA)

Dislocation patterning and the deformation of metals
M. Koslowski, Richard LeSar, Robb Thomson, Los Alamos National Laboratory (USA)

On the Role of Grain Boundaries in Plastic Deformation of Metals
R. J. Kurtz, C. H. Henager, Jr., Pacific Northwest National Laboratory (USA); R. G. Hoagland, Los Alamos National Laboratory (USA)

Modeling of microstructure evolution through deformation banding
S. Mahesh, C. N. Tome, Los Alamos National Laboratory (USA)

A diffuse interface model for the transfer coefficients across interfaces
G. Martin, Haut Commissaire à l'Énergie Atomique (France)

Dislocation glide in solid solutions from the atomic scale up
G. Martin, Haut Commissaire à l'Énergie Atomique (France); E. Rodary, L. Proville, CEA-Saclay (France); Y. Rodney, Y. Brechet, University of Grenoble (France)

Mesoscale Modeling of Fracture in Single Crystals and Polycrystals
D. S. Balint, V.S. Deshpande, Cambridge University (UK); J. Gullickson, A. Needleman**,** Brown University (USA); E. Van der Giessen, University of Groningen (The Netherlands)

Statistical treatments of deformation in polycrystals
M. Ortiz, California Institute of Technology (USA)

Evolution of dislocation link-length distributions during static annealing
Y. Tan, M. A. Przystupa, A. J. Ardell, University of California Los Angeles (USA)

Large Scale Simulations of Mesoscale Plasticity and Recrystallization of Aluminum Polycrystals
B. Radhakrishnan, G. B. Sarma, Oak Ridge National Laboratory (USA)

The effect of grain boundary geometry on local deformation behavior
A. D. Rollett, Carnegie Mellon University (USA); B. S. El-Dasher, D. P. Field, Washington State University (USA)

Modeling of Meso-scale Plasticity for Advanced Materials Processing
S. Roy, Y. Liu, H. Lu, R. Komanduri, Oklahoma State University (USA)

Three-Dimensional Atom-Probe Microscopy and the Temporal Evolution of Microstructures
D. N. Seidman, Northwestern University (USA)

Computer simulation at the atomic scale of twin boundary motion in the HCP metals.
A. Serra, Universitat Politecnica de Catalonia (Spain); D.J. Bacon, The University of Liverpool (UK); Yu.N. Osetsky, Oak Ridge National Laboratory (USA)

Dislocation Bypass Mechanism in Cu-Co Alloys: Molecular Dynamics Study
J.-H. Shim, B.D. Wirth, University of California Berkeley (USA)

Stage I-Stage II transition simulated by parallel discrete dislocation dynamics
C. S. Shin, M. C. Fivel, GPM2 (France); M. Verdier, LTPCM (France)

Micromechanics of Damage Evolution in Solid Propellants
F. Xu, P. Sofronis, University of Illinois at Urbana-Champaign (USA); N. Aravas, University of Thessaly (Greece)

On the Micromechanics of Void Growth by Prismatic Dislocation Loop Emission
D. C. Ahn, P. Sofronis, University of Illinois at Urbana-Champaign (USA); R. Minich, Lawrence Livermore National Laboratory (USA)

Symposium 4 Experimental Validation of Multiscale Models

Scale Change in the motion process of interstitial-type dislocation loops in iron with the growth of loops
K. Arakawa, H. Mori, Osaka University (Japan); E. Kuramoto, Kyushu University (USA); K. Ono, Shimane University (Japan)

2-D Mesoscale Analyses and Correlation with Continuum Measurement
S. K. Dwivedi, J. R. Asay, Y. M. Gupta, Washington State University (USA)

Statistical Description of White Beam Microdiffraction by Dislocations
R. Barabash, J. Pang, G. Ice, Oak Ridge National Laboratory (USA)

Heterogeneity of residuals strains in Zircaloy-4 after thermal creep: Link between diffraction and homogenization
N. Letouz, O. Castelnau, R. Brenner, Université Paris (France); J-L. Béchade, M-H. Mathon, CEA/Saclay (France)

Validation of a multiscale approach for modeling particle reinforced metal-matrix composites
P. Kenesei, A. Borbely, Eötvös Lorand University (Hungary); H.Biermann, Technische Universitat (Germany)

Assessment of the constitutive behavior of irradiated metals using non-standard mechanical tests and FEM calculations
E. N. Campitelli, R. Bonadé, C. Hellwig, Nuclear Energy and safety Research Department (Switzerland); P. Spätig, M.Victoria, Association EURATOM-Confederation Suisse (Switzerland)

Shape Change Studies of BCC Single Crystals Using a Non-Contact Image Correlation System
J. N. Florando, D. H. Lassila, M. M. Leblanc, G. Kay, S. A. Perfect, A. Arsenlis, M. Rhee, Lawrence Livermore National Laboratory (USA); E. T. Lilleodden, J. W. Morris Jr., University of California Berkeley (USA)

Mesoscale Studies of Plastic Deformation in Indented Cu Using Submicron-Resolution 3D X-Ray Microscopy
B. C. Larson, Oak Ridge National Laboratory (USA)

Precipitation-induced hardening of thermally aged Fe Cu alloys: a multiscale modelling study and its experimental validation
K. Verheyen, A. Almazouzi, L. Malerba, Belgian Nuclear Energy Research Centre (Belgium); C. Domain, EDF – R&D (France); J. Kuriplach, Charles University (Czech Republic); S. van Petegem, Paul Scherrer Institut (Switzerland)

Effect of Obstacle Size on the Mechanism of Dislocation-SFT Intersection
Y. Matsukawa, S.J. Zinkle, Oak Ridge National Laboratory (USA)

A Suite of Diffraction Experiments for Measuring Deformation Partitioning in Multiphase Alloys
M. Miller, J. Bernier, J-S. Park, Cornell University (USA)

Analysis of Embedded Nano-clusters by Positron Annihilation Spectroscopy
Y. Nagai, Z. Tang, M. Hasegawa, Tohoku University (Japan)

Through Process Modelling of Aluminium Processing for Anisotropic Property Prediction
L. Neumann, R. Kopp, M. Crumbach, M. Goerdeler, G. Gottstein, RWTH Aachen University (Germany)

Late Blooming Phases and Dose Rate Effects in RPV Steels: Integrated Experiments and Models
G. R. Odette, T. Yamamoto, University of California Santa Barbara (USA); B. D. Wirth, University of California Berkeley (USA)

Dislocation – stacking fault tetrahedra interaction: a comparison between in situ experiments and atomic-scale modeling
Y. N. Osetsky, R. E. Stoller, Y. Matsukawa, S.Zinkle, Oak Ridge National Laboratory (USA)

Dislocations, defects, and mechanical properties: combining experiments, simulation and modeling
I. M. Robertson, University of Illinois at Urbana Champaign (USA)

A direct comparison between surface slip marking growth in fatigue and discrete dislocation dynamics simulation results
C. Robertson, C. Déprés, CEA/SRMA Saclay (France); M.C. Fivel, CNRS/INPG (France); M. Verdier, LTPCM (France)

Comparison of Mesoscale Finite Element Deformation Modeling with Measurements using X-ray Microscopy
G. B. Sarma, B. Radhakrishnan, J.W.L. Pang, G.E. Ice, Oak Ridge National Laboratory (USA)

Three-Dimensional Atom-Probe Microscopy and its Application to Plasticity
D. N. Seidman, Northwestern University (USA)

In-situ nanoindentation: a novel technique for understanding nanoscale deformation mechanisms
E. A. Stach, A. M. Minor, Lawrence Berkeley National Laboratory (USA); M. Jin, D. Ge, University of California at Berkeley (USA); J.W. Morris, Jr., Drexel University (USA)

Nano Cu precipitate in pressure vessel steel of nuclear power reactor studied by positron annihilation and 3D atom probe
T. Toyama, Y. Nagai, M. Hasegawa, Tohoku University (Japan); Y. Nishiyama, M. Suzuki, Japan Atomic Energy Research Institute (Japan); T.Ohkubo, K. Hono, National Institute for Materials Science (Japan)

Understanding mechanical coupling via nanomechanical contact
K. J. Van Vliet, S.Y. Lee, J. Li, S. Suresh and S.Yip, Massachusetts Institute of Technology (USA); T. Zhu, Ohio State Univ. (USA)

Symposium 5 Multiscale Modeling of Biomaterials

On multiscale approach to modelling biological patterns
M. Alber, University of Notre Dame (USA)

Substructured Multibody Molecular Dynamics
P. Crozier, Sandia National Laboratories (USA)

Exploring the energy landscape of proteins
Angel E. Garcia, G. Gnanakaran, Hugh Nymeyer, Los Alamos National Laboratory (USA)

Predicting Protein Stability using Network Rigidity at Finite Temperatures
D. J. Jacobs, California State University Northridge (USA)

Mechanics of DNA Packaging in Viruses
W. S. Klug, University of California Los Angeles (USA); M. Ortiz, California Institute of Technology (USA)

An Analytic Model of Bone Remodeling
R. LeSar, A. Redondo, Los Alamos National Laboratory (USA)

Spectrin-level and FEM modeling of the equilibrium shapes of human red blood cell
J. Li, M. Dao, Ohio State University (USA); S. Suresh, Massachusetts Institute of Technology (USA)

Damage Evolution in Natural Hierarchical Structures
P. K. Nukala, S. Simunovic, Oak Ridge National Laboratory (USA)

Coarse-Graining DNA Energy Landscapes
J. Othmer, Niles A. Pierce, California Institute of Technology (USA)

Symposium 6 Mathematical & Computational foundations of Multiscale Modeling

A finite micropolar elastoplasticity model of crystalline metals containing dislocations and disclinations
D. J. Bammann, D. L. McDowell, Sandia National Laboratories (USA); J. D. Clayton, Georgia Institute of Technology (USA)

Multi-Scale Modeling of Fracture of Defective Carbon Nanotubes (CNTs)
T. Belytschko, S. Zhang, Northwestern University (USA)

Multiscale Computation and Systematic Upscaling
A. Brandt, University of California Los Angeles (USA)

Multiscale modeling of epitaxial growth processes: level sets and atomistic models
R. E. Caflisch, University of California Los Angeles (USA)

A Coupled Meso-Macro Scale Formulation for Modeling of Microstructure Evolution and Wrinkling Formation in Polycrystalline Materials
J. S. Chen, S. Mehraeen, University of California Los Angeles (USA)

Multiscale Modeling of Ductile Polycrystalline Metals at High Strain Rate
S. Kuchnicki, A. Cuitiño, Rutgers University (USA); R. Radovitzky, Massachusetts Institute of Technology (USA); L. Stainier, University of Liege (USA); M. Ortiz, California Institute of Technology (USA)

Use of the multiple regression method for more accurate analyzes of TTT processes of the material type 50 CrV 4
Z. Dudás, Budapest Technical University of Engineering and Economy (Hungary)

Thermodynamic Field Estimators for Atomistic-Continuum Hybrid Simulations
J. Eapen, S. Yip, Massachusetts Institute of Technology (USA), J. Li, Ohio State University (USA)

Numerical homogenization of nonlinear partial differential equations and its applictions
Y. Efendiev, Texas A&M University (USA)

Deformation Behavior Analysis in ECAP Using Arbitrary Lagrangian-Eulerian formulation
Jun-Hyun Han, Kwang-Koo Jee, Korea Institute of Science and Technology (Korea); Hyung-Joon Chang, Kyu Hwan Oh, Seoul National University (Korea)

Multiscale Modeling and Computation of Incompressible Flows in Heterogeneous Media
T. Y. Hou, California Institute of Technology (USA)

Combining coarse-grained-particles dynamics and molecular dynamics for multiscale simulation of materials
T. Igarashi, Japan Science and Technology Agency (Japan); Shuji Ogata, Nagoya Institute of Technology (Japan); Hiroshi Iyetomi, Niigata University (Japan)

Micromechanical Evolutionary Elastoplastic Damage Model for FRMMC With Complete Fiber Debonding
J. W. Ju, Y. F. Ko, University of California Los Angeles (USA); H. N. Ruan, Hohai University Nanjing (China)

Complex Lattice Quasicontinuum Theory and Its Application to Ferroelectrics
O. Kowalewsky, J. Knap, M. Ortiz, California Institute of Technology (USA)

About a Plastic Strain of Solid in the Prefractures Zone
N. Kontchakovav, Voronezh State Military Air Engineering University (Russia)

Mechanical model for deformation mechanisms in polycrystals and alloys at disparate length scales
B. Zhu, R. J. Asaro, P. Krysl, University of California San Diego (USA)

Multiscale modeling of the dynamics of solids at finite temperature
X. Li, W. E, Princeton University (USA)

Computational Design and Manufacturing with Multiscale Materials
W. K. Liu, Northwestern University (USA)

A Multi-scale Atomistic-continuum Approach Coupling Molecular Dynamics and Material Point Method
H. Lu, J. Ma, B. Wang, S. Roy, R. Komanduri, Oklahoma State University (USA)

Atomistic and Mesoscopic Simulations of Grain Boundary Migration and Grain Growth in Nanocrystalline Materials
D. Moldovan, Louisiana State University (USA); V. Yamakov, National Institute of Aerospace (USA); A. J. Haslam, Imperial College London (UK); D. Wolf, Argonne National Laboratory (USA); S.R. Phillpot, University of Florida (USA)

VIMES: A Graphical Interface for Multiscale Modeling
R. P. Muller, Sandia National Laboratories (USA)

Automatic and Optimal Force Field Fitting
M. Martin, Sandia National Laboratories (USA)

An Iterative Asymptotic Expansion Multi-scale Method for Elliptic Eigenvalue Problems
S. Mehraeen, J. S. Chen, University of California Los Angeles (USA)

Multiscale Instability Analysis of Corrugated Fiberboard
H. Noguchi, Keio University (Japan); N. Ohno, D. Okumura, Nagoya University (Japan)

An adaptive hybridization of electronic-density-functional-theory and molecular dynamics for multiscale modeling of nanostructured devices on a computation grid
S. Ogata, Nagoya Institute of Technology (Japan); T. Igarashi, Japan Science and Technology Agency (Japan)

A Levelset Method for Modeling Epitaxial Growth
C. Ratsch, University of California Los Angeles (USA)

Calibration of Elastic Composites with Error Control for Computational Meso-Macro-Scale Modeling
H. Johansson, F. Larsson, K. Runesson, Chalmers University of Technology (Sweden)

A seamless coupling of atomistic and continumm fields in the quasicontinuum method
T. Shimokawa, Kanazawa University (Japan); J. Schiøtz, J. J. Mortensen, K. W. Jacobsen, Technical University of Denmark (Denmark)

Parallel TBMD, Hybrid Classical/TB-MD, and their Application to Interfacial Phenomena in Nanostructured Semiconductors
K. Tsuruta, C. Totsuji, H. Totsuji, Okayama University (Japan); S. Ogata, Nagoya Institute of Technology (Japan)

Symposium 7 Multiscale Modeling of Irradiated and Aging Materials

Long-term behaviour of irradiated hcp Zr coupling molecular dynamics and Monte Carlo simulations
C. Arevalo, J. M. Perlado, Universidad Politécnica (Spain); M. J. Caturla, Universidad de Alicante (Spain)

Production of the Primary Damage State Under Irradiation
D. J. Bacon**,** The University of Liverpool (UK); C. Becquart, Universit'e de Lille 1 (France); C. Domain, K. Nordlund, EDF-R&D Department MMC (France); University of Helsinki (Finland); Y. N. Osetsky, R. Stoller, Oak Ridge National Laboratory (USA)

Simulation of point defect, interstitial cluster and copper atom diffusion in Fe-Cu alloys
A. C. Arokiam, A. V. Barashev**,** D. J. Bacon, The University of Liverpool (UK)

Simulation of phosphorus diffusion in α-iron under irradiation conditions
A. V. Barashev, The University of Liverpool (UK)

Object Kinetic Monte Carlo Simulation of radiation damage in ferritic model alloys
C. S. Becquart, , Universit'e de Lille 1 (France); C. Domain, EDF-R&D Department MMC (France); L. Malerba, Belgian Nuclear Energy Research Centre (Belgium)

Modeling Helium effects in irradiated materials
M. J. Caturla, Universidad de Alicante (Spain); M. Victoria, T. Diaz de la Rubia, Lawrence Livermore National Laboratory (USA)

Multi-scale modeling of the evolution of defect populations in electron-irradiated α-Fe
J. Dalla Torre, C. C. Fu, F. Willaime, J.-L. Bocquet, A. Barbu, CEA/Saclay (France)

A fast quantum-mechanical model for molecular dynamics simulations of transition metals
S. L. Dudarev, Culham Science Centre (UK)

The Interaction of He with Self Interstitial Atoms and Small Vacancy Clusters in α-Fe Studied by Long-Time Dynamics
F. Gao, H. L. Heinisch, R. J. Kurtz, Pacific Northwest National Laboratory (USA)

Investigations of Cavity Evolution in BCC Iron under Neutron and α-Particle Irradiation
S. I. Golubov, R.E. Stoller, Oak Ridge National Laboratory, (USA); B. N. Singh, M. Eldrup, Risø National Laboratory (Denmark); A.M. Ovcharenko, The Hong Kong Polytechnic University (Honk Kong)

The Interaction Of Helium Atoms With Edge Dislocations In α-Iron
H. L. Heinisch, F. Gao,R. J Kurtz, Pacific Northwest National Laboratory (USA)

KMC Studies of the Reaction Kinetics of Defects that Diffuse One-dimensionally with Occasional Transverse Migration
H. L. Heinisch, Pacific Northwest National Laboratory (USA); B. N. Singh, Risø National Laboratory (Denmark); H. Trinkaus, Institute für Festkörperforshung (Germany)

Strain Rate Effects on Dislocation Evolution in Irradiated FCC metals

M. Hiratani, V. Bulatov, Lawrence Livermore National Laboratory (USA)

RPV-1 : a Virtual Test Reactor to simulate irradiation effects in light water reactor pressure vessel steels
J. C. Van Duysen, S. Jumel, Electricité de France (France)

Molecular dynamics simulation of unfaulting and pinning mechanisms of dislocation loops in FCC metals
H. Kaburaki, T. Kadoyoshi, F. Shimizu, Japan Atomic Energy Research Institute (Japan); H. Kimizuka, The Japan Research Institute (Japan); S. Jitsukawa, Japan Atomic Energy Research Institute (Japan); J. Li Ohio State University (USA)

Atomistic simulation of multiple-dislocation emission from the crack tip in the dynamical fracture of fcc metals
H. Kimizuka, The Japan Research Institute (Japan); H. Kaburaki, T. Kadoyoshi, F. Shimizu, Japan Atomic Energy Research Institute (Japan); J. Li, Ohio State University (USA); S. Yip, Massachusetts Institute of Technology (USA)

Basic Aspects of Bias Mechanism under Irradiation in Fe
E. Kuramoto, K. Ohsawa, J. Imai, K. Obata, T. Tsutsumi, Kyushu University (Japan)

Dislocation - radiation obstacle interactions in Cu, Fe and Mo
H-J. Lee, B. D. Wirth, University of California, Berkeley California (USA); J-H. Shim Korea Institute of Science and Technology (Korea); J. Marian, California Institute of Technology (USA)

Transformation strain by chemical disordering in silicon carbide
J. Li, Ohio State University (USA)

On the binding energies and configurations of vacancy and copper-vacancy clusters in bcc iron: a computational study
D. Kulikov, M. Hou, Universite Libre de Bruxelles (Belgium); L. Malerba, Belgian Nuclear Energy Research Center (Belgium)

DUPAIR: a line tension model for a first assessment and interpretation of radiation-induced hardening experiments
C. Domain, G. Monnet, S. Jumel, J. C. van Duysen, Electricit'e deFrance (France); L. Malerba, K. Verheyen, Belgian Nuclear Energy Research Centre (USA)

Defect accumulation and diffusion in Fe and Fe-Cu Alloys using Kinetic Monte Carlo
E. Martinez, J. M. Perlado, Universidad Politécnica (Spain); M.J. Caturla, M. Hernández, Universidad Alicante (Spain); D. Gómez Briceño, CIEMAT (Spain)

Atomistic modeling of helium bubble formation in Fe during irradiation
K. Morishita, R. Sugano, Kyoto University (Japan)

Molecular dynamics simulations of defect production during irradiation in silica glass
F. Mota, J. M. Perlado, E. Dominguez, Universidad Politécnica (Spain); M.-J. Caturla, A. Kubota, Universidad Alicante (Spain);

Bridging electronic and atomistic levels of modelling for non-magnetic and magnetic bcc transition metal-based fusion materials
D. Nguyen-Manh, S.L. Dudarev, Culham Science Centre (UK); D.G. Pettifor, University of Oxford (UK); V. Vitek, University of Pennsylvania (USA)

Edge dislocation – copper precipitate interaction process in BCC iron
A. Nomoto, N. Soneda, Central Research Institute of Electric Power Industry (Japan); A. Takahashi, Tokyo University of Science (Japan); S. Ishino, Tokai University (Japan)

Multiscale Modeling of Helium Transport and Fate in Irradiated Nanostructured Ferritic Alloys
N G. R. Odette, T. Yamamoto, University of California Santa Barbara (USA); B. D. Wirth, University of California

Berkeley (USA); R. J. Kurtz, Pacific Northwest National Laboratory (USA)

Activation energy for a one-dimensional slip motion of a dislocation loop
K. Ohsawa, E. Kuramoto, Kyushu University (Japan)

Atomic-scale modeling of dislocation dynamics in radiation defect environments
D. Rodney, GPM2-INPG (France); B. D. Wirth, University of California Berkeley (USA); Yu. N. Osetsky, Oak Ridge National Laboratory (USA)

From point defects to diffusion and ionic conductivity in quartz and silica
G. Roma, Y. Limoge, CEA-Saclay (France)

The role of grain size and grain boundary structure in the primary damage state of irradiated nanocrystalline metals
M. Samaras, P. M. Derlet, H. Van Swygenhoven, Paul Scherrer Institute (Switzerland); M. Victoria, Ecole Polytechnique (Switzerland)

Deduction of He-Fe interaction potential from first-principle calculations
T. Seletskaia, Yu. Osetsky, R. E. Stoller, G. M. Stocks, Oak Ridge National Laboratory (USA)

Vacancy-related changes on the structure and mobility of interstitial clusters in cubic metals
M.A Puigvi, A. Serra, Universitat Politecnica de Catalunya (Spain); Yu. N. Osetsky, Oak Ridge National Laboratory (USA)

Modeling of temperature effect on the formation of matrix damage in bcc-Fe: combined MD and KMC study
N. Soneda, K. Dohi, S. Ishino, Central Research Institute of Electric Power Industry (Japan); A. Takahashi, Tokyo University of Science

Diffusion of SIA clusters in bcc iron alloys: a molecular dynamics study of the influence of chromium atoms
D. Terentyev, L. Malerba, SCK•CEN(Belgium) Y. Osetskiy, Oak Ridge National Laboratory (USA), A. Barashev The University of Liverpool (USA)

Impact of Impurities on the Diffusion Reaction Kinetics of SIA Clusters in Metals under Cascade Damage Conditions
H. Trinkaus, Forschungszentrum Jülich (Germany); B.N. Singh, Risø National Laboratory (Denmark); S. I. Golubov, Oak Ridge National Laboratory (USA)

Ab-initio study of the stability and mobility of self-interstitials and small interstitial clusters in α-Fe
F. Willaime, C.-C. Fu, CEA/Saclay (France)

Radiation Defect Properties and Interactions
B. D. Wirth, University of California Berkeley (USA); R. J. Kurtz, Pacific Northwest National Laboratory (USA); Y. N. Osetsky, Oak Ridge National Laboratory (USA); A. Serra, University Politechnia de Catalunya (Spain); N. Soneda, Central Research Institute of Electric Power Industry (Japan)

Interaction of Helium Impurities with Self-Interstitial Atom Clusters in Ferritic Alloys
L. Ventelon, B. D. Wirth, University of California Berkeley (USA);

Symposium 8 Thin Film Processing

Multiscale Transport and Thin Film Microstructure Development
M. O. Bloomfield, H. Huang, T. S. Cale, Rensselaer Polytechnic Institute (USA)

Atomistic modeling of pulsed laser deposition: effects of energetic particles on film morphologies
G. Gilmer, B. Sadigh, L. Zepeda-Ruiz, Lawrence Livermore National Laboratory (USA); J. Dalla Torre CEA

Saclay (France)

Structural and mechanical properties of amorphous silicon surfaces: A combination study of ab-initio and classical molecular dynamics
S. Hara, T. Kumagai, S. Izumi, S. Sakai, University of Tokyo (Japan)

Mechanics of Nanoplates and Nanowires
H. Huang, L. G. Zhou, H. W. Shima, T. S. Cale, Rensselaer Polytechnic Institute (USA)

Modeling, Scaling, and Microstructure Evolution in Magnetron Sputter Deposition
M. Johnson, P. Cote, M. Hussain, Benet Laboratories (USA)

Bulk and Surface Vibrational Instabilities in Thin Films
J. Li, Ohio State University (USA); S. V. Dmitriev, The University of Tokyo (Japan); T. Zhu, S. Yip, Massachusetts Institute of Technology (USA)

Multiple Scale Methods for Solid Mechanics
H. S. Park, E. G. Karpov. W. K. Liu, Northwestern University (USA); P. A. Klein, Sandia National Laboratories (USA)

A uniform methodology for the implementation of large-scale scientific simulations based on psi-calculus
J. E. Raynolds, L. R. Mullin, State University of New York (USA)

'Non-vacancy' self-diffusion in two-dimensional metals
G. Poletaev, M. Starostenkov, J. Patzeva, Altai State Technical University (Russian)

Relaxation of two-dimensional Al and Ni_3Al crystal structures at the impulsive heating
M. Starostenkov, G. Poletaev, M. Aksyonov, Altai State Technical University (Russian); I. Dyomina, East-Kazakhstan State University (Kazakhstan)

The research of the combustion synthesis process in two-dimensional crystals of Ni-Al system
M. Starostenkov, G. Poletaev, Altai State Technical University (Russian); G. Popova, East-Kazakhstan State University (Kazakhstan)

Simulation of the disordering process in a two-dimensional Cu_3Au crystal at impulsive thermoactivation
M. Starostenkov, Altai State Technical University (Russian); M. Skakov, I. Dyomina, East-Kazakhstan State University (Kazakhstan)

The thermoactivated stability of thin films of Ni_3Al-Al composites
M. Starostenkov, Altai State Technical University (Russian); M. Skakov, I. Dyomina, East-Kazakhstan State University (Kazakhstan)

Deformation Instabilities in Heteroepitaxial Growth
D. Walgraef, Universite Libre de Bruxelles (Belgium)

True upward adatom diffusion in island formation on fcc metal (110) surface
E. G. Wang, Chinese Academy of Sciences (China)

Multiscale Simulation of Static and Dynamic Grain Growth in Polycrystalline Thin Films
A. J. Haslam, Imperial College London (UK); V. Yamakov, National Institute of Aerospace (USA); D. Moldovan, Louisiana State University (USA); R. Ding, D. Wolf, Argonne National Laboratory (USA); S.R. Phillpot, University of Florida (USA)

Phase transition in thin films
C.H. Woo, B. Wang, Z. Man, Hong Kong Polytechnic University (Hong Kong); H. Huang, Rensselaer Polytechnic Institute (USA)

Contrasting growth modes of Mn on Ge(100) and Ge(111) surfaces: Subsurfactant action versus

intermixing

Z. Zhang, Oak Ridge National Laboratory (USA) & University of Tennessee (USA)

Conference Committee

Organizing Committee

Dr. Bulatov, Vasily	UCLA Los Angeles, CA
Prof. Caflisch, Russel	UCLA Los Angeles, CA
Prof. Chen, Jiun-Shyan	UCLA Los Angeles, CA
Dr. El-Azab, Anter	PNNL Richland, WA
Prof. Ghoniem, Nasr (Chair)	UCLA Los Angeles, CA
Dr. Henager, Charles H	PNL Richland, WA
Prof. Huang, Hanchen	RPI Troy, NY
Prof. Kioussis, Nick	CSUN Northridge, CA
Prof. Klug, William	UCLA Los Angeles, CA
Dr. Noronha, Silvester	UCLA Los Angeles, CA
Dr. Sharafat, Shahram	UCLA Los Angeles, CA
Prof. Sun, Lizhi	UIOWA Iowa City, IA
Prof. Wirth, Brian	UCB Berkeley, CA

International Advisory Committee

Prof. Bacon, David	Liverpool, UK
Dr. Baskes, Michael	LANL, USA
Prof. Busso, Esteban	Imperial, London, UK
Prof. Cale, Timothy S.	RPI, New York, USA
Dr. Diaz de la Rubia, Tomas	LLNL,USA
Prof. Ghoniem, Nasr (Chair)	UCLA, USA
Prof. Gumsch, Peter	Universitat Karlsruhe, Germany
Prof. Guo, Xiao	Queens, London,UK
Dr. Hartley, Craig	AFOSR/NAUSA
Prof. Iwata, Shuichi	University of Tokyo, Japan
Prof. Kratochvil, Jan	CTU, Prague, Czech Republic
Dr. Kubin, Ladislas	ONERA-LEM, France
Dr. LeSar, Richard	LANL, USA
Prof. Meguid, Shaker	Toronto, Canada
Prof. Needleman, Alan	Brown, USA
Prof. Odette, Robert	UCSB, USA
Prof. Ortiz, Michael	Caltech, USA
Prof. Pettifor, David	Oxford, UK
Prof. Phillips, Robert	Caltech, USA
Prof. Raabe, Dierk	Max-Planck Institut, Dusseldorf, Germany
Prof. Shibutani, Yoji	Osaka University, Japan
Prof. Shibutani, Yoji	Osaka University, Japan
Dr. Soneda, Naoki	Komae Research Laboratory, Japan
Prof. Srolovitz, David	Princeton,USA
Prof. Suresh, Subra	MIT, USA

Prof. Tomita, Yoshihiro	Kobe University, Japan
Prof. Van der Giessen, Erik	University of Groningen, The Netherlands
Prof. Walgraef, Daniel	Free University, Brussels,Belgium
Dr. Wolf, Dieter	ANL, USA
Prof. Yip, Sidney	MIT, USA
Dr. Zinkle, Steve	ORNL, USA

Introduction

Following several successful symposia on the multiscale modeling theme in prior years, the Organizing Committee (now expanded into the International Steering Committee) feels that a dedicated international conference on "Multiscale Materials Modeling" will provide a timely forum for the discussion of common materials and modeling issues. This conference brings together scientists, technologists and industrialists across various disciplines, including Materials, Chemistry, Physics, Applied Mathematics, Computer Science, Biology and Medicine. The event ensures that: 1) a concerted effort is gathered to push forward the multiscale modeling activity; 2) knowledge and expertise are shared across disciplines; 3) rapid progress in computing power is timely exploited; and 4) new materials (e.g. nanostructures) and processes are thoroughly characterized and rapidly brought to industry, for the benefit of the public.

The survival and success of the future industry rely much on engineered materials and products with improved performance available in a timely manner and at relatively low-costs. This demands not only the rapid development of new and improved processing techniques, but also better understanding and control of materials, chemistry, processing, structure, property, performance, durability, and more importantly, their relationships. This scenario usually involves multiple length (space) & time scales and multiple processing & performance stages, which are sometimes only accessible via. multi-scale / stage modeling or simulation. The main theme of the conference is to provide an international forum for the advances of multiscale modeling methodologies and for their applications in rapid process and material (product) developments. It is hoped that this conference will stimulate further interactions between the engineering and scientific communities, resulting in new development of more innovative and sophisticated physically-based approaches for design and performance prediction of materials.

I am thankful to the program committee members, session chairs and authors, as well as to the current members of the ‘Nano and Micro Mechanics Laboratory’, UCLA, for putting together an excellent conference.

Nasr Ghoniem

Plenary Talks

Coupling Quantum and Continuum Mechanics to Obtain Predictive Models of the Macroscopic Behavior of Materials

Emily A. Carter

Princeton University
Department of Mechanical and Aerospace Engineering
and
Program in Applied and Computational Mathematics
D404A Engineering Quadrangle
Princeton, NJ 08544
eac@princeton.edu

ABSTRACT

First principles quantum mechanics in various forms is used to enhance the predictive capability of engineering models of the mechanical response of materials. We will describe both algorithmic developments and applications of coupling first principles density functional theory to continuum models of deformation, microstructure formation, and fracture of metals. These algorithms are of two kinds: (1) on-the-fly coupling with feedback, in the case of a linear scaling density functional theory for metals and (2) informed continuum approaches, where the quantum mechanical information is generated ahead of time and used to increase the predictive reliability of more complex processes, such as formation of microstructure due to shock and stress-corrosion cracking.

1. Introduction

Engineering models of materials response historically have utilized macroscopic, continuum level properties as input. More recently, with advent of multiscale modeling, inputs from finer length scales have become more common. For example, information from the atomic level, via analytic potential energy functions that describe interactions between atoms, has become available to incorporate into higher length scale models. These analytic potentials are either fit to experimental data—so-called empirical potentials—or to, e.g, first principles quantum mechanical data. For many phenomena, these analytic potentials have proven to be robust and informative. However, in the case of complex materials and, e.g., chemical reactions, it is often the case that such analytic potentials are insufficiently accurate and thus do not provide *predictive* capability to the higher length scale engineering models. In such cases, one may turn to first principles quantum mechanical (QM) models for higher accuracy. Such QM models are characterized by a minimal number of well-controlled approximations to solving the Schroedinger equation. This talk is concerned with developing and applying multiscale models that are founded upon information gathered from quantum mechanics, in order to increase the fidelity and predictive quality of engineering models of materials response.

2. Procedure

As mentioned in the abstract, we have been developing two different approaches of coupling quantum mechanics to continuum mechanics: an on-the-fly approach with feedback between scales (orbital-free density functional theory local quasicontinuum method, OFDFT-LQC) and an informed continuum strategy, where the quantum mechanical information is generated in advance and made available to the continuum level model. The latter strategy is necessary in cases where the OFDFT method is not accurate enough for the material or chemistry of interest. Since the former approach, OFDFT-LQC, will be presented in a contributed talk by R. L. Hayes on Thursday, October 14, I will focus here on the second approach of informed continuum modeling. Here we generate needed information from Kohn-Sham density functional theory (such as equations of state and elastic constants), as well as using Kohn-Sham theory to explore phenomena, leading, e.g., to a new universal form for atomistically-derived cohesive laws [1] used to describe fracture. This talk will be concerned with two phenomena: (i) shock-induced formation of microstructure in iron [2] and, if time permits (ii) stress-corrosion cracking of steel [3, 4]. The latter will be presented also in a poster by S. Serebrinsky on Tuesday, October 12; hence, the focus here will be on the first application.

3. Numerical Methods

We use Kohn-Sham (KS) density functional theory, with accurate non-local ultrasoft pseudopotentials to represent the valence electrons' interactions with the core electrons and nuclei and the generalized gradient approximation for electron exchange and correlation within the VASP code [5]. The numerical parameters concerning the plane wave basis set expansion (kinetic energy cutoff for the plane waves) and Brillouin zone sampling (k-point grid) were fully numerically converged for the properties of interest. For example, a 24x24x24 k-point mesh was required to obtain the desired accuracy for the elastic constants of Fe. The multiscale model of pressure-induced microstructure in Fe involves a multi-well energy function incorporating the response of both bcc and hcp Fe. A sequential lamination algorithm developed by Aubry et al. [6] was employed to describe the pressure-induced microstructure.

A coupled stress-assisted diffusion-static mechanics approach was employed for the stress-corrosion cracking of Fe. KS DFT was used to define a hydrogen embrittlement function [3] used in a cohesive zone model of fracture [1]. The Langmuir-McLean isotherm was used to relate bulk hydrogen concentration to hydrogen coverage at the crack surfaces. Continuum J-2 flow theory of plasticity and a conventional power law hardening model were also employed.

4. Results

We will show that our multiscale model of pressure-induced microstructure provides new insight into the scatter in measured transition pressures and the observed pressure

hysteresis in the bcc-hcp phase transition. In particular, we find that: (i) shear is required for the transition to occur; (ii) differing amounts of shear are likely responsible for the scatter in measured transition pressures, and (iii) formation of kinematically compatible and equilibrated mixed phases explains the presence of a hysteresis loop [2].

If time permits, we will show that our stress-corrosion cracking model of steel, using the QM-based cohesive laws, is able to reproduce essential features (intermittent cracking, crack propagation velocities, critical stress intensity factors, etc.) of stress-corrosion cracking as a function of variables such as applied stress, yield strength of the steel, etc. At the same time, some new insight is gleaned into the crack propagation dynamics. Our results suggest that hydrogen-induced decohesion is a likely cause of corrosion-induced cracking in Fe but not in Al.

Acknowledgments

This work was done in collaboration with K. J. Caspersen, A. Lew, M. Ortiz, M. Fago, R. L. Hayes, D. E. Jiang, and S. Serebrinsky. The work was supported by the DoD-MURI and DOE-ASCI programs.

References

1. R. L. Hayes, M. Ortiz, and E. A. Carter, "Universal binding-energy relation for crystals that accounts for surface relaxation," *Phys. Rev. B*, **69**, 172104 (2004).
2. K. Caspersen, A. Lew, M. Ortiz, E. A. Carter, "Importance of Shear in the bcc-to-hcp Transformation in Iron," *Phys. Rev. Lett.,* in press (2004).
3. D.E. Jiang and E.A. Carter, "First Principles Assessment of Ideal Fracture Energies of Materials with Mobile Impurities: Implications for Hydrogen Embrittlement of Metals," *Acta Materialia*, **52**, 4801 (2004).
4. S. Serebrinsky, E. A. Carter, and M. Ortiz, "A multiscale quantitative model of hydrogen embrittlement," *J. Mech. Phys. Sol.*, in press (2004).
5. G.Kresse, J.Furthmüller, *VASP the Guide*. <http://cms.mip.univie.ac.at/VASP/>.
6. S. Aubry, M. Fago, and M. Ortiz, *Comput. Methods Appl. Mech. Eng*. **192**, 2823 (2003).

Multi-Scale and Material-by-Design

Jim C. I. Chang
Director, U.S. Army Research Office, PO Box 12211, Research Triangle Park, NC 27709-2211

The multi-scale treatment of natural and physical phenomenon has been carried out for decades without being labeled as "multi-scale." For example, the name mesomechanics was coined about fifteen years ago for the purpose of describing a "smooth transition" from micro- to macro-mechanics scale.

Recently, the fundamental discoveries in the different "scale" disciplines, i.e., chemistry, physics, materials, mechanics, structures and systems have enabled us to take "multi-scale" to the next level – better understanding the fundamental relationships among different scales and designing physical systems from the ground up. Additionally, there are two major advancements that are causing major changes in the science and technology landscape, and they are Nanotechnology and Biotechnology. It is my opinion that the so-called "Multi-Scale" must take on a new meaning. Many conventional framework which existed in the mechanics community are no longer valid and must be reexamined in this context. Put differently, it is up to the mechanics community to face-up to this challenge or become scientifically irrelevant.

Mechanics is a discipline where "continuity" has been a built-in assumption. The word "continuity" referred to here is a mathematical sense where the field equations and their associated conditions are satisfied by a set of mathematics describable "continuity". When the discontinuities associated with the scale differential, phase, property or geometrical boundaries can no longer be represented by a set of rigorous mathematical formulations, all mechanics principles cease to be valid.

Traditionally, the mechanics community has been treating the three different difficulty issues associated with the non-biological and non-nano-scale systems in a semi-pseudo way with some success fully knowing fundamental mechanics principles have been violated and butchered. These three issues are scale, heterogeneity and physics of failure. Specifically, mechanics principles that are derived for a "continuity" domain are extrapolated to the "non-continue" regime for the purpose of material and systems design. The reason for the limited success is because these explorations are constrained within a set of principles, such as energy, and they are done very carefully to assure that they are not too far off from the conditions where the continuity conditions govern. However, when treating these systems where deviations from the "continuity" conditions become "large", the "conventional" mechanics formulations break down. Composite materials failure and failure under severe environment, i.e. thermal or pressure, are typical examples. When the scale gets to the nanometer level or to the introduction of the biological materials/systems, the deficiencies get worse.

The holy grail of the multi-scale material/structural research is to achieve the so-called "material-by-design." Historically, it has been accomplished in a very limited sense, i.e. "best" materials are produced independently and the users pick from what is suitable and available. Over a decade's research in mechanics has helped us to gain more insight into "multi-scale", but we are still short of a set of consistent physics principles for describing the key fundamental issues – heterogeneity and scale effects.

Molecular Dynamics simulations, Monte Carlo Simulations and other type of simulation methods have been used by the chemists and physicists to address behavior at atomic and molecular scales with some success. In this case, the challenge is to bridge these simulation methods with the conventional mechanics descriptions and to assure that the "continuity" in and across different scales are consistent with the inherent properties of the systems components being investigated. Limited progress has been made, such as modeling and simulation of TiAl materials. However, it is still far short of the ultimate goal of "material-by-design". In this case, the conventional mechanics based on the "continuity" assumptions must be reexamined to assure their rigor. The goal of this undertaking is either for designing the materials/systems without a through fundamental understanding, or for opening the mechanics research frontier one more time for the development of a set of rigorous and consistent theory.

With the advancement in computing power, and the insurgence of nanotechnology and its associated experimental capabilities, it is an opportune time for a team of materials scientists and mechanicians to tackle the "material-by-design" challenge in spite of the mechanics limitations. However, one must understand the inherent mechanics limitations to do the job right. Additionally, it is essential that material-by-design is a collaborative effort among the theory, the experiment and modeling.

Biommetics, bio-inspired, bio-self assembly and hybrid man-made and biological systems are the cornerstones of pursuing biotechnology. Unfortunately, in this case, the existing mechanics fundamentals are found grossly inadequacy. On the one side, the "continuity" and "scale" between the man-made and the biological materials is definitely an issue. On the other side, the effects of biological systems from the mechanical means, force and deformation, are totally unknown. For example, limited studies have revealed that a biological system's conformational changes, binding, transport and kinetics are directly controlled by the biological factors as well as by the force and deformation experienced by this biological system. In this case, in order to achieve the "material-by-design", one must have detailed combined knowledge of biology, biochemistry and mechanics, and their nonlinear relationship to one another.

Much of the effort of this workshop is devoted to the computational aspect of the issue; therefore, this paper will concentrate on the collaborative effort, and on the integrated aspect of "materials-by-design". This paper is to address the issues inherent in multi-scale fundamentals – scale effect and heterogeneity where work is needed with the

coming of the nanotech and biotech age. This talk will also look into the opportunities and challenges facing the mechanics community in the context of nanotechnology and biotechnology development.

Structural Alloy Performance Prediction for Accelerated Use: Evolving Computational Materials Science & Multiscale Modeling

Dennis M. Dimiduk, T.A. Parthasarathy,* S.I. Rao,* Y-S. Choi,* M. Uchic, C. Woodward, and J.P Simmons

Air Force Research Laboratory, Materials and Manufacturing Directorate,
AFRL/MLLM, Wright-Patterson AFB, OH 45434
*UES, Inc., 4401 Dayton-Xenia Road, Dayton, OH 45432-1894

ABSTRACT

A simulation and testing architecture was developed through the DARPA Accelerated Insertion of Materials initiative. The architecture defines a framework for efficiently using both models and experiments to rapidly gain information that directly feeds the design and certification process for engineered systems. As a whole the new methodology will reduce the number of iterative large-scale cycles required to qualify a material's suitability for structural service, and provide an outlet for multiscale materials modeling.

1. Introduction

As recently as 1999, computational materials science was referred to as "…the era of applied quantum mechanics" [1]. However, a different view is needed for structural materials engineering. Realistically, predicting the engineering performance of materials through simulation may be described as a wild frontier of multiscale materials modeling (MMM); the field is disjointed. No quantum mechanical methods exist for multicomponent compositions, but structural alloys typically contain 10 elements or more by design. Atomistic methods have a fidelity limited by the quality of interatomic potentials. For many metals central-force potentials are inadequate, while more advanced methods have been slow to evolve. Discrete dislocation simulations (DDS) show emergent successes, but boundary conditions and selected length- and time-scaling issues are challenges. The links to continuum plasticity methods are tenuous at best; that being of little surprise since the local-continuum approximation breaks down at length scales greater than those treated in DDS. Generally, codes for continuum materials simulations are a patchwork of research efforts, having no standards or bench marks, few robust validation efforts and little or no linkage to engineering design. Similar concerns exist with the tractable time scales for kinetics and dynamics simulations for both structure evolution and mechanics [2]. On the whole, MMM may be described as a cottage industry dominated by academic research rather than a framework for value-added engineering.

Against the introductory backdrop it is reasonable to ask, "Why bother with MMM? An obvious answer is that one may infer that computational materials science will inevitably mature to the levels of computational structural mechanics and fluid dynamics that are backbones of design and selected materials-process modeling. However, in order for

MMM to be useful in the engineering context it has to evolve in a way which is readily accessible to the greater engineering community and prepares a framework for engineering use. Such a framework must proceed from the needs of the design engineer in making the decision to use a material in structural service, and that framework is inverted from the common "materials-by-design" or "first principles" approaches in MMM.

2. The AIM Methodology and New Paradigm

A few years ago, the US Defense Advanced Research Projects Agency (DARPA) sought to establish a method for materials and processes (M&P) development that focused on *reducing the time* required for first use of materials. The initiative, entitled "Accelerated Insertion of Materials" (AIM), sought to build and implement an integrated parallel methodology for materials engineering that takes full advantage of emerging MMM within the constraints of systems engineering [3,4]. A premise of the initiative was that design teams make decisions to use materials from the existence of a "designer knowledge base" (DKB). For a given material the DKB evolves principally heuristically today and includes information on design rules, cost models, supplier constraints and readiness, together with traditional M&P information regarding performance and properties. The AIM method is a paradigm for M&P that includes the full scope of materials readiness within and engineering optimization framework (see Fig. 1), but also recognizes the evolving fidelity of M&P knowledge that emerges with experience. The new paradigm is needed because the existing sequential paradigm demands an expensive and risky commitment to use a material before application-specific qualification data are available. The method recognizes that emerging MMM, employed in conjunction with focused validation experiments, should mitigate engineering risk early in development. With the AIM framework there is a realistic chance of objectively certifying materials in a portable fashion rather than having them certified only within the context of applications, as is done currently. The challenge remains to put MMM tools into the AIM engineering framework. Within the AIM method, MMM should be viewed as discrete capability packages, with integral experimental validation methods. These should be built hierarchically, starting from linked analytical models before absolute fidelity and accuracy of physics is imposed as a constraint. After all, today's engineering practice achieves much with incomplete numerical physics. In this sense, one should recognize that while being a natural framework for MMM products, the

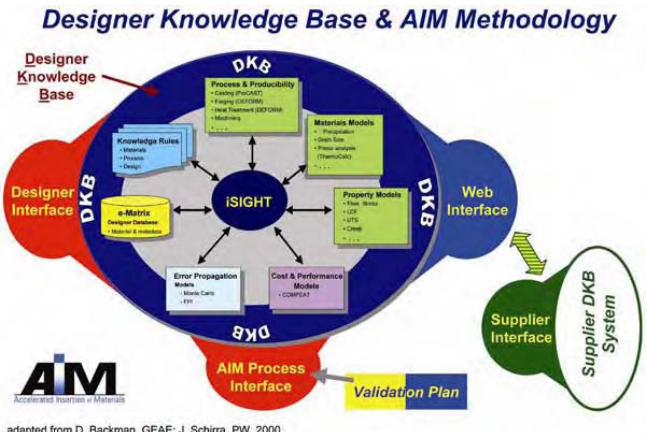

Fig. 1 Schematic of Designer Knowledge Base.

AIM methodology is attainable, with or without advanced MMM. Thus, the open questions are over the quantity and types of data needed for product engineering, and how much faster the necessary engineering information can be developed with MMM.

3. Emerging Capabilities and Longer-Range Challenges

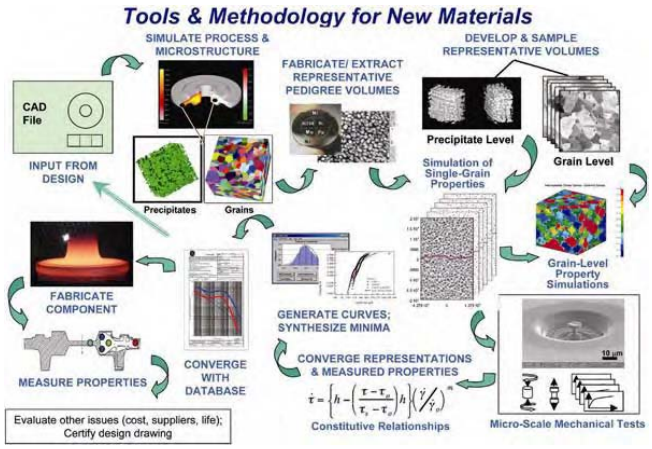

Fig. 2 Schematic of Integrated Models and Experiments.

There are emerging new experimental tools for high fidelity, multiscale 3D characterization of structure, and micromechanical measurements. One goal of the AIM method is to integrate those tools with simulations and error management techniques so that there is a convergence between the representative volumes for simulation and those for experiment. The schematic shown in Fig. 2 illustrates that integration for rapid materials development. Clearly these efforts demand growth in methods for quantitative kinetics, accurate constitutive descriptions at the micron scale, and alternate materials representation schemes that treat the necessary complexity and variability of real materials.

4. Acknowledgements

The authors acknowledge Dr. Dan Backman, and Mr. Jack Schirra for discussions, building the AIM method, and Fig. 1. Also acknowledged are Drs. S. Wax, L. Christodoulou, C. Hartley, L. Schwartz, H. Fraser, and R. Dutton who have made this effort possible.

5. References

1. J. Bernholc, Physics Today, **52**, 30 (1999).
2. N. M. Ghoniem, *et al*., Philosophical Magazine A, **83**, 3475 (2003).
3. D. M. Dimiduk, P. L. Martin, and R. Dutton, in *Gamma Titanium Alumindes 2003*, edited by Y-W. Kim, H. Clemens, and A.H. Rosenberger (TMS, Warrendale, PA 2003), p. 15.
4. D. M. Dimiduk, T. A. Parathasarathy, S. I. Rao, Y-S. Choi, and M. D. Uchic, in *Materials Processing and Design: Modeling, Simulation, and Applications, NUMIFORM 2004*, edited by S. Ghosh, J. M. Castro, and J. K. Lee (AIP CP712, American Institute of Physics, Springer-Verlag, New York, 2004), p. 1705.

Estimation and Control of Modeling Error in Computational Material Science

J. Tinsley Oden

Institute for Computational Engineering and Sciences
The University of Texas at Austin
201 East 24th Street, ACES 4.102
1 University Station C0200
Austin, Texas 78712
oden@ices.utexas.edu

ABSTRACT

The analysis of material bodies made up of heterogeneous materials, including the affects of phenomena at macro-, micro-, and smaller scales, is known to be a computational problem of enormous size and complexity. The present exposition develops a theoretical and computational framework for assessing error due to modeling at various scales. The key features of this approach are the calculation of *a posteriori* estimates of errors in quantities of interest and the adaptation of the model to meet specified tolerances on errors.

1. Introduction

We address a fundamental question in computational science at the heart of multiscale modeling of materials: *how can one systematically select appropriate mathematical models of physical events that occur at many spatial and temporal scales, so as to deliver accurate information on specific quantities of interest?*

In addressing this question, an issue of equal importance is also considered; namely, the development of an unambiguous, mathematically rigorous approach for constructing models in which various theories applicable to events at certain scales are appropriately woven together to produce a heterogeneous model capable of delivering results at a preset level of accuracy . We believe the answers to these questions lie in developing techniques for estimating and adaptively controlling modeling error.

2. Error Estimation and Adaptive Modeling

We begin by defining a *primal base model* of a class of physical events which may be completely intractable due to its size or complexity, but which will serve as a datum with respect to which other models are to be compared. In an abstract setting, the base problem may be of the form

$$\text{Find } \boldsymbol{u} \in \boldsymbol{V} \quad \text{such that} \quad \boldsymbol{B}(\boldsymbol{u};\boldsymbol{v}) = \boldsymbol{F}(\boldsymbol{v}) \qquad \forall\ \boldsymbol{v} \in \boldsymbol{V} \tag{1}$$

where V is an appropriate function space (a TVS), $B(\bullet; \bullet)$ is a semilinear form, nonlinear in u and linear in v, and F is continuous linear functional on V. We are only mildly interested in u; rather, our major goal is to compute values of a functional $Q(u)$, where Q: $V \rightarrow \Re$, the so-called *quantity of interest* (QoI). Finding $Q(u)$ subject to Eqn. (1) is an optimal control problem considered in [1].

Instead of attempting to solve Eqn. (1), we develop a sequence of *surrogate problems* which are tractable using available computational resources (i.e. we seek $u_0 \in V_0$ such that $B_0(u_0; v) = F(v) \quad \forall \ v \in V_0$), The modeling error in the QoI's can be shown to be

$$Q(u) - Q(u_0) = R(u_0, p) + r \tag{2}$$

where $R(u_0, p) = F(v) - B_0(u_0; v)$ is the residual functional, p is the solution to the dual problem for Q, and r is a term of higher order in the error components. Algorithms for estimating $R(u_0, p)$ and an appropriate sequence of surrogate models to reduce the error are referred to as goal-oriented methods, and are discussed in [1], [2], and [3].

3. Applications

Among applications of goal-oriented methods for modeling multiphase materials, we mention

1) two-phase, heterogeneous, linearly elastic composites [2], [3];
2) wave propagation in heterogeneous media [4];
3) Monte-Carlo analysis of random heterogeneous media [5]; and
4) Molecular-lattice models and their interface with continuum models [6].

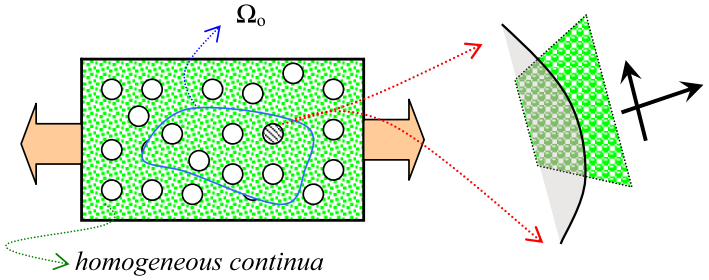

Figure 1. An example of a three-level model of a heterogeneous solid.

A brief description of the use of a goals algorithm for multiscale modeling involves the composite shown made of an aluminum matrix with cylindrical boron inclusions. The quantity of interest is, for example, the net radial and shear stresses on a sector of boron-aluminum atoms at the interface of corresponding lattices on a specific inclusion. The quantity of interest ultimately is whether debonding can occur. The full atomic lattice of the entire body, consisting of possibly millions of atomic sites, is the untractable base

model. Using standard methods, effective mechanical properties of boron and aluminum lattices are derived and used to define the matrix-constituent properties of two-phase macroscale model of a heterogeneous composite. This is, in turn, homogenized to produce a smeared model of homogenized elastic solid. This surrogate model is solved for a surrogate displacement field $\boldsymbol{u}_0$. The inclusion supporting the quantity of interest is surrounded by a domain Ω_o in which the full microstructure exists, but the boundary displacements on $\partial\Omega_o$ coincide with $\boldsymbol{u}_0$. This improved model is solved for correction field $\tilde{\boldsymbol{u}}_0$. The domain Ω_o is adaptively enlarged until such a $\tilde{\boldsymbol{u}}_0$ meets the preset error tolerance. This level of the process is described in [3]. Then $\tilde{\boldsymbol{u}}_0$ is mapped onto the lattice and the process is repeated, as described in [6], until the quantity of interest meets preset tolerances. There is thus *no fitting* of one model with another nor ambiguity concerning convergence of numerical approximations of models.

Acknowledgement: The support of this work by the Office of Naval Research under the contract N00014-25-0401 and the National Science Foundation under the grant EIA-0205181 is gratefully acknowledged.

References:

[1] Oden. J. T. and Prudhomme, S., "Estimation of Modeling Error in Computational Mechanics," *Journal of Computational Physics*, 182 (2002), pp. 496-515.

[2] Oden, J. T. and Vemaganti, K., "Estimation of Local Modeling error and Goal-Oriented Adaptive Modeling of Heterogeneous Materials; Part I: Error Estimates and Adaptive Algorithms," *Journal of Computational Physics*, 164 (2000), pp. 22-47.

[3] Vemaganti, K. and Oden, J. T., "Estimation of Local Modeling Error and Goal-Oriented Adaptive Modeling of Heterogeneous Materials. Part II A Computational Environment for Adaptive Modeling of Heterogeneous Elastic Solids," *Computer Methods in Applied Mechanics and Engineering*, 190 (2001), pp. 6089-6124.

[4] Romkes, A. and Oden, J. T., "Adaptive Modeling of Wave Propagation in Heterogeneous Elastic Solids," *Computer Methods in Applied Mechanics and Engineering,* 193 (2004), 539-559.

[5] Romkes, A., Vemaganti, K., and Oden, J. T., "Goal-Oriented Analysis of Random Heterogeneous Materials Using the Monte Carlo Method," *ICES Report* 04-21, Austin, Texas, 2004.

[6] Oden. J. T., Prudhomme, S., and Bauman, P., "On the Extension of Goal-Oriented Error Estimation and Hierarchical Modeling of Discrete Lattice Models," *Computer Methods in Applied Mechanics and Engineering* (to appear)[See also ICES Report 04-31, Austin, Texas, 2004, under the same title].

Atomistic Characterization of Shear Deformation in Solids

Ting Zhu[1], Ju Li[2], Shigenobu Ogata[3], Jinpeng Chang[1], Robert D. Boyer[1], and Sidney Yip[1]
[1]Massachusetts Institute of Technology, Cambridge, MA 02139 (USA)
[2]Ohio State University, Columbus, OH 43210 (USA)
[3]Osaka University, Osaka 565-0871 (Japan)

Abstract

The phenomenon of shear localization in solids is fundamental to our understanding of the mechanics of non-uniform deformation. Through atomistic simulations we examine how a dislocation or a deformation twin can nucleate and propagate in a crystal lattice. Three results will illustrate our recent attempts to formulate characteristic measures of shear localization at the nanoscale. By subjecting a perfect crystal to affine shear we find that the formation of a twin can be viewed as a nonlinear-wave instability. By analyzing the indentation of a single-crystal thin film we show that a local stiffness criterion can be developed to account for the individual displacement bursts observed in experiments. By reaction pathway sampling we determine the saddle-point configuration for the initial bowing out of a dislocation loop from a crack front.

Introduction

Shear deformation is a fundamental response of all materials systems. When a single crystal is subjected to uniform shear, a maximum strain is reached before structural instability sets in. By mapping out the stress-strain behavior by first-principles calculation one can thus define the ideal shear strength of the material [1]. The critical strain is a measure of the *shearability*, an intrinsic materials parameter that can be used to characterize metals and ceramics [2].

The onset of structural instability in a crystal under affine shear signals the spontaneous formation of a defect, in that the crystal undergoes a single slip between two adjacent planes (dislocation nucleation) or multiple slips between a group of adjacent planes (twin nucleation). How does one understand this localization as a collective behavior? In the absence of a general theory, we resort to specific case studies in atomistic simulation where homogenous nucleation can be unambiguously observed and analyzed.

I. Nucleation of Deformation Twin

In a recent molecular dynamics (MD) study of deformation twinning in bcc Mo, the formation and growth of a 3D embryo has been characterized [3]. Using a 1D-chain model of the reaction coordinates (minimum-energy path), one can probe the energetic competition between dislocation and twin nucleation, as well as the evolution scenario for the development of the twin embryo. With the help of a tiling technique, superimposing a small sinusoidal wave on the highly strained crystal just prior to the instability, we find that defect nucleation may be viewed as a nonlinear wave instability with 4 characteristic stages – linear growth, nonlinear growth, shear shock formation, and formation of an atomistic defect. We have compared the twinning pathways between fcc

and bcc structures [4]. Since empirical interatomic potentials are not quantitatively accurate, we have performed density-functional theory calculations to find that in Mo the minimum number of sliding layers required for twin formation is 5 [5].

II. Dislocation Nucleation by Nanoindentation

We have continued our analysis of nanoindentation-induced homogeneous dislocation nucleation in copper, where the strain localization event is triggered by an elastic instability of the crystal at finite strain [6]. A finite-element calculation, with Cauchy-Born constitutive relation based on an interatomic potential, is developed to characterize the instability, with the results validated by direct comparison with MD. An instability criterion involving bifurcation analysis is incorporated into the finite-element calculation to predict homogeneous dislocation nucleation. The criterion is superior to that based on the critical resolved shear stress in predicting both the nucleation site and the slip character of the defect, as demonstrated by further MD comparison. The critical configuration of homogeneous dislocation nucleation under a spherical indenter is quantified with full 3D finite-element calculations; the critical stress state at the nucleation site is found to be in quantitative agreement with first-principles density-functional theory calculation.

III. Dislocation Emission from a Crack Front

Semi-continuum models have given considerable insights into dislocation emission at a crack front; however, they are no substitutes for an atomistic description of this thermally activated process of longstanding interest. We have reported the first atomistic calculation of the saddle-point configuration and activation energy for the nucleation of a 3D dislocation loop from a mode-I loaded crack in single crystal Cu [7]. The transition state is identified by reaction pathway sampling methods which have not been applied much to mechanical deformation studies. This approach gives distributions of shear and opening displacements at the crack front which can be directly compared with previous semi-continuum analyses based on the Peierls concept. The latter results show a loop which is less wide and has a smaller forward extension than the atomistic configuration. At the saddle point one finds an activation energy of 1.1 eV, distinctly larger than the two previous estimates, a difference which is reasonable in view of the neglect of ledge production effects in all continuum treatments.

Another fundamental question in the atomistics of fracture is how a cleavage crack advances when the first few bonds are broken. In principle, simulation can address this issue because individual bond rupture as well as the cumulative effects of several bond breaking events can be followed in detail. However, most studies to date have been concerned with simulations in the plane-strain condition, in which case crack advancement is effectively treated as a two-dimensional problem. Such simulations therefore cannot describe the crack front distribution as the crack advances. We have again applied reaction pathway analysis to determine the minimum energy path for bond breaking along an atomically sharp crack front in Si [8]. Treating this path as a reaction coordinate we find that crack-front extension occurs through a kink mechanism, the nucleation of a double kink followed by the spreading of this kink across the front. This scenario is essentially the same as the mechanism for a screw dislocation to glide in the

diamond cubic lattice of Si. This investigation also leads to manifestations of lattice trapping and cleavage direction effects beyond those discussed in 2D or 3D-plane-strain simulations.

IV. Dynamic Localization in the Presence of Disorder

Since shear responses are ubiquitous, one might ask whether any useful connection exists between the phenomena discussed here and the responses to shear in disordered systems such as amorphous solids and highly viscous liquids. It would appear that atomistic simulations could give useful insights into crack propagation in glassy materials and shear relaxations in vitreous and colloidal systems. The question again would be to identify the unit process that triggers subsequent structural and dynamical responses. A system which might serve as a link between the fully ordered and the amorphous states is nanocrystals with variable grain size. The disorder in the glass is *distributed*, whereas the 'disorder' in the nanocrystal is *localized* in the grain-boundary regions. Whether in the limit of small grain size the nanocrystal would behave in the same way as the amorphous material [9, 10] is an interesting conjecture worthy of scrutiny.

Acknowledgements This work has been supported by NSF-ITR, Lawrence Livermore National Laboratory, and Honda R&D at MIT, and by Honda R&D and the Transprotation Research Endowment at Ohio State University.

References

[1] S. Ogata, J. Li, S. Yip, 'Ideal Pure Shear Strength of Aluminum and Copper', Science **298**, 807 (2002).
[2] S. Ogata, J. Li, N. Hirosaki, Y. Shibutani, S. Yip, 'Ideal Shear Strain of Metals and Ceramics', Phys. Rev. B (2004), in press.
[3] J.-P. Chang, 'Atomistics of Defect Nucleation and Mobility: Dislocations and Twinning', PhD Thesis, MIT (2003).
[4] R. D. Boyer, S. Ogata, D.-S. Xu, J.-P. Chang, J. Li, S. Yip, 'Multi-plane Generalized Stacking Fault Energies and Twinning Pathways in FCC and BCC Metals', this conference.
[5] S. Ogata, J. Li, S. Yip, 'Twinning Pathway in bcc Molydenum', Eur. Phys. Lett. (2004), in press.
[6] T. Zhu, J. Li, K. J. Van Vliet, S. Suresh, S. Ogata, S. Yip, 'Predictive Modeling of Nanoindentation-induced Homogeneous Dislocation Nucleation in Copper', J. Mech. Phys. Solids **52**, 691 (2004).
[7] T. Zhu, J. Li, S. Yip, 'Atomistic Study of Dislocation Loop Emission from a Crack Tip', Phys. Rev. Lett. **93**, 025503 (2004).
[8] T. Zhu, 'Atomistic Study of Mechanical Instability and Its Activation Mechanisms', Ph.D. Thesis, MIT (2004).
[9] T. G. Nieh and J. Wadsworth, 'Hall-Petch Relation in Nanocrystalline Solids', Scripta Metall. **25**, 955 (1991).
[10] S. Yip, 'The Strongest Size', Nature **391**, (1998).

Symposium -I

Micromechanics & Nanomechanics

Multi-plane Generalized Stacking Fault Energies and Twinning Pathways in FCC and BCC Metals

Robert D. Boyer[a], Shigenobu Ogata[b], Dong-Sheng Xu[c], Jin-Peng Chang[a], Ju Li[d], Sidney Yip[a]

[a]Department of Nuclear Engineering and Department of Materials Science and Engineering, Massachusetts Institute of Technology, Cambridge, MA 02139, USA
[b]Handai Frontier Research Center and Department of Mechanical Engineering and Systems, Osaka University, Osaka 565-0871, Japan
[c]Titanium Alloy Laboratory, Institute of Metal Research, Chinese Academy of Sciences, Shenyang 110016, China
[d]Department of Materials Science and Engineering, Ohio State University, Columbus, OH 43210, USA

ABSTRACT

Using empirical potentials and density functional theory (DFT), we compute the multi-plane generalized stacking fault energies of FCC Al, Cu and BCC Mo, from which the pathways for dislocation and twin nucleation are obtained and analyzed. In FCC Al and Cu, the qualities of the empirical potentials used are systematically checked against DFT calculations. While the Mishin potentials for Al and Cu are currently of the best quality, significant improvements should still be possible. Especially, we think Al could be modeled by short-ranged, but bond angle dependent interactions. For BCC Mo, the (211)[111] twinning energy pathway is determined for the first time using DFT, and intricate features up to 7-layer sliding are found. The thinnest metastable twin embryo is 2 layers. 3-layer twin embryo is unstable. The twin boundary formation energy is 610 mJ/m2, but the twin boundary migration energy is only 40 mJ/m^2 , suggesting twin partial dislocations in BCC Mo have very wide cores and high mobilities. These results will be discussed in the context of the Peierls-Rice-Tadmor analyses of crack-tip slip nucleation with attention to lengthscale issues.

1. Introduction

The most important parameter for the description of deformation twinning is the relative displacement, in the twinning direction, of a series of adjacent slip planes. By restricting all of the atoms in these planes such that they move as a single unit and limiting there motion to the twinning direction, the degrees of freedom required to model deformation twinning can be reduced from 3N, where N is the number of

particles in the system to n, the number of planes in the system. With these constraints the entire system can be described by the behavior of a one-dimensional chain of atoms with a representative from each plane. The deformation of the entire system can therefore be described by a series of displacements in the twinning direction between adjacent planes given by $\Delta x = (\Delta x_1, \Delta x_{2, \ldots}, \Delta x_{i, \ldots}, \Delta x_n)$. The significant decrease in degrees of freedom creates a tractable parameter space that allows for relatively straightforward analysis and visualization of shear deformation. Physically meaningful deformation mechanisms cannot be observed because local atomic relaxations are not allowed, but the elegance of the model allows for a strong intuitive understanding of the energetic barriers related to shear deformation.

The model described above has been applied, with both empirical potentials and ab initio energy calculations, to the {111}<112> system in the FCC metals and the {211}<111> system in BCC Mo. Embedded atom method (EAM) potentials developed by Mishin and collaborators are used to describe both Al and Cu [1,2] and a modified Finnis-Sinclair potential model for Mo [3]. We use the Vienna Ab-initio Simulation Package (VASP) with Perdew-Wang generalized gradient approximation (GGA) exchange-correlation density functional and ultrasoft (US) pseudopotential. The supercell is $e_1 \times e_2 \times me_3$ with $e_1 \equiv [111]a_0/2$, $e_2 \equiv [0\bar{1}1]a_0$, and $e_3 \equiv [2\bar{1}\bar{1}]a_0$, and 6 atoms per $e_1 \times e_2 \times e_3$. Brillouin zone (BZ) *k*-point sampling is performed using the Monkhorst-Pack algorithm. BZ integration follows the Methfessel-Paxton scheme with the smearing width chosen so the "-*TS*" term is less than 0.5 meV/atom. We use 233 eV planewave energy cutoff throughout the calculations.

3. Results

The energy penalty is calculated for FCC Al, Cu and BCC Mo using both empirical potentials and ab initio calculations as successive adjacent planes are sheared relative to one another by one partial Burger's vector, ***b***. The energy is then plotted as a function of the number of adjacent pairs of sheared planes. The relative stability of a series of planar shear-induced defects can be described using this energy function.

The energy barriers to the formation of one-layer planar faults, the unstable stacking energies, are calculated to be 171 mJ/m^2 for Al and 176 mJ/m^2 for Cu. The intrinsic stacking fault energies for the two FCC metals, which correspond to the energy of a single pair of adjacent planes sheared by ***b***, are 146mJ/m^2 for Al and 44mJ/m^2 for Cu. The energetic barrier to further slip and the formation of a two-layer twin embryo is 67 mJ/m^2 for Al and 156 mJ/m^2 for Cu. The energy for the formation of subsequent twinned layers is equal to barrier for the formation of the two-layer twin embryo.

In BCC Mo empirical potential calculations show that a one-layer planar fault is unstable, but that a two-layer twin embryo is stable. This is in contrast to the three-

layer embryo proposed previously [4]. The activation barrier to the formation of the two-layer twin embryo is calculated as 880mJ/m^2. The energy for twin boundary migration is calculated to be 83mJ/m^2 and applies to the growth of twins with three or more twinned planes. Ab initio calculations for molybdenum also indicate that the one-layer planar fault is unstable and the two-layer twin embryo is metastable. The energy barrier to two-layer twin formation is 1300mJ/m^2. However, with ab inito calculations the three and four-layer planar defaults are also unstable. From the two-layer twin embryo, which has an energy on 1150mJ/m^2, a five-layer twin embryo is formed with an energy barrier 1350 mJ/m^2. The barrier to layer-by-layer twin migration for twins greater than five layers is calculated to be 40mJ/m^2.

4. Discussion

In both FCC Al and Cu, partial dislocation nucleation and the formation of an intrinsic stacking fault are known to be stable and are shown to occur prior to the formation of a twinned structure in either of these two metals. However, despite the observation of twinned structures in Al and Cu, homogeneously nucleated deformation twinning does not seem viable in FCC metals. The (211)[111] twinning direction in the BCC structure does not contain an intrinsic stacking fault, and as a result, two-layer micro twins are homogeneously nucleated in BCC Mo.

Furthermore, unlike the FCC metals examined where layer-by-layer twin growth is immediately feasible, ab initio simulations of BCC Mo show that the metastable two-layer microtwin is followed by a five-layer twinned structure. This phenomena is attributed to proposed long-range interactions is Mo. We theorize that in the FCC structure the close-packed (111) planes more effectively shield the atomic interaction between all but adjacent planes making these interactions dominate. However, the relatively spares (211) planes in BCC Mo do not have the same shielding effect, and as a result longer range interaction play a key role in destabilizing three and four-layer twinned structures.

References

[1] Y. Mishin, D. Faraks, M.J. Mehl, D. A. Papaconstantopoulos, *Phys. Rev. B* **59** (1999) 3393.
[2] Y. Mishin, M.J. Mehl, D. A. Papaconstantopoulos, A.F. Voter, J. D. Kress, *Phys. Rev. B* **63** (2001) 224106.
[3] G. J. Ackland and M. W. Finnis, Phil. Mag. A, vol. 54, p.301, 1986.
[4] V. Vitek, Script. Metall., vol. 4, p. 725, 1970.

Overview of ONERA multiscale approaches in composite and polycrystals: applications to the design of components

N. Carrere and J.L. Chaboche
ONERA, Office National d'Etudes et de Recherches Aérospartiales, 92322 Chatillon, France

ABSTRACT

This paper presents the different multiscale methods studied and developed at Onera to describe the behavior of heterogeneous materials. Three main model classes are under investigation : (i) numerical techniques based on Finite Element calculations on a Representative Volume Element, (ii) analytical methods which consist of linearizing the local behavior and (iii) semi-analytical which can be considered as an approximation of numerical techniques. In this work, these different approaches are compared for structural calculations, in terms of computational cost, macroscopic results and local quantities.

1 Introduction

Many structures today are designed using heterogeneous materials such as composites or polycrystals. This requires knowledge of the coupling between non-elastic-behaviors at different length scales, and multiphysics problems (mechanical, ageing ...). It is a great challenge to model all these phenomena into a tool that can be used to optimise both the material and the structural design. At Onera, much research have been devoted to these subjects. Several multiscale strategies have been proposed to model the non-linear behavior of materials at different scales. If the homogenization of linear behaviors is now well-established, this is not the case in non-linear materials. The first class of models is numerical, generally developed on the assumption of a periodic microstructure. The local behavior is integrated in each sub-volume of the elementary volume element using a finite element method (FE^2 approach). The second class of models is analytical, first proposed in the general framework of polycrystal or of random microstructure which consist in linearizing the local behavior. Finally, the last model class is simplified methods (semi-analytical) which can be considered as an approximation of numerical techniques (TFA-like methods). The first part of this paper is devoted to a brief presentation of the different methods. In the second section comparisons and limitations of each model are given.

2 Presentation of the different methods

The FE^2 model [1, 2] The FE^2 model is an embedded finite element computation where the response of the representative volume element is computed using a finite element method. It is a general idea which is based on three ingredients:

1. a modeling of the mechanical behavior at the lower scale (the Representative Volume Element, RVE),

2. a localization rule which determines the local solutions inside the unit cell, for any given overall strain,

3. a homogenization rule giving the macroscopic stress tensor, knowing the micromechanical stress state.

Mean Field models [3, 4, 5, 6]. These analytical methods that were first proposed in the general polycrystals framework, or in random microstructure consist of linearizing the local behavior with a tangent, secant or second orders formulation. This allows to use a classical localization techniques for linear materials. The calculation of localization operators depends on the linearizing technique used.

Generalized Transformation Field Analysis [7, 8] This method, very similar in its principle to FE^2, is based on analytical tools. Two main steps are necessary to relate the macroscopic and the microscopic quantities. The local stress and strain fields are connected to the macroscopic ones by the relations:

$$\underset{\sim}{\sigma}_r = \underset{\approx}{\mathbf{B}}_r : \Sigma - \sum_{s=1}^{n} \underset{\approx}{\mathbf{F}}_{rs} : \underset{\approx}{\mathbf{L}}_s \underset{\sim}{\epsilon}^g_s \tag{1}$$

$$\underset{\sim}{\epsilon}_r = \underset{\approx}{\mathbf{A}}_r : \underset{\sim}{\mathbf{E}} + \sum_{s=1}^{n} \underset{\approx}{\mathbf{D}}_{rs} : \underset{\sim}{\epsilon}^g_s \tag{2}$$

where $\underset{\sim}{\epsilon}^g_s$ (called local generalized eigenstrain) represents all the uniform non-linear strain (due to plasticity or damage for instance) on the sub-volume s. $\underset{\approx}{\mathbf{F}}_{rs}$ and $\underset{\approx}{\mathbf{D}}_{rs}$ are the transformation influence tensors. Subscript rs is given for the influence of the sub-volume s on the sub-volume r. The computation of the influence tensors and the choice of the number of subvolumes are the keypoints of TFA method.

3 Some elements of comparison

The FE^2 method permit to obtain "exact" solution at the local and global scales but the computational cost is high. A major advantage of the FE^2 method is that all classical finite element capabilities are available for the local finite element computation (for example all material models, all kind of elements, boundary conditions, cohesive zone models…).

The mean field methods are very efficient in term of computational cost, but the macroscopic response is too "stiff" as compared with the reference solution provided by the FE modeling.

In TFA if the number of sub-volumes is not large enough, the plastic deformation is smoothed over many sub-volumes. This leads to an incorrect macroscopic response, which is too stiff. This is the reason why we have proposed two developments:

- a method called "sub-volume reduction" which is used to lower the number of subvolumes to consider in the TFA approach while preserving a correct mechanical response.

- a correction of the "total elastic localization rule" written as follows :

$$\underset{\sim}{\epsilon}_r = \underset{\sim}{\underset{\sim}{\mathbf{A}}}_r : \underset{\sim}{\mathbf{E}} + \sum_{s=1}^{n} \underset{\sim}{\underset{\sim}{\mathbf{D}}}_{rs} : \underset{\sim}{\underset{\sim}{\mathbf{K}}}_s \underset{\sim}{\epsilon}^g_s \tag{3}$$

  The tensor $\underset{\sim}{\underset{\sim}{\mathbf{K}}}_s$ depend on the shape of the RVE, the elastic properties and the asymptotic tangent stiffness.

These two corrections permit to obtain a good approximation of the global and local responses with a lower computational cost as compared with the FE^2 method.

References

[1] R.J.M. Smit, W.A.M. Brekelmans, and H.E.H. Meijer. Prediction of the mechanical behavior of nonlinear heterogeneous systems by multi-level finite element modeling. *Comput. Methods Appl. Mech. Engrg.*, 155:181–192, 1998.

[2] F. Feyel. *Application du calcul parallèle aux modèles à grand nombre de variables internes*. PhD thesis, Ecole National Supérieure des Mines de Paris, Paris, France, 1998.

[3] R. Hill. Continuum Micro-mechanisms of Elastoplastic Polycrystals. *J. Mech. Phys. Sol., Vol. 13, pp. 89-101*, 1965.

[4] J. W. Hutchinson. Elastic-Plastic Behaviour of Polycrystalline Metals and Composites. *Proc. Roy. Soc. Lond., Vol. A109, pp. 247-272*, 1966.

[5] M. Berveiller and A. Zaoui. An extension of the Self-Consistent Scheme to Plastically Flowing Polycrystals. *J. Mech. Phys. Sol., Vol. 6, pp. 325-344*, 1978.

[6] R. Masson, M. Bornert, P. Suquet, and A. Zaoui. An affine formulation for the prediction of the effective properties of non linear composites and polycristals. *J. Mech. Phys. Sol., Vol. 48, pp. 1203-1227*, 2000.

[7] G. Dvorak. Transformation field analysis of inelastic composite materials. *Proc. Roy. Soc. Lond.*, A437:311–327, 1992.

[8] J.-L. Chaboche, S. Kruch, J.-F. Maire, and T. Pottier. Towards a micromechanics based inelastic and damage modelling of composites. *Int. J. Plasticity*, 17:411–439, 2001.

Semi-Empirical Stress and Energy Analysis of Damage surrounding a Tip of a Propagating Crack

M. Chabaat[a]

[a]Built Environment Research Laboratory, Civil Engineering Faculty, University of Sciences and Technology Houari Boumediene, B.P. 32 El-Alia, Bab Ezzouar, Algiers 16111, ALGERIA, mchabaat2002@yahoo.com

ABSTRACT

In this work, evaluation of energy release rates in a model with a crack surrounded by a Damage Zone (DZ) is presented. The traditional approach identifies the process zone as a plastic one and employs the elastoplastic solution for the determination of the energy release rates, plastic zone, zone size, shape, etc…Herein, a Semi- Empirical Approach (SEA) using experimental data is proposed. On the basis of this latest, a more realistic model (displacement discontinuities of arbitrary shape rather than realistic microcracks) is suggested and for which the result can be obtained using experimental data and avoiding the difficulties of analytical solutions. It is also shown through this study that the kinematics of the DZ is characterized by few degrees of freedom (elementary movements) such as translation, rotation, isotropic expansion and distortion. Driving forces corresponding to the mentioned degrees of freedom are formulated within the framework of the plane problem of elastostatics.

There is sufficient experimental evidence that in most cases, a propagating crack is surrounded by a damage zone which often preceds the crack itself. This zone usually consists of slip lines or shear bands in metals [1], microcracks in ceramics and polymers [2], and crazes in amorphous polymers [3]. Thus, the existence of these defects affects progressively the propagation of cracks already present in some materials. These latest present at the local scale a brittle elastic behavior, but because of the presence of these microdefects their global behavior becomes complex.

The traditional approach identifies the process zone (PZ) as a plastic one and employs the elastoplastic solution for the determination of energy release rates, plastic zone size (length and width), shape, etc … However, there are some experimental results which show that the PZ can not be always modeled as a plastic zone [4]. Then, the plastic zone size through the thikness of the specimen is an important parameter for any type of plasticity theory employed and in which it results the use of yield criteria for plane strain and plane stress conditions in the interior and on the surface of the specimen, respectively. Besides, it is demonstrated in [4] that the shape of the process zone can also be difficult . Since, the damage zone consists of crazes or arbitrary oriented microcracks, then, the qualitative difference in the distribution of damage apparently, is a result of different micromechanisms of damage formation.

Because this damage can constitute an important toughening mechanism, problems dealing with crack microcracks interactions have received considerable research attention since they were introduced to fracture mechanics. As a result, a wide body of literature, on this topic, exists [5-7].

In this study, evaluation of energy release rates for the proposed model shown in Fig. 1 is considered. It is based first, on the determination of a stress field distribution induced during interactions between a main crack and surrounding microcracks by the use of a Semi-Empirical Approach (SEA) which relies on the Green's functions and second, by taking into consideration experimentally observed crack opening displacements as the solution to the multiple crack interactions problems.

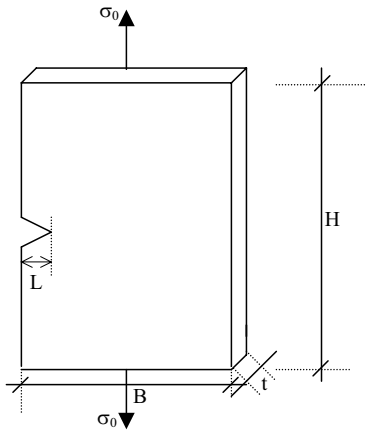

H = 80 mm
B = 20 mm
L = 1 mm
t = 0.5 mm
σ_0 = 16 MPa
E = 2.2 GPa

Fig.1 Geometry of the problem for general formulation.

Expressions for active parts of crack driving forces J, L, M and N corresponding to the translation, rotation, isotrope expansion and distorsion of the damage surrounding a crack can be obtained. In this study, only expressions for J (translation) and M (expansion) are considered.

If the specimen is loaded by a constant traction σ, then; the work is $A = 2\sigma.\delta\hat{U}$, the potential energy is $P = (-1/2).A$ and the corresponding variation is given by $\delta P = -\sigma.\delta\hat{U}$. Taking in consideration all of these latest, one can have the following relation;

$$-\delta P = \sigma[C.w.\Phi(x_{10}, H)+\int_0^l((\partial b/\partial l).\Phi(x, H).dx]\delta l + \sigma[2C.v.\Phi(x_{10}, H) + \int_0^l((\partial b/\partial e).\Phi(x, H).dx]\delta e \quad (1)$$

The first bracket in Eq. (1) is identified as being a J-integral and the second one as an M-integral and finally, one can write;

$$J = \sigma.[C.w.\Phi(x_{10}, H) + \int_0^l((\partial b/\partial l).\Phi(x, H).dx] \quad (2)$$

$$M = \sigma.[2C.v.\Phi(x_{10}, H) + \int_0^l((\partial b/\partial e).\Phi(x, H).dx] \quad (3)$$

In order to make use of expressions (2) and (3), one needs to know the concentration of damage C which can be taken from experimental photographs [8] and the second Green's

tensor Φ derived for the domain and can also be modeled by a semi-infinite domain of the crack (case where L/B<< 1) as shown in Fig. 2.

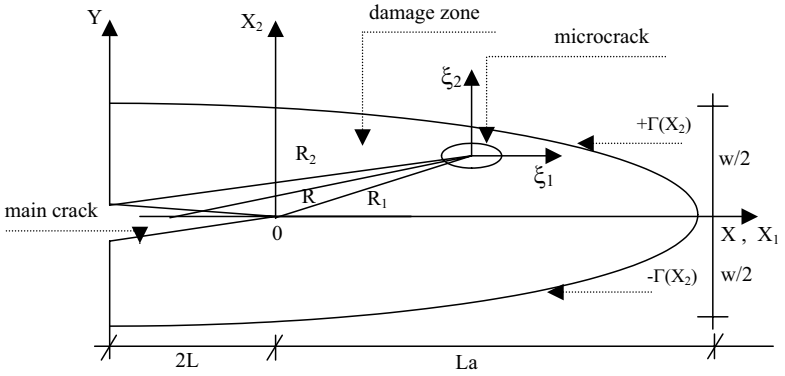

Fig.2 Schematic representation of the damage zone.

In conclusion theoretical expressions for translation (J) and isotrope expansion (M) representing the active parts of crack driving forces are formulated. It is also shown in this study that the measured δU experiments energy release rate which is usually represented by the area between the force and displacement curves obtained on a model with two incrementally different cracks where δP = J.δl. However, in a number of cases; J has a significant statistical distribution. The main reason for that is the expenditure of energy into various modes of crack propagation meaning the translational motion of the crack with the process zone unchanging on one hand and the expansion of the DZ on the other hand. The latter constitutes an important percentage of the total energy release rate. Besides, the distribution of energy into modes varies size from one experiment to the other as being a loading history dependant quantity.

BIBLIOGRAPHY

[1] J. Botsis, A. Chudnovsky and A. Moet, "Fatigue crack layer propagation in polystyrene", *Int. J. of Fracture,* Parts I and II, Vol. 33, 1987, pp.263-284.

[2] M. T. K. Takemori, "Fatigue fracture of polycarbonate", *Polymers Engng. and Sci.,* Vol. 22, 1982, pp. 937-645.

[3] M. Chabaat, "Comparison of minimal principal stress trajectories with crazes distribution", *Int. J. of Fracture,* Vol. 37, 1988, pp. 47-54.

[4] R. W. Hertzberg and J. A. Manson, Fatigue of engineering plastics, Academic Press, New York, 1980.

[5] L. R. F. Rose, "Microcrack interaction with a main crack", *Int. J. of Fracture,* Vol. 31, 1986, pp. 233-242.

[6] M. Chabaat and S. Djouder, "Crack-microcracks interactions using a semi-empirical approach", *submitted for publication in Int. J. of Mat. Sci. and Engng. A, 2004.*

[7] A. A. Rubinstein, "Remarks on macrocrack-microcrack and related problems", *Int. J. of Fracture,* Vol. 96, 1999, pp. 9-14.

[8] J. Botsis, "Faitgue crack layer propagation in polystyrene", Ph D Thesis, C.W.R.U., Cleveland Ohio, 1984.

Evolution of Dislocation Core Width with Dislocation Velocity: Influence of a Viscous Drag Mechanism.

C. Denoual, F. Bellencontre, Y.P. Pellegrini
CEA–DAM IdF, Département de Physique Théorique et Appliquée
F–91680 Bruyères le Châtel Cedex, France

ABSTRACT

A three-dimensional Element Free Galerkin method with an explicit formulation is used to model dislocations. As to the Peierls-Nabarro model, the proposed method states that dislocation core structure is the result of balance between elastic energy and stacking fault energy. This method allows for the modelling of complex boundary conditions as well as for studying dynamic and unsteady state problems. We study here the influence of the viscous drag on the width of the dislocation for a constant velocity, and compare to available analytical results.

1 Introduction

The velocity of a dislocation depends, in a quite complex manner, on macroscopic variables (like the loading or the temperature) but also on local features such as the dislocation core structure. Molecular dynamics is one of the powerful tools available to investigate dislocation motion, that has contributed to renew the understanding of some mechanisms previously considered well-known (see, e.g., [4] for the motion of a screw dislocation under high loading). This technique is however delicate to use for studying viscous effects since dislocation motion induces a local temperature increase. For this reason, simple analytical approaches like the Peierls-Nabarro model [2] and their extensions to fast propagating dislocations [5] can lead to a clearer picture of the relationship between viscosity and dislocation velocity, leaving aside thermal effects.

The aim of this study is to use a “dynamic” Peierls-Nabarro model to compare to a complete 2D calculation — at least in a phenomenological manner — some closed-form results provided by Rosakis [5], with emphasis on the relationship between the dislocation velocity, the microscopic viscosity and the core width.

The following section presents an outline of the method (an extended description can be found in [1]) whereas the second part shows some preliminary results.

2 Galerkin-Peierls-Nabarro method

The Peierls-Nabarro method consists in minimizing an elastic energy and a surface energy (the generalized stacking fault energy, E^{gsf}, or γ–surface) with respect to a field of displacement jump $\boldsymbol{f}$. When crossing the dislocation slip plane, the displacement $\boldsymbol{u}$ is therefore discontinuous ($[\![\boldsymbol{u}]\!] = \boldsymbol{f}$ on the slip plane). For transient loadings (i.e. shock waves or strongly accelerating dislocations), the elastic energy can no more be written as a function of the displacement field $\boldsymbol{f}$ but has to be defined through an integral of the elastic energy density over the whole volume. This problem is addressed in [1] in a way that amounts to using the action functional (a misprint on the sign of the kinetic energy is corrected here) :

$$\mathcal{A} = \int dt \left[\int_V \mathrm{d}V \left\{ \frac{1}{2}\rho \dot{\boldsymbol{u}}^2 - E^{\mathrm{e}}[\boldsymbol{u}, \bar{\boldsymbol{\eta}}] - \boldsymbol{u}\cdot\boldsymbol{B} \right\} - \int_S E^{\mathrm{isf}}[\bar{\boldsymbol{\eta}}]\ \mathrm{d}S \right]$$

with E^{e} the elastic energy, $\boldsymbol{u}$ the displacement field, $\boldsymbol{B}$ the bulk forces, $\bar{\boldsymbol{\eta}}$ a two-dimensional vector field that represents the plastic displacement when crossing the gliding surface, and E^{isf} a surface energy. The problem in $\boldsymbol{u}$ is solved by using an Element-Free Galerkin method with explicit time integration, and $\bar{\boldsymbol{\eta}}$ evolves according to a Time-Dependent Ginzburg-Landau equation (also used in the Phase Field method [6])

$$\frac{\partial \bar{\boldsymbol{\eta}}}{\partial t} = \frac{1}{\zeta}\frac{\delta \mathcal{A}}{\delta \bar{\boldsymbol{\eta}}}, \tag{1}$$

with ζ the viscosity of the slip plane (in Pa · m · s). The surface energy E^{isf} is defined by the equality $\min_{\bar{\boldsymbol{\eta}}} \left(\int_V \mathrm{d}V\, E^{\mathrm{e}}[\boldsymbol{u}(\boldsymbol{f}), \bar{\boldsymbol{\eta}}] + \int_S E^{\mathrm{isf}}[\bar{\boldsymbol{\eta}}]\ \mathrm{d}S \right) = E^{\mathrm{gsf}}(\boldsymbol{f})$ in the static configuration of two gliding *rigid* blocs (*i.e.*, the configuration used in *ab initio* methods to calculate E^{gsf}).

3 Results

Our 2D simulations are performed on an artificial isotropic material with $E^{\mathrm{gsf}} \propto \sin^2(2\pi f/b)$. An instantaneous shear loading is prescribed, leading to an acceleration of the edge dislocation followed by a stationary motion (only the 2^{nd} stage is considered in the following figures).

The relationship between the dislocation velocity v and the ratio $\sigma_{\mathrm{xy}}/\zeta$ can be observed on Fig. 1–a. However, only qualitative comparisons can be made with the closed-form solution because of the differences in the definition of the viscosity parameter (relative to $\boldsymbol{f}$ in [5] and relative to $\bar{\boldsymbol{\eta}}$ for [6, 1]). Figure 1–b shows that the evolution of the dislocation core width, as a function of the velocity, is qualitatively different from the closed-form solution. Actually, the width

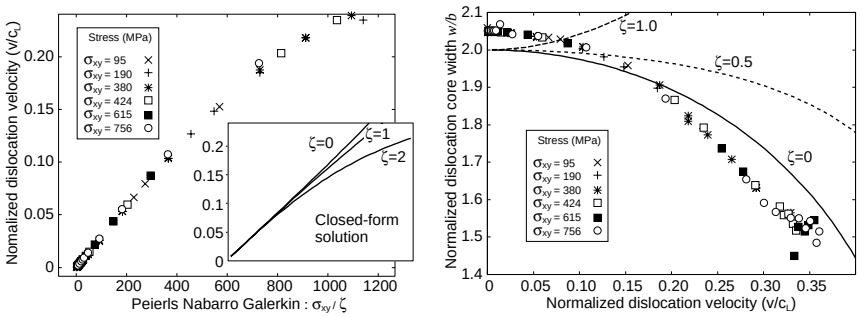

Figure 1: a– (left): Dislocation velocity normalized with the longitudinal celerity wrt. $\sigma_{\mathrm{xy}}/\zeta$. b– (right): Core width normalized with the Burgers norm as a function of the dislocation velocity. Lines display the closed form solution [5].

w decreases too fast and, for all the viscosities (even for the lowest ones), widths lower than 1.4 times the Burgers vector and velocities higher than $0.4c_{\mathrm{L}}$ cannot be reached. This surprisingly low limit for the velocity is related to a phenomenon of lattice wave emission [3], which leads to considerable energy loss and therefore to an extra drag force. This lattice emission appears when w becomes too small to be accurately represented by the element free Galerkin technique. This phenomenon seems to be an artifact of the simulation method since it can be removed by increasing the spatial resolution of the EFG technique.

References

[1] C. Denoual. Dynamic dislocation modeling by combining Peierls Nabarro and Galerkin methods. *Phys. Rev. B*, 70:024106, 2004.

[2] J. P. Hirth and J. Lothe. *Theory of Cristal Dislocations*. Krieger, 1982.

[3] H. Koisumi, H. O. K. Kirchner, and T. Suzuki. Lattice wave emission from a moving dislocation. *Phys. Rev. B*, 65:214104, 2002.

[4] J. Marian, W. Cai, and V. Bulatov. Dynamic transitions from smooth to rough to twinning in dislocation motion. *Nature Mat.*, 3:158–163, 2004.

[5] P. Rosakis. Supersonic dislocation kinetics from an augmented Peierls model. *Phys. Rev. Lett.*, 86(1):95–98, 2001.

[6] Y.U. Wang, Y.M. Jin, A.M. Cuitiño, and A.G. Khachaturyan. Nanoscale phase field microelasticity theory of dislocations: model and 3d simulations. *Acta mater.*, 49:1847–1857, 2001.

Numerical Analysis of Nanotube Based NEMS Devices

Changhong Ke and Horacio D. Espinosa

Dept. of Mech. Engineering, Northwestern University, Evanston, IL 60208, USA

E-mail: espinosa@northwestern.edu.

ABSTRACT

A non-linear analysis of nanotube based nano-electromechanical systems (NEMS) is presented. Singly and doubly clamped nanotubes under electrostatic actuation are examined by solving nonlinear elastic equations. The analysis emphasizes the importance of nonlinear effects, such as finite kinematics (i.e. large deformations) and charge concentrations at the tip of singly clamped nanotubes, in the prediction of the *pull-in* voltage of the device, a key design parameter. We show that nonlinear kinematics results in an important increase in the *pull-in* voltage of doubly clamped nanotube devices, but that it is negligible in the case of singly clamped devices. Likewise, we demonstrate that charge concentration at the tip of singly clamped devices results in a significant reduction in *pull-in* voltage. By comparing numerical results to analytical predictions, closed form formulas derived elsewhere are verified. The results reported in this work are particularly useful in the characterization of the electro-mechanical properties of nanotubes as well as in the optimal design of nanotube based NEMS devices.

1. Introduction

Carbon nanotubes (CNTs) have long been considered ideal building blocks for Nanoelectromechanical systems (NEMS) devices due to their superior electro-mechanical properties. The CNT-based NEMS reported in the literature, such as nanotweezers,[1-2] nonvolatile random access memory (RAM) devices,[3] and feedback-controlled nanocantilever NEMS devices,[4] can be simply modeled as CNT cantilevers or fixed-fixed CNTs hanging over an infinite conductive substrate. In order to design a functional NEMS device, its electro-mechanical characteristic should be well quantified in advance. Generally, multi-walled carbon nanotubes (MWNTs) can be modeled as homogeneous cylindrical beams and perfect conductors. In this paper, we investigate the electro-mechanical characteristics of singly and doubly clamped CNT-based NEMS, as illustrated in Fig.1: a biased MWNT cylinder of length L, placed above an infinite ground plane, at a height H. The inner radius and outer radius of MWNT are R_{int} and R_{ext}, respectively. The applied voltage between nanotube and substrate is V. In particular, two important but typically omitted effects in the modeling of nano-devices, such as concentrated charge at the free end for singly clamped nanotube and finite kinematics, which accounts for large displacements, are investigated in details. We consider devices with H ~0.1 μm in which the *van der Waals* force can be neglected

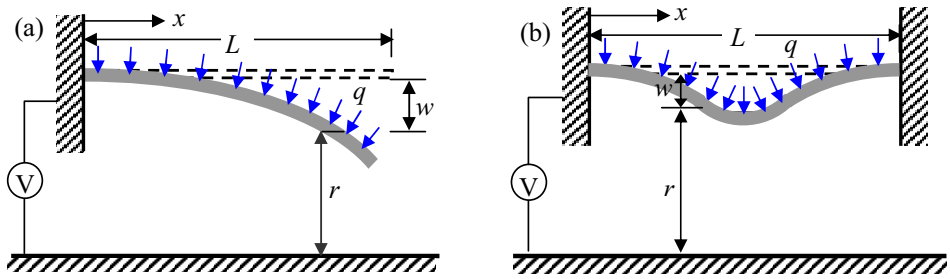

Fig. 1 Schematic of the finite kinematics configuration of a cantilever (a) and fixed-fixed (b) nanotube device subjected to electrostatic forces.

2. Modeling

The capacitance per unit length along the cantilever nanotube is approximated as[5]

$$C = C_d(r)\left\{1 + 0.85[(H + R_{ext})^2 R_{ext}]^{1/3}\,\delta(x - x_{tip})\right\} = C_d(r)\{1 + f_c\} \qquad (1)$$

where the first term in the bracket accounts for the uniform charge along the side surface of the tube and the second term, f_c, accounts for the concentrated charge at the end of the tube(For clamped-clamped nanotubes, $f_c = 0$). $x = x_{tip} \neq L$, as a result of the finite kinematics. $\delta(x)$ is the Dirac distribution function. $C_d(r)$ is the distributed capacitance along the side surface per unit length for an infinitely-long tube, which is given by $C_d(r) = 2\pi\varepsilon_0 / a\cosh(1 + r/R_{ext})$ where r is the distance between the lower fiber of the nanotube and the substrate, and ε_0 is the permittivity of vacuum. Thus, the electrostatic force per unit length of the nanotube is given as follows:

$$q = \frac{1}{2}V^2\frac{dC}{dr} = \frac{1}{2}V^2\left(\frac{dC_d}{dr}\right)\{1 + f_c\} \qquad (2)$$

If we just consider the bending of the singly clamped cantilever, the governing equation of the elastic line under finite kinematics is[6]

$$EI\frac{d^2}{dx^2}\left(\frac{d^2w}{dx^2}\left(1 + \left(\frac{dw}{dx}\right)^2\right)^{-\frac{3}{2}}\right) = q\sqrt{1 + \left(\frac{dw}{dx}\right)^2} \qquad (3)$$

where E is the Young Modulus, I is the moment of the inertia of the nanotube and w is the deflection of the nanotube. Eq. (3) clearly represents a more accurate description of the elastic behaviour of nanotubes than the more common equation assuming small displacements, i.e. $EI\frac{d^4w}{dx^4} = q$. For a doubly clamped nanotube, stretching becomes significant as a consequence of the rope-like behavior of a fixed-fixed nanotube subjected to finite kinematics. The elastic line equation becomes [6],

$$EI\frac{d^4w}{dx^4}-\frac{EA}{2L}\int_0^L\left(\frac{dw}{dx}\right)^2 dx\frac{d^2w}{dx^2}=q \tag{4}$$

3. Result and discussion

Solving numerically the previous nonlinear equations for singly, and doubly clamped nanotube NEMS devices, respectively, the *pull-in* voltage corresponding to the nanotube collapsing onto the ground substrate can be predicted. The comparison between results numerically obtained and the results of analytically derived formulas[7-8] obtained based on energy method is reported in Table 1.

Table 1: Comparison between pull-in voltages evaluated numerically and analytically for doubly (*D*) and singly (*S*) clamped nanotube devices, respectively. E=1 TPa, R_{int}=0. For cantilever nanotube device the symbol (w) denotes that the effect of charge concentration has been included.

Case	BC	H [nm]	L [nm]	$R=R_{ext}$ [nm]	V_{PI} [V] (theo. linear)	V_{PI} [V] (num. linear)	V_{PI} [V] (theo. non-linear)	V_{PI} [V] (num. non-linear)
1	*D*	100	4000	10	3.20	3.18	9.06	9.54
2	*D*	100	3000	10	5.69	5.66	16.14	16.95
3	*D*	200	3000	10	13.53	13.52	73.50	77.09
4	*D*	100	3000	20	19.21	18.74	31.57	32.16
5	*S*	100	500	10	27.28w)	27.05(w)	27.52(w)	27.41 (w)
6	*S*	100	500	10	27.28(w)	27.05(w)	30.87	31.66

It can be seen that the effect of finite kinematics is much significant for the doubly clamped boundary condition while for the singly clamped boundary condition, it is negligible. The effect of the concentrated charge for the singly clamped cantilever device is pronounced. The comparison between the numerical results and results of analytical close-form formula is in good agreement (with maximum discrepancy of 5 %).

Acknowledgements

The authors acknowledge the support from the FAA through Award No. DTFA03-01-C-00031 and the NSF through awards No. CMS-0120866 and EEC-0118025.

References

[1] S. Akita, et al, *Appl. Phys. Lett.*, 79(2001), 1691
[2] P. Kim and C. M. Lieber, *Science*, 126 (1999), 2148
[3] T. Rueckes, et al., *Science*, 289 (2000), 94.
[4] C. Ke and H. D Espinosa, *Appl. Phys. Lett.*, 85(2004), 681
[5] C. Ke, and H. D. Espinosa, "Analysis of electrostatic charge distribution in nanotubes and nanowires," submitted for publication to J. of Appl. Phys., 2004,
[6] M. Sathyamoorthy, *Nonlinear Analysis of Structures*, CRC Press, 1998.
[7] C-H. Ke, B. Peng, N. Pugno, and H. D. Espinosa, "Analytical modelling of nanotube based NEMS devices," submitted to *J. of Mech. and Phys. Solids*, 2004.
[8] N. Pugno, C-H. Ke and H. D. Espinosa, "Analysis of doubly-clamped nanotube devices under large displacements," Submitted to *J. of Appl. Mech*., 2004.

Multi-Scale Model for Damage Analysis in Fiber-Reinforced Composites With Debonding

Somnath Ghosh and Prasanna Raghavan

Department of Mechanical Engineering, The Ohio State University, Columbus, OH 43210

ABSTRACT

This paper presents an adaptive multi-level computational model for multi-scale analysis of composite structures with damage due to fiber/matrix interfacial debonding. The method combines continuum damage modeling with displacement based FEM with a microstructurally explicit modeling of interfacial debonding by the Voronoi cell FEM (VCFEM). Three computational levels of hierarchy with different resolutions are introduced to reduce modeling and discretization errors due to inappropriate resolution. They are: (a) level-0 of pure macroscopic analysis, for which a continuum damage mechanics (CDM) model is developed from homogenization of micromechanical variables that evolve with interfacial debonding; (b) level-1 of coupled macroscopic-microscopic modeling to implement adequate criteria for switching from macroscopic analyses to pure microscopic analyses; and (c) level-2 regions of pure microscopic modeling with explicit interfacial debonding. A numerical example of a composite joint is solved to demonstrate the limitations of CDM model and to demonstrate the effectiveness of the multi-scale in predicting failure due to interfacial debonding.

1. Introduction

Heterogeneous materials such as composites are conventionally analyzed with properties obtained from homogenization of response at smaller (meso-, micro-) length scales [1]. In this paper, the multi-level method is extended to optimally address the complex modeling of multi-scale damage of composites undergoing debonding at the fiber-matrix interface. The multi-level model consists of three essential levels, two of which adaptively evolve from the first from considerations of model deficiencies. The levels are: (i) a fully macroscopic domain (level-0) where the computational model uses homogenized material parameters; (ii) an intermediate level(level-1) consisting of the macroscopic analysis together with analysis of the microscopic representative volume element (RVE); and (iii) a purely microscopic domain (level-2) consisting of explicit description of the heterogeneities. A intermediate transition layer is placed between the macroscopic and microscopic domains for smooth transition from one scale to the next. For the level-0 computations, a continuum damage model (CDM) is developed from detailed

micromechanical analysis with interfacial debonding. The asymptotic homogenization method is used to evaluate macroscopic damage variables and their evolution laws for a fourth order strain-based anisotropic continuum damage model [7]. Numerical examples are conducted to demonstrate the effectiveness of the CDM model in predicting damage in composite structures.

2. The Adaptive Multi-Scale Computational Model

The overall heterogeneous computational domain is adaptively decomposed into a set of non-intersecting open subdomains, belonging to different levels as discussed next.

(a) Computational Subdomain Level-0 : corresponds to macroscopic regions where deformation variables like stresses and strains are relatively uniform in their macroscopic behavior. A continuum damage model is developed for this region to account for evolving damage in the microstructure [2]. The general form of CDM models introduce a fictitious effective stress $\tilde{\sigma}_{ij}$ in the damaged material using the fourth order damage effect tensor M_{ijkl} as $\sigma_{ij} = M_{ijkl}(D_{ijkl})\sigma_{kl}$ where D_{ijkl} is the damage tensor. This is accomplished by solving the micromechanical RVE boundary value problem with periodicity boundary conditions and evolving applied strain field [2].

Computational Subdomain Level-1 : Microscopic information from RVE-based analyses is used to decide whether the homogenization assumptions still apply in that region, or if microscopic computations are necessary. This domain adaptively emerges from level-0 simulations, at regions of locally increasing gradients of macroscopic variables. Computations in this region are still based on assumptions of macroscopic uniformity and periodicity of the RVE.

Computational Subdomain Level-2: Level-2 regions are characterized by significant microstructural non-uniformities in the form of high local stresses or strains that would occur e.g. near a crack tip or free edge. The microstructure-based Voronoi Cell Finite Element Model [3] is particularly effective for modeling level-2 elements because of its efficiency in modeling large heterogeneous regions For modeling interfacial debonding with VCFEM, the inclusion-matrix interface in each element is lined with a series of cohesive zone springs.

Transition Elements between Level-0/1 and Level-2 Elements : To facilitate smooth transition of scales across the element boundaries, a layer of transition elements is sandwiched between these elements.

3. Numerical Example of a Composite Joint with Microstructural Debonding

A double-lap bonded joint with boron-epoxy composite as the adherents is analyzed in this example. The joint is shown in Fig. 2. An adhesive is used to bond the two composite materials. A displacement u_x is applied at the face x=0. The composite material, at the microstructural level, consists of epoxy matrix with Young's modulus, E=4.6 GPa and Poisson's ratio, ν=0.4, and boron fiber with Young's modulus, E=210 GPa and Poisson's

ratio, ν=0.3. The material properties of the isotropic adhesive is Young's modulus E=3.45 GPa and Poisson's ratio, ν=0.34.

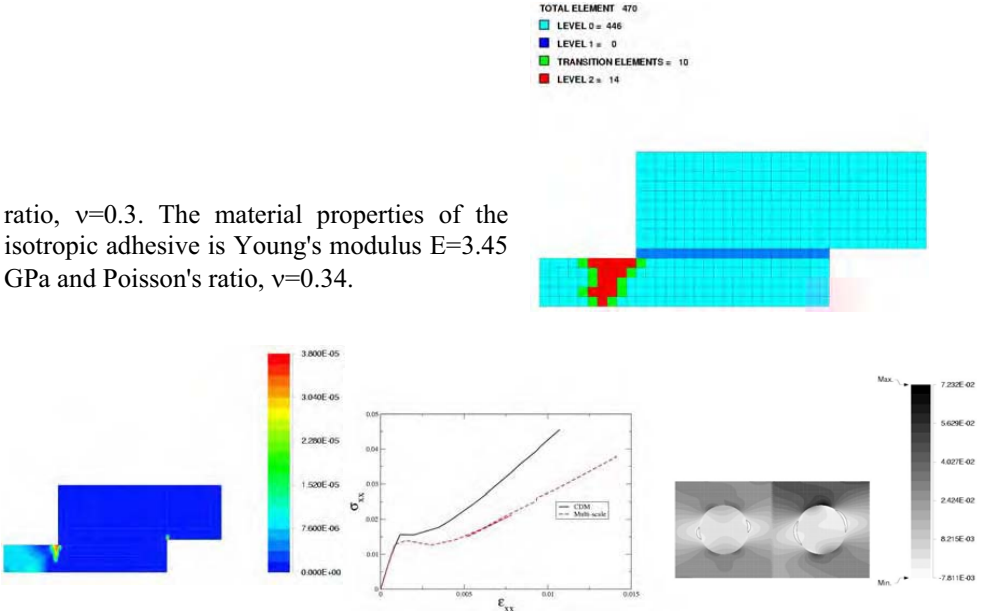

Figure 1. (a) Adhesively bonded composite joint, (b) multi-level mesh with level-0, 1, 2 and transition elements, (c) macroscopic damage distribution , (d) macroscopic stress-strain comparison between CDM and multi-scale model near point A and (e) microstructural stresses

A multi-level analysis is performed using the criteria for level-0 to level-1 transition. In the final increment, the multi-level mesh consists of 446 level-0 elements, 0 level-1 elements, 10 transition elements and 14 level-2 elements. The microscopic stress distribution and the debonding pattern compare very well for the two models. The error in the maximum stress is observed to be around 1%. Comparison is also made for the macroscopic stress-strain evolution at various locations in the structure. The CDM solution and the micromechanics solution are different in the neighborhood of localized damage at A, where level-2 solutions are needed. The limitations of the CDM in this region was observed from these results. In conclusion, the performance of the multi-level model is demonstrated to be superior from accuracy and efficiency point of view by comparing with macroscopic continuum, pure micromechanics and two-scale homogenization models. The multi-level model addresses difficult issues in solving multi-scale problems with damage and constitutes an essential tool for modeling this class of problems.

5. Acknowledgements : This work has been supported by the Air Force Office of Scientific Research through grant No. F49620-01-1-0305 and by the Army Research Office through grant No. DAAD19-02-1-0428.

6. References

1. Ghosh, S., Lee, K. and Raghavan, P., A multi-level computational model for multi-scale damage analysis in composite and porous materials, Int. J. Solids Struct., 2001, 38 (14) pp. 2335-2385.

2. Raghavan, P. and Ghosh, S. A continuum damage mechanics model for unidirectional composites undergoing interfacial debonding, Mech. of Mat. (in press)

3. Ghosh, S., Ling, Y., Majumdar, B. and Kim, R. Interfacial debonding analysis in multiple fiber reinforced composites, Mech. of Mat., 2000, 32, pp. 561-591.

VOID HARDENING IN BCC-IRON STUDIED BY ATOMIC-SCALE MODELLING

S. I. Golubov[1], Yu. N. Osetsky[2], and R. E. Stoller[1]

[1]Metals and Ceramics Division
[2]Computer Science and Mathematics Division
Metals and Ceramics division, Oak Ridge National Laboratory,
P. O. Box 2008, Oak Ridge, TN 37831-6138, Golubovsi@ornl.gov

ABSTRACT

Atomic-scale modelling permits detail simulation of the interactions between moving dislocations and particular obstacles. Such simulations should be of large enough scale to simulate a realistic dislocation density and obstacle spacing, and correctly treat long-range self-interaction between dislocation segments. Results obtained with a 2 nm void and two different atomic-scale techniques based on (1) a periodic array of dislocations (PAD) and (2) Green's function boundary conditions (GF) in alpha-Fe are presented. It is concluded that the both techniques reproduce the same critical resolved shear stress (CRSS), and similar void and dislocation modifications are observed.

1. Introduction

Understanding the dislocation processes that are controlled by atomic scale mechanisms require development of new modelling techniques. The interaction between gliding dislocations and an obstacle in its glide plane is an example of such a process. One of the most successful models [1] is based on a periodic array of dislocations (PAD) using an approach originally proposed by Baskes and Daw. PAD simulates a crystal containing initially straight edge dislocations with periodic boundary conditions along the dislocation line and in the direction of the Burgers vector. The model allows the correct configuration of the dislocation core structure to be simulated and has been successfully applied to study different type of obstacles in bcc and fcc metals (see e.g. [2, 3]). The model is simple and fast, but some limitations a rise when compared with results from macro-models based on the "single dislocation in infinite media" approach.

Another model proposed recently [4] employs 3D Green's function boundary relaxation conditions (GFBR) [5]. In this method, flexible GFBC are used along the Burgers vector and perpendicular to the slip plane. Periodicity is maintained along the dislocation line only to enable simulating the mobility of a single dislocation and its interaction with an array of obstacles [4, 6] (an efficient method to calculate the elastic displacement field was developed in [7]). This model has been used to calculate the interaction of edge dislocation with voids in bcc tungsten [4]. Since the PAD and GFBR methods are quite different, they have been applied to the same problem for comparative study. First results of such a study are presented for motion

of dislocation in perfect crystal and in crystal containing a row of 2 nm spherical voids in bcc Fe.

2. Calculation Details

An edge dislocation with Burgers vector ½[111] and {110} slip plane in bcc-iron was simulated using the many-body interatomic potential of Finnis-Sinclair type parameterized in [8]. The calculations by PAD are carried out in crystals containing (2-8)x10^6 mobile atoms whereas GFBC were applied in crystals having ~(0.2-1.0)x10^6mobile atoms. The crystal size is varied in the direction of Burgers vector only to test influence the dislocation-image interaction. To simulate motion of the dislocation a shear strain was incrementally increased with a step equal to 10^{-4}. In both types of calculation, a stress-strain curve, critical resolved shear stress (CRSS) and dislocation line shape at the CRSS has been obtained and analysed. The both techniques have been applied at T=0K.

3. Results

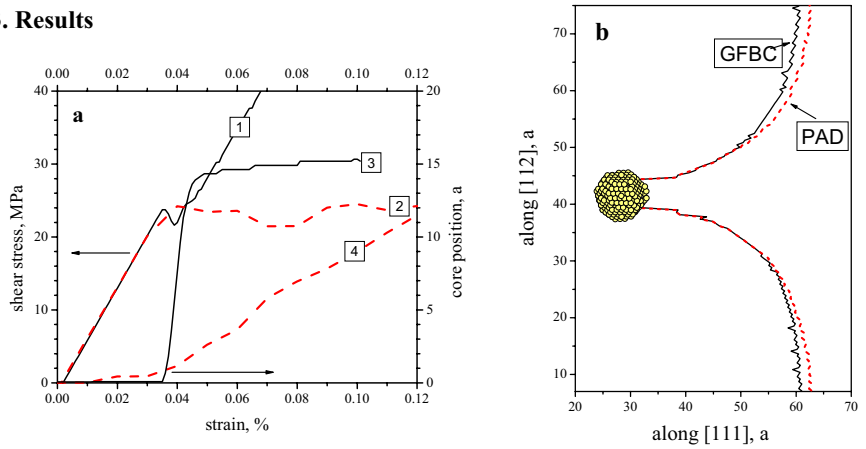

Fig. 1. (a) The stress-strain curves and core positions for the edge dislocation calculated via PAD and GFBC. 1, 2 – stress-strain for GFBC and PAD; 3, 4– core positions for GFBC and PAD. (b) Comparison of PAD and GFBC calculations of dislocation line shape at critical stress for 2 nm void at 0K.

An example of the stress-strain curves calculated for the case of dislocation glide in perfect crystal, together with the dislocation core displacement, is presented in Fig. 1. As can be seen the stress-strain curves are the same in linear elastic regime, i.e. before the dislocation moves. When the stress reaches a critical value, i.e. the Peierls stress, the dislocation moves and this motion is different in different models. Thus, in the case of PAD model the dislocation motion depends on dislocation density. In the case of GFBC, the dislocation moves continuously until interaction with boundaries compensates applied shear stress. Note that in the case of PAD the Peierls stress is the maximum stress generated in the system (curve 2 in Fig.1a) whereas in the case of GFBC the maximum stress can be infinitely high reflecting the repulsive force

between the dislocation and a boundary (curve 1 in Fig.1a). However, the value of Peierls stress calculated in the both cases is the same (τ_P~24MPa) as well as the critical strain: ε_P=0.033% (GFBC) and 0.035% (PAD).

In the case of dislocation-void interaction, a full stress-strain curve can be obtained only for the PAD [1, 2]. Therefore, a comparison between the models was made only for the dislocation line shape at the critical condition, i.e. just before it overcomes the obstacle out, and the line shape after the interaction. The former is presented in Fig.1b where one can see that both lines have very similar shape. It was observed earlier that the dislocation absorbs vacancies during the interaction with a void. It is found that in both cases the dislocation absorbs a similar number of vacancies, i.e. 11 for the GFBC and 10 for the PAD, and the shape of superjog created due to climb is also very similar.

4. Conclusions

Two atomistic-scale techniques, PAD and GFBC, have been used to study dislocation dynamics in perfect crystal and dislocation-void interaction in bcc-Fe. It was found that both techniques lead to similar results: including, the Peierls stress and strain, the dislocation line shape near the void at critical stress and atomic-scale structure of the dislocation line, and void shrinkage after dislocation-void interaction.

References

1. Yu. N. Osetsky, D.J. Bacon, An atomic level model for study the dynamic of edge dislocations in metals, Modelling Simulation Mater. Sci. Eng. 11 (2003) 427.
2. Yu. N. Osetsky, D.J. Bacon and V. Mohles, Atomic modelling of strength mechanisms due to voids and copper precipitates in α-iron, Phil. Mag. 83, Nos. 31-34 (2003) 3623.
3. Yu. N. Osetsky, D.J. Bacon, Void and precipitate strengthening in α-iron: what can we learn from atomic-level modelling?, J. Nucl. Mater. 323 (2003) 268.
4. Xiangli Liu, S.I. Golubov, C.H. Woo and Hanchen Huang, Atomistic simulations of dislocation-void interactions using Green's function boundary relaxation, Computer Modelling in Engineering & Sciences 5 /6 (2004) 527.
5. S. Rao, C Hernandez, J.P. Simmons, T.A. Parthasarathy and C. Woodward, Green's function boundary conditions in two-dimensional and three-dimensional atomistic simulations of dislocations, Phil. Mag. A 77 (1998) 231.
6. Xiangli Liu, S.I. Golubov, C.H. Woo and Hanchen Huang, Glide of Edge Dislocations In Tungsten and Molybdenum, Material Science and Engineering A365 (2004) 96.
7. Golubov S.I., Liu Xiangli, Huang Hanchen, Woo C.H., GFCUBHEX: Program to Calculate Elastic Green's functions and Displacements Fields for Applications in Atomistic Simulations of Defects in Cubic and HCP Crystals, Computer Physics Communications 137/2 (2001) 312-324.
8. G.J. Ackland, D.J. Bacon, A.F. Calder, T. Harry, 'Computer simulation of point defects in dilute Fe-Cu alloys using many-body interatomic potentials', *Philos. Mag., A* **71** (1997) 553.

Molecular Dynamics Simulations of Mechanical Properties of Boron-Nitride Nanotubes Embedded in Si-B-N Ceramics

Michael Griebel and Jan Hamaekers

**Department of Numerical Simulation, University of Bonn,
Wegelerstraße 6, D-53115 Bonn, Germany.
e-mail: griebel@ins.uni-bonn.de, hamaekers@ins.uni-bonn.de**

ABSTRACT

The elastic properties of BN-nanotubes embedded in amorphous Si-B-N matrices are examined by classical molecular dynamics simulations (MD) using the Parrinello-Rahman approach. To this end, all systems are modeled with a reactive many-body bond order potential due to Tersoff. We apply external stress and derive stress-strain curves for various tensile load cases at given temperature and pressure. In addition to Young moduli and Possion ratios, we compare radial distribution functions, average coordination numbers, ring statistics and self-diffusion coefficients in order to characterize the short-range, medium-range and long-range order of Si_3BN_5, $Si_3B_2N_6$ and $Si_3B_3N_7$ matrices. Here, our results show that $Si_3B_3N_7$ exhibits the highest Young modulus and the largest elastic range. Furthermore, we calculate stress-strain curves for BN-NTs embedded in Si-B-N matrices to predict the rates of reinforcement of the ceramics composites. Here the influence of the NT/matrix ratio on the elastic modulus is examined and we compare the derived Young moduli with predictions related to macroscopic rule-of-mixtures.

1 Introduction

Boron nitride nanotubes (BN-NTs) share many of the exceptional properties of carbon nanotubes (C-NTs). In particular, experimental studies and numerical simulations of their mechanical properties show that BN-NTs display a high Young modulus which is comparable to that of C-NTs. In contrast to C-NTs, BN-NTs exhibit an energy gap of about 4-5 eV independent of chirality, diameter and number of walls. Altogether, BN-NTs are one of the strongest insulating nanofibers and may find important uses in the reinforcement of amorphous materials. On the other hand, amorphous Si-N based systems containing B exhibit a diversity of industrial applications because of their unusual thermal and mechanical properties. Therefore, it can be expected that BN-NTs embedded in a Si-B-N matrix result in a promising future material. Note that, to our knowledge, composites of Si-B-N ceramics and BN-NTs have neither been theoretically studied nor been synthesized so far. Here, computational methods can be used to access and thus to predict, to describe and to explain characteristic properties of such future materials [1]. For large systems with thousand atoms and more, classical MD simulations are an important tool to better understand mechanical

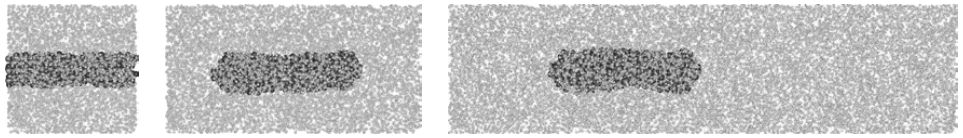

II III IV

Figure 1: Equilibrated System II, System III and System IV.

and thermal properties of BN-NT Si-B-N ceramics composites. In this work, we analyze the short-range, medium-range and long-range order and the mechanical and thermal properties of amorphous Si_3BN_5, $Si_3B_2N_6$ and $Si_3B_3N_7$ matrices by molecular dynamics simulations. Our results show that amorphous $Si_3B_3N_7$ exhibits the highest Young modulus and the largest elastic range. Therefore we concentrate on BN-NT $Si_3B_3N_7$ ceramics composites. Here, we derive stress-strain curves at various temperatures for different NT/matrix ratios. Finally, we compare our results with two macroscopic rule-of-mixtures, which are commonly used to predict the Young modulus and thus to derive the rate of reinforcement of composites.

2 Computational Methods

In our MD simulations, we use a reactive many-body bond-order potential model due to Tersoff, which is able to accurately describe covalent bonding. Because all interatomic terms are of short range, we use the well-known linked cell technique [1]. A straightforward domain decomposition approach then allows for a parallel implementation, which results in a parallel complexity of the order $\mathcal{O}(N/P)$ [2, 1]. Here, N denotes the number of particles and P the number of processors. To deal with the equilibration of the systems at given temperature and pressure, we apply a so-called Parrinello-Rahman-Nosé Lagrangian. Based on this method, we use an additional external stress-tensor to account for various tensile load cases [3, 4]. In particular, we increase or decrease linearly the uniaxial external stress components over time to generate stress-strain curves. Then, assuming a linear stress-strain relationship, we exploit Hooke's law to derive Young moduli and Poisson ratios. Furthermore, to characterize the short-range order of amorphous structures, we calculate pair correlation functions as well as average coordination numbers [5]. To characterize long-range order properties, like the atomic transport properties, we compute the mean square displacements to obtain the self-diffusion coefficients [1]. Finally, we analyze shortest-path rings of the interconnection networks, which are related to the medium-range order. Here, we improved the algorithm of Franzblau by exploiting the sparsity of the distance matrix of the interconnection graph. This way, we obtain a computational complexity of the order $\mathcal{O}(Nn^{\frac{k}{2}} \log k)$ instead of $\mathcal{O}(N^2)$ to calculate all shortest-path rings of maximal length k of a given interconnection network, where n denotes the maximal coordination number [5].

3 Numerical Experiments, Results and Discussion

We have incorporated the computational methods described in section 2 into our existing MD software package TREMOLO, which is a load-balanced distributed memory parallel code [1]. All experiments were performed on our PC cluster Parnass2, which consists of 128 Intel Pentium II 400 MHz processors connected by a 1.28 GBit/s switched Myrinet. We first equilibrated the following periodic systems under normal pressure at 300 K, 600 K, 900 K, 1200 K and 1500 K; see also Fig. 1:

- Amorphous Si_3BN_5, $Si_3B_2N_6$, and $Si_3B_3N_7$ with 3831, 4070, and 4254 atoms.
- An about 44 Å long capped BN-NT with 456 atoms.
- *System I*: An about 36 Å long $(12, 0)$ continuous BN-NT with 360 atoms.
- *System II*: BN-NT of System I embedded in a $Si_3B_3N_7$ matrix with 4254 atoms.
- *System III*: Capped BN-NT embedded in a $Si_3B_3N_7$ matrix with 8508 atoms.
- *System IV*: Capped BN-NT embedded in a $Si_3B_3N_7$ matrix with 17016 atoms.

For the Si_3BN_5, $Si_3B_2N_6$, and $Si_3B_3N_7$ matrices, we computed pair correlation functions $g_{\alpha-\beta}$, average coordination numbers $n_{\alpha-\beta}$ and self-diffusion coefficients D_α, where $\alpha, \beta \in \{\mathrm{Si}, \mathrm{B}, \mathrm{N}\}$; see also Fig. 2. Here, we exploited the minima of $g_{\alpha-\beta}$ to determine the bonding distances and thus to calculate the average coordination numbers as well as to analyze shortest-path rings. Our results show that the self-diffusion coefficients, the average coordination numbers $n_{\mathrm{Si-Si}}$, $n_{\mathrm{B-N}}$ and $n_{\mathrm{N-B}}$ significantly increase and the average coordination numbers $n_{\mathrm{Si-N}}$ and $n_{\mathrm{N-Si}}$ significantly decrease for temperatures larger than 1200 K. Also witch respect to the tensile test, our computed stress-strain curves show that the Young moduli for a temperature of 1500 K is significant lower than for 1200 K; see Fig. 3. Furthermore, the results of the tensile test show that the fraction of the shortest-path rings with length $5 \leq k \leq 10$ decrease with an increase of the external stress. Finally, the stress-strain curves show that $Si_3B_3N_7$ has the highest Young moduli and the largest the elastic range compared to $Si_3B_2N_6$ and Si_3BN_5; see Fig. 3.

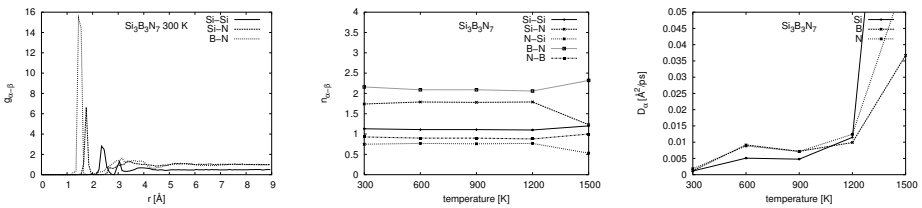

Figure 2: Partial radial distribution functions, average coordination numbers and self-diffusion coefficients for equilibrated $Si_3B_3N_7$.

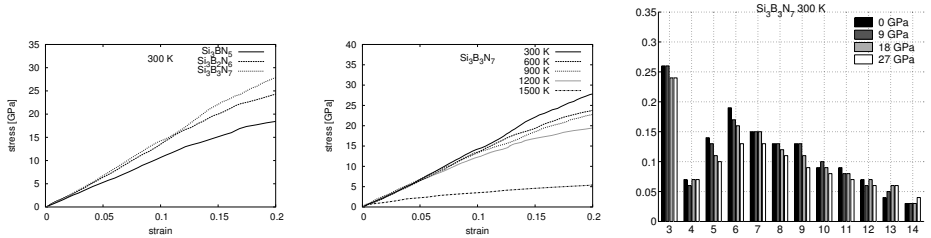

Figure 3: Stress-strain curves and distribution of shortest-ring paths for tensile tests.

For the composites System II, System III and System IV we performed tensile tests to compute the Young moduli and thus the reinforcement rates; see Tab. 1. Here, our results predict a reinforcement of about 12% in the case of System III and of about 6% in the case of System IV. For a nanocomposite, a macroscopic rule-of-mixtures (ROM) can be used to estimate its Young modulus depending on the volume fraction Ω_f of the nanofiber, the Young modulus E_f of the nanofiber and the Young modulus E_m of the matrix. This rule reads as

$$E_c = \Omega_f E_f + (1 - \Omega_f) E_m \,,$$

where E_c denotes the predicted Young modulus of the composite. For System II this estimation results in a relative error of 5% and less; see Tab. 2. For System IV we obtain values between 1.7% and 6.0% and for Sytem III we get values between 5.8% and 7.5% depending on the temperature. In the case of System III and System IV the relative error can be further reduced by using an extended ROM (EROM), which additionally takes the geometric distribution of the nanofiber into account:

$$E_c^{\mathrm{ex}} = \left(\frac{1}{E_m} \frac{(L - L_c)}{L} + \frac{1}{E_c} \frac{L_c}{L} \frac{A}{A_c} \right)^{-1} .$$

Here, E_c^{ex} denotes the predicted Young modulus of the composite, L_c denotes the length of the nanofiber, L denotes the length of the system in direction of the longitudinal axis, R_{in} denotes the inner radius of the nanotube, A denotes the area of the transverse section and A_c is defined as $A_c = A - \pi R_{\mathrm{in}}^2$; compare also Fig. 4.

Table 1: Calculated Young moduli E and Possion ratios ν.

	Tensile								
	$Si_3B_3N_7$		System I	System II		System III		System IV	
T [K]	E [GPa]	ν	E [GPa]	E [GPa]	ν	E [GPa]	ν	E [GPa]	ν
300	132.1	0.27	696.1	181.5	0.24	150.2	0.25	139.1	0.27
600	131.7	0.30	671.6	171.8	0.30	148.9	0.27	136.6	0.29
900	130.0	0.29	674.4	169.0	0.32	145.4	0.30	140.7	0.31
1200	129.5	0.32	657.8	164.2	0.30	145.1	0.32	140.1	0.36

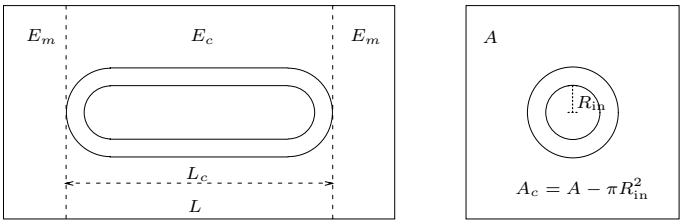

Figure 4: Schematic diagrams with respect to the EROM.

Table 2: The relative errors of the ROM and the EROM.

	System II	System III		System IV	
T [K]	ROM	ROM	EROM	ROM	EROM
300	-0.0284	0.0614	0.0356	0.0495	0.0279
600	0.0091	0.0580	0.0332	0.0598	0.0393
900	0.0143	0.0715	0.0456	0.0167	-0.0037
1200	0.0492	0.0749	0.0490	0.0198	-0.0012

4 Concluding Remarks

Our simulation results show that BN-NTs can be used to reinforce Si-B-N ceramics, at least theoretically. Now, experimental studies are needed to synthesize this suggested composite material also in practice and to determine its characteristic properties. More details related to our methods and results are given in [5].

5 Acknowledgments

This work was supported by a grant from the *Schwerpunktprogramm 1165* and the *Sonderforschungsbereich 611* of the *Deutsche Forschungsgemeinschaft*.

References

[1] M. Griebel, S. Knapek, G. Zumbusch, and A. Caglar. *Numerische Simulation in der Molekü ldynamik. Numerik, Algorithmen, Parallelisierung, Anwendungen*. Springer, Berlin, Heidelberg, 2003.

[2] A. Caglar and M. Griebel. On the numerical simulation of fullerene nanotubes: $C_{100.000.000}$ and beyond! In R. Esser, P. Grassberger, J. Grotendorst, and M. Lewerenz, editors, *Molecular Dynamics on Parallel Computers, NIC, Jülich 8-10 February 1999*. World Scientific, 2000.

[3] M. Griebel and J. Hamaekers. Molecular dynamics simulations of the elastic moduli of polymer-carbon nanotube composites. *Computer Methods in Applied Mechanics and Engineering*, 193(17–20):1773–1788, 2004.

[4] M. Griebel and J. Hamaekers. Molecular dynamics simulations of polymer-carbon nanotube composites. In M. Rieth and W. Schommers, editors, *Handbook of Theoretical and Computational Nanotechnology*. American Scientific Publishers, 2005. In preparation.

[5] M. Griebel and J. Hamaekers. Molecular dynamics simulations of mechanical properties of boron-nitride nanotubes embedded in Si-B-N ceramics. SFB 611 preprint, University of Bonn, 2004.

FIRST-PRINCIPLES EQUATION OF STATE FOR ENERGETIC INTERMETALLIC MIXTURE

X. Lu, and S. Hanagud
School of Aerospace Engineering, Georgia Institute of Technology, Atlanta, GA 30332-0150

Abstract: In this paper, thermodynamically complete equation of state P=P(ρ,T) for a intermetallic mixture of nickel and aluminum with porosity is obtained from first principle calculations for pressures up to 300GPa and temperatures up to 3000K. The calculations for the static-lattice equation of state (EOS) are carried out in the framework of density functional theory (DFT), using generalized gradient approximations, ultrasoft psuedopotentials and projector augmented wave approach. The phonon modes are calculated by density functional perturbation theory (DFPT). The lattice thermal contributions are obtained by populating phonon modes according to the Boltzmann statistics. The electronic thermal contributions are obtained by populating electron band structure according to the Fermi-Dirac statistics. Firstly, the EOS for each species is obtained by ab initio prediction of ground state energy and thermal contribution. Then, the EOS of mixture is obtained by using various mixture theories according to the mixture architecture. The effects of porosity on the EOS are introduced by considering the air as a third component in the mixture. The comparisons of the EOS for nickel and aluminum obtained from existing shock Hugoniot data show good agreement with the theoretical results.

Ab Initio Equation of State

The objective of this paper is to predict the isotropic equation of state (EOS) of an energetic intermetallic mixture of nickel and aluminum from quantum-mechanical methods. This type of intermetallic material can possess both high-energy content and high strength and therefore has great potentials in the applications of debris-free explosions after improving its energy release rate. The study of this type of materials in the shock physics includes the investigation of the shock-induced chemical reactions and the material synthesis techniques by using shock consolidation techniques. All of these studies require the complete information on EOS.

First, we discuss the approach to obtain EOS of a crystalline system. In crystalline phase, each ion vibrates about a fixed average position. The internal energy of the crystalline system can be obtained from *ab initio* calculations as the sum of ground state energy as a function of the specific volume and thermal contribution as a function of both the specific volume v (or density ρ) and temperature T. Specifically, the internal energy $e(v,T)$ can be split into the cold curve $e_c(v)$ (zero-temperature frozen-ion isotherm) and the thermal contributions from the ions $e_I(v,T)$ and electrons $e_e(v,T)$[1].

(a) *The cold curve energy* $e_c(v)$, also called as the electron ground state energy, is the energy of the system with electrons in the ground state and ions in their crystallographic sites associated with some specific volume. It is obtained from quantum mechanical calculations as the zero-point energy of the system for a given lattice parameter (a measure of the specific volume of the system). The configuration of the lattice is held not changed and only the scale (or lattice parameters) varies.

(b) *The electron thermal energies* $e_e(v,T)$ are caused by perturbations of the electron occupation numbers from their ground states. The electron thermal contribution is calculated from the electron band structure by populating the calculated states according to the Fermi-Dirac

[1] Swift, D. C., Ackland, G. J., Hauer, A. and Kyrala, G., A., First principle equations of state for simulations of shock wave in silicon. Phys. Rev. B, v. 64, 2001, pp. 214107 1- 214107 – 14

statistics. In the assumptions of the psuedopotential approach, the band structure refers to the outer electrons only and the core electrons are assumed to be occupied at all temperatures. The energy levels are used directly in estimating $e_e(v,T)$ or are collected into a numerical distribution function.

(c) *The lattice thermal energies* $e_l(v,T)$ is the contribution of thermal excitation of ions, which is calculated from phonon modes of lattice. Phonons represent the internal motions of a lattice about its center of mass by perturbations of the ion positions from their ground states. The phonon modes are then obtained from the eigenvalue problem of the structure defined by a given set of lattice parameters with the squared phonon frequencies representing the eigenvalues of the stiffness matrix. The variation of lattice thermal energy $e_l(T)$ with temperature at a given density is then found by populating the phonon modes according to the Boltzmann statistics.

(b) *Thermodynamically Complete EOS*: After obtaining the total internal energy of the lattice system, the associated free energy $f(v,T)$ can be obtained as $f(v,T) = e_c(v) + f_l(v,T)$. The thermodynamically complete EOS can be constructed by differentiating f with respect to the specific volume v, $P(v,T) = \frac{\partial f(v,T)}{\partial v}$ (1)

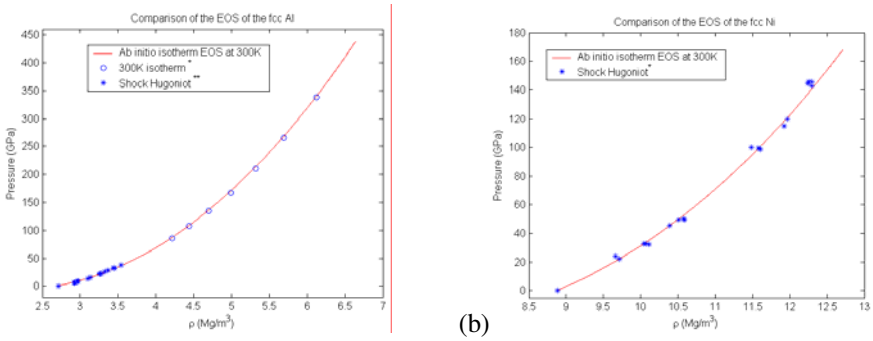

(a) (b)

Figure 1. Comparisons of EOS by ab initio isotherm EOS at 300K and shock Hugonioit. (a) Al, experimental data from Thadhani (low pressures) and ref[2] (high pressures, with assumed ρ_0=2.67kg/m^3); (b) Ni, experimental data from Los Alamos National Laboratory.

Results

For the calculations, we choose discrete lattice parameters 'a', i.e. discrete specific volume v. Therefore, we can calculate the free energy at discrete v and T values. The accuracy of the differential in equation (1) depends on the intervals of discrete v and T. Higher order polynomials are used to interpolate the values between these intervals. Discrete 'a', chosen for fcc Al, are the values from 3.0 to 4.0 Å at a selected interval. Extra calculations are made at the points close to the equilibrium lattice parameter 4.04 Å. Similarly, discrete 'a', chosen for the fcc Ni, are from 2.7 to 3.5 at a selected interval. Smaller interval is chosen for the values between 3.4 and 3.52Å, which is the equilibrium lattice parameter. Following the procedure, we obtained thermodynamically complete EOS for Al and Ni, respectively. The ab initio 300K isotherm EOS for Al and Ni is compared with their shock Hugoniot data. The comparisons are shown in Figure 1a and 1b, respectively.

A mixture theory is applied as a weighted combination of two limiting cases, one of which is equivalent to a series combination of the components (homobaric mixture theory) and the other

[2] Nellis, W.J, Moriarty, J.A., Mitchell, A.C., Ross, M. and Dandrea, G.R., "Metals physics at ultrahigh pressure: Aluminum, copper and lead as prototypes," Phys. Rev. Lett., v. 60, n. 4, 1988, pp. 1414 – 1417.

is equivalent to a parallel combination of the components (uniformly blended mixture theory). In the serial case, the interface between components is assumed to be in mechanical equilibrium, and every component occupies its own fractions of volume and mass. While in the parallel case, different components deform at the same strain. Initially, the EOS of each component is known or obtained by the ab initio techniques. For the homobaric mixture theory, given P and T, every component of mixture experiences the same P and T. We can obtain the density of every individual component $\rho_i(P,T)$ (i=1, 2, …, n) from its known EOS. For the uniformly blended mixture theory, given the density of mixture ρ, we can solve for the corresponding density of every component ρ_i. From the EOS of each component, we can determine the component pressure $P_i=P_i(\rho_i,T)$. The 300K isotherm EOS of mixture, obtained by using these two mixture theories, are compared in **Figure 1**. As expected, the EOS from homobaric mixture theory is 'softer' than that from uniformly blended mixture theory. In reality, the nature of mixture is intermediate to that of these two idealized mixtures and hence can be modeled as a weighted combination of the two cases.

Currently, the available techniques do not permit the synthesis of intermetallic mixtures up to a full density (without any voids). Usually, intermetallic mixtures synthesized in the laboratory only have densities in the range of 75% - 88% of the material with no voids. Some researchers think of that the existence of porosity and its collapse-induced dissipation is necessary to transfer energy to overcome the energy barriers for initiation of chemical reactions and release the stored energy in the energetic mixture. Therefore, the EOS of porous mixture is very important for the applications of these energetic materials.

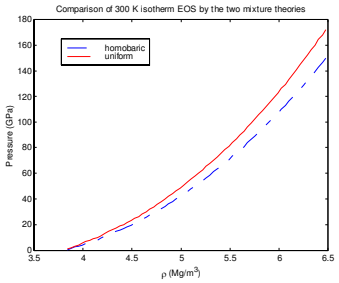

Figure 2. Comparison of the 300K isotherm EOS of mixture by using homobaric and uniform mixture theories.

To construct the EOS of a porous mixture, we introduce the porosity (or air) as a third component consisting of the mixture. We use van der Waals EOS for air, which is suitable at relatively high pressures (for a gas). When introducing air as the third component, which has no stiffness compared to the other two solid components, the mixture is very soft at low pressures, which is indicated by the observation that the pore collapse occurs at very low pressures. Therefore, the homobaric assumption is more appropriate to model the porous mixture at low pressures. For a 3Al+Ni mixture of 15% porosity, we use the homobaric mixture theory to approximate the EOS of porous mixture. Thermodynamically EOS is calculated and presented in Figure 3a. The 10^{-3}, 300 and 1000K isotherm EOS are presented in Figure 3b.

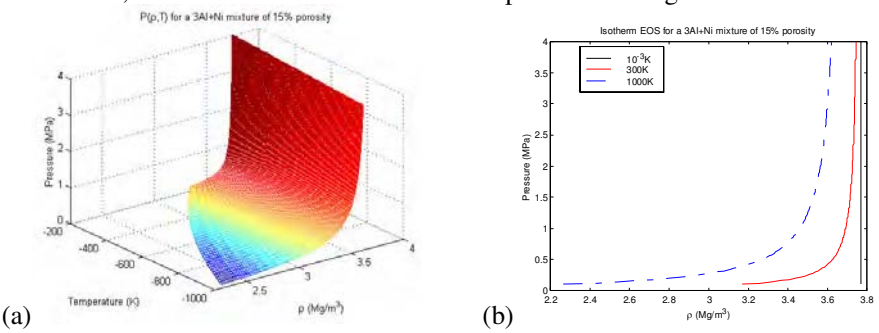

Figure 3. (a)The fully thermodynamically EOS of a 3Al+Ni mixture of 15% (volume) porosity; (b)The isotherm EOS of a 3Al+Ni mixture of 15% (volume) porosity at 10^{-3}, 300, and 1000 K.

REPRESENTATION OF THE DISLOCATION CONTENT BY A DISLOCATION DENSITY VECTOR

Craig S. Hartley

AFOSR, 4015 Wilson Blvd, Room 713, Arlington, VA 22203 USA

ABSTRACT

Describing deformation at the micro and nano-scale in terms of dislocation motion requires recognizing that deformation occurs by the collective motion of groups of dislocations. One of the chief challenges in relating continuum models of deformation to discrete dislocation theory is the difficulty of describing the dislocation content in terms of a field variable. This paper proposes a measure of dislocation content, the dislocation density vector, that specifies not only the resultant length of mobile dislocations on each active deformation system but also its net screw-edge character. The Nye tensor, which describes the resultant Burgers vector flux of dislocations crossing a plane of known orientation, is the sum of the dyadic products of the dislocation density vector and the Burgers vector for each active slip system. Although this vector is determined from volume averages of the quantities taken over a suitable Representative Volume Element (RVE) and does not reflect the non-local character of the distribution, it can be a useful concept in describing the deformation due to the collective motion of dislocations and in formulating constitutive equations based on specific models of rate-controlling mechanisms.

1. INTRODUCTION

In real physical systems, measurement of the dislocation content is difficult to accomplish directly. Early studies employed selective etching of strained regions where dislocations intersected the surface of crystals. Direct measurements are possible on thin sections observed in transmission electron microscopy and in crystals transparent to electromagnetic radiation provided the dislocation density is sufficiently low. Recent developments in microdiffraction techniques relate the lattice strain distribution to the distribution of dislocations from which they originate.

Dislocation arrays obtained by dislocation dynamics simulations present a more favorable situation for quantitative determination of parameters that describe the dislocation array, since direct measurements can be made of the lengths and orientations of dislocation

segments. This can be accomplished even more rapidly be applying stereological techniques to the simulated array. The following discussion presents a method of determining the distribution function for dislocation segments as a function of the orientation of the segment by counting the intersections of dislocations with planes of observation oriented at various angles with respect to reference directions. This procedure permits the determination of the length and orientation of the dislocation density vector, which is a description of the volume average of the length per unit volume of dislocation lines in a representative volume element (RVE) of the simulation.

2. THE DISLOCATION DENSITY VECTOR

The Nye tensor [1] (Geometrically Necessary Dislocation (GND) tensor), $\boldsymbol{\alpha}^{(\lambda)}$, gives the resultant Burgers vector flux*, $\mathbf{B}^{(\lambda)}$, due to all dislocations with Burgers vector $\mathbf{b}^{(\lambda)}$ on the λ^{th} slip system per unit area normal to the unit vector, $\mathbf{n}$:

$$\mathbf{B}^{(\lambda)} = \boldsymbol{\alpha}^{(\lambda)} \cdot \mathbf{n} \,. \tag{1}$$

The ij^{th} component of the Nye tensor is the component parallel to the x_i direction of the resultant Burgers vector flux per unit area normal to the x_j direction, so $\mathbf{B}^{(\lambda)}$ can be expressed as the algebraic sum of contributions due to dislocations of opposite sign. At the intersection of each dislocation segment with the section plane, assign a unit tangent vector, $\mathbf{t}^{(\lambda)}$, related to $\mathbf{b}^{(\lambda)}$ by the FS/RH rule of Bilby *et al*.[2] with positive unit normal to the slip plane, $\mathbf{v}^{(\lambda)} = (\mathbf{t}^{(\lambda)} \times \mathbf{b}^{(\lambda)})/|\mathbf{b}^{(\lambda)}|$. Give a dislocation segment and its intersection the sign of the product $(\mathbf{t}^{(\lambda)} \times \mathbf{b}^{(\lambda)}) \cdot \mathbf{v}^{(\lambda)}$. Pure screw segments are positive if $\mathbf{b}^{(\lambda)} \cdot \mathbf{t}^{(\lambda)} > 0$. The Nye tensor for the slip system, $\boldsymbol{\alpha}^{(\lambda)}$, can be expressed as the dyadic product of $\mathbf{b}^{(\lambda)}$ and a resultant dislocation density vector, $\overline{\boldsymbol{\rho}}^{(\lambda)} = \left(\boldsymbol{\rho}^{+(\lambda)} - \boldsymbol{\rho}^{-(\lambda)}\right)$:

$$\boldsymbol{\alpha}^{(\lambda)} = \mathbf{b}^{(\lambda)} \overline{\boldsymbol{\rho}}^{(\lambda)} \,. \tag{2}$$

The positive and negative dislocation density vectors, $\boldsymbol{\rho}^{\pm(\lambda)}$, have magnitudes equal to the total length per unit volume of positive and negative dislocation segments on the λ^{th} slip system. The directions of $\boldsymbol{\rho}^{\pm(\lambda)}$ depend on the edge-screw character and are determined as described below.

Consider a plane with unit normal, $\mathbf{n}$, and area, $A(\mathbf{n})$, passing through the centroid of a simulation cell. Denoting the number of positive and negative dislocation segments of the λ^{th} slip system intersecting $A(\mathbf{n})$ as $N^{+(\lambda)}$ and $N^{-(\lambda)}$, respectively, the length per unit volume of each type, projected parallel to $\mathbf{n}$ is

$$N^{\pm(\lambda)}(\mathbf{n}) = \boldsymbol{\rho}^{\pm(\lambda)} \cdot \mathbf{n} \,. \tag{3}$$

To determine $\boldsymbol{\rho}^{\pm(\lambda)}$ pass M section planes with unit normals $\mathbf{n}^{(M)}$ through the computational cell containing dislocation lines generated by a dislocation dynamics simulation. Then determine the number and sign of dislocation intersections for each slip system that intersects the plane, $N^{+(\lambda)}(\mathbf{n}^{(M)})$ and $N^{-(\lambda)}(\mathbf{n}^{(M)})$. This consists of counting the signed intersections of dislocation lines from each slip system using the convention

* Note that $B^{(\lambda)}$ has dimensions ℓ^{-1} since it represents the Burgers vector per unit area.

described above. Finally, form the (1 x M) matrices $\mathbf{N}^{+(\lambda)}$ and $\mathbf{N}^{-(\lambda)}$ with elements $N^{+(\lambda)}(\mathbf{n}^{(M)})$ and $N^{-(\lambda)}(\mathbf{n}^{(M)})$, respectively, and the (3 x M) matrix **S** whose columns are the components of the corresponding unit vectors, $\mathbf{n}^{(M)}$, along the reference coordinate axes. Then the components of $\boldsymbol{\rho}^{\pm(\lambda)}$ that minimize the residuals of equation (3) are given by [3]:

$$\mathbf{N}^{\pm(\lambda)} \cdot \left[\left(\tilde{\mathbf{S}} \right) \cdot \left(\mathbf{S} \cdot \tilde{\mathbf{S}} \right)^{-1} \right] = \boldsymbol{\rho}^{\pm(\lambda)} \tag{4}$$

where the tilde indicates the transpose and (-1), the inverse of the matrices. Repeating this procedure for all active slip systems gives the corresponding values of $\boldsymbol{\alpha}^{(\lambda)}$ by equation (2). The value of $\boldsymbol{\alpha}$ for the simulation volume is the sum of the contributions from each slip system.

The orientations of $\boldsymbol{\rho}^{\pm(\lambda)}$ relative to the slip direction are given by the angle, $\Psi^{\pm(\lambda)}$, where

$$\cos \Psi^{\pm(\lambda)} = \frac{\mathbf{b}^{(\lambda)} \cdot \boldsymbol{\rho}^{\pm(\lambda)}}{\left| \mathbf{b}^{(\lambda)} \right| \left| \boldsymbol{\rho}^{\pm(\lambda)} \right|} . \tag{5}$$

The normal to the slip plane of the system follows from its definition:

$$\mathbf{v}^{(\lambda)} = \frac{\pm \left(\boldsymbol{\rho}^{\pm(\lambda)} \times \mathbf{b}^{(\lambda)} \right)}{\left| \boldsymbol{\rho}^{\pm(\lambda)} \right| \left| \mathbf{b}^{(\lambda)} \right| \sin \Psi^{\pm(\lambda)}} . \tag{6}$$

The screw components of $\boldsymbol{\rho}^{\pm(\lambda)}$, $\rho_S^{\pm} = \left| \boldsymbol{\rho}^{\pm(\lambda)} \right| \cos \Psi^{\pm(\lambda)}$. The edge components of $\boldsymbol{\rho}^{\pm(\lambda)}$ lie in the slip plane, normal to $\mathbf{b}^{(\lambda)}$ with magnitude $\rho_E^{\pm} = \left| \boldsymbol{\rho}^{\pm(\lambda)} \right| \cos \Psi^{\pm(\lambda)}$. Corresponding components of the resultant dislocation density vector are formed from the definition above.

3. CONCLUSION

The dislocation density vectors, $\boldsymbol{\rho}^{\pm(\lambda)}$, are useful field variables for representing the dislocation content and character of a collection of dislocations from different slip systems contained in a RVE. The Nye tensor and curvature tensor can be expressed in terms of the resultant dislocation density vector, $\bar{\boldsymbol{\rho}}$, and defined as field variables associated with the centroid of the RVE [1].

4. REFERENCES

[1] J. F. Nye, "Some Geometrical Relationships in Dislocated Crystals", Acta Met., **1**, 153 (1953).

[2] B. A. Bilby, R. Bullough and E. Smith, "Continuous Distributions of Dislocations", Proc. Roy. Soc., A **231**, 263 (1955).

[3] O. Fischer, "Method of Least Squares", Survey of Applicable Mathematics, edited by K. Rektorys, The MIT Press, Cambridge, MA, 1285 (1969).

Interphase and size effect in nanocomposites. Elastic behavior

E.Hervé[1,2], V.Marcadon[1], A.Zaoui[1],

[1]Laboratoire de Mécanique des Solides, Ecole Polytechnique,
C.N.R.S, UMR 7649 F-91128 Palaiseau cedex, France.
[2]Université de Versailles, 45 Av des Etats Unis, 78035 Versailles Cedex, France,
herve@lms.polytechnique.fr

ABSTRACT

Reinforced polymers are expected to exhibit specific mechanical properties when the particle size tends towards the characteristic lengths of polymer chains. Such a size effect can be explained by the existence of an interphase of specific properties no longer negligible at nanoscopic and microscopic scales or, by the small distances between particles. To take into account those two effects, a speculative simple micromechanical model is used here.

1 INTRODUCTION

This paper reports on the possibilities of the micromechanical models derived from the so-called "morphologically representative pattern approach" (MRP-based approach) to express some particle size effect. In what follows, after a brief reminder of the way the MRP-based approach works (section 2), this method is first applied to the case of reinforced polymers with the presence of an interphase around the particles to show that there is an intrinsic size effect (section 3), and then is used to predict an indirect dependence of the overall behavior of matrix-inclusion composites on the particle size, scaled by the mean distance between nearest neighbor particles (section 4),.

2 THE MORPHOLOGICALLY REPRESENTATVE PATTER-BASED APPROACH

The MRP-based approach ([1], [2]) derives from a generalization of the basic idea of Hashin's Composite Sphere Assemblage. A special case of such a "generalized Hashin assemblage" is obtained when the different pattern families are constituted with n-layered spheres. The associated self-consistent model ([3]), which is derived with help of the so-called "(n+1)-phase model" [4] is used in the following for the description of various size effects. In the case of composites made of particles with the same size (with the diameter d), two morphologically representative pattern have been used: one made of particle surrounded by matrix (with or without an interphase) and the second one with matrix only. Let c_{max} denote the volume fraction of pattern 1 and (1- c_{max}) the volume

fraction of pattern 2. Let c and c_1 be the volume fraction of inclusions in the whole composite and in pattern 1, respectively. There is a relationship between those two volume fractions: $c_1 = \frac{c}{c_{\max}} = \left(\frac{d}{\lambda}\right)^3$, where λ denotes the mean distance between nearest neighbors. The matrix shell thickness of the composite sphere can then be estimated as half the mean distance between nearest neighbors in a random packing of spheres with the diameter *d*. Although the correspondence is only an indirect one because isotropy is supposed here, reference can be made to cubic lattices. c_{max} is considered here, for the sake of simplicity, as a single parameter depending on the type of packing.

3 EFFECT OF THE PRESENCE OF AN INTERPHASE

Several choices of micromechanical models (equivalent for small volume fraction of inclusions) have been made to deal with the presence of an interphase :

(a) One morphologically representative pattern-based model: by using the so-called "(n+1)-phase model" [3].

(b) A two morphologically representative pattern-based model: In the case of a composite made of particles with the same size, a second morphologically representative pattern has to be used and only matrix constitutes that second pattern. The volume fraction of pattern 1 (named c_{max}) has been chosen here as $\pi\sqrt{2}/6$ ($\approx .74$) .

(c) A two step-based model: to deal with composites with non percolated matrix.

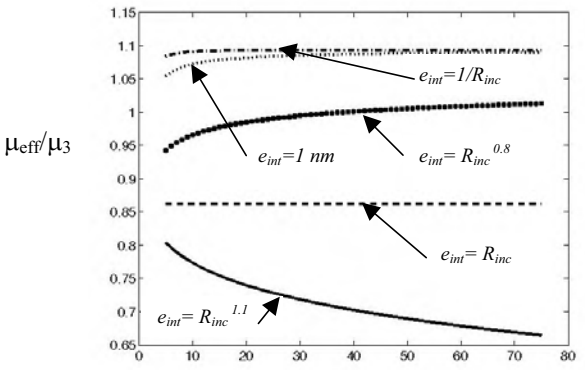

Figure 1: Normalized effective shear modulus μ_{eff}/μ_3 versus the radius of particles R_{inc} for $K_1/K_3=10$, $K_2/K_3=0.5$, $\nu_1=0.16$, $\nu_3=\nu_2=0.35$, C=0.45%

In order to study the behavior of composites where the thickness of the interface layer is not proportional to the radius of the corresponding particles (if yes, there is no size effect) let us write $e_{int}=f(R_{inc})$ where e_{int} denotes the thickness of the interphase and

R_{inc} the radius of the particles. Several functions have been considered and in each case, the size effect we get on the behavior of the studied composite is plotted in Fig. 1.

4 EFFECT OF THE DISTANCE BETWEEN PARTICLES

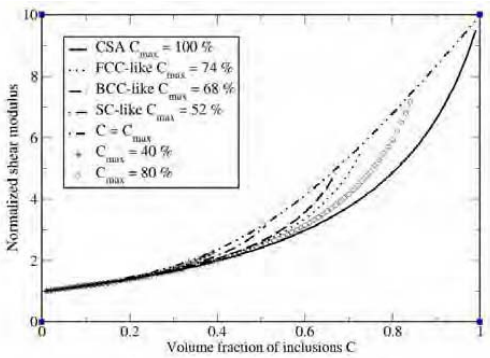

Figure 2: Particle size dependence of the effective shear modulus for different packings represented by c_{max} for $\mu_i/\mu_m = K_i/K_m = 100, \nu_i = \nu_m = 0.125$

In the previous section we have considered the presence of an interphase with a given value of the parameter c_{max}, which corresponds to a particular packing of spheres. A way of taking into account the mean distance between particles is to consider different values of c_{max} (cf Fig. 2) . It can be noticed that, for a given volume fraction c and a fixed value of λ the stiffening efficiency of the particles (which is minimum for the CSA) is increasing with the particle size.

4 CONCLUSION

The above examples are an illustration of the fact that improved micromechanical models, developed within a fully classical framework, can predict intrinsic as well as relative size effects through an adequate description of the material morphology

References

1. C. Stolz, A.Zaoui, Comptes Rendus de l'Académie des Sciences, 312, série II, 143 (1991)
2. M. Bornert, C. Stolz, A. Zaoui, J. Mech. Phys.Solids 44 (3), 307(1996).
3. M. Bornert, E. Hervé, C. Stolz, A. Zaoui, Appl. Mech. Rev., 47, Part 2, 66 (1994)
4. E. Hervé, A. Zaoui, International Journal of Engineering and Sciences 31 (1), 1 (1993)

Comparison of Mean Field Homogenisation Methods: Heterogeneous materials with random microstructure

P. Kanouté and J.L. Chaboche
Structure and Damage Mechanics Department
ONERA, Office National d'Etudes et de Recherches Aérospartiales,
92322 Chatillon, France

ABSTRACT

This paper investigates the quality and the relevance of different mean field homogenisation techniques for scale changes in the micro-to-macro elastoplastic analysis of heterogeneous materials. For this purpose, composite configurations with random or ordered microstructure are considered. Using reference solutions obtained by finite element analyses with periodic boundary conditions on unit cells, acting as representative volume elements (RVEs) of the material, we analyse the limitations and advantages of three mean field homogenisation techniques: the Incremental tangent method, the Affine method and the Transformation Field Analysis approach.

1 Introduction

The development of homogenisation procedures allowing to compute the non-linear effective behaviour of heterogeneous materials from the properties of their constituents or microstructure is a field of research that has undergone many upheavals in recent years and is still far from being stable. Non-linear estimates for the effective properties of heteregeneous materials can be traced back to the classical work of Taylor [1] on the elastoplasticity of polycristals, followed by the work of Kröner [2] through a self-consistent procedure. The incremental formulation of the self-consistent procedure is proposed later by Hill [3]. This work has spawned different models, namely the Affine method developed recently by R. Masson and A. Zaoui [5]. The present paper lies within this context by presenting the application of several homogenisation formulations, commonly used or recently developed, to predict the overall behaviour of such materials. It lays emphasis on the determination of the non-linear effective properties of composite materials made up of a random distribution of spherical or cylindrical inclusions in an elastoplastic matrix.

2 Numerical simulations of RVEs: random and ordered microstructures

Several simulations were first carried out in the framework of the periodic homogenisation which allows to describe the fields on the scale of the heterogeneities while respecting exacly equilibrium, compatibility and behaviour. Several inclusion repartitions were generated. The inclusions are isotropic elastic and the matrix is governed by a J_2-flow theory with a power law for isotropic hardening. The figure 1a illustrates an example of the plastic strain fields

obtained for a cylindrical inclusion arrangement among the materials. It has to be noticed that such material configuration allows to use a two-dimensional unit cell. The overall stress versus overall strain responses for uniaxial tensile loadings are given in the figure 1b for several random fiber arrangements and compared to a regular one. It can be observed that the composite with an ordered microstructure delivers a softer response than the composites with a random microstructure. This can be explained by the existence in random microstructure of regions containing closely packed fibers which constrain the matrix plastic flow.

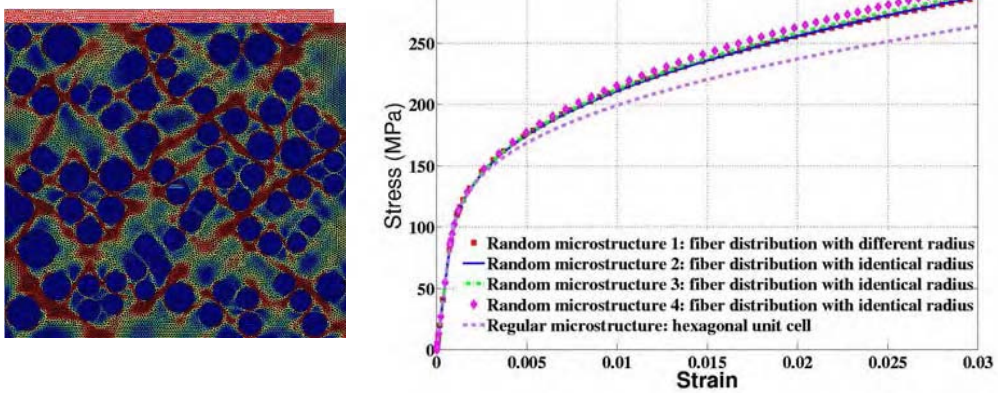

Figure 1: *(a) Plastic strain fields. (b) Overall stress-strain curves of the composite made up of a random distribution of cylindrical fibers,* $V_f = 32\%$.

3 Application of various mean-field methods

The particularity of mean field homogenisation techniques is that they apply the solution of the problem of a uniform ellipsoidal inclusion embedded in a infinite medium, originally introduced by Eshelby, to model the initial stages of elastoplasticity assimilating the situation of the most favorably oriented grains deforming plastically in an elastic matrix to that of Eshelby's inclusion. Three methods were chosen for our analysis. The Transformation Field analysis, initially introduced bt Dvorak [4] is based on the idea of a purely elastic redistribution of the macroscopic stress and strain and the use of uniform local eigenstresses or eigenstrains. On the contrary, the formulation introduced by Hill is based on a linearization in an incremental form of the local constitutive laws. The affine method still uses the current local tangent stiffness but replaces the incremental formulation (rates) of Hill by an elastic formulation with eigenstrains, with the tangent stiffness instead of the true elastic stiffness. For more details on these methods, one may consult the papers quoted in references. In each application of the mean field methods, the associated linear homogenisation rule chosen is the Mori-Tanaka's scheme. The results of the estimates are shown in Fig. 2.

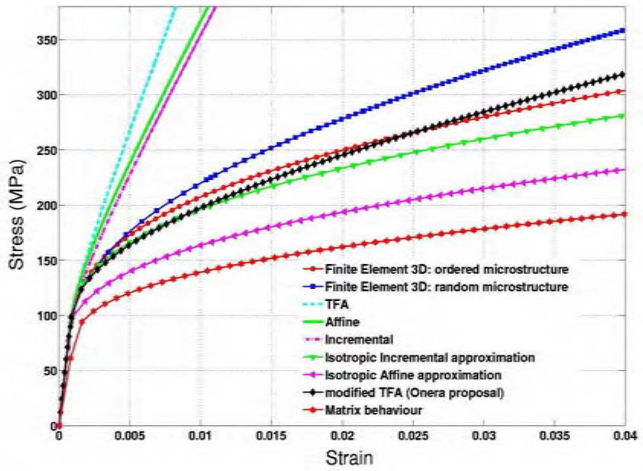

Figure 2: *Application of various mean field methods. The top curves use either elastic localisation or the anisotropic tangent operator. The lower curves employ an isotropic approximation of the tangent elastoplastic operator.*

4 Closure

This paper provides a review of different mean field homogenisation techniques, for some of them developed recently, to estimate the effective behaviour of non-linear heterogeneous materials. It has been noticed that the TFA, the incremental tangent and the affine methods significantly underestimate the overall strength and hardening of the composite with an ordered or with a random microstructure. Although this result is not completely new for the TFA and the incremental method, the effects observed are of an amplitude that does not seem to have reported until now. Moreover, a proposal made by Onera to modify the TFA method by introducing an asymptoptic elastoplastic modulus has appeared to offer a useful compromise between cost and accuracy.

References

[1] G.I. Taylor, Plastic strains in metals, *J.Inst.Metals*, 62, 307-324, 1938

[2] E. Kröner, Zur plastischen verformung des vielkristalls, *Acta. Metall. Mater.*, 9,155-161, 1961.

[3] R. Hill, Continuum micro-mechanics of elastoplastic polycrystals. *J. Mech. Phys. Solids.*, 13, 89-101, 1965. Environmental durability of glass-fiber composites. *Materials Science and Engineering*, 13, 265-324, 1994.

[4] G. Dvorak, Transformation fields analysis of inelastic composite materials. *Proc. Royal Soc. London*, A.437, 311-327, 1992.

[5] R. Masson and A. Zaoui, Self-consistent estimates for the rate dependent-elastoplastic behaviour of polycrystalline materials. *J. Mech. Phys. Solids*,1203-1227, 2000.

The Long March to Strain Hardening in FCC Crystals

L. Kubin[1], B. Devincre[1] and T. Hoc[2]

[1]Laboratoire d'Etude des Microstructures, CNRS-ONERA, 29 Av. de la Division Leclerc, BP 72, 92322 Châtillon Cedex, France (kubin@onera.fr)
[2]Laboratoire MSSMat, Ecole Centrale Paris, Grande Voie des Vignes, 92295 Châtenay-Malabry Cedex, France (hoc@mssmat.ecp.fr)

ABSTRACT

A summary is given of the steps involved in the modeling of the three-stage behavior of face-centered cubic crystals. Going up in scales, this involves dislocation dynamics simulations of individual reactions between dislocations and, further, measurements of the coefficients of interaction between slip systems. These coefficients are inserted into a dislocation-based, tensorial constitutive formulation for strain hardening. The latter is based on existing models; it only includes parameters having a well-defined physical meaning, of which the values are known within reasonable bounds. In a last step, this constitutive formulation is inserted into a crystal plasticity code, which allows predicting the dependence of the first-three stages of the stress-strain curves of single crystals as a function of orientation and stacking fault energy.

1. Mesoscopic Aspects

Interactions and reactions of dislocations are the main cause of strain hardening in face-centered cubic (fcc) crystals. As reactions between dislocations involve changes in line energy, they lead to the formation of strong obstacles, which can be treated by elasticity theory. This last assumption was checked in the past few years through a comparison between atomistic and purely elastic simulations (see [1] for a discussion). It is, however, necessary to make use of Discrete Dislocation Dynamics (DDD) simulations to estimate in an accurate manner the conditions for the formation and destruction of junctions between dislocations. The domain of existence of junctions and locks was first investigated in terms of geometrical parameters for each of the four types of reactions occurring in fcc crystals, viz. the Hirth and Lomer locks, the glissile junction and the collinear annihilation [2]. In the fcc structure, there are six possible types of interactions between slip planes, that is two non-contact interactions, the self-interaction and the coplanar interaction, plus the four reactions mentioned above. This allows defining an

interaction matrix between the twelve possible slip systems, as was done first by Franciosi and coworkers. The interaction coefficents are then determined from model DDD simulations. The hierarchy of the different types of interactions is found consistent with expectations, except for the collinear interaction, which is extremely strong and may account for about 30 percent of the hardening in multislip conditions [3].

2. The mechanical Response

If one wishes to predict the slip systems activity, it is necessary to go beyond traditional scalar models for strain hardening. Further, the limitation of DDD simulations to small strains can be by passed by combining them with constitutive formulations. The Kocks-Mecking framework is perfectly adapted for this purpose, once it is cast in a form accounting for the dislocations densities and interactions in each slip system. The formulation that is used in the present work derives from the model by Teodosiu and coworkers [4]. This model was adapted to include stage I behavior [5] and modified in several respects, which are not discussed here by lack of space. The parameters involved are the coefficients of the interaction matrix, the matrix of mean-free paths for the dislocations in each slip system and the critical annihilation distance of screw dislocations by cross-slip, which accounts for dynamic recovery. All parameters values are known within reasonable bounds from simulation, modeling or experiment. Fig. 1 shows, from an early stage of the model, stress-strain curves for copper, aluminum and silver crystals at room temperature obtained by inserting the constitutive formulation into a crystal plasticity code.

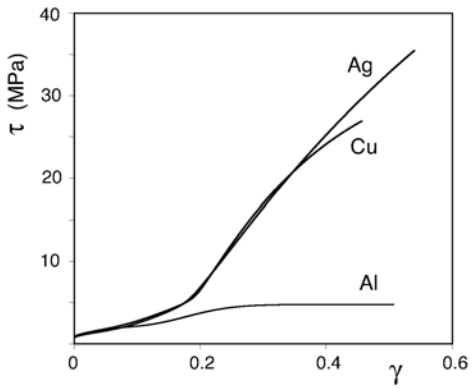

Fig. 1. Three-stage resolved stress-strain curves for $[\bar{1}35]$ fcc crystals at room temperature. The stacking fault energy of the material, which governs cross-slip processes, is for a large part responsible for the differences in mechanical response.

The main role of the crystal plasticity code is to account for the lattice rotations that accompany dislocation glide. As discussed in [5], the design of a model tensile specimen and the treatment of boundary conditions require some care, especially for stage I behavior. Preliminary results indicate that the cross-slip mechanism effectively governs the process of dynamic recovery, whereas the collinear interaction strongly affects the nature and number of activated slip systems in multislip conditions. A full account of the orientation and material dependence of the deformation curves of fcc crystals will be presented in a forthcoming publication.

Conclusions

The conclusions of this ongoing study are as follows. (i) Models based on uniform dislocation densities reproduce single crystal behavior in monotonic deformation because in such a case, the structure of the internal stress and the formation of dislocation patterns have little impact on the mechanical response. It would not be so if changes in strain path were performed. (ii) By combining DDD simulations, constitutive modeling and crystal plasticity codes, it is possible to establish physically-based and truly predictive models for plasticity. Thus, in favorable conditions, it is no longer justified to make use of parameter-fitting procedures. (iii) The cross-slip mechanism and the collinear interaction are key processes determining the mechanical response in multislip conditions.

References

[1] R. Madec, B. Devincre and L.P. Kubin, From dislocation junctions to forest hardening, Phys. Rev. Lett., **89**, 255508-1-4 (2002).

[2] L. P. Kubin, R. Madec and B. Devincre, Dislocation Intersections and Reactions in FCC and BCC Crystals, in *Multiscale Phenomena in Materials*, edited by H. M. Zbib, D.H. Lassila, L.E. Levine, K.J. Hemker (MRS, Warrendale, PA), MRS Proceedings Vol. 779, pp. 25-36 (2003).

[3] R. Madec, B. Devincre, L. Kubin, T. Hoc and D. Rodney, The role of collinear interaction in dislocation-induced hardening, Science, **301**, 1879-1882 (2004).

[4] C. Teodosiu, J.L. Raphanel and L. Tabourot, Finite element simulation of the large elastopastic deformation of multicrystals, in *Large Plastic Deformations*, edited by C. Teodosiu, J.L. Raphanel and F. Sidoroff (A.A. Balkema, Rotterdam), pp. 153-168 (1993).

[5] T. Hoc, B. Devincre and L.P. Kubin, Deformation stage I of fcc crystals: constitutive modelling, in *Evolution of Deformation Microstructures in 3D* (25th. Int. Symposium on Materials Science, Risoe Natl. Laboratory), in press.

Molecular Dynamics Simulation of Healing of an Ellipsoid Crack in Copper under Compressive Stress

M. Li[†‡], W. Y. Chu[†], K. W. Gao[†], L. J. Qiao[†]

[†]Dept. of Mater. Phys., Univ. of Sci. & Tech., Beijing, 100083, P. R. China

[‡]Dept. of Phys. & Astro., Cal. State Univ., Northridge, 91330-8268, U. S. A.

E-mail: mingli@csun.edu

ABSTRACT

Atomistic MD method is used to simulate healing of an ellipsoid crack inside copper under compressive stress with EAM potential. The result shows that dislocations are emitted firstly from the ellipsoid crack and move along <111> planes under a constant compressive stress of 0.34 GPa. The ellipsoid crack becomes smaller and smaller until it is healed through dislocation emission, motion, and annihilation on the surfaces. After crack healing, there are a residual dislocation net and some vacancy sites. It seems that the cavity inside the ellipsoid crack is transferred to crystal surfaces. In the same time, the crystal undergoes plastic deformation and its surfaces become rough.

1. Introduction

Crack healing is now considered to show promise in the recovery of the mechanical properties of the cracked materials. It has been reported that micro-cracks in hot-rolled 600 alloy were closed during heating over 870°C with a large compressive stress by the moving of grain boundaries because of recrystallization [1], and micro-cracks in cold-rolled Cu30Fe duplex alloy could be sealed after rolling exceeded 30% [2]. There have been also reports on atomistic MD simulation of micro-crack healing during heating and/or under compressive stress [3, 4]. The simulation results showed that a center penetrating microcrack in Cu or Al crystal could be healed under a compressive stress or by heating, and the role of compressive stress and heating in crack healing is additive. During micro-crack healing, dislocation emission and motion occurred and pre-existed dislocation could decrease the critical temperature or compressive stress necessary for microcrack healing. In the present paper, we present for the first time a three dimension atomistic MD simulation of healing of an ellipsoid crack in a copper single crystal.

2. Simulation Procedure

The single crystal copper is selected as the simulated material. The lengths of the

crystal along the x=[$1\bar{1}2$], y=[$1\bar{1}1$] and z=[110] directions are 17.9 nm, 16.9 nm and 15.6 nm, respectively. The total number of atoms is about 4×10^5. A flat ellipsoid hole (its lengths of its semi-axis are 2.21 nm, 2.21 nm and 0.247 nm respectively) is input in the center of the crystal, and then the configuration is relaxed for 1ps at 40 K until equilibrium is reached, as shown in Fig 1(a). A compressive stress along the z=[110] direction is applied with a loading rate of 57 MPa/ps. The time step is 10^{-3} ps. The inter-atomic potential used here is the embedded atom method (EAM) potential developed by Mishin et al. [5]. The motion of atoms follows the Newtonian Law. A leapfrog algorithm is utilized to integrate positions and velocities of atoms. The initial velocity is the Maxwell-Boltzmann distribution of a given temperature. The system temperature is maintained at 40K by scaling the atom velocities during the simulation.

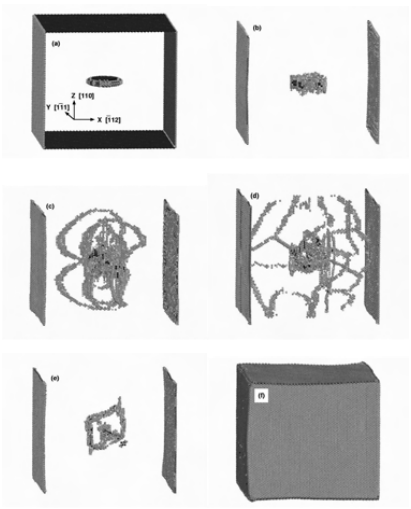

Fig.1 Healing of an ellipsoid crack under pressing, (a) an ellipsoid crack inside crystal, (b) dislocation emitting under compressive stress of 0.342 GPa, (c) dislocation emission and motion along the ($1\bar{1}1$) and ($\bar{1}11$) planes after keeping the constant compressive stress for 7 ps, (d) dislocation annihilation on the surfaces after relaxing for 10 ps, (e) crack being healed, and a dislocation net and vacancies resided within after relaxing for 37.5 ps, (f) crystal deformation after the crack is healed.

The potential energy of all lattice atoms distributes between –3.55 eV and –3.51 eV. The energy of atoms in the neighborhood of dislocation core is higher than average lattice atoms, and distributes between –3.49 eV and –3.45 eV after dislocation emission. These atoms with higher energy compose dislocation lines. The atoms with various energy distributions are distinguished using various colours. Therefore, the positions of all dislocations at any instant can be determined.

3. Result and Discussion

When the applied compressive stress is below the critical value necessary for dislocation emission, the energy of all atoms distributes between –3.55 eV and –3.51 eV, and there are no high energy atoms. When compressive stress increases to 0.342 GPa, high energy atoms appear ahead of the ellipsoid crack, as shown in Fig 1(b). Its shows that dislocations begin to emit from the ellipsoid crack tip, and the sites of the dislocations can be determined by the high energy atoms with deep colour. Keeping the constant compressive stress, dislocations are emitted and move continuously along the ($1\bar{1}1$) and ($\bar{1}11$) planes, as shown in Fig 1(c).

When dislocations move close to the surfaces of the crystal they are drawn toward the surfaces by the image force and annihilated on the surfaces, as shown in Fig 1(d). During dislocation emission and motion, the ellipsoid crack becomes smaller and smaller, and it seems that the cavity inside the ellipsoid crack is transferred to the surfaces through dislocation emission, motion and annihilation. After relaxing for 37.5 ps at the constant compressive stress, the ellipsoid crack has been healed completely and there exist a dislocation net and some vacancy sites, as shown in Fig 1(e). At the same time, the crystal undergoes plastic deformation, and the surfaces become rough because of annihilation of dislocation on the surfaces, as shown in Fig 1(f).

The simulation result shows that crack healing under a compressive stress is preceded by dislocation emission and motion. When temperature exceeds 200K, the energy distribution of the lattice atoms widens greatly and overlays with that of dislocation core. In such case, the site of dislocation core can not be determined according to energy distribution, i.e., the colour of the atoms. Therefore we cannot simulate three-dimensional crack healing during heating. For a penetrating crack in quasi-three dimensions simulation using a periodic boundary condition, all dislocations emitted from crack tip are straight lines penetrating the thickness, and can be determined according to the site of the half atomic plane [3, 4]. It may well be that crack healing during heating is preceded also by dislocation emission and motion, as that under compressive stress. This would be the subject of another MD exploration.

4. Summary

Under compressive stress, an ellipsoid crack becomes smaller and smaller until completely healed through dislocation emission, motion and annihilation on crystal surfaces. We observe that crack healing under compressive stress is preceded by dislocation emission and motion.

Acknowledgments

The present work was supported by the special Funds for the MSBRP (No G19990650) and by the NNSF of China (No 50141001 & No 50171012).

References

[1] E. Shapiro, G.E. Dietar, Metall. Trans. 1 (1970) 1711.
[2] J. Foct, N. Akdut, G. Gottstein, Scr. Metall. Mater. 27 (1992) 1033.
[3] S. Li, K.W. Gao, L.J. Qiao, F.X. Zhou, W.Y. Chu, Comput. Mater. Sci. 20 (2001) 143.
[4] G.H. Zhou, K.W. Gao, L.J. Qiao, Y.B. Wang, W.Y. Chu, Model. Simul. Mater. Sci. Eng. 8 (2000) 603.
[5] Y. Mishin, M.J. Mehl, D.A. Papaconstantopoulos, A.F. Voter and J.D. Kress, Phys. Rev. B, 63 (2001) 224106.

Nanovoid Cavitation by Dislocation Emission in Al.

Jaime Marian, Jaroslaw Knap and Michael Ortiz

Division of Engineering and Applied Science
California Institute of Technology
1200 E. California Blvd.
Pasadena, CA 91125
email: jaime@aero.caltech.edu

ABSTRACT

Void growth and coalescence are known to be important ductile fracture mechanisms in metals. Under shock conditions, such as those encountered in explosively loaded materials, the attendant high deformation rates may induce the formation of spall layers characterized by a large concentration of nano and microvoids arranged in spatial patterns. The diffusion, growth and coalescence of these voids can lead to material failure under these extreme conditions. Therefore, a detailed understanding of the main mechanisms by which these voids grow and interact is required in order to construct reliable multiscale models of spallation in metals. Recently, molecular dynamics (MD) simulations have revealed the nucleation of large dislocation loops in Cu and Al. However, the size constraints inherent to MD make it difficult to obtain a complete picture of the relevant mechanisms. At the same time, continuum methods neglect important processes occurring at very fine scales and cannot provide a detailed mechanistic picture of the relevant plastic phenomena. In this paper, we employ the quasicontinuum method in order to study voids and samples of realistic size under meaningful deformation conditions. Results for fcc Al under volumetric tension and simple shear are presented. Our analyses for both cases reveal several stages of pressure buildup separated by yield points. At each yield point, plastic deformation in the form of dislocation emission occurs, resulting in irreversible void growth. Stress yield maps are extracted from the different void sizes and loading conditions.

1. Introduction

Understanding materials response to high-strain-rate loading is needed in many technological and scientific applications, including explosion-induced spallation, high-speed machining of materials, impact experiments, interaction of intense pulsed lasers with solid targets, etc. Spall damage is characterized by a distribution of small independent cracks or voids in the region of the material subjected to tension and may result in the catastrophic failure of the material. Specifically, spall has been widely studied experimentally with methods such as plate impact (gas gun) and, more recently,

high-intensity, pulsed laser shock generators. The void formation is generally attributed to the emergence of reflected tensile waves inside the material. Voids then grow both intrinsically by extensive plastic flow, *i.e.* emitting dislocation loops and also by coalescing with neighboring bubbles. However, in these experiments, the combination of very high strain rates and sample size causes analyses based on traditional fracture mechanics, molecular dynamics or linear elasticity to be in many cases incomplete and insufficient. The technique we use in order to overcome these limitations is the three-dimensional version of the quasicontinuum (QC) method [1]. By adapting the spatial resolution to the structure of the deformation field, the QC method has allowed us to span realistic sample sizes (~1 micron), as well as isolate the surface of the void from the cell boundaries.

2. Results

The material under consideration here is single crystal fcc aluminum. We simulate cubic samples of various sizes containing spherical voids. Full atomistic resolution is provided initially within a small region surrounding the void, and the triangulation is rapidly coarsened with distance to the void elsewhere. With this coarsening scheme, a sample $432a_0 \times 432a_0 \times 432a_0$ in size is reduced to a mesh containing a total of 31,933 nodes as representative of the crystal with more than 3×10^7 lattice sites. Here we present results for samples under volumetric tension and simple shear and a void of $13a_0$ (~5.2 nm) diameter. By carrying out the analysis in quasistatic mode at 0 K we are able to explore the energy landscape and track the transition paths traversed by expanding nanovoids.

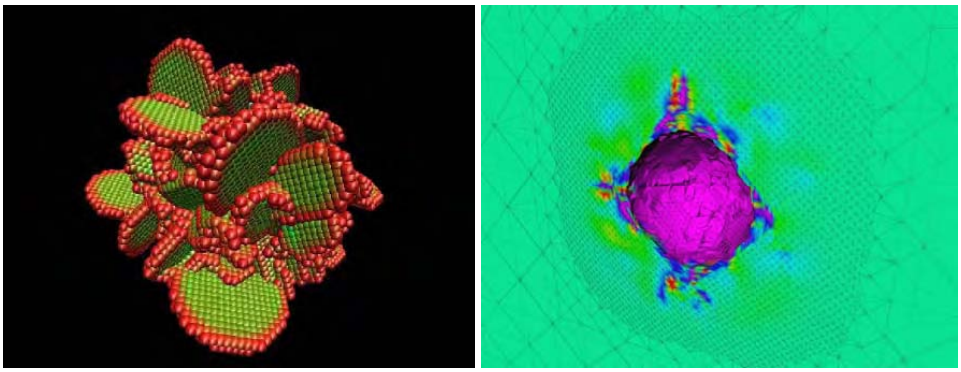

Figure 1: Atomistic (left) and finite-element (right) views of the $13a_0$-diameter void at a volumetric strain of 29%.

2.1 Volumetric strain

The material response is characterized by three main stages of rapid pressure buildup punctuated by inflection or yield points. The first yield point corresponds to the formation of highly stable tetrahedral dislocation junctions around the surfaces of the

void. The second yield point is caused by the dissolution of the tetrahedral structures and the emission of dislocation loops. Notably, we emphasize the observation of $\frac{1}{2}\langle 110\rangle\{001\}$ loops, in addition to the conventional $\frac{1}{2}\langle 110\rangle\{111\}$, which, albeit rare, have been observed experimentally [2]. Fig. 1 shows the dislocation distribution around the void after the second yield point.

2.1 Simple shear

In this case, the sample is subject to simple shear and the void's collapse gives rise to clean conventional $\frac{1}{2}\langle 110\rangle\{111\}$ dislocations loops. The void grows by the continued emission of loops, which bow out making room for new loops to be generated at the void. In this sense, the void acts as a very prolific dislocation source. Fig. 2 shows the QC mesh at 16% shear deformation and the equivalent dislocation structure.

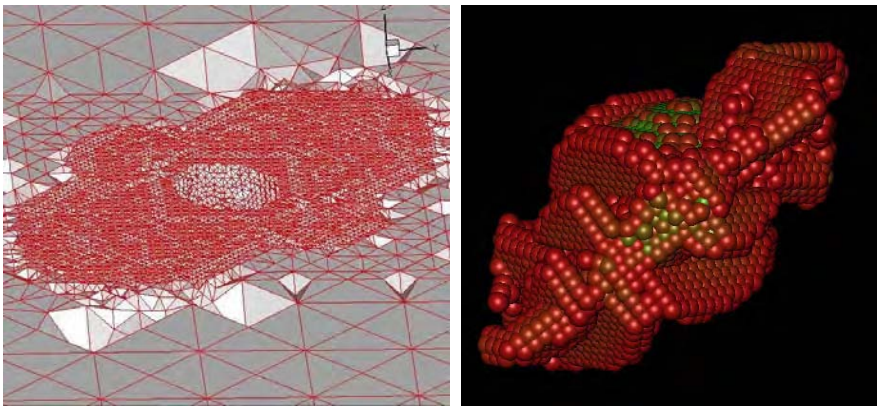

Figure 2: Detail of the QC mesh for a shear deformation of 16% (left), with the void clearly carved in the center. The growth of the atomistic mesh is, contrary to the volumetric case, heavily directional. On the right, equivalent dislocation structure.

Conclusions

In conclusion, we have studied the transition paths attendant to nanovoid growth in Al. Our analysis reveals several stages of pressure buildup separated by yield points for the hydrostatic case and a first failure point followed by continued emission of dislocation loops for simple shear. Our results suggest that the initial stages of deformation of a nanovoid in Al under stress are the result of a number of highly complex transitions that negotiate an exceedingly rugged energy landscape.

References

[1] J. Knap and M. Ortiz, *J. Mech. Phys. Solids* **49**, 1899 (2001).
[2] A. Korner and H. Karnthaler, *Philos. Mag*. **42**, 753 (1980).

MODELING OF MICROSTRUCTURAL EFFECTS ON THE LOCAL MECHANICAL FIELDS IN TEMPERED MARTENSITE AND BAINITE

S. Sekfali[(1)], C. Rey[(2)], B. Marini[(3)]

[(1)] PhD; [(2)] rey@mssmat.ecp.fr, LMSSMAT, CNRS-UMR 8579, Ecole Centrale Paris, F 92295 Châtenay-Malabry, France; [(3)] bernard.marini@cea.fr, CEA, DEN/SAC/DMN/SRMA, F-91191 Gif-sur-Yvette, France.

ABSTRACT

The local mechanical strain and stress fields in tempered bainite and martensite submitted to tensile tests have been computed from a crystalline modeling implemented in ABAQUS finite element code. The two aggregates were composed of one layer of actual grains which orientation, size and position are determined by EBSD technique. The model was validated from comparison of experimental and computed strain fields, the former deduced from micro-extensometry (micro-grids). The stress field in martensite was found larger and more heterogeneous than in bainite. This result is correlated with the thin microstructure of martensite. Stress amplification due to this miscrostructural effect may be an important parameter of the intergranular embrittlement sensitivity.

1 Introduction

Tempered martensite and bainite could present different susceptibilities to intergranular embrittlement generally attributed to some microstructural features, like lath boundaries and carbides, which can modify the segregation of chemical elements [1]. The present work is an attempt to determine the micro-mechanical effect of the differences in crystallographic units arrangements and relative sizes between the two microstructures. A crystalline approach of plasticity is used: the numerical model is implemented in a finite element code and the simulations are performed from actual descriptions of aggregates using EBSD method.

2 Numerical method

The crystal plasticity modeling presented a large kinematic description according to the framework developed by Peirce et al [2], with the hardening rule proposed by Teodosiu et al [3]. This model has shown great abilities to capture the main characteristics of multicrystals deformation during monotonic and sequential tests [4], [5]. Thus, only the main characteristics of this model are presented below. This model has been implemented in ABAQUS implicit finite element software using a User Subroutine UMAT. The numerical scheme is an explicit forward gradient procedure. The model accounts for crystallographic glide and lattice rotation. For b.c.c. metals at room temperature hardening is assumed to be caused by interactions between latent and active slip systems.

The glide velocity on a glide system is given by a classical viscoplastic power law using the resolved shear stress τ^s, the critical shear stress τ_c^s and the slip rate $\dot{\gamma}^s$ on the slip system (s):

$$\frac{\dot{\gamma}^s}{\dot{\gamma}_0} = \left|\frac{\tau^s}{\tau_c^s}\right|^{\frac{1}{m}} \mathrm{sgn}(\tau^s) \text{ with } \tau_c^s = \tau_0 + \mu b \sqrt{\sum_u a^{su}\rho^u} \quad (1\&2)$$

Where $\dot{\gamma}_0$ is a reference slip rate, ρ^u is the dislocation density on system (u) and a^{su} is the interaction matrix which describes the interactions between glide systems (s) and (u). The coefficient 1/m corresponds to the velocity exponent, μ and b are the shear modulus and the Burgers vector magnitude respectively. The τ_0 value corresponds here to a parameter describing the mean effect of carbides and lattice friction stress. The evolution of the dislocation density on a slip system (s) is governed by a production term and by an annihilation term

$$\frac{d\rho^S}{dt} = \frac{d\gamma^s}{dt}\left(\frac{\sqrt{\sum_{u\neq s}\rho^u}}{K} + \frac{1}{D} - g_c\rho^s\right) \quad (3)$$

Where D is the grain size, K and g_c are material constants. The hardening matrix is assumed isotropic and $\dot{\gamma}_0$ equal to $10^{-11}s^{-1}$. All material parameters are computed by inverse method from experimental tensile curves.

3 Experimental procedure

Bainite and martensite microstructures are elaborated from A508 C13 type steel with two different heat treatments. Samples were strained in a micro-machine designed for a SEM. Areas of 500x500µm^2 were analysed by Electron Back Scattering Diagram (EBSD) in order to built aggregates which grains orientation, size and position in the aggregate were measured. The EBSD analysis shows that the two microstructures are composed ex-gamma grains about 50µm with of ferrite lath packets presenting lattice orientation relation (fig.1). In bainite, the packets are about 10µm large and about 1 to 4 µm in martensite. The mean differences between the two microstructures are the size of lath packet and the carbides repartition. In the investigated zones of bainite microgrids (step 2µm) were deposed and three components of the experimental strain fields were computed using adequate software.

These aggregates are then computed in order to determine local mechanical fields.

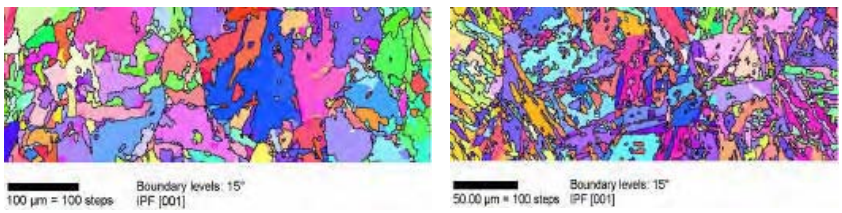

Fig1 : bainite (left) and martensite (right) microstructures, the bainite aggregate (600x200µm^2) is four time the martensite aggregate size (300x100µm^2).

4 Results

Experimental and numerical E11 component along tensile axis are compared for bainite on fig.2. The distribution curves are similar and support the computation. The widths of the curves, point out the inhomogeneities of the strain field at different applied macroscopic strain. Maps of the different Green Lagrange components allow analysis of the different kinds of deformation bands [5]. The computation gives access to the local evolution of different parameters. Fig.3 shows the local stress field in bainite and martensite respectively for the same macroscopic strain.

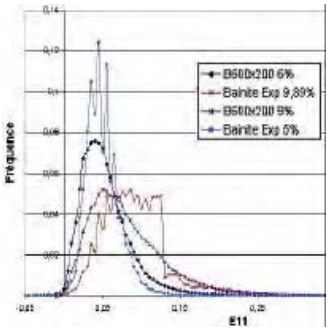

Fig.2: Comparison of experimental and numerical E11 distribution in bainite**.**

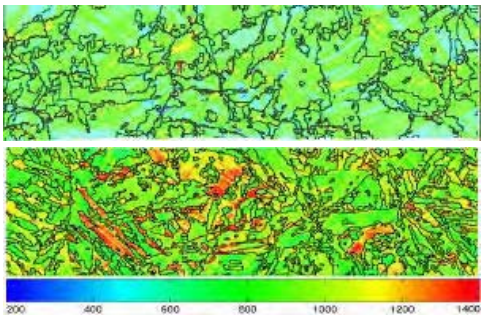

Fig 3 : S11 local stress map in bainite (high) and in martensite (low), for 7.5% elongation. The scale in MPa is the same for the two maps.

5 Discussion

The two microstructures have the same chemical composition but martensite is thinner than bainite. For a same amount of macroscopic strain (7.5%), the martensite presents in an ex-gamma grain, large variations of internal stresses (up to 1400MPa for a macroscopic stress of 978 MPa), whereas bainite presents a more homogeneous pattern. Simulations and EBSD analysis point out that internal stresses are larger for particular pair of lath orientations presenting large incompatibilities for the applied loading. We may assume that, in this case, the induced internal stresses which are not relaxed by slip in martensite thin laths increase the local loading at the ex-gamma grain boundaries and then, increase the probability of intergranular failure.

6 References

[1] S. Raoul, B. Marini et A. Pineau, Effect of microstructure on the susceptibility of a A533 steel to temper embrittlement, Jal of Nuc. Materials 257 (1998) 199-205.

[2] D.Peirce, R.Asaro, A. Needleman, Material rate dependance and localized deformation in crystalline solids. Acta Metall. 31, (1983) 1951-1976

[3] C. Teodosiu., J. Raphanel, L.Tabourot, (1993) Finite implementation of the large elastoplastic deformation of multicrystals, Proc. Int. seminar MECAMAT'91, 153-158.

[4] T. Hoc, C. Rey, J. Raphanel, Experimental and numerical analysis of localization during sequential tests for an IF-TI steel, Acta Mater. 48, (2000) 4893-4900.

[5] P. Erieau, C. Rey, Modeling of deformation bands and of deformation induced grain boundaries in IF steel during large strain compression. IJP 20, (2004) 1763-1788.

Density Functional Theory Study of Intrinsic Ductility of Solids

Shigenobu Ogata[1,3,4], Ju Li[5], Naoto Hirosaki[6]
Yoji Shibutani[4], and Sidney Yip[1,2]

[1]Department of Nuclear Engineering,
[2]Department of Materials Science and Engineering,
Massachusetts Institute of Technology, Cambridge, Massachusetts 02139, USA
[3]Handai Frontier Research Center,
[4]Department of Mechanical Engineering and Systems,
Osaka University, Osaka 565-0871, Japan
[5]Department of Materials Science and Engineering,
Ohio State University, Columbus, Ohio 43210, USA
[6]Advanced Materials Laboratory,
National Institute for Materials Science, Ibaraki, 305-0044, Japan
E-mail: ogata@mech.eng.osaka-u.ac.jp

ABSTRACT

Using density functional theory we analyze the stress-strain responses of 22 simple metals and ceramics to determine the maximum shear strain a homogeneous crystal can withstand, a property for which we suggest the name shearability. A shearability gap is found between metals and ceramics. Shearability of metals further correlates with the degree of valence charge localization and directional bonding. We hypothesize that the shearability is an important factor controlling the ductility of solids.

1. Introduction

The ductility of solids is controlled by the energy needed to break a bond by shear compared to that by tension [1]. It is characteristic of ceramics to have a larger ratio of shear to bulk moduli; however, little is known about the range of shear deformation in solids with different types of bonding. The maximum shear and tensile distortions that chemical bonding can withstand are particularly important for defects, e.g. dislocation cores and crack tips. A first step toward better understanding begins with two aspects of affine deformation of perfect crystals. One is the elastic constant describing the linear response of the lattice to small strain, and the other is a fundamental characterization of the large-strain nonlinear response. While use of the former in scaling relations is almost universal in defect mechanics, the question of whether the latter also factors into microstructure-controlling quantities such as the intrinsic stacking fault energy has been examined only recently [2]. Here we apply density functional theory (DFT) to compute

the shearability and tensibility of simple metals and ceramics, defined by the maximum shear and tensile strains at which a perfect crystal under affine deformation becomes unstable, to bring out the fundamental connection between critical mechanical response of a solid and the underlying electronic structure such as redistribution of valence charge density.

2. Theory and Method

We define shearability as $s_m \equiv \arg\max \sigma(s)$, where $\sigma(s)$ is the resolved shear stress and s is the engineering shear strain in a specified slip system. Similarly, tensibility is taken to be $t_m \equiv \arg\max -P((1+t)V_0)$, where $P(V)$ is the pressure-volume relation and V_0 is the equilibrium volume, $P(V_0) = 0$.

We have studied the following metals and ceramics using the Vienna Ab-initio Simulation Package [3]: FCC Ag, Cu, Au, ferromagnetic (FM) and paramagnetic (NM) Ni, Al; BCC W, Mo, Fe (FM); HCP Mg, Ti, Zn; $L1_0$ TiAl, $D0_{19}$ Ti_3Al; diamond cubic C, Si; β-SiC, α-, β-Si_3N_4; B1 NaCl, MgO, KBr, CaO. The exchange-correlation density functionals adopted are Perdew-Wang generalized gradient approximation (GGA) for metals except Au and Ag, and Ceperley-Alder local density approximation (LDA) for the others. Ultrasoft (US) pseudopotential is used in most cases, but for difficult systems we switch to the projector augmented-wave (PAW) method. Brillouin zone (BZ) ***k***-point sampling is performed using the Monkhorst-Pack algorithm. For metals, BZ integration follows the Methfessel-Paxton scheme with the smearing width chosen so the ``-*TS*'' term is less than 0.5 meV/atom. For non-metallic systems, the tetrahedron method with Blochl corrections is used.

Incremental affine shear strains are imposed on each crystal along experimentally determined common slip systems to obtain the corresponding relaxed energies and stresses, defined respectively by the conditions, $\sigma_{ij} = 0$ except for the resolved shear stress.

3. Results and Discussions

The relaxed ideal shear stress σ_m^r normalized by relaxed shear modulus G_r and the shearability s_m^r for different materials are plotted together in Fig. 1(a). From these results we see gaps in the distribution of s_m^r between the metals and the covalent solids. Moreover, among the metals the noble metals Au, Ag, Cu and the more directionally bonded Al[2] and BCC Mo, W, Fe (FM) are at opposite sides of the distributions. This suggests that directional bonding allows for longer-range shear distortion of the bonds before peak resistance is attained, which one can rationalize by observing that the greater the covalency, the more valence charge will concentrate in non-nuclear-centered regions.

The ``brittleness parameter'' of Rice[1] that compares the unstable stacking energy γ_{us} to the surface energy γ_m, may be very crudely estimated as

$$\beta \equiv \frac{\gamma_{us}}{\gamma_s} \propto \frac{Gs_m^2}{Bt_m^2} = \left(\frac{G}{B}\right)\left(\frac{s_m}{t_m}\right)^2 \qquad (1)$$

by scaling arguments. G/B is accessible experimentally and has been used as a performance predictor in alloy design, but s_m and t_m, while easy to obtain in *ab initio* calculations, are unavailable experimentally and therefore have never been used in a practical manner, despite having been theoretically established to be important. Our results indicate that a wide gap in β exists between metals and ceramics because G/B and s_m are governed not only by the crystal structure, but also by the nature of bonding (e.g., $s_m^r = 0.105$ in FCC Au vs. $s_m^r = 0.200$ in FCC Al). Besides the gap in β is mainly caused by s_m. On the other hand, the relative variation of G/B and t_m are less sensitive than s_m, and s_m has no spectral gap (see Fig. 1(b)). Therefore, we conclude that the shearability s_m is dominant factor controlling the ductility of solids.

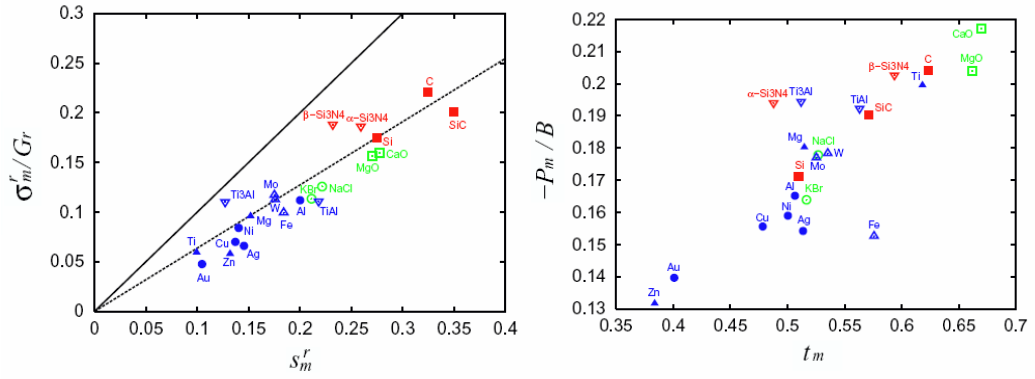

Figure 1 DFT calculation results of 22 materials (metallic: blue, ionic: green, covalent: red). (a) Relaxed ideal shear stress and shear strain, and (b) ideal tensile strength and tensibilities (volumetric). The solid line in (a) indicates a unit slope, while the dashed line corresponds to a slope of $2/\pi$.

References

[1] J.R. Rice, *J. Mech. Phys. Solids*, 40, 239 (1992).
[2] S. Ogata, J. Li, and S. Yip, *Science*, 298, 807 (2002).
[3] G. Kresse and J. Furthmuller, *Phys. Rev.* B, 54, 11169 (1996).

Acknowledgments

S.O. acknowledges support by Hattori-Houkoukai fellowship. J.L. acknowledges support by Honda R&D Co., Ltd. and the OSU Transportation Research Endowment Program. S.Y. acknowledges support by Honda R&D, AFOSR, DARPA, NSF, and LLNL.

Thermoelasticity at High Temperatures and Pressures for Ta

Daniel Orlikowski, Per Söderlind and John A. Moriarty
Lawrence Livermore National Laboratory, University of California,
P.O. Box 808, Livermore, CA 94550, email: orlikowski1@llnl.gov

ABSTRACT

A new methodology for calculating high temperature and pressure elastic moduli in metals has been developed accounting for both the electron-thermal and ion-thermal contributions. Anharmonic and quasi-harmonic thermoelasticity for bcc tantalum have thereby been calculated and compared as a function of temperature (<12,000 K) and pressure (<10 Mbar). In this approach, the full potential linear muffin-tin orbital (FP-LMTO) method for the cold and electron-thermal contributions is closely coupled with ion-thermal contributions obtained via multi-ion, quantum-based interatomic potentials derived from model generalized pseudopotential theory (MGPT). For the later contributions two separate approaches are used. In one approach, the quasi-harmonic ion-thermal contribution is obtained through a Brillouin zone sum of the strain derivatives of the phonons, and in the other the anharmonic ion-thermal contribution is obtained directly through Monte Carlo (MC) canonical distribution averages of strain derivatives on the multi-ion potentials themselves. The resulting elastic moduli compare well in each method and to available ultrasonic measurements and diamond-anvil-cell compression experiments indicating minimal anharmonic effects in bcc tantalum over the considered pressure range.

Existing methods to calculate the thermoelastic moduli for a single crystal material include, for example, molecular dynamics[1] and Monte Carlo techniques[2] where only the ionic contribution is calculated, or the particle-in-a-cell method[3] where both electronic and ionic contributions (treated only approximately) are calculated. We present here a new methodology for calculating the high temperature and pressure elastic moduli that separates the Helmholtz free energy into cold, electronic and ionic contributions and makes a full calculation for each component. Two methods of calculating the ion-thermal contributions are presented and compared: one within the quasi-harmonic phonon approximation and the other being fully anharmonic. Both ion-thermal treatments produce similar results in the case of Ta indicating negligible anharmonic effects for the high pressure phase diagram for this metal.

For high temperatures (300 K $\leq$ T $\leq$ T_{melt}) and pressures (P< 10 Mbar), we assume that the electron-phonon coupling is negligible for a metal and write the Helmholtz free energy as, $F(\Omega,T) = \Phi_o(\Omega,T=0) + F_e(\Omega,T) + F_H(\Omega,T) + F_A(\Omega,T)$, where $\Phi_o(\Omega,T=0)$ is the total energy of the electronic ground state, i.e. the frozen lattice, $F_e(\Omega,T)$ contains the electron-thermal contribution, $F_H(\Omega,T)$ holds the ion-thermal contribution, and $F_A(\Omega,T)$ has the anharmonic contributions. The specific volume Ω is the volume per atom. With this and through the definition of the

isothermal elastic moduli $C^T_{ijkl} = \Omega^{-1}\partial^2 F/\partial\eta_{ij}\partial\eta_{kl}\mid_{T\eta'}$, where η' indicates that all other strains are held fixed, the individual contributions to the elastic moduli are obtained, $C^T_{ijkl} = C^o_{ijkl} + C^e_{ijkl} + C^{ion}_{ijkl}$. For the C^e_{ijkl} term, temperature is incorporated into $F_e(\Omega, T) = U_e - TS_e$ through a broadening of the electron density of states, $n(\epsilon, \Omega)$, via the Fermi-Dirac distribution, $f(\epsilon)$, and through the electronic entropy, $S_e(\Omega, T) = -k_B \int d\epsilon\; n(\epsilon, \Omega)\{f(\epsilon)ln[f(\epsilon)] - (1-f(\epsilon))ln[1-f(\epsilon)]\}$. To calculate this term, the full-potential, linear muffin-tin orbital(FP-LMTO) electronic-structure method is used [4].

For the C^{ion}_{ijkl} contribution, we have implemented two different calculations to assess the anharmonic contribution: one within the quasi-harmonic(QH) approximation and one that is fully anharmonic(AH). Specifically for the QH method, following Wallace [5], the Helmholtz free energy for the lattice is written as a Brillouin zone and branch(κ) sum of the phonon frequencies ω_κ as $F_{ion} = \sum_\kappa 0.5\hbar\omega_\kappa + ln[1 - exp(-\hbar\omega_\kappa/kT)]$. Therefore, to obtain C^{ion}_{ijkl}, strain derivatives of F_{ion} lead to a summation over the Brillouin zone of strain derivatives of the phonon frequencies. To compute the fully AH lattice contribution to the elastic moduli, we have extended previous MC work[2], where the strain derivatives of the partition function are taken while accounting for periodic boundary conditions. This leads to a canonical assemble average of these derivatives evaluated at thermodynamic equilibrium for a given Ω and T via a standard Metropolis, MC algorithm. Two to three runs for each Ω and T point were performed with a run lasting at least 1.5×10^6 MC-steps. In both ion-thermal methods, we have used a quantum derived, multi-ion potential for Ta from the model generalized pseudopotential theory(MGPT) [6].

We first compare the calculated adiabatic moduli C^S_{ijkl} obtained from $C^T_{ijkl}(\Omega, T)$ with electronic plus QH thermal contributions against experimental data, Figs.(1 and 2). We have found that it is necessary to include

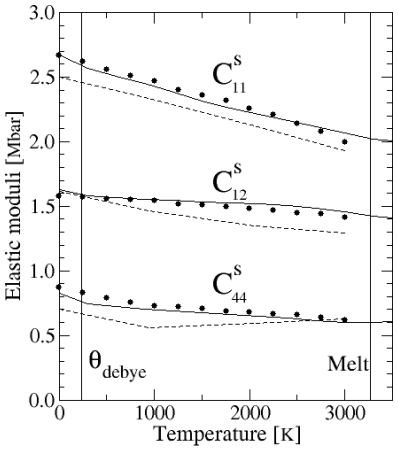

Fig. 1: The thermal dependence of the calculated C^S_{ijkl} (solid line) at ambient pressure up to T_m= 3376 K is compared to experiment[7] (circle). The dashed lines are from Gülseren and Cohen's work [3].

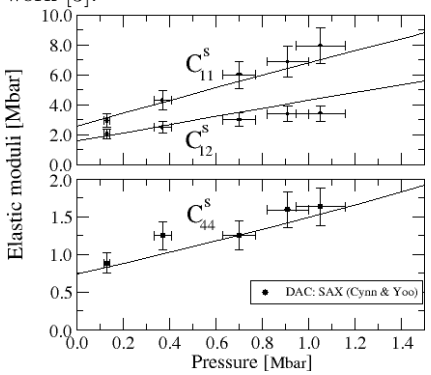

Fig. 2: The calculated C_{ijkl} (line) at T=300 K captures the pressure dependence as compared to SAX-DAC data[8](circle).

both the electron- and ion-thermal components of the C_{ijkl}, since each is of similar magnitude, roughly 0.1 Mbar at T= 2500 K and P= 0. Since the electron thermal plus QH ion-thermal calculation describe well the available experimental values, we now compare only the computation of $C^{ion}_{ijkl}(\Omega, T)$ by the QH and AH calculations. Overall the AH calculation yields similar values compared to the QH calculation, especially below 1 Mbar and even near T_m. As the pressure increases, the AH calculated values deviate from the QH values at temperatures just below T_m(see Fig. 3). At pressures above 6 Mbar, the AH calculated values only begin to deviate from the QH calculation within 80% of the T_m. This indicates that Ta has negligible anharmonic effects (deviation from high temperature, linear dependence) over a broad range of pressure with temperature nearing T_m. This linear temperature dependence of the C^T_{ijkl} leads to linear dependence in Voigt averaged shear modulus, albeit the pressure dependence of the cold shear modulus is non-linear above 6 Mbar.

This work was performed under the auspices of the U.S. Department of Energy by the University of California Lawrence Livermore National Laboratory under contract W-7405-Eng-48.

*

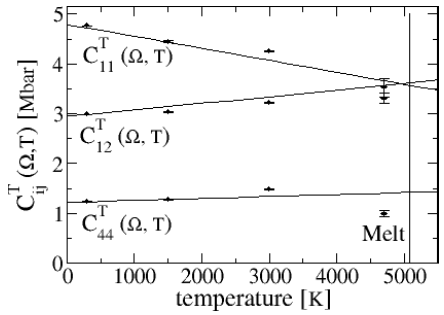

Fig. 3: The QH (line) and AH (circle) calculations of the $C^{ion}_{ijkl}(\Omega, T)$ term at Ω =102.2 a.u.^{3} for Ta. The pressure varies from 0.5 to 0.7 Mbar nearing T_m = 5074 K.

References

[1] R. J. Wolf, K. A. Mansour, M. W. Lee and J. R. Ray, *Temperature dependence of elastic constants of embedded-atom models of palladium*, Phys. Rev. B **46**, 8027 (1992).

[2] C. W. Greeff and J. A. Moriarty, *Ab initio thermoelasticity of magnesium*, Phys. Rev. B **59**, 3427 (1999).

[3] O. Gülseren and R. E. Cohen, *High-pressure thermoelasticity of body-centered-cubic tantalum*, Phys. Rev. B **65**, 064103 (2002).

[4] P. Söderlind and J. A. Moriarty, *First-principles theory of Ta up to 10 Mbar pressure: Structural and mechanical properties*, Phys. Rev. B **57**, 10340 (1998).

[5] D. C. Wallace, *Thermodynamics of crystals*, Dover: Mineola, NY (1998).

[6] J. A. Moriarty, et al. *Quantum-based atomistic simulation of materials properties in transition metals*, J. Phys.: Cond. Mat. **14**, 2825 (2002).

[7] E. Walker and P. Bujard, *Anomalous temperature behavior of the shear elastic constant C_{44} in tantalum*, Solid State Comm. **34**, 691 (1980).

[8] H. Cynn and C.-S. Yoo, *Single crystal elastic constants of tantalum to 105 GPa*, LLNL internal document UCRL-JC-137930 (unpublished).

Explicit Expression for Stress in Multi-level Line Structures and in Connecting Vertical Vias

Ares J. Rosakis[1], Tae-Soon Park[1], and Subra Suresh[2]

[1] Graduate Aeronautical Laboratories
California Institute of Technology
Pasadena, CA 91125
[2] Department of Materials Science and Engineering,
Massachusetts Institute of Technology,
Cambridge, MA 02139

ABSTRACT

Explicit expressions for volume-averaged thermal stresses in periodic metal and dielectric lines at a single Damascene layer deposited on a substrate are first presented. Individual stress components acting on these structures are expressed in terms of substrate curvature, temperature change, elastic properties and thermal expansion coefficients of individual phase. By observing that such stresses at different metalization levels are not influenced by the presence of additional layers, these expressions for the stress components in terms of total substrate curvatures are subsequently generalized to multi-level line structures by recourse to the concept of superimposition. For via plugs connecting lines at different metalization levels, the vertical stress component is also calculated in terms of the vertical stress components at the top and bottom lines and of mismatch stress from embedding dielectric materials. This stress component is directly related to critical tensile (via pull-out) and compressive (via push-in) failures of the via plugs recently reported in the literature. Full three-dimensional finite element analysis (FEA) is carried out for the purpose of verifying the generalized analytical stress models for both line and via structures. The analytically predicted and numerically calculated stress components are found to compare very well. Finally, thermal compatibility of various low-k dielectric materials with Cu is discussed in relation to probable failure mechanisms associated with the predicted stress amplification phenomenon at the vertical via plugs.

1. Introduction

The rate of yield loss is getting higher as the industry is pushing for ever increasing levels of metalization (high need of more integrated semiconductor chips) deposited on wafers of ever increasing diameters (smaller thickness to diameter aspect ratios). Among failure mechanisms associated with multi-level interconnect structures, pull-out or push-in of the via plugs connecting lines at different metalization levels is reported to occur during thermal cycling and/or after annealing. The nature of such mechanisms depends on the selection of embedding dielectric materials [1, 2]. Indeed voiding in vertical vias remains

a problem even in cases where voiding in lines has successfully been suppressed suggesting the occurrence of a mechanism of stress amplification in the vertical via plugs.

2. Analytical Modeling

Figure 1 shows a representative structure composed of vertical vias connecting horizontal periodic lines at the lower and upper levels following a Dual Damascene process and capping inter-layer deposition. The vias are cylindrical and periodic with a diameter of 2*R*, a pitch of *V*, and a height of $h_v=h_f-t$. As in Fig. 1, the vias connect horizontal lines of width *b* and pitch *d*. The material between the top of the lower line features and the bottom of the upper line features, surrounding the vias, is filled with the capping inter-layer dielectric (ILD) described in the previous section (materials properties E_c, ν_c, α_c). The average vertical stress in each via is now given as follow:

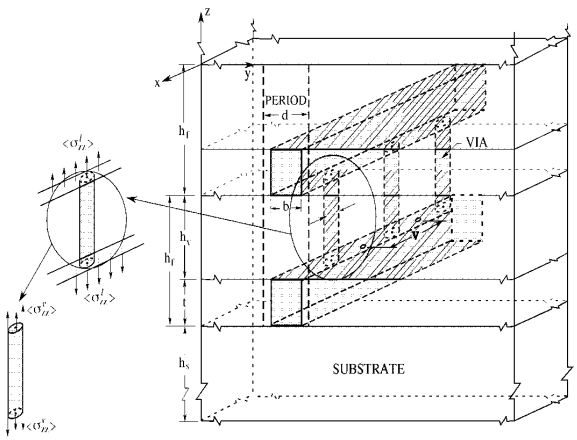

Figure 1. Schematic of a two level, periodic Cu interconnect line structure with vertical connecting vias at the lower and at the upper levels. Stress transfer at the vias is illustrated.

$$\left\langle \sigma_{zz}^{v} \right\rangle = \left\langle \sigma_{zz}^{v} \right\rangle (f_v, E_v, E_c, \alpha_v, \alpha_c, \left\langle \sigma_{zz}^{L} \right\rangle, \Delta T) \qquad (1)$$

Figure 2 shows computed amplification factors (ratios of $\langle\sigma_{zz}^{V}\rangle / \langle\sigma_{zz}^{l}\rangle$) as a function of the volume fraction of vias f_v for two commonly used encapsulating or passivating dielectrics (e.g. commercial materials under the trade names of TEOS and SILK) of a structure whose adjacent periodic line structures are connected by either Cu or W vias and is subjected to a $\Delta T=-380^{o}C$. The purpose of the figure is to use different material combinations to investigate the effect of material (mechanical and thermal) properties mismatch on the establishment of stress

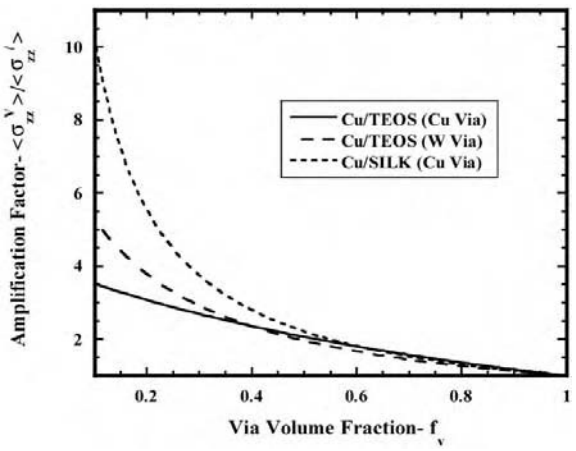

Figure 2. Ratios of volume-averaged stresses of connecting vertical vias to corresponding stress values of adjacent lower and upper lines as a function of via volume fractions based on analytical predictions.

concentration in vias. When a stiff metal (e.g. W) is used for a via plug, the vertical stresses are amplified to a much higher level in the vias (compared to their line equivalents), especially when the via volume fraction is small. When the embedding dielectric is compliant (e.g. polymer-based dielectric materials such as SILK), the vertical stress in the via become very high for isolated vias.

3. Numerical Modeling

Figure 3 shows FEA results on stress variations in elements lying along the path of the schematic (path along the interfaces between lines/via and an embedding dielectric) ranging from the bottom of the lower line, through the via, to the top of upper line. Stress values are fairly constant within each region. All stress components (both normal and shear stresses) are extremely well matched with analytical predictions on upper/lower lines and a via.

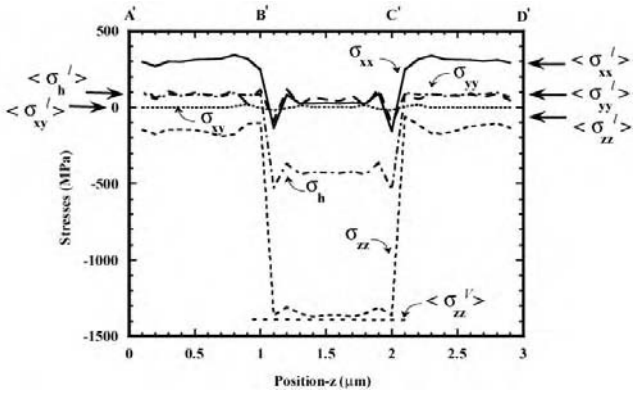

Figure 3. FEA results showing stress distribution along the path (along the vertical interfaces between Cu lines/via and an embedding SILK dielectric) from the bottom of the lower line through the via to the top of the upper line during cooling from 200°C to room temperature. Analytical predictions are also indicated for each feature.

4. References

1. S. Varadarajan, D. Kalakkad and T. Cacouris, Semiconductor International, 125 (2002)
2. G. Passemard and O. Demolliens, Advanced Metalization Conference, San Diego, CA (2000)

Strain Localization: Effects of Non-Glide Stresses

V. Racherla and J. L. Bassani

Department of Mechanical Engineering and Applied Mechanics, University of Pennsylvania, PA 19104, U.S.A. E-mail: vikranth@seas.upenn.edu

ABSTRACT

Simple isotropic yield and flow functions are proposed to represent polycrystal yield and flow surfaces in materials for which slip in individual grains depends upon non-glide stresses as well as the Schmid stress [1,2]. Constitutive models for rate-independent materials with non-associated flow are proposed that extend the ideas of Rudnicki and Rice [3] and satisfy conditions for uniqueness and stability for incremental boundary-value problems at small strains. Generally at large strains, uniqueness can be lost, and we demonstrate significant effects of non-associated flow on strain localization. In this paper we present results of bifurcations from uniform states of deformation in a thin sheet and forming limits corresponding to sheet necking (using a MK-model), both for biaxial proportional loading paths. The effects of non-glide stresses, which have their origin in dislocation mobility, are manifested at macroscopic scales and are found to significantly effect these and other failure mechanisms.

1. Introduction

For most engineering applications, problems involving plastic deformations are analyzed using so-called associated flow theories, but such theories are not appropriate to describe the inelastic behavior of a broad class of materials. For example, in non-close-packed crystals such as body centered cubic (BCC) metals and intermetallic compounds, or in granular materials, the inelastic material behavior is more accurately described using a non-associated flow theory. In BCC crystals, for example, the core of a screw dislocation spreads onto several non-parallel planes, in which case non-glide stresses can significantly affect their mobility. The plastic behavior in such materials is classified as non-associated in the sense that the flow is not normal to the yield surface and, therefore, a separate flow potential is required. Using Taylor model, Yin and Bassani [1] obtained yield and flow surfaces for random BCC polycrystals, incorporating the effects of non-glide stresses at the single crystal level based upon the yield criterion proposed by Qin and Bassani[2] . The aim of this work is to study the influence of non-glide stresses on the flow of polycrystals. Significant effects of non-glide stresses are also found at the macroscopic levels.

2. Yield and Flow Functions

The yield surface and flow potential for random polycrystals with non-glide stress effects are shown in Fig. 1a (see [1]; also the related paper in this conference by Bassani, et al, 2004, Effects of Non-Glide Stresses on Plastic Flow: From Atomistic Studies of

Dislocations to Macroscopic Failure Mechanisms). The yield surface is seen to depend on the sign of stress whereas the flow surface is independent of the sign of stress. Simple isotropic functions of stress (independent of pressure) for the yield function F and the flow function G that accurately represent the surfaces in Fig. 1a are given by

$$F = \sqrt{3}\left[\left(J_2\right)^{3/2} + bJ_3\right]^{1/3} \quad \text{and} \quad G = \sqrt{3J_2}\,, \tag{1}$$

where J_2 and J_3 are the second and third invariants of the deviatoric stress s_{ij}, respectively, and b is the non-associated flow parameter. The curve fits to the yield and flow surfaces are shown in Fig. 1b, where $b = -0.72$ for the yield function.

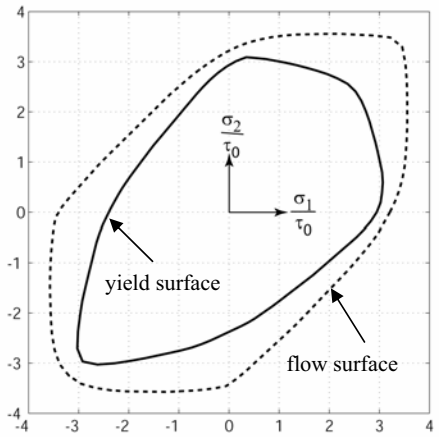

Fig. 1a. Yield and flow surfaces from [1]

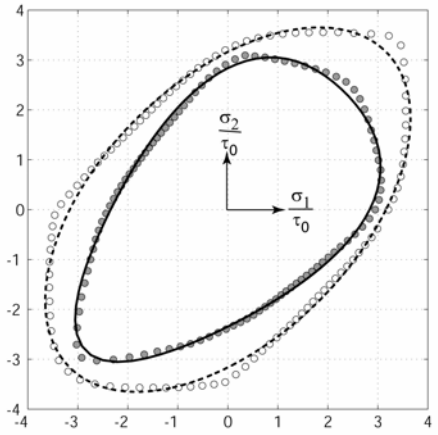

Fig. 1b. Fits to surfaces from Eqn. (1)

3. Non-Associated Flow Theory with Corner Effects

For a material exhibiting non-associated flow, to ensure uniqueness and stability of the solution to an incremental boundary value problem at small strains in the sense of Hill [4] and Drucker [5], corner effects are introduced similar to that adopted by Rudnicki and Rice [3]. In this work, the plastic strain rate $\dot{\varepsilon}_{ij}^{\mathrm{p}}$ is defined as

$$\dot{\varepsilon}_{ij}^{\mathrm{p}} = g\left(\boldsymbol{\sigma}, \varepsilon^{*}\right)\left[\frac{N_{kl}^{\mathrm{f}}\dot{\sigma}_{kl}}{h} N_{ij}^{\mathrm{g}} + \frac{\sqrt{N_{kl}^{\mathrm{f}}N_{kl}^{\mathrm{f}}}\sqrt{N_{kl}^{\mathrm{f}}N_{kl}^{\mathrm{f}}}}{h} g_0 \dot{s}_{ij}\right], \tag{2}$$

where g is an elastic-plastic transition function, $\dot{\sigma}_{ij}$ is the stress rate, h is the hardening modulus, g_0 is a material parameter and, N_{ij}^{f} and N_{ij}^{g} are the outward normals to the yield and flow surfaces, respectively.

4. Non-Glide Stress Effects on Macroscopic Failure Mechanisms

Bifurcations from a uniform state of deformation are studied under plane stress conditions in materials with varying strength-differential, $\mathrm{SD} = 2\left(\sigma_c - \sigma_t\right)/\left(\sigma_c + \sigma_t\right)$, where σ_t and σ_c are the uniaxial yield stresses in tension and compression, respectively. SD is given by a simple function of the parameter b in Eqn. (1); SD = -0.2, 0, 0.2 corresponds to b = -0.75, 0, 0.75, respectively. The critical strains at which bifurcations occur are plotted in Fig. 2a for various proportional loading paths. Next, a MK model is used to determine the strains at which necking occurs in the band, the forming limit. The critical strains at which necking occurs are shown in Fig. 2b.

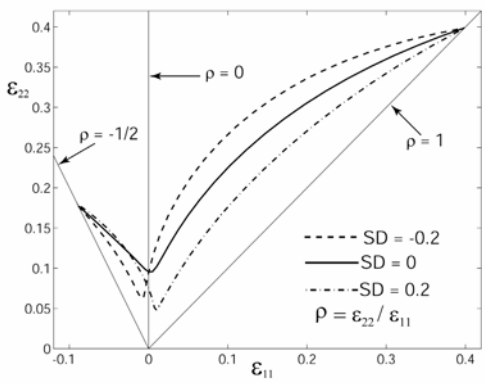

Fig. 2a. Plane stress bifurcations for various proportional loading paths

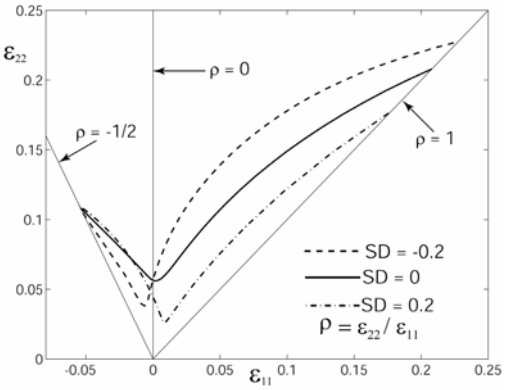

Fig. 2b. MK analysis for different loading paths

For a given value of $\rho = \varepsilon_{22}/\varepsilon_{11}$, both the bifurcation strain and the forming limit can depend significantly on SD. At any state in the deformation, the larger the angle between the outward normals to the yield and flow surfaces the larger the effect of non-associated flow.

References

[1] Yin, L. and Bassani, J. L. (2004) Non-associated flow of polycrystals with non-glide stress affects in single crystals. (to be submitted)

[2] Qin, Q. and Bassani, J. L. (1991) Non-Schmid yield behavior in single crystals. *J. Mech. Phys. Solids* **40**, 813-833.

[3] Rudnicki, J. W. and Rice, J. R. (1975) Conditions for localization of deformation in pressure-sensitive dilatant materials. *J. Mech. Phys. Solids* **23**, 371-394.

[4] Hill. R. (1958) A general theory of uniqueness and stability in elastic-plastic solids. *J. Mech. Phys. Solids* **23**, 236-249.

[5] Drucker, D. C. (1959) A definition of a stable inelastic material, ASME, *J. Appl. Mech.* **26**, 101-106.

Effect of shape and size-distribution on precipitate strengthening in superalloys

S.I. Rao*, T.A. Parthasarathy*, D.M. Dimiduk and P.M. Hazzledine*

Air Force Research Laboratory, Materials and Manufacturing Directorate,
AFRL/MLLM, Wright-Patterson AFB, OH 45433

*UES Inc., 4401 Dayton-Xenia Rd., Dayton, OH 45432

ABSTRACT

Discrete dislocation simulations are a tool to predict the athermal component of critical resolved shear stress (CRSS) for precipitation-strengthened superalloys (1). In this work, the effects of precipitate size, shape and APB energy on the CRSS are simulated, for the strong-pair cutting regime wherein the individual dislocations of a dislocation pair lie within the same precipitate. The APB energy and size dependencies of CRSS are found to be at odds with the analytical Reppich model (2,3). For a distribution of precipitate sizes, the CRSS can be described using an average effective size.

1. Simulations and Effect of APB Energy

A description of the simulations used to set up the γ-γ' microstructure and to drive dislocations through it has been given elsewhere (1). Fig. 1a gives the simulated CRSS for the a/2<110> 60° dislocation pair to overcome the precipitate barrier as a function of the APB energy for three different sizes of cubic precipitates ranging from 50 to 200 nm, edge length. The precipitates in these simulations were randomly-arranged for a volume fraction (v/o) = 0.4. CRSS results for APB energies of 150, 250 and 320 mJ/m^2 were used to generate the plot. The simulation is repeated for five 'microstructures' (i.e. five different sets of precipitate center positions for the same v/o). Fig. 1a shows that the variation of the CRSS with the APB energy is approximately linear, with the CRSS going

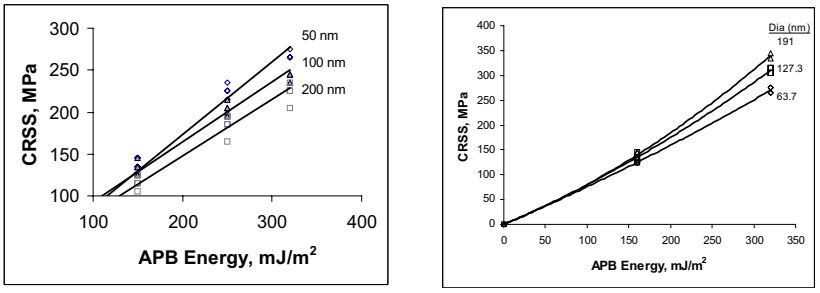

Fig. 1 (a) Simulated CRSS for an a/2<110> 60° dislocation pair cutting cubic precipitates (50, 100, and 200 nm edge lengths) as a function of APB energy at a 0.4 volume fraction. (b) CRSS obtained for an a/2<110> screw-character dislocation pair plotted against the APB energy, for 0.36 volume fraction of spherical precipitates at diameters of 63.7, 127.4 and 191 nm.

to zero at zero APB energy, for precipitate sizes of 50, 100 and 200nm, over the whole APB-energy range. Fig. 1b gives the same information for screw dislocations interacting with three different sizes of spherical precipitates ranging from 63.7 to 191 nm diameter. CRSS results for APB energies of 160 and 320 mJ/m^2 were used to generate the plot. The precipitates in these simulations were randomly arranged spheres for v/o = 0.36. Fig. 1b shows that the variation of CRSS with APB energy is slightly steeper than a linear APB-energy dependence, with the stress going to zero at zero APB energy. Also shown in Fig. 1 is the statistical fluctuation of the CRSS for the five different random distributions and this is seen to be small. For all of the precipitate sizes and APB energies considered in Fig. 1, the spacing between the individual dislocations in the pair remains smaller than the size of the precipitates; hence, the dislocation pair is in the strongly-coupled regime (2,3). Classical theories predict approximately a square-root dependence of the CRSS on the APB energy in the strongly-coupled cutting regime (2,3), which is at variance with the present simulation results. However, the present results for spherical precipitates can be rationalized from the results of simulations of homogenized precipitate structures and the Foreman and Makin simulation results for gliding dislocations interacting with point defects (1, 4-8). The difference between cubic and spherical precipitates is attributable to the different kinds of precipitate intersections on the octahedral plane that are prevalent for the two cases (1).

2. The size and size-distribution of precipitates

Fig. 2 gives the same data as Fig.1 replotted to show the dependence of CRSS on precipitate size. Cubic precipitates become weaker obstacles as their size increases whereas spherical precipitates show the opposite trend. In both cases the dependence of CRSS on size is weak, in disagreement with the inverse-square-root dependence predicted by analytical theories (2,3). Figs. 3a and 3b give the CRSS for two different standard deviations (σ) of the precipitate size distribution, 0.4L and L, for an average precipitate size (L) of 100 nm for cubes and spheres, respectively. Simulations were performed for APB energies of 160 and 320 mJ/m^2. In both cases, the distribution

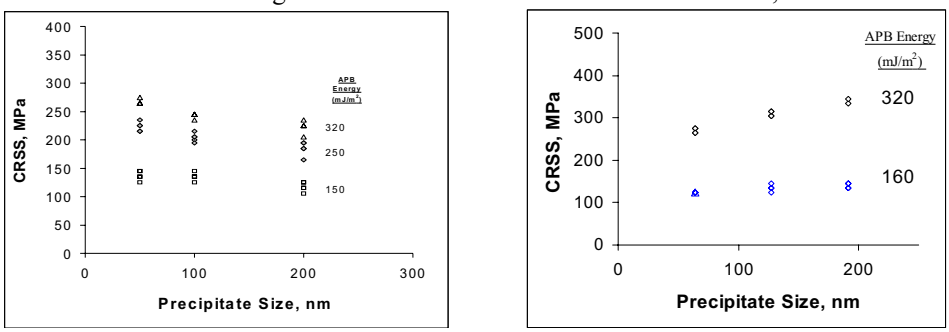

Fig. 2 (a) Effect of the size of cubic precipitates (50–200 nm) on the CRSS for an a/2<110> 60^0 dislocation pair, APB energies of 150, 250 and 320 mJm^{-2} and a volume fraction of 0.4. (b) Effect of the size of spherical precipitates (63.7–191 nm diameter) on the CRSS for an a/2<110> screw-character dislocation pair γ-γ', APB energies of 160 and 320 mJm^{-2} and a volume fraction 0.36.

considered was log normal. For σ = 0.4L five different sizes having probabilities according to the log-normal distribution were used to make up the distribution, whereas for the σ =L case, nine sizes were used. As before, CRSS results from five different microstructures were averaged. Fig. 3 shows that in the case of cubes, the CRSS decreases weakly with increasing σ of the distribution (10% at a σ of L) whereas for

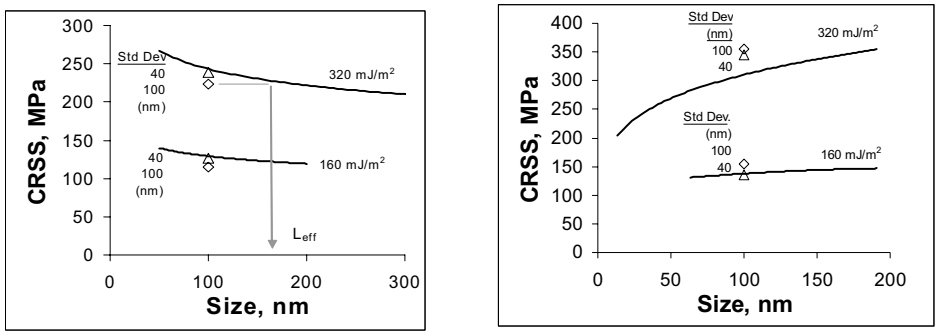

Fig. 3 (a) Effect of the size distribution of cubic precipitates on the CRSS for an a /2<110> 60^0 dislocation pair, at an average precipitate size of 100 nm. (b) Effect of the size distribution, for spherical precipitates having an average precipitate diameter of 127.4 nm, on the CRSS to move an a /2<110> screw-character dislocation pair. APB energies of 160 and 320 mJm^{-2} are considered at a volume fraction of 0.4.

spheres, the CRSS increases weakly with increasing σ of the distribution (15% at a σ of L), at both APB energies. Based on these results, it is suggested that the distributed sizes of precipitates can be replaced by an effective size that is somewhat larger than the average size of the distribution (see Fig. 3).

3. References

1) Rao, S.I., Parthasarathy, T.A. , Dimiduk, D.M. and Hazzledine, P.M., 2004, Phil.Mag., accepted for publication.
2) Reppich, B., 1982, Acta Metall., **30**, 87
3) Reppich, B., 1993, *Materials Science and Technology. A Comprehensive Treatment, vol 6,* edited by H. Mughrabi, et. al., (VCH, Weinheim, Germany), p113·
4) Foreman, A.J.E. and Makin, M.J., 1966, Phil.Mag., **14**, 911.
5) Foreman, A.J.E. and Makin, M.J., 1967, Can. Journ. of Phys., **45**, 511.
6) Ardell, A.J. , 1985, Metall. Trans. A, **16**, 2131.
7) Brown, L.M. and Ham, R.K., 1971, *Strengthening Methods in Crystals,* edited by A. Kelly and R.B. Nicholson, (London: Applied Science), p. 12.
8) Gil Sevilano, J., Ocana Arizcorreta, I. and Kubin, L.P. , 2001, Mat. Sci. and Engr. A, **309-310**, 393.

Toward On-the-fly Multiscale Modeling of Damage Localization

Robert E. Rudd and David Jefferson
Lawrence Livermore National Laboratory, L-045, Livermore, CA 94551

ABSTRACT

We present a preliminary investigation of damage localization as a model problem for adaptive sampling. The fine-scale material response involving void nucleation and growth is computed on the fly as needed at the coarse scale.

1 Adaptive Sampling of Fine-scale Physics

The construction of multiscale models is quite diverse, ranging from sequential approaches to concurrent methodologies [1]. Here we are particularly interested in the class of systems where the entirety of the state space at the fine scale(s) is too vast to permit pre-computation of the material response, but the scales are well separated and the fine-scale evolution only depends on the coarse-scale state locally. Then it is possible to envisage a methodology that computes the fine-scale material behavior on the fly, as it is needed by the coarse-scale simulation. For example, the fine-scale behavior may depend strongly on the initial microstructure and how it evolves under deformation. Both the initial configuration space and the possible histories may be vast and impossible to pre-compute. Nevertheless, it might be possible to compute a homogenized response such as a plastic strain increment for a given microstructure on the fly. Typically the fine-scale calculations are expensive computationally, so the challenge is to formulate an intelligent approach that allows the coarse-scale calculation to be completed at the desired level of accuracy with the minimal amount of fine-scale calculation. The key to the success of such an *adaptive sampling* approach is to minimize redundant or superfluous fine-scale calculations.

The application of interest here is damage localization. At the coarse scale the material deformation results from plastic flow in response to shear stresses and plastic dilation due to the increasing porosity. At the fine scale this porosity is resolved into voids that nucleate from second phase particles, grow and coalesce leading to material failure. We are interested in how the random distribution of void nucleation thresholds (related to the inclusion size distribution, etc.) and local heating affect the degree to which the deformation is localized in damage bands.

2 Numerical Methods

At the coarse scale we have a one-dimensional system (a beam) taken to be a viscous solid in expansion in the longitudinal direction. The system is taken to be periodic in the longitudinal direction, and elongated at a linearly increasing strain rate. The viscous response of the solid is given by $\sigma = \alpha(\dot{\varepsilon}_v)^n$ where σ is the stress and α and n are material constants. The viscous strain rate, $\dot{\varepsilon}_v$, is given by the difference between

the total strain rate and the rate of porosity increase $\dot{\varepsilon}_v = \dot{\varepsilon} - \dot{p}$ where $\dot{\varepsilon}$ is the total strain rate and p is the porosity. The dots denote time derivatives. The porosity is computed on the fly by a fine-scale model. Thermal conduction is also computed. The local temperature affects the development of porosity which in turn causes heating.

Ultimately, a sophisticated and expensive model of void growth will be used at the fine scale, but for the purposes of this preliminary work, the void growth is described by a DFRACT model [2]: $\dot{p}_i = p_i(\sigma - \sigma_0)/\nu$, where p_i is the volume fraction of the i^{th} void, σ is the mean (hydrostatic) stress, σ_0 is the mean stress threshold for growth, and ν is the viscosity. Void nucleation takes place at a mean tensile stress and void volume drawn from Gaussian distributions. These distributions are calculated at the beginning of the simulation, so the initial microstructure is completely specified. The input for the fine-scale model is the local stress and temperature, and the resulting output is the rate of porosity increase. We have found that it is necessary to compute the porosity rate implicitly in order to achieve numerical stability.

A coupling code provides an interface between the coarse-scale and fine-scale models, and it controls the adaptive sampling. In practice, just like the fine-scale model, its role is to provide the data $\dot{p}[\sigma(x,t), T(x,t); x]$ to the coarse-scale model. At each point, the coarse-scale model provides the temperature $T(x)$ and the stress $\sigma(x)$, and the coupling routine returns the rate of porosity increase. The coupling model appears to the coarse-scale code to be a material response database. This kind of interface is important for minimally invasive implementation of on-the-fly multiscale modeling. In practice it does one of two things. Based on a sampling criterion that incorporates knowledge of the finite temperature threshold, the coupling model either returns a database value for $\dot{p}$ where available or it queries (or spawns and queries) a fine-scale simulation to determine $\dot{p}$, and returns that value.

3 Results and Discussion

We have used the adaptive sampling algorithm described above to investigate the development of localized fracture with a particular interest in the effective speed up that can be obtained and how it depends on the degree to which the damage is localized. The results of two simulations are shown in Fig. 1. The porosity is plotted as a function of position in the one-dimensional system. The coarse-scale model consisted of 1000 finite elements with linear shape functions and single point quadrature. Each element contained 100 void nucleation sites with normally distributed random nucleation thresholds whose standard deviation was 20% of the mean. Failure occurred when the porosity in any one element reached 0.1. The difference in the two simulations was the temperature dependence of the void growth threshold. The system with a greater temperature dependence tended to localize the damage to one or a few elements, as the heat generated by the initial void growth promoted further void growth. The onset of this damage localization instability could also be triggered by changes in the strain rate, nucleation threshold distribution and growth viscosity.

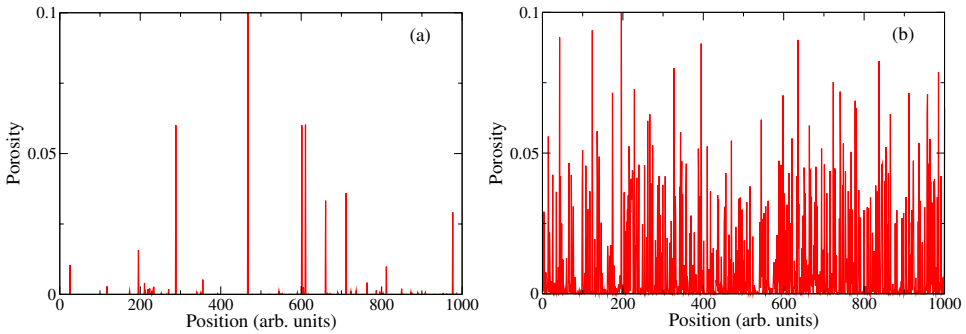

Figure 1: Porosity at failure due to void growth from a random distribution of nuclei: (a) greater damage localization due to heating and (b) negligible heating.

While these preliminary simulations were done with a fairly inexpensive void growth model, our goal is to use high fidelity fine-scale calculations including molecular dynamics. Then the fine-scale calculations will dominate the computational cost, and so we quantify the speed up as the ratio of the total number of material model calls in the coarse-scale elements to the number that involve a fine-scale calculation (a ratio of 1 indicates no speed up). The main result, for our purposes here, is that by adjusting the parameters of the model we have attained different levels of damage localization and quantified the speed up due to the adaptive sampling approach. In the highly localized case (Fig. 1a), the ratio of the total number of material model calls in the coarse-scale elements to the number that involve a fine-scale calculation was 203 and a total of 180 voids nucleated; in the poorly localized case (Fig. 1b), the sampling ratio was 26 and a total of 4282 voids nucleated.

These simple toy model calculations indicate that adaptive sampling may be used quite effectively in order to speed up multiscale simulations relying on on-the-fly calculation of fine-scale material response. The proof, of course, will lie in the implementation of this algorithm in more realistic simulations. As a by-product, the simple model indicates that damage localization may exhibit a rich physical phenomenology as thermal and mechanical materials properties are varied.

We thank R. Becker for important contributions in formulating adaptive sampling, and thank A. Arsenlis, N. Barton and V. Bulatov for useful discussions. This work was performed under the auspices of the U.S. Dept. of Energy by Univ. of California, Lawrence Livermore National Laboratory under Contract No. W-7405-Eng-48.

[1] R. E. Rudd and J. Q. Broughton, "Concurrent Multiscale Simulation of Solid State Systems," Phys. Stat. Sol. (b) **217**, 251 (2000).

[2] L. Seaman, D. R. Curran and D. A. Shockey, "Computational models for ductile and brittle fracture," J. Appl. Phys. **47**, 4814 (1976).

Dynamics Simulation of Material Interface Using Molecular Dynamics and SPH Methods

Ken-ichi Saitoh, Yuki Tateoka, and Noboru Shinke

Department of Mechanical Engineering, Faculty of Engineering,
Kansai University
3-3-35 Yamate-cho, Suita-shi, Osaka, 564-8680 Japan
E-mail: saitou@ipcku.kansai-u.ac.jp

ABSTRACT

Availability of two genuine particle methods, molecular dynamic (MD) and smoothed particle hydrodynamics (SPH), in framework of multi-scale mechanical analysis is discussed. We have developed SPH simulation of interface between isotropic solids with three-dimensional elastic constitutive equation. To compare with results of SPH, MD simulation by using simple Lennard-Jones potential is carried out. The dynamic behavior and stress distribution of these interface models are obtained. It is found that there is some similarity in the mechanism of stress concentration in interface region. Subsequently, an idea for hybrid simulation method between SPH and MD is proposed and numerical test using simple configuration is performed.

1. Introduction

Fatal fracture of engineering materials often occurs in interface region because inhomogeneous bonding between atoms or severe difference in material properties causes and incompatibility of deformation and residual stresses. For the purpose of evaluating such mechanical behavior in interface region, microscopic view (i.e. atomistic view) is inevitable, so molecular dynamics (MD) simulation is promising. However, it is difficult by applying only MD methodology to treat whole region. A multi-scale simulation, where MD simulation is combined with some macroscopic simulation, should be developed for mechanical analysis of materials interface. Several studies tried to implement such a hybrid-type simulation [1]. In this study, availability of SPH (smoothed particle hydrodynamics) as a partner for MD is investigated. The fact that both MD and SPH are genuine particle methods with moving particles on Lagrangian frame makes their combination very naturally. A hybrid computation model is proposed after evaluation of mechanical properties of bi-material including interface region by these two methods are carried out and compared.

2. Methods for SPH and MD simulations

SPH method for elastic solid materials is as follows [2][3]. Basic equations of SPH for dynamic analysis are Eqn.(1),(2), and (3), where α and β mean Cartesian components. The parameter h determines interaction range of kernel function, as $W_{ij} \equiv W(|\boldsymbol{r}_j - \boldsymbol{r}_i|, h)$. The comma used in subscript indicates derivative. Variables, r_i^α, v_i^α, ρ_i, m_i, $\varepsilon_i^{\alpha\beta}$, and $\sigma_i^{\alpha\beta}$ are velocity, density, mass, strain, and stress of a particle i, respectively. Π_{ij} is artificial

viscosity [4]. Stress tensor is obtained from strain tensor by constitutive equation for three-dimensional isotropic elastic solid.

$$\frac{\mathrm{d}\rho_i}{\mathrm{d}t} = \sum_j m_j (v_j^\beta - v_i^\beta) W_{ij,\beta} \tag{1}$$

$$\frac{\mathrm{d}v_i^\alpha}{\mathrm{d}t} = \sum_j m_j \left(\frac{\sigma_i^{\alpha\beta}}{\rho_i^2} + \frac{\sigma_j^{\alpha\beta}}{\rho_j^2} - \Pi_{ij} \right) W_{ij,\beta} \tag{2}$$

$$\frac{\mathrm{d}\varepsilon_i^{\alpha\beta}}{\mathrm{d}t} = \frac{1}{2} \sum_j \frac{m_j}{\rho_j} \left\{ (v_j^\alpha - v_i^\alpha) W_{ij,\beta} + (v_j^\beta - v_i^\beta) W_{ij,\alpha} \right\}, \ \sigma_j^{\alpha\beta} = C_j^{\alpha\beta\gamma\delta} \varepsilon_j^{\gamma\delta} \tag{3}$$

Materials joint model for SPH simulation is shown in Fig.1(a), which is surrounded by free surfaces and is composed of materials A, B, and interface material. The interface material, whose thickness is changeable, possesses medium properties between A and B. Calculation condition for SPH simulation is shown in Table 1. One of examples of materials pair, presented here, is copper(A) and steel(B). The computation model for MD analysis using Lennard-Jones potential is shown in Fig.1(b), where interface is corresponding to (100) crystalline plane of fcc. Calculation condition for MD analysis is shown in Table 2. Tensile loading is subjected to these models by pulling two chucking regions with constant velocity to the opposite directions ($\pm y$).

3. Results & Discussions

3.1 Comparison of Results Obtained by SPH and MD Methods

Fig.2(a) shows stress distribution of σ^{xx} averaged on SPH particles along y direction when total tensile strain ε^{yy} reaches 0.0014. Regional compressive and tensile stresses occur due to different Poisson's effect between materials A and B. Oscillation in the stress distribution means that precise propagation of stress wave has been caught. According to theory of elasticity stress in the edge of material interface should come to infinity, but finite value is obtained because of discretization in SPH. Maximum difference in σ^{xx} is about 40 MPa when tensile stress σ^{yy} is about 200 MPa. Fig.2(b) shows distribution of σ^{xx} averaged for MD results. Stress concentration behavior same as that of SPH is also detected for MD.

3.2 Discussion: Introduction of Hybrid Model between MD and SPH

Apart from difference in size (MD for atomic and SPH for macroscopic dimensions), concentration of stress in the interface region is reproduced adequately by SPH and MD method. For test of a hybrid simulation between MD and SPH, we adopt "force bridging method" (without overlapping region)[5]. In this methodology, for example, equation of motion of MD particle in transition region is considered as Eqn.(4). "N_{md1}" is the maximum number of standard MD interactions and "N_{sph2}" is that of interactions between SPH and MD particles. The second term in RHS of Eqn.(4) balances by also acting on SPH particles j.

$$\frac{\mathrm{d}v_i^\alpha}{\mathrm{d}t} = -\frac{1}{m_i} \sum_{j=1}^{N_{md1}} \frac{\partial \phi(r_{ij})}{\partial r_{ij}} \frac{r_{ij}^\alpha}{r_{ij}} + \sum_{j=1}^{N_{sph2}} m_j \left(\frac{\sigma_i^{\alpha\beta}}{\rho_i^2} + \frac{\sigma_j^{\alpha\beta}}{\rho_j^2} - \Pi_{ij} \right) \frac{\partial W_{ij}}{\partial r_i^\beta} \tag{4}$$

Fig.3 shows model and result of tensile test (in this case the material is monotonic fcc solid and dimension of the system is scaled down to nano-meter size for spatial compatibility). There seems to be no inconvenience in replacing MD particles by SPH particles.

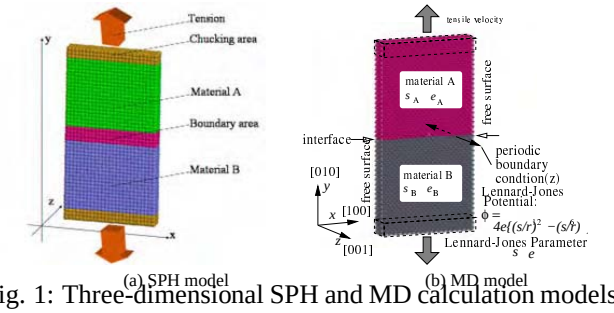

(a) SPH model (b) MD model

Fig. 1: Three-dimensional SPH and MD calculation models

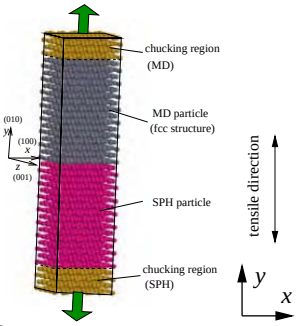

(a) computation model

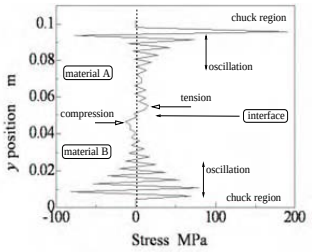

(a) Result obtained by SPH (ε^{yy}=0.0014)

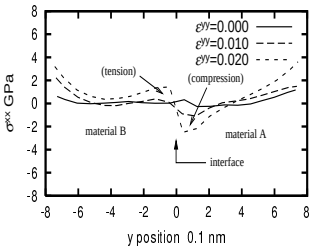

(b) Result obtained by MD

Fig. 2: Distribution of σ^{xx} along y direction

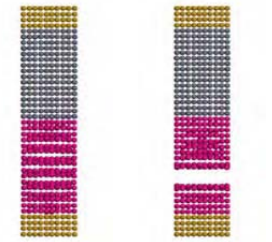

(b) ε^{yy}=2.93% (c) ε^{yy}=4.39%

Fig. 3: Hybrid model for SPH-MD analysis and result

Table 1: SPH calculation conditions

property	unit	value
Width×Length×Thickness ($x \times y \times z$)	mm	51.05× 100.0× 6.4
Distance between initial particles	mm	2.127 ($= R_x$)
Chuck length	mm	6.0
Boundary thickness	mm	4.2
Tensile speed	m/s	0.1
Time increment	s	1.0×10^{-9}
The number of Particles	-	4800
Type of kernel function	-	cubic spline
Kernel parameter h	R_x	1.5

Table 2: MD calculation conditions

value	unit	property
The number of atoms	-	13284
Lattice constant	nm	0.405
Size $x \times y \times z$	nm	8.10×16.20×1.62
Time increment	fs	0.5
Maximum temperature	K	5.0
Tensile speed	m/s	100.0
Periodic conditions		only in z direction
LJ parameter s	nm	0.2608
LJ parameter e/k_B	K	4948.0 (material B),
(k_B:Boltzmann const.)		24740 (material A)

References

[1] *For example:* Kohlhoff,P., *et al.*, Crack Propagation in b.c.c Crystals Studied with a Combined Finite-Element and Atomistic Model , *Philos.Mag.*, **64**-4(1991), 851-878.

[2] Sakai,Y. and Yamashita,A., Study on the Fundamental Characteristics of Structural Analysis by Particle Method based on SPH, Trans.Jpn.Mech.Eng.,Ser.A, **67**(2001),1093-1102. (in Japanese)

[3] Shintachi,T. and Sekine,H., Proposal of New Particle Generation Technique in SPH Analysis of Hypervelocity Impacts, Trans.Jpn.Mech.Eng.,Ser.A, **68**(2002),132-138. (in Japanese)

[4] Randles,P.W. and Libersky,L.D., Smoothed Particle Hydrodynamics: Some Recent Improvements and Applications, *Comput.Methods Appl.Mech.Engrg.*, **139**(1996), 375-408.

[5] Liu,G.R., and Liu,M.B., *Smoothed Particle Hydrodynamics; A Meshless Particle Method*, (2003), 341, World Scientific.

Ideal Interfacial Strength Between Vanadium and Oxide Ceramics

M.Satou[a], K.Abe[a], N.Kioussis[b] and N.Ghoniem[c]

[a] Dept. Quantum Sci. & Energy Engr., Tohoku Univeristy, Aramaki-aza-Aoba, Sendai 980-8579, JAPAN manabu.satou@qse.tohoku.ac.jp
[b] Dept. Physics & Astronomy, California State University, Northridge, CA 91330 U.S.A. nick.kioussis@csun.edu
[c] Mechanical & Aerospace Engr. Dept., University of California Los Angeles, Los Angeles, CA 90095 U.S.A. ghoniem@ucla.edu

ABSTRACT

We have studied the bonding interface using the model of oxide ceramics slab adhered to vanadium slab by means of the electronic structure calculation. The simple interface model of vanadium and CaO facing each other at the (001) plane was employed. Total energy and adhesive energy were evaluated. We found that the relation of adhesive energy and separation distance of the interface was described well by universal binding energy relation. The ideal strength of the interface was calculated to be 6.4GPa as the derivative of the energy with respect to the interfacial separation distance.

1. Introduction

Metal and ceramics interface is of interest from various fields of engineering materials including nano-particle strengthening steel and nuclear fusion blanket component. Fundamental understanding of metal and ceramics bonding will provide useful guideline to develop a robust interface for these applications. Vanadium alloy have been considered as a prime candidate structural material for liquid metal blanket design of nuclear fusion reactor. Insulator coating on the alloy is considered to be essential to reduce magneto-hydro dynamics effects of the system. Selected oxide ceramics have been studied for the application. In this paper, we will discuss about the ideal bonding strength of the interfaces between vanadium and oxide ceramics.

2.Procedures

A combination of CaO and V was selected in this study. CaO has passable properties for the nuclear fusion blanket applications. Although other candidate ceramics include Y_2O_3 and Er_2O_3 have much better compatibility with lithium at high temperatures, CaO was selected due to its rather simple structure. CaO has rock-salt structure with face centered cubic lattice. The experimental lattice parameter used in the calculation for CaO was 0.481059nm, and that for V was 0.30274nm with body centered cubic lattice. Previous electronic structure calculations indicated that early transition metals (V, Nb, Ti) and oxide ceramics have strong bonding. The metal atoms were located directly on the top of the oxide O ions [1]. In this paper, a simple interface model of CaO and V facing each other at the (001) plane was employed. The model we used here is that the V lattice

is rotated by (π/4-arctan(1/2)) degree around the [001] axis of the CaO lattice, so that one out of five V atoms in the (001) plane are located on the top of O ions of the CaO as show in Fig. 1. We used a supercell approach to simulate the interface. Three layers of CaO slab is adhered to both sides of three layers of V slabs. The experimental lattice constant of 0.30274nm was used for the V layers, so the CaO (a=0.481059nm) must shrink by 0.5% to be commensurate.

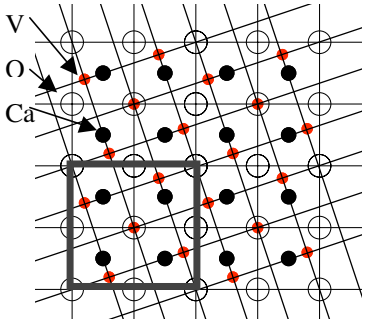

Fig.1. Geometry of the top view CaO/V interface model. Vanadium and CaO are facing each other at the (001) plane in the interface. Square box is calculation cell.

For calculations of the electronic structure of the interface we have used the WIEN package [2], that uses density functional theory based on the full-potential linearized augmented plane-wave and local orbitals method. Detailed procedure of calculation was described in elsewhere [3]. Total energy and adhesive energy of the interface model were evaluated. A charge convergence limit of 0.0001 was applied to all calculation. The numerical accuracy of the energy was less than 0.1meV/atom.

3.Results and Discussion

The calculated total energy as a function of the interface separation distance between CaO and V had the minimum at the distance of 0.32nm, which was considered to be corresponding to the equilibrium separation. The adhesive energy (E_a) of the interface is defined as follow:

$$E_a=(E_{CaO/V} - (E_{CaO} + E_V))/2A. \quad (1)$$

$E_{CaO/V}$ is the total energy of the supercell containing the CaO and V interfaces, E_{CaO} and E_V refer to the energy of a slab of CaO or V, respectively, separated by vacuum. The area of an interface is A, and the factor 2 represents the two interfaces in the supercell. The calculated adhesive energy as a function of the interface distance had minimum as shown in Fig.2. The minimum energy at the equilibrium separation is defined as the ideal adhesive energy (E_0) of the interface.

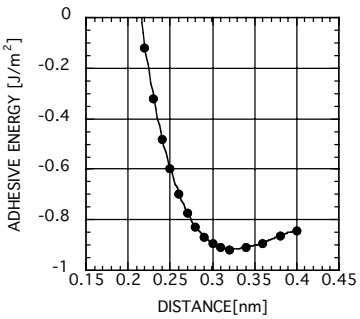

Fig.2. Adhesive energy as a function of separation distance of the CaO/V interface.

Relationship between adhesive energy and separation distance of covalent or metallic bond phases was described by universal binding energy relation as follow [4]:

$$E^*(a^*)= - (1+a^*) \exp(-a^*), \quad (2)$$

$$a^*=(d-d_0)/l . \quad (3)$$

$E^*(a^*)$ is a scaled adhesive energy, which is the adhesive energy (E_a) divided by the ideal adhesive energy (E_0), d is the separation distance, d_0 is the equilibrium separation distance and l is a scaling length. As shown in Fig.3, the function describes well the relation of adhesive energy and separation distance for the CaO and V interface as

far as 0.5 of the scaled distance.

The stress can be defined as the derivative of the energy as a function of the separation distance. The ideal peak interfacial strength was derived from the relation of the ideal adhesive energy as follow [5].

$$\sigma_{max} = 2E_0 / le \,, \qquad (6)$$

where E_0=0.92J/m^2, l =0.105nm in the case of the CaO and V interface from Fig.3 and e is the base of the natural logarithm. Thus the ideal strength of the interface is calculated to be 6.4GPa.

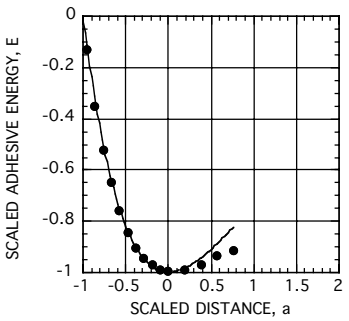

Fig.3. Scaled adhesive energy as a function of scaled separation distance of the CaO/V interface. The solid line is a plot of the universal binding energy relation.

The procedure described here can be utilized for more complex system such as Y_2O_3 and Er_2O_3 and alloys, however, to discuss the actual interfacial strength, it may need to deal with a large-scale atomistic picture of the interface that includes misfit dislocations and micro cracks. The small-size atomistic view described here should be a subset of such large-scale view. Moreover, advanced experimental methods to measure the interface strength corresponding to their stress mode such as shear, tensile or twist, could be utilized for validation of this calculation.

4.Summary

Ideal tensile strength of the interface between metal and ceramics was calculated. Procedure described here could be applied much complex systems, which may be suitable for practical applications.

Acknowledgements

This work was partly supported by the Japan/US collaborative JUPITER-II program in fusion materials research. A part of the calculation was done at supercomputing system, Information Synergy Center at Tohoku University.

References

[1] S.Kostlmeier and C.Elsasser, *Ab-Initio Investigation of Metal-Ceramic Bonding: M(001)/MgAl2O4(001), M = Al, Ag*, Interface Sci., **8**, 41(2000).
[2] Wien2k:P.Blaha, K.Schwarz, G.K.H.Madsen, D.Kvasnicka and J.Luitz, *WIEN2k, An Augmented Plane Wave + Local Orbitals Program for Calculating Crystal Properties* (Karlheinz Schwarz, Techn. Universitat Wien, Austria), 2001. ISBN 3-9501031-1-2.
[3] M.Satou, N. Komatsu, T. Sawada, K. Abe, *Calculation of electronic structure at bonding interface between vanadium and oxide ceramics for insulator coating applications*, J.Nucl. Mater., **329-333**, 1571 (2004).
[4] A.Banerjea and J.R.Smith, *Origins of the universal binding-energy relation*, Phys. Rev. B, **37**, 6632 (1988).
[5] T.Hong, J.R.Smith and D.J.Srolovitz, *Impurity effects on adhesion: Nb, C, O, B, and S at a Mo/MoSi$_2$ interface*, Phys. Rev. B, **47**, 13615 (1993).

Growth of Dislocations in Nonuniform Fields --- A Microelectronics Perspective

K.W. Schwarz [a] **and D. Chidambarrao** [b]

[a] IBM Watson Research Center, P.O. Box 218, Yorktown Heights, NY 10589
[b] IBM Systems and Technology Group, SRDC, Hopewell Junction, NY 12533

ABSTRACT

Semiconductor processing involves large stresses, high temperatures, crystal damage, and other factors favoring the appearance of dislocations. Yet a few dislocations in the wrong places on wafer containing hundreds of millions of devices can cause failure. It is important, therefore, to develop practical ways of estimating when and where dislocations are likely to nucleate, and to determine their final configurations. Dislocation modeling can be useful in this context. Fundamental issues that need further clarification include the nucleation and growth of dislocations in highly nonuniform fields, and the effects of crystal damage on dislocation nucleation. Even greater challenges are presented by current plans to utilize strained-silicon layers grown pseudomorphically on relaxed SiGe/Si or SiGe/SOI layers. Here the goal is to control the dislocation behavior so that the SiGe layer relaxes to leave a uniform distribution of misfit dislocations at the SiGe/Si interface, with very few dislocations threading the layer. Detailed comparisons between particularly promising experiments and large-scale simulations have been carried out, and excellent agreement is obtained.

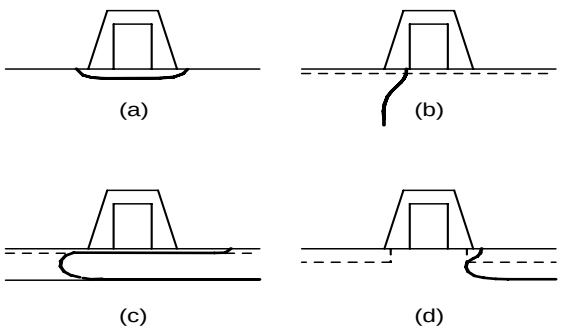

Fig. 1. Some likely dislocation fails. (a) stable configurations in bulk silicon due to source-drain pinning; (b) threading dislocation from a graded buffer layer extending into the Si cap; (c) shorting misfit created by motion in an SGOI layer; (d) possible stable configuration in an embedded-SiGe device.

1. Dislocations in Devices

Figure 1 shows some typical transistor fails due to dislocations. To understand such unwanted 'intruder' dislocations in a device, the challenge is to model single dislocations in the extremely complicated processing environment. Usually, the greatest difficulty lies in determining the stress fields in the device at various stages of the manufacturing process. In addition to the standard finite-element stress modeling approaches, process-

modeling codes likes TSUPREM4 and TAURUS are required to deal with stresses resulting from chemical processes such as oxidation and nitride deposition. Such codes are more qualitative, and have other goals than accurate stress prediction, but we have had success in using them to predict dislocation behavior quantitatively [1]. From the dislocation-modeling point of view, such problems require the ability to deal with arbitrarily complicated stress and stress fields. The approach adopted in our DD code PARANOID [2,3] is to convert the usual unstructured FEM stress table into a tree of Cartesian tables, and to deal with surfaces in terms of the usual unstructured table of triangular tiles. A typical model calculation is shown in Fig. 2.

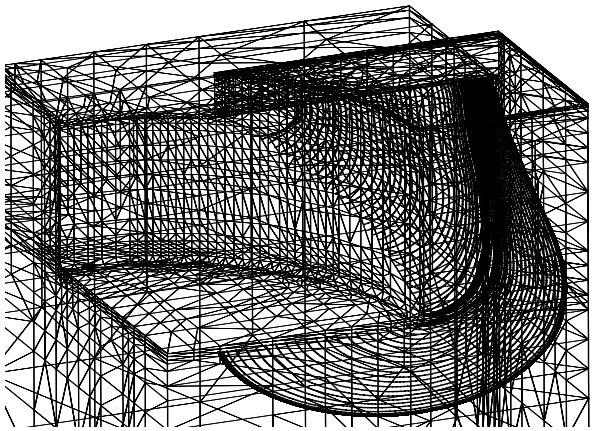

Fig. 2. Model calculation of dislocation motion in one quadrant of a DRAM cell.

Aside from the practical difficulty of characterizing the environment, there is the physical issue of understanding dislocation nucleation. Here the DD code can be used to identify the location and size of the minimal dislocation loops required, allowing one to estimate whether such a loop is likely to be injected into the system thermally or as the result of crystal damage. Controlled experiments are being carried out to explore the usefulness of such estimates.

2. Strained-Silicon Substrates

The basic feature of many of the strained-silicon schemes is the pseudomorphic growth of a thin layer of strained Si on top of a relaxed SiGe layer, either graded on bulk Si or sitting directly on a buried oxide. As indicated in Fig. 3, the relaxation of the SiGe substrate proceeds by the motion of threading arms through the layer, leaving behind a 2D array of misfit dislocations in the interface. Both the uniformity of the resulting misfit array and the residual density of threading arms are crucial factors in determining the usefulness of the relaxed substrate. The primary challenge in modeling layer relaxation, or the related problem of layer strength, is the necessity of treating many interacting dislocations. The PARANOID code implements sophisticated methods of approximating the strong interactions that occur between colliding dislocations [3], allowing us to treat such large problems with relatively modest computational resources.

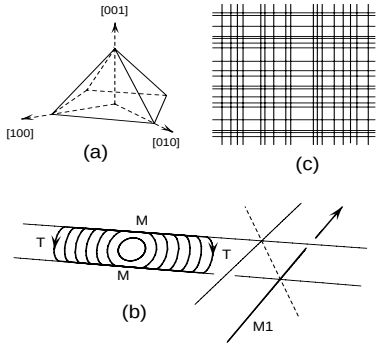

Fig. 3. Elements of layer relaxation. (a) slip systems for a (001) layer; (b) dislocation loop growing to form threading (T) and misfit (M) arms, interacting with another misfit (M1); (c) planview of idealized misfit array.

Again, the dislocation-nucleation mechanism is a problem, in that a typical layer often reaches many times the critical thickness before it begins to relax via some unknown dislocation-creation mechanism (open symbols in Fig. 4). Using ion-implantation techniques [4,5], however, it is possible to introduce a known initial density of threading dislocations into such a layer, leading to maximal possible relaxation for all layer thickness (closed symbols in Fig. 4), and making it possible to simulate the relaxation. As shown by the crosses in Fig. 4, such simulations are in excellent quantitative agreement with the experimental observations.

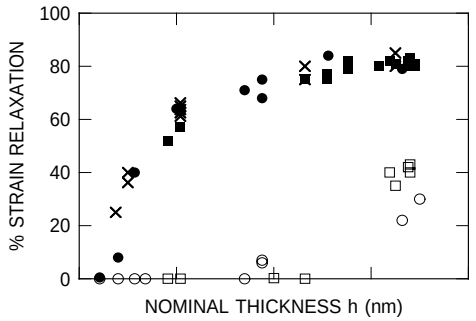

Fig. 4. Experiments (solid symbols) and theory (x marks) for implant-induced layer relaxation [6].

References

[1] D. Chidambarrao, X.H. Liu, and K.W. Schwarz, J. Appl. Phys. **92**, 6278 (2002).
[2] K.W. Schwarz, J. Appl. Phys. **85**, 108 (1999).
[3] K.W. Schwarz, Modell. Simul. Mater. Sci. Eng. **11**, 609 (2003).
[4] H. Trinkaus, B. Hollander, St. Rongen, s. Mantl, H.-J. Herzog, J. Kuchenbecker, and T. Hackbarth, Phys. Lett. **76**, 3552 (2000).
[5] S.H. Christiansen, P.M. Mooney, J.O. Chu, and A. Grill, Mater. Res. Soc. Symp. Proc. **686,** 27 (2002).
[6] K.W. Schwarz, J. Cai, and P.M. Mooney, App. Phys. Lett. (in press).

Combining Quantum and Continuum Mechanics to Model Hydrogen Embrittlement

S. SEREBRINSKY[1], E. A. CARTER[2] AND M. ORTIZ[3]

[1]Division of Engineering and Applied Science, California Institute of Technology, Pasadena, CA 91125, USA. serebrin@caltech.edu

[2]Department of Chemistry and Biochemistry, University of California at Los Angeles, Los Angeles, CA 90095-1569, USA. eac@princeton.edu

[3]Division of Engineering and Applied Science, California Institute of Technology, Pasadena, CA 91125, USA. ortiz@aero.caltech.edu

ABSTRACT

A model of hydrogen embrittlement (HE) is developed, based upon: 1) a cohesive law dependent on interface impurity coverage that is calculated *ab initio*; 2) a stress-assisted diffusion equation related to the environment; 3) a continuum analysis of crack growth; and 4) the Langmuir equilibrium determining the impurity coverage from its nearby bulk concentration. We consider the effect of several parameters, applying the model to calculate HE properties in high-strength steels (HSS) and high-strength aluminum alloys (HSAA). The calculations reproduce qualitatively the existence of stages I and II of crack growth, and may give intermittent crack. For HSS, the predictions of the model are in general quantitative agreement with available measurements, suggesting that hydrogen-induced degradation of cohesion is a likely mechanism for hydrogen-assisted cracking. For HSAA, calculations show a measurable HE, but lesser than experimentally observed.

1. Introduction and Model

Stress-corrosion cracking (SCC) and hydrogen embrittlement (HE) are related, long-standing problems, commonly described under the name of environment-assisted cracking (EAC), which remain incompletely understood from the mechanistic point of view. Accordingly, the prediction of the lifetime of engineering components undergoing EAC remains an elusive goal.

We endeavor here to develop a model of HE that contains several improvements on most previous works, namely: 1) embedding of *ab initio* calculations; 2) calculation of properties directly comparable with experiments. The three basic steps in the model are: 1) hydrogen is introduced into the metal through the boundaries; 2) atomic hydrogen is transported through the metal lattice towards the tensile-stressed surroundings of the crack tip; 3) the local combined action of stress and hydrogen concentration around the crack tip leads to failure of the metal in an embrittled zone.

Step 2 is accounted for by the stress-assisted diffusion equation for the hydrogen concentration C that includes the effect of a term $E_p=pV_H$ in the hydrogen chemical potential. p is the hydrostatic stress (or pressure), V_H is the molar volume of solution of hydrogen. Step 1 corresponds with the boundary condition on the crack flanks $C = C_{eq}(p) = C_{eq,0}\exp(pV_H / RT)$ for the diffusion equation. $C_{eq,0}=C_{eq}(0)$ is the concentration in an unstressed solid in equilibrium with its environment. Step 3 is incorporated via cohesive theories of fracture. The properties of the cohesive surface are derived by a combination of first principles calculations [1], a renormalization procedure and an elastic correction [2]. The resulting cohesive law $\sigma(\delta,\theta)$, remarkably, contains information from first principles calculations and at the same time is suitable for continuum level calculations. The particular form is $\sigma(\delta,\theta)=\sigma_c(\theta)(1-\delta/\delta_c)$ for $\delta<\delta_c$, and zero otherwise, where the dependence of the critical traction $\sigma_c(\theta)=\sigma_c(0)[1-\omega(\theta)]$ on interface coverage θ is given by the embrittlement function $\omega(\theta)$, calculated by first principles [1]. The critical opening displacement δ_c is quite independent of θ. We consider the bulk material as a J_2-plastic with power-law strain hardening.

E_p gives the effect of mechanics on concentration. The effect of concentration on mechanics is given by the cohesive law depending on θ, along with the Langmuir equilibrium $\theta=C/[C+\exp(-\Delta g_b^0/RT)]$ between the cracking interface and the adjoining bulk, where Δg_b^0 is the free energy difference between the standard states of hydrogen adsorbed at the cracking interface and bulk interstitial.

2. Simulations, Discussion and Conclusions

Each simulation corresponds to an applied stress intensity K, yield stress σ_y, and given environmental conditions. A typical evolution in time for HSS is shown in Fig. 1. There is an incubation time t_i while hydrogen builds-up around the cohesive zone, dragged by the stress p (the term E_p), and the traction free point at x_f does not move. After that the crack advances intermittently, again due to some time needed for hydrogen accumulation around the crack tip, in an *average* steady state with constant cohesive zone length L_{coh} and velocity V_P. These features agree with experimental observations. The concentration and plastic strain fields follow the jerky advancement. For each value of σ_y, a curve V_P-K is extracted, leading to a threshold K_H for crack propagation, a steep increase of V_P above K_H (stage I), and a plateau at velocity $V_{P,II}$ (stage II), in agreement with the general form of an experimental curve V_P-K in EAC. The derived plots of K_H-σ_y and V_P-σ_y display

very good agreement with experimental data. When increasing the environmental activity, experiments show a decrease and later some saturation of K_H. The calculations show a similar behavior when increasing $C_{eq,0}$. The measurements reflect thus the saturation of the interface, as roughly shown by $\sigma_c(C)=\sigma_c(\theta(C))$. Such a saturating law should replace the often used linear relation $\sigma_c(C)=\sigma_c(0)-\alpha C$. Overall, the agreement suggests that decohesion is a likely mechanism for HE of HSS.

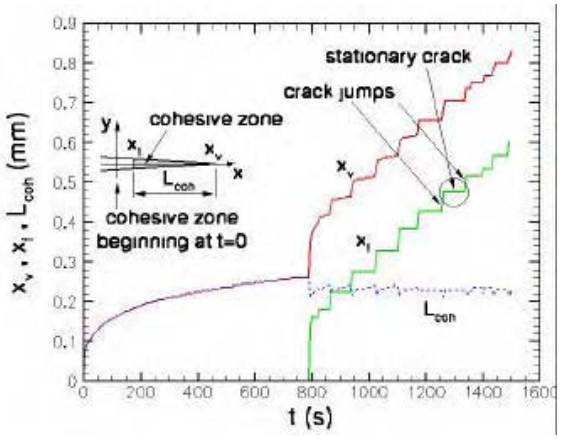

Figure 1. Evolution in time of the crack vertex and traction free points, for a typical simulation for HSS.

When applying the model to HSAA, the crack advances continuously. Experiments show that there exist crack jumps, but much smaller than in the case of HSS. The model gives thus the correct trend. Incorporation of details of microstructure of grain boundaries (GBs) may be relevant to account for jerky propagation. We also see here both stages I and II, but at values of K_H higher and $V_{P,II}$ lower as compared to experiments. The milder calculated embrittlement may be due to: 1) additional mechanisms involved; 2) embrittlement laws for GBs are required; 3) effects of microstructure lead to different equations with the same mechanistic ingredients.

Acknowledgements

E.A.C. and M.O. thank the U.S. Dept. of Defense for support provided through Brown University's MURI Center for the "Design and Testing of Materials by Computation: A Multi-Scale Approach." M.O. acknowledges the Office of Naval Research for partial support provided under grant N00014-96-1-0068.

References

[1] a) A. van der Ven, and G. Ceder, *The thermodynamics of decohesion*, Acta Mater. **52**, 1223 (2004); b) D. E. Jiang, and E. A. Carter, *First principles assessment of hydrogen embrittlement in Fe and Al crystals*, Phys. Rev. B (to be submitted).

[2] S. Serebrinsky, E. A. Carter, and M. Ortiz, *A quantum-mechanically informed continuum model of hydrogen embrittlement*, J. Mech. Phys. Sol. (in press).

Crack Propagation of Silicon by Hybrid Tight-binding Molecular Dynamics

Y. Shibutani*, N. Hori*, S. Ogata* and P. Gumbsch**

*** Dept. of Mechanical Eng. & Systems, Osaka University, 2-1 Yamadaoka, Suita, Osaka 565-0871, Japan E-mail: sibutani@mech.eng.osaka-u.ac.jp**

**** Fraunhofer Institute for Mechanics of Materials IWM, Woehlerestr.11, 79108 Frieburg, Germany E-mail: peter.gumbsch@iwm.fraunhofer.de**

ABSTRACT

Highly strained crack-tip field of silicon is analyzed using hybridized computational scheme coupling with the order *N* tight-binding (TB) method and the empirical modified Tersoff potential. The modeling on the treatment of so-called ghost forces coming up in the atomistic conjoining region is suggested and the exact total energy description in the whole system is formulated. In order to eliminate the initial residual stresses due to mismatching the equilibrium properties between two schemes, the empirical Tersoff potential parameter set is refitted by the simulated annealing method. Inspecting numerical conformity of the coupling region, it is applied to solve the crack propagation problem in silicon to discuss the effect of the boundary constraints to the anoisotropic propagation on the (110) crack surface dependent on the crack propagation direction.

1. Introduction

Most simplified understanding of a crack problem is reduced to coupling between dislocation emission and bond breaking of the crack tip. A sensing tool for the bond breaking behavior of the brittle materials with the highest resolution could be an atomistic simulation. The crack problem with (011) crack surface of silicon has been discussed by the density functional theory (DFT) [1] and the tight-binding (TB) method [2] in order to understand the anisotropy of the crack propagation direction. The issues on the surface reconstruction and the bond breaking by the exacter electric charge distribution has there been emphasized. However, the boundary constraint problem due to the limited number of the atoms remains.

In the present paper, the hybridized computational scheme between the order *N* TB

method and the empirical Tersoff type potential with refitted parameter set is proposed to improve the size-limitation problem. The modeling on the treatment of so-called ghost forces coming up in the atomistic conjoining region is suggested and the exact total energy description in the whole system is formulated. In order to eliminate the initial residual stresses due to mismatching the equilibrium properties between two schemes, the Tersoff potential parameter set is refitted by the simulated annealing (SA) method.

2. Hybridization between TB and Tersoff potential

The hopping parameters and the pairwise repulsive potential of the present TB model are described by the environment-dependent TB potential proposed by Wang *et al*. [3]. To reduce the computational time, the TB scheme has been scaled into the order *N* using the density matrix (DM) method initially proposed by Li *et al*. [4]. Since the most of the atoms containing in the crack problem deform infinitesimally except the localized highly-strained crack region, the TB region is patched only at the crack tip surrounded by the atoms driven by the empirical Tersoff potential, as shown in Fig.1. The total energy of the whole system is first summed by the TB energy, E_{ab}, and the Tersoff poteintial part, E_{em}, as follows.

$$E_{tot} = E_{ab} + E_{em}$$

$$E_{ab} = E^{\mathrm{TB(TI)+TR}} = \sum_{n}^{occ} \sum_{\alpha \in \mathrm{TB+TR},l} C_{\alpha l}^{n*} C_{\alpha l}^{n} E_{\alpha l} + \sum_{n}^{occ} \sum_{\alpha \in \mathrm{TB+TR},l} \sum_{\beta \in \mathrm{TB+TR},l'} C_{\alpha l}^{n*} C_{\beta l'}^{n} H_{\alpha l \beta l'}, \quad (1)$$

$$E_{em} = E^{\mathrm{TR+TE}} = \sum_{\alpha \in \mathrm{TR+TE}} E^{\alpha}(\boldsymbol{r}^{\mathrm{TR}}, \boldsymbol{r}^{\mathrm{TE}}, \boldsymbol{r}^{\mathrm{TI}})$$

where $C_{\alpha l}^{n}$ is the *n*-th eigenvectror of the *l* atomic orbital of α atom. Due to each nonlocal property of the TB and Tersoff potential with the different cutoff radius, the energy is intrinsically overestimated in Eqn.(1). Therefore, the work done by the so-called ghost forces emerging in the TI and TR regions, where TI is within the TB region also within the cutoff radius of the Tersoff potential in the TR, should be subtracted from

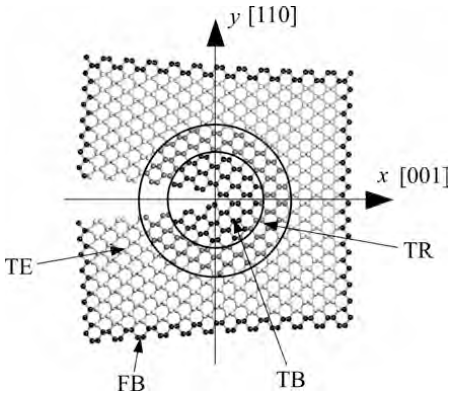

Fig.1 Hybridized MD with TB for crack model.

Eqn.(1).

$$E_{tot} = E_{ab} + E_{em} - \sum_{\gamma} \int_0^{\boldsymbol{u}^\gamma} \boldsymbol{g}^\gamma(\boldsymbol{u}^\gamma) \cdot d\boldsymbol{u}^\gamma$$
$$= E^{\mathrm{TB(TI)+TR}} + E^{\mathrm{TR+TE}} - \sum_{\gamma} \int_0^{\boldsymbol{u}^\gamma} \boldsymbol{g}^\gamma(\boldsymbol{u}^\gamma) \cdot d\boldsymbol{u}^\gamma \quad , \tag{2}$$

where $\boldsymbol{g}^\gamma(\boldsymbol{u}^\gamma)$ $(\gamma \in \mathrm{TI}, \mathrm{TR})$ is the ghost force of the atom γ in the TI or TR region. Since $\boldsymbol{g}^\gamma(\boldsymbol{u}^\gamma)$ changes according to the deformation, it should been updated at each time step. If the external loads $\tilde{\boldsymbol{f}}^\beta$ are applied on the group of atoms β, the total potential energy Π in the system should be written as the following.

$$\Pi = E_{tot} - \sum_{\beta} \int_0^{\boldsymbol{u}^\beta} \tilde{\boldsymbol{f}}^\beta(\boldsymbol{u}^\beta) \cdot d\boldsymbol{u}^\beta$$
$$= \left(E^{\mathrm{TB(TI)+TR}} + E^{\mathrm{TR+TE}} - \sum_{\gamma} \int_0^{\boldsymbol{u}^\gamma} \boldsymbol{g}^\gamma(\boldsymbol{u}^\gamma) \cdot d\boldsymbol{u}^\gamma \right) - \sum_{\beta} \int_0^{\boldsymbol{u}^\beta} \tilde{\boldsymbol{f}}^\beta(\boldsymbol{u}^\beta) \cdot d\boldsymbol{u}^\beta \quad . \tag{3}$$

3. Refitting Potential Parameter Set

The physical properties obtained by the original Tersoff potential [5] and the TB are so different that the residual stress field may occur after the sufficient relaxation. The current misfit volume strain is about 1.5% due to the different lattice parameters. The new parameter set is shown in Table1 after being refitted by the SA method. It is noticeable that the lattice constant and C_{44} are especially improved.

Table 1 Physical properties by refitted Tersoff potential parameter set.

	C_{11} [GPa]	C_{12} [GPa]	C_{44} [GPa]	C_{11}-C_{12} [GPa]	Lattice const. [nm]	Cohesive Energy [eV]
TB	149.6	45.3	62.5	104.3	0.5459	-4.5618
Refitted Tersoff	135.6	30.6	62.6	105.0	0.5459	-4.5686
Error [%]	9.5	32.7	0.1	0.8	0	0.01
Error of original Tersoff[%]	11.9	43.9	27.4	2.0	0.49	1.5

Acknowledgements

The author (YS) would like to acknowledge the support from Grants-in-Aid for Scientific Research (B)(15360054).

References

[1] R.Pérez and P.Gumbsch, Acta. Mater., **48** (2000), 4517-4530.
[2] Y.Shibutani, T.Kugimiya and P.Gumbsch, Proc. of Int. Conf. on DIS'02, (2002-11), 101-108,
[3] C.Z.Wang, B.C.Pan and K.M.Ho, J.Phys: Condens. Matter, **11** (1999), 2043-2049.
[4] X.P.Li, R.W.Nunes and D.Vanderbilt, Phys. Rev. B, **47** (1993), 10891-10894.
[5] J.Tersoff, Phys. Rev. B, **38** (1988), 9902-9905.

Dislocation Evolution in Thin Film-Substrate Systems

E.H. Tan and L.Z. Sun

Department of Civil and Environmental Engineering and Center for Computer-Aided Design, The University of Iowa, Iowa City, IA 52242-1527, U.S.A.
Email: lzsun@engineering.uiowa.edu

ABSTRACT

A discrete dislocation dynamics method is developed to simulate dislocation evolution in thin films. The interactions among the dislocation loop, the free surface and interface are rigorously computed by decomposing this complicated problem into two relatively simple sub-problems. Dislocation loops are discretized into segments, each of which is represented by a parametric space curve. This method is successfully applied to determine the critical thickness of film for a surface half loop to nucleate and to simulate how a surface loop evolves into two threading dislocations.

1. Introduction

Various types of discrete dislocation dynamics (DDD) methods [1-4] have been developed for infinitely extended homogenous solids. Hartmaier et al. [5] further simulated the dislocation movement in half-space solids. For the widely used thin film-substrate systems, however, due to the complexity arising from the inhomogeneities and free surface boundary conditions, most research work still treats them as an infinitely extended homogeneous solid with a prescribed misfit strain [e.g., 6].

In this paper, with the assumption that materials are isotropic and the dislocations glide in their own slip planes, an effective DDD algorithm for thin film-substrate systems is proposed. The basic idea of the algorithm is first described, and then examples concerning dislocation movements and critical radii for dislocation loops emerging from free surfaces are given. Finally, several conclusions are reached.

2. Algorithm

It is very difficult to directly obtain stresses induced by dislocation loops in thin film-substrate systems. Actually, we decompose this problem into the supposition of two problems: (a) the occurrence of dislocation loops in an infinite extended bi-material medium, which will create a traction field $T_i(\mathbf{x})$ on the virtual free surface, and (b) the loading of a traction field $-T_i(\mathbf{x})$ on the free surface of the thin film-substrate system.

In our case, the local stresses at a point on the dislocation loop are induced by three factors: the misfit strain, other dislocations and the dislocation itself. The first two

components can be obtained by Freund method and the method we have just discussed. We use Brown method to find the third component. Then the Peach-Kohler formula is employed to find the local force $\boldsymbol{f}(s)$ acting on a dislocation line.

In most cases, the dislocation speed and the stress are small enough so that we can neglect the inertial effects and write the governing equation in a linear form:

$$\boldsymbol{B}\cdot\mathbf{v}(s)-\boldsymbol{f}(s)=0 \tag{1}$$

where $\boldsymbol{B}$ is dislocation mobility, $\mathbf{v}(s)$ is the dislocation velocity.

The Galerkin method is used to construct the weak form of equation (1) and further obtain the global governing equation during the ith time step t_i. Solving the global equation, we obtain the node velocities $\{V\}_{t_i}$. Then the node coordinates of the dislocation line at t_{i+1} can be written as:

$$\{X\}_{t_{i+1}}=\{X\}_{t_i}+\{V_e\}_{t_i}\left(t_{i+1}-t_i\right) \tag{2}$$

The dislocation position at t_{i+1} can be totally determined by the node coordinates $\{X\}_{t_{i+1}}$.

3. Example and Conclusions

Consider a dislocation half loop emerging from the free surface in a thin film-substrate system as shown in Fig. 1. The thin film is $0.1\mu m$ thick. Its Young's modulus, Poisson ratio and lattice constant are $E_f=85.5GPa$, $\nu_f=0.31$ and $a_f=5.653$ Å respectively. The corresponding substrate parameters are: $E_s=165.5GPa$, $\nu_s=0.25$ and $a_s=3.834$ Å. The misfit strain is $\varepsilon_0=4\%$. The dislocation's Burgers vector is $b=3.834$ Å. The angle between the slip plane of the dislocation loop and the horizontal plane is 60^0.

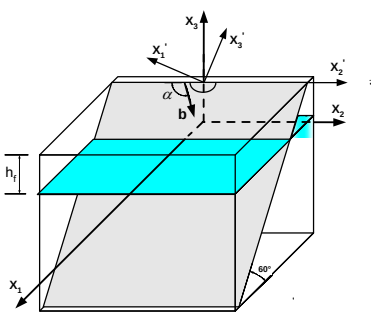

Fig. 1 Model

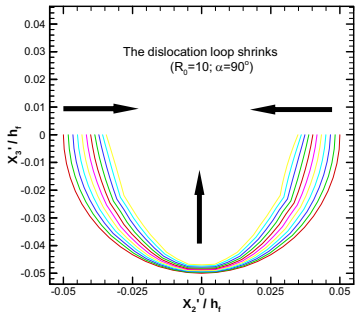

Fig. 2 Dislocation shrinking

Fig. 2 shows that when the initial radius is reduced to $R_0 = 10nm$, the dislocation will shrink and finally leave out of the system. While Fig. 3 indicates that if $R_0 = 25nm$ the dislocation will continuously expand, finally becoming two threading dislocations with a misfit segment along the interface. So the critical radius in this case should satisfy $10nm < R_c < 25nm$. Fig. 4 gives the plot of critical thickness versus misfit strain. The solid curve is given by setting the total generalized force acting on the threading dislocation to be zero. The discrete points are estimated by the numerical simulations of the nucleation of a surface half loop with the assumption that the external energy fluctuation is 7.2×10^{-19} *Joules*. Obviously, the critical thickness for the nucleation of a surface half loop is much greater that that for a threading dislocation to advance.

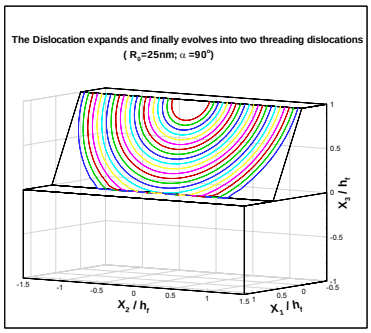

Fig. 3 Dislocation expansion

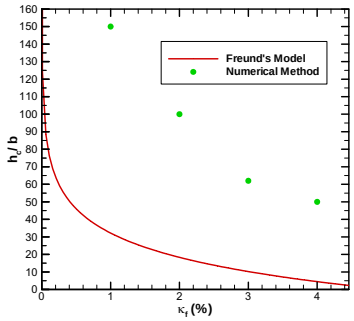

Fig. 4 Critical thickness comparison

It is seen that the method we propose successfully incorporate both the free surface effect and the interface effects in simulating dislocation evolution. It provides a more reasonable way to find the thin film critical thickness because more energy is needed for a dislocation to nucleate than expand.

4. Acknowledgements

The authors gratefully acknowledge the financial support of NSF under contract no. DMR 0113172.

Reference

1. H.M. Zbib, M.Rhee and J.P. Hirth, Int. J. Mech. Sci. **40**, 113 (1998)
2. N.M. Ghoneim, S.-H. Tong and L.Z. Su, Phys. Rev. B **61**, 913 (2000)
3. Y.U. Wang, Y.M. Jin et al, Acta mater. **49**, 1847 (2001)
4. M. Koslowski, A.M. Cuitiño and M. Ortiz, J. Mech. Phys. Solids **50**, (2002)
5. A. Hartmaier, M.C. Fivel et al, Modeling Simul. Mater. Sci. Eng. **7**, 781 (1999)
6. B. von Blanckenhagen, P. Gumbsch et al, Modeling Simul. Mater. Sci. Eng. **9**, 157 (2001)

Size Effects in Thin Films: Discrete Dislocations and Strain Gradients

E. van der Giessen and L. Nicola

Netherlands Institute for Metals Research/Department of Applied Physics, University of Groningen, Nyenborgh 4, 9747 AG Groningen, The Netherlands
E-mail: Giessen@phys.rug.nl

1 Introduction

Experiments have shown that stress evolution in films with a thickness on the order of micrometers is size dependent. Two-dimensional, plane strain simulations are presented where plastic deformation arises from the nucleation and motion of discrete dislocations in a thin film bonded to a stiff substrate. We subsequently study the ability of one of the strain gradient theories currently available to pick-up these size effects, viz. the one proposed by Gurtin[1].

2 Summary of DD Results for Single Crystal Thin Films

The problem of a thin film on a semi-infinite substrate subjected to thermal loading as illustrated in Fig. 1 has been studied using discrete dislocation (DD) simulations in [2] and [3]. As the temperature is reduced from a stress-free and dislocation-free state, the substrate undergoes unconstrained contraction but, due to the mismatch between the thermal expansion coefficient of film (α_f) and substrate (α_s), stress develops in the film; tensile for $\alpha_f > \alpha_s$. After an initial elastic response, dislocations nucleate in the film and partially relax the stress in the film by gliding on three sets of parallel slip planes. We focus on two crystal orientations: $\phi_{60} = (0^\circ, 60^\circ, 120^\circ)$ and $\phi_{30} = (30^\circ, 90^\circ, 150^\circ)$.

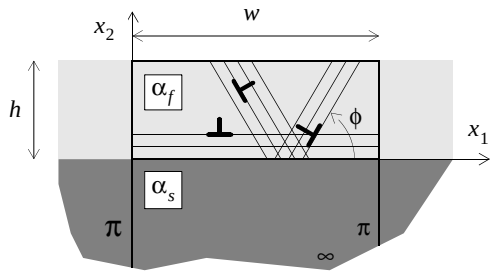

Figure 1: Geometry of the film-substrate problem. A unit cell of width w is analyzed and the height of the substrate is taken large enough to represent a half space.

Results obtained for three different film thicknesses —$h = 1\mu$m, 0.5μm and 0.25μm— show that the average in-plane stress in the films is dependent on the film thickness. Results also show that hardening depends on crystal orientation: relaxation in films with orientation

ϕ_{30} is higher than in films with slip planes oriented ϕ_{60}. Moreover, the size effect is more evident for the ϕ_{60} orientation.

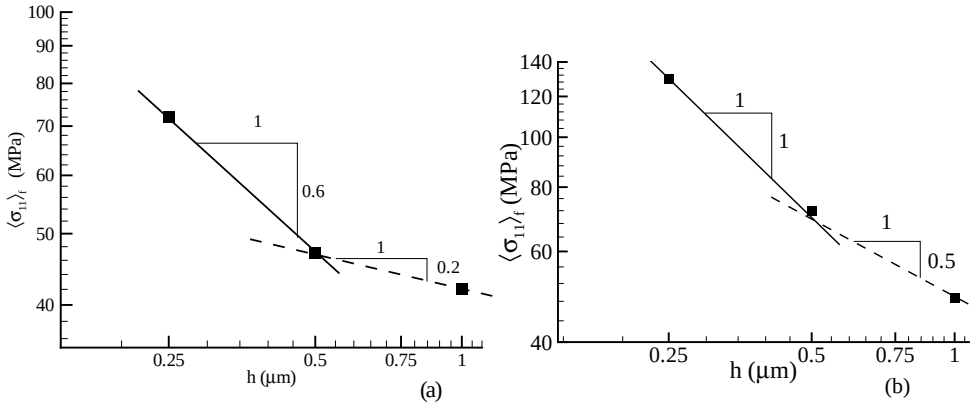

Figure 2: DD predictions [2] of the average film stress versus film thickness for (a) ϕ_{30} and (b) ϕ_{60}. The data points are fitted to a power law of the form $\langle\sigma_{11}\rangle_f \propto h^{-p}$.

In both crystal orientations, the size dependence originates from the large stress gradient at the film-substrate interface, caused by dislocation pile-ups. Instead of a uniform stress distribution across the film height, as in the elastic state or according to classical local plasticity, the stress increases as the interface is approached. As a consequence, the stress left inside the film after relaxation depends on the film thickness

3 Strain Gradient Crystal Plasticity

Gurtin's theory[1] is a continuum plasticity theory designed for single crystals with a finite set of slip systems (identified by a superscript $^{(\beta)}$). The key characteristic is that it assumes the free energy ψ to be additively decomposed of the standard elastic strain energy and a defect energy Ψ_D that is quadratic in the gradients of the slip, $\boldsymbol{\nabla}\gamma^{(\beta)}$. This results into a back stress on each slip system that depends on the slip gradients on (possibly) all slip systems. We confine attention here to only this strain gradient effect in symmetric double slip (and in plane strain).

The form of $\Psi_D(\boldsymbol{\nabla}\gamma^{(\beta)})$ is a constitutive assumption and there are very few guidelines except invariance principles. Originally, Gurtin proposed the isotropic expression [1]

$$\Psi_I = \tfrac{1}{2}\ell^2\pi_0|\boldsymbol{g}|^2 \tag{1}$$

for Ψ_D, where π_0 is the initial yield shear stress and ℓ a constitutive length parameter. The slip gradient in this case enters through the net-Burgers vector $\boldsymbol{g} = \sum_\beta \partial^{(\beta)}\gamma^{(\beta)}\boldsymbol{s}^{(\beta)}$, where for each slip system β, $\partial^{(\beta)}$ is the derivative in the direction of slip. The closed-form solution in [4] demonstrated that this version of the theory is capable to describe the results

for the orientation ϕ_{30} but not for ϕ_{60}. In fact, the predicted stress field is independent of orientation.

Motivated by the presence of numerous pile-ups in the DD simulations, we consider, amongst others, a defect energy determined directly by the measure $\partial^{(\beta)}\gamma^{(\beta)}$, i.e.

$$\Psi_P = \tfrac{1}{2}\ell^2\pi_0 \sum_{\beta} (\partial^{(\beta)}\gamma^{(\beta)})^2. \tag{2}$$

π_0 is the same initial yield stress as in (1), but ℓ is a different length parameter. The latter is the single free parameter that controls the size effect. A value $\ell = 3\mu$m gives a pretty good agreement with the DD resuls, for both orientations as shown in Fig. 3.

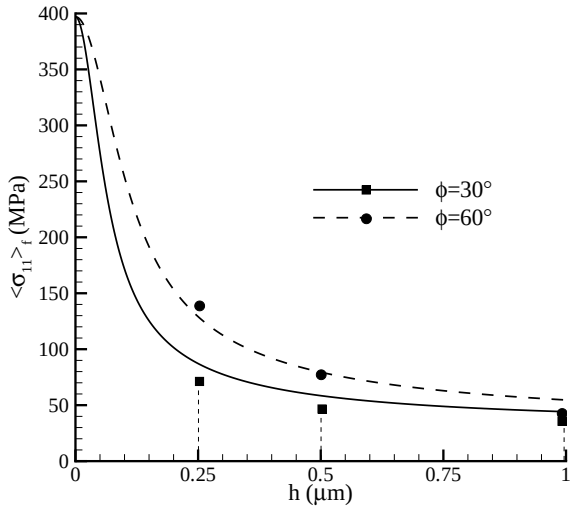

Figure 3: Film-average tensile stress as a function of film thickness *h* for two orientations according to the pile-up theory.

References

[1] M.E. Gurtin, *J. Mech. Phys. Solids*, vol. 50, pp. 5–32, 2002.

[2] L. Nicola, E. van der Giessen and A. Needleman, *J. Appl. Phys.*, vol. 93, pp. 5920-5928, 2003.

[3] L. Nicola, E. van der Giessen, A. Needleman, "Two hardening mechanisms in single crystal thin films studied by discrete dislocation plasticity", *Phil. Mag.* submitted for publication.

[4] L. Nicola, E. van der Giessen, A. Needleman, "Nonlocal modeling of size-dependent response of thin films", in Proceedings of ICM9, May 25-29, Geneva 2003 (CD-ROM: 273.pdf).

Bridging between QM and mesoscale: development and application of ReaxFF reactive potentials for Ru/Pt metal and metal oxide surface catalysis

Adri van Duin, Yunhee Jang, Timo Jacob and William Goddard

Materials and Process Simulation Center, California Institute of Technology, Pasadena CA 91106, E-mail duin@wag.caltech.edu

ABSTRACT

The high computational expense of quantumchemical (QM) methods greatly hinders application of these methods to dynamic simulations of the interaction of metal and metal oxide surfaces with their catalytic substrates. As such, application of QM methods tends to be limited to idealized, static simulations. While such simulations have provided valuable insights in metal and metal oxide surface catalysis, they cannot provide a full picture of the chemical complexity and the influence of reaction conditions (temperature, pressure, chemical composition) on the catalytic process.

To provide a dynamic picture of chemical reactivity at metal/metal oxide surfaces for large (>1000 atoms) systems we have extended the ReaxFF reactive potentials [1-4] to Ru/Pt metal and metal oxides and their interaction with first-row elements. We have fitted ReaxFF parameters to extensive QM-databases covering both ground state systems and relevant reaction pathways. Using this method we have performed dynamical simulations of oxygen interactions with Ru/Pt metal systems and have managed to abstract reaction kinetic data from these simulations that can be used to train mesoscale fuel cell models.

1. Introduction

Chemical reactions at metal and metal oxide surfaces play a crucial part in many catalytic processes. Obtaining detailed atomistic-scale information for the reaction dynamics at these surfaces, crucial for optimizing catalyst design, is far from trivial. Experimental measurements can provide information on stable surface species, but cannot easily access the microscopical length scales and femtosecond-time scale required to obtain information on reaction pathways. Computational methods, on the other hand, suffer from the reverse problem. While quantumchemical (QM) methods are certainly capable of providing detailed reaction information, the computational expense associated with these methods limits their general application to small, static systems, making it virtually impossible to apply these methods to generate a full, dynamic picture of the chemistry occurring at configurationally and compositionally complicated metal/metal oxide surfaces. Force field-based (FF) methods do, in principle, allow simulations on systems sizes and time-lengths suitable for capturing surface reactivity, but traditionally

these methods have mostly been parameterized to describe systems at or near equilibrium and cannot simulate bond dissociation or formation. To remedy this situation we have been developing a new branch of FFs, ReaxFF [1-4], which combines the computational speed of FF-methods with the QM-ability to simulate chemical reactions. Here we report on the extension of the ReaxFF method to Ru- and Pt metal and metal oxides.

2. Methods

The periodic QM calculations were performed using the SeqQuest periodic DFT program with Gaussian basis sets. The non-periodic QM-calculations were performed using the Jaguar-program (Schrödinger Inc.) using the DFT/B3LYP/6-311G** for the first row elements and the LAC3P effective core potential and basis set for the metal atoms.

3. Results/Discussion

3.1 Force field development.

To determine ReaxFF parameters for Pt/Ru/O systems we constructed a substantial and diverse QM-derived training set. This set contained data for the following systems:

- Equations of state (EOS) for Pt- and Ru 12, 8, 6 and 4-coordinate bulk metal phases.
- EOS for various Pt/Ru alloys.
- Surface energies for metal, alloy and metal oxides.
- Pt- and Ru metal clusters ranging from 2 to 35 atoms.
- EOS and relative heats of formation for Pt- and Ru-oxide bulk phases, covering multiple oxidation states (PtII-PtIV, RuII-RuVIII).
- Oxygen binding energies to various surface sites.
- Full single- and double metal-oxygen bond dissociation.
- Distortion energies for relevant valence angles.

We successfully fitted ReaxFF parameters to reproduce these QM-data, thus generating a fast computational method able to describe the reaction dynamics related with oxidation at Ru/Pt metal and alloy surfaces.

3.2 Application to ozone-reaction with Pt/Ru alloy slabs.

To demonstrate the potential of ReaxFF for investigating transition metal surface chemistry we performed NVT-MD simulations at 1200K on Pt- and Ru surface oxidation by ozone. We find that, in case of Ru, the oxidation reaction leads to the formation of several Ru-oxide layers on top of the slab, while in the case of Pt the oxygen atoms remain on the surface and do not migrate into the bulk (Figure 2).

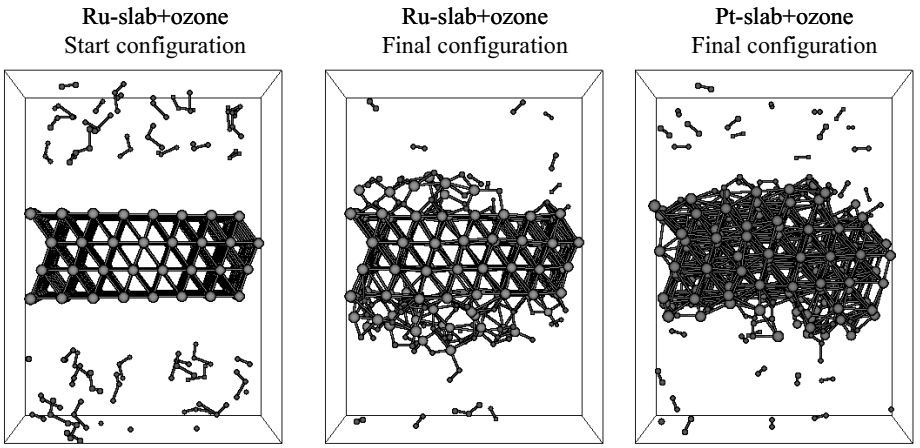

Figure 2. Initial and final configurations obtained from a 1200K NVT-MD simulation of the ozone reaction with a Ru- and a Pt-(111) slab.

4. Conclusion

By fitting force field parameters to a substantial QM-derived training set, containing both ground state systems as well as transition state structures, we managed to construct a reactive force field method (ReaxFF) suitable for describing oxidation reactions at Ru- and Pt-surfaces. Application of this method to high-temperature (1200K) surface oxidation by ozone indicates that Ru will form several oxide layers under these conditions, while the oxygen atoms cannot migrate into the Pt-bulk.

References

[1] A.C.T. van Duin, S. Dasgupta, F. Lorant and W.A. Goddard *ReaxFF: A Reactive Force Field for Hydrocarbons* . J. Phys. Chem. A **105**, 9396-9409 (2001).

[2] A. Strachan, A.C.T. van Duin, D. Chakraborty, S. Dasgupta and W.A. Goddard *Shock waves in High-Energy Materials: The Initial Chemical Events in Nitramine RDX.* Phys. Rev. Letters **91**, 098301-1 (2003).

[3] A.C.T. van Duin, A. Strachan, S. Stewman, Q. Zhang, X. Xu and W.A. Goddard *$ReaxFF_{SiO}$ Reactive Force Field for Silicon and Silicon Oxide Systems*. J. Phys. Chem. A **107**, 3803-3811 (2003).

[4] Q. Zhang, T. Cagin, A.C.T. van Duin, W.A.Goddard, Y. Qi and L.G. Hector *Adhesion and nonwetting-wetting transition in the Al/α-Al_2O_3 interface.* Phys. Rev. B **69**, 045423 (2004).

First Principles Simulation of Dislocation Cores

C. Woodward, SI, Rao,* and D. Trinkle
Materials and Manufacturing Directorate, Air Force Research Laboratory
AFRL/MLLM, Wright-Patterson AFB, OH 45433-7817
***UES, Inc., 4401 Dayton-Xenia Road, Dayton, OH 45432-1894**
christopher.woodward@wpafb.af.mil

ABSTRACT

In order to understand the "chemistry of deformation" an adequate description of the strain field near the center of dislocations (the core) is required. We have developed a first-principles flexible boundary-condition method for simulating isolated dislocations in metals and alloys. The method self-consistently couples the local dislocation strain field to the long-range elastic field. The problem is divided into two parts: a solution for the nonlinear dislocation-core region and a solution for the long-range elastic response. Solving these problems is straightforward and by iteratively coupling the two solutions we can efficiently solve for the strain field in all space. This effectively reduces the mesoscopic atomistic simulation to one involving only degrees of freedom near the dislocation core. We have used this method to study dislocations cores and the Peierls stress in: bcc Mo and Ta, and $L1_0$ TiAl.

1. Introduction

Many materials properties are directly related to the structure and mobility of dislocations. While continuum elasticity methods have been very successful in describing long-range stress fields of dislocations, these methods diverge close to the center of a dislocation (i.e. the core region) and cannot describe the strain field produced there. Atomistic methods have shown that the forces produced at the dislocation core and their coupling to the applied stress can have a dramatic effect on plasticity. However, atomistic methods are limited by the fidelity of the assumed interaction model and for this reason are at best semi-empirical. In order to understand the "chemistry of deformation" it is necessary to produce an accurate representation of the atomic forces produced near the dislocation core. Here we derive theses forces using an electronic structure method combined with a flexible boundary condition method which correctly couples the local strain field to the long range elastic field. This allows for simulation cell sizes which are substantially smaller than conventional methods (by more than 90%) while retaining the integrity of the simulation [1].

2. Numerical Procedure

The electronic structure calculations have been performed using an *ab-initio* total-energy and molecular dynamics program, the Vienna *Ab-initio* Simulation Package (VASP), which was developed at the Institut für Theoretische Physik, Technische Universitat

Wien [2]. Details of the calculations for a/2<111> screw dislocations in bcc Mo and Ta and a/2<110] screw dislocations in $L1_0$ TiAl can be found in the literature [3,4,5].

The strain field of the dislocation core is contained using the 2-dimensional lattice Greens function. The dislocation is placed within two concentric cylindrical regions (Fig. 1) where region 3 is used to isolate the dislocation core from the domain boundary formed at the edge of the simulation cell [4,5]. An initial atomic displacement field, from anisotropic elasticity theory, is then relaxed in region 1 using the Hellmann Feynman forces from the first principles calculation. Incompatibility forces, generated for atoms in region 2, are removed by displacing all the atoms within the simulation cell according to the Greens function (GF) solution:

$$u_i^m = \sum_{j,n} G_{ij}^{mn}(R_{mn}) f_j^n \qquad (1)$$

where the indices m, n denote atoms, the indices i, j denote the Cartesian components, $R_{mn}=R_n-R_m$ and f_j are the Hellmann-Feynman forces. This process is repeated until the atomic forces in regions 1 and 2 are converged. The required elastic GF and the lattice Greens function are generated from the reference calculations of the elastic constants and a simple numerical procedure respectively [1]. In the first principles adaptation of the GFBC the atoms are moved according to the derived Hellmann-Feynman forces at all steps of the optimization procedure.

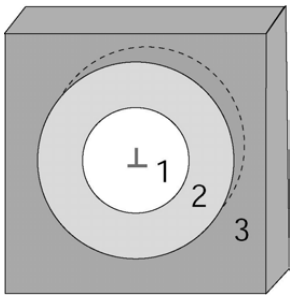

Figure 1.
Schematic of simulation cell geometry.

3. Results and Discussion

We have calculated the equilibrium displacement field and the lattice friction stress for a/2<111> screws dislocations in the bcc transitions metals (Mo and Ta) and a/2<110] screw dislocation in $L1_0$ TiAl. The derived equilibrium dislocation cores are shown in Figure 2. using the method of differential displacements.

It is widely accepted that one source of non-Schmidt effects in the bcc metals is the spreading of the screw dislocation cores on to more than one glide plane. Previous atomistic simulations of the bcc transition metals predicted dislocation cores which spread into three {110} planes with the shapes of the cores falling into two distinct classes. The group V (Ta) metals exhibited a core spread symmetrically about a central point while the core for the group VI (Mo) metals spreads asymmetrically about this central point. The first principles dislocation core for Mo and Ta are almost identical (Fig. 2) in contrast to previous atomistic results [4]. This has led to a reassessment of the atomistic potentials for the bcc transition metals. The predicted lattice friction stresses, for pure shear stress, show pronounced deviations from Schmid's law as a function of the angle of the maximum

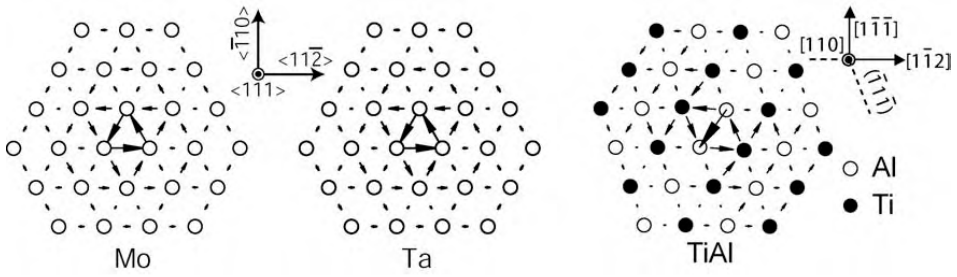

Figure 2.
Differential displacement plots (screw components) of the a/2<111> screw dislocation in Mo and Ta and the a/2<110] screw dislocation in $L1_0$ TiAl. The respective dislocation coordinate systems are shown for each crystal structure.

resolved shear stress plane to the (110) plane. We also find that Mo has a large tension-compression asymmetry for uni-axial stress along (100) and (110) [3]. Similar to the bcc metals the predicted ordinary screw dislocation in TiAl (Fig. 2) spreads on two {111} glide planes [5]. We expect that this configuration will easily cross slip, consistent with high temperature strengthening models for γ–TiAl.

4. Acknowledgements

The authors acknowledge the support of: Lawrence Livermore National Laboratory, US Department of Energy under contract B346019, the Air Force Office of Scientific Research under contract F33615-96-C-5258 and a grant of computer time from the US Department of Defense High Performance Computing Modernization Program, at the Aeronautical Systems Center-Major Shared Resource Center, on the IBM-SP2 and IBM-SP3.

5. References

[1] "Greens Function Boundary Conditions in 2 and 3 Dimensional Atomistic Simulations of Dislocations", S. Rao, C. Hernandez, J. Simmons, T.A. Partharasarthy, and C. Woodward, Phil. Mag. A **77**, 231-56 (1998).

[2] "Efficient Iterative Schemes for ab initio Total Energy Calculations Using a Plane-Wave Basis Set", Kresse, G., and Furthmueller, J., *Phys. Rev*. B, **55**, 11169-86 (1996); "*Ab Initio* Molecular Dynamics For Liquid Metals", Kresse, G., and Hafner, J., *Phys. Rev*. B, **47**, 558–561 (1993).

[3] "Flexible Ab-Initio Boundary Conditions: Simulating Isolated Dislocations in bcc Mo and Ta", C. Woodward and S.I. Rao, Phys. Rev. Lett, **88**, 216402-1-4 (2002).

[4] "*Ab-initio* simulation of isolated screw dislocations in bcc Mo and Ta", C. Woodward and S.I. Rao, Phil. Mag. **81**, 1305-1316 (2001).

[5] "*Ab-initio* simulation of (a/2)<110] screw dislocations in γ–TiAl", C. Woodward and S.I. Rao, *Phil. Mag.*, **84**, 401-413, (2004).

MD / DDD Study on Dislocation Behaviors at Matrix-Precipitate Interface in Nickel-Based Superalloys

K. Yashiro, Y. Tabata, F. Kurose, Y. Tomita, H. M. Zbib

Kobe University, 1-1, Rokkodai, Nada, Kobe 657-8501, JAPAN
yashiro@mech.kobe-u.ac.jp

ABSTRACT

Dislocation behaviors in the matrix-precipitate microstructure of Ni-based superalloys are investigated by means of molecular dynamics (MD) and discrete dislocation (DD) dynamics simulations. MD results suggest that a dislocation is not blocked by the matrix-precipitate interface but decelerated by the stress field around the precipitate. A DDD–FEM analysis is then implemented to evaluate the stress field and treat the image force on dislocations from precipitates, showing good agreement with the MD results.

1. Introduction

Ni-based superalloys possess the characteristic microstructure where cuboidal γ' phases are precipitated in the γ matrix. The precipitates are decreased in the size down to about 0.5μm, and arranged with the distance of less than 0.1μm in the matrix. The dislocation behavior in the array of γ' precipitates has attracted intense interest with respect to the understanding of the deformation mechanism of superalloys. In the present study, the dislocation behaviors at the γ / γ' interface are investigated by means of MD and DDD simulations.

2. MD simulation

The MD simulation is implemented with a slab cell that mimics a local part of an apex of cuboidal Ni_3Al precipitate in a Ni matrix, as schematically illustrated in Fig. 1(a), with about 3 million atoms. Mode II type displacement is applied on the cell to nucleate edge dislocations and proceed them toward the precipitate. Here, the γ' precipitate is slightly pushed-in or pulled-out as shown in Figs. 1(b) and (c), in order to increase/decrease the compressive internal stress of γ' precipitate due to the lattice misfit. The former cell is referred as "Model C" while the later as "Model T". The dislocation motions observed in the simulations are also shown in the figures. In the Model C, the first dislocation is decelerated at the front of the precipitate while it continues to glide at the other part, resulting in the dislocation bending. It is noteworthy that the slow-down takes place at far point about 3 nm from the interface. Then the bent dislocation begins to cut into the precipitate. On the other hand, the dislocation in Model T reaches the interface with constant speed and penetrates into the precipitate without any obstruction. This different behavior is explained in terms of the Peach-Koehlor (PK) force by the stress field around the precipitate. Figure 2 shows the distribution of shear stress, τ_{zx}, which generates the PK force on the edge dislocation in the direction advanced. Negative stress can be found at the front of γ' precipitate in Model C, so

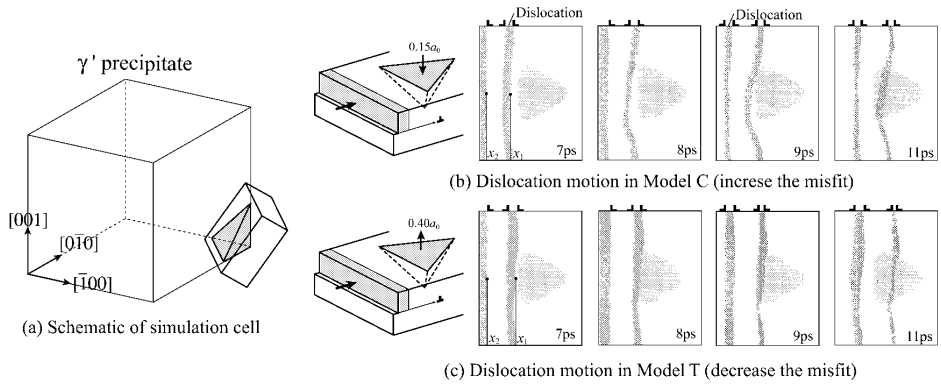

Fig. 1 Model and result of MD simulations.

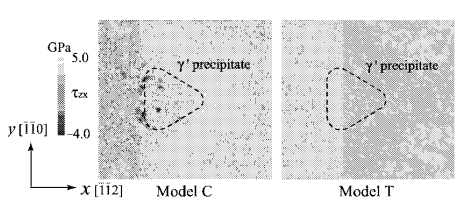

Fig. 2 Distribution of shear stress, τ_{zx}, on the slip plane.

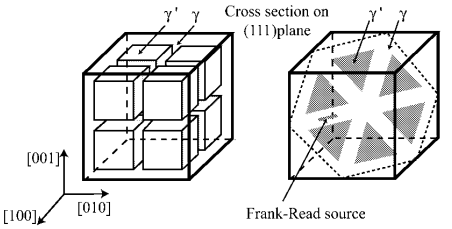

Fig. 3 DDD–FEM simulation model.

that we can deduce this negative stress causes repulsive force on the approaching dislocation and decelerate it. This MD result suggests that the γ/γ' interface is rather continuum and the stress field around the precipitate would dominate the dislocation behavior in the γ/γ' microstructure. Details of the simulation is shown in our previous report [2].

3. DDD Simulation

All dislocation lines and loops of arbitrary shape are discretized into short line segments, and the time evolution of each dislocation is pursued by calculating the force acting on each segment on the basis of the dislocation theory. The PK force on the node i at the position vector $\mathbf{p}$ is calculated by the following equation,

$$\mathbf{F}_i = \sum_{j=1}^{N-1} \left(\boldsymbol{\sigma}^{\mathrm{D}}_{j,j+1}(\mathbf{p}) + \boldsymbol{\sigma}^{\mathrm{a}}(\mathbf{p}) \right) \cdot \mathbf{b}_i \times \boldsymbol{\xi}_i + \mathbf{F}_{i-\mathrm{self}} \tag{1}$$

where $\sigma^{\mathrm{D}}_{j,j+1}(\mathbf{p})$ is the stress at $\mathbf{p}$ generated by a remote segment [1], $\sigma^{\mathrm{a}}(\mathbf{p})$ the applied stress, N the number of all nodes, $\mathbf{b}_i$ and $\boldsymbol{\xi}_i$ are the Burgers vector and line sense vector at node i, respectively. $\mathbf{F}_{i-\mathrm{self}}$ represents the line tension evaluated by the curvature at the node i.

The formulation of $\sigma^{\mathrm{D}}_{j,j+1}(\mathbf{p})$ is defined in the infinite body of homogeneous material, so that it could not be directly applied to the problem containing surface or heterogeneous interface. In order to treat such problem, the DDD simulation

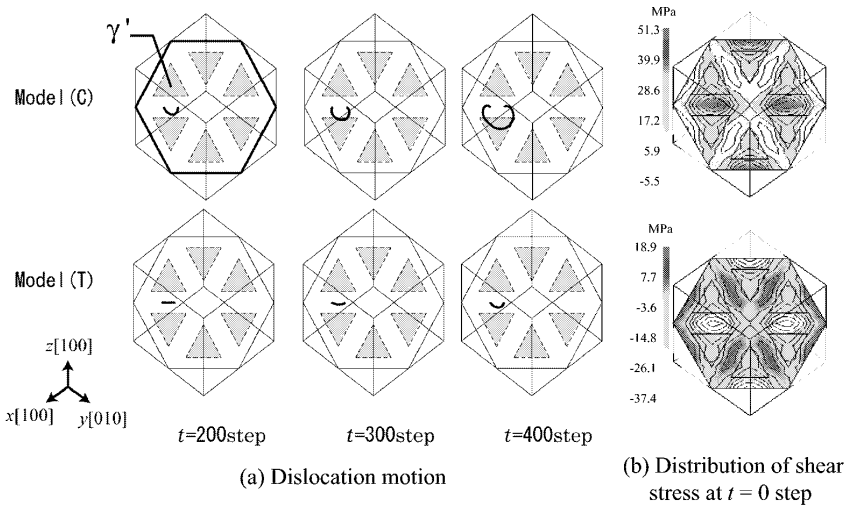

(a) Dislocation motion

(b) Distribution of shear stress at $t = 0$ step

Fig. 4 Results of DDD-FEM simulations

is coupled with the FEM analysis [1]. We used the DDD-FEM code proposed by Zbib and Diaz de la Rubia [1]. Our DDD-FEM simulation is implemented with the cubic cell containing 8 cuboidal precipitates as schematically illustrated in Fig. 3(a). The length of the cubic cell is 3.56μm while that of one precipitate is 1.18μm. The cubic cell is discretized into $12 \times 12 \times 12$ mesh blocks in the FEM analysis. A Frank-Read source, of which width is 0.5 nm and Burgers vector $[01\bar{1}]$, is set in the γ channel as shown in Fig. 3(b). The dislocation propagates from the source and approaches the precipitate under the loading condition of $\dot{u} = 5.0 \times 10^8$/sec in the [001] direction. Here the positive/negative mean stress of 200 MPa is applied as body force on the FEM mesh of the precipitates, mimicing the misfit stress. The shear moduli of matrix and precipitate are 80 GPa and 85 GPa, respectively. Poisson's ratio is set at 0.3 for both materials.

Figure 4(a) illustrates the motion of dislocation on the (111) slip plane simulated by the DDD-FEM analysis. In the figure, the model with negative mean stress on the precipitate is refered as "Model C" while the other as "Model T". It is clear that the dislocation in Model T propagates slower than that in Model C. Figure 4(b) shows the distribution of shear stress along the $[01\bar{1}]$ due to the applied misfit stress. The positive stress in the γ channel accelerates the dislocation toward the $[01\bar{1}]$ in Model C, while the negative one in Model T decelerates it. Taking the opposite character of Burgers vector into account, this result coincides with that of MD simulation.

References

[1] Zbib, H. M. and Diaz de la Rubia, T. (2002): "A multiscale model of plasticity", *International Journal of Plasticity*, Vol. 18, pp. 1133-1163.

[2] Yashiro, K., Tabata, Y. and Tomita, Y. (2004): "Molecular Dynamics Study on the Characterisitics of Edge and Screw Dislocations in Gamma/Gamma-Prime Microstructure in Ni-based Superalloy", *Solid mechanics and its applications*, Vol. 115, pp. 59–60, Kluwer Academic Publishers.

Constitutive Modeling of $L1_2$ Crystals Based on a Modified Superkink Bypassing Model and the Self-unlocking Model

Y. Yuan and **D.M. Parks**

Department of Mechanical Engineering, MIT

77 Mass Ave. RM 1-321, Cambridge MA, 02139，USA, yiny@mit.edu

ABSTRACT

A single-crystal constitutive model of the $L1_2$ structure intermetallic compound Ni_3Al is developed, based on recent theoretical developments in dislocation mechanics and experimental evidence. Hirsch's superkink bypassing model and Caillard's self-unlocking mechanism have been modified and combined to describe dislocation dynamics in the yield anomaly region. Results of numerical simulations successfully capture major features of temperature dependence of the tensile yield strength and hardening rate over a range of crystallographic orientations.

1. Introduction

Since the observation of the anomalous yield behavior in Ni_3Al in 1957, intensive research has focused on understanding the mechanical behaviors of $L1_2$ compounds, especially in the temperature regime of yield anomaly. It is now commonly accepted that the positive temperature-dependence of yield strength is associated with hindered movements of (101) screws on the octahedral planes. Obstacles to the motion, the K-W locks, are formed by thermally-activated cross-slipping of screws from the octahedral to the cube plane. Above the temperature of peak yield strength, where cube slip dominates, the temperature/strength relation returns to normal. Based on this understanding, we develop a physically-based single-crystal constitutive model, which captures the anomalous temperature dependence both in yielding and hardening for $L1_2$ crystals.

2. General Constitutive Framework

Major equations of the single-crystal constitutive framework were described by Kalidindi, *et al.* [1]. The plastic flow rate, L^p, is comprised of the superposition over the active slipping system α of the crystallographic plastic shear rates ($L^p = \sum_\alpha \dot{\gamma}^\alpha \, \mathrm{m}_0^\alpha \otimes \mathrm{n}_0^\alpha$), where $\mathbf{m}_\mathbf{0}^\alpha$ and $\mathbf{n}_\mathbf{0}^\alpha$ are unit lattice vectors, denoting slip direction and slip plane normal, respectively. The plastic shearing strain rate on each system, $\dot{\gamma}^\alpha$, is given by the Orowan's equation, $\dot{\gamma}^\alpha = \rho_m^\alpha b \bar{v}^\alpha$, which provides a connection between macro-deformation and the micro-dislocation-dynamics. Here ρ_m^α is the density of the mobile

dislocations for slipping system α, b is the magnitude of the Burgers vector, and $\bar{v}^{\alpha}$ is the average dislocation velocity.

3. Dislocation Mechanics

Hirsch indicated that when the effective stress level on an octahedral plane is low (low-temperature part of the yield anomaly region), after the first cross-slip of the leading superpartial, the screw will progressively develop into a complete K-W lock [2]. He proposed a superkink bypassing model, in which flow of an octahedral slipping system was simplified, represented by a single screw with equally-separated superkinks of the same height. The resulting average dislocation velocity was given by $\bar{v} = v_f \exp[-(H_u - H_l)/kT]$, where v_f is the free-flight velocity, H_l is the locking enthalpy, and H_u is the unlocking activation enthalpy. Unlocking is presumed to be rate-controlling, with enthalpy $H_u = H_{u0} - V(l)\tau$. Here H_{u0} is a constant (~2 ev), and V is the activation volume, proportional to the superkink height, l. In the modified model, we assume that the superkinks' population shows an exponential form distribution over its height, $f_1(l) = C_0 \exp(-l/l_o)$, as observed by Couret, *et al.* [3]. C_0 and l_o are temperature-related parameters governing the distribution. Yield anomaly is attributed to the decrease of superkink height, caused by the increased locking frequency at higher temperatures. The plastic strain rate of each octahedral slipping system achieved via the superkink bypassing mechanism is defined by:

$$\dot{\gamma}_{(1)}{}^{\alpha} = b v_f \rho_{total}^{\alpha} \int_0^{l_{\max}^{\alpha}} f_1(l^{\alpha}) \exp\left(-\frac{H_u(l^{\alpha}, \tau^{\alpha}) - H_l}{kT}\right) dl^{\alpha} \qquad (\alpha = 1-12); \tag{1}$$

Because the activation volume V is large (~$100\,b^3$), the integral of Eqn. (1) is dominated by its upper limit, $l_{\max}$. Thus, at any given stress, only the screws with the longest superkinks have a chance to be unlocked. When these screws relock, the newly-generated superkinks obey the same exponential form distribution and are mostly very short. Originally mobile screws become sessile, and to sustain flow, the stress must be increased to activate screws with the next longest superkinks. Thus, the hardening rate is closely related with the evolution of $l_{\max}$, which is:

$$\dot{l}_{\max} = \frac{dl_{\max}}{dt} = \frac{dl_{\max}\dot{\gamma}}{d\gamma} \approx \frac{\Delta l_{\max}\dot{\gamma}}{\Delta\rho b l_{\max}} \approx \frac{-\dot{\gamma}}{f_1(l_{\max})\rho_{total} b l_{\max}} \tag{2}$$

At the high-temperature end of the yield anomaly region, octahedral stress levels may become high enough to reach a critical value, $\tau_{critical}$, such that sessile screws lacking mobile superkinks can be unlocked by a self-unlocking mechanism proposed by Caillard [4]. $\tau_{critical}$ is a function of the geometrical factor w, measuring the APB width on the cube plane, and material variables including fault energies and the elastic anisotropy factor. The octahedral system plastic strain rate achieved by this mechanism is given by:

$$\dot{\gamma}_{(2)}{}^{\alpha} = b \rho_{total}^{\alpha} \int_0^{w_{\max}} f_2(w) v_{(2)}{}^{\alpha}(w, \tau)\, dw \qquad (\alpha = 1-12); \tag{3}$$

where $f_2(w)$ is assumed to be a normal distribution of w, centered at $\bar{w}(T)$, an increasing function of temperature. The average dislocation velocity $v_{(2)}{}^{\alpha}$ is defined as:

$$v_{(s)}{}^{\alpha} = v_f \left[\left(\frac{\tau^{\alpha}}{\tau_{critical}}\right)^{m_1} - 1\right] \qquad \text{If } \tau^{\alpha} > \tau_{critical}\,; \qquad v^{\alpha} = 0 \qquad \text{Otherwise} \tag{4}$$

where m_1 is a rate sensitive exponent. The total plastic strain rate for the octahedral planes, $\dot{\gamma}^{\alpha}$, is the summation of Eqns (1) and (3): $\dot{\gamma}^{\alpha} = \dot{\gamma}_{(1)}{}^{\alpha} + \dot{\gamma}_{(2)}{}^{\alpha}$, $(\alpha = 1-12)$.

For cube slip, $\dot{\gamma}^{\alpha}$ is represented by a power-law form, $\dot{\gamma}^{\alpha} = \dot{\gamma}_o \left(\tau^{\alpha} / s^{\alpha}\right)^{m_2}$, $\alpha = (13-18)$. The evolution of cube resistance, s^{α} is given by $\dot{s}^{\alpha} / s^{\alpha} = C_2 \dot{\gamma}^{\alpha}$, with an initial value s_o^{α} linearly decreasing with temperature. Here $\dot{\gamma}_o$, m_2 and C_2 are constants.

4. Simulation Results and Discussion

The proposed constitutive model is applied in simulation of uniaxial-tension of single crystals under an applied strain-rate of 10^{-4}/s for the three corner orientations of the spherical triangle. Simulation results of the temperature-dependence of tensile yield strength and tensile hardening modulus, $\bar{h}$, are shown in Figures (1) and (2), respectively:

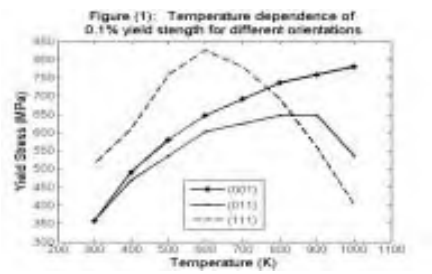

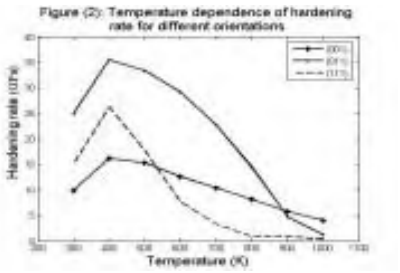

Both the yield strength and the hardening rate increase with increasing temperature for all orientations until the respective peak temperatures, $T_{p,\tau}$ and $T_{p,h}$. Orientation dependence of $T_{p,\tau}$ is due to the different Schmid factors of cube planes for these orientations: largest in (111), zero in (001). $T_{p,h}$ is clearly smaller than $T_{p,\tau}$, as expected. Decreases of $\bar{h}$ for (001) and (011) orientations are due to the self-unlocking mechanism activated at high temperature. For (111) orientation, decrease of $\bar{h}$ is also partially due to the activation of cube slip, consistent with observations of Lall, *et al.* [5], that cube slip has already been activated for orientations close to (111) at the temperatures lower than $T_{p,\tau}$.

5. References

[1] Kalidindi, S. R., Bronkhorst, C. A., and Anand, L., *J. Mech. Phys. Solids*, Vol. 40, 537 - 569, 1992.

[2] Hirsch P. B., *Phil. Mag. A*, Vol. 65, No. 3, 569-612, 1992.

[3] Couret A., Sun Y. Q. and Hirsch P. B., *Phil. Mag. A*, Vol.67, No.1, 29-50,1992.

[4] Caillard D. and Paidar V. , *Acta mater.*, Vol. 44, No.7, 2759-2771, 1995.

[5] Lall C., Chin S. and Pope D.P., , *Metall. Trans.*, Vol. 10A, 1323-1332, 1979.

Hierarchical Modeling of Failure Mechanisms and Grain-Boundary Effects in Crystalline Aggregates

T. Kameda[+]
[+]**University of Tsukuba and North Carolina State University**
M.A. Zikry, A.M. Rajendran*, *, D. Brenner*
***North Carolina State University**
Raleigh, NC 27695-7910
zikry@ncsu.edu

ABSTRACT

New hierarchical computational methodologies have been developed to predict dominant material behavior and mechanisms at scales ranging from the nano to the micro. Physically based scaling relations have been formulated to characterize mechanisms and grain-boundary effects in crystalline materials. These scaling relations have been used to link molecular dynamic and microstructural finite-element modeling to delineate the interrelated effects of grain boundary orientation and structure, dislocation transmission, absorption, and blockage through GBs, such that dominant failure mechanisms can be accurately identified and predicted from initiation to unstable growth.

1. Introduction

Grain-boundary (GB) structure, orientation, and distribution are essential microstructural features that characterize the initiation and evolution of failure modes in crystalline metals, alloys, and intermetallics (see, for example, [1]). Physically based constitutive descriptions are needed that can account for dominant physical mechanisms that may occur at different physical scales. The challenge is to determine at what scale to characterize material failure. The primary purpose of this study is the coupling of molecular dynamic calculations of dislocation nucleation to an inelastic dislocation density-based multiple-slip crystalline microstructural computational framework that can be used to obtain a detailed understanding and accurate prediction of interrelated local mechanisms that control and affect global failure modes in f.c.c. polycrystalline aggregates with CSL GB orientations and distributions. Most polycrystalline formulations generally do not account for GB effects such as dislocation-density and slip transmission, blockage, and absorption. These effects could result due to GB orientation, structure, or interfacial stress mismatches (see Kameda and Zikry [2] for a more detailed review). In this study, GB effects are accounted for by the introduction of interfacial regions that are used to track slip and dislocation density transmissions and intersections.

2. Approach

In this section, the formulation for the multiple-slip crystal plasticity rate-dependent constitutive relations, and the derivation of the evolutionary equations for the mobile and immobile dislocation densities are presented. A detailed presentation is given by Kameda and Zikry [2]. In that formulation, it has been assumed that the deformation

gradient can be decomposed into elastic and inelastic components and that the inelastic deformation-rate tensor can be defined in terms of the crystallographic slip-rates.

To gain a fundamental understanding of the effects of dislocation motion, interaction, and transmission on material failure modes, the multiple-slip crystal plasticity constitutive formulation is coupled to internal variables that account, in an average sense, for a local description of the dislocation structure in each crystal. Specifically, we have used the mobile and the immobile dislocation densities as the internal variables to describe inelastic behavior and the evolution and the characteristics of the microstructure are governed by dislocation production and dynamic recovery. We have assumed that during an increment of strain, an immobile dislocation density rate is generated, which will be denoted by $\dot{\rho}_{\mathrm{im}}^{(\alpha)+}$, and an immobile dislocation density rate is annihilated, which will be denoted by $\dot{\rho}_{\mathrm{im}}^{(\alpha)-}$. We also assumed that $\dot{\rho}_{\mathrm{m}}^{(\alpha)+}$ corresponds to a generation of mobile dislocation densities, and $\dot{\rho}_{\mathrm{m}}^{(\alpha)-}$ corresponds to an annihilation of mobile dislocation densities. Using balance laws pertaining to the generation and annihilation of mobile and immobile dislocations, we have derived the following coupled equations that account for the evolution of mobile and immobile dislocation densities that correspond to dislocation generation, interaction, trapping, and recovery,

$$\frac{d\rho_m^{(\alpha)}}{dt} = \dot{\gamma}^{(\alpha)}\left(\frac{g_{sour}}{b^2}\left(\frac{\rho_{im}^{(\alpha)}}{\rho_m^{(\alpha)}}\right) - \frac{g_{minter}}{b^2}\exp(-\frac{H}{kT}) - \frac{g_{immob}}{b}\sqrt{\rho}_{im}^{(\alpha)}\right), \qquad (1)$$

$$\frac{d\rho_{im}^{(\alpha)}}{dt} = \dot{\gamma}^{(\alpha)}\left(\frac{g_{minter}}{b^2}\exp(-\frac{H}{kT}) + \frac{g_{immob}}{b}\sqrt{\rho}_{im}^{(\alpha)} - g_{recov}\exp(-\frac{H}{kT})\rho_{im}^{(\alpha)}\right), \quad (2)$$

where g_{sour} is a coefficient pertaining to an increase in the mobile dislocation density due to dislocation sources, g_{minter} is a coefficient related to the trapping of mobile dislocations due to forest intersections, cross-slip around obstacles, or dislocation interactions, g_{recov} is a coefficient related to the rearrangement and annihilation of immobile dislocations, g_{immob} is a coefficient related to the immobilization of mobile dislocations, H is the activation enthalpy, k is Boltzmann's constant, and T is the temperature. As these evolutionary equations indicate, the dislocation activities related to recovery and trapping are coupled to thermal activation. Two general conditions, pertinent to the evolution of dislocation densities in crystalline materials, have been used: (i) that the mobile and immobile densities saturate at large strains; (ii) that the relaxation of the mobile dislocation density to a quasi-steady state value occurs much faster than the variation of the immobile density.

Dislocation behavior adjacent to the GB is critical for characterizing intergranular and transgranular failure. Hence, it is necessary to take this effect into account to predict accurately the phenomena around GB. In this study, our dislocation-density based FEM formulation is coupled to the MD computations through the evolution of the dislocation densities on the dominant slip-systems adjacent to the GB region. The MD computations are used to determine the dislocation nucleation sites, and these dislocations are then statistically used as a database for the FEM calculations.

3. Results

The behavior of f.c.c. copper bicrystals with Σ3 and Σ9 CSL GBs with a symmetric tilt axis were investigated by both the microstructurally based finite element approach and the MD simulations under tensile deformations. The total potential energy was minimized every 1% strain for the MD simulations. Specimens with different aspect ratios were used (Table 1). Furthermore, the number of atoms was varied to investigate convergence and energy stability. Representative results indicating dislocation nucleation are shown in Figure 1for a Σ3 bicrystal.

Table 1. Specimen Dimensions

	Specimen Dimensions (Å)	Number of atoms
Type 1	26 x 100 x 30	7056
Type 2	44 x 100 x 46	17640
Type 3	88 x 200 x 86	131920

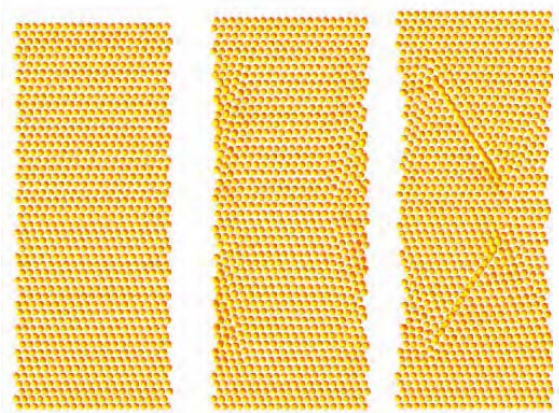

(a) 6 % (b) 8 % (c) 10 %

Fig. 1. Representative results for atom positions and dislocation nucleation corresponding to different nominal strains of Type 2.

REFERENCES

1. Watanabe T. (1994), *Materials Science And Engineering A-Structural Materials Properties Microstructure And Processing*176, 39-49

2. T. Kameda and M.A. Zikry (1998), *International Journal of Plasticity* 14, 689-703.

Symposium -2

Statistical Mechanics of Plasticity

A Dynamical Approach to the Spatio-temporal Features of the Portevin-Le Chatelier Effect

G.Ananthakrishna
Materials Research Centre, Indian Institute of Science
Bangalore-560012, India, email:garani@mrc.iisc.erent.in

ABSTRACT

We show that an extension of Ananthakrishna's model exhibits all the features of the Portevin - Le Chatelier effect including the three types of bands and the recently observed crossover from a chaotic state at medium strain rates to a power law state of stress drops at high strain rates. Most dislocations are shown to be in the pinned stated in the chaotic regime and at the edge of unpinning in the power law regime.

1. Introduction

Explaining the rich spatio-temporal dynamics of the Portevin - Le Chatelier (PLC) effect [1] has remained a challenging problem for a long time. The inherent nonlinearity and the presence of multiple time and length scales demands nonlinear dynamical approach. Here, we follow the Ananthakrishna's model which provides a natural basis [2]. The model predicts several generic features of the PLC effect including the negative strain rate sensitivity of the flow stress [2]. One prediction specific to the model is the existence of chaotic stress drops subsequently verified by using methods of time series analysis [3]. More recently an intriguing crossover from a low dimensional chaotic state found at medium strain rates to a high dimensional power law state of stress drops at high strain rates has been reported [4]. The power law state is reminiscent of self-organized criticality [5]. We show that the extended Ananthakrishna's model explains this crossover as well as different types of PLC bands.

2. The Ananthakrishna's Model

We follow the notation of Ref. [6] to which we also refer the reader for details of the mechanisms included in the model. The equations for the three scaled densities, the mobile $\rho_m(x,t)$, the immobile $\rho_{im}(x,t)$, and the Cottrell's type density $\rho_c(x,t)$ coupled to the scaled stress ϕ are

$$\frac{\partial \rho_m}{\partial t} = -b_0\rho_m^2 - \rho_m\rho_{im} + \rho_{im} - a\rho_m + \phi_{eff}^m\rho_m + \frac{D}{\rho_{im}}\frac{\partial^2(\phi_{eff}^m(x)\rho_m)}{\partial x^2}, \quad (1)$$

$$\frac{\partial \rho_{im}}{\partial t} = b_0(b_0\rho_m^2 - \rho_m\rho_{im} - \rho_{im} + a\rho_c), \quad (2)$$

$$\frac{\partial \rho_c}{\partial t} = c(\rho_m - \rho_c), \quad (3)$$

$$\frac{d\phi(t)}{dt} = d[\dot{\epsilon} - \frac{1}{l}\int_0^l \rho_m(x,t)\phi_{eff}^m(x,t)dx] = d[\dot{\epsilon} - \dot{\epsilon}_p]. \quad (4)$$

The PLC state is seen for $10 < \dot{\epsilon} < 2000$ when other parameter values are in the instability limit (set here to $a = 0.8, b_0 = 0.0005, c = 0.08, d = 0.00006, m = 3.0, h = 0.07$ and $D = 0.5$). These equations are solved with appropriate boundary conditions.

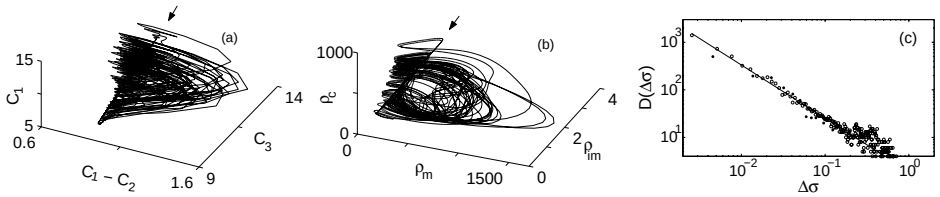

Figure 1: (a,b): Reconstructed strange attractor for a chaotic experimental stress-time series for $\dot{\epsilon}_a = 1.7 \times 10^{-5} s^{-1}$ and the strange attractor from the model for $\dot{\epsilon} = 120$. (c): The power law distribution of stress drops from the model for $\dot{\epsilon} = 280$.

3. Dynamics of Crossover

We summarize the results and compare them with experiments wherever possible.
a) We have earlier shown that the stress - strain curves (from Cu-Al alloys) in the medium strain rate regime are chaotic with a correlation dimension, $\nu = 2.3$, [1,3]. Likewise, the model is chaotic at low and medium strain rates. The largest Lyapunov exponent of the model becomes positive around $\dot{\epsilon} \sim 30$ peaking around 120 and nearly vanishes beyond 240 ($\sim 5 \times 10^{-4}$) with a finite density of null (almost vanishing) exponents. The experimental attractor visualized using singular value decomposition shown in Fig. 1a in the space of the first three principal directions [6] is similar to the attractor from the model shown in Fig. 1b for $\dot{\epsilon} = 120$ in the chaotic regime.
b) In experiments, at high strain rates, stress drops obey a power law statistics. Similarly, the stress drop distribution $D(\Delta\phi)$ for the stress-time series beyond $\dot{\epsilon} \sim 260$ obtained from the model shows a power law $D(\Delta\phi) \sim \Delta\phi^{-\alpha}$. This is shown in Fig. 1c ($\circ$) for $\dot{\epsilon} \sim 280$ along with the experimental points ($\bullet$) corresponding to $\dot{\epsilon}_a = 8.3 \times 10^{-5} s^{-1}$ with the same exponent value $\alpha \approx 1.1$.
c) The finite density of null exponents at high $\dot{\epsilon}$ implies that most dislocations are close to the unpinning threshold. The dislocation configuration can be visualized in terms of a parameter which physically corresponds to an effective unpinning stress $\delta = \phi^m - \rho_{im}(j) - a$. δ negative, positive and zero correspond respectively to the pinned (small ρ_m), unpinned (large ρ_m) and unpinning threshold state. The dislocation configuration in the power law state in Figs.2(a,b) shows that most dislocations are at the unpinning threshold both before and after the yield drop. In the chaotic state, most dislocations are in the pinned state.
d)For strain rates, $30 \leq \dot{\epsilon} < 70$, we get uncorrelated static dislocation bands [6]. In the range $70 \leq \dot{\epsilon} < 180$, we find *hopping bands*. At high strain rates we see

continuously propagating bands starting from $\dot{\epsilon} = 240$ as can be seen from Fig. 2c. The velocity of the bands given by $v = 2\sqrt{\frac{D\dot{\epsilon}}{\bar{\rho}_m \rho_{im}}(\frac{\dot{\epsilon}}{\bar{\rho}_m} - a - \rho_{im})}$ which shows that it is proportional to $\dot{\epsilon}$ and $v \propto \bar{\rho}_m^{-1}$ consistent with known experimental results.

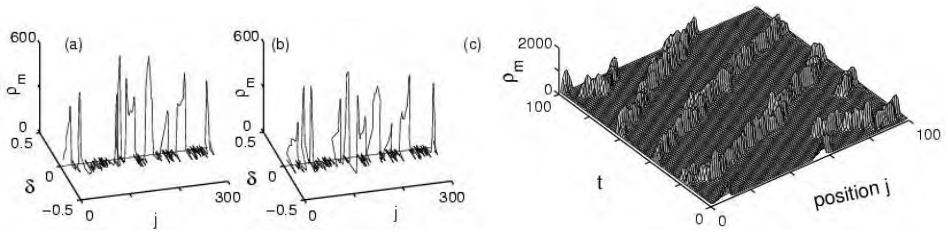

Figure 2: (a,b): Dislocation configuration before and after a typical yield drop in the power law regime for $\dot{\epsilon} = 280, j = 50, N = 100$. (c): Propagating type of bands.

4. Conclusions

Thus, the model captures all the dominant features of the PLC effect including the nature of bands and the crossover from chaos to power law state. The latter is characterized by the changes in the Lyapunov spectrum. At high $\dot{\epsilon}$ where power law stress drops is seen, most dislocations are seen to be at the threshold of unpinning.

The author wishes to thank Dr. M. S. Bharathi for the collaborative work. This work is supported by Department of Science and Technology, New Delhi, India.

References:

1. L.P. Kubin, C. Fressengeas and G. Ananthakrishna, in *Collective Behavior of Dislocations*, edited by F.R.N. Nabarro and M.S. Deusbery, *Dislocations in Solids* Vol.11 (North-Holland, Amsterdam, 2002).
2. G. Ananthakrishna and M. C. Valsakumar, *Repeated yield drop phenomenon : a temporal dissipative structure*, J. Phys. D **15**, L171 (1982).
3. S.J. Noronha, *et al.*, *Chaos in the Portevin - Le Chatelier effect,* Int. Jl. of Bifurcation and Chaos **7**, 2577 (1997) and references therein.
4. G. Ananthakrishna *et al.*, *Croossover from chaotic to self-organized critical dynamics in jerky flow,* Phys. Rev. E. **60**, 5455 (1999); M.S. Bharathi, *et al.*,*Multifractal burst in the spatio-temporal dynamics of jerky flow,* Phys.Rev.Lett.**87**,165508(2001).
5. P.Bak,C.Tang and K.Wiesenfeld,*Self-organized criticality*, Phys.Rev.**A38**,364(1988).
6. G. Ananthakrishna and M. S. Bharathi, *A Dynamical Approach to the Spatio-temporal dynamics of the Portevin-Le Chatelier effect: Chaos, turbulence and band propagation*, Phys. Rev. E **70**, 026111 (2004) and the references therein.

Effects of Non-Glide Stresses on Plastic Flow: From Atomistic Studies of Dislocations to Macroscopic Failure Mechanisms

J. L. Bassani[a], **V. Vitek**[b], **and V. Racherla**[a]

[a]**Department of Mechanical Engineering and Applied Mechanics,** [b]**Department of Materials Science and Engineering, University of Pennsylvania, Philadelphia, PA 19104 U.S.A. E-mail: bassani@seas.upenn.edu.**

ABSTRACT

In non-closely packed crystals, like in bcc metals and intermetallics, the dislocation cores can spread significantly onto several non-parallel planes. As a consequence, stress components in addition to the Schmid stress affect the dislocation mobility. Atomic-level simulations are utilized to identify the important non-glide stress components that affect the dislocation motion. With direct input from atomistics, multiple-slip constitutive relations are developed for single crystals that are of the non-associated flow type. Taylor averages are used to construct the yield and the flow potential surfaces for both random and textured polycrystals. Polycrystalline behavior is also non-associated flow, and this has significant consequence on macroscopic behavior including strain localization.

1. Introduction

Ample evidence now exists for a broad range of crystalline materials, particularly those with non-close packed lattices, that dislocation core structures are generally non-planar, particularly for screw segments, and such structures have a direct influence on macroscopic plastic flow. Common signatures of core effects are: unexpected deformation modes and slip geometries; strong and unusual dependence of flow stresses on crystal orientation and temperature; and, most commonly, a break-down of Schmid's law (which states that glide on a slip system, defined by a slip plane and direction of slip, commences when the resolved shear stress on that system, the Schmid stress, reaches a critical value). This paper focuses on the effects of non-Schmid (or non-glide) stresses on non-planar cores with the aim of incorporating these effects into the constitutive relations for macroscopic continuum models of plastically deforming single- and poly-crystals.

2. Atomistic Study of the Glide of $1/2\langle 111\rangle$ Screw Dislocations

The atomistic studies presented in this paper are based on the Finnis-Sinclair many-body potential for molybdenum. The calculated (static) core structure of the $1/2<111>$ screw dislocation is shown in Fig. 1, where the arrows depict differential displacements between atoms. As clearly seen, the primary displacements are on three $\{1\bar{1}0\}$ planes containing the Burgers vector. Glide of the screw dislocation arising from a shear stress parallel to the Burgers vector, but not necessarily on the slip plane, depends strongly on the orientation of the maximum resolved shear stress plane (MRSSP) defined by the

angle χ that it makes with the $(\bar{1}01)$ slip plane. The critical resolved shear stress on the MRSSP, τ_{M}, at the onset of dislocation motion versus χ is plotted in Fig. 2 (see [1]). The $\tau_{\mathrm{M}} - \chi$ relation does not follow the $1/\cos(\chi)$ dependence given by Schmid's law.

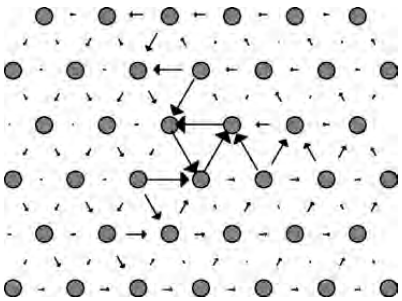

Fig. 1 Calculated Structure of ½[111] screw dislocation core in Molybdenum.

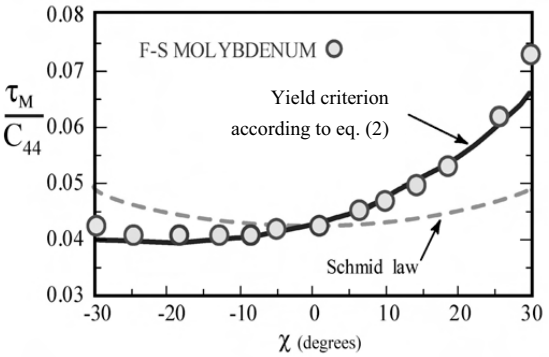

Fig. 2 Dependence of CRSS on χ.

3. Slip System Yield Criteria

To include the effects of non-glide components of stress in a single crystal yield criterion, Qin and Bassani [2] proposed that slip system α is at yield when a generalization of Schmid's law holds given in terms of the effective yield stress:

$$\tau^{*\alpha} = \tau^{\alpha} + \sum_{\eta} \alpha_{\eta}^{\alpha} \tau_{\mathrm{cr}}^{*\alpha}, \tag{1}$$

where τ^{α} is the Schmid stress, τ_{η}^{α} are the non-glide stresses and a_{η}^{α} are the corresponding material parameters that determine the relative importance of the different non-glide components ($\eta = 1, M$), and $\tau_{\mathrm{cr}}^{*\alpha}$ is the critical value of the effective stress for that system. Corresponding to the atomistic results of Fig. 2, a non-glide stress is taken to be the shear stress on $(0\bar{1}1)$ plane in [111] direction for the motion of the dislocation on $(\bar{1}01)$ plane, and in this case the yield criterion Eqn. (1) becomes:

$$\tau + a\tau_{(0\bar{1}1)} = \tau_{\mathrm{M}} \left[\cos(\chi) + a \cos(\chi + 60) \right] = \tau_{\mathrm{cr}}^{*\alpha}. \tag{2}$$

The least square fit to the dependence of the atomistically calculated values of τ_{M} versus χ gives a value of $a = 0.64$, and the corresponding curve from Eqn. (2) is plotted as the solid line in Fig. 2. We see that the generalized yield criterion more accurately reproduces the dependence of τ_{M} on χ for the screw dislocation as compared to Schmid's law.

4. Polycrystalline Response

A Taylor model (uniform strain) is used to estimate the polycrystalline response for materials whose single crystal yield criteria incorporate the effects of non-glide stresses

as given by Eqn. (2). An important manifestation of non-glide-stress effects at the polycrystal level is a uniaxial tension-compression asymmetry in yield, which is plotted in Fig. 3 as a function of the non-glide-stress parameter *a* for a random polycrystal. The yield and flow surfaces for the random polycrystal are plotted in Fig. 4.

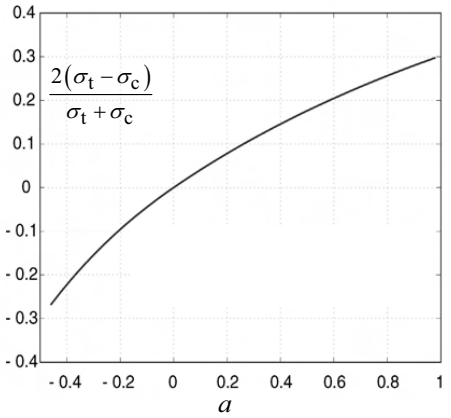

Fig. 3 Variation of tension-compression asymmetry with non-glide stress parameter *a.*

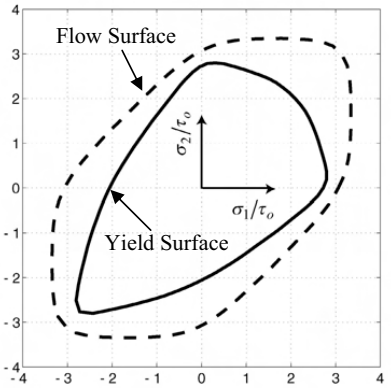

Fig. 4 Yield and flow surfaces in two dimensional stress space

5. Conclusions

Utilizing atomistic simulations of dislocation behavior, we have demonstrated a methodology to develop a physically-based theory of crystal plasticity that incorporates the significant effects of non-glide stresses. This paper has focused on bcc metals, but the phenomenon of stress-state dependence of the Peierls barrier is found in a wide range of materials for which dislocations possess non-planar core structures. The implications are not only striking at the single crystal level, but significant effects also are predicted at the polycrystalline level.

In related work reported in this conference (Racherla, V. and Bassani, J. L., 2004, Strain Localization: Effects of Non-Glide Stresses), simple functions of stress invariants are shown to accurately represent the macroscopic yield and flow potential surfaces for random polycrystals (Fig. 4). These isotropic functions are incorporated into studies of strain localization, and the effects of non-associated flow are predicted to be significant.

References

[1] Bassani, J. L, Ito K. and Vitek V. (2001) Complex macroscopic plastic flow arising from non-planar dislocation core structures. *Mater. Sci. Eng. A* **319-321**, 97-101.

[2] Qin, Q. and Bassani, J. L. (1991) Non-Schmid yield behavior in single crystals. *J. Mech. Phys. Solids* **40**, 813-833.

Anomalous Hall-Petch Behavior of Ni_3Al: a Model Based on the Statistics of Weak Links

Priam Pillai and D. C. Chrzan

Department of Materials Science and Engineering, University of California, Berkeley, CA 94720-1760; email: dcchrzan@socrates.berkeley.edu.

ABSTRACT

Constant strain rate simulations of dislocation dynamics reflecting the statistics of the exhaustion of dislocation motion are used to analyze the constant strain rate response of Ni_3Al. Specifically, Hall-Petch type experiments are modelled. The resulting Hall-Petch exponents are more negative than $-1/2$.

1. Introduction

The anomalous mechanical properties of some Ni_3Al alloys are well documented. Most notably, the strength of many of these alloys is observed to increase with increasing temperature. This so-called yield strength anomaly is accompanied by other anomalous properties, including an anomalously high hardening rate [1] and, for certain alloys, a Hall-Petch exponent more negative than $-1/2$ [2].

Prior work [3, 4] has linked the strain hardening rates to the dynamics of the dislocations mediating the slip process. The dislocations are composed of segments elongated along screw orientation and connected by (sometimes) mobile segments known as superkinks. The glide of the dislocation is mediated by the lateral motion of the superkinks. Superkinks are mobile if they exceed a critical length that scales inversely with the net stress acting on the dislocation.

As a dislocation propagates, the number and lengths of superkinks along it fluctuate. At lower stresses, the dislocation may attain a configuration in which it contains *no* mobile superkinks. The dislocation is consequently pinned, and the density of mobile dislocations is reduced. Maintaining the constant strain rate condition requires an increase in stress. This increase has two consequences. First, the velocity of the mobile dislocations increases. Second, some immobile dislocations may become mobile.

A statistical model of the strain hardening has been proposed [4]. This analysis leads one to expect that materials with shorter dislocations will be intrinsically stronger at any given strain because they display higher strain hardening rates. If the length of the dislocations is dictated by the grain size, this property will impact the observed Hall-Petch behavior.

2. Simulations

In order to model a constant strain rate response, one must construct a velocity law for the individual dislocations, one must allow for dislocation production and annihilation, and one must establish the conservation law that leads to the desired constant strain rate conditions.

Simulations of dislocation dynamics [5] suggest that a velocity law of the form

$$v_i = \frac{\sigma_i b}{2B}\left(\tanh\frac{|\sigma_i| - \sigma_i^c}{\alpha} + 1\right) \tag{1}$$

is a reasonable description of the dislocation dynamics. Here,v_i is the velocity of the ith dislocation, σ_i is the net stress on the ith dislocation, b is the dislocation Burgers vector, B is a drag coefficient, and α is a parameter that can be chosen to mimic the effects of thermal depinning. The parameter σ_i^c represents the zero temperature critical stress needed for dislocation i to be mobile. This parameter scales inversely with the length of the longest superkink along the dislocation, and is governed by the probability distributions given in reference [4].

The dislocations are generated from a number of isolated, one-sided dislocation sources. The dislocations associated with a single source interact through their mutual stress/strain fields. The interaction between dislocations generated from different sources is dynamic only and maintained by the constant strain rate condition (the conservation law). The source produces a new dislocation whenever the net stress at the source exceeds a predefined critical stress. Each source has a finite length. When dislocations move out beyond that finite length, they are removed from the simulation. Each dislocation is assumed to have a finite width. This width defines a length dependent strain hardening rate for the dislocations.

3. Results and Conclusions

Figure 1 displays the predicted stress/strain response for dislocations of different lengths. Note that as the dislocations increase in length, the applied stress necessary to achieve the imposed strain rate decreases. Note also that the fluctuations in stress during a single experiment are substantial, in part a result of the finite number of dislocations considered in the simulations. Choosing the stress at 0.2% plastic strain as a measure of the yield stress, one finds that the apparent yield strength increases rapidly with decreasing dislocation length. Fitting the "observed" yield strength to the Hall-Petch relation yields an exponent near -1.1.

The origins of this increase in Hall-Petch exponent within the simulations is clear. Although defined to be preyield, some dislocations are mobile at the onset of deformation. These motion of these mobile dislocations may be exhausted rapidly

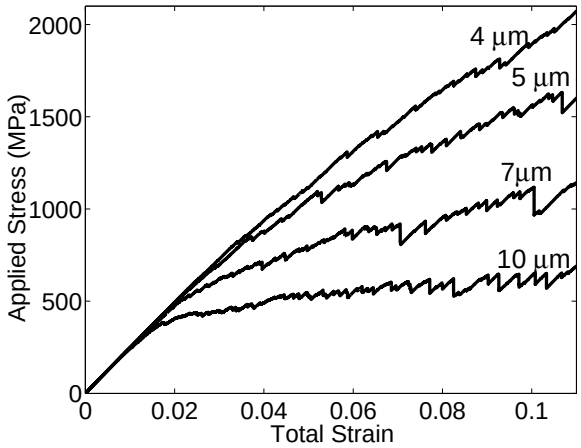

Figure 1: Stress versus strain for dislocations of different lengths. The imposed strain rate is 1/sec. Fifty dislocation sources are modeled. The initial average superkink length is 2.5×10^{-8} m, B is taken to be 2×10^{-3} Pa-sec, and α is taken to be 10^7 Pa. The burgers vector is taken to be 5 Å, and the shear modulus is 5×10^{10} Pa.

because in the early stages of the simulation, the applied stresses are not large. This preyield hardening is more pronounced for short dislocations than for large dislocations. Hence, in addition to the tendency for dislocations to form pileups, leading to the well known Hall-Petch exponent, $-1/2$, there is another contribution to the strength of smaller grained materials. This additional contribution serves to decrease the observed Hall-Petch exponent.

This work is supported by the National Science Foundation Grant No. DMR-0304629.

References

[1] C. Bontemps-Neveu, These de Doctorate (Univ. Paris-Sud, Orsay, France) (1991).

[2] E. M. Schulson, T. P. Weihs, D. V. Viens, and I. Baker, Acta Metallurgica **33**, 1587 (1985).

[3] M. J. Mills and D. C. Chrzan, Acta Matallurgica et Materialia **40**, 3051 (1992).

[4] D. C. Chrzan, M.D.Uchic, and W.D.Nix, Philosophical Magazine A **79**, 2397 (1999).

[5] D. C. Chrzan and M. S. Daw, Physical Review B **55**, 798 (1997).

Characterization of Dislocation Structures in the Presence of Precipitates in Precipitation Hardening Aluminum Alloys

R.S. Yassar, and P. Trivedi, D.P. Field

School of Mechanical and Materials Engineering, P.O. Box 642920
Washington State University, Pullman, WA 99164-2920
reza-sh@mail.wsu.edu, ptrivedi@mail.wsu.edu, field@mme.wsu.edu

ABSTRACT

Dislocation structure evolution during deformation of aluminum alloys was investigated experimentally using channel die compression followed by electron backscatter diffraction (EBSD) and TEM. Polycrystal AA6022 samples were aged and then deformed up to 10% strain. Local misorientation associated geometrically necessary dislocation content was studied for large grains with <110> orientations as a function of precipitate characteristics. It is found that precipitate morphology affects the density and distribution of geometrically necessary dislocations.

1. Introduction:

Non-uniform plastic deformations give rise to the development of the so-called geometrically necessary dislocation (GND) densities which are required to accommodate lattice curvature [1]. Although the concept of geometrically necessary dislocations (GNDs) has been a subject of extensive discussion in the literature (e.g., [1] and [2]), the formation and evolution mechanisms of the GND cell structures are not well established yet. In a previous study, the effect of crystal lattice orientation and the orientations and topology of neighboring grains on the evolution of dislocations was investigated [3]. In the present paper and in a complementary work, the evolution of GNDs in the presence of different precipitate morphologies is investigated.

2. Procedure:

To produce precipitates with different morphologies, aluminum alloy 6022 (Al-0.55%Mg-1.1%wt Si was solutionized for 3 hours at 550ºC and subsequently quenched in water. The specimens were aged at 175ºC in salt bath furnace and the precipitates were characterized by TEM prior to deformation. EBSD analysis on the aged samples showed that very large grains (~2mm diameter) with orientation of <110> are present in the

microstructure. It is assumed that the deformation behavior of these grains is dominant over the deformation behavior of small grains and thus these large grains were subjected to EBSD analysis during plastic deformation. After ageing, channel die compression experiments were performed up to a level of 10% deformation. Subsequently orientation measurements were obtained by EBSD at a 3 micron step size from large grains near the central region of the channel die deformed specimens. The other existing orientations in the EBSD scan were excluded from the data.

3. Results and Discussion:

Fig. 1 shows the bright field TEM micrograph of specimens aged for 40min, 500min and 5500min. The ageing kinetics and precipitation sequence of this alloy has been investigated by the authors [4] and the results show that the precipitates in Fig. 1a and b are β″ and β+Si+Q respectively. β″ precipitates are needle shaped and are aligned in $<100>_{Al}$ direction of matrix. Si precipitates with various morphologies are seen with β-Mg_2Si platelets and Q lath shaped precipitates in Fig. 1b.

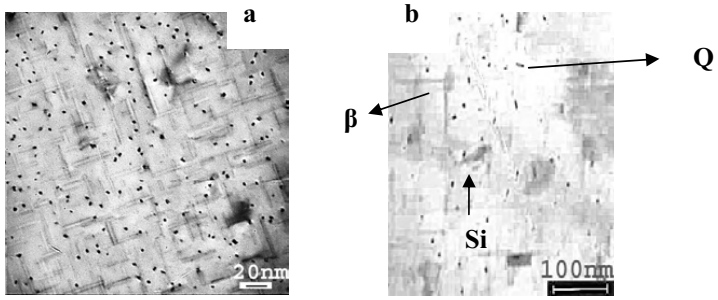

Fig. 1) AA6022 samples aged at 175ºC for (a) 500min and (b) 5500min.

The GND density can be obtained according to Nye [5] equation which relates the second-rank curvature tensor, κ_{ij}, directly to the dislocation density tensor, α_{ij}:

$$\alpha_{ij} = \kappa_{ij} - \delta_{ij}\kappa_{kk} \tag{1}$$

where δ_{ij} is the Kronecker delta and the summation convention is adopted. According to the recent work of El-Dasher et al [6,7] the curvature tensor can be measured by automated EBSD technique and for FCC materials the density of geometrically necessary dislocations can be obtained by

$$\rho_{GN} = \mathbf{A}^T\left(\mathbf{A}\mathbf{A}^T\right)^{-1}\boldsymbol{\alpha} \tag{2}$$

where the matrix **A** represents a component of the dislocation dyadic. Based on this method the total GND density for the large grains with <110> orientations in two different samples with different precipitate morphologies were calculated and the GND

distribution in the grains were plotted in Fig. 2a and b. The total GND density in the sample aged up to the peak of hardness (~500min) is 25% higher than the overaged (~5500min) sample. The reason can be explained by the fact that the needle shaped precipitates are the strongest barrier to the motion of dislocations and therefore more dislocations are expected to pile up around these precipitates. Thus the lattice rotation associated with these precipitates would be higher. In contrast, the overaged precipitates are large and the space between them is wide, therefore the dislocations can overcome them more easily and the lattice rotation would be less for this type of structure. From these results one can conclude that the precipitate morphology strongly affects dislocation flow and patterning, which yields a change in the GND densities and their distribution.

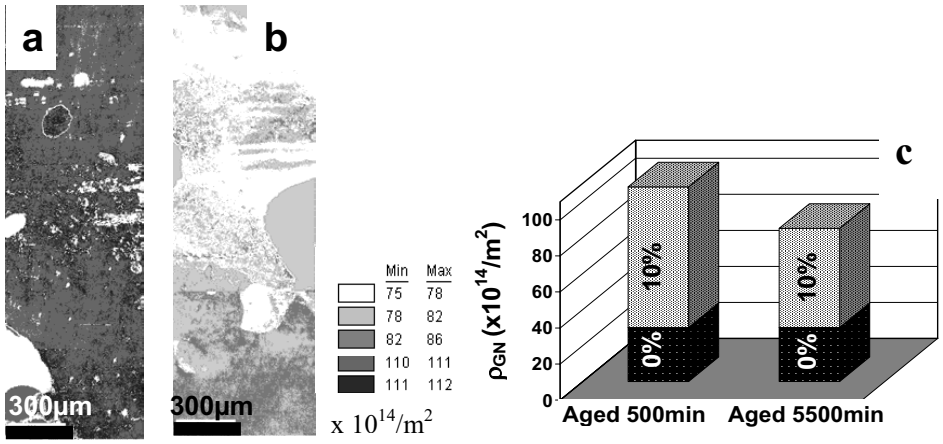

Fig. 2) GND distribution plot for the samples aged (a) 500min (b) 5500min and then deformed 10% (c) GND density comparison for these two samples after 0 and 10% deformation

Acknowledgement
This work was supported by DOE under grant no. DE-FC07-01ID 14189. The authors would like to thank Dr. Hasso Weiland for his helpful discussions.

References

[1] M.F. Ashby, Phil. Mag., vol. 21 (1970), 399–424.
[2] A. Arsenlis, D.M. Parks, Acta Mater., vol. 47 (1999), 1597–1611.
[3] P. Trivedi, D.P. Field, H. Weiland, Int. J. plasticity, vol. 20 (2004), 459-476
[4] R. S. Yassar, D.P. Field, H. Weiland, Mater. Sci. Eng., 2004, (submitted)
[5] J.F. Nye, Acta Metall., vol. 1 (1953), 153
[6] D.P. Field, S.I. Wright, P. Trivedi, Mat. Sci. Forum, vols. 426-432 (2003), 3739-3744
[7] B.S. El-Dasher, B.L. Adams, A.D. Rollett, Scripta Mater. vol. 48 (2003), 141.

Modelling In-plane Torsion: A Case of Particular Interest Relating GND and Plastic Strain Gradients

A. Luque, J. Aldazabal, J.M. Martínez-Esnaola and J. Gil Sevillano

CEIT, Centro de Estudios e Investigaciones Técnicas de Gipuzkoa and TECNUN, Technological Campus of the University of Navarra. Manuel Lardizabal 15, 20018 San Sebastián, Spain. Corresponding author e-mail: jgil@ceit.es

ABSTRACT

This paper presents simple 2-D analysis of the in-plane torsion test of disks using continuum, crystalline or atomistic plasticity models. Such test could be useful for the study of mechanistic strain gradient plasticity (SGP) theories of crystalline materials, because in the in-plane shear specimen the plastic gradients are much stronger than in the out-of-plane shear of cylindrical samples deformed by conventional torsion.

1. Introduction

Torsion testing of cylindrical specimens is a routine tool for assessing large strain plastic behaviour and ductility of materials. From a more fundamental point of view of current interest, the size effect shown by the torsional response of cylinders is crucial for demonstrating the relevance of the hardening effects of geometrically necessary dislocations (GND) associated to extrinsic plastic strain gradients [1-3]. By contrast, in-plane torsion of annular specimens has been a very rarely used test [4-6]. Nevertheless with the denomination of Corbino disk test, the in plane torsion of vortex crystal matter is nowadays being the object of much interest both from the experimental and from the modelling points of view (see [7] and references therein). A simple continuum analysis evidences that such test is very appropriated for the study of mechanistic SGP theories of crystalline materials, because in the annular in-plane shear specimen the plastic gradients are much stronger than in the out-of-plane shear of cylindrical samples deformed by conventional torsion. This paper presents simple 2-D analysis of the in-plane torsion test of disks or rings spanning from the macroscopic to the nanoscopic scales.

2. Macroscopic (Continuum) Analysis of the In-plane Torsion Test

If we consider a flat ring of radius $r_1 \le r \le r_2$, and we induce an in-plane torsion by application of a torque **T** (perpendicular to the disk plane) through the inner (or the outer) surface, the outer (inner) one being rigidly fixed, a non-homogeneous deformation occurs in the ring. For planar isotropy, the non-homogeneity is given by a radial simple shear gradient, $\gamma(r)$. Assuming a rigid-plastic power-law hardening for the macroscopic flow stress, $\tau \propto \gamma^n$, from equilibrium it is immediate to see that the shear stress gradient is

$$\chi(r) = \frac{\partial \gamma(r)}{\partial r} = -\frac{2\gamma(r)}{nr} \qquad (1)$$

By contrast, the gradient in a twisted cylindrical bar is constant and amounts to

$\chi = \gamma(r)/r$. For accommodation of the plastic gradient of the ring, given by (1), it will be geometrically necessary to store the GND dislocation density

$$\rho_G(r) = \frac{M_G}{b}|\chi(r)| = \frac{2M_G\gamma(r)}{nbr} \tag{2}$$

where b is the modulus of the Burgers vector and M_G an orientation factor of the order of unity. It may be seen that for moderate γ values and $0 \le n \le 0.5$, the predicted GND density will be very high for rings of small dimensions (i.e., $r \approx 1$ mm).

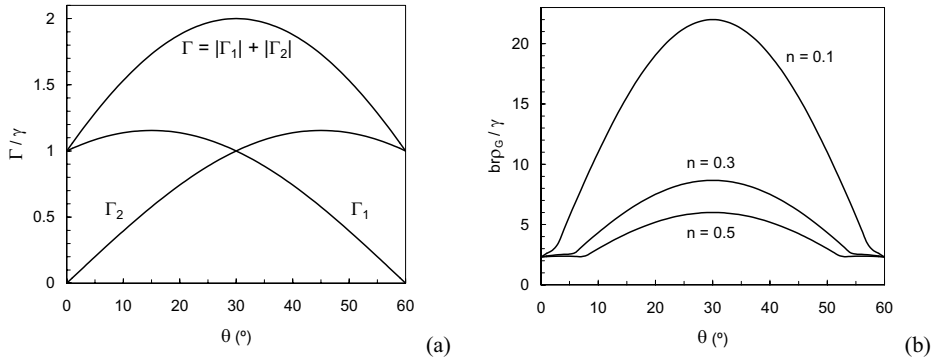

Figure 1. (a) Crystallographic slip in the active systems. (b) Normalised densities of GNDs as a function of the angular position for different hardening exponents.

3. Crystal Plasticity Analysis of a Simple Case of In-Plane Torsion

We will consider a very simple case. If the disk is made of a power-law hardening HCP single crystal deforming preferentially by prismatic <*a*> slip and the torsion axis is parallel to the hexagonal *c* axis, any circumferential simple shear deformation is resolved by activation of two prismatic slip planes. Assuming a radial gradient of the shear, as before (what seems reasonable for this particular case but not valid for other orientations with stronger planar anisotropy) and making a Taylor type calculation of the tangential dependence of the crystallographic slips, the result for each sector of 60º is presented in Fig. 1a, where the origin of the tangential coordinate θ is a $[10\bar{1}0]$ direction on the (0001) surface of the disk. From such result the slip gradient for each system at any tangential position can be deduced, and assuming the GND density being constituted of trapped slip dislocations, the GND density is given by

$$\rho_G = \frac{1}{b}\sum_{i=1}^{s}|\vec{n}_i \times \nabla\Gamma_i| \tag{3}$$

with s being the available slip systems. Figure 1b presents the normalised GND dislocation densities for our disk for three values of the strain hardening exponent n.

4. An Atomistic 2-D Simulation

Figure 2 shows the results of a 0 K atomistic simulation of the in-plane torsion of a

compact 2-D Copper crystal of (111) orientation, i.e., the 2-D crystalline version of the previous section. The calculation is made using the EAM method with the Cu potential from ref. [8]. The diameters of the ring are 10 nm and 20 nm. Twisting of the initially perfect crystal induces the emission of gliding dislocations from the inner rigid circumference (a rigid layer three to four atoms thick has been located at the inner and outer circumferences). GNDs are progressively stored (first 6, then 12, and so on) near the inner part of the ring where deformation is strongly concentrated, creating a boundary of increasing misorientation.

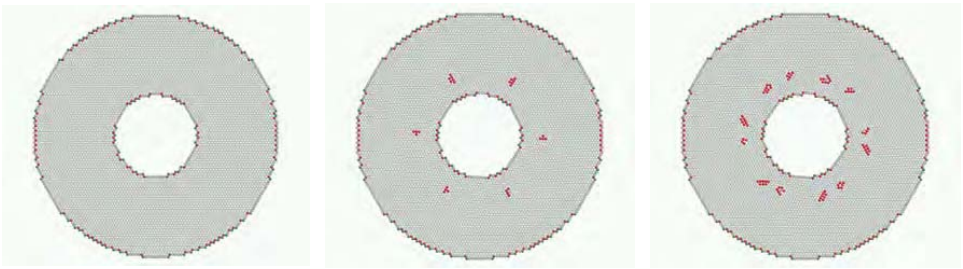

Initial configuration $\gamma = 0.16$ (6 GND) $\gamma = 0.24$ (12 GND)

Figure 2. Atomistic simulation of in-plane torsion.

Acknowledgements: Support from the Spanish MCYT, through projects MAT2000-0603 and MAT2003-04314, and to the Departamento de Educación, Universidades e Investigación of the Basque Government is gratefully acknowledged.

References

[1] N.A.Fleck, G.M.Muller, M.F.Ashby and J.W.Hutchinson, "Strain gradient plasticity: theory and experiment", *Acta Metal. Mater.*, 42, 475 (1994).

[2] F.Székely, I.Groma and J.Lendvai, "Nonlocal effects in torsional deformation", *Mater. Sci. Eng.*, A277, 148-153 (2000).

[3] J.M.Martínez-Esnaola, M.Montagnat, P.Duval and J.Gil Sevillano, "Geometrically necessary dislocations in a c-axis oriented cylindrical bar of basal-slipping hexagonal crystals deformed in torsion", *Scripta Mater.*, 50, 273-278 (2004).

[4] Z.Marziniak and J.Kolodziezski, "Assessment of sheet metal failure sensitivity by meted of torsioning the rings", *Proc. of 7th Biannual Congr. of the IDDRG*, 61-64, Amsterdam, 1972.

[5] R.Sowerby, "On in-plane torsion testing of sheet metal", *J. Mech. Eng. Sci.*, 19, 213-220 (1977).

[6] A.E.Tekkaya and K.Pöhlandt, "Determining stress-strain curves of sheet metal in the plane torsion test", *Annals of the CIRP*, 31, 171-174 (1982).

[7] M.C.Miguel and S.Zapperi, "Tearing transition and plastic flow in superconducting thin films", *Nature Materials*, 2, 477-481 (2003).

[8] Y.Mishin, D.Farkas, M.J.Mehl and D.A.Papaconstantopoulos, "Interatomic potentials for monoatomic metals from experimental data and ab-initio calculations", *Phys. Rev. B*, 59, 3393-3406 (1999).

Theoretical and Numerical Modeling of Strain-Rate Softening Instabilities: On the Velocity Selection of Propagating Portevin–Le Chatelier Deformation Bands

Peter Hähner[1,2], **Verena Grützun**[2], **Egidio Rizzi**[3]

[1]**Structural and Functional Materials, Institute for Energy, DG-Joint Research Centre, European Commission, PO Box 2, NL-1755 ZG Petten, The Netherlands (email: peter.haehner@jrc.nl)**

[2]**Institut für Metallphysik und Nukleare Festkörperphysik, Technische Universität Braunschweig, Mendelssohnstrasse 3, D-38106 Braunschweig, Germany**

[3]**Facoltà di Ingegneria, Dipartimento di Progettazione e Tecnologie, Università degli Studi di Bergamo, viale G. Marconi 5, I-24044 Dalmine (BG), Italy**

ABSTRACT

Uniformly propagating Portevin–Le Chatelier (PLC) plastic deformation bands are studied theoretically and numerically in terms of a model which incorporates the dynamic strain ageing kinetics and the effect of long-range dislocation interactions. PLC deformation banding is traced back to a wave propagation phenomenon, and the problem of propagation velocity selection is addressed for both strain- and stress-controlled tensile tests. According to the control mode, the model reveals fundamental differences in the velocity selection mechanism, which compare favourably with numerical simulations and experimental observations.

1. Introduction

The Portevin–Le Chatelier (PLC) effect, also known as jerky flow, denotes the serrated yielding of solid solutions. The PLC effect represents a strain-rate softening instability (a negative strain-rate sensitivity (SRS) of the flow stress), the microphysical reason of which consists in a repeated break-away of dislocations from, and subsequent recapture by, mobile solute atoms, *i.e.* dynamic strain ageing (DSA).

Recently, a new PLC model has been introduced [1, 2]. Its implications on the velocity selection problem during band propagation are to be discussed in the present work, in particular, as far as tensile tests at constant *stress* rate are concerned ($\dot{\sigma} = \text{const}$). In this case, staircase-type stress–strain curves go along with PLC bands propagating rapidly at virtually constant stress, while quasi-elastic loading intervals separate the nucleation/propagation of successive bands. From the characteristic times involved (the duration of band propagation $t_{\rm prop} \approx 10^{-1}$ s is much less than the duration of the intermediate loading phases $t_{\rm load} \approx 10$ s) we conclude that most of ageing occurs during elastic loading. In fact, as the characteristic time of solute diffusion largely exceeds $t_{\rm prop}$, *dynamic* strain ageing during band propagation is not significant, but *static* ageing occurs during elastic loading transients.

2. DSA-based model of the PLC effect

Consider a plastically-deforming material described by an Arrhenius law for the plastic strain rate $\epsilon_{,t}$, which depends on an effective Gibbs' free activation enthalpy $G = G_0 + \Delta G$, with an additional enthalpy ΔG in proportion to the solute content accumulated at glide dislocations: $\epsilon_{,t} = \nu\,\Omega\,\exp\left[-\frac{G_0+\Delta G}{kT} + \frac{\sigma_{\rm eff}}{S_0}\right] \equiv \eta\,\Omega\exp[-g]\,f$. Here a generalized driving force f and the reduced additional enthalpy g have been defined by:

$$f = \frac{\nu}{\eta}\exp\left[-\frac{G_0}{kT}\right]\exp\left[\frac{\sigma_{\rm eff}}{S_0}\right]\,, \qquad \text{and} \qquad g = \frac{\Delta G}{kT}\,, \tag{1}$$

where ν is an appropriate attack frequency, Ω is the elementary strain associated with a single activation step, G_0 is the basic activation enthalpy in the absence of DSA, k is Boltzmann constant and T absolute temperature. S_0 denotes the *instantaneous* SRS of the flow stress. By the parameter η we have introduced the ageing rate ($\propto$ solute mobility) as a relevant model time scale (*cf.* Eqs. (2,3)), such that the generalized driving force f and the scaled DSA-related activation enthalpy g are the dimensionless dynamical variables of the model. Expressed in non-dimensional terms the evolution equations of the model read [1, 2]:

$$\dot{f} \;=\; \dot{\sigma} f - \theta\,\exp[-g] f^2\,, \tag{2}$$

$$\dot{g} \;=\; g'' + (g/g_\infty)^{-(1-n)/n}(g_\infty - g) - f\exp[-g]\,g\,. \tag{3}$$

Here dots stand for differentiation with respect to dimensionless time $\tilde{t} = \eta t$. Dimensionless parameters have been introduced by scaling the external stress rate $\sigma_{{\rm ext},t}$ and the strain hardening coefficient h according to $\dot{\sigma} = \sigma_{{\rm ext},t}/(\eta S_0)$, $\theta = \Omega h/S_0$, and g_∞ denotes the asymptotic value of g associated with completely aged dislocations (saturation value of g). The exponent n governs the initial ageing kinetics, $g \propto t^n$, well before saturation sets in.

The effective stress in Eq. (1) is defined as the externally applied stress $\sigma_{\rm ext}$ (flow stress) minus the internal stress $\sigma_{\rm int}$ (athermal back stress), $\sigma_{\rm eff} = \sigma_{\rm ext} - \sigma_{\rm int}$. Accordingly, the driving force f changes owing to the external stress rate $\sigma_{{\rm ext},t}$ diminished by the contribution from strain hardening, $\sigma_{{\rm int},t} = h\epsilon_{,t}$. Eq. (2) then expresses the balance between external loading and strain hardening of the specimen. The term $g_\infty - g$ in Eq. (3) describes the effect of ageing: g approaches the saturation value at unit rate on the non-dimensional time scale $\tilde{t}$. The last term on the r.h.s. of Eq. (3), which is equivalent to $-g\epsilon_{,t}/(\eta\Omega)$ expresses the loss of solute content g in the glide dislocations owing to thermally activated unpinning at the dimensionless rate $\epsilon_{,t}/(\eta\Omega)$.

The spatial coupling term g'' of Eq. (3) represents a second order gradient with respect to the tensile direction x in terms of the non-dimensional coordinate $\tilde{x} = \sqrt{\eta/D}\,x$. In the present case, the diffusion-like coupling coefficient $D = \beta(\mu/S_0)\epsilon_{{\rm b},t}s^2$ (where $\beta \approx 0.1$ is a numerical prefactor, μ the shear modulus) is traced back to long-range dislocation interactions associated with gradients in glide velocity [1].

In the following sections tensile tests at constant strain rate ($\dot{\epsilon} = $ const) and at constant stress rate ($\dot{\sigma} = $ const) will be considered separately. We investigate the problem of propagation velocity selection of solitary deformation bands, *i.e.* uniformly translating strain-rate profiles of the form $\epsilon_{,t} = \epsilon_{,t}(x - c_{\rm b}t)$. As we shall see, the solution to this problem depends on the test control mode.

3. Velocity selection for $\dot{\epsilon} = \text{const}$

The plastically deforming solid solution is an excitable medium in which various types of waves may nucleate/propagate. The most regular excitation is a Type-A PLC band, which represents a solitary wave propagating at constant speed c_b. The derivation of the band parameters has been presented in [1]. Here we focus on a qualitative discussion on band speed selection. To this end we note that a PLC band represents a zone of almost unaged dislocations (g small) which propagates into an aged state (g near g_∞). The unpinning of dislocations in the front of the band occurs at near constant f, as this is a comparatively slow variable unable to follow rapid ageing changes. So we may concentrate on the dynamics of a solitary wave in g with $\dot{g} = -c\,g'$ and $c = (D\eta)^{-1/2} c_\mathrm{b}$ denoting the non-dimensional band speed. Consider Eq. (3) rewritten in the form ($n = 1$, for simplicity):

$$g'' + cg' = -\frac{\partial U}{\partial g} \quad \text{with} \quad U = g_\infty g - \frac{1}{2}g^2 + f(g+1)\exp[-g]\,. \tag{4}$$

The dynamical 'potential' U is plotted in Fig. 1 for various f values. For intermediate values $f_\mathrm{min}<f<f_\mathrm{max}$, U exhibits two stationary points corresponding to dynamically stable steady states (the strongly aged state in front of the advancing band and the almost unaged state within the band), separated by a minimum (unstable steady state at intermediate g). The value f_max at which the strongly aged steady state disappears corresponds to the upper yield point associated with the nucleation of a new band. Band propagation occurs as band nucleation goes along with a certain stress drop. The switching of one stable state to the other, which is associated with the passage of the band front, can then be interpreted in terms of a simple mechanical analogue: Eq. (4) is tantamount to the equation of motion of a unit mass particle in the 'potential' U subjected to dynamic friction with 'damping coefficient' c. The solitary wave solution corresponds to a situation where the particle originates from the left maximum at 'time' $\tilde{x}\to -\infty$, moves through the potential valley, and comes to rest again at the right maximum for $\tilde{x}\to\infty$. Obviously, this particular trajectory exists only for a certain value of 'damping coefficient', such that the propagation velocity c is well-defined [1].

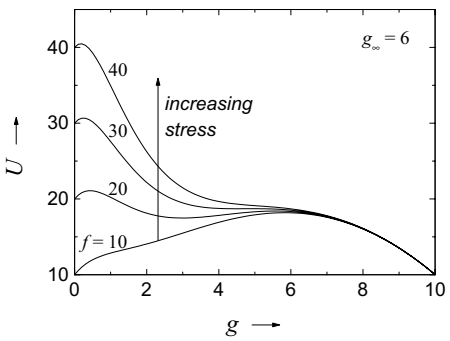

Figure 1: Illustration of the dynamic potential U defined in Eq. (4) for various values of the generalized driving force f (and $g_\infty = 6$).

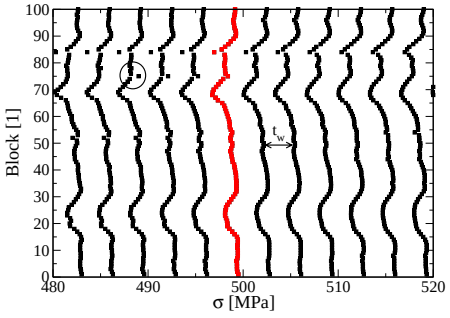

Figure 2: Spatio-temporal band correlation for a numerical tensile test at constant stress-rate: $n = 1/3$, $\dot{\sigma} = 0.5$ MPa/s.

4. Velocity selection for $\dot{\sigma} = \text{const}$

As compared to strain control ($\dot{\epsilon} = \text{const}$), the description of stress controlled tests with $\dot{\sigma} = \text{const}$ is formally simplified by the fact that the 'machine equation' does not affect the dynamics. The non-local feedback provided by the tensile machine may induce additional deformation modes, i.e. intermittent bands of Type B and randomly nucleating bands of Type C [1, 2]. Therefore $\dot{\sigma} = \text{const}$ tests do not reveal analogues of Types B and C. Also, the propagation velocity of strain-controlled Type-A bands is determined by the imposed deformation rate $\dot{\epsilon}$, while it is not clear what controls velocity in a $\dot{\sigma} = \text{const}$ test. In principle, the strain bursts could propagate at any speed. Experimental investigations show that the band velocities c_b may significantly exceed those observed for $\dot{\epsilon} = \text{const}$. Moreover, one notes two important differences. Firstly, for $\dot{\sigma} = \text{const}$, the stress rise occurring between two successive PLC bands goes along with quasi-elastic deformation, until a critical stress level for the next nucleation is reached. As band nucleation occurs without stress drop, the specimen is prepared in a marginally stable state (the horizontal inflection point for $f \approx 30$ in Fig. 1), into which the band propagates. This is to be distinguished from the propagation into a metastable state as it was discussed in Section 3. Secondly, most of ageing occurs *statically* during quasi-elastic loadings, while *dynamic* strain ageing is negligible during short propagation periods. The PLC band dynamics depends on the degree of static ageing that the specimen in front of the band was subjected to and, hence, on the applied stress rate $\dot{\sigma}$: the shorter the elastic loading phase, *i.e.* the higher $\dot{\sigma}$, the less ageing has occurred.

Again, Fig. 1 can be invoked to illustrate the velocity selection problem. Now the solution in question (the particle originates from the dynamically stable unaged state associated with the left maximum and comes asymptotically to rest at the horizontal inflection point corresponding to the marginally stable state in front of the band) exists for any 'damping' $c > c^*$. Apart from this lower limit velocity c^* (corresponding to the marginally stable case where group velocity and phase velocity of the plastic wave coincide), a particular propagation speed does not exist. Accordingly, we expect a less regular space-time correlation of deformation bands exhibiting a spectrum of propagation velocities.

That was confirmed by numerical simulations of the model, with specimen discretized in 100 segments ('blocks'). Fig. 2 shows a typical space-time(stress) correlation pattern of the local extrema of the plastic strain rate. One notes that the deformation bands propagate at any velocity (the slope of the space-time trajectories). Hence the propagation velocity is no longer a well-defined quantity, while the recurrence time still is, as in the case of solitary Type-A bands under strain control. Owing to that well-defined recurrence time, however, one observes a regular stair-case type stress-strain curve, which must not be confused with solitary wave propagation at constant speed. This has also been confirmed experimentally by laser-extensometric monitoring of stress-controlled tensile tests on a Cu-Al alloy [3].

References

[1] P. Hähner, A. Ziegenbein, E. Rizzi, H. Neuhäuser, *Spatiotemporal Analysis of Portevin–Le Chatelier Deformation Bands: Theory, Simulation and Experiment*, Phys. Rev. B **65** (2002) 134109.

[2] E. Rizzi, P. Hähner, *On the Portevin–Le Chatelier Effect: Theoretical Modeling and Numerical Results*, Int. J. Plast. **20** (2004) 121.

[3] F. Klose, these proceedings.

A Continuum Theory of Dislocation Motion

Thomas Hochrainer

Universität Karlsruhe (TH)
Institut für Zuverlässigkeit von Bauteilen und Systemen
Kaiserstr. 12, 76131 Karlsruhe, Germany
thomas.hochrainer@izbs.uni-karlsruhe.de

ABSTRACT

Physically founded continuum descriptions of dislocation-based crystal plasticity must be formulated in terms of dislocation densities. Classical dislocation density measures, as the Kroener-Nye tensor, can account for the kinematic evolution of dislocation systems only if they are considered on the discrete dislocation level. At the beginning of a three-dimensional continuum theory of dislocation motion therefore stands the definition of a dislocation density measure which retains the macroscopically relevant information about the dislocation system, together with the derivation of a kinematic evolution equation for it. A 3D dislocation density measure is proposed as a differential form on the space of directions and curvatures at each point of a crystal. A kinematic evolution equation for the proposed density is derived solely from the assumption that curved dislocation segments move according to a given velocity field. Relations with other density-based models of dislocation systems are discussed.

1. Introduction

The plastic behavior of metals in small dimensions shows size-effects not covered by conventional continuum plasticity. Dislocation density based models of plastic flow therefore gained new attention as physically based continuum descriptions of plasticity. There are promising approaches in two dimensions, e.g. Zaiser and Groma [1], but the three dimensional case still faces the problem of defining an appropriate measure of a dislocation density. The Kroener-Nye tensor does not account for dislocation distributions with zero net Burgers vector and is thus not suited to describe dislocation systems on an averaged level. Several authors proposed dislocation density measures beyond the Kroener-Nye tensor, as for example Kosevich [2], El Azab [3] and Sedlacek, Kratochvil and Werner [4]. All these measures categorize dislocations according to their line-direction and in the last case also to their curvature and are said to measure a line-length per unit volume. But a mathematical definition for an object of this dimensionality is not given. Consequently when deriving evolution equations these objects are treated as volume-densities.
In the present approach, a dislocation density measure is defined as a differential form. The evolution equation for this measure accounts for changes of line-direction and curvature and reflects line length increase (or decrease) by bowing of dislocations. It is derived naturally from the measures formal definition and needs no further

phenomenological add-ons. The general approach furthermore assures that no terms are missed.

2. Definition of the Dislocation Density Measure

For a fixed Burgers vector b we define a measure for a density of curved dislocation lines as $\alpha(p,l,k) = \rho(p,l,k)dA^l d\phi^k dK$. Here dK is the volume element around the point k in curvature space, dL^k is the angular element orthogonal to the vector k (viewed as angular velocity) at the point l in directional space (sphere of directions) and dA^l is the unit area element perpendicular to the unit vector l at the point p in physical space. The function $\alpha(p,l,k)$ accordingly gives the number of dislocations at p having a line-direction contained in dL^k around l (piercing thus orthogonally through an area element dA^l) and a curvature vector contained in dK around k. After integrating over curvature space, ρ has the physical dimension of [1/*Area*]. The calculus for such a differential form is in principle well known from abstract differential geometry.

3. Evolution of line-length, line-direction and curvature

The evolution of the dislocation density measure introduced above should account for all important features of the motion of a single dislocation. When a dislocation is moving according to a given velocity field v, the line-length, the line-direction and the curvature vector will change. Preparing a large strain formulation, the dislocation is viewed as a curve c in a Riemannian manifold with a metric tensor g equipped with a metric connection ∇ that is not necessarily symmetric. Without loss of generality c is taken to be parameterized by arc-length. At a point $c(s)$ on the curve the line direction and the curvature vector are then given as $l = \partial_s c$ and $k = \nabla_s l$, whereby ∇_s denotes the covariant derivative along c induced by the metric connection. With standard calculus of variations the resulting *infinitesimal elongation* (or *contraction*) λ, the *directional velocity* ϑ and the *curvature velocity* κ are found as

$$\lambda = g(\nabla_s v + T(v,l),l) = -g(v,k) + g(T(v,l),l),$$
$$\vartheta = \nabla_s v + T(v,l) - \lambda \cdot l = (\nabla_s v + T(v,l))^{\perp} \text{ and}$$
$$\kappa = -\lambda \cdot k + \nabla_s \vartheta + R(v,l,l).$$

Here T and R denote the torsion tensor respectively the curvature tensor of the given connection. The symbol $(\,)^{\perp}$ denotes the part of a vector orthogonal to the line-direction.

4. Evolution of the density measure

The notation used in the last two paragraphs requires a repeated application of the splitting of the double tangent bundle due to Dombrowski [5]. Using this to define a Sasaki type metric on the third order tangent bundle and making the density function ρ given in Sec.2 time-dependent, the evolution equation for this is found as

$$\partial_t \rho(t,p,l,k) = -\mathrm{div}^S(\rho v) - \mathrm{div}^D(\rho\vartheta) - \mathrm{div}^C(\rho\kappa) + \rho\lambda = -\mathrm{DIV}(\rho \cdot (v,\vartheta,\kappa)) + \rho\lambda .$$

The operators div^S, div^D and div^C denote divergence-like operations in space, directional space and curvature space, respectively. These together form a divergence operator DIV on the configuration space.
Integrating over all directions D and curvatures C in a volume Ω, which is dislocation free in a surrounding of its boundary, gives the change of line length in the volume Ω as

$$\partial_t \int_\Omega \int_D \int_C \rho = \int_\Omega \int_D \int_C \partial_t \rho = \int_\Omega \int_D \int_C \rho\lambda ,$$

by using the general version of Stokes theorem. This reflects exactly what is expected from the discrete dislocation case, when the density would be a generalized function and the integral over the configuration space reduces to a line-integral along the curve:

$$\int_\Omega \int_D \int_C \rho\lambda = \oint_c \lambda$$

5. Conclusion

A dislocation density measure was defined as a differential form on directional and curvature space. The velocity fields induced from a velocity field on a dislocation line in directional and curvature space were given. An evolution equation for the density measure subject to a velocity field was derived in the setting of a Riemannian manifold with a general metric connection. This evolution equation inherently accounts for line-element rotation, elongation and curvature evolution during the motion of dislocation lines. Line-length increase leads to an according net gain in overall dislocation content.

Acknowledgements

The author expresses his thanks to Michael Zaiser and Peter Gumbsch for fruitful discussions and encouragements and gratefully acknowledges that parts of the work were done with support of the European Commission (Contract No. MRTN-CT-2003-504634).

References

[1] M. Zaiser, M. Carmen Miguel, I. Groma "Statistical dynamics of dislocation systems: the influence of dislocation dislocation correlations" *Phys Rev B* **64** (2001), 224102

[2] A. M. Kosevich in *Dislocations in Solids*, edited by F.R. Nabarro (Amsterdam: North-Holland, 1979), Vol. 1, 33-142

[3] A. El Azab "Statistical mechanics treatment of the evolution of dislocation distributions in single crystals" *Phys Rev B* **61** (18) (2000), 11956-11966

[4] A. Sedlacek, J. Kratochvil, E. Werner "The importance of being curved: bowing dislocations in a continuum description" *Phil Mag*, 1, **83** (2003), 3735-3752

[5] P. Dombrowski "On the Geometry of the Tangent Bundle" *J. Reine Angew. Math*, **210** (1962), 73-88

Dislocation Dynamics versus Kinetics

U. F. Kocks
Retired Fellow, Los Alamos National Laboratory
P.O. Box 89, Placerville, CO 81430
kocks@starband.net

Presented in honor of the pioneering and thoughtful works of Ladislas Kubin and of Hartmut Neuhäuser.

ABSTRACT

It is re-emphasized that 'normal' plasticity is a problem in the Statistical Mechanics (of lines) and is characterized by mechanical equilibrium situations punctuated by release events that are governed by thermal-activation kinetics; dynamics and cooperative effects enter in a significant way only in the special situation of macroscopic flow instabilities. Similarly, dislocation structure evolution is governed (in pure metals) by 'invasion percolation with storage', punctuated by dynamic recovery events under thermal-activation kinetics, and not by collisions or by 'pattern formation'. In general, simulation of dislocation behavior can aid model building – the important step – by illuminating local processes more so than in 'multi-scale' effects. Some local problems worthy of sophisticated simulation and/or experiments are outlined.

1. Statistical Mechanics of Dislocation Movement

The resistance to dislocation glide may be modeled by a two-dimensional random array of point-like obstacles; this may represent actual localized centers of 'strong' resistance [1] or even any non-regular distribution of glide resistances [2]. In such an arrangement, long dislocation lines (or dislocation loops) may be in mechanical equilibrium under stresses so low that none of the obstacles touched by the dislocation is overcome; a dislocation in such a situation is termed a 'hard line'. As the stress is raised, the important question is not whether any particular ('average') obstacle gets overcome, but whether, once it is overcome, the dislocation configuration changes such that other obstacles are immediately overcome also; the situation where no equilibrium configuration can any longer be found on the slip plane may be called 'dislocation percolation' (a term not yet used in [2]). The evolution of the dislocation configuration toward that critical state is illustrated in Fig. 1: at a low stress (a), regions that are 'soft' are insular, embedded in a matrix of regions that are still 'hard' under this stress; at a stress that is only slightly higher (b), the topology in inverted: free regions are contiguous and hard regions are insular. The final events leading to macroscopic slip on this plane occur at 'critical gates'.

It is easy to imagine a situation where a hard line exists that has one link almost penetrated – the 'critical gate' – and where, therefore, thermal-activation kinetics may cause a release with the most likelihood. After this one activation, many further links may give -- for geometric reasons, not dynamical: the dislocations are normally overdamped [2]. Typical times: are about 1 second waiting for thermal activation at the critical link [2], about 10^{-4} s for the ensuing slip over the entire plane [4].

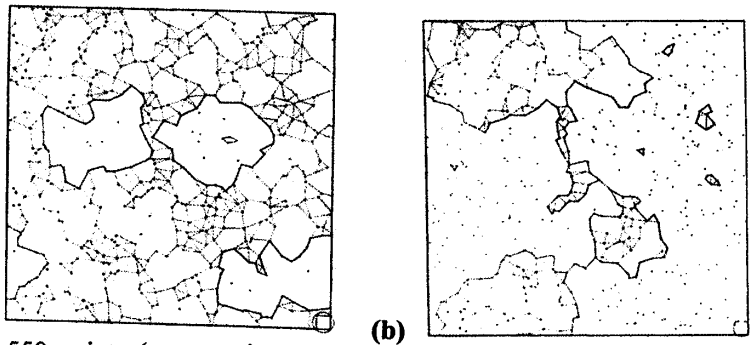

(a) (b)

Fig. 1 – 550 points (representing 'strong' obstacles) placed at random, with periodic boundary conditions, and connected by lines when they cannot be bypassed by a dislocation under the stress characterized by the circle in the lower-right corner (where the square contains in the average 1 point). After Kocks 1966 [2].

In this model, hard lines serve to separate topologies and tend to be 'concave loops'; in 'dislocation dynamics' simulations, one starts with a straight dislocation at one edge, and considers *long-range slip* to be achieved, when it reaches the opposite edge. This simulates one particular, path-dependent case: it needs further abstraction to generalize this for an overall model. (Note that the work for Fig. 1 simulated one particular slip plane – but an equation was found to characterize the topological flip-over.

An advantage of our model [2] is that it leads naturally to heterogeneity of the structure – without any need for 'pattern formation' or the like; and it is inherently stable against unloading. A disadvantage is that the 'naturally heterogeneous' structure is two-dimensional. A three-dimensional structure would ensue due to plastic relaxation of the 'forward' internal stresses inside the unslipped islands (which may be looked upon as being surrounded by 'dipole pile-ups') [2]. This relaxation is especially effective when slip on other planes is available in the structure. (It need only be short-range for this purpose, although it would normally be long-range in polyslip [5]). Such a relaxed, 3-D dislocation arrangement would also be stable against dissolution by next-arriving dislocations. The local three-dimensional structure is a special kind of tangle; it is inherently polarized and is under an internal stress that would tend to shrink it.

2. Dislocation Structure Evolution

The storage of 'concave loops' [2] around insular hard regions provides the primary cause of dislocation accumulation. (Dislocation collisions are negligible, according to time proportions mentioned above.) The rate of accumulation is small and could perhaps be quantitatively determined from simulations of 'invasion percolation with storeage'. Dynamic recovery may take place inside the tangles, under the driving force of the forward internal stress and with the aid of thermal activation. It is these processes within tangles (plastic relaxation and dynamic recovery) that could substantially benefit from local simulations; they could also quantify the *rotations* ensuing inside the tangle. The situation is schematically illustrated in Fig. 2, where the *thin* lines are from plastic relaxation and may extend into the third dimension. The formation of closed-looking *cells* occurs only in the process of *stopping* slip on a particular plane [5].

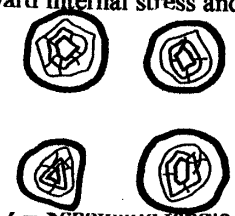

Fig. 2 – Schematic tangles.

In the extreme, dynamic recovery within the tangles can lead to the formation of two subboundaries of opposite sign and eventually to only a single subboundary corresponding to any *net* dislocation content of the original tangle. (so-called 'geometrically necessary dislocations').
A detailed model has been built upon the above 'picture' and extensive phenomenological investigations. [5]; it was developed for pure FCC polycrystals, but the basic ideas should apply to many other materials, the only real condition being planar glide (which ensues from a similarity of the glide resistance to screw and edge dislocations, common for 'strong' obstacles [1], such as forest dislocations). BCC polycrystals are presumed to behave in a similar manner at high temperatures; in the regime of high lattice resistance, on the other hand, screws are much harder to move and thus glide becomes more 'lineal' than planar and the storage rate is lower; solution-hardened materials could underlie similar restrictions (the edges being harder to move), but such an effect has not yet been observed.

3. 'Dynamic Strain Aging'
This term is commonly applied (as DSA) to the case of simultaneous kinetics of thermally-activated dislocation glide and thermally-activated solute diffusion. It is characterized by a negative contribution to the strain-rate sensitivity of both flow stress and strain-hardening, during homogeneous deformation. Only when the total strain-rate sensitivity becomes negative (sufficiently negative), does deformation become macroscopically instable and, typically, band propagation ensues.

4. Dynamics of Macroscopic Instabilities
A truly dynamic phenomenon has recently been discovered by Ananthakrishna and co-workers.[6] This occurs when the strain-rate sensitivity has become (sufficiently) negative and produces jerky flow, with PLC-bands of various characteristics. A sophisticated phenomenological analysis provides insight into the kind of statistics obeyed; collective behavior of dislocations is important in this instance.

Acknowledgments
Most of this work was performed under the auspices of the DOE Office of Basic Energy Sciences, Materials Sciences Branch, at Los Alamos National Laboratory. Many extensive discussions with Ladislas Kubin are gratefully acknowledged. Discussions with Profs. A. Beaudoin, H. Neuhäuser, and Ch. Schwink have also been very helpful.

References
[1] J. Gil Sevillano, J. Bouchaud, L.P. Kubin, "The fractal nature of gliding dislocation lines" (1991): *Scripta Metall.* **25**, 355.
[2] U.F. Kocks, "A statistical theory of flow stress and work hardening" (1966): *Philos. Mag.* **13**, 541-566; see also [5] Chap. 4..
[3] U.F. Kocks, A.S. Argon, and M.F. Ashby, "Thermodynamics and kinetics of slip" (1975): *Prog. Mater. Sci.* **19**, 300 pp.; U.F. Kocks, "Plastic deformation: thermal-activation approach" (2001): *Encyclopedia of Materials Science and Technology* (Elsevier Science) pp.7084-7088.
[4] H. Neuhäuser (1983): *Dislocation in Solids* **6**, 319, F.R.N. Nabarro, ed. (Elsevier Science)
[5] U.F. Kocks and H. Mecking, "The physics and phenomenology of strain hardening: the FCC case" (2003): *Prog. Mater. Sci.* **48**, 171-273.
[6] M.S. Bharati, M. Lebyodkin, G. Ananthkrishna, C. Fressengeas, L.P. Kubin, "The hidden order behind jerky flow" (2001): *Acta Mater.* **50**, 2813-2824

Mechanisms Controlling the Size of Misoriented Dislocation Cells

Jan Kratochvíl[1] **and Radan Sedláček**[2]

[1] Czech Technical University, Faculty of Civil Engineering, Dept. Physics, Thákurova 7, 166 29 Prague, Czech Republic, e-mail: kratochvil@fsv.cvut.cz

[2] Technische Universität München, Lehrstuhl für Werkstoffkunde und Werkstoffmechanik, Christian-Doppler Laboratorium für moderne Mehrphasenstähle, Boltzmannstr. 15, 85747 Garching, Germany

ABSTRACT

One of the most distinguished types of dislocation structure, the misoriented cells, is treated as an instability of plastic flow in pre-stressed solids. In the standard (local) approach, the continuum theory predicts an infinitesimally small cell size. To study the mechanisms controlling the finite cell size, selected short-range dislocation interactions have been introduced into the continuum description of dislocation flow: (i) the self-force of curved glide dislocations considered in the line-tension approximation, (ii) the short-range interactions among the glide dislocations themselves. Both interactions introduce nonlocal terms into the theory. Within the proposed framework, the cell size is a result of a compromise: the bulk strain and dissipative energy tends to decrease the cell size whereas the nonlocal interactions restrict this tendency.

1. Introduction

Deformation microstructure controls plastic, fatigue and fracture properties of ductile materials. There are two basic types of microstructure of a different physical nature: the *dipolar structures* which occur typically in easy cross-slip materials at early stages of single slip deformation (tangles, veins, walls) and the *lamellar structures* consisting of lamellae of differing slip. The reason for the slip differences is a tendency to decrease locally the number of active slip systems and in that way to minimize the energy of the deformation process. In the case of single slip, the plastic strain is localized into shear-band or kink-band lamellae. In case of double or multi slip, the plastic strain may occur in several systems of lamellae that simultaneously form a pattern of misoriented cells.

A convenient framework for description of a dislocation structure formation is provided by the refined continuum theory of dislocations complemented by a constitutive equation for dislocation velocity [1, 2]. The dislocation self-force and interactions among the glide dislocations represent nonlocal effects that introduce intrinsic length scales into the model. The introduction of the latter mechanism was inspired by the statistical dislocation dynamics worked out by Groma et al. [3].

An experimentally well documented prototype of the misoriented cells is the sheet structure observed in some cubic metal crystals, originally oriented for single slip in tension. The simplest form of the sheets seems to occur in certain bcc metals [4, 5]. In

the sheet structure, most of the dislocations are arranged in thin planar layers which are nearly parallel to the primary slip plane. The sheets consist of crossed grids of primary screw and secondary dislocations. In one particular grid, all the primary and secondary dislocations are of one sign only. The sheets occur in pairs. The crystal lattice of two neighboring layers adjacent to a sheet is misoriented: the alternate sheets display alternate changes in the sense of lattice rotation. According to [4], the sheets are formed in two stages. At the end of the easy glide region, the bundles of primary dipolar loops start to dissolve, causing avalanches. The avalanches spread over a distance of several bundles in the direction of primary Burgers vector. At the crossing with the bundles, the density of primary dislocations decreases and the bundles are dissolved. During the dissolution, long parallel primary screw dislocations remain stretched out among the remaining bundles, forming warps of one sign only. In the second stage, the secondary dislocations are caught on the warps. In that way, the primary and secondary dislocations interact in the avalanche regions, forming crossed grids. The avalanches and the screw dislocation warps are the factors which influence the characteristic size of the sheet structure. In the next section, the physical nature of the avalanches is briefly analyzed.

2. The Model

The avalanches are interpreted as primary-slip shear bands with an inner dislocation structure. A crystal deformed by single slip is considered. The slip planes are parallel to the xOz plane, the slip vector coincides with the x direction, t means time. The model consists of the small-strain 3D continuum mechanics equations: stress equilibrium, compatibility of total strain consisting of elastic and plastic parts, and the isotropic Hooke's law for elastic strain. The plastic strain is related to dislocation motion by Orowan equation. The dislocation orientation β measured with respect to the slip direction, and the density ϱ of dislocations of a specific initial orientation have to satisfy the dynamic law of conservation of Burgers vector (for details see [1, 2]),

$$\varrho\frac{\partial\beta}{\partial t} - \cos\beta\frac{\partial\varrho v}{\partial x} - \sin\beta\frac{\partial\varrho v}{\partial z} = 0\,, \qquad \frac{\partial\varrho}{\partial t} - \sin\beta\frac{\partial\varrho v}{\partial x} + \cos\beta\frac{\partial\varrho v}{\partial z} = 0\,. \tag{1}$$

The dislocation velocity v is controlled by the forces exerted on glide dislocation segments (the equation is considered for each initial orientation separately). In the rate-independent limit we have

$$b\sigma_{xy} + \kappa(\cos\beta\frac{\partial\beta}{\partial x} + \sin\beta\frac{\partial\beta}{\partial z}) + \xi(\sin\beta\frac{\partial\varrho}{\partial x} - \cos\beta\frac{\partial\varrho}{\partial z}) - b\tau_0 - Ab\int v\varrho dt = 0\,, \tag{2}$$

where b is the magnitude of Burgers vector. The second term represents the self-force taken in the line-tension approximation, κ is the line tension, and the rest of the term is the dislocation curvature. The third term represents the short range interactions among parallel dislocations derived in the special case of straight edge dislocations by Groma et al. [3]. Here $\xi = \mu b^2 D/(2\pi(1-\nu)\bar{\varrho})$ is the parameter expressing the difference between short-range ordered and random arrangements of dislocations,

$D \approx 0.8$, and $\bar{\varrho}$ is an average dislocation density. The rest of the third term is the gradient of density in the direction of the dislocation motion. In the fourth term, τ_0 is a friction stress and the last term represents the softening of the primary slip system caused by the dissolution of the bundles; $A > 0$ is a softening coefficient.

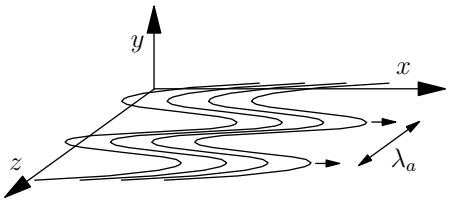

Figure 1: Avalanches in a shear band spreading in the primary slip direction.

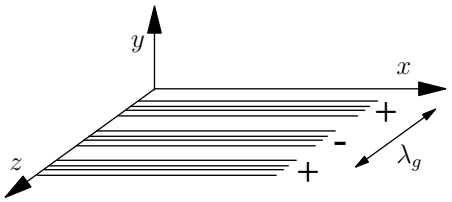

Figure 2: Warps of primary screw dislocations forming 'embryonic grids'.

The stability analysis of the model at the softening stage predicts formation of thin inhomogeneous shear bands. The initially edge primary dislocations coming from the dissolving bundles and controlled by the line tension produce the avalanches sketched in Fig. 1. The evaluated distance between the avalanches is $\lambda_a = 2\pi\sqrt{\kappa/b\bar{\varrho}A}$. When, under the influence of the short-range order interaction, the screw dislocations start to form the warps, the stability analysis predicts a periodic arrangement of screw dislocations into "embryonic grids" sketched in Fig. 2. The wavelength of this arrangement is $\lambda_g = 2\pi\sqrt{\xi/bA}$. The softening coefficient A can be estimated from the deviation of the grids from the primary slip plane. The small deviation has been observed [4, 6], and is predicted by the model. Taking the deviation to be of $\sim 1°$, using the measured primary dislocation density $10^{12}\,\mathrm{m}^{-2} < \varrho < 10^{14}\,\mathrm{m}^{-2}$ [4, 5, 7], and employing the estimate of the parameter ξ from [3], we get $10\,\mu\mathrm{m} < \lambda_a, \lambda_g < 100\,\mu\mathrm{m}$, i.e. λ_a and λ_g are roughly of the order of the size of the observed sheet structure pattern [4, 5, 7].

Acknowledgements

This research has been supported by grants GAČR 106/03/0826 and VZ J00021 (JK) and DFG We 2351/8-1 (RS).

References

[1] J. Kratochvíl and R. Sedláček. *Phys. Rev. B* 67 (2003) 094105.
[2] R. Sedláček, J. Kratochvíl, and E. Werner. *Philos. Mag.* 83 (2003) 3735.
[3] I. Groma, F. F. Csikor, and M. Zaiser. *Acta Mater.* 51 (2003) 1271.
[4] S. Libovický and B. Šesták. *Philos. Mag. A* 47 (1983) 63.
[5] W. Wasserbach. *Philos. Mag. A* 53 (1986) 335.
[6] D. A. Hughes et al. *Mater. Sci. Eng. A* 309-310 (2001) 220.
[7] J. W. Steeds. *Proc. R. Soc. A* 292 (1966) 343.

Experimental Research of Dynamic Strain Ageing and Portevin-LeChatelier Effect in Cu-Based Alloys at the Technical University of Braunschweig

H. Neuhäuser, Ch. Schwink

Institute of Metal Physics and Nuclear Solid State Physics
Technical University of Braunschweig38106 Braunschweig, Germany
e-mail: h.neuhaeuser@tu-bs.de

In our first studies [1] of Cu-30%Zn and Cu-Ge alloy single crystals it was realized that the „athermal" plateau of the temperature dependence of the critical resolved shear stress in fact results from a superposition of the thermally activated decrease of stress to overcome local solute obstacles and the increasing stress due to diffusional effects by mobile solute atoms. Slip line observations showed a very rapid evolution of slip band clusters during the load drops in the PLC regime, but recording failed because the location of the next avalanche could not be predicted. First observations with successful micro-cinematographic recordings were achieved by M.Schülke and J.Plessing [2] with Cu-Al alloy single crystals showing the local kinetics of avalanche formation [3] suggesting rapid dislocation multiplication after first breakaway of a source dislocation interacting with solute obstacles, and rapid local work hardening in the very small slipped volume where a very high local strain develops.

It became clear from the very beginning that dynamic strain ageing (DSA), i.e. the additional obstruction of dislocation mobility by solutes segregating to the dislocation cores, plays a decisive role for the appearance of the PLC effect, as even at much lower temperatures local atomic rearrangements in the dislocation core region could be evidenced in stress relaxation experiments and yield points on reloading [4]. Furthermore, the local stresses due to the development of extended dislocation groups owing to the destruction of short-range order [5, 6], involved in the nucleation and propagation of slip bands [7], were recognized to be important, supporting ideas by A.Korbel [8] and W.Pawelek [9] who, however, relied on the stress concentrations only.

The effects of DSA were studied extensively in the group of Ch.Schwink in the stable regimes near the transition to plastic instabilities (e.g., [10 - 12]), while Neuhäuser's group was concentrating on the instabilities themselves. The alloy systems Cu-Mn and Cu-Al were compared, the former with constant stacking fault energy (like Cu), the second showing a strong decrease of the stacking fault energy with increasing solute content (which enhances slip localization considerably). The dependence of DSA on solute type and concentration, temperature and strain rate as well as work-hardening state (i.e. effective stress), provided quantitative results on the limits of PLC regimes [10 – 12] as well as on the activation parameters and

modes of solute diffusion. In particular it was found that in all PLC regimes solute diffusion along dislocation cores is rate controlling, and with increasing temperature a change of processes occurs [11]: at relatively low temperature, diffusion along the core of partial dislocations from aged forest dislocations to the intersection regions with mobile dislocation produces additional "intersection strengthening" (process I) [13]. Then diffusion of solutes along the mobile dislocations (process II) occurs and/or atomic rearrangements along the mobile dislocations waiting for thermal activation lead to additional "line strengthening" (process II), while at even more elevated temperature, the diffusion in the stacking fault ribbon (Cottrell and Suzuki cloud) prevails (process III). Due to the increasing number of diffusion paths and intersection regions with increasing strain (stress) along the work-hardening curve, each of these processes may exhaust before the next sets in or they may overlap, depending on the alloy system [11]. The high temperature end of the PLC regime is determined by exhaustion of process III, while the transition to homogeneous glide occurs when volume diffusion is fast enough to reconstruct local obstacles so rapidly during the waiting times that the solute atmospheres are "dragged along" with the moving dislocations and the "athermal" stress contribution strongly decreases with temperature [14]. These pictures are supported by the experimentally determined activation energies [11, 12] and activation volumes [15] and are in accord with microstructural observations [5, 6].

The studies on the PLC instabilities have strongly profited from a laser scanning extensometer developed in the 90s by Fiedler Optoelektronik, which permits to follow in-situ the propagating PLC bands with a spatial resolution of about 1 μm and temporal resolution of 20 ms, yielding a resolution in local strain of 0.05% in 2 mm wide segments along the specimen. This instrument has mostly been applied in investigations of PLC band propagation of types A [16], B [17], and C in Cu-15at%Al polycrystals. Another essential push came from the presence of P.Hähner in our group, who had already developed profound concepts (correcting and extending earlier ones) for modeling the PLC effect [18] and now, in close contact with the experimentalists, worked out his model further with respect to the PLC types and band propagation, obtaining very good agreement with the observations [19, 20].

These studies have been continued with strain-rate controlled [17, 21, 22] and stress-rate controlled experiments [23], with the aim to elucidate the controlling mechanism for PLC band propagation. All experiments (and theoretical estimations [18, 19]) indicate that the local stress concentrations of dislocation groups, i.e. the intensive interaction of dislocations through their far-reaching stress field – the second prerequisite, besides DSA, for the PLC effect to occur [18, 23] – causes and controls the band propagation (similar to the case of Lüders band propagation [6]), as shown in particular by the results of acoustic emission during strain controlled [24] and of laser extensometry in stress-controlled experiments [25].

Acknowledgements. The authors are indebted to their numerous coworkers over the years for their engaged work, to many colleagues for fruitful discussions, as well as to the Deutsche Forschungsgemeinschaft and Volkswagenstiftung for financial support.

References

[1] H. Traub, H. Neuhäuser, Ch. Schwink: Acta Metall. **25** (1977) 437-446.
[2] H. Neuhäuser, M. Schülke, J. Plessing: J.Mech.Beh.Metals **2** (1990) 231-257.
[3] C. Engelke, J. Plessing, H. Neuhäuser: Mater.Sci.Eng.A **164** (1963) 235-239.
[4] H. Neuhäuser, H. Flor: Scripta Metall. **12** (1978) 443-448; H. Flor, H. Neuhäuser: Acta Metall. **28** (1980) 939-948.
[5] J. Olfe, H. Neuhäuser: phys.stat.sol. **109** (1988) 149-160; J. Plessing, Ch. Achmus, H. Neuhäuser, B. Schönfeld, G. Kostorz: Z.Metallk. **88** (1997) 630-635.
[6] S. Flor, H. Dierke, A. Nortmann, H. Neuhäuser: Z.Metallk. **94** (2003) 572-579.
[7] A. Hampel, T.Kammler, H. Neuhäuser: phys.stat.sol.(a) **135** (1993) 405-416; H. Neuhäuser, A. Hampel: Scripta Metall.Mater. **29** (1993) 1151-1157.
[8] A. Korbel, J. Zsadadzinski, Z. Sieklucka: Acta Metall. **24** (1976) 919-923.
[9] A. Pawelek, Z.Metallk. **80** (1989) 614-618:
[10] A. Kalk, A.Nortmann, Ch. Schwink: Phil.Mag.A **72** (1995) 1239-1259.
[11] A. Nortmann, Ch. Schwink: Acta Metall.Mater. **45** (1997) 2043-2050; 2051-2058.
[12] Ch. Schwink, A. Nortmann: Mater.Sci.Eng.A **234-236** (1997) 1-7.
[13] R.A. Mulford, U.F. Kocks: Acta Metall. **27** (1979) 1125-1134.
[14] A. Nortmann, H. Neuhäuser: phys.stat.sol.(a) **168** (1998) 87-107.
[15] F. Springer, A. Nortmann, Ch. Schwink: phys.stat.sol.(a) **170** (1998) 63-81.
[16] A. Ziegenbein, P. Hähner, H. Neuhäuser: Comput.Mater.Sci. **19** (2000) 27-34; Mater.Sci.Eng.A **309-310** (2001) 336-339.
[17] F. Klose, A. Ziegenbein, J. Weidenmüller, H. Neuhäuser, P. Hähner: Comput.Mater.Sci. **26** (2003) 80-86.
[18] P. Hähner: Mater.Sci.Eng.A **207** (1996) 208-215; 216-223; Acta Metall. Mater. **45** (1997) 3695-3707.
[19] P. Hähner, A. Ziegenbein, E. Rizzi, H. Neuhäuser: Phys.Rev.B **65** (2002) 134109 (1-20).
[20] E. Rizzi, P. Hähner: Int.J.Plasticity **20** (2004) 121-165: P. Hähner, E. Rizzi: Acta Mater. **51** (2003) 3385-3397.
[21] L. Casarotto, R. Tutsch, R. Ritter, J. Weidenmüller, A. Ziegenbein, F. Klose, H. Neuhäuser: Comput.Mater.Sci. **26** (2003) 210-218.
[22] F. Klose, J. Weidenmüller, A. Ziegenbein, P. Hähner, H. Neuhäuser: Phil.Mag.A **84** (2004) 467-480; F.B. Klose, A. Ziegenbein, H. Neuhäuser, M.Abbadi, P. Hähner, A. Zeghloul: Mater.Sci.Eng.A 364 (2004) 70-81.
[23] F. Chmelik, A. Ziegenbein, H. Neuhäuser, P. Lukac: Mater.Sci.Eng.A **324** (2002) 200-207.
[24] S. Bross, P. Hähner, E.A. Steck, Comput.Mater.Sci. **26** (2003) 46-55.
[25] F.B. Klose, F. Hagemann, P. Hähner, H. Neuhäuser: Mater.Sci.Eng.A (in print); H. Neuhäuser, F.B. Klose, F. Hagemann, J. Weidenmüller, H. Dierke, P. Hähner: J.Alloys Comp. **378** (2004) 13-18; F. Klose, PhD thesis, TU Braunschweig (2004): http://opus.tu-bs.de/opus/volltexte/2004/571/

Bending and torsion of thin samples in continuum dislocation-based approach

Radan Sedláček[1] and **Jan Kratochvíl**[2]

[1] Technische Universität München, Lehrstuhl für Werkstoffkunde und Werkstoffmechanik, Christian-Doppler Laboratorium für moderne Mehrphasenstähle, Boltzmannstr. 15, 85747 Garching, Germany, e-mail: sedlacek@lam.mw.tum.de

[2] Czech Technical University, Faculty of Civil Engineering, Dept. Physics, Thákurova 7, 166 29 Prague, Czech Republic

ABSTRACT

The continuum dislocation-based model of plastic deformation is applied to bending of thin strips and torsion of thin wires. It is shown that the size effects observed on the micrometer scale can be ascribed to the bowing of dislocations penetrating from the free surfaces of the samples.

1. Introduction

The recently proposed continuum dislocation-based model of plastic deformation [1] is applied to modelling of size effects in bending of thin crystalline strips and torsion of thin wires. The approach is based on the refined averaging in the continuum theory of dislocations and its coupling with the continuum crystal plasticity. Introduction of the line-tension controlled self-force of curved dislocations renders the theory nonlocal. In confined plasticity, the bowing of dislocations between impenetrable interfaces leads to a size effect [2, 3]. It is shown here that also in inhomogeneous plastic deformation of free standing samples, the size effects on the micrometer scale can be ascribed to the bowing of dislocations.

In elastic regime, the pure bending of a strip gives rise to a linear distribution of normal stress. Plastic yielding begins simultaneously at the inner and outer surfaces and propagates towards the neutral plane. In terms of dislocations, these can be pictured as being nucleated at the free surfaces and gliding towards the center of the strip. The image forces acting on the dislocations near the free surfaces cause the dislocations to be oriented approximately perpendicular to the surface, thus being forced to bow out. The size effect is due to the self-force of the curved dislocations. In small samples, the dislocations must curve more strongly than in large ones, so that the self-force opposing the deformation is stronger. The situation is quite analogous in torsion of thin wires, Fig. 1. The bending of thin crystalline strips has been treated in detail in Refs. [4, 5]. The model for torsion of a thin crystalline wire is set up in the following.

2. The Model

A thin wire with a circular section of radius R, its axis parallel to z, is considered in

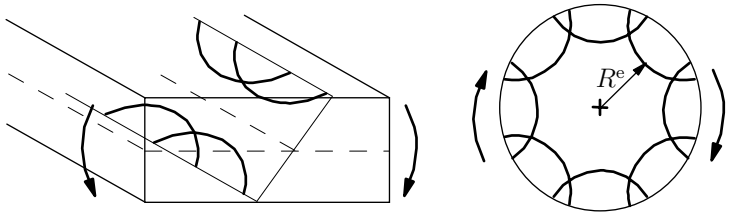

Figure 1: Curved dislocations penetrating into a bent strip (left) and a twisted wire (right) from the free surfaces. R^{e} is the boundary of the elastic core.

cylindrical coordinates r, θ, z. A twist per unit length, $\varkappa$, is applied, resulting in the material shear strain $\gamma \equiv \gamma_{\theta z} = r\varkappa$. Additive decomposition of the material shear in an elastic and a plastic part, and application of Hooke's law yield the shear stress

$$\tau \equiv \tau_{\theta z} = \mu(r\varkappa - \gamma^{\mathrm{p}})\,, \tag{1}$$

where μ is shear modulus. The plastic shear γ^{p} is assumed to be produced by continuously distributed dislocations that nucleate at the free surface of the wire and glide in the shearing planes towards the center, Fig. 1. The dislocation interactions are considered only indirectly, via the yield stress that is introduced below. Supposing three coplanar slip systems, we assume for simplicity that everywhere along the cylinder, there is a Burgers vector in the tangential direction and with magnitude b available, so that the deformation is homogeneous along the concentric circles in the section. Thus, the problems becomes one-dimensional, the independent variable being the radius r. The geometric quantities used in the model are introduced in Fig. 2.

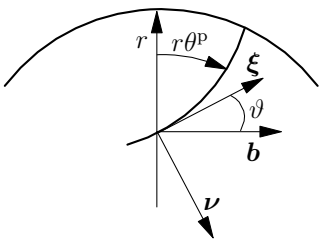

Figure 2: A curved dislocation near the surface of the wire. The indicated quantities are: Burgers vector $\boldsymbol{b}$, dislocation displacement in the slip direction $r\theta^{\mathrm{p}}$, local dislocation orientation ϑ, unit tangent $\boldsymbol{\xi} = (\xi_r, \xi_\theta) = (\sin\vartheta, \cos\vartheta)$ and unit normal $\boldsymbol{\nu} = (\nu_r, \nu_\theta) = (-\cos\vartheta, \sin\vartheta)$ to the dislocation.

In a quasistatic approximation, the self-force of the curved dislocations is in equilibrium with the Peach-Koehler force,

$$(\tau - \hat{\tau})b + T\kappa = 0\,. \tag{2}$$

Here $\hat{\tau} \approx \alpha\mu b\sqrt{\bar{\varrho}}$ is the yield stress, $T \approx \mu b^2$ is the line tension, $\kappa = -\operatorname{div}\boldsymbol{\nu} = (1/r)(d(r\nu_r)/dr)$ is the dislocation curvature. Using the substitution $\cos\vartheta(r) = y(r)$, we get $\kappa = y/r + y'$. Twice the number of dislocations per unit length of the section's circumference has been denoted by $\bar{\varrho}$. Then, the Orowan relation yields the plastic shear as

$$\gamma^{\mathrm{p}} = b\bar{\varrho}r\theta^{\mathrm{p}}\,, \tag{3}$$

where $r\theta^{\mathrm{p}}$ is the dislocation displacement in the slip (i.e. tangential) direction, Fig. 2. Equations (1) to (3) yield an ordinary differential equation for $y(r)$,

$$y' = \frac{y}{r} + \bar{\varrho}r\theta^{\mathrm{p}} - \frac{r\varkappa}{b} + \alpha\sqrt{\bar{\varrho}}\,. \tag{4}$$

The geometrical relation $d(r\theta^{\mathrm{p}}(r))/dr = 1/\tan\vartheta$, cf. Fig. 2, yields a differential equation for $\theta^{\mathrm{p}}(r)$,

$$\theta^{\mathrm{p}\prime} = -\frac{\theta^{\mathrm{p}}}{r} + \frac{y}{r\sqrt{1-y^2}}\,. \tag{5}$$

Equations (4) and (5) must be complemented by boundary conditions. Due to the image forces, the dislocations are assumed to be perpendicular to the free surface,

$$y(R) = 0\,. \tag{6}$$

As distinct from the classical case, the boundary R^{e} between the elastic core and plastic mantle is not known a priori. It depends on how deep the curved dislocation half-loops penetrate, Fig. 1. The two halves of the half-loops penetrating from the surface are symmetric to each other. Moreover, $\gamma^{\mathrm{p}}(R^{\mathrm{e}}) = 0$. Thus we have

$$y(R^{\mathrm{e}}) = 1\,, \qquad \text{and} \qquad \theta^{\mathrm{p}}(R^{\mathrm{e}}) = 0\,, \tag{7}$$

cf. eqn. (3).

We have set up a system of two differential equations, eqns. (4) and (5), complemented by three boundary conditions, eqns. (6) and (7). The dislocation orientation $\vartheta(r)$ (represented by $y(r)$), the plastic slip $\gamma^{\mathrm{p}}(r)$ (represented by $\theta^{\mathrm{p}}(r)$), and the penetration depth expressed through R^{e} are the unknown quantities. The model reflects the size-dependent response of the thin wire known from the experiments [6].

Acknowledgements

This research has been supported by grants DFG We 2351/8-1 (RS) and GAČR 106/03/0826 and VZ J00021 (JK).

References

[1] R. Sedláček, J. Kratochvíl, and E. Werner. *Philos. Mag.* 83 (2003) 3735.
[2] R. Sedláček and S. Forest. *phys. stat. sol. (b)* 221 (2000) 583.
[3] R. Sedláček and E. Werner. *Phys. Rev. B* 69 (2004) 134114.
[4] R. Sedláček. *Mater. Sci. Eng. A*, submitted.
[5] R. Sedláček. In preparation.
[6] N. A. Fleck et al. *Acta Metall. Mater.* 42 (1994) 475.

Multiple slip in a statistical-mechanics based strain-gradient plasticity model

E. van der Giessen and S. Yefimov

Netherlands Institute for Metals Research/Department of Applied Physics, University of Groningen, Nyenborgh 4, 9747 AG Groningen, The Netherlands
E-mail: Giessen@phys.rug.nl

1 Introduction

While most strain-gradient plasticity theories are completely phenomenological, we have been concerned with an alternative approach: a recently proposed nonlocal crystal plasticity theory [1] that augments a standard crystal plasticity description with a statistical-mechanics description of the collective behavior of dislocations [2]. Initially, the theory was proposed in single slip [1]. In the present paper we discuss its extension to multiple slip.

2 Nonlocal Continuum Plasticity

To define a continuum dislocation dynamics in multiple slip, we apply the single slip dynamics [1] for each slip α system individually. Thus, each slip system is characterized by a dislocation density field ρ^α and a net-Burgers vector density k^α, which are governed by

$$\frac{\partial \rho^\alpha}{\partial t} + \frac{\partial}{\partial \boldsymbol{r}} \cdot (k^\alpha \boldsymbol{v}^\alpha) = f^\alpha; \quad \frac{\partial k^\alpha}{\partial t} + \frac{\partial}{\partial \boldsymbol{r}} \cdot (\rho^\alpha \boldsymbol{v}^\alpha) = 0\,. \tag{1}$$

Here, $\boldsymbol{v}^\alpha$ is the continuum dislocation glide velocity, defined as $\boldsymbol{v}^\alpha = B^{-1}\boldsymbol{b}^\alpha(\tau^\alpha - \tau^\alpha_{\rm tot})$, in terms of the resolved shear stress $\tau^\alpha = \boldsymbol{m}^\alpha \cdot \boldsymbol{\sigma} \cdot \boldsymbol{s}^\alpha$ and the total back stress $\tau^\alpha_{\rm tot}$ on the slip system α. The actual form of $\tau^\alpha_{\rm tot}$ will be discussed later. The function f^α in the right-hand side of (1)a governs the rate of production and annihilation of dislocations. The slip rate $\dot\gamma^\alpha$ is linked to the average continuum dislocation glide velocity $\boldsymbol{v}^\alpha$ according to $\dot\gamma^\alpha = \rho^\alpha \boldsymbol{b}^\alpha \cdot \boldsymbol{v}^\alpha$. These slip rates then contribute to the plastic part $\dot{\boldsymbol{\varepsilon}}^{\rm p}$ of the strain rate.

Awaiting a proper statistical treatment of two-dimensional dislocation dynamics in multiple slip, we adopt a purely phenomenological approach, where the total back stress $\tau^\alpha_{\rm tot}$ is defined as a superposition of the single slip measures of back stress of all available slip systems with orientation dependent weight factors. Thus, we define $\tau^\alpha_{\rm tot}$ as

$$\tau^\alpha_{\rm tot} = \sum_{\alpha=1}^{N} S^{\alpha\beta}\tau^\beta_{\rm s}; \quad \tau^\alpha_{\rm s} = \frac{\mu \boldsymbol{b}^\alpha}{2\pi(1-\nu)\rho^\alpha} \cdot D\frac{\partial k^\alpha}{\partial \boldsymbol{r}}\,, \tag{2}$$

with $\tau^\alpha_{\rm s}$ the back stress from the single slip approximation. Here, we study the following three forms of the projection matrix $S^{\alpha\beta}$:

version 1: $S^{\alpha\beta} = \boldsymbol{m}^\alpha \cdot (\boldsymbol{m}^\beta \otimes \boldsymbol{s}^\beta) \cdot \boldsymbol{s}^\alpha = (\boldsymbol{m}^\alpha \cdot \boldsymbol{m}^\beta)(\boldsymbol{s}^\alpha \cdot \boldsymbol{s}^\beta)$

version 2: $S^{\alpha\beta} = \boldsymbol{m}^\alpha \cdot (\boldsymbol{s}^\beta \otimes \boldsymbol{m}^\beta + \boldsymbol{m}^\beta \otimes \boldsymbol{s}^\beta) \cdot \boldsymbol{s}^\alpha$

version 3: $S^{\alpha\beta} = \boldsymbol{s}^\alpha \cdot \boldsymbol{s}^\beta$

The second of these is the symmetrized version of the first, and the third is similar to that used by Gurtin [4].

3 Sensitivity of nonlocal interaction laws for constrained simple shear

The three interaction laws proposed above are benchmarked by considering the simple shearing of a crystalline strip constrained between two rigid and impenetrable walls, as illustrated in Figure 1a. In case of a classical local plasticity theory, the solution to this sim-

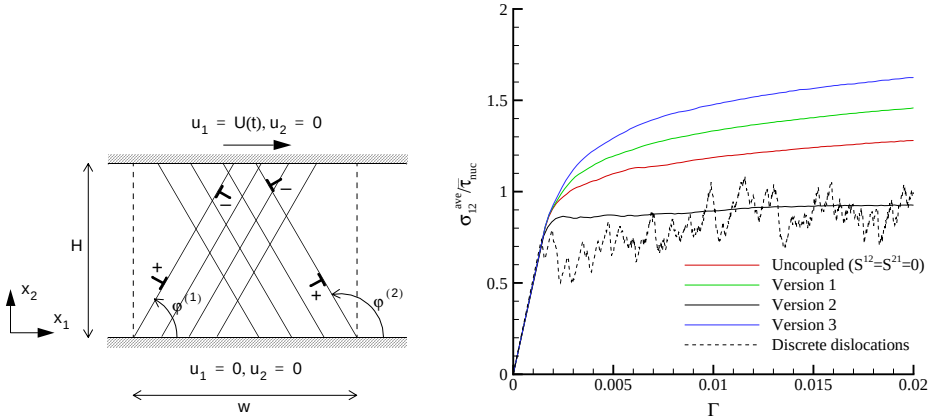

Figure 1: (a) Simple shear of a crystal with two slip systems between two impenetrable walls. (b) Average shear stress σ_{12}^{ave} versus applied shear strain Γ response for different slip systems interaction laws. Discrete dislocation results [5] shown for comparison. $H = 1\mu$m.

ple shearing boundary value problem for a homogeneous material and for uniform initial conditions is such that the only nonvanishing strain component, ε_{12}, is spatially uniform.

This changes drastically however in discrete dislocation (DD) when it is assumed that the dislocations cannot penetrate the top and bottom boundaries, i.e. $\boldsymbol{v}^{(\alpha)} \cdot \boldsymbol{n} = 0$, where $\boldsymbol{n}$ is the unit normal to the top and bottom surfaces. In the analysis no dislocations are present initially and obstacles are not taken into account. The parameters for drag, nucleation and annihilation are taken to be the same for the DD simulations and for the present continuum theory. The values of the remaining material constants in the continuum theory are the same as those fitted by Yefimov *et al.* [1] to DD simulations of two-dimensional composite material in single slip. Figure 1b shows that the best match with DD is achieved by applying the interaction rule denoted as 'version 2'.

4 Bending of a single crystal

The second benchmark problem is bending of a single crystal in double slip Traction-free boundary conditions are imposed along the top and bottom sides of the strip and slip by the motion of edge dislocations on two slip systems occurs inside the highlighted area of the strip.

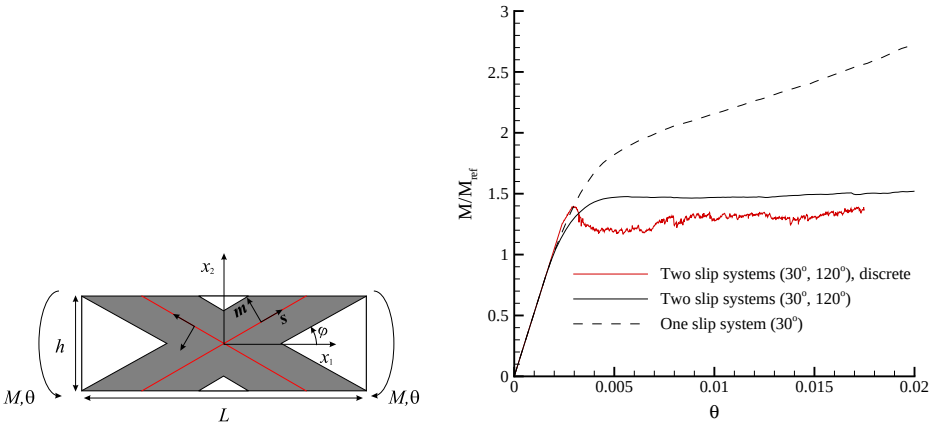

Figure 2: (a) Plastic bending of a two-dimensional strip with two symmetric slip systems. (b) Comparison of bending response for a crystal with $(30°, 150°)$ according to nonlocal continuum and DD plasticity. $L = 12\mu$m and $h = 4\mu$m.

Using the same material parameters as in the previous problem, the bending moment response to the imposed rotation is shown in Fig. 2b. The prediction by the continuum model of the total dislocation density evolution is also in good agreement with the discrete dislocation simulations. Calculations with different specimen sizes (but the same shape) reveal that the theory is capable of predicting size effects, in bending as well as in the simple shearing problem.

5 Conclusion

The present study for multiple slip, together with the previous ones for single slip [1, 3], have shown that the proposed nonlocal continuum theory is able to handle various boundary value problems with different types of boundary conditions and to capture nonlocal effects. The length scale in this theory is not a constant, as in all phenomenological theories to date, but is controlled by the dislocation density which generally evolves with deformation.

References

[1] S. Yefimov, I. Groma, E. Van der Giessen, *J. Mech. Phys. Solids*, vol. 52, pp. 279–300, 2004.

[2] I. Groma, *Phys. Rev. B*, vol. 56, pp. 5807–5813, 1997.

[3] S. Yefimov, I. Groma, E. Van der Giessen, Bending of a single crystal: discrete dislocation and nonlocal crystal plasticity simulations, *Mod. Simul. Mat. Sci. Engrg.* (in print).

[4] M.E. Gurtin, *J. Mech. Phys. Solids*, vol. 50, pp. 5–32, 2002.

[5] J.Y. Shu, N.A. Fleck, E. Van der Giessen, A. Needleman, *J. Mech. Phys. Solids*, vol. 49, pp. 1361–1395, 2001.

Dislocation avalanches : role of temperature, grain size and strain hardening

Thiebaud Richeton, Jérôme Weiss and François Louchet

LGGE-CNRS, 54 rue Molière, BP 96, 38402 St Martin d'Hères Cedex, France
weiss@lgge.obs.ujf-grenoble.fr

ABSTRACT

The role of temperature, grain size and strain hardening on the scale free, critical dynamics observed during the collective motion of dislocations is analysed from acoustic emission measurements of dislocation avalanches in ice single- and poly-crystals. It is shown that an increase of temperature, though strongly increasing the mobility of individual dislocations, does not modify this critical dynamics that results from elastic long-ranged interactions. On the other hand, grain boundaries act as barriers to the dynamic propagation of avalanches, leading to a finite size effect on the distributions of avalanche sizes in polycrystals. Finally, the strain hardening observed in polycrystals reduces the relaxation time of the avalanches.

1. Introduction

It is now well established that the plastic deformation of crystalline materials with a dominant slip system and/or a high dislocation mobility may be characterized by a strong spatial heterogeneity of deformation and scale invariant dislocation patterning [1] as well as a strong intermittency of plastic flow [2]: plastic deformation occurs through transient and strongly localized episodes called dislocation avalanches [3]. Acoustic emission (AE) has been used for several years to explore this complexity of dislocation dynamics, as dislocation avalanches generate acoustic waves whose properties can be used to characterize the avalanche properties [4]. In former works, we performed experiments on single crystals of ice Ih, a HCP material with a high dislocation mobility and a strong plastic anisotropy leading to a dominant slip system, along the basal planes [5]. It was shown that the dynamics of an assembly of interacting dislocations self-organized into a scale-free pattern characterized by power law distributions of avalanche sizes (that is, of AE amplitudes A), $P(A) \sim A^{-\tau}$ [2], and a fractal spatial patterning of avalanche locations [3]. This argued for an out-of-equilibrium system close to criticality, therefore supposedly with a high degree of universality of the statistical behavior.

Here, we continue our exploration of dislocation avalanche phenomena in crystalline plasticity from acoustic emission by exploring the role of temperature, grain size, and strain hardening on these avalanches. All the experiments were performed on ice Ih considered here as a model material, either on single- and poly-crystals.

2. Role of temperature

To explore the role of temperature on the self-organization of collective dislocation dynamics, we performed uniaxial compression creep tests on ice single crystals at –3°C, -

10°C and –20°C. Once renormalized by the total number of avalanches, the three avalanche size distributions collapse perfectly, showing that the scale-free pattern is independent of the temperature (Fig. 1). Note that the applied shear stress resolved on the basal planes was different for these three tests, but former work demonstrated that avalanches size distributions are also independent of the driving force to dislocation motion. These results confirm that the scale free critical dynamics is independent of the individual behavior of the dislocations, instead results from the long-ranged elastic interactions between dislocations and exhibits a high degree of universality. Indeed, from –20°C to –3°C, the mobility of an individual basal dislocation increases by a factor of about 15 [6], without changing the critical dynamics of collective dislocation motion.

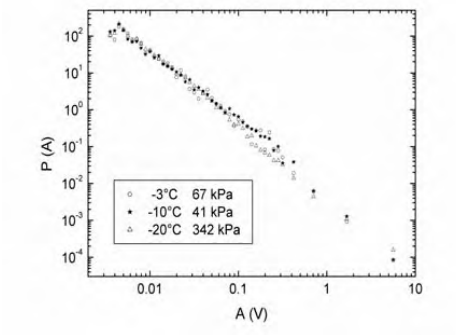

Fig. 1. AE amplitude (that is, avalanche size) distributions for three ice single crystals loaded under compression creep at different temperatures.

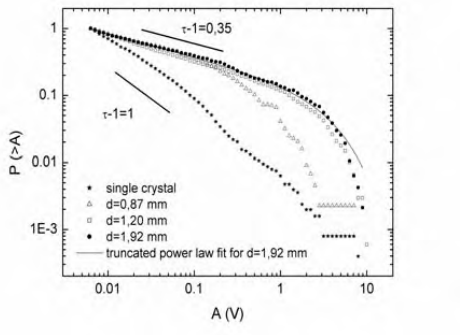

Fig. 2. Cumulative AE amplitude distributions for one single crystal and three polycrystals of ice loaded under compression creep at –10°C. The distributions for polycrystals show a lower power law exponent τ, as well as an exponential cut-off towards large A.

3. Role of grain size

Interactions between dislocations and grain boundaries (GB) are numerous and complex: GB can act as dislocation sources, whereas dislocations can pile up against GB. This suggests that GB could be strong barriers to the dynamic propagation of dislocation avalanches. This is confirmed by the AE data collected during compression creep tests on ice polycrystals with different grain sizes (Fig. 2). The avalanche size cumulative distributions for polycrystals show a finite size effect expressed by an exponential cut-off of the power laws, $P(>A) \sim A^{-\tau} \exp(-A/A_c)$, with the cut-off amplitude A_c which decreases with decreasing grain size. A_c scales as d^2, where d is the grain size. This indicates that dislocation avalanches cannot spread, in average, over more than the grain "area". An important consequence of this finite size effect is the possibility to homogenize the intermittency and heterogeneity of plastic deformation for scales significantly larger than the average grain size.

4. Role of strain hardening

Unlike ice single crystals, polycrystals exhibit significant strain hardening, with a significant contribution of kinematic hardening [5]. The level of hardening, which increases with decreasing grain size, does not seem to significantly modify the nature of the critical dynamics. However, it modifies the characteristics of the avalanches, particularly their relaxation. The larger the strain hardening, the shorter the avalanche durations. The larger durations are observed for a single crystal that did not hardened (Fig. 3). This can be interpreted as a role of the back stress resulting from strain hardening on the avalanches that damp more quickly. This is an illustration of the connection between the microscopic properties of plastic instabilities and the macroscopic response of the material.

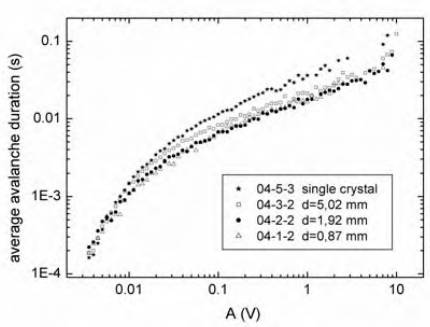

Fig. 3. Average avalanche duration vs AE amplitude for dislocation avalanches recorded during the compression creep at –10°C of one single-crystal and three poly-crystals of ice.

Acknowledgments

We would like to thank A. Manouvrier for technical assistance.

References

1. Zaiser, M. and A. Seeger, *Long-range internal stresses, dislocation patterning and work-hardening in crystal plasticity*, in *Dislocations in solids*, F.R.N. Nabarro and M.S. Duesbury, Editors. 2002, Elsevier.
2. Miguel, M.C., *et al.*, *Intermittent dislocation flow in viscoplastic deformation.* Nature, 2001. **410**: p. 667-671.
3. Weiss, J. and D. Marsan, *Three dimensional mapping of dislocation avalanches: clustering and space/time coupling.* Science, 2003. **299**(5603): p. 89-92.
4. Weiss, J. and J.R. Grasso, *Acoustic emission in single crystals of ice.* J. Phys. Chem., 1997. **101**: p. 6113-6117.
5. Duval, P., M.F. Ashby, and I. Andermann, *Rate-controlling Processes in the creep of polycrystalline ice.* J. Phys. Chem., 1983. **87**: p. 4066-4074.
6. Petrenko, V.F. and R.W. Whitworth, *Physics of ice*. 1999, Oxford: Oxford University Press.

Continuum Representation of Dislocation Dynamics

Michael Zaiser[1] , Anter El-Azab[2] and Istvan Groma[3]

[1]Centre for Materials Science and Engineering, The University of Edinburgh, King's Buildings, Sanderson Building, Edinburgh EH93JL, UK, m.zaiser@ed.ac.uk
[2]Department of Mechanical Engineering, Florida State University 2525 Pottsdamer Street, Room A229, Tallahasee, FL 32310, USA, anter@eng.fsu.edu
[3]Department of General Physics, Eotvos University Budapest, Pazmany P. setany 1/A, 1117 Budapest, Hungary, groma@metal.elte.hu

ABSTRACT

We discuss some of the key issues which must be resolved in order to arrive at viable continuum descriptions of dislocation dynamics in two and three dimensions. In particular, we address alternative formulations of dislocation kinetics including dislocation multiplication and reactions, averaging procedures, and the question how to describe dislocation interactions in a continuum framework.

1. Introduction

A main goal of crystal plasticity theory is the derivation of continuum constitutive relations from the underlying dynamics of systems of discrete dislocations. One approach is to perform the discrete-to-continuum transition on the dislocation dynamics level by considering the evolution of appropriately defined dislocation densities. While many phenomenological models of dislocation density evolution have been proposed over the years, the idea of obtaining density-based descriptions of dislocation systems from systematic statistical averaging is only recently being pursued. Here we present a brief review of current approaches and formulate some criteria which, in our view, a successful statistical model of dislocation dynamics should fulfill. For illustration of concepts, we will resort at some points to the simple special case of an effectively two-dimensional system of parallel straight dislocations [1,2]. This example is instructive both in showing what can be done by straightforward adaptation of methods from particle dynamics, and in illustrating how much more needs to be done before a true continuum representation of dislocation dynamics in three dimensions is achieved.

2. Dislocation Kinetics

A consistent continuum theory of dislocation dynamics must first of all correctly capture the dislocation kinetics. The motion of a dislocation line/segment under a given stress depends on the dislocation's slip system and line direction. Because of this simple fact, a

continuum theory of dislocation dynamics, and indeed of plastic flow, cannot directly be built upon the basis of the classical continuum theory of dislocations. (To demonstrate this it is sufficient to consider the simplest conceivable deformation state, namely a homogeneous shear flow mediated by the motion of dislocations on a single slip system. The dislocation density tensor $\boldsymbol{\alpha}$ is zero above the scale of the discrete dislocations, the dislocation fluxes are spatially constant, and hence the fundamental kinetic equation $\partial_t \boldsymbol{\alpha} + \nabla \times \mathbf{J} = 0$, where $\mathbf{J}$ is the dislocation flux tensor, is trivially fulfilled – irrespective of whether plastic flow occurs or not.) However, any continuum theory of dislocations should be able to recover the classical theory in order to correctly represent the relations between dislocation arrangement, plastic distortion, and internal stress fields.

In two dimensions the problem of correctly representing the kinetics can be solved straightforwardly by distinguishing dislocations into different 'species' (β,s) according to their sign s and slip system β [1,2]. Under a given local stress $\boldsymbol{\sigma}(\mathbf{r})$, each of these species moves in a different manner depending on the 'configurational coordinates' (β,s). In this case, the kinetics of the discrete dislocations is simply given by

$$\partial_t \mathbf{r}_i = \mathbf{v}(\beta_i, s_i, \boldsymbol{\sigma}(\mathbf{r}_i)) \quad . \tag{1}$$

By introducing discrete densities $\rho_{\mathrm{D}}(\beta,s,\mathbf{r})=\Sigma_j \delta_{\beta\beta[j]}\delta_{ss[j]}\delta(\mathbf{r}-\mathbf{r}_j)$ this set of kinetic equations can be formally cast into the shape of continuity equations for the 'species' (β,s):

$$\partial_t \rho_{\mathrm{D}}(\beta, s, \mathbf{r}) + \nabla[\rho_{\mathrm{D}}(\beta, s, \mathbf{r})\mathbf{v}(\beta, s, \boldsymbol{\sigma}(\mathbf{r})] = 0 \tag{2}$$

By appropriate averaging these may be transformed into true continuum equations (cf. below). Extending the approach to 3D dislocation systems is, however, not straightforward. Two complications arise: (i) The direction of motion of dislocation segments depends on the line direction, which is a continuous variable, (ii) since the kinetics must maintain connectivity of the dislocation lines, the motion of curved dislocations changes their length. Hence, even the kinetics of a discrete dislocation system is not easily cast into a mathematical formulation, although such a formulation is implicit in 3D discrete dislocation dynamics codes. Two distinct approaches have been proposed: (i) El-Azab proposed to distinguish dislocation segments by their line direction θ [3], which replaces the (discrete) sign s as a configurational coordinate. This approach 'attaches' the kinetic properties to the segment 'species' in a manner which is very similar to the procedure outlined above for the 2D case. The most straightforward way to account for changes in line length may be to further extend this approach by including the curvature κ as another configurational coordinate, though alternative formulations are possible [4]. A formal derivation of a 3D continuum equation for densities $\rho(\beta,\theta,\kappa,\mathbf{r})$ has recently been given by Hochrainer [5]. (ii) An alternative approach has been pursued by Sedlacek and co-workers [6]. They consider the line direction as a second field $\theta(\beta,\mathbf{r})$, which leads to a description of dislocation dynamics in terms of the evolution of coupled fields $\theta(\beta,\mathbf{r})$, and $\rho(\beta,\mathbf{r})$. As long as these are considered on the level of discrete dislocations, the description is equivalent to the approach of El-Azab et. al. However, a problem arise when it comes to averaging, which may lead to non-unique director fields.

3. Averaging and Dislocation-Dislocation Correlations

Many phenomena in dislocation systems including cell formation and size effects governed by boundary layers [1,2,6] occur on scales of a few dislocation spacings. Hence, averages should be envisaged as ensemble averages rather than spatial averages over volumes containing many dislocations. In discrete simulations, ensemble averages correspond to averages over many simulations with different, but statistically equivalent, initial conditions. Formally, the ensemble of these initial conditions can be characterized by initial density functions which then evolve under the ensemble-averaged kinetics. As an example, for the glide motion of dislocations on a single slip system with a velocity proportional to the local shear stress, the discrete dynamics can be written as

$$\partial_t \rho_{\mathrm{D}}(\mathbf{r},s) = Bbs\,\partial_x \left[\tau_{\mathrm{ext}} \rho_{\mathrm{D}}(\mathbf{r},s) + \rho_{\mathrm{D}}(\mathbf{r},s) \sum_{s'} s' \int \tau(\mathbf{r}-\mathbf{r}') \rho_{\mathrm{D}}(\mathbf{r}',s') \mathrm{d}^2 r' \right] \tag{3}$$

and averaging gives

$$\partial_t \rho(\mathbf{r},s) = Bbs \partial_x \left[\tau_{\mathrm{ext}} \rho(\mathbf{r},s) + \sum_{s'} s' \int \tau(\mathbf{r}-\mathbf{r}') \rho_{(2)}(\mathbf{r},s,\mathbf{r}',s') \mathrm{d}^2 r' \right] \tag{4}$$

where the $\rho_{(2)}(\mathbf{r},s,\mathbf{r}',s') = < \Sigma_{ij}\ \delta_{\mathrm{ss}[i]}\delta_{s's[j]}\delta(\mathbf{r}-\mathbf{r}_i)\delta(\mathbf{r}'-\mathbf{r}_j) >$ are pair-density functions which differ from products of densities by correlation functions, $\rho_{(2)}(\mathbf{r},s,\mathbf{r}',s') = \rho(\mathbf{r},s)\ \rho(\mathbf{r}',s')\ [1+d\ (\mathbf{r},s,\mathbf{r}',s')]$. These correlation functions are crucial for the dynamics, since they contain relevant information on short-range interactions which govern the flow stress [2] and are also indispensable for correctly representing the internal stress patterns and associated energetics. The approach may be generalized to 3D, where the rate of dislocation multiplication may expressed in terms of a correlation function between the density and curvature of segments of a given orientation [4].

References

[1] M. Zaiser, M. Carmen Miguel, I. Groma "Statistical dynamics of dislocation systems: the influence of dislocation dislocation correlations" *Phys Rev B* **64** (2001), 224102

[2] I. Groma, F. Csikor, M. Zaiser "Spatial Correlations and Higher-Order Gradient Terms in a Continuum Description of Dislocation Dynamics", Acta Mater. **51** (2003), 1271 – 1281.

[3] A. El Azab "Statistical mechanics treatment of the evolution of dislocation distributions in single crystals" *Phys Rev B* **61** (18) (2000), 11956-11966

[4] M. Zaiser, A. El-Azab, "Statistical Statistical Dislocation Dynamics – Multiplication and Long-Range Interactions", MRS Proceedings Vol. 779, 2004, W5.7 1-6.

[5] T. Hochrainer, "A Continuum Theory of Dislocation Motion", this volume.

[6] A. Sedlacek, J. Kratochvil, E. Werner "The importance of being curved: bowing dislocations in a continuum description" *Phil Mag*, 1, **83** (2003), 3735-3752

Symposium -3

Microstructure Effects on the Mechanics of Materials

The Effects of Grain Size on the Strengthening Behavior of Polycrystals: The Dislocation Density Tensor Approach

S.B. Biner[1] **and J.R. Morris**[2]

[1]Materials and Engineering Physics, Ames Laboratory (USDOE),
Iowa State University, Ames, IA 50011-3020, biner@ameslab.gov
[2]Metals and Ceramic Division, Oak Ridge National Laboratory,
Oak Ridge, TN 37831-6115, morrisj@ornl.gov

ABSTRACT

In this study, a dislocation pile-up model based on the dislocation density tensor approach was implemented in a 2D finite element code. The analyses were confined to a single slip system. The evolution of the flow stress from grain sizes ranging from 160 microns down to 75 nanometers under shear deformation was examined. The results were compared with those obtained from 2D discrete dislocation simulations in which the number of dislocations approached nearly 20 000. Both approaches gave almost identical stress-strain curves and dislocation densities for similar grain sizes. For the grain size ranges considered, an inverse relationship between the grain size and 0.2% offset flow stress in the form of Hall-Petch relationship $[d]^{-1/2}$ was observed. The evolution of flow stress follows a narrow band when expressed as a function of dislocation density, suggesting a scaling with the grain size as seen in our earlier studies.

1. Introduction

Hall [1] and Petch [2] first correlated yield strength with the inverse square root of grain size, in mild steel. Specifically, for yield or flow stress the relationship is observed to be

$$\sigma = M\ \tau = M\left(\tau_0 + Kd^{-1/2}\right) \qquad (1)$$

where M is the Taylor orientation factor, τ is the critical resolved shear stress, d is the mean grain size, and τ_0 and K are material parameters. There are a number of models that have been proposed to account for the grain size dependence implied in Eq. 1. We have studied the strengthening behavior described by Eq. 1 by taking into account the collective behavior of a large number of dislocations, on the order of 20 000, in a two dimensional setting in [3,4]. In these studies, not only the role of grain size, but also the roles of grain morphology, dislocation source density and simulation cell sizes were investigated. The results supported the evolution the flow strength with the grain sizes as described by Eq. 1 and also indicated the insensitivity of the solutions to dislocation source density and their locations. Moreover, we observed the scaling of the flow stress with the dislocation density normalized by the grain size

In this study, a dislocation pile-up model based on the dislocation density tensor approach was implemented in a 2D finite element code. This enabled us to study the evolution of

the strengthening behavior grain sizes ranging from 160 micron to 75 nanometers and up to 5% strains with extremely high computational efficiency.

1.1 The Numerical Approach. Here, we very briefly describe our numerical implementation; a more detailed description can be found in [5]. The non-zero components of the dislocation density tensor, resulting from the equilibrium density of dislocations in a pile-up as schematically shown in Fig. 1a, is given by [6]:

$$\alpha_{31}(x,y)=\frac{D_0 bx}{\left(a^2-x^2\right)^{1/2}}\delta(y)\left[H(x+a)-H(x-a)\right]$$
$$D_0=2\pi(1-\upsilon)\frac{\tau-\tau_0}{\mu b} \tag{2}$$

where $\delta(y)$ is the Dirac's delta function, $H(x)$ is the Heaviside step function, υ is the Possion's ratio, μ is the shear modulus and b is the magnitude of the burgers vector. τ is the resolved shear stress and τ_0 is the threshold stress for the nucleation of dislocations. The number of dislocation in the equilibrium is given by

$$N=\int_0^a \frac{D_0}{\left(a^2-x^2\right)^{1/2}}xdx \tag{3}$$

and the resulting eigenstrain is given by

$$\varepsilon^*_{12}=\int_{-a}^{a}\alpha_{31}dx \tag{4}$$

Once the eigenstrain is determined for given dislocation distribution, then the solution reduces to an internal stress problem in elasticity theory. We have solved this elasticity problem with the FEM shown in Fig. 1b. We have introduced a threshold shear stress τ_0=70MPa±0.2Std for dislocation nucleation to the slip planes shown in Fig. 1b which were initially dislocation free.

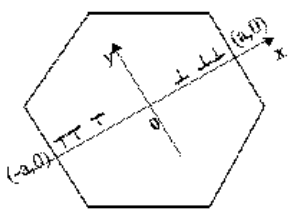

Fig. 1a

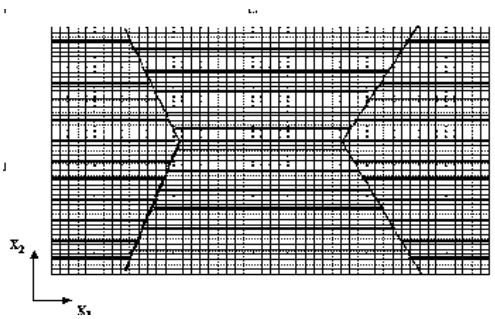

Fig. 1b

Fully periodic boundary conditions were maintained during the solution, and loading was achieved in pure shear loading mode with prescribed displacements to top edge and

resulting nominal stress values were calculated from the resulting reaction forces at the constrained bottom edge.

2. Results and Concluding Remarks

The resulting stress-strain curves for grain sizes ranging from 160 micron and to 75 nanometer is shown in Fig. 2. Due to computational efficiency, we are able to carry these simulations up to 5% strain level.

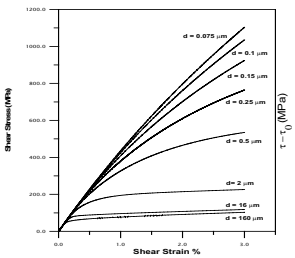

Fig. 2

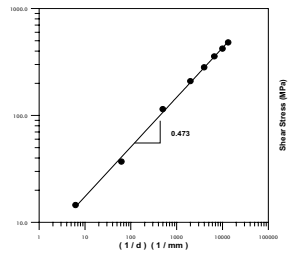

Fig. 3

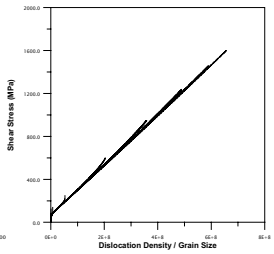

Fig. 4

The resulting correlation of the 0.2% offset flow stress with the grain size is given in Fig. 3. As can be seen, the resulting slope is 0.47 which is close agreement with Eq. 1. The evolution of the flow stress with the dislocation density normalized by the grain size is given in Fig. 4. As in our earlier studies [3,4], all the curves unify into a single curve. The correlation of the dislocation densities and stress-strain curves for similar grain sizes from those obtained from discrete dislocation dynamics are also very good and are given in [5].

Although this work is confined to a single slip system, the computational efficiency in comparison to 2D discrete dislocation dynamics is extremely high, and the extension of this solution procedure to multiple slip systems is currently under way.

3. References

1. E.O. Hall, Proc. Phys. Soc. B, 64, 747, 1951.
2. N.J. Petch, J. Iron Steel Inst. Lond. 174, 25, 1953.
3. S.B. Biner and J.R. Morris, Modell. Simul. Mater. Sci. Eng. 10, 617, 2002.
4. S.B. Biner and J.R. Morris, Philos. Mag. 83, 31, 2003.
5. S.B. Biner and J.R. Morris, (To be published).
6. T. Mura, Micromechanics of Solids, Martinuss Nijhoff Publishers, 1982.

4. Acknowledgement

This work was performed for the United States Department of Energy by Iowa State University under contract W-7405-Eng-82 and by Oak Ridge National Laboratory under contract DE-AC05-00OR-22725 with UT-Battelle, LLC. This research was supported by the Director of Energy Research, Office of Basic Sciences.

Connection of Hierarchical Multiscale Models in Simulating Phase Transformation of Ferroelectric Polymer

Shanfu Zheng[1], **Haibin Su**[2], **Alejandro Strachan**[3], **Alberto M. Cuitiño**[1] and **William A. Goddard, III**[2]

[1]**Mechanical and Aerospace Engineering, Rutgers University, cuitino@jove.rutgers.edu**
[2]**Materials and Process Simulation Center, Caltech**
[3]**Theoretical Division, Los Alamos National Laboratory**

ABSTRACT

We developed a physics-based, multi-scale model (from the nanoscale to the mesoscale and continuum) to simulate the phase transformations in the ferroelectric polymer poly(vinylidene-fluoride) (PVDF) and its copolytmers with trifluoroethylene. In the nanoscale, Molecular Dynamics (MD) simulations using *ab initio*-based Force Fields (FF) and first principles quantum mechanics (QM) calculations are to predict the fundamental properties that govern the electromechanical properties of these polymers, such as energetics and structure of various phases, elastic and dielectric constants, nucleation and propagation of a phase transition, and ferroelectric domain boundaries. These properties are relevant for materials design and serve as input into mesoscale and continuum models. Based on the properties, a tracking surface approach is used to follow the phase-transformation process from non-polar α-phase to the polar β-phase of crystallized polymer. This approach is rooted on the global minimization of Gibbs free energy that includes the mechanical and electrical contributions under combined electromechanical loads. The driving force for the interface evolution arises from the reduction of the free energy that is estimated by a homogenization technique, which is well developed in dealing with composite materials, based on the current stress state. The applications on two restricted polarization propagations of PVDF, one is along the molecular chain and the other is perpendicular to it, indicates the connected multiscale models are capable of predicting material properties from the fundamental structures.

1. Methodology

Poly(vinylidene fluoride) (PVDF) based co- and ter-polymers exhibit excellent electro-mechanical properties such as ferroelectricity, piezoelectricity, pyroelectricity, and nonlinear optical properties. Very recently, Zhang and collaborators[1] showed that it is possible to make use of electric field-induced phase transformations between polar and non-polar phases in nano-structured (via electron irradiation) P(VDF-TrFE) to obtain large electrostrictive strains (about 5%) at high frequencies (1000 KHz) and with good energy densities (comparable to the best piezoceramics). In order to best design the material, a physics-based, multi-scale model from *ab initio* QM calculations to meso-scale simulation is developed to predict the material properties.

The *ab initio* QM calculations in this paper were performed using the DFT pseudopotential code SeqQuest[11] which uses Gaussian basis sets. We used the Perdew, Burke, and Ernzerhof implementation of the Generalized Gradient Approximation (GGA)[12]. The SeqQuest code calculates atomic forces and the stress tensor, which were used to relax positions and cell parameters. In order to accelerate the computation, we use the First Principles based force field MSXX[4] with MD to study energetics, nucleation energies, interface mobility, and viscoelastic properties. The TrFE segments is described in the way that the fluorine atom in the CHF group as the F atoms in VDF (same atom type and charge), the corresponding carbon is treated as the CF_2 carbon in MSXX with its charge modified to maintain charge neutrality.

The meso-scale model is based on the principle that the phase transformation minimizes the Gibbs free energy of the system. If the material is assumed to be linear in the continuum scale, the Gibbs' free energy at a generic state under the electromechanical load ($\boldsymbol{\sigma}$, E) can be expressed as

$$\mathrm{G}(\sigma, E) = \frac{1}{2}\int_V \sigma_{ij}(\varepsilon_{ij} - \varepsilon_{ij}^s)dV - \int_S F_i u_i dS + \frac{1}{2}\int_V E_i(D_i - D_i^s)dV + \int_S \phi D_i n_i dS \qquad (1)$$

where $F_i = \sigma_{ij} n_j$ and ϕ are the mechanical traction and electrical potential applied on the boundary with unit outward normal n_i. The spontaneous strain ε_{ij}^s and the spontaneous polarization D_i^s are due to the phase transformation. To determine where the new phase transformation occurs needs to solve many times of a complex electromechanical boundary problem by assigning new phase at the untransformed region. The new phase transformation occurs at the point that will reduce the free energy at most. To do it numerically is very expensive. Here we employ a homogenization technique [2], which is well used in composite materials, to estimate the change of Gibbs' free energy when a new site of polarization occurs.

If a homogeneous reference phase (the stress and electric field are uniformly equal to the applied $\overline{\sigma}_{ij}$ and $\overline{E}_i$) is introduced, the change of the Gibbs energy is

$$\Delta \mathrm{G} = -\boldsymbol{G}_1 - \boldsymbol{G}_2 - \boldsymbol{G}_3, \qquad (2)$$

where

$$\begin{aligned}
\mathrm{G}_1 &= \frac{1}{2}\int_V \overline{\sigma}_{ij}(\varepsilon_{ij}^s + \varepsilon_{ij}^*)\boldsymbol{dV} + \frac{1}{2}\int_V \overline{\boldsymbol{E}}_i(\boldsymbol{D}_i^s + \boldsymbol{D}_i^*)\boldsymbol{dV}, \\
\mathrm{G}_2 &= \frac{1}{2}\int_V \sigma_{ij}\varepsilon_{ij}^s \boldsymbol{dV} + \frac{1}{2}\int_V \boldsymbol{E}_i \boldsymbol{D}_i^s \boldsymbol{dV}, \qquad (3) \\
\mathrm{G}_3 &= \frac{1}{2}\int_V \sigma_{ij}^{pt}\varepsilon_{ij}^s \boldsymbol{dV} + \frac{1}{2}\int_V \boldsymbol{E}_i^{pt} \boldsymbol{D}_i^s \boldsymbol{dV}.
\end{aligned}$$

and $\varepsilon_{ij}^*, D_i^*$ are the equivalent eigenstrain and eigenpolarization in the sense of Edhelby [3] but cast in the electromechanical context so that the transformed phase can be replaced by the reference phase. As an initial model we assume the phase transformation occurs only surround the already transformed phase, mobility of the interface, the G_3 doesn't change much for different locations of transformation. The term G_2 plays the criterion of determining where the new phase transformation happens.

2. Results and conclusions

Elastic and dielectric constants are critical material properties for meso- and macroscopic simulations. Using the MSXX force field we calculated the elastic constants for T- and T_3G_{au}- phases of P(VDF-TrFE) using analytical second derivatives, the results are shown in Table 1 and Table 2.

Table 1. Elastic constants of T phase (GPa)

23.77	5.73	4.19	0.00	0.00	2.94
5.73	18.85	4.86	0.00	0.00	-0.45
4.19	4.86	267.54	0.00	0.00	1.46
0.00	0.00	0.00	5.18	2.87	0.00
0.00	0.00	0.00	2.87	5.02	0.00
2.94	-0.45	1.46	0.00	0.00	5.62

Table 2. Elastic constants of T_3G_{au} phase (GPa)

15.63	6.62	0.39	0.00	-1.00	0.00
6.62	15.48	11.71	0.00	0.59	0.00
0.39	11.71	114.78	0.00	1.67	0.00
0.00	0.00	0.00	2.90	0.00	1.10
-1.00	0.59	1.67	0.00	1.73	0.00
0.00	0.00	0.00	1.10	0.00	5.26

A key issue to understand the electro-mechanical properties of these polymers is the relative energies and structural changes among the various phases and the origins of such differences. Our simulations explored two extreme cases of chain-chain separations: perfect crystals and isolated chains; our results are consistent with the observation in Zhang's experiments[1] and quantify the effect of inter-chain cohesive energy. In summary, we find that the lowest energy phase for PVDF is a non-polar crystal with a combination of trans (T) and gauche (G) bonds; in the case of the copolymer the role of the extra (bulkier) F atoms is to stabilize T bonds. This leads to the higher crystallinity and piezoelectricity observed experimentally. Using the material properties calculated from MD and Eqn (1) we also reach the same conclusions.

Using the methodology described in Sec 1, the propagation of the phase transformation is simulated both by MD and meso-scale model. Both of the simulations indicate the molecular chain is the major direction of the phase transformation.

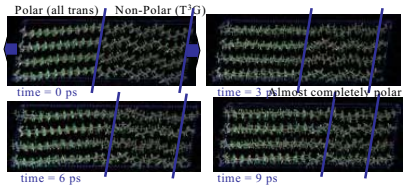

Fig. 1 Propagation of phase transformation in crystal PVDF substrate simulated by MD model

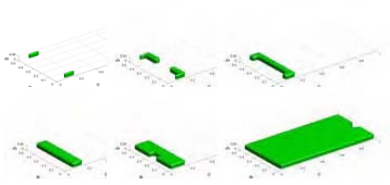

Fig. 2 Propagation of phase transformation in crystal PVDF substrate simulated by meso-scale model

3. Reference

[1] Q. M. Zhang, V. Bharti, and X. Zhao, Science **280**, 2101 (1998).
[2] J. Li and G. J. Weng, Proc. R. Soc., Lond. A, **455**, 3493 (1999).
[3] J. D. Eshelby, Proc. R. Soc., Lond. A, **241**, 376 (1957).

Mesoscale Simulation of Grain-Boundary Diffusion Creep*

R. Ding [a], D. Moldovan [b], V. Yamakov [c], D. Wolf [a] and S.R. Phillpot [d]

[a] Materials Science Division, Argonne National Laboratory, Argonne, IL 60439, e-mail: rong@anl.gov
[b] Department of Mechanical Engineering, Louisiana State University, Baton Rouge, LA 70803
[c] National Institute of Aerospace, Hampton, VA 23666
[d] Department of Materials Science and Engineering, University of Florida, Gainesville, FL 32611

ABSTRACT

The effects of microstructural inhomogeneity on grain-boundary diffusion creep with and without accommodation by grain-boundary migration are investigated using mesoscale simulations based on the variational principle of dissipated power. By selectively turning GB migration on and off, the grain growth in the inhomogeneous system is shown to result from two distinct processes. In addition to the growth due to the conventional mechanism of curvature-driven grain-boundary migration, even in the absence of grain-boundary migration the diffusion creep itself induces topological discontinuities resulting in grain growth. In combination, these two processes enable the deformation to proceed in a stable manner to rather large strains while preserving nearly equiaxed grain shapes. By contrast, if the accommodation of the deformation by grain-boundary migration is suppressed, microstructural and topological instabilities occur already for rather small strains.

1. Introduction

Grain boundary (GB) diffusion creep (Coble creep) is the dominant deformation mechanism in fine-grained polycrystalline materials under low stress and at elevated temperature [1]. Because of the complexity of Coble creep in topologically inhomogeneous polycrystalline materials, a systematic study of the intricate coupling between the kinetic and topological aspects of the deformation has yet to be carried out. In this paper we use mesoscale simulation to investigate the coupling between GB migration and GB diffusion creep in polycrystalline materials with inhomogeneous microstructure. The present mesoscale simulation method is based on the variational principle for dissipative systems and uses an implementation technique developed by Pan and Cocks [2,3] to solve the full GB field equations and determine the detailed stress and velocity fields for a wide range of grain geometries and microstructural inhomogeneities. The characteristics of the microstructural evolution, i.e., grain growth and grain

elongation, are investigated. The influence of both the geometrical and physical inhomogeneities on Coble creep is analyzed.

2. Simulation methodology

Our simulation model is based on the variational principle of dissipated power, and the detailed equations can be found in Refs. [2,3]. In the present simulation, two dissipative processes are considered: GB diffusion and GB migration. The microstructure is updated at each time step according to the velocity fields, including the velocities of the grain centers, the rates of grain rotation and the migration velocities of GB junctions. A two-dimensional general inhomogeneous polycrystalline microstructure containing 553 grains with discretized GBs is used in order to simulate the behavior of the curved GBs in the real situation.

3. Simulation results

Four snapshots capturing the microstructural evolution during Coble creep accommodated by GB migration are shown in Fig. 1. It can be seen that the grain shape remains almost equiaxed even at the strain of 1.0, compared with the elongated grain shape and unstable microstructure seen in our previous simulations of Coble creep without accommodation by GB migration [4]. Fig. 2(a) compares the variation of the grain aspect ratio during Coble creep with and without accommodation by GB migration. The grains become elongated and the grain aspect ratio reaches 1.5 at the strain of 0.8. By contrast, during Coble creep with accommodation by GB migration, the grain aspect ratio increases much less from 1.14 to 1.3 at the strain of 1.0. The comparison of the variation of the average grain size under the two different deformation conditions is shown in Fig. 2(b). It can be seen that the rate of the static grain growth (i.e., growth driven by GB migration) is much higher than the dynamic grain growth induced by GB diffusion only. The variation of the strain rate with strain at the normalized stresses $\overline{\sigma}$ ($\overline{\sigma} = \sigma d / \gamma_{GB}$, where σ the actual applied stress, d the mean grain size and γ_{GB} the GB energy. $\overline{\sigma}$ varies only with σ in the same microstructure) of 0.8 and 2.0 is shown in Figs. 3(a) and (b), respectively. The comparison reveals that the strain rate decreases at the low stress because of the larger static grain growth. By contrast, at the higher stress, the strain rates even increase because of the higher rate of grain switching and small-grain disappearance.

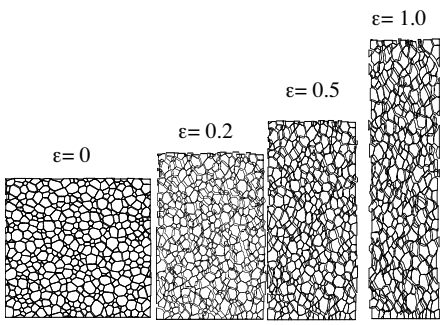

Fig. 1. Snapshots of the microstructure at different strains during Coble creep under GB diffusion accommodated by GB migration for the normalized stress $\overline{\sigma}$=1. The grains remain almost equiaxed even after 100% plastic strain and after the occurrence of grain growth.

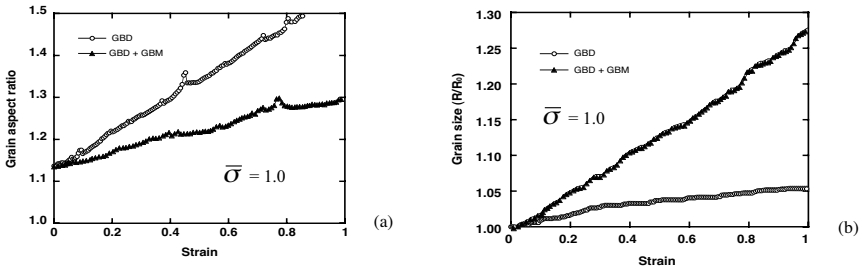

Fig. 2. Variation of (a) the grain aspect ratio and (b) the grain size during GB diffusion (GBD) creep with and without accommodation by GB migration (GBM). The role of the GBM is to produce a more equiaxed grain shape, and the rate of the static grain growth driven by the GBM is much higher than that of dynamic grain growth induced by the topological inhomogeneity in the polycrystalline microstructure.

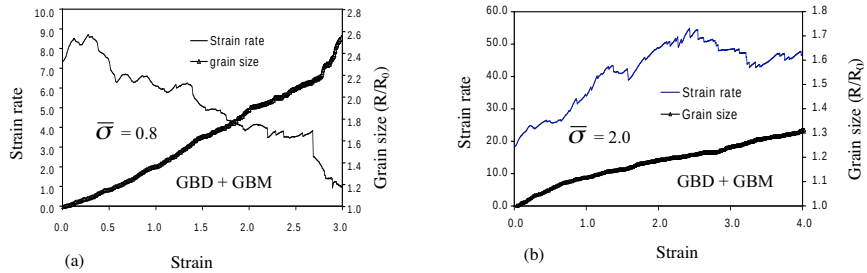

Fig. 3. Variation of the strain rate (left scale) and the grain size (right scale) with strain at the normalized stresses of (a) $\overline{\sigma}$=0.8 and (b) $\overline{\sigma}$=2.0.

4. Conclusions

The grain growth during Coble creep results from two distinct processes: the static grain growth driven by GB migration, and in a topologically inhomogeneous microstructure, the dynamic grain growth induced by the grain switching and small-grain disappearance. The strain rate *decreases* with strain at the lower stresses because of the larger static grain growth, but *increases* at higher stress because of the higher rate of stress-induced grain switching and small-grain disappearance. The grains remain almost equiaxed during Coble creep *with* accommodation by GB migration.

* This work was supported by the US Department of Energy, Basic Enery Sciences-Materials Sciences, under Contract W-31-109-Eng-38.

References

[1] R. L. Coble, J. Appl Phys. **34**, 1679 (1963).
[2] J. Pan and A.C.F. Cocks, Comp. Mater. Sci. **1**, 95 (1993).
[3] J. Pan, A.C.F. Cocks and S. Kucherenko, Proc. R. Soc. Lond. **A453**, 2161 (1997).
[4] R. Ding, D. Moldovan, V. Yamakov, D. Wolf and S.R. Phillpot, submitted to Acta Mater.

Intense Slip Band Formation and Crack Initiation in Fatigued 316L Explained by Discrete Dislocation Simulations

C.J. Déprés[1,2], C.F. Robertson[2], M. C. Fivel[1]

[1] GPM2, 101 rue de la Physique, 38402 Saint Martin d'Hères, France,
Marc.Fivel@inpg.fr
[2] CEA/Saclay, SRMA, bât. 455, 91191 Gif-sur-Yvette, France

ABSTRACT

In f.c.c. single crystals, fatigue is characterised by strain localization into persistent slip bands. Elimination of dislocations at the free surfaces of the sample creates steps that may remain and accumulate from one cycle to another resulting into localized extrusions and intrusions. Depending on the loading conditions; this irreversibility character of the behaviour finally creates microcracks leading to damage.

In this presentation the early stages of the formation of the dislocation microstructure in low strain fatigue are analysed using three dimensional discrete dislocation simulations. The simulation is adapted to the case of 316L stainless steel.

The code is validated by comparing both the dislocation microstructures and the associated mechanical behaviour with experiments performed in single slip and double slip loading conditions. A complete and detailed scheme for the microstructure formation is described from simulation snapshots. It appears that the cross-slip plays a crucial role: during the first cycles, cross-slip events spread the plasticity whereas after few cycles it localizes and lock the dislocation structure pinned in the bands. Finally, the relief of the free surface is computed and the evolution of the extrusion size versus the cycles is derived from the simulation so that fatigue life can be estimated.

1. Introduction

During the past few decades, the need to understand the physical causes for fatigue microstructures formation and crack initiation, associated with the tremendous increase of computer capabilities have stimulated the development of new multi-scale modelling tools. One promising method to help studying intra-granular plasticity is three dimensional Discrete Dislocation Dynamics (DDD)[1,2]. Using DDD, the description of the plastic deformation directly emerges from the collective effect of a large number of discrete dislocation entities whose constitutive rules for motion, annihilation, cross-slip are implemented explicitly. When applied to cyclic plasticity, this numerical model provides:

- direct observations of the dislocation structure into Persistent Slip Band,
- computation of the associated surface displacements.

The present DDD model is based on a simple edge-screw discretisation of the dislocation segments, in FCC crystals. The material parameters are those of a 316L stainless steel [3]. For all the simulations, a cylindrical simulation volume is considered. Dislocation can escape through the top surface (free surface). The other cylinder surfaces are strong obstacles to dislocation motion (grain boundary). Cyclic loading conditions are imposed in term of plastic strain amplitude: stress is applied in a quasi-static manner, and reversed when the maximal plastic strain is attained. More information on the characteristics of the simulations can be found in [3].

2. Self organization of the dislocation microstructure

A typical numerically generated dislocation microstructure obtained after 23 cycles is represented in Fig. 1a. Here the imposed plastic strain amplitude is 10^{-3}, in single slip conditions. The dislocation microstructure fills the whole grain, localized in a set of intense slip bands. Fig. 1b shows only dislocation segments within a 0.6 µm thick crystal slice containing a single PSB. A detailed analysis of the bands reveals that the presence of "channels" made of single row of prismatic loops, edge dipoles and multi-poles. The channels are always embedded in dislocation tangles of various shape and size. We also observe that small dislocation pile-ups are present in the slip plane separating the band from the matrix.

The interaction between the activated slip system (primary) and the associated cross-slip system is found to be crucial in the formation of the PSB microstructure. First, the cross-slip events spread the dislocation microstructure inside the grain. As the cycles proceed, the interaction between cross-slip dislocations and primary dislocations contribute to gradually form both the channel and the tangle structures.

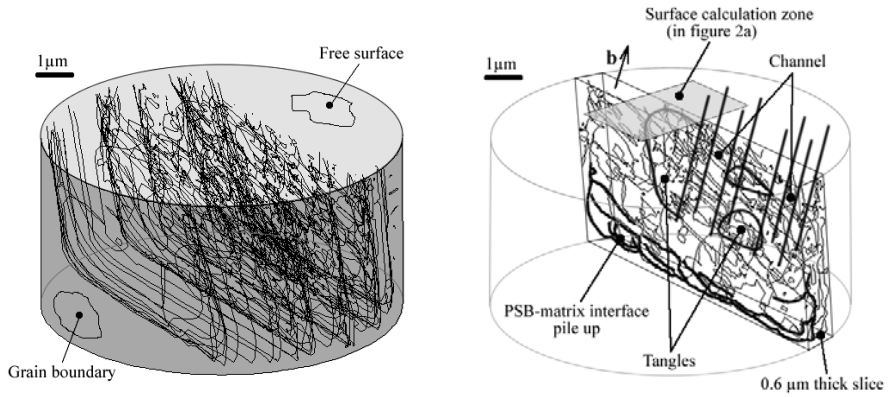

Fig. 1: (a) Typical dislocation microstructure obtained after 23 cycles ($\Delta\gamma_{pl}$=1.6 10^{-3}). (b) Details of a single PSB microstructure.

3. Surface damage accumulation

A typical surface relief resulting from the emergence of dislocations lines of a given intense slip band through the free surface is plotted in Fig. 2a. The calculation zone position is marked in Fig. 1b. The four represented snapshots are all taken at ε_p=0. During a short initial regime (first 3 cycles), most of the surface steps are reversible: steps formed during forward loading are erased when the load is reversed. These reversible steps are associated with the early formed pile-ups. After about five cycles, irreversible markings start forming in a few locations. Unlike the reversible slip markings, the irreversible surface markings are not erased upon load suppression or reversal. This process results in a gradual extrusion or intrusion growth.

As illustrated in Fig. 2b, the comparison between the surface profile computed at ε_p=0 (point1) and the same profile computed at $\varepsilon_p = \varepsilon_p^{max}$ (point2) shows that the plastic accommodation is localized at the PSB edges, which has been experimentally observed by [4]. Detailed analyses of successive snapshots from the DDD give insights on the dynamical surface relief behaviour. The dislocations inside the band, namely those making up the tangles and channels, slip on short distance during the cycles, hopping from one multi-pole trap to another. Therefore the inner dislocations have a small associated plastic strain. Conversely, the dislocations located at the band interface move over long distances during the cycles, forming highly polarized microstructures such as pile-ups. The latter accommodate the largest part of the imposed macroscopic strain (point 2, Fig. 2b). A quantitative prediction of the irreversible slip in the grain surface is computed as a function of the number N of cycles. It is found that the total slip evolution can be fitted by a $N^{1/2}$ law.

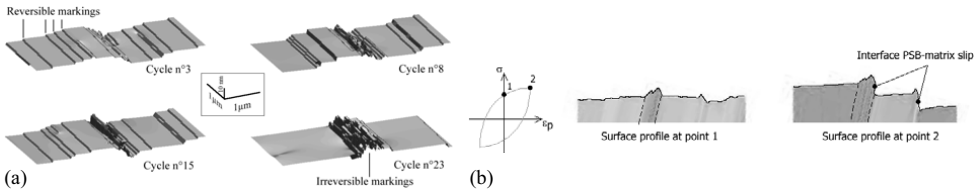

Fig. 2: (a) Computation of the surface slip during the cycling. (b) Surface profiles computed at zero strain (point1) and at maximum strain (point2).

References

[1] M. Verdier, M. Fivel, I. Groma, Mod. Sim. Mat. Sci. Eng., Vol. 6 (1998), p. 755.

[2] D. Weygand, L.H. Friedman,Van der Giessen, Mod. Sim. Mat. Sci. Eng., Vol. 10 (2003), p. 437.

[3] C. Déprés, M. Fivel, C. Robertson, Phil. Mag., Vol. 84, (2004),p. 2257.

[4] J.M. Finney, C. Laird, Phil. Mag., Vol. 31 (1975), p. 339.

Multiscale modeling of interfacial phenomena in particle-solidification front interactions

J.W. Garvin[1], Yi Yang[1], H.S. Udaykumar[1]

[1]Department of Mechanical Engineering
The University of Iowa, Iowa City, IA 52242
Email: jwgarvin@engineering.uiowa.edu

ABSTRACT

The interaction between a particle and a solidification front is important in many applications, ranging from metal-matrix composite manufacture to frost heaving in soils to cryopreservation. The particle-front interaction is a multiscale process as the dynamic interactions in the nano-scale gap between the particle and the front play an important role in the overall evolution of the system at the microscale. For two objects that are of order of microns in size or greater, the full solution of the Navier-Stokes equations in the nano-scale gap between their interacting surfaces is impossible due to the fine mesh requirement needed. An embedded multiscale model is therefore developed. The multiscale model assumes that the gap between the particle and the solidification front acts as a lubrication layer. Assuming a lubrication layer in the gap eliminates the need for a mesh in one direction. The solution to the lubrication model is coupled to the flow and temperature field outside the gap that is solved using the Navier-Stokes equations. The interfaces are tracked using a sharp-interface level-set method along the lines of that developed by Osher. Results are obtained for the interaction between a particle and an advancing solidification front.

2. Introduction

Depending on the thermosolutal conditions, the interaction of solidification fronts with embedded micron-sized particles can result in pushing or engulfment of the particles by the front [1]. Such interactions are important in several applications, including metal matrix composite manufacture, frost heaving, and cryobiology. For example, in the processing of metal-matrix composites, embedded particles are deliberately introduced in the melt so that they may serve as a reinforcement mechanism for the final solidified sample. The particles embedded in the melt need to be uniformly distributed in order to provide such reinforcing properties and to ensure continuity of the mechanical properties throughout the composite. The development of the solidified microstructure in such systems depends on complex interactions between non-planar solidification fronts and multiple particles. The particle-front interaction is a multiscale process as the dynamics at the micro- (i.e. particle) scale hinges on the interactions between the phase boundary and the particle which occurs across a nano-scale gap. This makes the study of such a

phenomenon quite challenging due to the bridging of vastly different length and time-scales.

In the sections that follow, a very brief description is given of a numerical method that can be used to capture the dynamics of interacting micro-sized interfaces. This method takes into account disjoining pressure and premelting effects due to intermolecular forces in between the gap of the surfaces. This method is then used to study particle-solidification front interactions.

2. Numerical Method

The general method used for the microscale calculations was developed in Marella *et al*. [2] for simulating three-dimensional incompressible flows and heat and mass transport around complex stationary or moving solid boundaries. In this method, the flow and temperature fields are solved using a second-order accurate Cartesian based finite-difference scheme to discretize the incompressible Navier-Stokes equations. The moving interfaces are represented and tracked using a sharp-interface, mesh-based level set method.

The problem with modeling the interaction between a particle and a solidification front is that the interfaces will not interact with each other until the gap between them is of order of nano-meters in size. Capturing the dynamics in such a thin gap would require too fine a mesh that the calculations would quickly become impossible. A model is therefore needed to capture the dynamics of the two interacting interfaces. A lubrication model in the gap between the particle and the solidification front is used to circumvent this problem. The model includes disjoining pressure effects due to the intermolecular forces that are important at the nano-meter length scale. The pressure in the gap, and hence the force acting on the particle, is calculated using the lubrication model. With this force, the particle velocity can be calculated in order to advect the particle accordingly. The solution of the lubrication model in the gap is then coupled to the solution of the flow field that is solved using the Navier-Stokes equations.

The details of the simulation setup for the solidification calculation are given in Garvin and Udaykumar [3].

3. Results

Figure 1 contains the tip velocity and particle velocity vs. time plot (on the left) and the *d* vs. time plot (on the right) for a system where the particle radius is 1 micron, the pull velocity is 500μ/s, and the Hamaker constant is -5.0×10^{-19} Joules. Figure 1 is qualitatively very similar to results obtained from previous simplified models [3]. A pressure contour plot and a velocity vector plot are given in Figure 2. Figure 2 gives very reasonable results for the outer flow field.

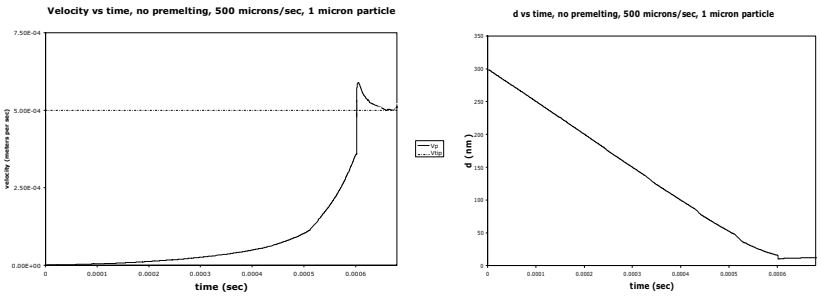

Figure 1: On the left, particle velocity (solid line) and tip velocity (dash-dot line) versus time. On the right, d versus time.

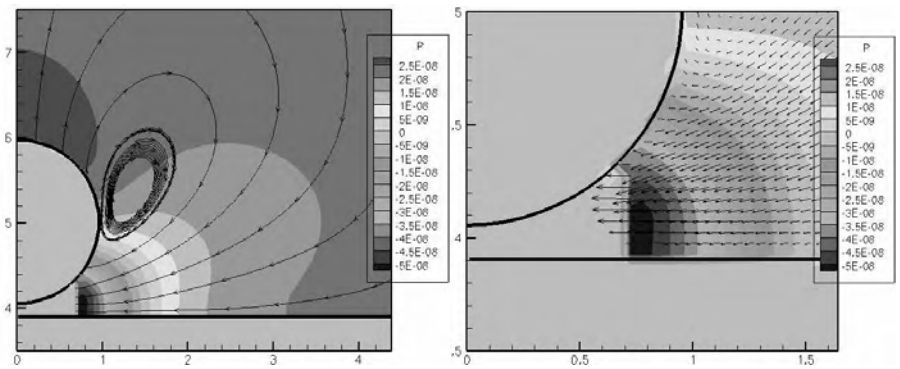

Figure 2: Pressure profiles and streamlines on the left. Zoomed-in view of the velocity vectors at the matching region on the right.

4. References

1. S.N. Omenyi and A.W. Neumann, "Thermodynamic aspects of particle engulfment by solidifying melts", *Journal of Applied Physics*, Vol. 47, No. 9, pp. 3956-3962(1976)

2. S. Marella, S. Krishnan, H. Liu, H.S. Udaykumar, "An easily implemented sharp interface Cartesian grid method for 3D moving boundary computations", *Journal of Computational Physics* (submitted).

3. J.W. Garvin, H.S. Udaykumar, "Particle-Solidification Front Dynamics Using a Fully Coupled Approach, Part I: Methodology", *Journal of Crystal Growth*, 252 (2003), 451-466.

Mechanical behaviour of high yttria content fully stabilized zirconia. An overview.

D. Gómez-García, A. Gallardo-López, A. Domínguez-Rodríguez and L. P. Kubin

Departamento de Física de la Materia Condensada-Universidad de Sevilla, Apartado 1065, 41080 Sevilla (SPAIN), dgomez@us.es

Laboratoire d'Etude des Microstructures (LEM-CNRS, ONERA), 22 avenue de la Division Leclerc, 92322 Châtillon Cedex (FRANCE) ladislas.kubin@onera.fr

ABSTRACT

A number of mechanisms can be found in the system ZrO_2 doped with high Y_2O_3 concentrations regarding its mechanical properties at intermediate and high temperatures. At temperatures between 1573 and 1673 ºC, a competition between pinning and unpinning dislocations by mobile point defects controls the plasticity. When the temperature increases until around 1773 K, the plasticity is controlled by dislocation dragging of point defects which have a velocity comparable with that of mobile dislocations. In this case, dislocations glide become difficult therefore, controlling plasticity. At higher temperatures point defects move so fast that dislocation climb controls now the plasticity. The nature of the point defects in this system and the mechanisms controlling plasticity in terms of dislocations and point defects interaction will be analysed in this overview.

1. Introduction.

Zirconia ceramics have been the objective of extensive research since the discovery of the martensitic transformation by Garvie et al [1]. This has been motivated by the promising applications linked to the design of toughened ceramic materials. A good proof of this extraordinary effort was put into evidence through a series of monographic meetings on the field.

Among the rich variety of zirconia ceramics, that of yttria-doped zirconia is likely to be the most attractive one, due to the capability of alloying in a wide range of yttria concentration forming a solid solution; as well as the diversity of different phases originated. In particular, when zirconia is alloyed with yttria at concentrations higher than 8 mol%, a cubic fluorite structure is found. This structure is commonly known as the fully-stabilised zirconia (YFSZ).

Regarding the mechanical properties, its interest is based upon two essential reasons: Firstly, YFSZ is a component of many composites ceramics used as hard materials or tailored systems for structural high temperature applications. Secondly, mechanical behaviour itself from a basic point of view, can give the source for some piece of information on essential properties, as defects diffusion, dislocation-defect interaction or dislocation dynamics, which is certainly relevant for a scientific improvement of the mechanical behaviour in YFSZ-based systems for high temperature applications.

This work is focused on the high temperature mechanical behaviour of YFSZ, with a particular emphasis on the analysis of the main experimental facts occurring at this range, all of them due to the peculiar dislocation dynamics taken place, and the way how they have been modelled.

2. Experimental procedure.

YFSZ single crystals with different amounts of yttria (from 9.4 mol% up to 32 mol%) have been prepared for uniaxial plastic deformation in creep at high temperatures (T≥1673 K) in a prototype testing machine. The minor details on the experimental set up are described elsewhere [2,3]. What is a major fact is the orientation for compression, chosen in such a way that only a primary slip system is activated: (001)[110]. The steady state creep regime is analysed according to the standard high temperature creep equation:

$$\dot{\varepsilon} = A\frac{\mu b}{kT}\left(\frac{\sigma}{\mu}\right)^{n} D_0 \exp\left(\frac{-Q}{kT}\right) \tag{1}$$

where $\dot{\varepsilon}$ is the steady state strain rate, A is dimensionless empirical constant, μ being the shear modulus, b the Burgers vectors, σ the applied stress, D_0 the preexponential factor of the diffusion coefficient of the deformation-controlling species, Q the corresponding activation energy, n the stress exponent, both of them accounting for the deformation controlling creep; and k and T has their usual meaning in statistical physics.

In addition to the creep tests, constant cross-head speed tests at different temperatures as well as microstructural characterization of both the as-received and deformed samples was carried out through transmission electron microscopy (TEM). The standard procedure for sample preparation for TEM observation is described also in [2,3].

3. Results.

Creep test results are illustrated in Fig. 1, in which the steady state strain rate versus the inverse of temperature is displayed. What is notorious in this plot is the significant change in the Arrhenius fit of the strain rate versus 1/T depending on the temperature range. In fact, two different fits must be done; one of them for data measured at temperatures higher than 1773 K and the other one for those achieved in creep tests at temperatures lower than 1773 K. This mathematical fact puts into evidence a different plastic behaviour, which is also confirmed by the different values of the stress exponents and the activation energies recorded at the two different temperature domains. Table 1 illustrates quantitatively the existence of two deformation regimes: creep parameters differ notably from each other. The existence of two different deformation mechanisms is also proved by TEM observations. According to these ones, dislocation dynamics is radically different at the different temperature ranges: Whereas dislocation recovery through climb turns to be very active at the very high temperature regime (T>1773 K), producing comparable dislocation densities in both the primary slip planes and the climb ones; this is no longer the case in the “low temperature” regime (T<1773 K). In this second case, dislocation density at the climb planes is negligible, most dislocations being concentrated in the primary slip plane.

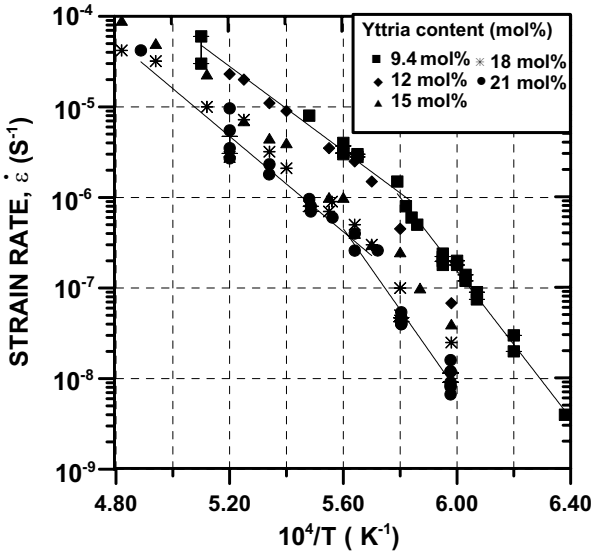

Figure 1: Strain rate versus the inverse of the temperature for a set of YFSZ samples with different yttria concentrations.

Table I: Stress exponent (n) and activation energy (Q) measured from creep test in YFSZ.

Creep parameters	T<1773 K	T>1773 K
n	5.0±0.5	3.0±0.5
Q (eV/atom)	7.5±0.7	5.3±0.7

Finally, constant cross-head speed tests at temperatures around 1673 K shows the existence of plastic instabilities in the stress-strain curves, displayed by means of serrations. This fact is only detected in a very narrow window of temperatures. Further experimental details on the matter are reported in [2].

4. Discussion.

The two deformation mechanisms at temperatures higher than 1673 K can be interpreted in the frame of a model due to Burton et al. [2]. According to this model, deformation mechanism change is induced by the activation of the dislocation glide mobility when temperature increases. Thence, dislocation mobility along the primary glide plane is relatively slow compared to that of climb in the low temperature regime, being dislocation glide kinetics the deformation-controlling process; while it

increases rapidly when temperature increases, in such a way that the picture inverses in the high temperature regime: dislocation glide mobility becomes much higher than that for climb, being dislocation climb kinetics the deformation-controlling process at these conditions. The model accounts quantitatively for the values of both activation energy and the stress exponent. These two mechanical parameters are a function of the ratio of dislocation glide-dislocation climb mobility.

Finally, the origin of the low dislocation glide mobility has been proposed to be related to the strong dislocation-point defect interaction due to the remarkable size effect induced by the yttrium atoms [3]. A strong support to this idea is given by the existence of plastic instabilities in the stress-strain curves in a small temperature interval well inside the low temperature regime. These serrations have been definitively proved to be compatible with a Portevin-Le Chatelier effect quite recently [4].

5. Acknowledgements.

The authors would like to acknowledge the financial support awarded by the Spanish "Ministerio de Educación y Ciencia" through the research projects MAT2000-0622 and MAT2003-04199-CO2-O2. The financial support of the "Acción Integrada Hispanofrancesa" HF2001-0125 is also acknowledged.

6. References.

1-R. C. Garvie, R. C. Hannick and R. T. Pascoe, "Ceramic steel?", Nature 258, 703-704, (1975).

2-D. Gómez-García, J. Martínez-Fernández, A. Domínguez-Rodríguez, P. Eveno and J. Castaing; "Deformation mechanisms for high temperature creep of high yttria content stabilised zirconia single crystals", Acta mater. 44, 991-999, (1996).

3- D. Gómez-García, J. Martínez-Fernández, A. Domínguez-Rodríguez and J. Castaing, "Mechanisms of High-Temperature Creep of Fully Stabilized Zirconia Single Crystals as a Function of the Yttria Content", J. Am. Ceram. Soc. 80 [7], 1668-72 (1997).

4- A. Gallardo-López, D. Gómez-García, A. Domínguez-Rodríguez and L. P. Kubin, "Portevin-Le Chatelier effect in Y_2O_3-ZrO_2 single crystals", Scripta mater. 51, 203-207 (2004).

Cluster Dynamics in Al(Zr,Sc) Alloys

L. Lae, P.Guyot

LTPCM, INPG, BP 75, 38402 Saint Martin d'Hères, France.
ludovic.lae@ltpcm.inpg.fr, pguyot@ltpcm.inpg.fr

ABSTRACT

Cluster dynamics (CD) is used to model at a mesoscopic scale the precipitation kinetics in a solid solution undergoing a first order ordering transformation when lowering the temperature. The chosen sytems are binary AlZr and AlSc and ternary Al(Zr,Sc) alloys. The clusters (precipitates) have the $L1_2$ structure with stochiometry $Al_3(Zr_xSc_{1-x})$. The time evolution of the sytem is controlled by solute monomer exchanges between adjacent (n-1), n, (n+1)-mer clusters. Emission (absorption) of monomers corresponds to the shrinkage (growth) of the clusters. The formation and time evolution of the cluster size distribution is calculated by numerical solution of a set of master differential equations. Any quantity of interest, mean cluster size, cluster volume fraction.., is deduced from this distribution. CD appears very efficient to describe the behaviour of the ternary alloy, enlighting some experimental results which will be discussed.

1. Introduction

Precipitation kinetics is usually modelled assuming that three successive stages can be distinguished and separately solved: initial nucleation step, growth and coarsening. This description has the advantage of simplicity and easy numerical handling. But all steps operate instead simultaneously and the previous approach can be misleading. The CD method, ([1]-[3]) solves this problem and gives at a mesoscopic scale a global description of the time evolution of the whole cluster/precipitate assembly which appears in supersaturated solid solutions. Initially developed for clustering (segregation) we adapted it to a first order phase transformation, the ordering of a Al(Zr,Sc) solid solution.

2. Cluster dynamics in a binary (AlZr or AlSc) alloys

In a binary alloy the isolated Zr(Sc) solute atoms (monomers) gather to form with Al clusters of chemical composition $Al_3Zr(Sc)$ with a $L1_2$ structure. These clusters react through the exchange of monomers Zr(Sc). Accordingly the clusters grow (shrink) by monomer absorption (emission). The time evolution of the cluster size distribution then follows a set of master differential equations:

$$\left(\partial C_n/\partial t\right)_{n\geq 2} = \alpha_{n+1}C_{n+1} + \beta_{n-1}C_{n-1} - \left(\beta_n + \alpha_n\right)C_n \qquad (1)$$

C_n is the concentration of the clusters of size n, the number of solute atoms within the cluster. β_n is the probability that a cluster of size n catches a monomer and transforms into a (n+1) cluster (absorption rate), α_n is its probability to emit a monomer to

transform into a (n-1) cluster (emission rate). Given α_n and β_n and initial t=0 conditions, the cluster size distribution $C_n(t)$ is obtained by numerical integration of Eqn. (1). From $C_n(t)$ one deduces any physical quantity of interest: the amount of solute within the clusters and in solid solution, the number density of clusters, the nucleation current, the cluster average size, etc.

β_n results from solute long range diffusion in the matrix, and possibly from its integration in the $L1_2$ structure once it impinges a cluster interface. Only long range diffusion is here considered. Then:

$$\beta_n = S_n D C_1 / R_n \Omega$$

D is the Zr(Sc) diffusion coefficient in Al, C_1 is the monomer concentration in the matrix; Ω is the Al atomic volume, S_n and R_n are the surface area and radius of a *n*-cluster. The emission rate α_n is evaluated, as for the classical nucleation theory, using the principle of detailed balance applied to a constrained equilibrium cluster distribution:

$$\alpha_{n+1} / \beta_n = \overline{C_n} / \overline{C_{n+1}}$$

The equilibrium concentration $\overline{C_n}$ is given, within a cluster gas description of the clustered solid solution, by:

$$\overline{C}_n = \exp\left(-\left(F_n - n(F_1 + kT \ln \overline{X}_1)\right)/kT\right)/\Omega$$

F_n is the free enthalpy of a *n*-cluster. It is evaluated in terms of first and second neighbours interactions and using the capillary approximation. The numerical solution of Eqn. (1) operates by an iterative procedure. The cluster size distribution is truncated at a maximum size of presently $n=3.10^6$.

3. Extension to ternary Al(Zr,Sc) alloys

The clusters have the stochiometry $Al_3Sc_xZr_{1-x}$, Sc and Zr are randomly distributed on their sublattice. A cluster class is now characterized by 2 integers i(j), number of Sc (Zr) atoms in the cluster, and its concentration $C_{i,j}(t)$. Eqn. (1) becomes:

$$\begin{aligned} \partial C_{i,j}/\partial t = {} & \beta_{i-1\to i,j} C_{i-1,j} - \alpha_{i\to i-1,j} C_{i,j} + \alpha_{i+1\to i,j} C_{i+1,j} - \beta_{i\to i+1,j} C_{i,j} + \beta_{i,j-1\to j} C_{i,j-1} \\ & - \alpha_{i,j\to j-1} C_{i,j} + \alpha_{i,j+1\to j} C_{i,j+1} - \beta_{i,j\to j+1} C_{i,j} \end{aligned} \qquad (2)$$

A (i, j) class has 4 kinetic coefficients:

$$\beta_{i,j\to j+1} = S_{i+j} D_{Zr} C_{Zr} / R_{i+j}\,\Omega = \beta^0_{i,j\to j+1} X_{Zr}$$

$$\alpha_{i,j+1\to j} = \beta_{i,j\to j+1}\, \overline{C}_{i,j} / \overline{C}_{i,j+1} = \beta^0_{i,j\to j+1} \exp\left(-\left(F_{i,j+1} - F_{i,j} - F_1^{Zr}\right)/k_B T\right)$$

and similar expressions for Sc. The free energy of a (i,j) cluster is, with the capillary approximation:

$$F_{i,j} \approx -kTLn\left((i+j)!/(i!\,j!)\right) + S_{i+j} < \gamma > +12\left(i\varpi_{1,Sc} + j\varpi_{1,Zr}\right)$$

$<\gamma>$ is the surface energy of the cluster, $\omega_{1,Zr(Sc)}$ is the first neighbours pair interaction.

4. Simulation results and discussion

The kinetics has first been solved for the binary alloys, varying the ageing temperature and the alloy composition. The kinetics is characteristic of a nucleation-growth process followed at late stage by LSW coarsening, and is predominantly controlled by the solute diffusion (which is for Sc 100 times faster than for Zr at 450°C). The precipitation path is obtained by numerical solving of Eqn. (2), written in an explicit

matrix form. It gives $C_{i,j}$ versus i,j and t, from which the cluster number density, their mean size, the partitioning of Zr and Sc in the clusters, are deduced. Results are given in Fig. 1 to 3 for Al-0.5at%Zr(Sc) and Al-0.5at%Zr-0.5at%Sc aged at 450°C. Fig.4 stands for various ternary alloys. The principal findings of the simulations are: i) the addition of Zr to AlSc alloy slows down the growth and coarsening. ii) in the same time nucleation is stimulated and the precipitate number density increases. iii) due to the different Sc and Zr diffusivities the chemical composition of the $L1_2$ phase varies continuously with time; Fig.3; at first Sc rich clusters get rounded by a rich Zr shell, Fig.4, which may explain the known LSW coarsening resistance of the ternary alloys.

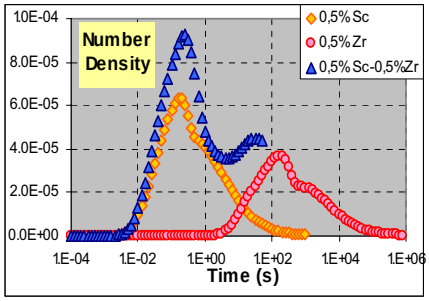

Figure 1: Number density vs time of clusters of size i,j or (i+j)>6

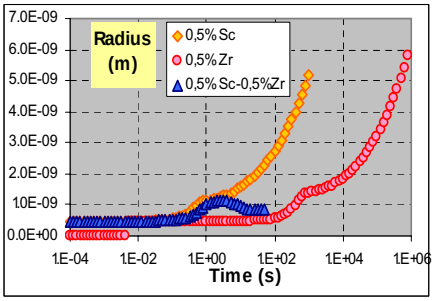

Figure 2: Mean radius vs. time

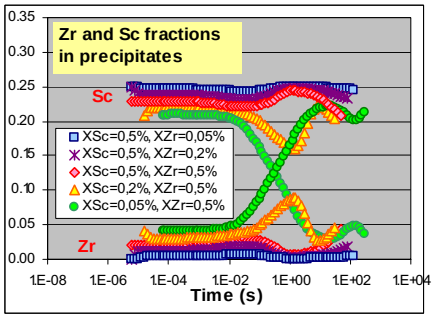

Figure 3: Zr and Sc concentrations in clusters

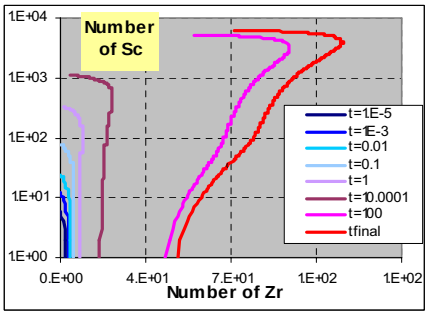

Figure 4: i vs j,t at $C_{i,j}=10^{-20}$. 0.1%Zr, 0.5%Sc

Acknowledgements:
This work was supported by CNRS and Pechiney-CRV, Alcan. They are greatly acknowledged as well as for the grant of L Lae.

References

[1] K. Binder and D. Stauffer*: Statistical theory of nucleation, condensation and coagulation*, Adv. in Phys., 25, 343 (1976)
[2] K.F. Kelton, A.L. Greer, C.V. Thompson: *Transient nucleation in condensed systems*, J. Chem. Phys., 79, 6261 (1983)
[3] P. Guyot, L.Lae, C. Sigli, *Cluster dynamics*, Thermodynamics, Microstructures and Plasticity, 107, Kluwer Acad. Publishers, (2003)

Direct Computation of the Hall-Petch Coefficient in FCC Metals from Dislocation-Grain Boundary Simulations

C. H. Henager, Jr., R. J. Kurtz

Materials Science Division
902 Battelle Blvd., MS: P8-15
PNNL, Richland, WA 99352
chuck.henager@pnl.gov

ABSTRACT

Atomistic modeling of dislocation–grain boundary (GB) interactions using 2D simulations of lattice dislocations impinging on symmetric and asymmetric Σ11 tilt GBs in Al, Cu, and Ni are presented to understand GB transmission, which can provide basic understanding of the Hall-Petch relation. A single partial dislocation is used in these simulations so that all pile-up and Escaig forces are zero and the critical resolved glide stress to transmit the partial dislocation is determined and used to calculate the Hall-Petch coefficients for these FCC metals. This research has implications with regard to the current debate of the role of partial dislocations in deformation of nanocrystalline metals.

1. Introduction

The Hall-Petch relation [1] relates yield stress to grain size as

$$\sigma_y = \sigma_0 + k_y d^{-n} \tag{1}$$

where σ_0 is a friction stress, k_y is the Hall-Petch coefficient, d is the grain size, and exponent n is usually about 0.5. The analysis based on dislocation pile-ups at GBs gives the Hall-Petch coefficient in terms of τ_c, a critical stress to initiate slip transmission across GBs as

$$k_y \cong \left(\frac{4\mu b \tau_c}{\pi(1-\nu)} \right) \tag{2}$$

where μ is the shear modulus, b is the Burgers vector magnitude, and ν is Poisson's ratio. The term τ_c represents an average of the critical stress required for grain boundary transmission for a single dislocation in a polycrystals. Atomistic models can provide an

estimate of τ_c for direct determination of the Hall-Petch coefficient. Plus, such models provide information that is not contained in the Hall-Petch relation, namely details of the transmission/nucleation events, which can guide understanding of the Hall-Petch relation. In particular, there is considerable interest in a regime of nanocrystalline grain sizes where the Hall-Petch relation no longer prevails. In nanocrystalline FCC metals this regime apparently coincides with MD simulations showing that deformation is mediated by partial dislocations, which suggests that there may be some connection between hall-Petch breakdown and partial dislocation mediated plastic flow.

2. Procedure

Rectangular models were constructed with either one of two boundaries, both belonging to the same Σ11 coincident site lattice. One of the GBs is a Σ11 <101> {131} symmetric tilt boundary and the other a Σ11 <101> {252}|{414} asymmetric tilt boundary. Dislocations were introduced into the models by applying the fully anisotropic displacement field for a dislocation on an interface between two elastically dissimilar materials. The dislocation lines were parallel to the tilt axis were placed on suitable (111)-planes in the upper grain adjacent to the boundary plane. Either the **βA** or the **CA** dislocation was inserted on the $(1\bar{1}\,\bar{1})$ plane (plane A in Fig. 1). Straining was accomplished by applying a strain gradient tensor to the upper and lower grain atoms calculated to apply a force that would move the upper grain dislocation toward the GB. A quasi-static straining method was used in which the models were strained in small increments and then relaxed, followed by repeated straining until an event was observed.

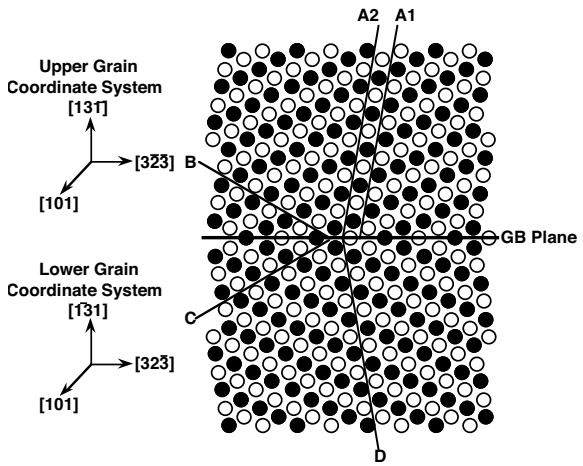

Figure 1. Orientation relationship for the Σ11 <101> {131} symmetric tilt GB.

3. Results

Grain boundaries are strong obstacles to dislocation motion, as is well known, and the simulations confirm that understanding, but also indicate that many other events occur prior to, during, and after GB transmission. Single partial dislocations are transmitted at critical resolved stresses of greater than 650 MPa in our simulations on symmetric Σ11 GBs, which corresponds to a significant glide barrier. The results for the symmetric Σ11 GB are tabulated in Table 1 for each FCC metal and are in reasonable agreement with published values for the Hall-Petch coefficient for each material. However, we also observe GB dislocation emission, GB migration, and cases where no transmission occurs. Transmission is more difficult for partial dislocations compared to dissociated perfect dislocations due to the absence of Escaig forces for the single partials. Qualitative observations suggest that this causes more GB migration compared to dissociated perfect dislocations as GB transmission proceeds, which suggests that nanocrystalline plasticity mediated by partial dislocations will exhibit enhanced GB migration and rotation compared to larger grain size materials [2-5].

Table 1. Calculated Hall-Petch coefficients for FCC metals

Metal	Critical Stress (MPa)	Calculated k_y (MPa$\sqrt{m}$)	Experimental k_y (MPa$\sqrt{m}$)
Al	650-700	0.08	0.06-0.17
Cu	1300	0.14	0.11-0.17
Ni	1800	0.21	0.13-0.22

4. References

[1] Friedman, L. H., Scripta Materialia, Towards a full analytic treatment of the Hall - Petch behavior in multilayers: putting the pieces together, **50**, 763 (2004).

[2] Van Swygenhoven, H., P. M. Derlet and A. Hasnaoui, NATO Science Series, II: Mathematics, Physics and Chemistry, Grain size effect of plasticity modelled by molecular dynamics, **108**, 253 (2003).

[3] Yamakov, V., D. Wolf, S. R. Phillpot, A. K. Mukherjee and H. Gleiter, Philosophical Magazine Letters, Deformation mechanism crossover and mechanical behaviour in nanocrystalline materials, **83**, 385 (2003).

[4] Schiotz, J., Scripta Materialia, Atomic-scale modeling of plastic deformation of nanocrystalline copper, **51**, 837 (2004).

[5] Shan, Z., E. A. Stach, J. M. K. Wiezorek, J. A. Knapp, D. M. Follstaedt and S. X. Mao, Science, Grain Boundary-Mediated Plasticity in Nanocrystalline Nickel, **305(5684)**, 654 (2004).

Interaction Between Grain and Specimen Size: Measurements of Strain and Orientation Gradients in Single Grains as a Function of the Applied Load

Mark Henning[*], Horst Vehoff[+]

Universität des Saarlandes, Werkstoffwissenschaften und Methodik (WWM), Geb. 43B, D-66123 Saarbrücken, Germany
Email: [*)] mh@homolog.de [+)] vehoff@matsci.uni-sb.de

ABSTRACT

In coarse grained tensile sheets grain orientation, deformation, slip band formation and orientation distribution within each grain were measured as a function of the applied load. From the results the shape change, rotation and hardening distribution of each grain were obtained. Additionally, FE-meshes were constructed for the direct use in FE-simulations.

1. Introduction

One of the tasks of modern micromechanics is the prediction of the local mechanical behaviour in polycrystalline crystals [1]. The micromechanical models not only need a global stress-strain curve for their verification, but also the local mechanical response of each grain. This means the nucleation and formation of slip bands and the local rotation of grains must be measured.

Therefore appropriate characterization methods were developed to obtain the necessary data, i.e. grain orientation and rotation, slip band distribution, grain deformation and local orientation gradients. The measurements were performed in-situ within a SEM as a function of the applied load.

2. Experimental methods

Coarse grained tensile sheets were produced by an appropriate heat treatment. The sheets, one mm in thickness, were incrementally loaded. After each loading step, the orientation of each grain, the slip band distribution and the grain shape was measured. In addition, the orientation distribution within a grain was measured and evaluated as a function of the load. From the mean orientation of each grain, the grain rotation was obtained, and from the orientation distribution within the grains, the orientation gradient $\max(\Delta_x,\Delta_y)$ was calculated, whereas Δ_x and Δ_y are the misorientation angles between neighbouring points in x- and y-direction, respectively.

3. Results

Fig. 1a-d show typical results for the slip band distribution, their prediction, the mean deformation and grain orientation. Fig. 2 shows an example of the orientation gradient for different strains. These data were gathered for different specimens, as well as the stress strain curves, shown in Fig. 3. Details are given in [2].

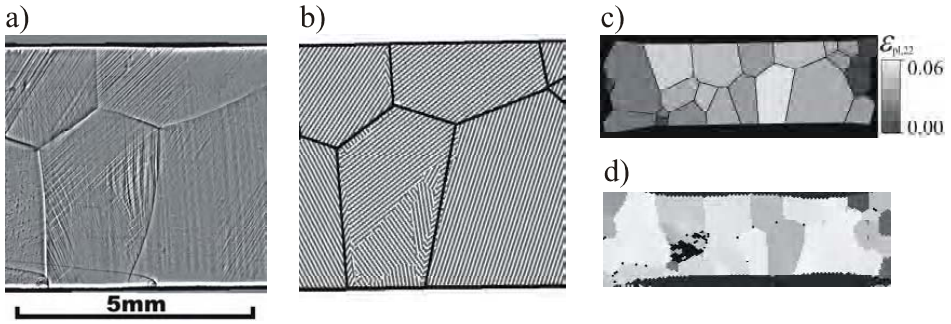

Fig. 1: a) Observed slip bands at ε_{pl}≈1.5%. b) Predicted slip bands. c) Measured average deformation of grains in tensile direction at ε_{pl}≈4%. d) Orientation measurement by means of EBSD at ε_{pl}≈4%

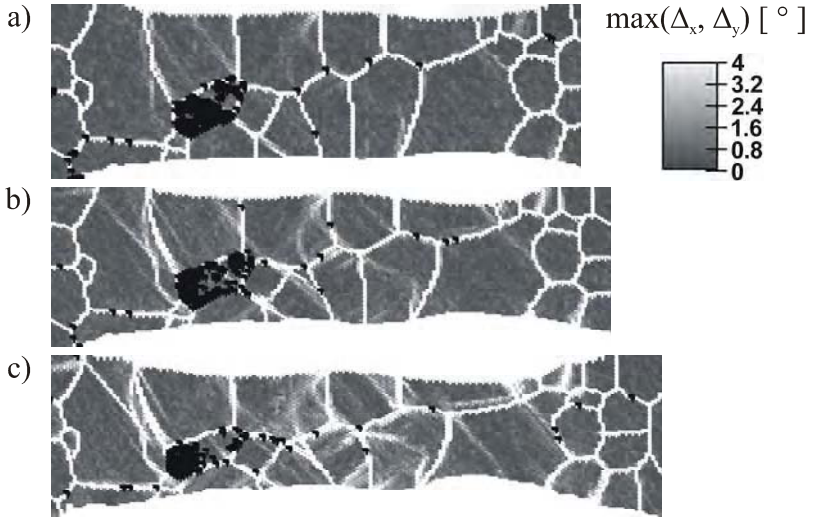

Fig. 2: Orientation gradient maps (OGM) for different strains. a-c) ε_{pl}≈{4%;10%;19.5%}

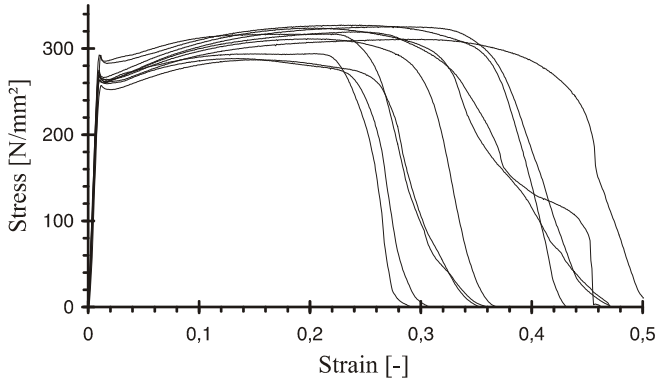

Fig. 3: Stress-strain curves of different specimens.

4. Discussion

FE meshes of the real 3-d grain structure of each specimen were constructed for the direct use in the commercial FE-software ABAQUS. The nucleation of slip bands and the initial slip band distribution could be predicted by a simple anisotropic-elastic calculation (Fig. 1a and b). The grain deformation and rotation results are currently used to compare the predictions of different elastic-plastic models locally [3, 4]. First results show that the necking location agrees with the experiment. However the stress-strain curves and deformation distribution were not correctly predicted. The local orientation gradients (Fig. 2) are connected with the hardening distribution. Therefore these results can be used to incorporate local hardening in the FE-model and to fit the necessary hardening law locally.

6. Acknowledgment

This work was supported by the German research foundation (DFG) under contract number Ve 132/21-1.

7. References

[1] S. R. Kalidindi, A. Bhattacharyya, R. D. Doherty, How do polycrystalline materials deform plastically?, Adv. Mater. 15 (16) (2003) 1345-1348.

[2] M. Henning, H. Vehoff, Local mechanical behavior and slip band formation of thin sheets with large grains, submitted to Acta Mat.

[3] S. Berveiller et al., to be published.

[4] B. Svendsen et al., to be published.

Modelling Low Temperature Brittle Fracture of Polycrystalline Zinc

G E Smith*, G M Hughes P E J Flewitt** and A G Crocker***

* Department of Physics, University of Surrey, Guildford, Surrey GU2 7XH, UK
** Interface Analysis Centre, University of Bristol, Bristol BS2 8BS, UK
Gillian.Smith @surrey.ac.uk; gareth.hughes@bristol.ac.uk;
peter.flewitt@magnox.co.uk; a.crocker@surrey.ac.uk

ABSTRACT

An integrated programme of research, involving modelling and experimental work on the brittle fracture of polycrystalline zinc is being carried out. The experimental results demonstrate that the fracture processes are more complex than anticipated and the models are being extended to take this into account. Some multiscale effects, arising from different grain sizes, have been noted.

1. Introduction

The present authors have been involved in modelling the fracture of polycrystalline materials and comparing the predictions with available experimental results for several years.[1,2] The principal aim has been to determine the proportions of different fracture modes, e.g. brittle and ductile, transgranular and intergranular, which occur in different materials under different conditions, and to predict the overall fracture behaviour of the materials from these results. Some of the research has been based on regular three-dimensional (3-d) models and has produced some striking results. For example, in low temperature brittle fracture, because cleavage planes in adjacent grains do not in general meet in a line in their common grain boundary, a substantial amount of grain boundary failure, or some other accommodation mechanism, must occur. However, models with regular geometry do not provide a satisfactory representation of the complex shapes of grains in real polycrystalline materials.

Much of the research has therefore been based on models in which the locations of the grains and their crystallographic orientations are allocated randomly. Using computer simulation a crack is then propagated across the model, the choice of fracture mode adopted at each stage being selected using energy-based criteria. Mainly we have used 2-d models, working towards 3-d representations.[3] These have been applied to the fracture of ferritic steels and have generated interesting predictions. For example, the models can be used to describe the role of impurity element segregation to grain boundaries or cavitation/decoherence on overall

fracture strength. However, making direct comparisons between 2-d predictions and 3-d experimental results, especially on steels in which fracture may be greatly influenced by alloying elements and substructure, such as martensite or bainite, is very difficult. Also, reliable key information, such as the energies of different fracture modes, is needed. It was therefore decided to carry out a series of fracture experiments on a material with a different structure to bcc α-iron and steel and to compare the experimental results with a new set of predictions. Polycrystalline hcp zinc, which is well known to cleave on the unique basal plane rather than on one or more of the three cube planes available in ferritic steels, was selected, in anticipation of large amounts of grain boundary brittle failure. The initial results have been far more dramatic than this and have demonstrated emphatically the need for realistic 3-d modelling.

2. Experimental results on the low temperature brittle fracture of zinc

Polycrystalline zinc specimens have been notch-fractured at 77K. The fracture surfaces were imaged using ion-induced secondary electrons using a focussed ion beam (FIB) workstation. Ion beam microscopy has several advantages over a conventional SEM for fractography, including an enhanced crystallographic contrast, resulting from ion channelling, and the ability to mill cross-sections to obtain sub-surface information at points of interest. Electron back-scattered diffraction is used to provide information on the orientation of cleavage facets and other features. As expected, cleavage occurs on basal (0001) planes but there is only a small amount of brittle failure on grain boundaries. However, a substantial amount of cleavage is observed on prismatic planes, encompassing variants of the {10-10} and {11-20} families. In addition, failure occurs on some of the six {10-12} twin boundaries. As a result of these additional variants, the brittle fracture modes are therefore complex. Some results have also been obtained on the effect of grain size on brittle fracture mechanisms.

3. Computational modelling of the low temperature brittle fracture of zinc

In tandem with the experiments, preliminary modelling work was carried out. For regular grains with a single cleavage plane, about 67% accommodating failure is required. Clearly this was not consistent with the experimental observations. The 2-d models were therefore adapted to include both basal and prismatic cleavage with different cleavage energies, incorporating a factor to allow for the different multiplicities. In addition, twin boundaries were introduced and these were given a third energy. Finally the grain boundaries were allocated a fourth energy. Different ratios have been used for these energies but as they are linked to 2-d features it is difficult to match them with 3-d experimental values on polycrystals.

A substantial amount of work has therefore been carried out developing appropriate 3-d models. Initially this has concentrated on generating random arrays of polyhedra. The aim is to obtain predictions using such models with a range of energy ratios for the different fracture mechanisms. Multiscale effects are being considered by monitoring the proximity of grain corners to cleavage and sub-boundary planes and therefore determining their influence. The results will be compared with the experimental observations and deductions made about the properties of the various planes and boundaries on which brittle fracture occurs.

4. Conclusions

Although 2-d models have provided some useful information on the fracture of polycrystalline materials, realistic 3-d models are needed to obtain predictions that can be matched to most experimental results.

Focussed iron beam (FIB) microscopy provides a very powerful tool for investigating fracture surfaces and, by milling cross-sections, the details of sub-surface features.

Close interactions between investigators developing and using models and those generating experimental results is essential if a better understanding of the mechanisms which control material properties is to be obtained.

Acknowledgements

Discussions with John Knott, Robert Moskovic and Valerie Randle are acknowledged. The work is supported by EPSRC. PEJF thanks BNFL British Nuclear Group for allocating time to work at Bristol University.

References

1. A G Crocker, P E J Flewitt and G E Smith, Computational Modelling of Fracture in Polycrystalline Materials, International Materials Reviews, in the press.

2. G E Smith, A G Crocker, R Moskovic and P E J Flewitt, Models to describe brittle and ductile fracture in ferritic steels, Philos. Mag. A, 2002, **82**, 3443-53.

3. G E Smith, A G Crocker, P E J Flewitt and R Moskovic, Brittle Fracture of Polycrystals: a New Pseudo Three-dimensional Model, in Fracture Mechanics Beyond 2000, Neimitz et al, eds, EMAS, 2002, **3**, 325-32.

On the Role of Grain Boundaries In Plastic Deformation of Metals

R. J Kurtz[1], C. H. Henager, Jr.[1], and R. G. Hoagland[2]

[1] Materials Science Division, Pacific Northwest National Laboratory
P.O. Box 999, Richland WA 99352 USA rj.kurtz@pnl.gov
[2]Los Alamos National Laboratory, P.O. Box 1663, Los Alamos, NM 87545

ABSTRACT

In this paper we describe results of atomic-scale simulations to explore the relationship between grain boundary (GB) structure and sliding resistance. Certain extrinsic GB defects have been found to dramatically lower the resistance to shear [1]. Introduction of substitutional solutes such as Mg in the vicinity of the GB are found to increase resistance to homogeneous shear and inhibit the motion of GB dislocations.

1. Introduction

Grain boundaries strongly influence the mechanical properties of metals. At low temperatures, they are barriers for the motion of lattice dislocations and give rise to the grain size dependence of the flow stress. During recrystallization, migrating GBs absorb lattice dislocations in highly strained material to reduce the stored energy of the system. Impingement and emission of lattice dislocations from GBs play significant roles in determining the sliding resistance of GBs and, therefore, are significant in various high temperature deformation phenomena such as creep and superplasticity. Atomistic simulations are useful for probing the fundamental mechanisms governing GB sliding in metals. Here we explore the effect of Mg on the sliding resistance of Al GBs.

2. Procedure

Briefly, the model [1,2] consists of a two part computational cell, rectangular in shape. One part, Region 1 contains movable atoms embedded in a semi-rigid part, Region 2. The GB approximately bisects the model as shown in Fig 1. Equilibrium, ~0 K, structures are obtained via relaxation using molecular dynamics with an energy quench. The two grains are free to move and undergo homogenous displacement in all three directions and this movement occurs during the relaxation via a viscous drag algorithm. Periodic border conditions were employed parallel to the z-direction, i.e. parallel to the

tilt axis. The embedded atom method potential derived by Ercolessi and Adams [3] for Al was used along with the Al-Mg potentials derived by Liu, et. al. [4]. The GB selected was a Σ11 <101> {131} symmetric tilt boundary in Al. We employed nudged elastic band methods to determine the shapes of energy paths connecting local minima on the gamma surface [6], the gradients of which are the maximum shear stresses to slide a GB.

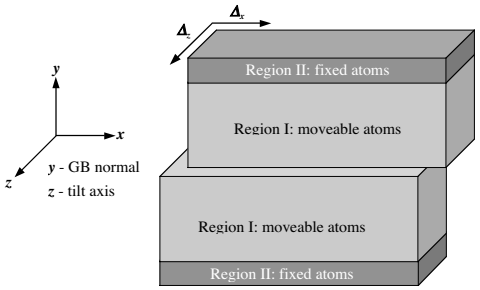

Figure 1. Model geometry used in GB simulations. Models are periodic in the z-direction. Δ_x and Δ_z are translation vectors parallel to the GB plane.

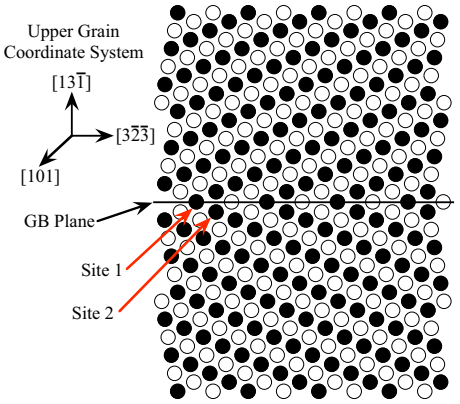

Figure 2. Relaxed structure of the Σ11 <101> {131} Al GB. Open and full symbols correspond to different {101} planes.

3. Results and Discussion

The lowest-energy configuration for the Σ11 <101> {131} GB is shown in Fig 2. The energy of this GB is 0.13 J/m^2. Homogeneous shear of this GB was studied by translating the upper grain relative to the lower grain along paths that left the configuration unchanged except for a shift of the GB plane by one atomic layer in the y-direction. The shear vectors that result in equivalent GB structures are depicted in Fig 3 on the cell of non-identical displacements, which is a two-dimensional periodic arrangement of atoms in the plane of the GB (x-z plane). The energetics of the system were explored as the upper grain was translated relative to the lower grain along each of these shear vectors. Nudged elastic band calculations were performed to map the variation of GB energy as a function of shear displacement separating minimum energy end state configurations. These calculations were carried out for pure Al GBs and for GBs containing Mg atoms in the GB plane (Site 1), and adjacent to the GB plane (Site 2), Fig 2. The results of these calculations are presented in Fig 4. The shear stress associated with the shortest shear vector is considerably smaller than the other three larger shear vectors in all cases. Shear in the direction of the tilt axis is easier than in the

x-direction. These maximum stresses are quite large and are equal to or greater than the theoretical strength for shear on the {111} planes. Molecular statics reveal that Mg atoms prefer to reside directly on the GB plane (Site 1) and there is a significant barrier to move Mg off of the GB (Site 2). When Mg atoms occupy Site 1, or Sites 1 and 2 the sliding stress increases except in the direction of the tilt axis. From previous work [2,5] it was observed that sliding stresses are substantially lowered by GB dislocations.

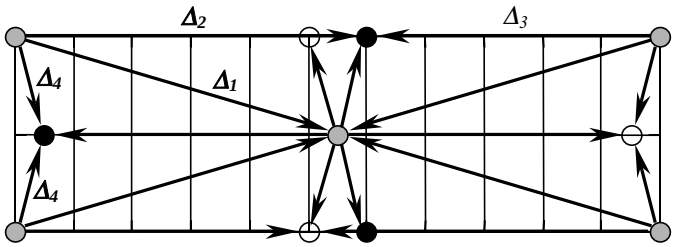

Figure 3. The cell of non-identical displacements for the Σ11 <101> {131} GB showing the low-energy configurations as gray circles. The black and white circles are equivalent low-energy configurations with the GB plane displaced up or down one layer. Allowable shear vectors translate from gray to gray, no GB migration, or from gray to black moving the GB up, or from gray to white moving the GB down.

Acknowledgements

This work was supported by the U.S. DOE, OBES under contract DE-AC06-76RLO 1830.

References

[1] R.J Kurtz, R.G. Hoagland, J.P. Hirth, Phil. Mag. A79 (1999) 683.
[2] R.J Kurtz, R.G. Hoagland, J.P. Hirth, Phil. Mag. A79 (1999) 665.
[3] F. Ercolessi and J. B. Adams, Europhys. Lett. 26 (1994) 583.
[4] X.Y. Liu, P.P. Ohotnicky, J.B. Adams, C.L. Rohrer, RW Hyland, Jr., Surf. Sci. 373 (1997) 357.
[5] R.G. Hoagland, R.J Kurtz, Phil. Mag. A82 (2002) 1073.
[6] G. Mills, H. Jonsson, G.K. Schenter Surf. Sci. 324 (1995) 305.

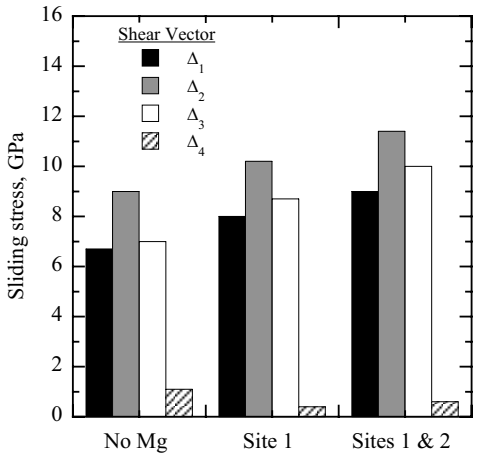

Figure 4. Sliding stress for homogeneous shear of a Σ11 <101> {131} GB in pure Al and with Mg atoms occupying Site 1, or Sites 1 and 2.

Diffuse Interface Model for the Interfacial Transfer Coefficient

G. Martin

CEA-Cabinet du Haut Commissaire, 33 rue de la Fédération, 75015 Paris Cedex 15, France

ABSTRACT

The transfer coefficients matrix, across a coherent interface, can be viewed as a correction to the Onsager matrix of mobility coefficients, when a diffuse interface model is replaced by an abrupt interface. We show that the matrix of transfer coefficients writes as : $\overline{\overline{K}}_{\alpha\beta} = \left[(N-1)\overline{\overline{\Lambda}}^{-1} - \left((N_\alpha - 1)\overline{\overline{L}}_\alpha^{-1} + (N_\beta - 1)\overline{\overline{L}}_\beta^{-1}\right)\right]^1$ where $\overline{\overline{K}}_{\alpha\beta}$ and $\overline{\overline{\Lambda}}, \overline{\overline{L}}_\alpha, \overline{\overline{L}}_\beta$ are respectively the matrixes of transfer coefficients across the α–β interface and the Onsager matrixes which describe diffusion, respectively along the inhomogeneous equilibrium concentration profile, in the α phase and in the β phase. N_α, N_β are the number of lattice planes respectively in the α and the β phases ($N = N_\alpha + N_\beta$). For a system with S components (including vacancies in the case of vacancy diffusion mechanism), the above (S-1)x(S-1) matrixes give the fluxes respectively as a function of the difference of chemical potentials (relative to one of the components, e.g. vacancies) across the α–β interface, and as a function of the gradient of the latter chemical potentials, in the system under considerations.

1. Introduction

Any heterogeneous reaction, such as precipitate growth, thickening of a reaction layers etc… implies two processes acting in series: diffusion to the interface and transfer across the interface. Diffusion fluxes and transfer fluxes are proportional respectively to the gradients of chemical potentials, and to the differences of chemical potentials across the interface. In a multi-component alloy, the atomic mobility and transfer coefficient are matrices, rather than scalars. While the atomistic theory of diffusion permits to express the mobilities as a function of the atomic jump frequencies, in dilute as well as concentrated alloys, no general link of the transfer coefficient to atomistic processes has yet been established to our knowledge. One reason for that is the complexity of real interfaces, at the atomic level. However, in view of the success of phase field models, which smoothen out the interface between two phases into a continuous transition region, it is of interest to propose a diffuse interface model of the transfer coefficient. Also, lattice models are widely used to describe the development of microstructures in the course of coherent phase separation [1]. We propose a general formalism to express the transfer coefficient across a planar coherent interface, as a function of

atomic jump frequencies, under stationary conditions; the expression is fully consistent with the expressions used for the diffusion coefficients in the bulk phases. The present paper generalizes a previous work [2].

2. Technique

Consider N parallel lattice planes (labeled p =1 to N), N_α of which (p=1 to N_α) are in the α phase and the remaining N_β (p = N_α+1 to N) are in the β phase. At equilibrium a smooth concentration profile extends from p=1 to N; the *diffusion potential* of any alloy constituent, along this profile, is uniform, i.e. independent of the lattice plane. The diffusion potential is the chemical potential of the species minus that of one of the constituents, taken as a reference (e.g. the vacancies for the vacancy diffusion mechanism). For a system with S constituents (labeled s=1 to S), we represent the diffusion potentials, at each plane p, by a column vector $\tilde{\mu}_p$ with S-1 components (μ_s-μ_S). *Close to equilibrium*, $\tilde{\mu}_p$ varies slowly with p, and a diffusion flux results: from plane p to p+1, $\tilde{J}_{p,p+1}$ is proportional to the difference in diffusion potentials between the two planes. This writes: $\tilde{J}_{p,p+1} = -\overline{\overline{L}}_{p,p+1}(\tilde{\mu}_{p+1} - \tilde{\mu}_p)$. From the second law of thermodynamics, the $\overline{\overline{L}}_{p,p+1}$'s are positive *definite* matrices. The $\overline{\overline{L}}$*'s* are defined *along the equilibrium concentration profile* and in general are function of the local concentration [3]. If we impose the flux to be uniform ($\tilde{J}_{p,p+1} = \tilde{j}$), diffusion will occur along a *stationary concentration profile* (no accumulation of any constituent at any plane). The latter profile is smooth, i.e. exhibits no discontinuity and is defined by: $\tilde{\mu}_{p+1} - \tilde{\mu}_p = -\overline{\overline{L}}^{-1}_{p,p+1}\,\tilde{j}$, where $\overline{\overline{L}}^{-1}_{p,p+1}$ is the inverse mobility matrix. Summing from p=1 to N-1, we get:

$$\tilde{\mu}_N - \tilde{\mu}_1 = -\sum_{p=1}^{N-1} \overline{\overline{L}}^{-1}_{p,p+1}\,\tilde{j} \quad ; \quad \tilde{j} = -\overline{\overline{\Lambda}}\,\frac{\tilde{\mu}_N - \tilde{\mu}_1}{N-1} \; with \quad \overline{\overline{\Lambda}}^{-1} = \sum_{p=1}^{N-1} \overline{\overline{L}}^{-1}_{p,p+1} \qquad (1)$$

At the macroscopic scale, the system is a two-phase one, with the α phase (N_α planes thick) in contact along the α–β interface with the β phase (N-N_α planes thick). Matter transport across the two-phase sample implies three processes in series: diffusion through the α phase, with, for $\overline{\overline{L}}_{p,p+1}$, the constant value in the α phase, far away from the interface ($\overline{\overline{L}}_\alpha = \overline{\overline{L}}_{p,p+1}$, p << N_α), transfer across the interface, located between the planes N_α and N_α+1, with an unknown transfer matrix $\overline{\overline{K}}_{\alpha\beta}$ and diffusion through the β phase, with $\overline{\overline{L}}_\beta = \overline{\overline{L}}_{p,p+1}$, in the β phase, far away from the interface, i.e. for p ≈ N_β. For the thicknesses of the phases to be stationary, the three fluxes must have identical values:

$$\tilde{j} = -\overline{\overline{L}}_\alpha \frac{\tilde{\mu}_{N_\alpha} - \tilde{\mu}_1}{N_\alpha - 1} = -\overline{\overline{K}}_{\alpha\beta}(\tilde{\mu}_{N_\alpha+1} - \tilde{\mu}_{N_\alpha}) = -\overline{\overline{L}}_\beta \frac{\tilde{\mu}_N - \tilde{\mu}_{N_\alpha+1}}{N_\beta - 1} \qquad (2)$$

3. Result and Discussion

Taking advantage of Eqn. (1) and (2), we find:

$$\overline{\overline{K}}_{\alpha\beta} = \left[(N-1)\overline{\overline{\Lambda}}^{-1} - \left((N_\alpha - 1)\overline{\overline{L}}_\alpha^{-1} + (N_\beta - 1)\overline{\overline{L}}_\beta^{-1}\right)\right]^1 \qquad (3)$$

Eqn. (3) generalizes the result of Ref. [2] to any number of constituents and any diffusion mechanism. It proves that the transfer coefficients across a coherent interface are defined by the value of the mobility matrices along the equilibrium composition profile (see Eqn, (1)). The transfer coefficient as defined in Eqn. (3) appears as a correcting term to be introduced in the mobility matrixes, when a sharp interface model is superimposed to a diffuse physical interface. As a consequence, there is no a priori reason why this correcting term should be positive. Indeed, in the special case studied in [2], K was found negative.

Atomistic expressions of the coefficients of the $\overline{\overline{L}}$ matrices for concentrated solid solutions are rare, but steady progresses are being made along this line [3].

In the particular case where the diffusivities are the same in both phases ($\overline{\overline{L}}_\alpha = \overline{\overline{L}}_\beta = \overline{\overline{L}}$), the value of the transfer coefficients does not depend on the (somewhat arbitrary) choice of the location of the interface (N_α): indeed, eqn. (3) reduces to $\overline{\overline{K}}_{\alpha\beta} = \left[(N-1)\overline{\overline{\Lambda}}^{-1} - (N-2)\overline{\overline{L}}^{-1}\right]^1$. This, however, is not the general case, since diffusivities are usually distinct in both phases. As discussed by Cahn [4], a surface quantity (such as $\overline{\overline{K}}_{\alpha\beta}$), the value of which depends on the choice for the location of the interface, may be of experimental interest, but has no theoretical use. Based on Cahn's work, we may define relative transfer coefficients, independent of the choice for the location of the interface; the meaning of these latter coefficients is however not clear for the time being. This point will be discussed elsewhere.

Acknowledgements: This work started during my Eshbach Scholar visit at the Department of Materials Science and Engineering of Northwestern University.

References

[1] e.g. V.G. Vaks, Kinetics of $L1_2$-Type Ordering in Alloys, *JETP Letters, Vol. 78, 2003, 168–178.*

[2] P. Maugis, G. Martin, Interface Transfer Coefficient. *Phys.Rev.* ***B49****, 1994, 11580-11587*

[3] e.g. M. Nastar, V.Yu Dobretsov, G. Martin, Selfconsistent Formulation of Configurational Kinetics Close to Equilibrium. *Phil. Mag.* ***A80****, 2000, 155-184.*

[4] J.W. Cahn, Thermodynamics of Solid and Fluid Surfaces, in *ASM Seminar on Interfacial Segregation, W.C. Johnson and J.M. Blakely eds., Metals Park, USA, 1977, 3-23.*

Evolution of dislocation link-length distributions during static annealing

Yi Tan, Marek A. Przystupa and Alan J. Ardell

**Department of Materials Science and Engineering,
University of California, Los Angeles; Los Angeles, CA 90095**

ABSTRACT

Using methodologies of the theory of particle coarsening it is possible to show that the evolution of the dislocation link lengths during the initial stages of static annealing should be similar to that of particle sizes during coarsening of precipitates. This also means that the link-length distributions should be time-invariant when scaled using an appropriate time-dependent measure of link lengths. In this study theoretical predictions have been compared with experimental data obtained by high temperature annealing of pure aluminum samples. The samples were pre-deformed in compression at 913 K and subsequently annealed for various times at the same temperature. The dislocation link-length distributions at all stages of annealing were determined using the etch-pit method.

1. Introduction

Recent studies of the coarsening of dislocation networks during Harper-Dorn (H-D) creep suggested that the evolution of the dislocation link-length distributions during both H-D creep and the initial stages of annealing should be similar and adequately described by the network coarsening theory [1]. This theory assumes that the relation describing link growth rate, $g(L,t)$, has the following form:

$$g(L,t) = \frac{dL}{dt} = \frac{k}{L^*(t)} \frac{u-1}{u^m} \tag{1}$$

where L is the link length, k and m are stress-independent material constants and $u = L/L^*(t)$ is a normalized link length. $L^*(t)$ is a characteristic length serving as a natural scaling factor; links larger than $L^*(t)$ grow while those smaller than $L^*(t)$ shrink. Eq. (1) embodies, among other things, the requirement of non-vanishing flux of links at both ends of the link-length distribution. From the coarsening theory it also follows that the average value of $\langle u \rangle = \langle L \rangle / L^*$ is a material constant [2] and that, after assuming that the average link length, $\langle L \rangle$, is related to dislocation density, ρ, through the relationship $\langle L \rangle = \beta \rho^{-1/2}$, the change of ρ with time is governed by the equation:

$$\frac{1}{\rho} - \frac{1}{\rho_o} = \left(\frac{\langle u \rangle}{\beta} \right)^2 \frac{2m^m}{(m+1)^{m+1}} k \cdot t = \kappa \cdot t \tag{2}$$

where ρ_o is an initial dislocation density. The theory also predicts that the standard link-length distribution function, $\phi(L)$, when plotted in normalized form as $\phi(L)\langle L \rangle / N$ vs.

$L/\langle L \rangle$ should be time invariant (N is the number of links per unit volume) [1]. The purpose of this work was to check these predictions.

2. Experimental Procedures

The pure aluminum polycrystalline samples used in this study were first chemically polished to remove possible surface damage and then soaked for 72 h at 913 K (0.98 T_{melt}). They were then compressed at 913 K under a stress of 0.08 MPa for 180 s and cooled under load to preserve the high temperature dislocation network structure. After loading, the samples were sliced into 6 mm thick disks which were subsequently annealed at 913 K for times ranging from 300 s to 2 h. The obtained dislocation network structures were then characterized using the etch pit procedure described in detail elsewhere [3].

3. Summary of Results

Two representative annealed dislocation etch pit structures are shown in Fig.1. There is a slight tendency to dislocation alignment during the initial stages of annealing, Fig. 1a, but eventually the distribution of dislocation etch pits becomes uniform, Fig. 1b. The variation of $1/\rho$ with annealing time, t, is shown in Fig 2a. According to Eq. (2) the dependence should be linear; despite the scatter of the data in Fig. 2a, a linear fit is reasonable. Fig. 2b shows comparison of the initial and annealed dislocation link-length distributions. The data from the five distributions collapse onto a single curve, supporting our theoretical expectation of scaling behavior.

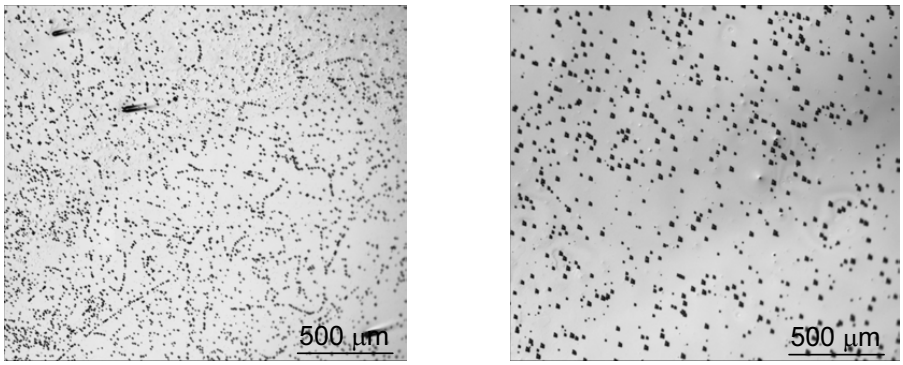

(a) (b)

Figure 1. Dislocations structures of pure aluminum samples loaded for 180 s at 913 K and then annealed for (a) 300 s and (b) 7200 s at the same temperature.

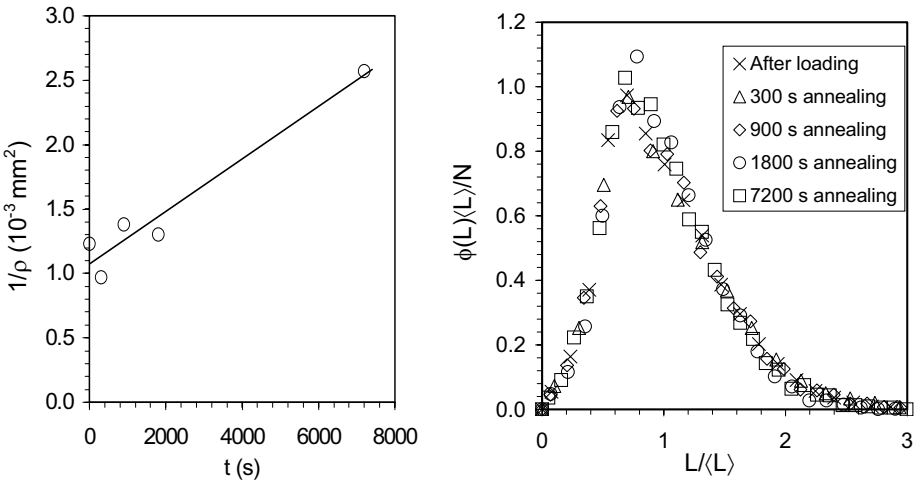

(a) (b)

Figure 2. Experimental results showing (a) change of the dislocation density with annealing time and (b) comparison of the normalized dislocation link-length distributions for various annealing times for pure aluminum annealed at 913 K (0.98 T_{melt}).

We conclude that our results convincingly show that the evolution of the dislocation network during static annealing can be indeed adequately described by the coarsening theory in conjunction with the proposed link growth law, Eq. (1). This means that (1) the kinetics of other processes involving growth of dislocation networks, such as creep, can be also described by the same relationships and that (2) for all those processes the scaled link-length distributions are time invariant.

4. Acknowledgements

The authors would like to thank the Department of Energy, Office of Basic Sciences, for supporting this research under Grant No. DE-FG02-03ER46077.

5. References

1. M. A. Przystupa and A. J. Ardell, ”Predictive Capabilities of the Dislocation-Network Theory of Harper-Dorn Creep”, Metall. and Mat. Trans. A, **33A**, 231 (2002).
2. I. M. Lifshitz and V.V. Slezov:”Kinetics of Diffusive Decomposition of Supersaturated Solid Solutions”, Soviet Physics JETP, **35**, 331 (1959).
3. P. Lin, M. A. Przystupa, and A. J. Ardell, “Dislocation Network Dynamics During Creep Deformation of Monocrystalline Sodium Chloride” in *Strength of Metals and Alloys*, ICSMA-7, edited by H. K. McQueen et al. (Pergamon Press, Oxford, 1985), p. 595.

Large Scale Simulations of Mesoscale Plasticity and Recrystallization of Aluminum Polycrystals

B. Radhakrishnan[1] and G.B. Sarma

[1]Computer Science and Mathematics Division
Oak Ridge National Laboratory
Oak Ridge, TN 37831-6008

ABSTRACT

The deformation of polycrystalline aluminum is simulated at the microstructural length scale using a crystal-plasticity based finite element technique. The deformation substructure is extracted from the finite element results, and the evolution of the deformation substructure during subsequent annealing is simulated using a Monte Carlo approach. Both the finite element and the Monte Carlo simulations are implemented for large, three-dimensional domains using the massively parallel computational capabilities at Oak Ridge National Laboratory. The simulations are able to capture for the first time, the formation of a strong Cube component following recrystallization from an initial grain structure containing a small volume fraction of Cube. The microstructural and kinetic aspects of cube texture evolution are discussed.

1. Introduction

The key to the successful production of aluminum sheet for high formability applications is the ability to control the crystallographic texture in the hot band. A strong Cube texture component following hot deformation and coiling is an essential requirement for many applications of aluminum sheet. It has been known for quite some time that the Cube texture component originates from Cube bands that survive the hot deformation process. Careful experiments using slip trace analysis [1] have shown that the stability of Cube during hot deformation is due to slip activity on the {110} <110> non-octahedral slip systems in addition to the usual {111} <110> octahedral slip systems. Recent experiments using aluminum bi-crystals [2] have shown that the stored energy inside the Cube grains is lower than in other deformation components such as S, Copper and Brass. The above experimental results have been captured adequately by recent microstructural deformation simulations based on crystal plasticity concepts [3]. The authors have developed an approach [3, 4] to extract a deformation substructure from the results of the deformation simulations by assuming that the deformation substructure exists in the form of a well-defined subgrain structure, where the local subgrain size and/or the mean misorientation varies according to the stored energy, and evolving the reconstructed subgrains during annealing using a Monte Carlo approach. Although the simulations were able to capture the annealing behavior of deformed bi-crystals [3], the evolution of a strong Cube texture from an initial polycrystalline sample containing very little Cube

component has not been successfully simulated. This paper presents our initial simulations of Cube texture evolution in polycrystals using large scale, three-dimensional simulations of deformation and recrystallization.

2. Mesoscale Simulations

The initial grain structure used in the deformation simulations was generated using a three-dimensional, Monte Carlo simulation of grain growth in a 60×60×60 simple cubic lattice by considering the first-, second- and third-nearest neighbors of a site for local energy calculations. A random texture was introduced to this grain structure, and four Cube-oriented grains were randomly introduced in the grain structure. The total volume fraction of initial cube was roughly 0.01. The initial grain structure had a total of 412 grains. The deformation was carried out in plane strain compression to a compressive strain of −0.7 and −1.2 at a strain rate of 1.0 s^{-1}. Slip on both octahedral and non-octahedral slip systems was included in the polycrystal deformation calculations. The deformation substructure was extracted using a procedure that has been outlined elsewhere [3, 4]. Each element was assumed to consist of 27 subgrains whose orientations were scattered around the mean element orientation, and the mean misorientation among the subgrains was calculated based on the stored energy of the element. The stored energy within the element was assumed to be proportional to the square of the slip system critical resolved shear stress within the element.

3. Results and Discussion

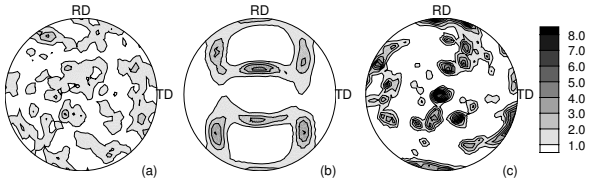

Figure 1: (100) pole figures showing (a) initial texture, (b) deformation texture for e = −1.2, and (c) recrystallized texture.

The initial, deformed and recrystallized textures are shown in Fig. 1. The initial texture is random. The deformation texture after a compressive strain of −1.2 is a typical face centered cubic (fcc) rolling texture. The texture after recrystallization shows strengthening of the Cube component. The stored energy of deformation and the misorientation from the Cube orientation are shown in Fig. 2. Careful analysis revealed that the regions that are close to Cube orientation are surrounded by regions with higher stored energy. The mechanism of Cube nucleation involves the migration of the boundary between the Cube and the surrounding non-Cube regions, leading to the consumption of the non-Cube regions by the Cube regions. In the early stages of growth, some of the migrating boundaries had a misorientation close to 40° <111> thus indicating the presence of near Σ7 boundaries. However, during the course of recrystallization, the special boundaries disappeared because of the changing orientation of the surrounding grains.

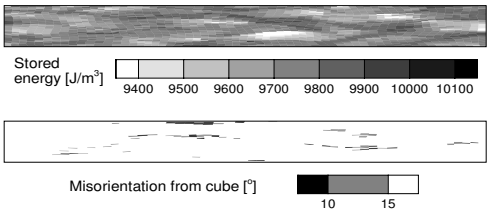

Figure 2: Stored energy of deformation (top) and the misorientation from Cube (bottom) for e = −1.2.

The evolution of the Cube component during recrystallization appears to depend upon the amount of deformation. Fig. 3 shows the temporal evolution of the cube for prior deformations of e = −0.7 and e = −1.2. The Cube fraction initially increases but then drops for e = −0.7 while for e = −1.2, the Cube fraction increases continuously. It appears that large strains favor stronger Cube fraction after recrystallization.

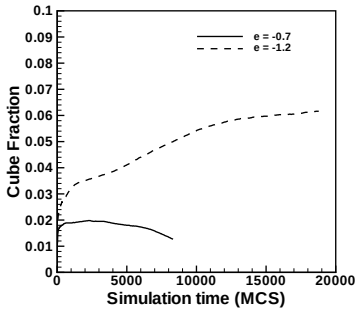

Figure 3: Effect of prior deformation on Cube evolution.

The current simulations involve several simplifying assumptions about the dislocation substructure. However, deformation structures are more complex in commercial alloys containing impurities and second phase particles. A theory that can deal with the evolution of dislocation substructures at the mesoscale for large deformations, and that can be coupled with crystal plasticity simulations, is needed in order to make realistic predictions of recrystallization in commercial alloys.

Acknowledgements

This research was sponsored by the Division of Materials Sciences and Engineering, U.S. Department of Energy, and used resources of the Center for Computational Sciences at Oak Ridge National Laboratory, which is supported by the Office of Science of the U.S. Department of Energy, under contract DE-AC05-00OR22725 with UT-Battelle, LLC.

References

1. C. Maurice and J.H. Driver, “Hot rolling textures of fcc metals–Part I. Experimental results on Al single and polycrystals,” Acta Mater, **45**, 4627 (1997).
2. M.C. Theyssier and J.H. Driver, “Recrystallization nucleation mechanism along boundaries in hot deformed aluminum bicrystals,” Mater. Sci. Eng., **A272**, 73 (1999).
3. B. Radhakrishnan and G. Sarma, “Simulating the deformation and recrystallization of aluminum bicrystals,” JOM, **56**, 55 (2004).
4. B. Radhakrishnan and G. Sarma, “The effect of coarse non-deformable particles on the deformation and static recrystallization of aluminium alloys,” Phil. Mag., **84**, 2341 (2004).

Modeling Meso-scale Plasticity Using Combined FEM and Nanoindentation Approach

S. Roy, Y. Liu, B. Wang, M. Yoshino, H. Lu, and R. Komanduri*

School of Mechanical and Aerospace Engineering
Oklahoma State University
Stillwater, OK 74078, USA
***e-mail: ranga@ceat.okstate.edu**

ABSTRACT

Constitutive laws are critical in the investigation of mechanical behavior of single crystal/polycrystalline materials in applications spanning from microscale to macroscale. An FEM/nanoindentation approach has been developed to determine the material behavior of single crystal copper incorporating the mesoplastic constitutive model. Nanoindentation on a single crystal copper was modeled using the multiscale simulation technique involving mesoplasticity and continuum elasticity. The meso-mechanical behavior of crystalline structures and the effects of the mesoplastic parameters on the nanoindentation load-displacement curves were investigated. Nanoindentation tests were conducted on single crystal copper to determine load-displacement relationships. Appropriate parameters in the mesoplastic constitutive model were determined through fitting the simulated load-displacement relation to the experimental data. The topography of nanoindentation impression was compared with the results from finite element simulation, yielding reasonably good agreement.

1. Introduction

Material behavior at all scales spanning from atomistic to continuum involves such processes as elastic deformation, dislocation generation and multiplication, cleavage, formation of voids and their coalescence into microcracks, alignment of microcracks to macrocracks, and final failure. In multiscale simulations [1-2], mesoplasticity serves as an appropriate formalism bridging atomistic mechanisms of deformation and fracture to macroscopic behavior [3-4]. This reinforces the importance of investigating material behavior under mesoscale. Ductile single crystals are of considerable interest in many applications, such as micro-electro-mechanical systems (MEMS). On the experimental side, the nanoindentation technique has become a very useful tool to probe into the mechanical behavior of materials at very small size. In finite element method (FEM) analysis, Yoshino *et al*. [5] applied the mesoplasticity theory to simulate the dislocation generation and propagation during indentation of single crystal silicon for the 2D case. In the literature, quantitative comparison of results between mesoplastic/orthotropic coupling simulation and nanoindentation/micro-tension results is not available and it is the objective of this investigation to address this issue.

2. Mesoplasticity Model

Plastic deformation in a single crystal is confined to well-defined slip systems. In an FCC lattice, there are 12 slip systems, which govern the mesoscopic distortion of the crystal [5]. Shear strain rate can be expressed as $\dot{\gamma}^{(k)} = \dot{\gamma}_0 \,\mathrm{sgn}(\tau^{(k)}) \left| \frac{\tau^{(k)}}{\tau_0^{(k)}} \right|^{\frac{1}{m}}$, where $\tau^{(k)}$ is the shear stress, m is the rate sensitivity exponent, $\dot{\gamma}_0$ is the shear strain rate at a reference condition and $\tau_0^{(k)}$ denotes the current shear strength of the slip system. The mesoplastic constitutive equation is $\overset{\nabla}{\boldsymbol{\sigma}} = \mathbf{C}^e : \mathbf{D} - \sum_{k=1}^{12} [(\mathbf{W}^{(k)} \cdot \boldsymbol{\sigma} - \boldsymbol{\sigma} \cdot \mathbf{W}^{(k)}) + \mathbf{C}^e : \mathbf{P}^{(k)}] \, \dot{\gamma}^{(k)}$. In this investigation, the mesoplastic constitutive model is implemented in a commercial FEM code (ABAQUS/Explicit) using a user-defined subroutine VUMAT.

3. Nanoindentation Tests and FEM Simulations

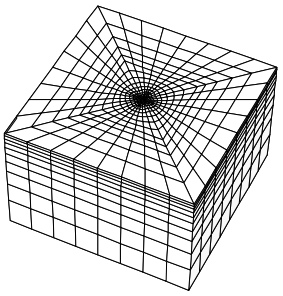

Fig. 1. FEM mesh for indentation simulations

An MTS Nano Indenter XP system was used for nanoindentation tests on a single crystal Cu to obtain load-displacement relationships. Each free surface in the specimen corresponds to <100>, and the upper and lower surfaces are the (100) faces. A 3D FEM analysis of nanoindentation was conducted on a single crystal Cu. The dimensions of the workpiece are 15×15×10 μm. The FEM mesh is shown in Fig. 1. Nanoindentation simulations involve multiple length scales, which are implemented using constitutive models at meso- and continuum- scales. The workpiece is partitioned into two parts and the corresponding constitutive relationships are assigned in these two parts of the model, i.e., meso-scale crystal plasticity and continuum-scale orthotropic elasticity. The single crystal copper is oriented in the [100] direction. A spherical indenter, assumed rigid, is used. A frictionless contact pair between the indenter and the workpiece is defined. Total time step increments of 66,967 were used in the simulation, including loading, intermediate transition and unloading.

4. Results and discussion

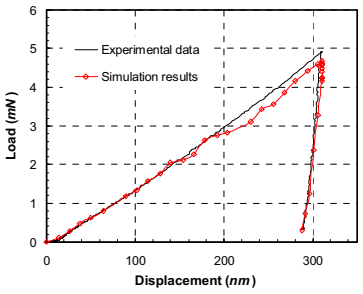

Fig. 2. Load-displacement curves at a 310 *nm* depth

Appropriate parameters in the mesoplastic constitutive model were determined by fitting simulation results with the corresponding experimental data, as shown in Fig. 2. Fig. 3(a) is FEM results of the distribution of out-of-plane displacement profiles on the indentation surface,

showing a four-fold symmetry of the deformation on (100) orientated surface. Fig. 3(b) shows an AFM image at an indentation depth of 310 *nm* for comparison. Both show a four-fold symmetry, and the profiles are in reasonably good agreement.

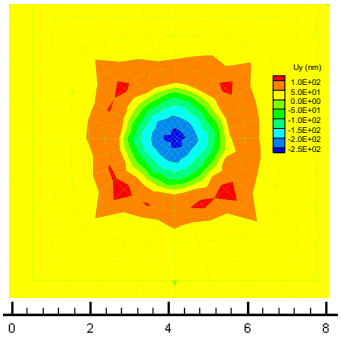

(a) Numerical results.

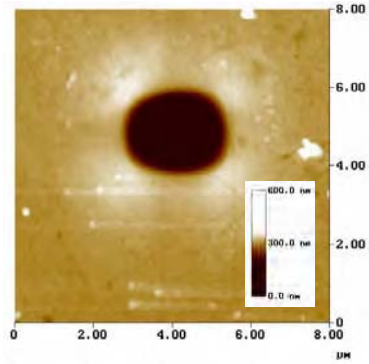

(b) AFM image.

Fig. 3. Out-of-plane displacement

6. Concluding Remarks

A multiscale FEM model involving meso-plasticity and continuum elasticity has been implemented to simulate nanoindentation. The meso-mechanical behavior of the crystalline structure was investigated using FEM modeling. Nanoindentation tests were conducted on a single crystal Cu to obtain load-displacement curves. Material parameters in the mesoplastic constitutive model were determined for single crystal Cu using the combined FEM/ nanoindentation approach by fitting numerical nanoindentation load-displacement curves with the experimental data. Good agreement was obtained between numerical and experimental results.

Acknowledgements: The work was supported by a grant from the Air Force Office of Scientific Research (AFOSR) through a DEPSCoR grant (No. F49620-03-1-0281). The authors thank Dr. Craig S. Hartley, Program Manager for Metallic Materials Program at AFOSR for his interest and support of this work.

References:

[1] Ogata, S., Lidorikis, E., Shimojo, F., Nakano, A., Vashishta, P., and Kalia, R., "Hybrid FE/MD/EDF approach to materials simulations on parallel computers," Computer Phys. Commu. **138**, 143 (2001).

[2] Smith, G. S., Tadmor, E. B., Bernstein, N., and Kaxiras, E., "Multiscale simulations of silicon nanoindentation," Acta Mater. **49**, 4089 (2001).

[3] Komanduri, R., Lu. H., Roy, S., Wang, B. and Raff, L., "Multiscale modeling and simulation of materials processing," Proceedings of the Annual Grantees Meeting, AFOSR Metallic Material Program, Wintergreen, August 16-18 (2004).

[4] Hartley, C. S., "A method for linking thermally activated dislocation mechanisms of yielding with continuum plasticity theory," Philos. Mag. **83**, 3783 (2003).

[5] Yoshino, M., Aoki, T., Chandrasekaran, N., Shirakashi, T., and Komanduri, R., "Finite element simulation of plane strain plastic-elastic indentation on single crystal silicon," Int. J. Mech. Sci. **43**, 313 (2001).

Three-dimensional atom-probe microscopy and the temporal evolution of microstructures

Chantal K. Sudbrack[1], Kevin E. Yoon[1], Ronald D. Noebe[2], and David N. Seidman[1†]

[1]Northwestern University, Dept. of Materials Science & Engineering; 2220 Campus Drive; Evanston, IL 60208-3108 USA [2]NASA John H. Glenn Research Center; 21000 Brookpark Road; Cleveland, OH 44135 USA [†] d-seidman@northwestern.edu

ABSTRACT

The temporal evolution of the early to the later stages of precipitation of ordered γ'-precipitates ($L1_2$) in Ni-5.2 Al-14.2 Cr at.% are studied at 873 K. Precipitates with sub-nanometer radii are characterized completely by three-dimensional atom-probe (3DAP) microscopy. Contrary to what is often assumed by theory or in models, the average precipitate composition is shown to evolve with time, such that solute concentrations decrease toward an equilibrium value given by the solvus lines. Power-law time dependencies of the number density, mean radius, and supersaturations of Al and Cr are presented and discussed.

1. Introduction

The precipitation of γ'-phase from a supersaturated solution (γ) in a temperature range where nucleation and growth are observable has been studied in Ni-Al alloys by direct imaging techniques [1,2]. In the present investigation, 3DAP microscopy is employed to characterize the identical, ternary alloy, Ni-5.2 Al-14.2 Cr at.%, aged at 873 K, as studied by references [3,4]. 3DAP microscopy allows the direct, spatial characterization of the chemical composition on a sub-nano- to nanometer scale via the reconstruction of a volume of material, typically 10^5 nm^3 and 10^7 nm^3 for the conventional 3DAP and the local electrode atom-probe (*LEAP*) [5] microscopes, respectively. The experimental procedures are described in [6].

2. Results and Discussion

After homogenization, Ni-5.2 Al-14.2 Cr at.% decomposes at 873 K into a high number density, N_v, of nanometer-sized, spheroidal γ'-precipitates. The lattice parameter misfit between the γ (f.c.c.) and γ' ($L1_2$) phases is 0.11 % [6], and the precipitates are coherent and spheroidal up to 1024 h [6]. The γ'-precipitation is first observed after 0.17 h of aging and the precipitates' average radius, $<R>$, and volume fraction, $V_f^{\gamma'}$, are determined to be 0.74 nm and 0.11 %, as shown in Fig. 1. A sharp increase in N_v at a constant $<R>$ value is observed between 0.17 and 0.25 h aging times, indicating that nucleation predominates. 3DAP microscopy detects precipitates as small as $<R> = 0.45$

nm (20 atoms). After 0.25 h and until 256 h, precipitate coalescence is observed, as seen for 4 h in Fig. 2. Given the precipitate radii and small lattice parameter misfit, this is not believed to be a result of elastically driven particle migration, and marks the finest scale, as well as smallest $V_f^{\gamma'}$, where this phenomenon has been observed in the solid state. Peak N_v, (3.2 ± 0.6) x 10^{24} m^{-3}, is achieved after 4 h of aging, after which the transformation enters a quasi steady-state regime with a constant power-law dependence of $t^{-0.64\pm0.06}$. In this regime, $V_f^{\gamma'}$ steadily increases (*upper panel,* Fig. 1), indicating that the transformation is not complete, yet $<R>$ has a temporal dependence of 0.30 ± 0.04, which is approximately consistent with the $t^{1/3}$ prediction for the coarsening of a ternary alloy.

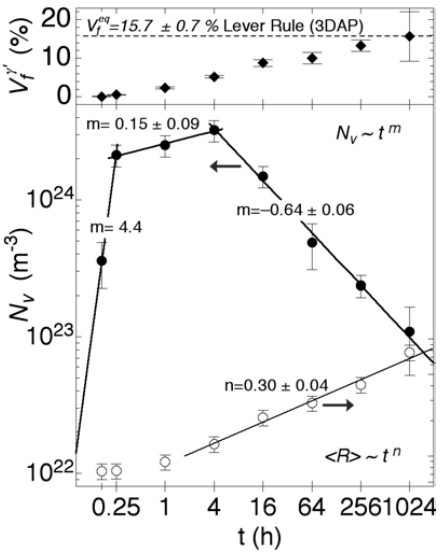

Figure 1. The temporal evolution of the γ'-precipitate volume fraction ($V_f^{\gamma'}$), number density (N_v), and average radius ($<R>$) in Ni-5.2 Al-14.2 Cr at.% aged at 873 K.

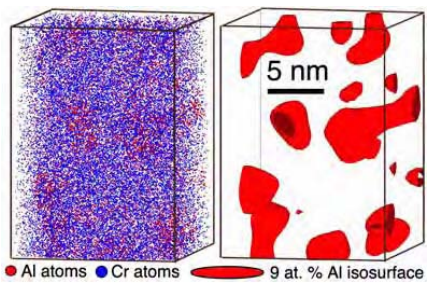

Figure 2. 15x15x20 nm^3 subset of a 3DAP microscope reconstructed volume of Ni-5.2 Al-14.2 Cr at.% aged at 873 K for 4 h (Ni atoms omitted). 30 % of the γ'-precipitates are coalesced.

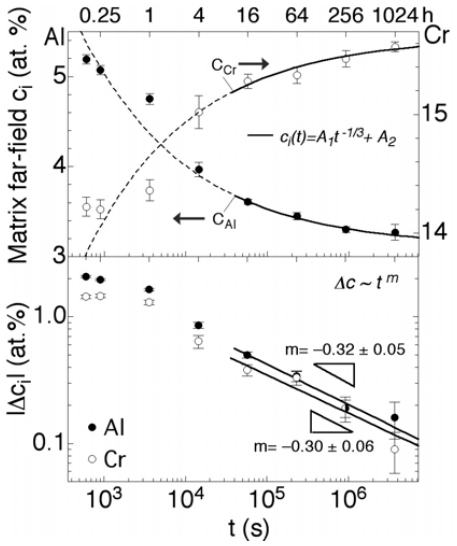

Figure 3. The average far-field concentrations and supersaturation in the matrix obtained by 3DAP microscopy in Ni-5.2 Al-14.2 Cr at.% aged at 873 K.

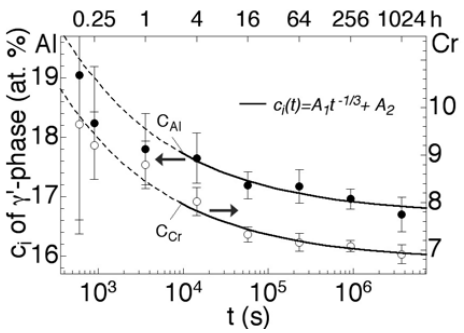

Figure 4. Average composition in the precipitates' interiors obtained by 3DAP microscopy in Ni-5.2 Al-14.2 Cr at.% aged at 873 K.

The average compositions of the γ (Fig. 3) and γ'-precipitates (Fig. 4) continually evolve temporally. The matrix becomes more enriched in Ni and Cr and depleted in Al with time. Between 4 and 16 h, the solute far-field concentrations change slowly (dc/dt → 0), and the quasi-stationary approximation can be applied after 16 h. Assuming this approximation, Marquis and Seidman [7] recently determined the solid solubilities, c_i^{eq}, in a ternary alloy. They applied $c_i(t) = \kappa t^{-1/3} + c_i^{eq}$ to fit the experimental data. Employing their approach c_i^{eq} are 16.69 ± 0.22 at.% for Al and 6.77 ± 0.15 at.% for Cr. Straightforwardly, the matrix supersaturations, $\Delta c_i = c_i(t) - c_i^{eq}$, are determined (Fig. 3). Their temporal behavior is in approximate agreement with the prediction of $\Delta c \sim t^{-1/3}$ for coarsening in a ternary alloy [8,9]. The classical theory of nucleation and growth assumes that the precipitates' composition is at their equilibrium value at the reaction's onset. Contrary to this assumption, it is found that the precipitates are highly saturated with Al (19.1 ± 2.8 at.%) and Cr (9.7 ± 2.1 at.%) at t = 0.17 h, and continuously decrease to 16.70 ± 0.29 at.% Al and 6.91 ± 0.20 at.% Cr at 1024 h. With the evolving composition, a $c_i(t) = \kappa t^{-1/3} + c_i^{eq}$ law fits the experimental data (Fig. 4) for the γ'-precipitates. This fit yields equilibrium values of 3.11 ± 0.05 at.% for Al and 15.66 ± 0.05 at.% for Cr. Utilizing the lever rule, the equilibrium $V_f^{\gamma'}$ is determined to be 15.7 ± 0.7 %

3. Acknowledgements

This research was sponsored by the National Science Foundation under grant DMR-0241928. C. K. Sudbrack and K. E. Yoon received partial support from NSF and NASA graduate research fellowships, respectively. We also would like to extend our gratitude to Dr. T. F. Kelly for use of Imago Scientific Instruments' LEAP™ microscope.

4. References

[1] H. Wendt and P. Haasen, Acta Metall. **31,** 1649 (1983).
[2] S. Q. Xiao and P. Haasen, Acta Metall. **39**, 651 (1991).
[3] C. Schmuck, P. Caron, A. Hauet, and D. Blavette, Phil. Mag. A **76**, 527 (1997).
[4] C. Pareige, F. Soisson, G. Martin, and D. Blavette, Acta Mater. **47**, 1889 (1999).
[5] T. F. Kelly, P. P. Camus, D. J. Larson, L. M. Holzman, and S. S. Bajikav, Ultramicroscopy, **62**, 29 (1996); T. F. Kelly et al., Microsc. Microanal. **10**, 373-383 (2004).
[6] C. K. Sudbrack, Ph.D. Thesis, Northwestern University, 2004.
[7] E. A. Marquis and D. N. Seidman, to be submitted to Acta Mater., 2004.; E. A. Marquis, Ph.D. Thesis, Northwestern University, 2002.
[8] A. Umantsev and G. B. Olson, Scr. Mater. **29**, 905-908 (1993).
[9] C. Kuehmann and P. W. Voorhees, Metall. Trans. Mater. A 27, 937-943 (1996).

Computer Simulation at the Atomic Scale of Twin Boundary Motion in the HCP Metals.

A. Serra[1], D. J. Bacon[2] and Yu.N.Osetsky[3]

1. **Departament de Matemàtica Aplicada III. Universitat Politècnica de Catalunya. Jordi Girona 1-3, C-2, 08034 Barcelona, Spain; a.serra@upc.es**
2. **Materials Science and Engineering, Department of Engineering. The University of Liverpool, Brownlow Hill, Liverpool L69 3GH, UK; djbacon@liv.ac.uk**
3. **Computational Materials Science Group, Oak Ridge National Laboratory, One Bethel Valley Road, P.O.Box 2008, MS-6138, Oak Ridge, TN37831, USA; osetskiyyn@orln.org**

ABSTRACT

An atomic-scale computer simulation method has been developed to simulate a dislocation with step character in a boundary with full periodicity in the boundary plane, i.e. along both the direction of the line of the defect and its direction of motion. It may be used for investigating the properties of such interfaces as the defects in them move over large distances. With the exception of the $\{11\bar{2}1\}$ twin, atomic shuffles are required for glide of twinning dislocations in the hcp metals and hence boundary movement may be temperature dependent. In the present work, we apply the static variant of the simulation method (T = 0K) to determine the critical stress, i.e. Peierls stress, for motion of twinning dislocations in the $\{10\bar{1}2\}$ twin boundary of zirconium. The influence of temperature and applied stress is being studied with the dynamic variant of the method and is illustrated here by the mechanism and velocity of motion of twinning dislocations in the $\{11\bar{2}2\}$ boundary at 300K and 600K.

1. Introduction

Deformation twinning plays an important role in the plasticity of the HCP metals, but little is known about the dynamics of the mechanisms that control twin boundary motion. Conservative motion of the twin boundary can be achieved by the glide of line defects that step the boundary and have dislocation character, namely, disconnections. In previous studies we have used computer simulation to study the atomic structure of twinning disconnections [1-3]. The conventional model used for simulation is periodic along the dislocation line, in order to simulate infinite length, and has fixed boundary conditions in the other two orthogonal directions. This model has been used to study the interaction of crystal dislocations with the twin boundary and it proved to be successful in revealing a new mechanism of creation of twinning dislocations in the $(10\bar{1}2)$ twin which leads to high mobility of the interface [3]. However, the method does not

permit quantitative study of dislocation dynamics because the interaction of the moving dislocation with the fixed boundaries restricts dislocation motion under an applied stress or strain. To overcome these problems, a technique for the simulation of a periodic array of dislocations has been implemented by Osetsky and Bacon [4] for modelling the dynamics of an initially straight edge dislocation in a single crystal, with periodic boundary conditions applied not only along the dislocation line but also the Burgers vector direction. This model may be applied to simulate long distance motion of a dislocation under a variety of loading and temperature conditions. Recently it has been applied to the simulation of interfacial defects with both dislocation and step character [5]. In this paper we show two extreme cases of twinning dislocation mobility: the highly mobile $\mathbf{b}_2$ dislocation of the $\{10\bar{1}2\}$ twin boundary and the low mobility $\mathbf{b}_3$ dislocation of the $\{11\bar{2}2\}$ twin boundary; the subindex n in $\mathbf{b}_n$ indicates the number of lattice planes parallel to the twin habit plane that intercept the step due to the dislocation.

2. Method

The principle underlying the method is that **b** of a perfect dislocation in a single crystal is the difference between two lattice vectors. Similarly, in a bicrystal formed by two half crystals (λ and μ), **b** of an interfacial defect that separates interfaces with identical structure is the difference between two lattice translation vectors from λ and μ respectively. For both situations, the defect is created by joining the two half crystals and selecting the two translation vectors $\mathbf{t}_\lambda$ and $\mathbf{t}_\mu$ whose difference is the Burgers vector of the chosen defect: $\mathbf{b} = \mathbf{t}_\lambda - \mathbf{t}_\mu$. To achieve the joining process, λ and μ have to be strained to bring $\mathbf{t}_\lambda$ and $\mathbf{t}_\mu$ into coincidence. The simulation model exploits the fact that the vector used to generate periodicity along the direction of motion of the defect, i.e. the translation vector, $\mathbf{t}^*$, of the model supercell, can be chosen to be $\mathbf{t}^* = \frac{1}{2}(\mathbf{t}_\lambda + \mathbf{t}_\mu)$. Thus, after the straining process, both λ and μ have a lattice translation equal to $\mathbf{t}^*$. A Finnis-Sinclair type interatomic potential derived by Ackland [6] representing zirconium has been used.

3. Results

To determine the critical stress, i.e. Peierls stress, for motion of the $\mathbf{b}_2$ dislocation in the $\{10\bar{1}2\}$ twin boundary, strain was applied incrementally with relaxation of the crystallite to the minimum potential energy at each step. A wide core, easy shuffles and low energy barrier make the dislocation extremely mobile. Thus, the strain increment had to be small, $\Delta\varepsilon=10^{-5}$, to control the process. Fig.1 shows the stress-strain curve; the maximum stress corresponds to the Peierls stress, σ_p=2.5MPa. At a temperature of only 0.1K the stress necessary to move the dislocation diminished by two orders of magnitude, i.e., a shear stress of 5kPa induces a velocity of 715 m/s. The $\mathbf{b}_3$ twinning dislocation in the $\{11\bar{2}2\}$ twin boundary has a narrow core with difficult shuffling since two rows of atoms have to move in opposite senses and in a direction perpendicular to $\mathbf{b}_3$ during dislocation glide. As a consequence glide has to be thermally assisted. Fig.2 shows the velocity of the $\mathbf{b}_3$ dislocation as a function of applied stress and T. Up to 500MPa the velocity increases with T, which is opposite to the effect observed due to phonon

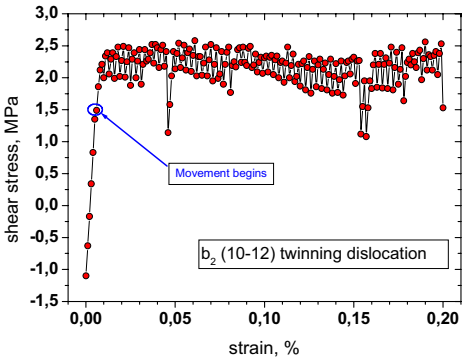

Figure 1. Stress-strain dependence obtained by static modelling of dislocation motion.

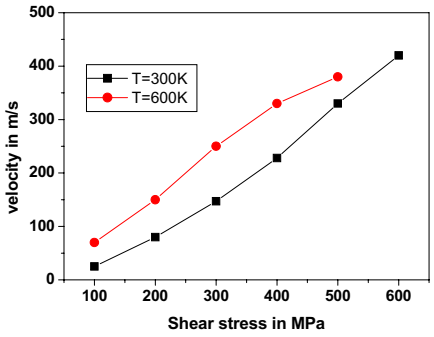

Figure 2. Dislocation velocity versus shear stress for the b_3 dislocation in a {11-22} twin boundary

scattering in single crystals [4]. This emphasizes the significance of boundary structure and shuffles. At T=600K and stress bigger than 550MPa a dipole pair with Burgers vector $\pm\mathbf{b_1}$ is created at the core of the $\mathbf{b}_3$ dislocation and one $\mathbf{b}_1$ glides away from the $\mathbf{b_3}$ defect. When this process occurs three times the ($\mathbf{b_3} - 3\mathbf{b_1}$) complex converts to a (**c+a**) crystal dislocation and the twin boundary moves away at high speed due to the high mobility of the remaining $\mathbf{b}_1$ twinning dislocations in the twin boundary. The details of the process will be described elsewhere.

Acknowledgments

We acknowledge support from the project BFM2003-08211-C03-03 of the Spanish M. C. y T. Part of the computing has been done in CESCA (Centre de Supercomputació de Catalunya)

References

[1] A. Serra, R.C. Pond, D.J. Bacon, "Computer simulation of the structure and mobility of twinning dislocations in h.c.p. metals" *Acta Met. & Mater.*, **39** (1991), 1469

[2] A. Serra, D.J. Bacon, "Computer simulation of screw dislocation interactions with twin boundaries in h.c.p. metals". *Acta Met. & Mater.*, **43**, (1995), 4465.

[3] A. Serra, D.J. Bacon, "A new model for (10-12) twin growth in h.c.p. metals", *Phil. Mag. A*, (1996), **73**, 333

[4] Yu.N. Osetsky and D.J. Bacon, "An atomic-level model for studying the dynamics of edge dislocations in metals", *Modelling Simul. Mat. Sci. Eng.,* **11** (2003) 427.

[5] A. Serra and D.J. Bacon, "A model for simulating the motion of line defects in twin boundaries in the HCP metals", *Zeitschrift für Metallkunde*, (2004), **95**, 4.

[6] G.J. Ackland, S.J. Wooding and D.J. Bacon, 'Defect, surface and displacement-threshold properties of α-Zr simulated with a many-body potential', *Phil. Mag. A*, **71** (1995) 553

Dislocation Bypass Mechanism in Cu-Co Alloys: Molecular Dynamics Study

J.-H. Shim [a,b] and B.D. Wirth [a]
[a] **Department of Nuclear Engineering, University of California, Berkeley, CA 94720, USA** (jhshim@nuc.berkeley.edu)
[b] **Nano-Materials Research Center, Korea Institute of Science and Technology, Seoul 136-791, Republic of Korea**

ABSTRACT

Molecular dynamics simulations of the interaction between screw or edge dislocations with coherent Co precipitates embedded in Cu-Co alloys are presented. The simulations provide insight into the sequence of events controlling the interaction and bypass mechanisms, in addition to quantitative information on the critical resolved shear stress. The simulations reveal a temperature dependent dislocation bypass mechanism, which involves a new interaction mechanism at low temperature.

1. Introduction

Cu-Co alloys, which exhibit giant magnetoresistance (GMR) behavior as either multilayer thin films or alloys with embedded cobalt nanoparticles, have been studied as a model precipitate-hardened alloy system for more than three decades. Ferromagnetic cobalt has limited solubility in copper, and a relatively small lattice mismatch (< 2%). Thus, cobalt precipitates rapidly form following thermal aging from super-saturated solutions and maintain a coherent, fcc phase until losing coherency and transforming to the preferred hcp phase [1].

Büttner and Nembach [2] found an anomalous temperature dependence of the critical resolved shear stress (CRSS) of Cu-Co single crystals containing coherent Co precipitates. In the precipitate hardened alloys, the critical resolved shear stress increases with temperature to a maximum value about 200 K and then decreases to a value at 500 K similar or a little below the critical resolved shear stress measured at 12 K. The entire temperature dependence and, in particular, the maximum CRSS at relatively low temperature of about 200 K are not entirely understood. The purpose of this study is to provide detailed atomistic insight into the mechanisms of the dislocation–precipitate interaction in order to understand the temperature dependence of the critical resolved shear stress.

2. Computational Procedures

Large-scale molecular dynamics (MD) simulations were performed of the interaction between moving edge dislocations and 3 nm diameter, coherent cobalt precipitates over a temperature range of 10 to 400 K. The MD used a modified version of the MDCASK code, with embedded atom method (EAM) potentials [3].

The simulation cell consists of an fcc lattice, bounded by {111}, {110} and {112} faces in *X*, *Y* and *Z* directions, respectively. The cell dimensions are approximately 32 x 38 x 27 nm (*X*, *Y* and *Z* directions) containing about 2.7 million atoms for the edge dislocation simulations and 31 x 26 x 66 nm containing 4.5 million atoms for the screw dislocation simulations. Periodic boundary conditions are applied in the *Y* and *Z* directions, while the *X* surface is initially free, but is subject to a constant surface

traction following equilibration. The surface traction provides a shear stress to drive dislocation motion. A coherent fcc Co precipitate, about 3 nm in diameter, is inserted, maintaining the cube-cube orientation relationship with the matrix. A constant shear stress of 100 MPa is applied by superimposing a constant (equal and opposite) force in the [110] direction on the atoms in the two $(\bar{1}11)$ surfaces.

3. Results and Discussion

Fig. 1 shows snapshots from an MD simulation at 300K and an applied shear stress of 100 MPa[1]. During equilibration, the 3 nm Co precipitate maintains coherency with the Cu matrix, without any indication of impending structural transformation or interface instability leading to misfit dislocation formation. The edge dislocation is noticeably split into two Shockley partials, which glide in the *Y* direction. After about 16 ps of applied stress, the leading partial initially contacts the Co precipitate (Fig. 1a). By about 23 ps, the leading partial shears the precipitate, noticeably bowing with a critical angle of about 80°(Fig. 1b). As the leading partial moves past the particle, the trailing partial begins to interact with the precipitate (Fig. 1c). By about 44 ps, the leading partial has moved through the periodic boundary conditions and re-entered the cell from the bottom (Figs. 1c and 1d), while the trailing partial continues to be pinned by the precipitate. 44.8 ps after the applied stress, the trailing partial dislocation bypasses the precipitate by the expected shear mechanism. Noticeably, the resistance due to the precipitate is stronger for the trailing rather than the leading partial, with a critical bypass angle of approximately 55° as the trailing partial detaches from the precipitate (Fig 1e). MD simulations at 400 K reveal a similar sequence of events and detachment mechanism, namely that both the leading and trailing Shockley partial dislocations bypass the coherent Co precipitate by the expected shear mechanism, with the trailing partial experiencing more resistance

The MD simulations at lower temperatures revealed a different bypass mechanism for the trailing partial dislocation. The leading partial shears past the precipitate by about 22 ps, noticeably bowing with a critical angle of about 80°. As the leading partial moves past the particle, the trailing partial begins to interact with the precipitate. By about 41 ps, the leading partial has moved through the periodic boundary conditions and re-entered the cell from the bottom, while the trailing partial continues to be pinned by the precipitate, bowing to a critical angle of nearly 0°. As the trailing partial nearly completely surrounds the precipitate, the partial dislocation segments just beyond the precipitate strongly interact and annihilate. This releases the trailing partial dislocation from the precipitate and leaves a partial (Orowan) dislocation loop around the precipitate. The resulting glide loop is not energetically stable at this size and collapses, resulting in the additional shear of the precipitate, as the trailing partial continues to move beyond the particle. All of the MD simulations of edge dislocation – Co precipitate interaction performed at 100 MPa applied shear stress and temperatures between 10 and 200 K showed the same bypass mechanism, namely mixed shear and Orowan looping.

The change in the dislocation bypass mechanism from the mixed shear/Orowan mechanism at low temperature to the shear mechanism at higher temperatures,

[1] Movies of the MD simulation results at 300 and 100 K can be viewed at http://iron.nuc.berkeley.edu/~bdwirth/Public/WRG/CuCo.html.

indicates a decreased precipitate resistance with increasing temperature. This temperature dependence of the dislocation bypass mechanism might explain the reported anomalous temperature dependence of the CRSS, combined with the dislocation dynamic effect due to frozen phonon drag at very low temperatures. For the screw dislocation interactions, nearly same dislocation bypass behavior is observed, although the detail of the results is not presented here. In that case, the mixed shear/Orowan mechanism operates below about 300 K, with shear at higher temperatures.

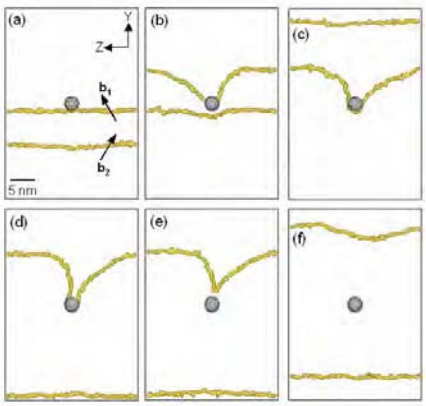

Figure 1. Snapshots of an edge dislocation cobalt precipitate interaction at 300 K and 100 MPa applied stress at a) 16.2, b) 23.0, c) 40.2, d) 44.2, e) 44.8 and f) 50.2 ps.

None of the precipitate strengthening mechanisms, including modulus or lattice mismatch, should differ substantially for the two Shockley partial dislocations, nor have a strong temperature dependence. For the specific case of coherent cobalt precipitates embedded in an fcc Cu matrix, an additional crystallographic transformation strengthening mechanism operates, which is different for each of the two Shockley partial dislocations. Precipitate bypass by the leading partial shears the precipitate by 1/6<112>, thereby introducing a plane of hcp stacking (e.g., the fcc stacking fault which separates partial dislocations) within the precipitate on the dislocation glide plane. hcp Co is energetically favored to fcc Co, and thus, additional work is required to transform the hcp glide plane within the precipitate back to fcc. This imparts an additional resistance which acts against only the trailing Shockley partial dislocation. The energy difference between fcc and hcp Co will decrease with increasing temperature, because hcp Co transform to fcc Co at 695 K. Therefore, the precipitate resistance to the trailing partial decreases with the increasing temperatures, which might cause the temperature dependence of the dislocation bypass mechanism.

References

[1] G.Y. Yang et al., "Precipitation of Nanoscale Co Particles in a Granular Cu-Co Alloy with Giant Magnetoresistance," Mater. Res. Bull. **35**, 875 (2000).

[2] N. Büttner and E. Nembach, " Low Temperature Anomalies of Precipitation Hardening in the System Copper-Cobalt," Z. Metallkd. **76**, 82 (1985).

[3] K. Nordlund and R.S. Averback, "Inverse Kirkendall Mixing in Collision Cascades," Phys. Rev. B **59**, 20 (1999).

Micromechanics of Damage Evolution in Solid Propellants

[1]N. Aravas, [2]F. Xu, [2]P. Sofronis

[1]Department of Mechanical and Industrial Engineering
University of Thessaly, Pedion Areos, 38334 Volos, Greece; Email:aravas@uth.gr

[2]University of Illinois at Urbana-Champaign,
Department of Theoretical and Applied Mechanics
104 South Wright Street, Urbana, IL 61801, USA; Email: sofronis@uiuc.edu

ABSTRACT

Solid propellants are composite materials with complex microstructure. In a generic form, the material consists of polymeric binder, ceramic oxidizer, and fuel particles (e.g. aluminum). Damage induced by severe stress and extreme temperatures is manifested in decohesion along particle/binder interfaces followed by void formation and opening. With the use of rigorous composite-material homogenization theory, a macroscopic constitutive model is proposed that accounts for continuous void nucleation and growth upon straining. Numerical simulations for the uniaxial tension test reveal: i) an initial elastic regime; (ii) a following viscoplastic regime in which void formation competes with hardening in the matrix; (iii) a final softening regime.

1. Introduction

The microstructure of a typical solid propellant material consists of polymeric binder, oxidizer, metal fuel, and some other additives for improved bonding and burning (1). The binder is a rubbery material that behaves viscoelastically. The oxidizer, e.g. ammonium perchlorate, is an organic crystal whose response is elastic. The fuel is elastoplastic owing to its metallic nature. An additional complexity in the characterization of the overall constitutive response is the onset of decohesion at particle/binder interfaces upon straining, a phenomenon called dewetting. Dewetting induces interfacial microcracks or holes, and therefore it is a source of strong macroscopic nonlinearity.

Characterization of the constitutive response of solid propellant materials in the presence of damage has been the objective of several other investigations in the past 30 years. For a thorough review of previous work in the area of propellant constitutive modeling, one can look at the most recent work of Schapery and co-workers, e.g. [2], and that of Ozupek and Becker [1, 3]. While the theoretical predictions of previous models agree with the experimental results in many respects, the models employ a number of phenomenological parameters to describe material characteristics such as the overall propellant dilatation and damage. These parameters are difficult to determine experimentally.

The objective of the present work is to introduce a rigorous solid mechanics methodology to analyze the response of a solid propellant as affected by damage. The

goal is to suggest a general 3-D model, possibly with no fitting parameters, and capable of accounting for the evolution of the microstructure with straining. The development of the model is based on some recent advances of rigorous homogenization theory for nonlinear viscous composites [4]. Material data are for a model system as experimental data were not available.

2. Material model

The binder is assumed to be incompressible, linearly elastic with shear modulus μ_m, and viscous. The viscous response is allowed to be nonlinear to account for chain straining and reorientation with a stress-strain rate law in uniaxial tension given by

$$\dot{\varepsilon}_m(\sigma_m) = \dot{\varepsilon}_0 \left[\zeta \frac{\sigma_m}{\sigma_0} + (1-\zeta)\left(\frac{\sigma_m}{\sigma_0}\right)^2 \right], \tag{1}$$

where $\dot{\varepsilon}_m$ is the strain rate in response to the stress σ_m, $\dot{\varepsilon}_0$ and σ_0 are material constants, and ζ is a parameter used to explore linear, $\zeta = 1$, or nonlinear, $\zeta = 0$, viscous effects. To a first approximation, the fuel and oxidizer particles are treated as rigid. The microstructure of the solid propellant is treated as evolving with deformation. In other words, as the straining proceeds and the local dewetting criterion is met voids are forming around oxidizer particles while existing voids enlarge. Details on the treatment of the microstructural evolution and the applied homogenization procedure can be found in the work of Aravas *et al*. [5].

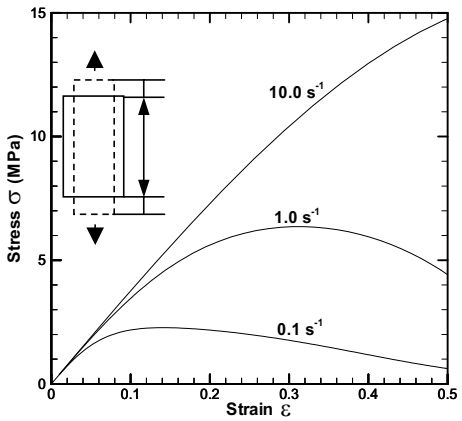

3. Results

The response of a solid propellant material was simulated in uniaxial tension under prescribed constant displacement rate. The procedure was implement in the finite element code Abaqus through a "User Subroutine" (UMAT). Before the application of the load, the initial volume fraction of the oxidizer particles, i.e. of those particles in the model that could turn into voids upon straining, was 0.615. The volume fraction of the fuel particles was 0.10, and hence the initial value of the volume fraction of the total number of particles (oxidizer and fuel) was 0.715. The initial volume fraction of the binder in the composite was 0.275. It was also assumed that the propellant had a small amount of an initial porosity 0.01 which in a real-world material can be attributed to long range chemical reactions. The shear modulus of the matrix was 1.7MPa and the parameters for the

matrix viscous response in Eqn. (1) were taken those for PMMA, i.e. $\dot{\varepsilon}_0 = 1.0\,\mathrm{s}^{-1}$, $\sigma_0 = 2.5\,\mathrm{MPa\ s}^{-1}$, and $\zeta = 0.037$. The response of the homogenized propellant in uniaxial tension is shown in Fig. 1, where the stress σ in response to three fixed strain rates $\Delta\dot{u}/L$ is plotted as a function of the logarithmic strain $\varepsilon = \ln(1 + u/L)$ in which L is the undeformed length before straining, and Δu is the increment of the displacement u. Clearly there is a strong strain rate effect which derives from the response of the polymeric binder (cf. Eqn. (1)). At the beginning of loading the response is linear and this reflects the elasticity of the binder and the linear component of the viscosity of the binder. The linear regime is followed by a hardening regime which apparently reflects the interaction between the rigid particles and the nonlinearity of the binder. At macroscopic strains greater than 0.08, 0.15, and 0.23 respectively for the three loading strain rates 0.1, 1.0, and $10\mathrm{s}^{-1}$, substantial void formation accompanied by particle decohesion is the case. As straining continues and void formation becomes profuse, a critical strain is reached after which the softening effect prevails and the stress-strain curve begins to drop.

4. Summary

The homogenization theory of Ponte Castaneda [4] for non-linear composites has been used to propose a nonlinear model for the constitutive response of solid propellant materials. The model accounts for the evolution of the microstructure upon straining as is demonstrated by void formation and growth. The prediction that there are three strain rate dependent regimes of deformation, namely linear, hardening, and softening agrees well with experiment.

Acknowledgements

This work was supported by the Center for Simulation of Advanced Rockets, funded by the U.S. Department of Energy under subcontract number DOE/LLNL/B523819. The finite element calculations were carried out at the National Center for Supercomputing Applications at the University of Illinois at Urbana-Champaign.

References

1. Ozupek, S. and Becker, E. B. (1992) Constitutive modeling of high-elongation solid propellants, J. Engng Mater. Technology, ASME, 114, 111-115.
2. Ha, K. and Schapery, R. A. (1998) Three-dimensional viscoelastic constitutive model for particulate composites with growing damage and its experimental validation, Int. J. Solids Structures, 35, 3497-3517.
3. Ozupek, S. and Becker, E. B. (1997) Constitutive equations for solid propellants, J. Engng Mater. Technology, ASME, 119, 125-132.
4. Ponte Castaneda, P. (1991) The effective mechanical properties of nonlinear isotropic composites, J. Mech. Phys. Solids, 39, 45-71.
5. Aravas, N., Xu, F., Sofronis, P. (2004) Micromechanics of Damage in Solid Propellants," Proceedings of the JANNAF 36th Structures and Mechanical Behavior Subcommittee meeting, New Orleans, Luisiana, March 30-April 1, 2004.

Symposium -4

Experimental Validation of Multiscale Models

Change in the motion process of interstitial-type dislocation loops in iron with the growth of loops

K. Arakawa[1], H. Mori[1], E. Kuramoto[2] and K. Ono[3]

[1]Research Center for Ultra-High Voltage Electron Microscopy, Osaka University, Yamada-Oka, Suita, Osaka 565-0871, Japan, arakawak@uhvem.osaka-u.ac.jp, mori@uhvem.osaka-u.ac.jp
[2]Research Institute for Applied Mechanics, Kyushu University, 6-1 Kasuga-koen Kasuga Fukuoka 816-8580, Japan, kuramoto@riam.kyushu-u.ac.jp
[3]Department of Material Science, Shimane University, 1060 Nishikawatsu, Matsue 690-8504, Japan, onok@shimane-u.ac.jp

ABSTRACT

Extensive simulations based on classical molecular dynamics have shown that small interstitial-type perfect dislocation loops in various metals and alloys have the structure of bundles of crowdions and loops can easily move one-dimensionally. The present study dynamically examines the variation in the motion process of loops in pure iron with the growth of loops under 1 MeV electron irradiation by high-voltage electron microscopy. Two types of loops were formed by irradiation. Loops of one type possessed the Burgers vector of 1/2<111> and the habit plane of {011}, and loops of the other type were <001> {001}. Loops of the former type made back-and-forth motion and expansion towards the direction along their Burgers vectors when they were smaller than about a few ten nanometers in diameter. Loops of the latter type only rarely moved more slowly when they were smaller than about the same size. When loops of the both types grew larger than about 50 nm, the characteristics of the motion of loops changed drastically. Dislocation segments of each large loop made long-distance glide independently of their opposite segments. This kind of motion means that self-interstitial atoms at the central region of such large loops are no longer the crowdions.

1. INTRODUCTION

Extensive simulation studies based on classical molecular dynamics have shown that small interstitial-type perfect dislocation loops consisting of several to several tens self-interstitial atoms (SIAs) in fcc and bcc metals and alloys have the structure of bundles of crowdions and a loop can make the one-dimensional motion by the collective motion of the whole crowdions belonging to the loop [*e.g.* 1, 2]. In addition, several experimental studies using transmission electron microscopy (TEM) have revealed the back-and-forth motion of small loops of a few to a few ten nanometers in diameter along the "crowdion direction" parallel to their Burgers vector [3-5]. These experimental studies also clarified that loops move thermally [5], and indirectly indicated that loops move by a stress [3-5]. However, the mechanism of the motion of loops has not been experimentally clarified yet.

In contrast, as a loop grows, the atomic structure around the extra-half plane in the loop will approach that of a perfect crystal which should not be regarded as the bundle of crowdions any longer. Additionally, theoretical studies suggested that the distribution of atomic distance along a crowdion axis in a loop becomes extended and the "effective mass" of the crowdion increases as the SIA is far from the periphery of the loop [6, 7]. Such a variation in the structure of loops with their growth is expected to cause a remarkable dependence of the motion process of loops with their size. In the present study, we examined the motion process of loops in iron under energetic-particle irradiation using TEM over a wide range of the loop size from a few to a few hundred nanometers in diameter.

2. EXPERIMENTAL PROCEDURES

The specimen of pure bcc Fe (99.999%) supplied by Showa Denko Inc. was used. It was rolled down to 0.08 mm in thickness. The sheets of pure Fe were pre-annealed at 1120 K for 1 hour in a hydrogen atmosphere. Then, they were electrochemically polished for TEM.

High-energy electron irradiation and in-situ observation was performed in a high-voltage electron microscope H-3000 (Hitachi) operated at an acceleration voltage of 1000 kV at temperatures ranging from 110 to 300 K. The main beam axis was <001>. The beam flux was mainly $1x10^{24}$ e^-/m^2s, and $1x10^{23}$ e^-/m^2s for a weak irradiation.

For in-situ TEM observation, bright-field imaging was used. The reflection adopted was mainly **g** = 110 and **g**=200 with the deviation parameter from the exact Bragg condition *s* of 0.03 nm^{-1}. The images were recorded through a CCD camera with a time resolution of 1/30 s.

3. RESULTS AND DISCUSSION

Two types of loops were formed by irradiation. Loops of one type had the Burgers vector of 1/2<111> and the habit plane of {011}, and loops of the other type were <001> {001}. Loops of the former type were mobile when they were smaller than about a few ten nanometers; whilst loops of the latter type were almost immobile. Some of 1/2<111> loops occasionally exhibited the repetition of the expansion of their image towards the Burgers vector and shrinkage into the original platelet. The Burgers vector of these loops often spontaneously rotated into another 1/2<111> or <001> direction [8]. These phenomena are likely attributed to the independent motion of each crowdion belonging to the loop; these strongly support the idea that a small mobile loop has the structure of the bundle of crowdions and the loop moves by the collective motion of the whole crowdions.

When loops of the both types grew larger than about 50 nm, the characteristics of the motion of loops drastically changed. Dislocation segments of such a large loop made long-distance glide independently of its opposite segment as shown in Fig. 1. This kind of motion means that the SIAs located at the central region of such large loops are no longer a crowdion, and each dislocation segment moves as a conventional dislocation.

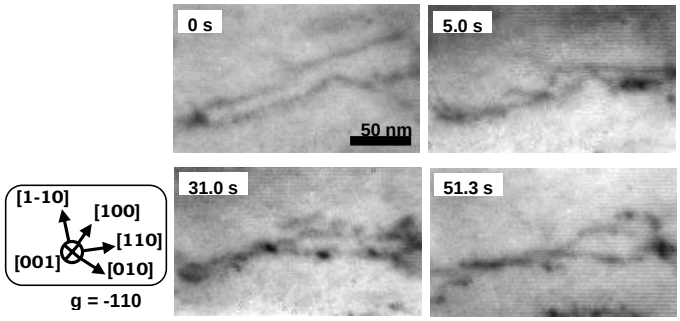

Fig. 1 The behavior of a large loop whose Burgers vector **b** equals 1/2[1-11] or 1/2[1-1-1] under high-energy electron irradiation at 290 K.

Further, small loops located near a dislocation segment of a large loop moved in sync with the dislocation. This directly shows the motion of small loops is induced by a stress. Meanwhile, the mobility of both small and large loops was remarkably reduced by lowering the electron-beam intensity; hence loops are likely to move not by thermal energy but mainly by a stress at temperatures examined. From the difference between the motion processes of large and small loops, the origin moving a large loop will be shear stress acting on each dislocation segment via the Peach-Koehler force; whilst the origin moving a small loop is expected to be mainly the spatial gradient of the compression and expansion strain field acting on the whole crowdions in the loop as claimed by Kiritani [3] rather than the inhomogeneous or co-axial shear stress acting on each dislocation segment.

References

1. B. D. Wirth, G. R. Odette, D. Maroudas, and G. E. Lucas, "Dislocation loop structure, energy and mobility of self-interstitial atom clusters in iron", J. Nucl. Mater. **276,** 33 (2000).
2. Yu. N. Osetsky, D. J. Bacon. A. Serra, B. N. Singh, and S. I. Goulubov, "One-dimensional atomic transport by clusters of self-interstitial atoms in iron and copper", Phil. Mag. **83**, 61 (2003).
3. Kiritani, "Defect interaction processes controlling the accumulation of defects produced by high energy recoils", J. Nucl. Mater. **251**, 237 (1997).
4. T. Hayashi, K. Fukumoto, and H. Matsui, "In situ observation of glide motions of SIA-type loops in vanadium and V-5Ti under HVEM irradiation", J. Nucl. Mater. **307-311**, 993 (2002).
5. K. Arakawa, M. Hatanaka, H. Mori, and K. Ono, "Effects of chromium on the one-dimensional motion of interstitial-type dislocation loops in iron", J. Nucl. Mater. **329-333**, 1194 (2004).
6. E. Kuramoto, "Computer simulation of fundamental behaviours of interstitial clusters in Fe and Ni", J. Nucl. Mater. **276**, 143 (2000).
7. S. L. Dudarev, "Coherent motion of interstitial defects in a crystalline material", Philos. Mag. **83**, 3577 (2003).
8. K. Arakawa, E. Kuramoto, K. Ono, H. Mori, in preparation.

Heterogeneity of residuals strains in Zircaloy-4 after thermal creep, link between diffraction and homogenization.

Nils Letouzé[a,b], Rénald Brenner[a], Jean-Luc Béchade[b], Marie-Hélène Mathon[c], Olivier Castelnau[a]

[a] LPMTM, UPR901, Université Paris 13, Av. J.B. Clément, 93230 Villetaneuse (France) (nl@lpmtm.univ-paris13.fr, oc@lpmtm.univ-paris13.fr,)
[b] CEA/DEN, Service de Recherches Métallurgiques Appliquées, CEA/Saclay, 91191 Gif-sur-Yvette Cedex (France)(jean-luc.bechade@cea.fr,)
[c] Laboratoire Léon Brillouin (CEA-CNRS), CEA/Saclay, 91191 Gif-sur-Yvette Cedex (France)(mathon@llb.saclay.cea.fr)

ABSTRACT

Zirconium polycrystals, used in the nuclear industry, can be considered as composite materials made of grains with soft and hard crystallographic orientations for plastic deformation, leading to a strongly heterogeneous deformation [1]. A better understanding of the effective (overall) mechanical properties of Zr alloys is suited for the improvement of alloys actually in use, for the development of new alloys, and for the optimisation of elaboration processes. This requires (i) the accurate knowledge of the local mechanical behaviour of grains, and (ii) a scale transition scheme (from the grain to the polycrystal) adapted to the material microstructure.
However, grain local behaviour is particularly difficult to be measured directly, eg. by mechanical tests, owing to the difficulty of growing large single crystals. This difficulty can be circumvented by coupling diffraction measurements to scale transition models, as proposed in this paper.

1. Introduction

The distribution of elastic strain in a plastically deformed zirconium alloys is a signature of the deformation path and can therefore be used to determine the constitutive behaviour of the material at the grain level. Two complementary ways are undertaken to investigate this distribution: experimentally using diffraction techniques (X-ray and neutron diffraction), and numerically with a modelling approach using homogenization techniques.

- ✓ On one hand, diffraction gives a statistical analysis of average elastic strains and of their fluctuations in the investigated volume (the whole sample volume in the case of neutron diffraction). These mechanical parameters can be extracted respectively from the position and the shape of the peak.
- ✓ On the other hand, the elastic strain distribution can also be predicted by homogenisation techniques, providing that the (non-linear) local mechanical behaviour and the microstructure of the material are known. For polycrystals, the self-consistent scheme is well adapted owing to the random character of the microstructure [2]. However, the extension of the self-consistent scheme to non-linear behaviour is only approximate [3].

2. Results : confrontation of the modelling with experiments

Comparison between elastic strain distribution obtained (a) by neutron diffraction experiments performed at the diffractometer 6T1 at LLB and (b) by a thermo-elasto-visco-plastic self-consistent model [4] have been performed. Figure 1 shows the (0002) pole figure of the Zircaloy-4 specimen deformed by creep at 400°C in tension up to 5%.

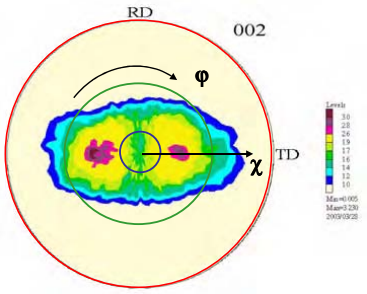

Fig. 1 : (0002) pole figure measured on a Zircaloy-4 deformed by creep at 400°C in tension up to 5%. (RD is the rolling direction and TD is the transverse direction)

One can see on Fig. 2 the good agreement between the experimentally determined elastic strains obtained for different orientations in (0002) pole figure defined by their tilt angle χ and rotation angle φ (open circles) and the micromechanical modelling calculation (continuous line)

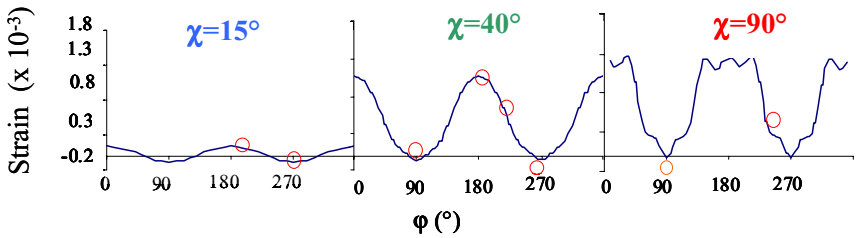

Fig. 2 : Strain map after thermal creep for different χ angles.

The results obtained show also how diffraction data can be used for the validation of the scale transition model [5] used in the frame of homogenisation methods. These methods make it possible to estimate or bound the effective behaviour of heterogeneous materials starting from the statistical description of the microstructure (texture) and the knowledge of the mechanical behaviour of the constituents (in this work, we label "phase" a set of grains with the same orientation). They also allow to estimate the intra- and inter-phase fluctuations of the mechanical fields. So the comparison of experimental and calculated strain maps using different non linear approaches, is a promising way for determining the best linearization procedure.

Fig. 3 gives an example of the influence of the linearization procedure on the prediction of the elastic strain for different orientations. In this case, viscoplastic

simulation has been performed, using Zircaloy-4 real texture with thermal creep loading in tension at 127 MPa stress level. We used the secant and affine Self Consistent schemes (2 ways of linearization assuming both in–homogeneity of stress and strain) as well as Reuss (stress homogeneity) and Taylor (strain homogeneity) bounds to calculate the phase average stress. Focusing for a particular orientation, here for example at χ=55°, significant differences between several polycrystals models are shown.

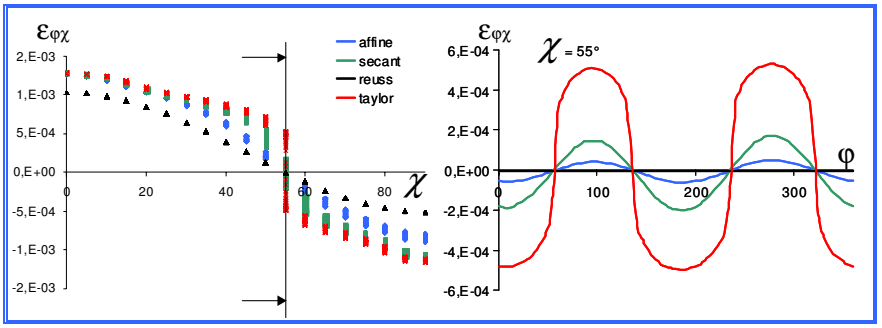

Fig. 3 : Evolution of the elastic strains calculated with several polycrystal models and comparisons for a particular orientation at χ=55°.

On main result is that the Reuss model does not predict any residual strain around the principal orientation (at χ=55°), which is absolutely not realistic. The secant formulation is closer to the prediction of the Taylor bound, whatever χ angle is, the Taylor formulation showing a strain level 10 times higher, for example at χ=55°, and the affine one a strain level 2 times lower compared to the secant formulation. Finally these large discrepancies between different linearization procedures would be enough to select the best one when experimental data will be acquired and compared to.

3. Conclusion

Diffraction experiments (here using neutrons) provide a volume measurement of the elastic strain distribution in polycrystals on a plastically deformed Zircaloy-4 specimen. Taking into account that these data can be compared rigorously to the results of homogenisation schemes as shown in [5], and therefore they may be used for a reliable determination of the local constitutive relation and a good way for determining the best linearization procedure in the case of non linear behaviour.
An application to creep loading shows an excellent agreement with the prediction of the affine self-consistent scheme for non linear elasto-viscoplasticity.

References

[1] - Brenner R., PhD thesis, Université Paris XIII, France 2001.
[2] – Kröner E., *J. Phys. F: Metal Phys*. **8**, 2261-2267, 1978.
[3] – Ponte Castañeda P., Suquet P., *Adv. Appl. Mech.* **34**, 171-302, 1998.
[4] Masson R., Zaoui A., *J. Mech. Phys. Solids* **47**, 1543-1568, 1999.
[5] Letouzé N., R. Brenner, O. Castelnau, J.L. Béchade, M.H. Mathon, *Scripta Mater.* **47**, p. 595-599, 2002.

Assessment of the Constitutive Behavior of Irradiated Metals Using Non-Standard Mechanical Tests and FEM Calculations

E. N. Campitelli[1], P. Spätig[2], R. Bonadé[2], M. Victoria[2], C. Hellwig[1]

1) Laboratory for Materials Behaviour,

Nuclear Energy and Safety Research Department, Paul Scherrer Institute

5232 Villigen PSI, Switzerland

emiliano.campitelli@psi.ch

2) Fusion Technology–Materials, CRPP - EPFL

Association EURATOM-Confederation Suisse

5232 Villigen PSI, Switzerland

ABSTRACT

Based upon DIN standard tensile tests and three different kinds of non-standard mechanical tests, finite element models were validated and the constitutive behavior for reactor-irradiated zircaloy cladding tubes and proton irradiated tempered martensitic steels was assessed. These tests are the curved longitudinal tensile test, the ring tensile test and the small ball punch test. The mechanical tests were carried out on unirradiated material in order to determine the constitutive behavior for this condition first. In the case of zircaloy, the optimal sets of plastic anisotropy parameters were also determined. The constitutive behaviors that we use for the simulations are based upon a phenomenological description of the dislocation structure evolution with strain, characterized by key parameters like the dislocation mean free path and the dislocation annihilation distance for instance. Due to limitations on the dose to personnel, only small ball punch tests were chosen and employed for testing the irradiated zircaloy and steels. The evaluation of the evolution of the critical parameters of the constitutive behavior after irradiation is discussed in the light of the changes observed on the experimental and corresponding simulated punch test curves.

1. Introduction, recount of previous work.

In a previous paper [1] we have completed the experimental validation of a finite element model (FEM) for small ball punch test experiments (SBPT). The purpose of such a validation was to show the viability of making an assessment on the mechanical constitutive behaviour of isotropic metals by employing SBPT experimental data. In particular, we have shown to what an extent the constitutive parameters that describe the flow properties, such as the yield stress and the strain hardening capacity (*plastic option* in the FEM) govern the shape of the SBPT force-deflection curves (f-d). We have also analysed the effect on these curves of other model parameters as the sample thickness and the sample-ball interaction surface friction coefficient. From the practical point of view, the small volume of SBPT samples together with other experimental aspects, allow testing of irradiated material under fulfilment of very constringent radiation protection standards. The purpose of the present work is twofold: First, to expand the model capability and the experimental validation, so as to take into account the effects of possible anisotropic flow properties of the sample metal. This is done in order to allow us dealing with a metal such as Zircaloy. Second, to make an assessment regarding the effect that neutron irradiation has on changing the yield stress of Zircaloy. In an expanded version of this manuscript we will also present results on the assessment of irradiation hardening for tempered martensitic steels and for the validation via FEM of other non-standard mechanical tests.

2. Assessment of the mechanical anisotropy of Zircaloy, FEM implementation.

The root of the anisotropic behavior in Zircaloy and other HCP based alloys is a combination of facts of the deformation at the single crystal as well as at the polycrystal level [2]. In this work we have modeled the plastic flow of Zircaloy using the Hill anisotropic yield function [Hill] (*potential option* in the FEM). The finite element model thus, contains as a description of the flow properties, two kinds of parameters: On one hand, the plastic option as used previously for isotropic materials [1], and on the other hand a set of "anisotropic yield stress ratios", $R_{11}$and R_{22}, which measure the ratio of yield stress in a direction perpendicular to the sample disc surface and another direction on the plane of the disc respectively, with respect to the yield stress used in the *plastic option*. Comparison of experimental and calculated curves for the unirradiated condition (next section) leads to $R_{11} = 1.1$ and $R_{22} = 1.22$ as the best matching (entry C on Fig.1 below)

3. Assessment of the irradiation hardening of Zircaloy.

The Zircaloy material used in this work consists exclusively of cladding material. Samples were punch tested in the reference, unirradiated condition as well as neutron irradiated at ~280 °C after 3 cycles in service at LWR. The total estimated dose is ~10 dpa [3]. The irradiated samples posses no tracks of fission products (no alpha contamination) and only a very low activity remains from a Tin isotope. As they were

obtained from the central portion of the cladding wall thickness, they contain no hydrides. The assessment provided on the yield stress increase is then exclusively an effect of irradiation. Fig. 1 shows an experimental curve for irradiated Zircaloy, the unirradiated is included for comparison. The higher force levels are an indication of increased yield stress. We can estimate this increase using the validated rule [1] for estimating it from the proportionality with the load level previously defined as P_y. From figure 1 we obtain for P_y 45 N and 80 N for the unirradiated and irradiated Zircaloy respectively (sample thickness is the same in both cases). We must have then, an approximate increase of yield stress by a factor (80/45) ≅ 1.77. As the unirradiated yield stress was measured to be 388 MPa, we obtain ~688 ± 20 MPa for the irradiated condition, that is, an increase of ~300 MPa induced by irradiation. After introducing this modification in the plastic option, the calculated f-d curve reproduces well the experimental one (up to maximum load) as we expected.

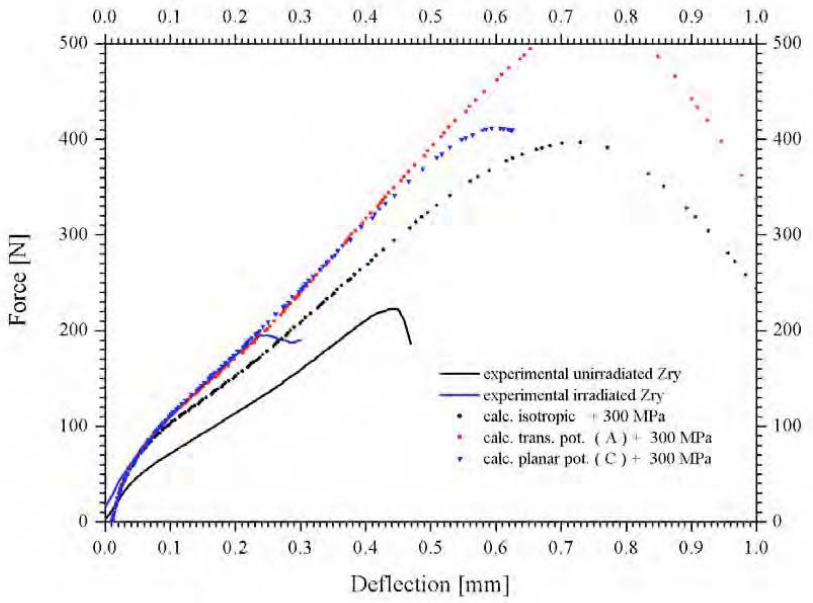

Figure 1: Assessment of the yield stress increase in Zircaloy after neutron irradiation at LWR.

4. References

[1] E. Campitelli et. al., **"Assessment of constitutive properties from small ball punch test: Experiment and modeling"**, accepted for publication in Journal of Nuclear Materials.

[2] E. Tenckhoff, **"Deformation mechanisms, texture, and anisotropy in Zircaloy"**, ASTM (STP 966), 1988.

[3] C. Lemaignan, A. T. Motta, **"Zirconium alloys in Nuclear Applications"**, Materials Science and Technology, Volume 10 B (1993), Nuclear Materials Part II.

Shape Change Studies of BCC Single Crystals Using a Non-Contact Image Correlation System

J.N. Florando[*], D.H. Lassila[*], M.M. Leblanc[*], G.J. Kay[*], S.A. Perfect[*], A. Arsenlis[*], M. Rhee[*], K.R. Magid[**], E.T. Lilleodden[***], J. W. Morris Jr.[**]

[*]Lawrence Livermore National Laboratory, PO Box 808, Livermore, CA 94551, [+]florando1@llnl.gov, [++]lassila1@llnl.gov, [+++]leblanc2@llnl.gov, [++++]kay1@llnl.gov, [+++++]perfect1@llnl.gov, [++++++]arsenlis1@llnl.gov, [+++++++]rhee1@llnl.gov

[**] Department of Materials Science & Engineering, University of California-Berkeley, Berkeley, CA 94720, [+]kmagid@berkeley.edu, [++]jwmorris@berkeley.edu

[***] Institut für Materialforschung II, Forschungszentrum Karlsruhe, D-76021 Karlsruhe, Germany, Erica.Lilleodden@imf.fzk.de

ABSTRACT

A 3-D image correlation system has been used to study the deformation behavior of high purity molybdenum single crystals. This system, in conjunction with a recently developed experimental apparatus, provides the full field displacement and strain data needed to validate dislocation dynamics simulations. The accuracy of the image correlation system was verified by comparing the results with data taken from conventional strain gage rosettes. In addition, a stress analysis has been performed to examine the non-uniformities in stress. The results of the analysis show that after the sample has been strain 2%, the axial stress in the sample varies by ± 20%.

1. Introduction

With the continuing development of a massively parallel dislocation dynamics simulation to achieve appreciable strains [1], there is a continuing need to develop experiments to validate these simulations. Recently, a "6 Degrees of Freedom" (6 DOF) experiment was developed to validate dislocation dynamics simulations of plastic flow of bcc single crystals up to strains of approximately 1% [2]. This unique experiment essentially imposes a compressive uniaxial stress state on the sample, while allowing the crystal to deform in 3 orthogonal translation directions and 3 rotation/tilt axes. At larger strains (> 2%), the anisotropic nature of slip in single crystals may cause severe shape changes to develop. Traditional strain gages, while accurate, only measure strain at one point, and are limited by the amount of strain they can measure (< 1.5%). Shape changes may also lead to non-uniformities in the applied stress state, making it difficult to directly compare with simulations. Therefore, a full 3-D strain measurement in conjunction with finite element analysis is needed. A commercial 3-D non-contact image correlation system, from Trilion Quality Systems, was used to measure the full-field strains during a 6 DOF experiment on high-purity single crystal molybdenum samples.

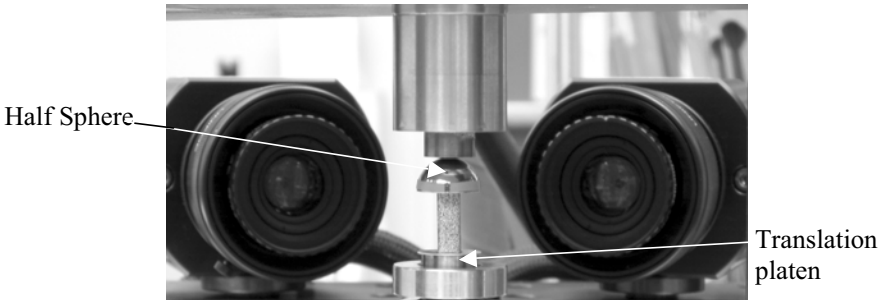

Figure 1-Picture of the large strain testing set-up.

In the 3-D image correlation method, a random speckled pattern is applied to the surface of the sample before deformation. A CCD (charged couple device) camera takes a picture of the sample before and after a given strain amount. The two photos are compared using commercial image correlation software, and the displacements of the spots are measured [3]. Knowledge of the displacements allow for the calculation of the strains. By using 2 cameras/face, the complete 3-D displacement field can be measured and the rigid body motion can be eliminated. A picture of the testing set-up is shown in Fig. 1. The compressive load is applied to a half sphere, which allows the sample to tilt, while the translation platen allows for full range of motion in the x-y plane. Unlike traditional testing techniques, this unique set-up allows essentially unconstrained deformation of the crystal.

2. Results and Discussion

As shown in Fig. 2, an axial strain map can be superimposed onto a picture of the sample. For this example, the global axial strain was 2% and the results show that while most of the sample has uniform strain, there are areas that show differences in strain. For instance, the triangular area of maximum strain that occurs in the middle of the sample corresponds to an area bounded by the crystallographic planes where the maximum slip activity is calculated to have occurred [2]. Fig. 2 also shows the corresponding stress and strain data in comparison with strain gage data. The axial strains for the image correlation experiment are calculated by averaging the strains over an area similar to the active region of a strain gage. The close match between the two experiments verifies the accuracy of the image correlation technique.

Since the sample can distort during the deformation experiment, a detailed FEM analysis has been performed on a deformed sample to examine the non-uniformities in the stress state. Using the FEM package NIKE3D, a mesh was created from the dimensions of the deformed sample and then an elastic load was applied. This analysis gives an approximation of the stress state without having to assume any plasticity laws. The

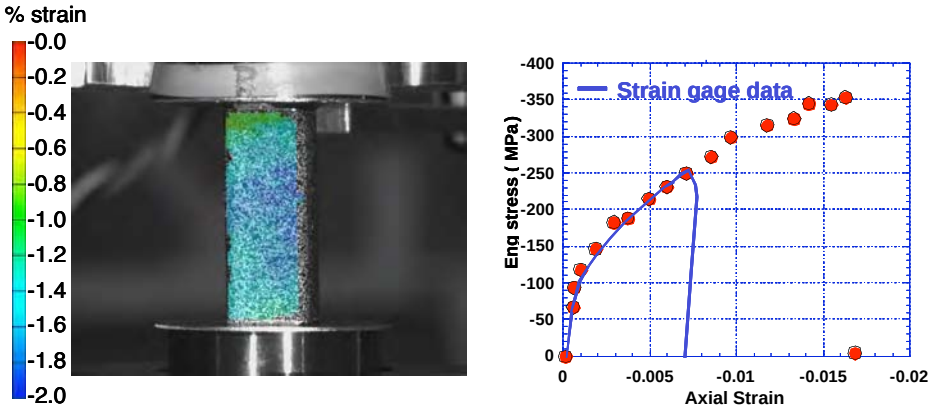

Figure 2- Axial strain results using the image correlation system. The corresponding stress strain curve is shown on the right.

results of the analysis show that at 2% strain the uniaxial stress in a horizontal cut though the center of the sample varies by ± 20%.

3. Conclusions

A commercial image correlation system has been used to examine the deformation response of a molybdenum single crystal to 2% strain. The results show good agreement with previous experiments conducted with strain gages. The image correlation method is also able to examine the full field strains, and areas of high strain correspond to planes of maximum deformation. A stress analysis has also been performed and shows that the due to the distortion of the crystal, the axial stress in the sample varies by ± 20%.

4. Acknowledgments

This work was performed under the auspices of the U.S. Department of Energy by the University of California, Lawrence Livermore National Laboratory under Contract W-7405-Eng-48.

5. References

[1] V.V. Bulatov,"Current Developments and Trends in Dislocation Dynamics" J. Comput-Aided Mat. Design. **9**, 133 (2002).

[2] D.H. Lassila, M.M. Leblanc, and G. J. Kay, "Uniaxial Stress Deformation Experiments for Validation of 3-D Dislocation Dynamics Simulations", J. Eng. Mat. Tech., **124**, 290 (2002).

[3] T. Schmidt, J. Tyson, K. Galanulis, "Full-Field Displacement and Strain Measurement using Advanced 3D Image Correlation Photogrammetry: Part I", Exp. Techniques, **27**, 47 (2003).

Mesoscale Studies of Plastic Deformation in Indented Cu Using Submicron-Resolution 3D X-Ray Microscopy

B. C. Larson[1], Wenge Yang[1], G. M. Pharr[2], J. Z. Tischler[1], and G. E. Ice[2]

[1]Condensed Matter Sciences Division; [2]Metals and Ceramics Division
Oak Ridge National Laboratory, Oak Ridge, TN 37831 bcl@ornl.gov

ABSTRACT

The availability of high-brilliance synchrotron x-ray sources and the development of new microbeam x-ray diffraction techniques now makes investigations of plastic deformation possible with submicron resolution in three-dimensions. Microbeam x-ray measurements of plastic deformation from a spherical indent in dislocation-free Cu single crystals are presented. Observations of indent induced lattice rotations with large rotations and sharply defined microstructural features over length scales of tens of microns underscore the need for advanced modeling techniques to predict deformation microstructure at the mesoscale. Indentation inherently confines the deformation field to volumes that are feasible for both measurements and computations. Thus, direct testing of computer simulations and multi-scale modeling on mesoscopic length scales is now possible in investigations of fundamental aspects of deformation on mesoscopic length scales

1. Introduction

Because of its scientific and technological importance, the prediction of deformation and microstructure evolution has been a central research topic in materials science and mechanics. Although significant progress has been made by conventional crystal plasticity, strain-gradient theories, and discrete dislocation computations, it is not possible to handle deformation and microstructure evolution on mesoscopic length scales (~tenths to hundreds of microns) adequately to be a truly predictive science. The problem is of course exceedingly difficult because of the need to address both the local grain structure and the deformation-induced microstructure. Moreover, the situation has been exacerbated by the fact that nondestructive microstructural measurements with the needed micron or submicron point-to-point resolution have not been available for comparison with simulations and multi-scale modeling.

2. Experimental Methods

Three-dimensional x-ray microscopy measurements were performed using the polychromatic x-ray microbeam diffraction facility of the UNICAT-II beamline at the Advanced Photon Source (APS) at Argonne National Laboratory. Figure 1 shows a schematic view of the recently developed [1] differential-aperture x-ray structural microscopy (DAXM) facility that is capable of performing spatially-resolved measurements of local crystal structure and microstructure. This facility can be used to determine the crystallographic phase, orientation, morphology, and elastic and plastic strain tensors with submicron

point-to-point spatial resolution in single crystals, polycrystals, deformed materials, composites, and functionally graded materials.

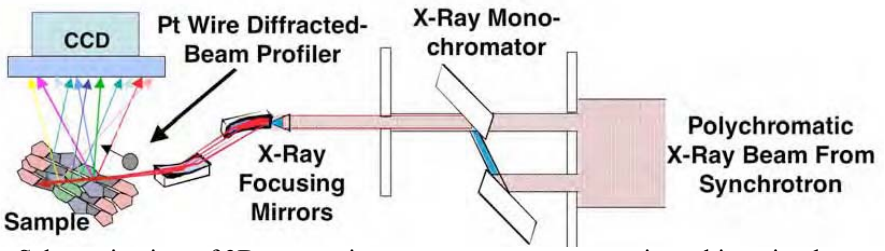

Fig. 1. Schematic view of 3D x-ray microscopy measurements using white microbeams

As described in more detail elsewhere [1-3], a ~0.5 μm diameter polychromatic microbeam that is focused at the sample (~500 μm depth of field) inherently provides spatial resolution in the two dimensions perpendicular to the beam direction. Depth resolution along the beam is more difficult and is obtained by exploiting the fact that polychromatic (i.e. white) x-ray beams produce a full Laue diffraction pattern from every segment of the sample along the beam. The structure, orientation, and elastic and plastic strain tensors from each position along the beam are determined after differential-aperture depth profiling of the diffraction patterns; that is, (1) taking submicron steps of the (knife-edge) Pt wire profiler, (2) collecting CCD diffraction pattern images after each step, (3) subtracting and collating images, and (4) computer reconstructing scattering from each micron. This provides full diffraction patterns from ~0.5x0.5x1 μm^3 voxels along the beam [1-3]. The diffraction patterns are computer indexed to obtain local orientations with ~0.01 degrees angular resolution and least-squares analyzed to obtain ~10^{-4} resolution elastic strain tensors. The local orientation measurements also provide a measure of continuous rotation gradients, making it possible to determine local plastic deformation and dislocation tensors [4] with submicron spatial resolution.

Nondestructive measurements of the local deformation under a (69 μm radius; 100 mN) spherical indent in Cu were made using the geometry shown in Fig. 2. The position of the indent tip (dotted outline), the distorted lattice planes, and the probing microbeam are illustrated. Depth resolving the scattered x-ray Laue Bragg reflections provides a direct measure of the rotation angles along the microbeam, from which local the orientation gradients and plastic deformation are obtained.

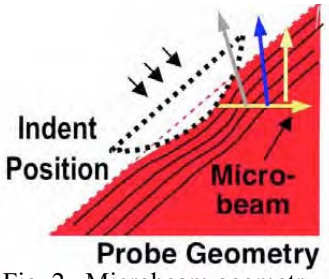

Fig. 2. Microbeam geometry

3. Results and Discussion

Figure 3 is a composite-view demonstration of the depth-resolved Laue pattern method for nondestructive measurements of local lattice orientations. Panel (a) is a magnified view of the (hhh) reflection of the full Laue pattern in panel (b), where each reflection is

streaked by plastic deformation. Panel (c) is an enlarged view of a micron-by-micron depth-resolved (111) pole corresponding to (a), where "s" denotes the surface position and "X" represents the undistorted orientation deep in the crystal along the microbeam. Note the sharp changes in rotation direction and the non-uniform angular spacing. Panel (d) shows the nominal rotation directions as a function of depth, a log-plot of the magnitudes of the misorientation/micron along the beam, and the relative position of the x-ray microbeam within the indent crater. We note highly heterogeneous rotations and the presence of lattice curvatures ranging from ~0.02 to 1 degree per μm along the beam in (d). Rotation gradients along a single direction are not sufficient to specify the deformation; however, a 2D array of such depth-resolved measurements spanning the indent region will provide a measure of the full 3D deformation distribution. *The 3D spatial distribution of local orientations and their gradients then produces a direct, micron resolution connection with computer simulations and multi-scale modeling for deformations on the mesoscale under well-defined boundary conditions.*

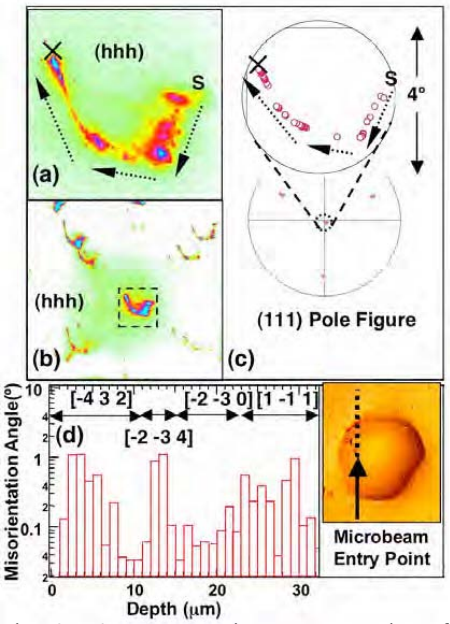

Fig. 3. 3D x-ray microscopy probe of spherical indent induced lattice rotations in Cu. Depth resolution of white beam Laue patterns (a), (b) yield depth depenent pole figure (c) and micron step misorientations (d).

Acknowledgements: Work at the APS supported by the DOE Office of Science, DMS under contract with ORNL, managed by UT-Battelle, LLC; UNICAT is supported by UIUC, ORNL, NIST and UOP Res., Inc.; the APS is supported by DOE

References

1. B. C. Larson, W. Yang, G. E. Ice, J. D. Budai, and J. Z. Tischler, "Three-Dimensional X-Ray Structural Microscopy With Submicron Resolution," *Nature* **415**, 887 (2002).
2. W. Yang, B.C. Larson, J.Z. Tischler, G.E. Ice, J.D. Budai and W. Liu, "Differential-Aperture X-Ray Structural Microscopy: A Submicron-Resolution Three-Dimensional Probe of Local Microstructure and Strain," *Micron* **35**, 431 (2004).
3. W. Yang, B.C. Larson, G.M. Pharr, G.E. Ice, J.D. Budai, J.Z. Tischler and W. Liu,"Deformation Microstructure Under Microindents in Single-Crystal Cu Using 3D X-Ray Structural Microscopy," *J. of Mat. Res.* **19**, 66 (2004).
4. Anter El-Azab, "Statistical Mechanics Treatment of the Evolution of Dislocation Distributions in Single Crystals," *Phys. Rev.* B **61**,11956 (2000).

Precipitation-Induced Hardening Of Thermally Aged Fe-Cu Alloys: A Multiscale Modelling Study And Its Experimental Validation.

K. Verheyen[1], A. Almazouzi[1], L. Malerba[1], C. Domain[2], J. Kuriplach[3], S. van Petegem[4]

[1] SCK•CEN, Department RMO, Boeretang 200, B-2400 Mol (Belgium), kverheye@sckcen.be, aalmazou@sckcen.be, lmalerba@sckcen.be
[2] EDF – R&D, Les Renardières, Dpt MMC, F-77250 Moret sur Loing, France, christophe.domain@edf.fr
[3] Dept. of Low Temperature Physics, Charles University, V Holesovickach 2, CZ-18000 Prague, Czech Republic, honzakr@mbox.troja.mff.cuni.cz
[4] NUM/ASQ, Paul Scherrer Institut, CH-5232 Villigen PSI, Switzerland, steven.vanpetegem@psi.ch

ABSTRACT

Cu precipitation in Fe-1%wtCu specimens aged at 500°C from few minutes to hours was characterised using positron annihilation (PA) and small-angle neutron scattering (SANS). Transmission electron microscopy (TEM) examinations were started and hardness measurements and tensile tests were performed. The ageing process was simulated by atomistic kinetic Monte Carlo (AKMC) and the results favourably compared with SANS data on mean size. By coupling AKMC distributions to positron response calculations the specific positron trapping rate of Cu precipitates was deduced. Finally, a line-tension computational model, describing the motion of a dislocation in an array of precipitates, reasonably reproduced the experimental hardening data.

1. Introduction

The aim of multiscale-modelling is to describe phenomena occurring in materials, from the atomic-level to their macroscopic consequences, linking suitable computational tools. Dedicated experiments must be designed to validate the model, which in turn should help interpret experimental results. Here, precipitation-induced hardening after thermal-ageing of Fe-Cu alloys is studied explicitly with a view to testing the possible interplay between simulation and experiments, for a better understanding of materials behaviour.

2. Experimental

A binary Fe-1wt%Cu alloy containing less than 20 ppm interstitial impurity was prepared by vacuum melting. After solution annealing, specimens were thermally aged at 500°C for times from 10 min to a few hours. After each aging time the specimens were analysed

using PA (coincidence Doppler broadening) and SANS. Also hardness and tensile tests were performed, while some specimens were observed by TEM.
Cu atoms are known to have high affinity to positrons, for which they constitute local traps [1]. Thus, PA can detect the presence and growth of Cu-precipitates, in terms of signal ratio to pure Fe. In the as-quenched and 10-min-aged sample this ratio is close to 1: the influence of Cu clusters is weak. After 90 min a clear signal reveals that positrons are predominantly trapped by Cu-precipitates. After 180 min the positron signal saturates: the ratio curve coincides with that for pure Cu and all positrons annihilate at Cu-precipitates.
SANS can characterise Cu precipitation in terms of size-distribution and density [2], but is only sensitive to sufficiently large precipitates. Thus, for ageing times < 180 min most precipitates were too small and had a too low volume fraction to be seen by SANS, although PA clearly shows their existence. However, in the 90-min-aged samples a small volume fraction (0.022%) of fairly large precipitates (~20 nm) was detected, whose existence is supported by TEM observations. From 180 min onwards, a clear bimodal distribution was found, dominated by small precipitates with a size of a few nm.

3. AKMC simulations versus experiments

AKMC simulations are based on the idea of diffusion events through vacancy jump on a rigid lattice. The corresponding jump frequencies are computed according to a simple energetic model [3], using an interatomic potential [4] for total energy calculations. The results of the AKMC simulations of Cu precipitation in terms of mean precipitate size are compared with SANS results in Fig.1.

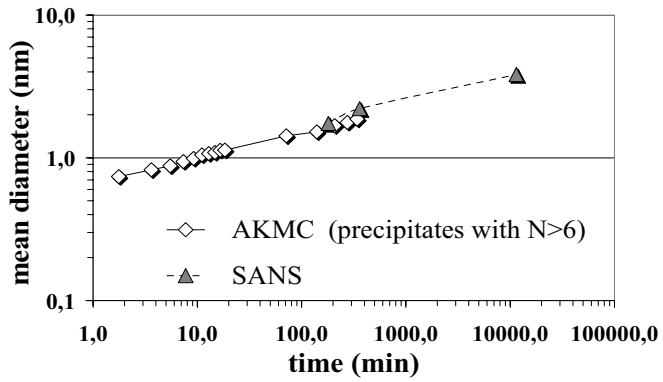

Fig.1 – Precipitate mean diameter vs ageing time in simulation and SANS.

Box size limitations prevent AKMC from simulating a bimodal distribution, but it has been checked that the model can properly reproduce copper diffusion and solubility limit in bcc iron. If only precipitates containing more than 6 elements (which are present already in the initial, as-quenched, random Cu distribution) are counted, the simulated mean size is in good agreement with SANS data.

4. Specific trapping rate to Cu precipitates

The positron specific trapping rate (STR) is so far not known for Cu-precipitates in Fe but it is an essential positron quantity, whose knowledge allows the precipitate concentration to be deduced from PA studies. Based on AKMC simulations the dependence of the positron response on the precipitate size was calculated [5]. By comparing calculated and measured response, the STR to Cu precipitates is determined. In general, the obtained STR is at least one order of magnitude lower than that for vacancy clusters in Fe.

5. Hardening

Hardening predictions were made with a line tension code [5] using as input the defect distribution from AKMC simulation. Fig.2 shows a fairly favourable comparison between simulation results and experimental measurement of yield strength increase.

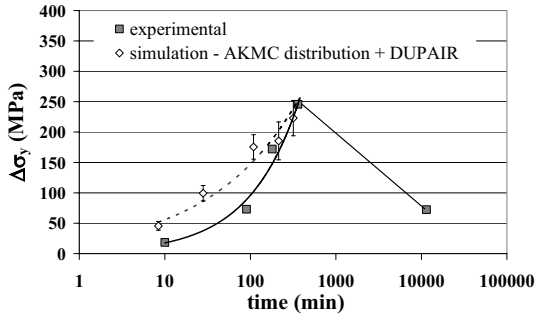

Fig.2 – Comparison between experimental and simulated hardening.

References

[1] Y. Nagai, M. Hasegawa, Z. Tang, A. Hempel, K. Yubuta, T. Shimamura, Y. Kawazoe, A. Kawai and F. Kano, Phys. Rev. B 61 (2000) 6574.

[2] J. T. Buswell, W. J. Phythian, R. J. McElroy, S. Dumbill, P. H. N. Ray, J. Mace and R. N. Sinclair, J. Nuc. Mat. 225 (1995) 196

[3] C. Domain, C.S. Becquart and J.-C. van Duysen, MRS Symp. Proc., vol. 650**,** G. E. Lucas, L. L. Snead, M. A. Kirk Jr. and R. G. Elliman Eds, R3.25.

[4] M. Ludwig, D. Farkas, D. Pedraza and S.Schmauder, Modelling Simul. Mater. Sci. Eng. 6 (1998) 19-28.

[5] J. Kuriplach, F. Becvar, J. Cizek and I. Prochazka, Mater. Sci. Forum, 445-446 (2004) 132-134.

[6] C. Domain, L. Malerba, G. Monnet, K. Verheyen, S. Jumel and J.-C. van Duysen, "DUPAIR: a line tension model for a first assessment and interpretation of radiation-induced hardening experiments", this conference.

Effect of Obstacle Size on the Collapse of SFT by Interaction with Gliding Dislocations

Y. Matsukawa, Yu N. Osetsky, R.E. Stoller and S.J. Zinkle

Metals and Ceramics Division, Oak Ridge National Laboratory,

P.O. Box 2008, TN 37831-6138, U.S.A., E-mail: ym2@ornl.gov

ABSTRACT

The effect of SFT size on the collapse of SFTs in gold during interaction with gliding dislocations was examined by TEM *in-situ* straining experiments. Small SFTs (~9nm edge length) were more resistant to collapse by gliding dislocations than large SFTs which were in the energetically-metastable size range (> ~23nm) [1]. Large SFTs (~27nm) collapsed when intersected by a gliding dislocation near the base triangle, but never when intersected near the apex. However, small SFTs did not collapse even after multiple dislocations intersected near the base triangle. The variation of atom configuration induced by intersection with dislocations was examined by considering Burgers vectors of intersecting dislocations. Energetically unfavorable overlapping atom configuration inevitably appeared at I-ledge by intersection with perfect dislocations, which is a conceivable driving force for the SFT collapse. The speculations derived from this geometry consideration were in qualitatively good agreement with the features of SFT collapse confirmed in experiments, including SFT size effect.

Introduction

The stacking fault tetrahedron (SFT) is a common vacancy cluster produced by neutron irradiation in many fcc metals. Hence, interaction of SFTs with gliding dislocations is currently of particular interest in nuclear materials research, in relation to both irradiation-induced hardening and ductility reduction [2]. Nevertheless, the process of SFT-dislocation interaction still remains unclear. This is mainly due to the complicated crystallographic geometry of SFT. Computational simulations using molecular dynamics (MD) codes [3-4] and *in-situ* straining experiments using a transmission electron microscope (TEM) [2,5] are currently used to study this topic. Here, we report the results of TEM *in-situ* straining experiments, focusing on the SFT size effect on the collapse of SFT in quenched gold by intersection with gliding dislocations. The SFT size was varied

by changing the anneal and quench conditions.

Large SFT-dislocation Interaction

Fig. 1 shows the interaction between a gliding dislocation and a large SFT, whose size is about 27nm. The SFT collapsed when directly interacted with the dislocation, leaving a small SFT as a remnant of the collapse. The small SFT corresponded to an apex portion of the original SFT, divided by the gliding plane of the dislocation: in other words, only the base portion divided by the intersection annihilated, while the apex portion remained intact [5]. Besides the small SFT, there was another remnant created on the dislocation that collapsed the SFT. The remnant shrunk as the dislocation bowed out, and simultaneously a super jog gradually developed on the dislocation, indicating that the remnant is an aggregate of vacancies formally contained in the base portion of the original SFT. No remarkable super jogs were present on the dislocation at the moment of SFT collapse, indicating that the dislocation did not cross-slip on the SFT but simply cut through it. Assuming that dislocation cross-slip was not involved in the collapse process, this type of SFT collapse may be induced by dislocations irrespective of its type, whether screw or edge [5]. The number of intersections was not the primary factor dominating the collapse: some SFTs collapsed by multiple intersections (maximum number was 3 as far as we clearly confirmed), whereas some collapsed by single intersection. The dislocation collapsing the SFT was a perfect dislocation or a pair of Shockley partials, whose dissociation distance was extremely narrow (less than a few nanometers). An important factor for the SFT collapse was the intersection position: SFT collapse always occurred when intersected at the middle or near the base triangle, but never when intersected near the apex.

Small SFT-dislocation Interaction

Fig. 2 shows the interaction between a pile-up dislocation and a small SFT, whose size is about 9nm. The encircled SFT was completely intersected by the first four dislocations in the pile-up: the first two of four were perfect dislocations, whereas the rest of them were Shockley partials having identical Burgers vector, gliding on adjacent (111) plane, finally resulting in formation of a twin band. Judging from the geometry of interaction, the small SFT was intersected by dislocations near the base triangle; nevertheless the small SFT did not collapse. In order to make more definitive statements, further work is required;

however, the present study clearly indicates that small SFTs are more resistant to collapse than large SFTs.

References

[1] T. Jøssang and J.P. Hirth, *Phil. Mag.* **13**, (1966) 657-670.
[2] S.J. Zinkle et al. *MRS Symp. Proc.* **792**, (2004) R1.1.1-1.1.10.
[3] B.D. Wirth et al. *J. Eng. Mater. Sci. Tech.* **124**, (2000) 329-334.
[4] Yu. N. Osetsky et al. *J. Nucl. Mat.* (2004) in press.
[5] Y. Matsukawa and S.J. Zinkle, *J. Nucl. Mat.* (2004) in press.

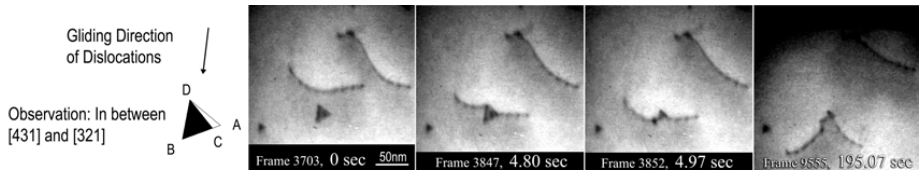

Fig. 1 Large SFT-dislocation interaction: the SFT edge length was 27nm, and the foil thickness was 99nm.

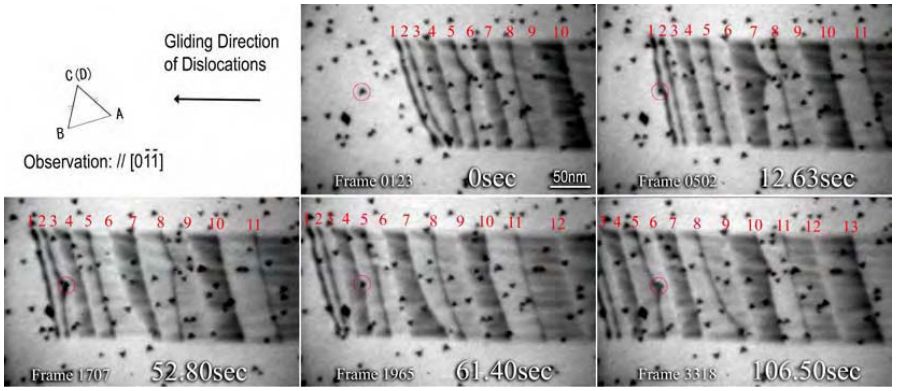

Fig. 2 Small SFT-dislocations interaction: the SFT edge length was 9 nm, and specimen foil thickness was 128 nm.

A Suite of Diffraction Experiments for Measuring Deformation Partitioning in Multiphase Alloys.

Joel V. Bernier, Jun Sang Park and Matthew P. Miller
Sibley School of Mechanical & Aerospace Engineering
Cornell University • Ithaca, NY 14853
mpm4@cornell.edu

ABSTRACT

Diffraction experiments that measure distributions of lattice strains can be employed to better understand the micromechanical state within a deforming multiphase, polycrystalline material. In this work, lattice strains were measured in several iron/copper alloys via sets of in-situ mechanical loading/diffraction experiments. Two suites of experiments were conducted: A set of uniaxial compression/neutron diffraction experiments at the Spectrometer for MAterials Research at Temperature and Stress (SMARTS) facility at the Los Alamos Neutron Science Center (LANSCE), followed by set of uniaxial tension/X-ray diffraction experiments at the A2 experimental station within the Cornell High Energy Synchrotron Source (CHESS). While the strain resolution is higher at SMARTS [1], the increased number of scattering vectors available at CHESS allows for a more complete understanding of the micromechanical state and its evolution with deformation. The pre-yield diffraction moduli observed in both alloys agree well across experiments. Both data sets also show that the crystal strains differ significantly from uniaxial tension as the weaker (Cu) phase begins to yield. These experiments contribute to a material design framework we refer to as the Digital Material. Simulations of the SMARTS experiments via virtual specimens from the Digital Material accurately capture the observed lattice strain evolution.

1. Introduction

Deformation partitioning within a multiphase alloy is a complicated process that depends on the stiffness, strength, volume fraction, orientation distribution and spatial distribution of each constituent phase. The accurate prediction of the behavior of a multiphase system thus depends strongly on the ability to model behaviors on multiple size scales. Even under simple macroscopic loading cases such as uniaxial tension, grains in each phase can be experiencing multiaxial stress states due to complex neighborhood interactions. Lattice strain data from in-situ mechanical loading/diffraction experiments provides 'snapshots' of the micromechanical state; coupled with quantitative microstructural characterization, they are invaluable for motivating and validating models.

This paper describes a set of diffraction experiments designed to measure lattice strains and their evolution under uniaxial deformation in iron/copper alloys. The ultimate goal is the ability to predict aggregate-averaged responses that are critical to materials selection, such as stiffness and strength, by virtual of capturing the proper phase/grain interactions.

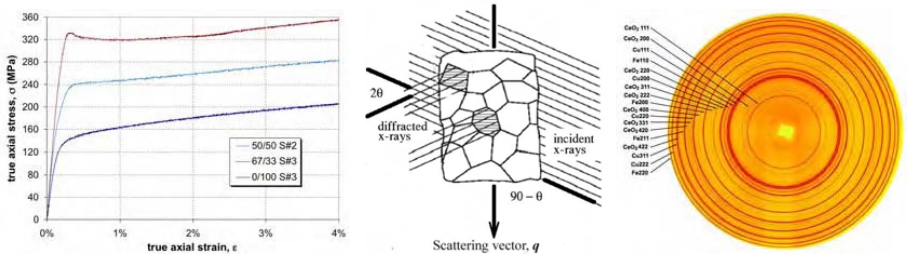

(a) (b) (c)

Figure 1: 1(a) Tensile test data for Fe/Cu alloys. 1(b) Diffraction from a polycrystal. 1(c) Diffraction image of Fe/Cu 50/50 with CeO_2 paste applied for calibration.

2. Material

The accurate measurement of each phases' properties is more easily realized if pure samples of each are available, particularly in terms of analyzing diffraction data. Hence sintered alloys of α-Fe(BCC) and Cu(FCC) powders in volume fractions of 67/33 and 50/50 (Fe/Cu) were chosen as model alloy systems [2]. Advantages include the mutual insolubility of the constituents as well as the well-quantified property differences, the latter of which is evident in Fig. 1(a).

3. In-situ Diffraction Experiments

Diffraction in crystalline solids is fundamentally described by Bragg's law:

$$2d_n \sin\theta_n = \lambda. \tag{1}$$

Diffracted intensity is measured at an angle $2\theta_n$ related to the wavelength λ from the subset of crystals having crystallographic planes $\{hkl\}$ with normal $\boldsymbol{n}$ (and spacing d_n) aligned with the sample direction $\boldsymbol{q}$ (see Fig. 1(b)). The mean plane spacing, $\bar{\boldsymbol{d}}_{\boldsymbol{n}}$, for $\{hkl\}$ in those grains satisfying a particular Bragg condition is the fundamental piece of information available from the diffraction experiment. Given a set of reference plane spacings (usually from an 'unstrained' state), d_n^0, we define the lattice strain for the planes associated with d_n along a particular sample direction $\boldsymbol{q}$ as

$$\varepsilon_{\{hkl\}}(\boldsymbol{q}) \equiv \varepsilon_n(\boldsymbol{q}) = \frac{\bar{d}_n - d_n^0}{d_n^0}, \text{ where } \boldsymbol{n}||\boldsymbol{q}. \tag{2}$$

A distinct advantage of using synchrotron x-rays over neutrons for these experiments is the availability of large, position sensitive area detectors, enabling the collection of data along many $\boldsymbol{q}$ for many $\{hkl\}$ simultaneously (see Fig. 1(c)). By measuring changes in $2\theta_n$ with applied load, we can employ Eqn. 1 along with the detector geometry to calculate $\varepsilon_n(\boldsymbol{q})$ for each $\boldsymbol{q}$, $\{hkl\}$ pair measured in each phase. Fig. 2(a) shows $\varepsilon_n(\boldsymbol{q})$ at specific $\boldsymbol{q}$ for two directions in each phase of Fe/Cu 50/50 at various macroscopic stress levels. The lattice strains are nominally tensile in the loading

direction, changing to compressive in the direction transverse to the loading axis. The strain levels also vary with $\boldsymbol{n}$ in a manner consistent with the the single crystal moduli and yield strengths.

4. Validation of Experiments and Comparison to Simulations

The $\varepsilon_n(\boldsymbol{q})$ data obtained from SMARTS served to validate our experimental method at CHESS. Fig. 2(b) shows $\varepsilon^{Fe}_{[211]}(\boldsymbol{q})$ and $\varepsilon^{Cu}_{[311]}(\boldsymbol{q})$ from both CHESS and SMARTS for $\boldsymbol{q}$ aligned with both the loading and transverse axes. The diffraction moduli compare well across experiments up until the Cu phase begins to yield, after which differences in loading state and sample geometry may dominate.

The diffraction experiments form a critical component in the material design/selection framework we refer to as the Digital Material [3]. Results from the modeling component agree well with the SMARTS data (see Fig. 2(c)). The model captures several important trends in the lattice strain evolution; in particular, the apparent change of the straining direction of the weaker Cu phase.

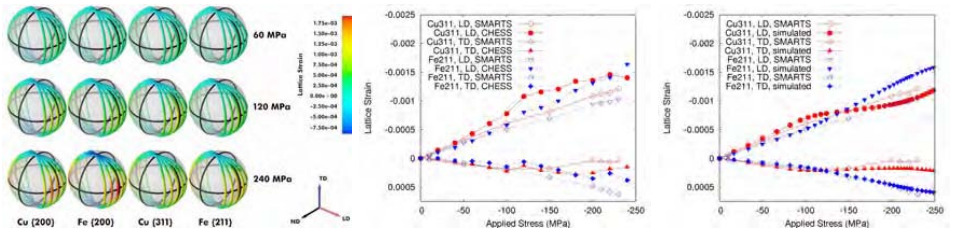

(a) (b) (c)

Figure 2: 2(a) 50/50 LSPFs from CHESS data demonstrating the evolution of $\varepsilon_{\{hkl\}}(\boldsymbol{q})$ with mechanical loading.2(b) Evolution of $\varepsilon_{\{hkl\}}(\boldsymbol{q})$ for Cu{311} and Fe{211} and $\boldsymbol{q}||LD$, $\boldsymbol{q}||TD$ from SMARTS and CHESS. Note that the sign for the applied stress of the CHESS experiments is opposite of that shown. 2(c) Similar comparisons of SMARTS and simulated $\varepsilon_{\{hkl\}}(\boldsymbol{q})$.

5. Acknowledgments

This work was sponsored (in part) by the Air Force Office of Scientific Research, USAF, under grant/contract number F49620-02-1-0047.

References

[1] D. H. Carter and M. A. M. Bourke. Neutron diffraction study of the deformation behavior of beryllium-aluminium composites. *Acta. Mat.*, 31(A):1543–1555, 2000.

[2] B. Commentz, C. Hartig, and H. Mecking. Micromechanical interaction in two-phase iron-copper polycrystals. *Comp. Mat. Sci.*, 6:237–247, 1999.

[3] P. Dawson, M. Miller, T.-S. Han, and J. Bernier. An accelerated methodology for the evaluation of critical properties in polyphase alloys. *Met. Trans.*, in review, 2004.

Analysis of Embedded Nano-clusters by Positron Annihilation Spectroscopy

Yasuyoshi NAGAI[1], Zheng TANG[2] and Masayuki HASEGAWA[1,2]

[1] The Oarai Branch, Institute for Materials Research, Tohoku University Oarai, Ibaraki 311-1313, Japan,
e-mail: nagai@imr.tohoku.ac.jp, hasegawa@imr.tohoku.ac.jp
[2] Institute for Materials Research, Tohoku University, Sendai 980-8577, Japan,
e-mail: tang@imr.tohoku.ac.jp

ABSTRACT

We introduce *positron* as a sensitive probe of embedded nano-clusters. As good examples, bcc Cu clusters in Fe, fcc Zn clusters in Al and AgAl clusters in Al are studied using state-of-the-art positron annihilation techniques, including coincidence Doppler broadening (CDB), two-dimensional angular correlation of positron annihilation radiation (2D-ACAR), positron lifetime and positron age-momentum correlation (AMOC) methods. We show how the atomic and electronic structure of the clusters, solute concentration in the clusters and the size of the clusters are revealed.

1. Introduction

The advantage to use *positron* for analysis of embedded nano clusters originates from its *self-seeking* and *site-selective* behavior. If there are any positron affinitive sites in the material (typically more than a few ten ppm in atomic fraction), thermalized positrons are sensitively trapped at the sites during diffusion. After trapping, they annihilate with one of the electrons around the trapping site. It is well known that vacancy-type defects are the positron affinitive sites. However, they are not the only positron affinitive site. Recently, we have found that some kind of clusters embedded in materials without any

open volume can also trap positrons sensitively [1-4], which extend the applicability of positron annihilation in materials science.

In our talk, we report, as the good examples, the studies of bcc Cu clusters in Fe, fcc Zn clusters in Al and AgAl clusters in Al using CDB, 2D-ACAR, and AMOC methods. The atomic and electronic structure of the clusters, solute concentration in the clusters and size estimation of the clusters are discussed. Because of the limited space for this proceeding paper, here we briefly show the size estimation of the Cu (sub)nano clusters in Fe using 2D-ACAR.

2. Experimental

Electron momentum distribution in nano clusters is different from that in bulk because of the electron localization effect. Especially, the distribution is smeared around the Fermi momentum. The smearing is inversely proportional to the cluster radius [5]. Thus, we can estimate the radius of the clusters by measuring precisely the momentum smearing using 2D-ACAR.

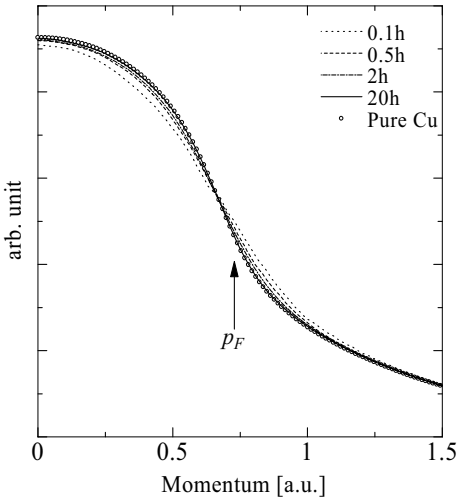

Fig.1: Isotropic component of 2D-ACAR of Cu clusters.

We prepared the Cu nano cluster samples by aging a polycrystalline Fe-1.0wt.%Cu alloy. It was heated to 825ºC and kept 4h, followed by quenching into ice water. Cu atoms were isolated in a supersaturated solid solution in the as-quenched state. The samples were thermally aged at 475ºC for 0.1-20 h after quenching; the Cu atoms are aggregated to clusters in the range from sub nm to few nm.

In the 2D-ACAR spectra, Fe matrix component as well as Cu cluster component is included. We extracted the 2D-ACAR component of the Cu clusters by subtracting the matrix one using the CDB intensities.

3. Results

Figure 1 shows the isotropic component of 2D-ACAR spectra of the Cu clusters.

Clearly, the smearing around the Fermi momentum, p_F, is observed. The relationship between the smearing Δp and the cluster radius r is estimated theoretically as $\Delta p / p_F = 1.13 \times (3/4\pi n)^{1/3} / r$, where n is electron density [5]. Using this equation, we estimated the cluster radius as a function of aging time. The results are shown in Fig.2. For a reference, the cluster radii estimated from 3D-Atom probe (3D-AP) spectroscopy are also shown. The agreement is very good. It should be mentioned that this method using 2D-ACAR can estimate the size of the ultrafine Cu clusters which cannot be observed even by 3D-AP formed in the samples aged for shorter time than 0.5h.

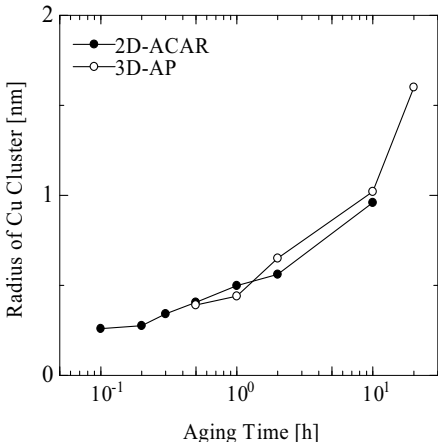

Fig.2: Radius of Cu cluster as a function of aging time for Fe-1.0wt.%Cu alloy.

Acknowledgement

This work is partly supported by Radioactive Waste Management Funding and Research Center, Grant-in-Aid for Scientific Research of the Ministry of Education, Science and Culture (No. 14740199, 15106015 and 15360330) and the REIMEI Research Resources of Japan Atomic Energy Research Institute.

References

[1] M. J. Puska and R. M. Nieminen, "Theory of Positrons in Solids and on Solid Surfaces," Rev. Mod. Phys. 66, 841 (1994).

[2] Y. Nagai et al, "Positron Confinement in Ultrafine Embedded Particles: Quantum-Dot-Like State in an Fe-Cu Alloy," Phys. Rev. B 61, 6574 (2000).

[3] Y. Nagai et al., "Irradiation-Induced Cu Aggregations in Fe: An Origin of Embrittlement of Reactor Pressure Vessel Steels," Phys. Rev. B 63, 134110 (2001).

[4] Y. Nagai et al., "Fermi surface of nanocrystalline embedded particles inn materials: bcc Cu in Fe," Phys. Rev. Lett. 87, 176402 (2001).

[5] R. Sainz et al., "Compton scattering, positron annihilation, and the electron properties of quantum dots," Phys. Rev. B 65, 245310 (2002).

Through Process Modelling of Aluminium Processing for Anisotropic Property Prediction

L. Neumann[1], R. Kopp[1], M. Crumbach[2], M. Goerdeler[2], G. Gottstein[2]

[1] Institut für Bildsame Formgebung, RWTH Aachen University, Intzestr. 10, 52056 Aachen, Germany (e-mail: neumann@ibf.rwth-aachen.de)

[2] Institut für Metallkunde und Metallphysik, RWTH Aachen University, Kopernikusstr. 14, 52056 Aachen, Germany

ABSTRACT

Work has been carried out to link models of the microstructural level to the process level, the latter of which is simulated by means of the finite element method (FEM). One major advantage of physics based microstructure models is the possibility - in principle - to extrapolate beyond the scope of the data used for the fitting of the model. Furthermore, microstructure models use microstructural variables of state for the description of material behaviour making them ideal for multi-stage processing, where the material history plays an important role. The present article shows the production steps of hot and cold rolling. Subsequently, cup-drawing is treated. All steps are simulated numerically and carried out experimentally (for later simulation validation). The modelling set-up consists of a dislocation density based flow-stress model coupled to a full constraints (FC) Taylor texture model. Both run directly coupled to FEM allowing for dislocation density based flow stress prediction in the process level. In the cup-drawing stage, the same modelling set-up includes phenomenological yield-loci for anisotropic flow prediction. The used yield loci can be interactively updated with directional yield stresses delivered by the flow-stress and texture models. The final property predicted is the earing profile. All models and simulation steps will be discussed and compared with experimental results.

1. Introduction

The properties of aluminium sheets are determined by the processing parameters according to which it has been produced. The processing begins by the correct alloying before casting and continues on through the thermo-mechanical processing steps of hot and cold rolling as well as annealing. In the final stage of sheet forming the sheet's flow behaviour is dictated by the properties it has developed during processing and the layout of the sheet metal forming process itself. An overview of all models used in the entire processing chain is given in [1].

2. Models used and how they are coupled

As computational power continues to increase significantly, the use of physical plasticity models has become an option in the simulation of thermo-mechanical processing. Physical plasticity models simulate the processing based on the underlying physical phenomena. A number of such models is implemented into the commercial FEM software LARSTRAN. All relevant data from casting and homogenisation simulations are input to the (hot and cold) rolling and the annealing steps, where hardening, softening, and texture play a predominant role (see Section 2.1). The results of these simulations are, in turn, input to the simulation of sheet forming, where focus is put on the prediction of plastic anisotropy (see Section 2.2). The evolution of the latter is also regarded. The coupling of all models is depicted in Fig. 1 and has been previously presented [2,3].

2.1 Hardening, softening, and deformation texture

During hot and cold rolling the FEM-package delivers the incremental displacement gradient of an element to a full-constraints Taylor model [4]. This is done if the element's summed up strain for the calculated increment(s) has reached a preset value (usually of 0.02). The setting of such a value avoids starting the (computationally intensive) texture module for an element which is not in the forming zone. The texture module then calculates the new orientation distribution for the element and passes the Taylor factor on to the dislocation density based flow stress model (three-internal-variable model or 3IVM [5,6]). Taking previous values of dislocation density populations as well as the temperature, strain, and strain rate into account, 3IVM returns a value of the flow stress to the FEM-package. The new orientation distribution, the values of dislocation densities, and the Taylor factor are stored as well, thus accounting for the element's processing history.

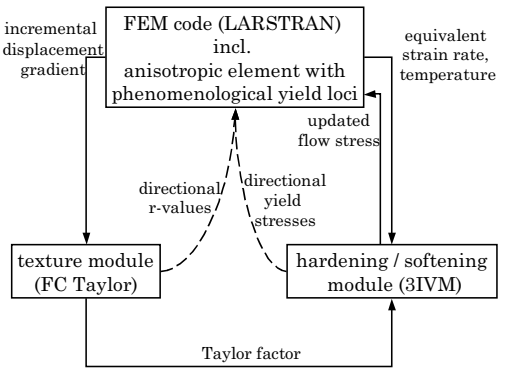

Figure 1: Flow chart showing the coupling of texture and work hardening modules in FEM (solid lines) as well as anisotropy update (dashed lines).

2.2 Plastic anisotropy

The anisotropic FEM formulation presented in [3] was used here. The microstructure modules 3IVM and texture can be used for online calculation of directional yield stresses for each finite element. These values are then used as parameters for a Hill48 [7] yield surface.

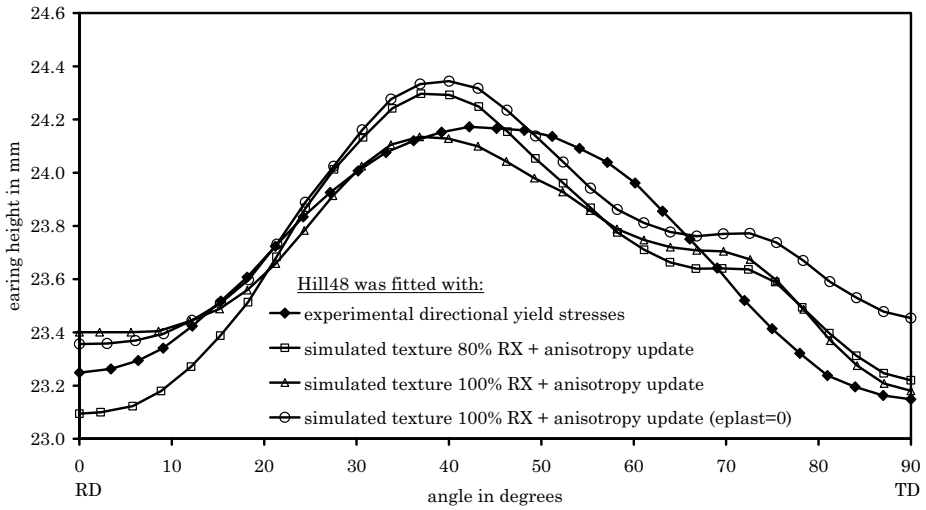

Figure 2: Earing profiles for current coupling strategy with experimentally determined yield stresses (no anisotropy update) and different simulation settings for cup drawing with anisotropy update. ('eplast' refers to the value of summed up strain ε_{plast} that must be reached before texture simulation and anisotropy update are called.)

Most recent results of earing profiles as simulated are shown in Fig. 2. Agreement of the earing prediction using anisotropy update with the experimentally calibrated yield locus is satisfactory. The saddle point in the profile is an unwanted effect of the coupling strategy and subject of ongoing research.

Acknowledgements

The authors gratefully acknowledge the financial support of the Deutsche Forschungsgemeinschaft (DFG) within the Collaborative Research Centre (Sonderforschungsbereich) 370 'Integral Materials Modelling'.

References

[1] L. Neumann, R. Kopp, A. Ludwig, M. Wu, A. Bührig-Polaczek, M. Schneider, M. Crumbach, G. Gottstein, Modelling Simul. Mater. Sci. Eng. 12 (2004) S19.
[2] L. Neumann, H. Aretz, R. Kopp, M. Goerdeler, M. Crumbach, G. Gottstein, Z. Metallkd. 94 (2003) 5.
[3] L. Neumann, H. Aretz, R. Kopp, M. Crumbach, M. Goerdeler, G. Gottstein, AIP Conf. Proc. 712, 388 (2004).
[4] G.I. Taylor, J. Inst. Met. 62 (1938) 307.
[5] F. Roters, D. Raabe, G. Gottstein, Acta Mater. 48 (2000) 4181.
[6] M. Goerdeler, M. Crumbach, M. Schneider, G. Gottstein, L. Neumann, H. Aretz, R. Kopp, Dislocation density based modeling of work hardening in the context of integrative modeling of aluminum processing, Materials Science and Engineering A, In Press.
[7] R. Hill, The Mathematical Theory of Plasticity, Oxford University Press (1950) 318.

Comparison of Mesoscale Finite Element Deformation Modeling With Measurements Using X-Ray Microscopy*

G.B. Sarma[1], B. Radhakrishnan[1], J.W.L. Pang[2], and G.E. Ice[2]

[1]Computer Science and Mathematics Division
[2]Metals and Ceramics Division
Oak Ridge National Laboratory
Oak Ridge, TN 37831-6008

ABSTRACT

The deformation of a nickel bi-crystal in uniaxial tension is simulated using a mesoscale finite element model, and the results are compared with corresponding experiments. The simulations make use of crystal plasticity to model the material constitutive response, and discretization of the bi-crystal with a large number of elements to capture the heterogeneous deformation of each grain. The simulations predict changes in the local orientation of each crystal during deformation, and the results are compared with experimental measurements of grain reorientations. The measurements are made using a polychromatic three-dimensional X-ray microscope, which provides in-situ spatially resolved orientation data at the sub-micron scale in individual grains during deformation of polycrystalline samples. Such detailed comparisons provide a valuable means to evaluate the capability of the crystal plasticity based finite element simulations to model the heterogeneous microstructure evolution during deformation of polycrystalline materials.

1. Introduction

It is well known that the deformation of metals, while seemingly homogeneous at the continuum scale, is an inherently heterogeneous process at the scale of individual grains. The variations in deformation among different grains are strongly influenced by the crystallographic orientations of the grains. Modeling the deformation of metals at the mesoscale has been accomplished in recent years by combining the explicit discretization of the microstructure using the finite element method with crystal plasticity theory to incorporate the anisotropy in the material constitutive response based on the crystal orientation [1]. In this paper we apply mesoscale finite element simulations to the deformation of a nickel bi-crystal in uniaxial tension, and compare the model predictions with corresponding experimental measurements of grain orientations made using a polychromatic three-dimensional X-ray microscope [2].

---

2. Mesoscale Simulations and Experimental Measurements

The finite element discretization consisted of 80×20×20 hexahedral elements, with each crystal comprised of 40 elements along the direction of extension (x-axis). Material parameters for the crystal plasticity model were obtained by fitting a polycrystal model based on the Taylor mean field assumption to the stress-strain response for nickel. Initial orientations with appropriate spread in the two grains were assigned based on experimental data. The measurements were carried out using a polychromatic X-ray beam, and depth resolution was achieved using the differential aperture microscopy method developed by Larson et al. [2].

3. Results

The finite element mesh after deformation under uniaxial tension to a strain of 8% is shown in Fig. 1, along with the contours of the misorientation angle. The misorientation has been calculated for each element relative to its initial orientation, and therefore represents the change in orientation during deformation. It is evident from both the mesh distortion and the misorientation values that grain A has accommodated a larger share of the overall strain, with higher misorientation and greater heterogeneity, while grain B has deformed in more uniform fashion with relatively smaller change in orientation, as also seen from the deformed sample shown in Fig.1.

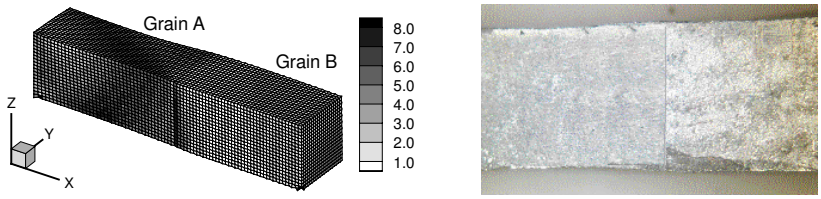

Figure 1: Deformed mesh showing misorientation in [°] from the initial orientation (left) and deformed sample from the experiment (right).

The experimental measurements of orientation after 8% tensile strain were taken at three locations along the z-axis at the grain boundary, and at distances of 5 and 10 μm from the grain boundary along the tensile axis in each grain. At each location, orientation data were measured at 1 μm intervals along the y-axis up to depths of 38 μm (or roughly halfway) into the sample. Results are presented as misorientation values calculated relative to the first orientation measured along the scan direction. Figure 2 shows the misorientations in grain A for points A-1 and A-2. Since the crystal plasticity model used in the simulations does not have an inherent length scale, the corresponding results from the mesoscale model are shown for elements at different distances from the grain boundary, at x=21, 36, 39 and 40, at z=10 for grain A. Since grain A is composed of 40 elements along the x-axis, x=21 is roughly halfway from the grain boundary to the end, and corresponds to a point in the grain interior, while x=40 is right next to the boundary. The experimental data show slightly higher misorientations developing at A-2, which is

closer to the grain boundary, compared to A-1, although the difference in the range of values is not very large. The model predictions show a similar range of misorientations, especially through element 10 which is halfway into the sample, although locations closer to and further away from the grain boundary do not show much difference in the values.

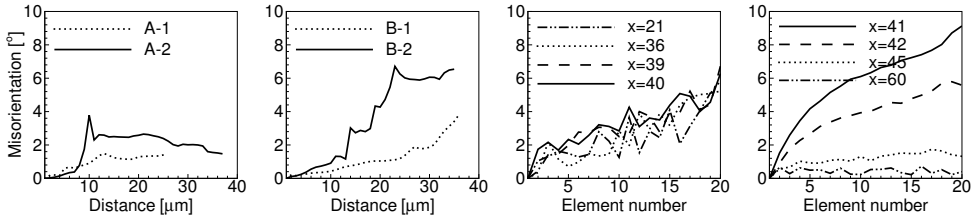

Figure 2: Misorientations along the scan direction relative to the first orientation from experiments (two left figures) and simulations (two right figures) for grains A and B.

Similar results on misorientation values are also shown in Fig. 2 for grain B. In this case, unlike for grain A, there is a larger difference in the misorientation values at the two locations, with the values at B-2, which is closer to the grain boundary, being much higher than the values at B-1. The simulation results in this case show a similar trend of higher misorientations closer to the grain boundary (x=41, 42) and much lower values further away (x=45, 60). The results indicate that the grain boundary has a stronger influence on the deformation of grain B than on grain A.

Comparisons of misorientation values along the scan lines in the two grains show that the model predictions match both the range and the overall trends in the experimental data. Further work is required in terms of measurements at more locations and at greater distances from the boundary, as well as more detailed modeling with higher mesh resolution near the grain boundary to capture the sharp orientation gradients as in grain B, to enable more meaningful comparisons between the simulations and the experiments.

Acknowledgements

This research was sponsored by the Division of Materials Sciences and Engineering, U.S. Department of Energy, and used resources of the Center for Computational Sciences at Oak Ridge National Laboratory, which is supported by the Office of Science of the U.S. Department of Energy, under contract DE-AC05-00OR22725 with UT-Battelle, LLC.

References

1. G.B. Sarma *et al*., "Mesoscale Modeling of Microstructure and Texture Evolution During Deformation Processing of Metals," Adv. Eng. Mater., **4**, 509 (2002).
2. B.C. Larson *et al*., "Three-Dimensional X-Ray Structural Microscopy With Submicrometre Resolution," Nature, **415**, 887 (2002).

Three-dimensional atom-probe microscopy and the temporal evolution of microstructures

Chantal K. Sudbrack[1], Kevin E. Yoon[1], Ronald D. Noebe[2], and David N. Seidman[1†]

[1]Northwestern University, Dept. of Materials Science & Engineering; 2220 Campus Drive; Evanston, IL 60208-3108 USA [2]NASA John H. Glenn Research Center; 21000 Brookpark Road; Cleveland, OH 44135 USA [†] d-seidman@northwestern.edu

ABSTRACT

The temporal evolution of the early to the later stages of precipitation of ordered γ'-precipitates ($L1_2$) in Ni-5.2 Al-14.2 Cr at.% are studied at 873 K. Precipitates with sub-nanometer radii are characterized completely by three-dimensional atom-probe (3DAP) microscopy. Contrary to what is often assumed by theory or in models, the average precipitate composition is shown to evolve with time, such that solute concentrations decrease toward an equilibrium value given by the solvus lines. Power-law time dependencies of the number density, mean radius, and supersaturations of Al and Cr are presented and discussed.

1. Introduction

The precipitation of γ'-phase from a supersaturated solution (γ) in a temperature range where nucleation and growth are observable has been studied in Ni-Al alloys by direct imaging techniques [1,2]. In the present investigation, 3DAP microscopy is employed to characterize the identical, ternary alloy, Ni-5.2 Al-14.2 Cr at.%, aged at 873 K, as studied by references [3,4]. 3DAP microscopy allows the direct, spatial characterization of the chemical composition on a sub-nano- to nanometer scale via the reconstruction of a volume of material, typically 10^5 nm^3 and 10^7 nm^3 for the conventional 3DAP and the local electrode atom-probe (*LEAP*) [5] microscopes, respectively. The experimental procedures are described in [6].

2. Results and Discussion

After homogenization, Ni-5.2 Al-14.2 Cr at.% decomposes at 873 K into a high number density, N_v, of nanometer-sized, spheroidal γ'-precipitates. The lattice parameter misfit between the γ (f.c.c.) and γ' ($L1_2$) phases is 0.11 % [6], and the precipitates are coherent and spheroidal up to 1024 h [6]. The γ'-precipitation is first observed after 0.17 h of aging and the precipitates' average radius, $\langle R \rangle$, and volume fraction, $V_f^{\gamma'}$, are determined to be 0.74 nm and 0.11 %, as shown in Fig. 1. A sharp increase in N_v at a constant $\langle R \rangle$ value is observed between 0.17 and 0.25 h aging times, indicating that

nucleation predominates. 3DAP microscopy detects precipitates as small as $\langle R \rangle$ = 0.45 nm (20 atoms). After 0.25 h and until 256 h, precipitate coalescence is observed, as seen for 4 h in Fig. 2. Given the precipitate radii and small lattice parameter misfit, this is not believed to be a result of elastically driven particle migration, and marks the finest scale, as well as smallest $V_f^{\gamma'}$, where this phenomenon has been observed in the solid state. Peak N_v, (3.2 ± 0.6) x 10^{24} m^{-3}, is achieved after 4 h of aging, after which the transformation enters a quasi steady-state regime with a constant power-law dependence of $t^{-0.64\pm0.06}$. In this regime, $V_f^{\gamma'}$ steadily increases (*upper panel* in Fig. 1), indicating that the transformation is not complete, yet $\langle R \rangle$ has a temporal dependence of 0.30 ± 0.04, which is approximately consistent with the $t^{1/3}$ prediction for the coarsening of a ternary alloy.

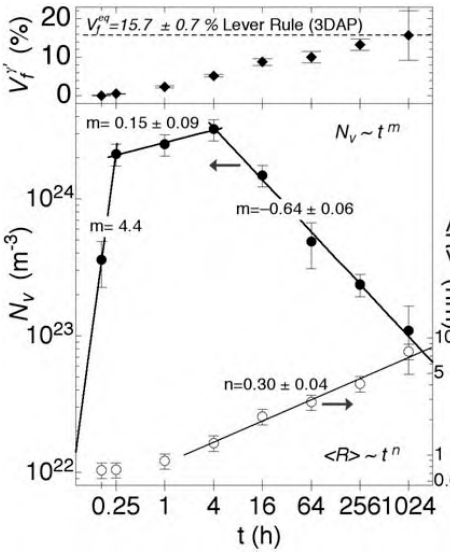

Figure 1. The temporal evolution of the γ'-precipitate volume fraction ($V_f^{\gamma'}$), number density (N_v), and average radius ($\langle R \rangle$) in Ni-5.2 Al-14.2 Cr at.% aged at 873 K.

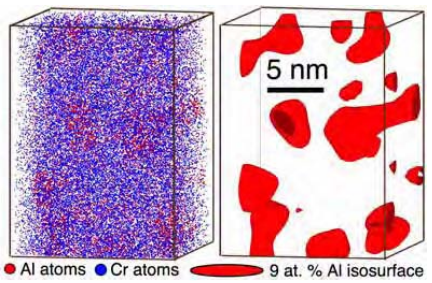

Figure 2. 15x15x20 nm^3 subset of a 3DAP microscope reconstructed volume of Ni-5.2 Al-14.2 Cr at.% aged at 873 K for 4 h (Ni atoms omitted). 30 % of the γ'-precipitates are coalesced.

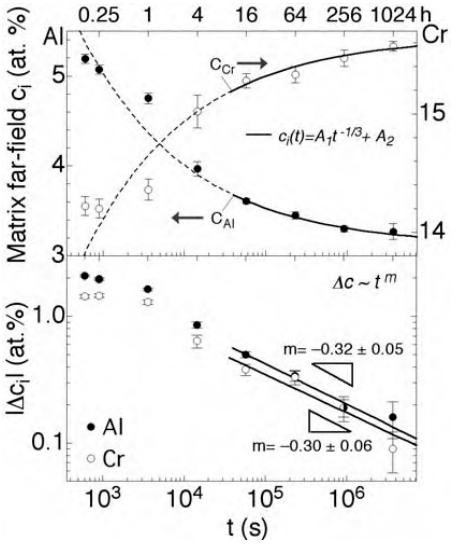

Figure 3. The average far-field concentrations and supersaturation in the matrix obtained by 3DAP microscopy in Ni-5.2 Al-14.2 Cr at.% aged at 873 K.

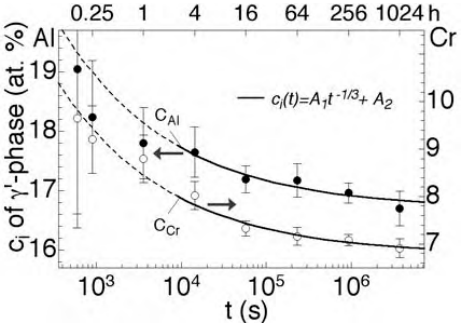

Figure 4. Average composition in the precipitates' interiors obtained by 3DAP microscopy in Ni-5.2 Al-14.2 Cr at.% aged at 873 K.

The average compositions of the γ (Fig. 3) and γ'-precipitates (Fig. 4) continually evolve temporally. The matrix becomes more enriched in Ni and Cr and depleted in Al with time. Between 4 and 16 h, the solute far-field concentrations change slowly (dc/dt → 0), and the quasi-stationary approximation can be applied after 16 h. Assuming this approximation, Marquis and Seidman [7] recently determined the solid solubilities, c_i^{eq}, in a ternary alloy. They applied $c_i(t) = \kappa t^{-1/3} + c_i^{eq}$ to fit the experimental data. Employing their approach c_i^{eq} are 16.69 ± 0.22 at.% for Al and 6.77 ± 0.15 at.% for Cr. Straightforwardly, the matrix supersaturations, $\Delta c_i = c_i(t) - c_i^{eq}$, are determined (Fig. 3). Their temporal behavior is in approximate agreement with the prediction of $\Delta c \sim t^{-1/3}$ for coarsening in a ternary alloy [8,9]. The classical theory of nucleation and growth assumes that the precipitates' composition is at their equilibrium value at the reaction's onset. Contrary to this assumption, it is found that the precipitates are highly saturated with Al (19.1 ± 2.8 at.%) and Cr (9.7 ± 2.1 at.%) at t = 0.17 h, and continuously decrease to 16.70 ± 0.29 at.% Al and 6.91 ± 0.20 at.% Cr at 1024 h. With the evolving composition, a $c_i(t) = \kappa t^{-1/3} + c_i^{eq}$ law fits the experimental data (Fig. 4) for the γ'-precipitates. This fit yields equilibrium values of 3.11 ± 0.05 at.% for Al and 15.66 ± 0.05 at.% for Cr. Utilizing the lever rule, the equilibrium $V_f^{\gamma'}$ is determined to be 15.7 ± 0.7 %

3. Acknowledgements

This research was sponsored by the National Science Foundation under grant DMR-0241928. C. K. Sudbrack and K. E. Yoon received partial support from NSF and NASA graduate research fellowships, respectively. We also would like to extend our gratitude to Dr. T. F. Kelly for use of Imago Scientific Instruments' LEAP™ microscope.

4. References

[1] H. Wendt and P. Haasen, Acta Metall. **31,** 1649 (1983).
[2] S. Q. Xiao and P. Haasen, Acta Metall. **39**, 651 (1991).
[3] C. Schmuck, P. Caron, A. Hauet, and D. Blavette, Phil. Mag. A **76**, 527 (1997).
[4] C. Pareige, F. Soisson, G. Martin, and D. Blavette, Acta Mater. **47**, 1889 (1999).
[5] T. F. Kelly, P. P. Camus, D. J. Larson, L. M. Holzman, and S. S. Bajikav, Ultramicroscopy, **62**, 29 (1996); T. F. Kelly et al., Microsc. Microanal. **10**, 373-383 (2004).
[6] C. K. Sudbrack, Ph.D. Thesis, Northwestern University, 2004.
[7] E. A. Marquis and D. N. Seidman, to be submitted to Acta Mater., 2004.; E. A. Marquis, Ph.D. Thesis, Northwestern University, 2002.
[8] A. Umantsev and G. B. Olson, Scripta Mater. ??
[9] C. Kuehmann and P. W. Voorhees, Metall. Trans. Mater. A ???

Nano Cu Precipitation in Pressure Vessel Steel of Nuclear Power Reactor Studied by Positron Annihilation and 3D Atom Probe

Takeshi TOYAMA [1], Yasuyoshi NAGAI [1], Yutaka NISHIYAMA [2], Masahide SUZUKI [2], Tadakatsu OHKUBO [3], Kazuhiro HONO [3], Masayuki HASEGAWA [1].

[1] The Oarai Center, Institute for Materials Research, Tohoku University, Oarai, Ibaraki 311-1313, Japan.
[2] Japan Atomic Energy Research Institute, Tokai, Ibaraki 319-1195, Japan.
[3] National Institute for Materials Science, 1-2-1 Sengen, Tsukuba, Ibaraki 305-0047, Japan.

ABSTRACT

We have investigated the effects of neutron irradiation flux on the embrittlement mechanisms of RPV steels of a British Calder Hall-type (CH) reactor in Japan using positron annihilation and three-dimensional atom probe. It is found that the Cu precipitation is enhanced by the low flux irradiation in CH reactor and gives rise to the embrittlement. On the contrary, after the high flux irradiation in a materials testing reactor, the usual irradiation-induced defects are formed to cause almost the same strengthening as that for the CH reactor irradiation, but no Cu precipitation is observed.

1. Introduction

The embrittlement of the nuclear reactor pressure vessel (RPV) steels is one of the most important topical issues in the safe operation of commercial nuclear power plants. The microscopic mechanisms of irradiation-induced embrittlement of RPV steels have been studied by the accelerated tests with material testing reactors (MTRs), where the irradiation flux is at least two orders higher than those for the commercial nuclear reactors (BWR and PWR). However, the details of the flux effects for the embrittlement mechanisms have not been clarified yet. In particular, it has been pointed out that the Cu precipitation, which is one of the main reasons of the embrittlement, is enhanced even by very low flux irradiation, but no clear evidence for it is reported.

In this work, we investigate the microscopic mechanisms of embrittlement for the surveillance specimens of a British Calder Hall-type (CH) reactor in Japan, and for the same material irradiated with almost four orders of magnitude higher flux in a Japan

Materials Testing Reactor (JMTR). We have employed positron annihilation techniques (Coincidence Doppler Broadening: CDB and positron lifetime) for observation of both Cu nano-precipitates and vacancy-type defects, and three-dimensional atom probe (3D-AP) for elemental mapping of alloying species.

2. Experimental

The chemical composition of the RPV specimens, Al-killed C-Mn steel [1], is listed in Table 1. The irradiation conditions are shown in Table 2.

The details of the CDB measurement are described in ref. [2]. The CDB ratio spectrum shown as Fig.1 was obtained by normalizing the momentum distribution of each spectrum to that of the well annealed (defect-free) pure Fe. Positron lifetime measurements were carried out using a conventional fast-fast spectrometer with a time resolution of 190 ps (FWHM). The 3D-AP measurements were performed with an energy compensated 3D-AP system at ~60K, under vacuum of ~1×10^{-7} Pa.

Table1: Chemical composition of the specimens of C-Mn steel (wt.%).

C	Si	Mn	P	S	Ni	Cr	Cu	Mo	Al	N
0.10	0.23	1.1	0.014	0.015	0.17	0.096	0.14-0.19	0.054	0.027	0.0060

Table2: Irradiation conditions.

Irradiation	Fluence (n/cm^2)	Flux (n/cm^2-s)	Irradiation Period	Temperature (ºC)
Calder Hall Reactor	2.7×10^{17}	4.2×10^{8}	20 y	240
JMTR	2.2×10^{18}	3.6×10^{12}	7 d	220

3. Results and Discussion

Fig.1 shows CDB ratio spectra. For the surveillance specimen of the CH reactor, a broad peak around 24×10^{-3} m_0c, where c is the speed of light and m_0 is the rest mass of electron, is clearly observed, whereas the spectrum for the unirradiated specimen shows no broad peak. The broad peak is the characteristic of Cu 3d electrons and shows the formation of Cu nano precipitates [3, 4]. A positron lifetime spectrum for the surveillance specimen demonstrates only one lifetime component of 120 ps, close to that of bulk Fe or Cu, showing almost no vacancy-type defects. Thus, the embrittlement in the CH surveillance specimen is due to the enhanced Cu nano-precipitation.

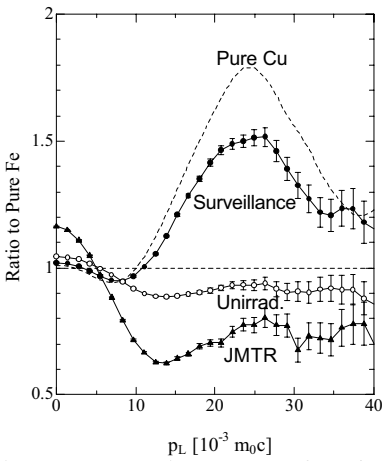

Fig.1: CDB ratio spectra for the irradiated and unirradiated specimens.

On the other hand, the spectrum for the JMTR specimen in Fig.1 exhibits an enhancement in the low momentum region ($p_L < 5\times10^{-3}m_0c$) together with a dehancement at high momentum ($p_L > 10\times10^{-3}m_0c$). This is specific feature of positron trapping at vacancy-type defects [3]. The positron lifetime spectrum is decomposed into two components; the longer one (t_2) is 176 ps (I_2 = 82%) and shorter one (t_1) is 20 ps. The value of 176 ps corresponds to the positron lifetime in monovacancies in Fe. Thus, the matrix defects, such as vacancy-type defects and dislocation loops, cause the embrittlement in the JMTR specimen and give almost the same strengthening as that of the CH surveillance specimen.

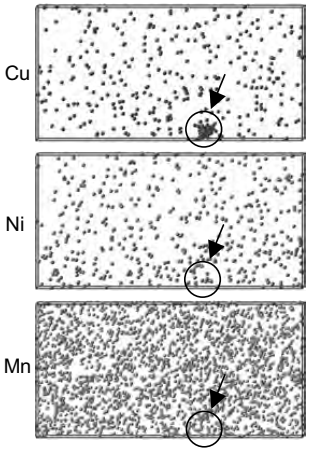

Fig.2: 3D-AP elemental maps for the surveillance specimen (~10×10×20 nm).

The Cu nano-precipitation in the surveillance specimen are also observed by 3D-AP (Fig.2) which exhibits elemental maps of Cu, Ni and Mn. Clearly there is no enrichment of Ni and Mn in the Cu precipitate. We have also examined the JMTR specimen for ~15×15×300 nm region. However, no precipitate has been observed, which supports the CDB result.

In conclusion, very low flux irradiation for 20 years in the British Calder Hall-type reactor induced the Cu nano-precipitates but no vacancy-type defects in the RPV surveillance specimen. On the contrary, after accelerated irradiation with the higher flux for 7 days in JMTR, we observed only vacancies but no Cu nano-precipitates.

Acknowledgement

This work is partly supported by Radioactive Waste Management Funding and Research Center, Grant-in-Aid for Scientific Research of the Ministry of Education, Science and Culture (No. 14740199, 15106015 and 15360330) and the REIMEI Research Resources of Japan Atomic Energy Research Institute.

References

[1] M. Suzuki et al., Effects of Radiation on Materials: 18th International Symposium, ASTM STP 1325, 379 (1999).

[2] For Example, P. Asoka-Kumar et al., “Increased Elemental Specificity of Positron Annihilation Spectra”, Phys. Rev. Lett. 77, 2097 (1996).

[3] Y. Nagai et al., “Irradiation-Induced Cu Aggregations in Fe: An Origin of Embrittlement of Reactor Pressure Vessel Steels”, Phys. Rev. B 63, 134110 (2001).

[4] Z. Tang et al., “First-principles calculation of coincidence Doppler broadening of positron annihilation radiation”, Phys. Rev. B 65, 045108 (2002).

Understanding mechanical coupling via nanomechanical contact

K.J. Van Vliet[a], T. Zhu[b], J. Li[d], S. Suresh[a] and S.Yip[a,c]

[a]Dept of Materials Science & Engineering, MIT, Room 8-237, 77 Massachusetts Avenue, Cambridge, MA 02139. krystyn@mit.edu
[b]Dept of Mechanical Engineering & [c]Dept of Nuclear Engineering, MIT
[d]Dept of Materials Science & Engineering, Ohio State University

ABSTRACT

Local mechanical deformation can be used to induce critical changes in the structure of materials, thereby coupling the mechanical state to the functional behavior and properties of the macrostructure. By investigating such processes at the length and force scales of atomistic/molecular deformation, we can understand the physical basis of such mechanical coupling. This knowledge can be applied toward both the prevention of undesirable material changes –such as the uncontrolled nucleation of defects in an electromechancial structure –and the exploi tation of mechanical coupling for sensing, actuating, and transduction of mechanical signals –such as in the evolution of phenotype in living cells. Here, we discuss the development of an atomistic defect nucleation criterion, through the use of nanomechanical experiments, simple models, and sophisticated simulations, and what this tells us about the integrity and performance of evershrinking films and lines in integrated circuits. We also discuss how nanoscale mechanical stimuli can be used to induce and to measure changes in cell structure and function, particularly in the context of endothelial cells that line capillary blood vessels.

1. Introduction

There now exists a range of experimental tools which enable mechanical probing of material structures and processes defined by length scales of 10^{-9} m. This capability has created unprecedented opportunities to develop computational tools and simulations that capture with high fidelity the atomistic and molecular mechanisms that control deformation at microscopic and macroscopic length scales. Here, we present two collaborative efforts that highlight our investigation of mechanically coupled instabilities. First, we summarize the development and implications of atomic-scale prediction of defect nucleation in metallic crystals. Second, we demonstrate application of these approaches in biological problems including mechanical control of phenotype and identification of molecular receptors on living mammalian cells.

2. Nanomechanical instabilities in metallic crystals

Several researchers have established that face-centered cubic (FCC) metallic crystals including Au, Al, and Cu exhibit discrete bursts of deformation at GPa-level stresses when subjected to nanoindentation via a rigid probe of ~100 nm radius [1]. This experimental phenomenon may be attributed to dislocation nucleation within the bulk, and thus present an opportunity to observe and model homogeneous nucleation of crystalline defects. The soap bubble raft of FCC crystals developed by Bragg et al. [2] is a simple two-dimensional (2D) model of this experiment, and confirms that dislocation nucleation indeed occurs within the bulk in the absence of surface tractions.

Motivated by these observations, a continuum-level analytical model of elastic instability was extended to the atomic-scale [3]. According to this model, elastic wave amplitude is nonlinear and unbounded, and thus a crystalline defect is nucleated, when:

$$\Lambda_{min} = \min(C_{ijkl} w_i w_k + \tau_{jl}) k_j k_l \leq 0 \qquad (1)$$

where $\boldsymbol{w}$ and $\boldsymbol{k}$ are unit vectors equivalent to the slip direction and slip plane normal, respectively, $\underline{\underline{\boldsymbol{C}}}$ are the elastic moduli, and $\underline{\boldsymbol{\tau}}$ is the Cauchy-Born stress component. By defining the defect nucleation criterion with reference to $\boldsymbol{\tau}$, this criterion can be validated at both the atomistic level through direct molecular dynamics simulations for which $\underline{\underline{\boldsymbol{C}}}$ can be computed locally and at the continuum level where the Cauchy-Born hypothesis of affine deformation is assumed. This criterion has been validated in both 2D and 3D, and predicts the site and slip character of homogeneously nucleated defects more accurately than does the position of maximum shear stress [4]. Extension of this combined experiment/simulation approach to elastic instability has also shown (1) that there is a critical average grain size d_c on the order of 10 nm in FCC metals, such that polycrystals of $d < d_c$ exhibit a reduction in resistance to plastic deformation [5] as grain size decreases; and (2) that the yield strength of nanoscaled FCC metal lines decreases with decreasing aspect ratio due to the relaxation provided by the migration of dislocations to line sidewalls [6].

3. Nanomechanical instabilities in living biological cells

Biological systems such as cells and molecules can be investigated through similar experimental approaches, in that the length scale relevant to biological processes in these structures ranges 10^{-6}–10^{-9} m [7]. In these material systems, there is significant coupling between the mechanical and structural/functional states—a reality which motivates and complicates understanding of biological mechanisms. For example, it is known that mechanical force such as fluid shear flow causes microvascular endothelial cells that line capillaries to align in the direction of flow. Here, we show that cyclic deformation of endothelial cells, representing super-physiological stress concentrations (e.g., due to

tumor encroachment) induces reorganization of cell populations from a single layer into capillary tube-like structures [8]. Multiscale modeling of such large-scale changes in cells is one focus of computational biology. Further, we show that the presence and function of molecules on the cell surface can be identified through nanomechanical measurement of rupture forces between molecules, but that the extent to which these forces are unique to given molecular pairs remains an open and important question which multiscale simulations will help to answer.

4. Conclusions

Here, we demonstrate nanomechanical experimental approaches that can guide and validate computational modeling of discrete changes in material structure and function. These general methods impose deformation through localized mechanical contact, and quantify resulting changes in local stiffness in applications ranging from dislocation nucleation in crystals to molecular receptor identification in living biological cells. By coupling these experimental approaches with simulations ranging from the atomistic/molecular to continuum levels, we can better understand the mechanisms of these fundamental material transformation processes.

References

1. J.D. Kiely and J.E. Houston. Nanomechanical properties of Au (111), (001), and (110) surfaces. Phys. Rev. B. **57**, 12 588 (1998).
2. L. Bragg, W. M. Lomer and J.F. Nye, Experiments with the bubble model of a metal structure, 17-minute MS movie (originally 16mm), producer N. S. Marqueen (1954).
3. J. Li, K.J. Van Vliet, T. Zhu, S. Yip and S. Suresh. Atomistic mechanisms governing elastic limit and incipient plasticity in crystals. Nature **418** 307 (2002).
4. K.J. Van Vliet, J. Li, T. Zhu, S. Yip and S. Suresh. Quantifying the early stages of plasticity through nanoscale experiments and simulations, Phys. Rev. B **67**, 104 105 (2003).
5. S. Yip. Mapping plasticity, Nature Mat. **3**, 11 (2004).
6. Y. Choi, K.J. Van Vliet, J. Li and S. Suresh. Size effects on the onset of plastic deformation during nanoindentation of thin films and patterened lines, J. Appl. Phys. **94**, 6050 (2003).
7. K.J. Van Vliet, G. Bao and S. Suresh. The biomechanics toolbox: experimental approaches for living cells and biomolecules, Acta Mater. **51**, 5881 (2003).
8. A. Shukla, A.R. Dunn, M.A. Moses and K.J. Van Vliet. Endothelial cells as mechanical transducers: Enzymatic activity and network formation under cyclic strain. (2004, submitted).

Symposium – 5

Multiscale Modeling of Biomaterials

On Multiscale Approach to Modeling Biological Patterns

M. Alber and R. Chaturvedi

Department of Mathematics and Interdisciplinary Center for the study of Biocomplexity, University of Notre Dame, Notre Dame, IN 46556. Email: malber@nd.edu, rchaturv@nd.edu

ABSTRACT

A three-dimensional (3D), hybrid, multiscale model framework is presented for modeling biological pattern formation. The general approach is demonstrated for vertebrate skeletogenesis in the limb.

1. Introduction

We present a *3D* multiscale framework for modeling *morphogenesis* (structural development of an organism or its organs) during embryonic development in vertebrates. At subcellular and molecular scales, morphogenetic molecules are secreted, diffuse and interact. At cellular scale, morphogenesis involves cell growth, proliferation, differentiation, migration and death. At larger scales, bulk changes in tissue shapes produce dramatic patterns of tissues and organs. Genes specify products necessary for morphogenesis. Experiments suggest that *TGF-beta* and *fibronectin* are key molecules in vertebrate limb skeletogenesis. Initial multipotent stem cells diversify into distinct specialized *differentiation types* of the developed organism. We use the specific example of *chondrogenesis* (cartilage development) of vertebrate limb, where a sequence of cartilage elements forms in proximo-distal sequence.

2. Physical and mathematical submodels and their integration

CPM framework for modeling cellular and tissue scales: Adhesive interactions between cells allow cells to form stable clumps. Combined with cell motility, this causes different types of cells to sort into clusters of like type due to their different adhesivity [1]. CPM, our framework for modeling cells and their dynamics, describes cell behaviors using an effective energy, E, comprised of real (*e.g.*, cell-cell adhesion) and effective (*e.g.*, cell response to chemical gradient) energies and constraints [2]. CPM uses a lattice to describe cells. A cell is a set of discrete components (lattice sites) that can rearrange, resulting in cell shape changes and motions. Extra Cellular Matrix (ECM) is modeled as a generalized cell of distinct type. A phenomenological parameter drives cell-membrane fluctuations. Proposed changes in lattice configuration are accepted based on changes in E.

$$E = E_{contact} + E_{volume} + E_{chemical}. \qquad (1)$$

$E_{contact}$ describes the net adhesion between two cell membranes. A cell of type τ has a prescribed target volume and surface area. E_{volume} implements an energy penalty for deviations from targets. Actual volume and surface area fluctuate due to changes in osmotic pressure, pseudopodal motion of cells, growth and division of cells. Cells can respond to chemical signals by moving along concentration gradients. The chemotaxis/haptotaxis model requires a chemical *concentration field*, and an *interface* to connect the field to the CPM framework for cells [2, 3, 4]. Our extensions to CPM also provide for (i) variations in cell adhesivity (ii) cell growth, and (iii) division (*mitosis*).

Reaction-Diffusion equations for modeling molecular scales: Interactions of reacting and diffusing chemicals (at least one autocatalytic *activator* species and one *inhibitor* species which represses the activator) can produce self-organizing instabilities that might explain biological patterning. To model TGF-beta in the limb, we use RD and chemotactic coupling to the cells. Thus, the response of cells to TGF- beta depends on the RD *pre-pattern* of TGF- beta. Details of the RD equations used in limb chondrogenesis are available in [5] and [6].

Production modeling of macromolecular scales of fibronectin: Cells respond to the TGF- beta signal by producing a substratum adhesion molecule (SAM) (identified with fibronectin) and a cell-cell adhesion molecule (CAM) (identified with N-cadherin). We treat SAM as non-diffusing. Cells undergo haptotaxis in the direction of increasing SAM. SAM signal also upregulates cell-cell adhesion, enhancing cell clustering in regions of high SAM. Further, more SAM is secreted within those regions. Although the Turing-instability derived TGF- beta prepattern *initiates* SAM patterning, self-enhancing *positive feedback* of SAM secretion and CAM upregulation cause *subsequent* patterning.

Cell Types and the Type Transition Model: We model the major behavioral groups of cells as cell types and differentiation by a *Type Transition Model* (*TT*). It models regulatory networks by defining the rules governing type change, *e.g.* accounting for the intra- and inter-cellular effects of chemical fields. All cells of a particular differentiation type share a set of parameters describing their state; different cell types (*e.g.*, muscle and bone) have different parameter sets. Genetic and external cues influence both cells' type and state. In the avian limb, initial *precartilage mesenchymal* cell can translocate, divide, and produce various morphogens and ECM molecules. *Apical zone cells* (region extending from the distal end) are in a labile state. Unlike apical zone cells, *active zone cells* (region of condensation next to the distally located apical zone) respond to activator, inhibitor, and SAM. On sensing a threshold concentration of activator, such a cell's type changes to *SAM-producing*, which can upregulate its cell-cell adhesion. Cells that have not experienced threshold levels of activator respond to, but do not produce, SAM.

Integration of submodels at the scale of the organ: We integrate the CPM (stochastic, discrete), RD (continuum, PDEs) and TT (rule based state automaton) submodels while maintaining modularity, *e.g.* by: (i) Matching the spatial grid for the

continuum and stochastic models and (ii) Defining the relative number of iterations for RD and CPM evolvers. SAM and CAM submodels form a positive (upregulatory) feedback loop, providing the *biologically motivated* interface between the RD-based TGF- beta prepattern and the CPM-based cell dynamics. Other sub-modules implement different cell responses, *e.g.*, cell growth and mitosis. Criteria for interfacing various grids and time scales specify simulation protocol. CompuCell web site[1], distributes our Open Source software.

3. Results

The combined behavior of morphogens, cell dynamics and cell differentiation results in a biologically realistic, roughly periodic pattern of the major chondrogenic elements. For a full range of simulations and their discussions, including abnormal development in chicken limb, see [7].

Acknowledgements: We acknowledge support from NSF grant IBN-0083653.

References:

1. Steinberg, M. S., Reconstruction of tissues by dissociated cells, Science 141 (1963) 401-408.
2. Glazier, J. A. and Graner, F., A simulation of the differential adhesion driven rearrangement of biological cells, *Phys. Rev. E* 47 (1993) 2128-2154.
3. Chaturvedi, R., Izaguirre, J. A., Huang, C., Cickovski, T., Virtue, P, Thomas, G., Forgacs, G., Alber, M., Hentschel, G., Newman, S. A., and Glazier, J. A., Computational Science - ICCS 2003: International Conference Melbourne, Australia and St. Petersburg, Russia, June 2-4, 2003. Proceedings, Part III, P. M. A.Sloot, D. Abramson, A. V. Bogdanov, J. J. Dongarra, A. Y. Zomaya and Y. E. Gorbachev editors (LNCS Volume 2659, Springer-Verlag, New York), (2003) 39-49.
4. Izaguirre, J. A., Chaturvedi, R., Huang, C., Cickovski, T., Coffland, J., Thomas, G., Forgacs, G., Alber, M., Hentschel, G., Newman, S. A., and Glazier, J. A., CompuCell, a multi-model framework for simulation of morphogenesis, Bioinformatics 20 (2004) 1129-1137.
5. Alber, M., Glimm, T., Hentschel, H. G. E., Kazmierczak, B. and Newman, S. A., Stability of n-Dimensional Patterns in a Generalized Turing System: Implications for Biological Pattern Formation, to appear in Nonlinearity (2004).
6. Hentschel, H. G. E., Glimm, T., Glazier, J. A., Newman, S. A., Dynamical mechanisms for skeletal pattern formation in the vertebrate limb, to appear in Proceedings R. Soc. Lond: Bio. Sciences (2004).
7. Chaturvedi, R., Huang, C., Kazmierczak, B., Schneider, T., Izaguirre, J. A., Glimm, T., Hentschel, H. G. E., Newman, S. A., and Glazier, J. A., Alber, M., On multiscale approaches to 3-dimensional modeling of morphogenesis, submitted (2004).

[1] http://www.nd.edu/~lcls/compucell

Substructured Multibody Molecular Dynamics

Paul S. Crozier, Richard B. Lehoucq, Steven J. Plimpton, and Mark J. Stevens

Computational Materials and Molecular Biology Dept., Sandia National Laboratories, Albuquerque, NM 87185-0310, e-mail: pscrozi@sandia.gov

ABSTRACT

We are developing a substructured, multibody, molecular dynamics (SMMD) simulation framework [1] for multiscale modeling of materials and molecular biology systems. This simulation capability will give insights into the operation of large complex bio- and nano-systems. For example, the number of atoms in a motor protein is too large and the dynamics too slow for study by atomistic molecular dynamics (MD). However, large parts of the motor protein move as fairly rigid bodies linked by flexible connections. The SMMD method decomposes the protein complex into atomistic, flexible-body, and rigid-body regions, depending on each region's relevant internal motion. This allows the use of conventional atomistic force fields while gaining tremendous speedup by freezing non-essential degrees of freedom. We are building this SMMD simulation capability into our parallel MD code, LAMMPS, with the goal of enabling multiscale simulation on time scales that are currently beyond the capability of all-atom MD. Our ongoing efforts in implementation and testing of implicit solvent methods and development of a robust procedure for automatic substructure specification will widen the appeal of SMMD for multiscale modeling of materials and molecular biology systems.

1. Introduction

Molecular machines continue to be a critical component in the expanding and increasingly overlapping fields of nanoscience and molecular biology. Simulation methods are essential for gaining an understanding of how molecular machines work and how to manipulate and control them in nanodevices. However, currently available methods for the simulation of molecular machines have timescale limitations. For example, motor proteins such as kinesin are fundamental mechanical parts of cells and are something that researchers in nanotechnology would like to mimic and/or manipulate. The simulation of motor proteins, which are extremely large (e.g. 50,000 atoms), is impractical with present MD methods. There are a myriad of such systems, with motor proteins prototypical examples. Because these systems are typically so large, computing forces between all of the atoms is expensive, and this severely limits the total time span one can treat. Yet, in these large macromolecular assemblies, significant fractions of the atoms do not move independently—they effectively act as rigid bodies. If these parts of the macromolecular system were treated as rigid, the necessary computation for the forces would be greatly reduced and the treatable time span would be expanded commensurately. Molecular machine modelers need to be able to capture the essential

molecular physics through computationally efficient and relatively simple models. Simulations must be able to include seamlessly integrated multigranularity (disparate levels of detail) and the capability to simulate system sizes on the order of 100 nanometers on time scales much longer than currently possible.

2. SMMD Approach

Multibody substructuring allows the simulation of large complex systems using varying degrees of detail, from rigid bodies to atomistic regions, simultaneously where needed in one simulation. Rigid body treatment is useful for the simulation of large parts that move in unison, like those found in motor proteins. This significantly reduces the computational cost. But rigid body treatment inside the framework of atomistic simulation requires an efficient means of defining rigid parts and efficient algorithms for calculating rigid body dynamics. Moreover, the coupling of the dynamics between flexible and rigid parts must be self-consistent. SMMD is an approach that resolves these issues [1]. The SMMD method allows three levels of detail: rigid bodies, flexible bodies, and atomistic regions. Small-scale harmonic vibrations that contribute little to the overall protein dynamics are suppressed, thereby yielding good computational speed-up. Yet the SMMD approach allows dynamic simulation in much the same way as traditional MD simulation, utilizing all-atom force fields, and producing all-atom trajectories. SMMD is not just another sampling scheme, but rather a true energy-conserving dynamics approach to simulation. Substructuring divides the system into regions that are treated independently and then synthesized to provide information for the entire system. Substructuring enables rapid MD simulation with the appropriate degree of detail given to each part of the system under investigation. For example, for regions where little anharmonic motion is expected, or where the motion is unimportant to the phenomena under investigation, the atoms can be lumped together and modeled as rigid bodies. If a modest amount of motion is expected, a particular region is modeled as a flexible body. Regions that contain atoms where key motion occurs are modeled as small rigid bodies or individual atoms. The careful synthesis of the substructures results in an efficient representation of the entire system. The dynamics are simulated using a multiple time stepping scheme in which the high frequency motions in the atomistic regions are advanced on the inner loop, with the slower motions of the flexible and rigid bodies on successive outer loops.

3. SMMD Simulation of RuBisCO

RuBisCO is a molecular machine of great interest to the Genomes to Life (GTL) [2] project. It is the critical enzyme in the carbon fixation process in plants and seawater bacteria which catalyzes the conversion of CO_2 to a 3-carbon organic sugar. Two proteins (RuBisCO large and small) form a complex that creates the catalytic site. Reactants and products diffuse to and from the site by passing through a 3-stage trapdoor formed by specific loops and residues of the surrounding proteins. In solution the

trapdoor opens and closes to regulate the reaction. The majority of the RuBisCO complex serves as a rigid template which gives structure to the active site.

New SMMD features have been added to LAMMPS and enabled us to efficiently simulate a model of "trapdoor" conformational change in the RuBisCO protein. 14,350 atoms of the 14,546-atom RuBisCO complex were frozen, leaving 196 mobile atoms. Using these new features along with replica exchange molecular dynamics, we were then able to simulate trapdoor dynamics for more than a microsecond of total simulation time and observe a partial closing event by the C-terminus chain, the outermost portion of the trapdoor. By contrast, doing full dynamics on a model of the same complex with explicit solvent (52,419 atoms) would have required roughly 4000x more compute time. However, it would be desirable to model RuBisCO more realistically than was done with the simplistic 196 mobile atoms model. For example, the RuBisCO complex described above might be modeled more accurately as a few large rigid sections (free to move with respect to each other), rather than as one frozen mass. We are hopeful that future SMMD development will make this possible.

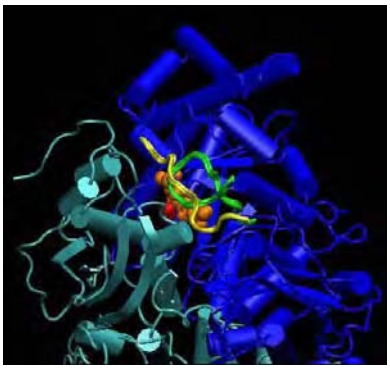

Figure 1. SMMD simulation of two RuBisCO large subunits (blue and cyan) with C-terminus in yellow, loop 6 in green, CO_2 in red, and ribulose-1,5-bisphosphate in orange.

4. Conclusion

The goal of SMMD modeling is to enable biomolecular simulation on time scales not accessible to traditional MD simulation. It is a true multi-scale approach with well-integrated subdomain regions at varying level of detail: atomistic, flexible, and rigid. We are working to make SMMD an efficient easy-to-use tool within the parallel LAMMPS simulation package.

Acknowledgement

Research partly funded by the U.S. Dept. of Energy's Genomes to Life program [3] under project, "Carbon Sequestration in Synechococcus…" [2]. Sandia is a multiprogram laboratory operated by Sandia Corporation, a Lockheed Martin Company for the US DOE's National Nuclear Security Administration under contract DE-AC04-94AL85000.

References

[1] H. M. Chun, et al., "MBO(N)D: A Multibody Method for Long-Time Molecular Dynamics Simulations," *J. Comp. Chem.*, 2000, 21, 159.
[2] http://www.genomes2life.org/
[3] http://www.doegenomestolife.org

Modeling DNA Bubble Formation at the Atomic Scale

Violeta Beleva[1], Kim Rasmussen1[2], and Angel E. Garcia[1,2]
[1]Center for Non Linear Studies (CNLS) and [2]Theoretical Division, T10 MS K710,
Los Alamos National Laboratory, Los Alamos, NM 87545
(axg@lanl.gov)

ABSTRACT

We describe the fluctuations of double stranded DNA molecules using a minimalist Go model over a wide range of temperatures. Minimalist models allow us to describe, at the atomic level, the opening and formation of bubbles in DNA double helices. This model includes all the geometrical constraints in helix melting imposed by the 3D structure of the molecule. The DNA forms melted bubbles within double helices. These bubbles form and break as a function of time. The equilibrium average number of broken base pairs shows a sharp change as a function of T. We observe a temperature profile of sequence dependent bubble formation similar to those measured by Zeng et al. (*1*).

1. Introduction

Long nuclei acid molecules melt partially through the formations of bubbles. It is known that CG rich sequences melt at higher temperatures than AT rich sequences. The melting temperature, however, is not solely determined by the CG content, but by the sequence through base stacking and solvent interactions (*2*). Recently, models that incorporate the sequence and nonlinear dynamics of DNA double strands have shown that DNA exhibits a very rich dynamics (*3*). Recent extensions of the Peyrard-Bishop model show that fluctuations in the DNA structure lead to opening in localized regions, and that these regions in the DNA are associated with transcription initiation sites(*4*). 1D and 2D models of DNA may contain enough information about stacking and base pairing interactions, but lack the coupling between twisting, bending and base pair opening imposed by the double helical structure of DNA that all atom models easily describe. However, the complexity of the energy function used in all atom simulations (including solvent, ions, etc) does not allow for the description of DNA folding/unfolding events that occur in the microsecond time scale.

2. Methods

We have developed an all atom model of DNA that contain these couplings, but with a simplified set of interactions, similar to the Go models used for protein folding (*5, 6*). The Go model defines a minimally frustrated, funnel-like, energy landscape(*7*). We use a minimalist representation of the interaction potential which includes base pairing, screened Coulomb, and stacking interactions. Based on the secondary structure of the native structure (i.e., the folded state), we classify atomic interactions as native, and non native. Native interactions are stacking and hydrogen bond interactions that are present in the folded state. Non native interactions are modeled as excluded volume interactions between all other pair of atoms not interacting in the native state. All atoms in the nucleic acid bases interact with neighboring bases in the sequence, and with the atoms in the neighboring bases of their base pair partners. For example, in the double helix $d[CGCG]_2$

(shown below) we define as native interactions the Watson-Crick hydrogen bond interactions between C1 and G8, G2 and C7, C3 and G6, and G5 and C5. Other base pairs are not considered native. We also define as native stacking interactions between all atoms in the G2 base with atoms in C1, C3, G6, and G8—but not with G4 and C5.

C1 G2 C3 G4
G8 C7 G6 C5

All atoms in the backbone interact via the non native potential, regardless of base pairing. In addition, all pairs of P atoms in the phosphates interact via a screened Coulomb potential, with a screening length, L_D, determined by the Debye-Huckel theory—assuming a homogeneous monovalent salt solution in water. Stacking interactions are modeled by a Lennard Jones potential ($\varepsilon_s[(\sigma/r)^{12} - 2(\sigma/r)^6]$ with σ_s = 3.5 A), hydrogen bonding are modeled by a 10-12 potential ($\varepsilon_{HB}[5(\sigma/r)^{12} - 6(\sigma/r)^{10}]$ with σ_{HB} = 3.0 A), and non native interactions are modeled by a repulsive $\varepsilon_{NN}(\sigma/r)^{12}$, with σ_{NN} = 2.0 A. The native hydrogen bonding, stacking, and non-native parameters are taken to be of order 1, 0.1, and 0.01, respectively, with ε_{HB}/RT_m =1 at 350 K. All bonding interactions are modeled using the Amber united atom force field (*8*). The overall ratio of energy over T is scaled such that we observe a sharp dependence in the opening/closing of base pairs at a fixed T. All calculations are done with a screening length L_D = 10 A. All bonding interactions are modeled using the Amber united atom force field (*8*).

3. Results

To test for the simplified Hamiltonian shown above we model the base pair opening and closing of a 60 base pairs molecule studied by Zeng et al. (*1*). First we determined a set of energy parameters that will show a melting transition at a fixed temperature, T_m= 350 K (Fig. 1). In Fig. 2 we show the dynamics of base pair opening and closing at temperatures below and above the transition T (defined as the T at which half the bases are opened). DNA bubbles are formed at all temperatures, but larger bubbles are formed at higher T.

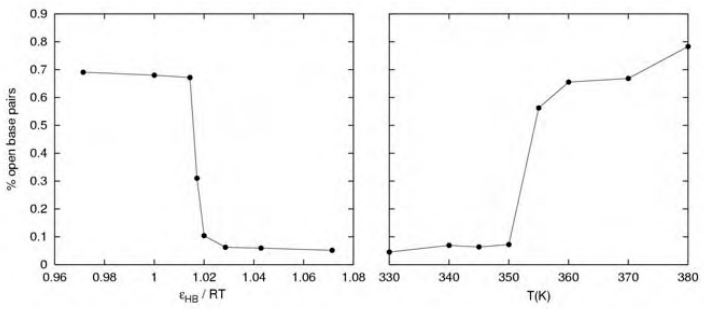

Fig. 1. Fraction of open base pairs as a function of the non-bonding interaction energy ε_{HB}/RT, at a fixed temperature, T=350 K (lhs). The curves are calculated from 20 ns trajectories. Fraction of open base pairs as a function of T, for ε_{HB}/RT =1.02 (rhs).

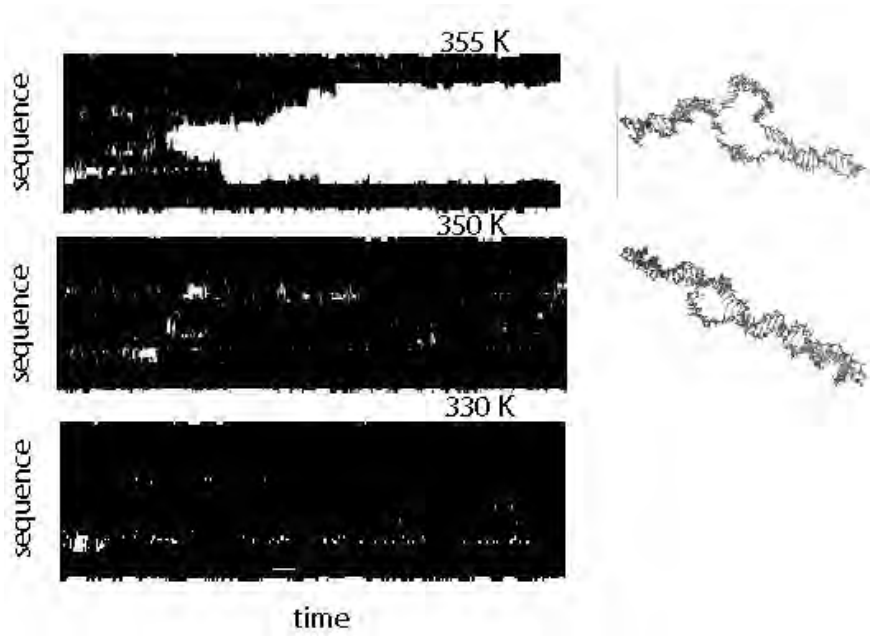

Fig. 2. Time series of base opening (white) and closing (black) during three different 20 ns trajectories at 330 K (bottom), 350 K (center), and 355 K (top). The right hand side plot shows DNA double helical configurations showing bubbles of different sizes. The CG rich sequence at the ends melt at much higher T, while the AT rich region open at $T < T_m$.

4. Conclusions

We have shown that simple minimalist models with atomic detail can reproduce observed bubble formation fluctuations in DNA. Bubbles form at temperatures well below the transition T. Small bubbles are 5 – 10 base pairs long, while large bubbles are as large as the AT rich segment of the DNA molecule.

1. Y. Zeng, A. Montrichok, G. Zocchi, *Phys. Rev. Lett.* **91**, 148101 (2003).
2. K. J. Breslauer, R. Frank, H. Blocker, L. A. Marky, *Proc. Nat. Acad. Sci. (USA)* **83**, 3746-3750 (1986).
3. M. Peyrard, A. R. Bishop, *Phys. Rev. Lett.* **62**, 2755-8 (1989).
4. C. H. Choi *et al.*, *Nuc. Acids Res.* **32**, 1584-1590 (2004).
5. N. Go, *Ann. Rev. Biophys. & Bioeng.* **12**, 183-210 (1983).
6. C. Clementi, A. E. Garcia, J. N. Onuchic, *J. Mol. Bio.* **326**, 933-954 (2003).
7. J. D. Bryngelson, J. N. Onuchic, N. D. Socci, P. G. Wolynes, *Proteins Struct. Funct. & Gen.* **21**, 167-195 (1995).
8. S. J. Weiner *et al.*, *J. Amer. Chem. Soc.* **106**, 765-84 (1984).

LAUR-04-6051

Understanding Protein Stability And Flexibility Using Network Rigidity

D. J. Jacobs

Physics and Astronomy, California State University, Northridge 18111 Nordhoff St. Northridge CA 91330-8268 U.S.A. donald.jacobs@csun.edu

ABSTRACT

Protein structure is represented as a mechanical framework defined by constraint topology. Various constraint types are used to model covalent bonds, hydrogen bonds, salt bridges and torsion angles. The set of constraint types defines a decomposition of free energy where each constraint is quantified by a local molecular free energy function, having enthalpy and entropy contributions. A coarse grain statistical mechanical Distance Constraint Model (DCM) is presented that explicitly accounts for network rigidity among constraints. For each constraint topology, the well-known problem of non-additivity of component entropies from a free-energy decomposition is explicitly accounted for using network rigidity. Network rigidity is a long-range underlying mechanical interaction that provides a mechanism for enthalpy-entropy compensation. For fixed constraint topology, an efficient graph algorithm is employed to identify flexible and rigid regions, and to determine independent constraints. Total enthalpy is obtained by summing over all enthalpy contributions. Total conformational entropy is obtained by summing entropy contributions from preferentially selected independent constraints to provide a lowest upper bound estimate. Ensemble averaging over accessible constraint topologies allows thermodynamic stability and molecular cooperativity (flexibility) to be predicted. The DCM provides a novel modeling scheme that probes stability-flexibility relationships important for protein engineering. A hybrid computational method that combines Monte Carlo sampling and Landau theory is employed. Phenomenological DCM parameters are determined by fitting to measured heat capacity data. Flexibility characteristics, stability curves and free energy landscapes are calculated. The DCM runs 10 orders of magnitude faster than Molecular Dynamics to obtain comparable sampling statistics.

1. Introduction

Since the late 1950s with the introduction of phenomenological Ising-like models to explain the alpha-helix to coil transition, there has been a desire for *reduced protein models* to capture the essential physics of protein folding. Also important, are many related issues pertaining to protein stability and molecular cooperativity that need to be accurately modeled so that function efficacy can be engineered by computer aided design in fast turn-around times. To this end, it would be desirable to have a simple model that will balance accurate estimations of energy and entropy among molecular constituents, while representing solvation effects in terms of enthalpy and entropy component contributions. A common approach that can satisfy the *simple* and *fast* criteria has been to invoke free energy decomposition schemes. Unfortunately, models based on the additivity assumption of free energy components become inaccurate when component

parts within a protein or associated with protein-solvent interactions strongly couple. These long-standing problems are directly addressed using a *Distance Constraint Model* (DCM) [1] that provides a computationally tractable approximation scheme. The DCM is based on free energy decomposition, but it invokes network rigidity as an underlying mechanical interaction to accurately account for non-additivity in component entropies.

2. Method

Microscopic interactions are modeled as constraints that may be quenched or fluctuate. Generally, a constraint, t, consists of m_t (more than one) elementary distance constraints. The DCM obtains thermodynamic properties by working with an ensemble of distinct constraint topologies, each defining a mechanical framework, $\mathcal{F}$. The DCM is solved within Landau theory by defining a macrostate of a protein in terms of (N_{hb}, N_{nt}) giving the number of (crosslinking H-bonds, native-like torsion-angles). Moreover, these two order parameters define a two-dimensional grid in constraint space. For each node on the grid, a Landau free energy is written in terms of phenomenological parameters as:

$$G(N_{hb},N_{nt}) = \Sigma_t E_t \overline{\eta_t} - u N_{hb} + v N_{nt} - RT \Sigma_t [\gamma_t \overline{\sigma_t} - [p_t \ln(p_t) + (1-p_t) \ln(1-p_t)]] \quad (1)$$

where constraint type, t, has an energy, E_t, and maximal *local* conformational entropy, γ_t. Energy of H-bonding to solvent is accounted for by u, ($u < 0$ is favorable), and v being negative favors native-like torsion constraints. An Ising-like variable η_t is (0,1) when a fluctuating constraint (is not, is) present. Variable σ_t gives the number of independent elementary distance constraints, ranging between 0 to m_t requiring non-trivial calculation. Distance constraints within framework $\mathcal{F}$ are sorted from smallest γ_t to largest $\forall$ t. A test for independence employs a generic rigidity graph-algorithm [2], except here, the order of constraint placement is defined by the sorted list. This preferential ordering provides a lowest upper bound estimate for conformational entropy, where $S_c(\mathcal{F}) \leq R \Sigma_t \gamma_t \sigma_t$. Mixing entropy, $S_m(\mathcal{F})$, is accounted for in Eqn. (1) by the last two terms where p_t has the form of a Fermi-Dirac occupation probability because each constraint acts as a two level system.

The known native 3D protein structure is used as a starting template. An ensemble of frameworks is constructed by perturbing away from this template. This simplification allows us to consider the variables E_t and γ_t fixed. Using empirical formulae for E_t, and assuming γ_t is a linear function of E_t, a 5-parameter model has been developed --- two are modeled as independent of protein and solvent conditions, and 3 remain as effective phenomenological parameters to be determined. With these simplifications, $\{p_t\}$ provides mean-field probabilities that are self-consistently calculated using Lagrange multipliers to fix the desired total number of constraints on the protein conformation per node. Random constraint topologies are then generated using Monte Carlo sampling within each node in accordance with a product probability measure built from $\{p_t\}$ to calculate Eqn. (1). By adaptive grid sampling, a free energy landscape is calculated from which thermodynamic response functions follow. Three free-parameters are determined by fitting heat capacity predictions to experimental data using simulated annealing with LAM-MPI parallel code.

3. Results

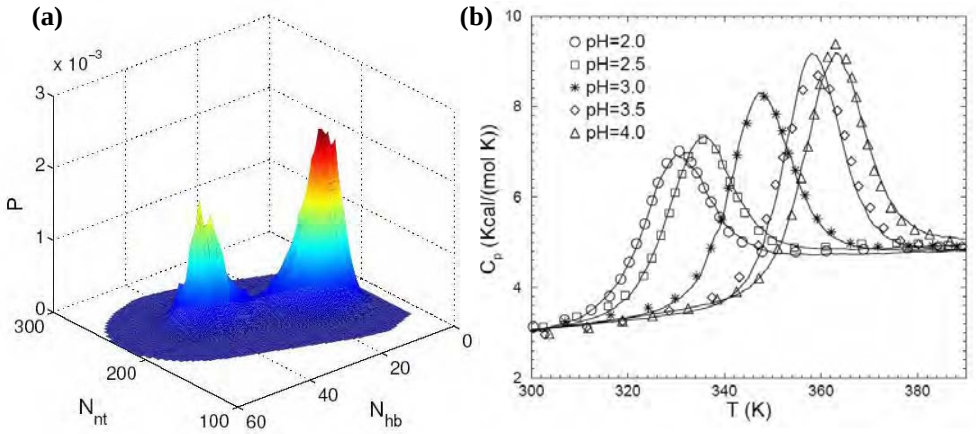

Figure 1: (a) Probability for the protein to have N_{hb} H-bond crosslinks and N_{nt} native-like torsion constraints for ubiquitin (at pH 3.0). **(b)** Corresponding 3 parameter DCM fits to the heat capacity data taken by P.L. Wintrode et al, *Proteins* **18** 246-253 (1994).

Typical free energy landscapes show two deep basins associated with the native and unfolded states (see Fig. 1a). Considering phenomenological parameters as functions of pH, the essential features of heat capacity are reproduced well, with typical results shown in Fig. 1b. Further, the DCM directly relates protein stability and flexibility in 10^{10} faster CPU time than MD to obtain similar sampling statistics. Current performance scales as $O(N^2)$, taking 2 hrs of CPU time on one 2.4 GHz processor for a N=238 residue protein. The goal is to obtain transferable parameters based on local molecular partition functions.

Acknowledgements

Research supported by NIH S06 GM48680-0952 and Research Corporation CC5141.

References

[1] D.J. Jacobs, S. Dallakyan, G.G. Wood, and A. Heckathorne, *Network rigidity at finite temperature: relationships between thermodynamic stability, the nonadditivity of entropy, and cooperativity in molecular systems*, *Phys. Rev. E.* **68** 061109-21 (2003); D.J. Jacobs, and G.G. Wood, *Understanding the alpha-helix to coil transition in polypeptides using network rigidity: predicting heat and cold denaturation in mixed solvent conditions*, Biopolymers **75** 1-31 (2004).

[2] D. J. Jacobs, A. J. Rader, L. A. Kuhn, and M. E. Thorpe, *Protein flexibility predictions using graph theory*, Proteins **44** 150-165 (2001).

Mechanics of Packaging DNA in Viruses

W.S. Klug
Mechanical and Aerospace Engineering Department,
University of California, Los Angeles, California 90095
email: klug@seas.ucla.edu

M. Ortiz
Division of Engineering and Applied Science,
California Institute of Technology, Pasadena, CA 91125
email: ortiz@aero.caltech.edu

ABSTRACT

Scientific advances in Biology brought about by the recent development of techniques for single-molecule mechanical experimentation are revealing clearly that mechanics plays a very important role in cellular biology. One particularly fascinating set of mechanically driven processes is the packaging and ejection of viral DNA. The packaging of DNA into a typical bacteriophage virus can be thought of as geometrically analogous to fitting 400 feet of electrical extension cord into a basketball. Nature's performance of such a remarkable feat is both impressive and necessary to the function of the virus. We can view it as an interesting challenge to analyze and understand the mechanics of genetic material in such confinement. We present a continuum theory of viral DNA packaging based on a director-field representation of the packaged DNA. Packaged conformations are identified as minimizers of a total free energy functional, which is composed of mechanical and electrostatic contributions. We discuss the usefulness of this approach for gaining insight into established packaging models and for suggesting new packing motifs, and compare analytical and numerical predictions of the theory to experimental observations.

1 Introduction

From a simplistic view point, a virus can be considered as a container which transports a piece of genetic material—a genome (either RNA or DNA). The virus attacks or infects a host cell by releasing its genome inside the cell. The machinery of the host cell then processes the genetic information of the virus and is thereby "hijacked", and tricked into producing all of the components for new progeny viruses. For most viruses, once assembly of the protein shell or *capsid* of a new virus is complete, the newly replicated genome is threaded inside, segment by segment. Impressive recent advances in structural biology and techniques of single-biomolecule experimentation have produced a number of observations about the mechanics of DNA as it is packaged into viruses. Cryo-electron microscopy [e.g., 1] has provided observational evidence supporting an axisymmetric packing motif known as the *inverse spool* [2], depicted in Fig. 1. Single-molecule experiments measuring the stiffness properties of DNA [e.g., 3] have enabled the formulation of quantitative, coarse-grained theories of packing mechanics.

2 DNA Director Field

Toward this end of understanding viral packaging mechanics, we have developed a continuum description of packaged DNA in terms of a director field which contains information about the local direction and interaxial spacing of the DNA at every point within the virus[4]. In the context of viral DNA packing, where the spacing between sections of the packaged DNA strand can be exceedingly small, a director-field description offers natural advantages over a strand-based approach. Instead of tracking the DNA segment by segment down the strand (a one-dimensional continuum), the director-field approach views the DNA conformations as spatial fields. The *DNA director field* is a vector field $\boldsymbol{m}(\boldsymbol{x})$ with the following defining properties: (i) its magnitude, $u(\boldsymbol{x}) = |\boldsymbol{m}(\boldsymbol{x})|$ gives the local DNA length density per unit volume, and (ii) its direction, $\boldsymbol{t} = \boldsymbol{m}(\boldsymbol{x})/|\boldsymbol{m}(\boldsymbol{x})|$ is the unit vector locally tangent to the DNA. As shown in [4] the free energy of the packaged genome can be modeled as

$$E(\boldsymbol{m}) = \int_{\Omega} [\, W(\boldsymbol{m}, \nabla\boldsymbol{m}, \nabla\nabla\boldsymbol{m}) + \phi(|\boldsymbol{m}|) \,]\, dV \tag{1}$$

i.e., the sum of the strain energy density W and the electrostatic interaction potential ϕ. Equilibrium can be sought by minimizing the free energy E.

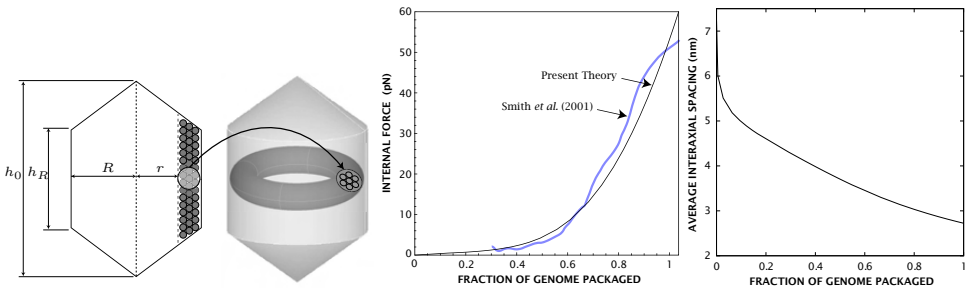

Figure 1: The inverse spool conformation. (a) Assumed geometry of bacteriophage ϕ29. (b) Theoretical predictions of packing force compared to experiments of Smith et al. [5]. (c) Average interaxial spacing as predicted by the director-field theory.

3 Results

For a simple *ansatz* such as the so-called inverse spool, minimization can be carried out solving analytically for the director field, resulting in predictions about the forces and densities required to package the genome, as shown in Fig. 1 (more details can be found in [4]). The close correspondence of these results to experimental findings (see figure) adds further support to the spool hypothesis. To model more general configurations, the director-field

can be discretized on a computational lattice, and minimization effected in terms of the finite number of degrees of freedom. Results obtained through this strategy are shown in Fig. 2 (see [6] for more details). These results also support the spool hypothesis, with the exception of the buckling-type behavior in the central core of the spool, which is conceivably a response to the high bending energy cost in this region.

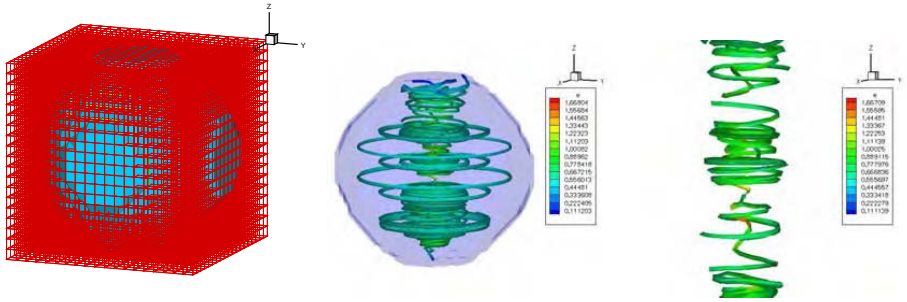

Figure 2: Lattice models of a bacteriophage λ: (a) computational grid, (b&c) Stream traces of the director field (full-view and close-up), indicating the direction of DNA at various positions within the capsid. (Color indicates energy density.)

References

[1] M.E. Cerritelli, N.Q. Cheng, A.H. Rosenberg, C.E. McPherson, F.P. Booy, and A.C. Steven. Encapsidated conformation of bacteriophage T7 DNA. *Cell*, 91(2):271–280, 1997.

[2] W.C. Earnshaw and S.C. Harrison. DNA arrangement in isometric phage heads. *Nature*, 268(5621):598–602, 1977.

[3] S.B. Smith, L. Finzi, and C. Bustamante. Direct mechanical measurements of the elasticity of single DNA-molecules by using magnetic beads. *Science*, 258(5085): 1122–1126, 1992.

[4] W.S. Klug and M. Ortiz. A director-field model of DNA packaging in viral capsids. *Journal of the Mechanics and Physics of Solids*, 51:1815–1847, 2003.

[5] D.E. Smith, S.J. Tans, S.B. Smith, S. Grimes, D.L. Anderson, and C. Bustamante. The bacteriophage ϕ29 portal motor can package DNA against a large internal force. *Nature*, 413(6857):748–752, 2001.

[6] W.S. Klug, M.T. Feldmann, and M. Ortiz. Three-dimensional director-field predictions of viral DNA packing arrangements. To appear in The Journal of Computational Mechanics, 2004.

Damage Evolution in Natural Hierarchical Structures

Phani Kumar V. V. Nukala and Srdjan Simunovic

Computer Science and Mathematics Division,
Oak Ridge National Laboratory, Oak Ridge, TN 37831-6359, USA
nukalapk@ornl.gov

ABSTRACT

Natural materials like seashells (e.g. nacre, conch) exhibit phenomenal fracture strength and toughness properties due to their hierarchical architecture at different length scales and due to the excellent adhesive properties of organic polymers that bond nacre tablets. Understanding the mechanisms of damage tolerance of these structures further enhances the ability to design novel materials for innovative practical applications. This study investigates the evolution of damage in these structures using discrete lattice models with modular damage evolution. Using the presented numerical model, it is possible to compare the contribution of the hierarchical structural form with the modular deformation of the polymer adhesive towards fracture strength of these natural materials.

1. Introduction

Natural materials such as nacre exhibit phenomenal fracture strength and toughness properties despite the brittle nature of their constituents [1-4]. This material comprises about 95% brittle inorganic phase (aragonite, a mineral form of $CaCO_3$) and only a few percent of the soft organic material [3,4]. The material forms a composite structure in which the aragonite nacre tablets are bonded together by soft organic interlamellar sheets with a fibrous core at the middle such that the composite is in the form of interlaced bricks separated by soft layers. Although the stiffness of these biocomposites is similar to that of the mineral constituent, their fracture energy is about 3000 times stronger than the corresponding single crystal mineral constituent [3,4]. The excellent fracture characteristics of these biocomposite materials are in general attributed to their hierarchical structural architecture that extends over several distinct length scales [2] and to the modular nature of the organic material that binds the nacre tablets [1].

This study investigates the progressive damage evolution in these materials by essentially capturing their salient features; namely, the hierarchical structure of the material and the modular damage evolution in the organic interface. In particular, we are interested in qualitative understanding of the basic mechanism that explains the observed phenomenal fracture characteristics of nacre. Discrete lattice models have often been used to

understand the scaling properties of fracture in disordered materials. A very well studied model is the random fuse model (RFM), where a lattice of fuses with random thresholds is subject to an increasing voltage [5,6,7]. A resistor network represents a scalar analog of an elastic medium and is thus relatively simple to analyze, while retaining the essential characteristic features of the problem. However, in order to capture the modular damage evolution in the organic interface that binds the nacre tablets, we introduce a continuous damage random thresholds fuse model (CDRFM), wherein damage evolves in a modular fashion corresponding to the saw tooth-like force-extension behavior of the organic polymer adhesive that bonds nacre tablets. A similar model for fiber bundle models has been introduced earlier in the Ref. 8. It should be noted that spring and beam lattice networks may also be used. However, in comparison with the spring and beam lattice models, CDRFM is a relatively simple model that captures the essential characteristic features of fracture problem.

At the lowest length scale, the structural architecture of nacre is that of a staggered brick-and-mortar structure, in which the aragonite platelets with a large aspect ratio (200-500 nm thick and a few mm long) are arranged in a staggered brick layer structure that are bonded together by organic collagen-rich protein matrix (mortar). In the CDRFM, this brick-and-mortar structure is modeled by a square lattice network as shown in Fig. 1. The tension elements (fuses), *T*, connect the short edges of the aragonite platelets and the shear elements (fuses), *S*, connect the long edges of the aragonite platelets.

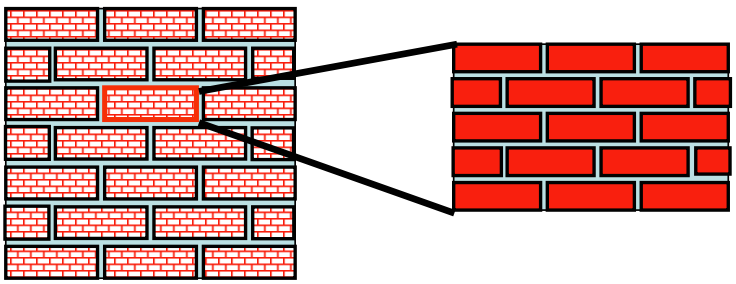

Figure 1: Hierarchical brick-and-mortar structural architecture of nacre

2. Model

In the continuous damage random thresholds fuse model (CDRFM), the lattice is initially fully intact with bonds having the same conductance, but the bond breaking thresholds, *t*, are randomly distributed based on a thresholds probability distribution, *p(t)*. Whenever the electrical current in the fuse exceeds the breaking threshold current value, *t*, of the fuse, the conductance of the fuse is reduced by a factor *a* ($0<a<1$). The characterization of damage by a continuous parameter corresponds to a description of the system on length scales larger than the typical crack size.

In the CDRFM, multiple failures of the fuses are allowed. That is, in principle, a fuse can fail more than once, and we define k_{max} as the maximum number of failures allowed per fuse. In addition, once a fuse has failed, we can either keep the same failure threshold (quenched disorder) or choose a different threshold (annealed disorder) based on the same probability distribution, $p(t)$. Furthermore, once a fuse has failed k_{max} number of times, we allow for brittle failure of the fuse. That is, the fuse is burnt irreversibly after k_{max} number of failures. A schematic of fuse behavior in the CDRFM for quenched and annealed disorders is presented in Fig. 2. Periodic boundary conditions are imposed in the horizontal direction to simulate an infinite system and a constant voltage difference, V, is applied between the top and the bottom of lattice system bus bars.

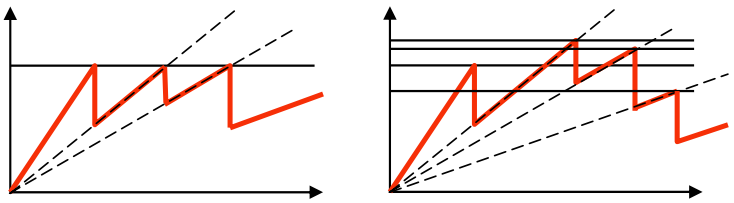

Figure 2: *I-V* fuse response in the CDRFM model; quenched disorder (left) and annealed disorder (right)

Numerically, a unit voltage difference, $V=1$, is set between the bus bars and the Kirchhoff equations are solved to determine the current flowing in each of the fuses. Subsequently, for each fuse j, the ratio between the current i_j and the breaking threshold t_j is evaluated, and the conductance of the bond j_c having the largest value, $max_j\ i_j/t_j$, is reduced by a factor a ($0<a<1$). If the fuse j_c fails more than k_{max} number of times, the fuse j_c is irreversibly removed (burnt), otherwise, the breaking threshold of the fuse j_c is either unchanged (quenched disorder) or a different threshold t is chosen for the fuse j_c based on the probability distribution $p(t)$. The current is redistributed instantaneously after the fuse failure implying that the current relaxation in the lattice system is much faster than the failure of a fuse. Each time a fuse fails, it is necessary to re-calculate the current redistribution in the lattice to determine the subsequent failure of a fuse. The process of fuse failures, one at a time, is repeated until the lattice system falls apart. In this work, we consider a uniform probability distribution, which is constant between 0 and 1 for the thresholds distribution $p(t)$.

Numerical simulation of fracture using large fuse networks is often hampered due to the high computational cost associated with solving a new large set of linear equations every time a new lattice bond fails. The authors have developed rank-1 sparse Cholesky factorization updating algorithm for simulating fracture using discrete lattice systems [7]. In comparison with the Fourier accelerated iterative schemes used for modeling lattice breakdown, this algorithm significantly reduced the computational time required for solving large lattice systems. Using this numerical algorithm, we were able to investigate damage evolution in larger square lattice systems. For many lattice system sizes, the

number of sample configurations, used are excessively large to reduce the statistical error in the numerical results.

3. Numerical Results

As mentioned earlier, two basic mechanisms, namely, the modular damage evolution of the organic polymer adhesive and the hierarchical structural architecture that extends over several length scales are the reasons behind the excellent fracture characteristics of biocomposites such as nacre.

3.1 Modular Damage Evolution

In order to simulate modular damage evolution, the protein matrix that binds the aragonite platelets is modeled by continuous damage random threshold fuse elements with threshold values randomly assigned between 0 and 1, and the aragonite platelet is modeled by fuses with very high breaking threshold value. Figures 3(a)-(d) present the typical *I-V* responses for the cases k_{max} = 1,2,3 and 5 using the CDRFM. When modular damage evolution in the protein matrix is simulated using the CDRFM fuses with multiple failures ($k_{max} > 1$), the fracture toughness (area under the *I-V* response curve) is significantly (at least two orders) higher compared with the no modular damage evolution case ($k_{max} = 1$).

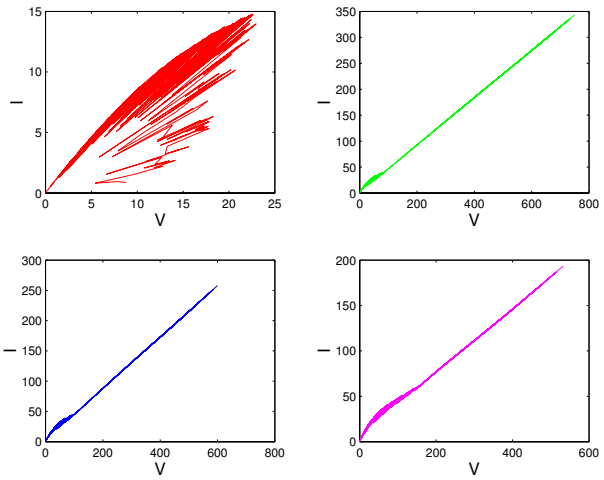

Figure 3: Typical *I-V* response curves of CDRFM model. (a) k_{max} = 1 (same as RFM model) (b) k_{max} = 2 (c) k_{max} = 3 (d) k_{max} = 5. Clearly, the fracture toughness (area under the *I-V* curves) for the cases $k_{max} > 1$ is at least two orders of magnitude greater than that of k_{max} = 1. This indicates that the modular damage evolution of organic protein matrix contributes significantly to the excellent fracture properties of nacre.

3.2 Hierarchical Structural Architecture

The effect of hierarchical structural architecture can be modeled using the CDRFM by adopting the Renormalization Group (RG) or Coarse Graining (CG) approach. Consider the basic staggered brick-and-mortar structure at the lowest length scale as shown in Fig. 1. At the next hierarchical length scale, the response of this basic staggered brick-and-mortar structure is coarse grained such that the response of the brick element in the higher hierarchical length scale is that of the renormalized response of the staggered brick-and-mortar structure at the lower length scale. Figure 3(a) represents the staggered brick-and-mortar response at the lowest length scale using the CDRFM (k_{max} = 1). Qualitatively, this response (Fig. 3(a)) is similar to the continuous damage random threshold fuse response with multiple failures and annealed disorder. In order to simulate the effect of hierarchical length scales (only), the protein matrix that binds the aragonite platelets is modeled by random threshold fuse elements (k_{max} = 1) with threshold values randomly assigned between 0 and 1, and the renormalized brick response from the lower length scale is modeled by continuous damage fuses (CDRFM) with multiple failure and uniformly distributed random threshold values. Figure 4 presents the effect of multiple hierarchies. In particular, Fig. 4 presents the effect of modeling the lower length scale response using the continuous damage fuse models with multiple failures (k_{max} = 1,3 and 5). Based on the results presented in Fig. 4, it is clear that the hierarchical structural architecture increases the fracture toughness by an order of magnitude compared with the staggered brick-and-mortar response at the lowest length scale.

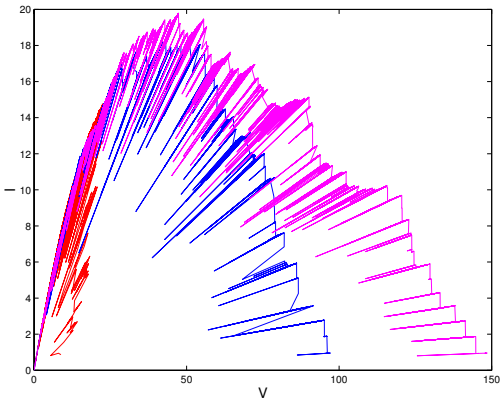

Figure 4: Effect of multiple hierarchical length scales on the fracture toughness. The staggered brick-and-mortar response at the lowest length scale is shown in red color. This also corresponds to the scenario in which the brick response at the higher length scale is modeled using a fuse element with k_{max} = 1. When the brick response at the higher length scale is modeled by continuous damage fuse elements with multiple failures so as to simulate the response from lower length scales, the fracture toughness is increased by an order of magnitude (k_{max} = 3 and 5 are represented by blue and magenta lines)

4. Conclusions

This study investigates the evolution of damage in natural biocomposites such as nacre using the discrete lattice models. In particular, continuous damage random thresholds fuse model is used to simulate the modular damage evolution of the organic protein matrix and the hierarchical structural architecture. Qualitatively, the results presented in this work indicate that the modular damage evolution of the organic protein matrix increases the fracture toughness by two orders of magnitude whereas the hierarchical structural architecture increases the fracture toughness by an order of magnitude.

Acknowledgements

This research is sponsored by the Mathematical, Information and Computational Sciences Division, Office of Advanced Scientific Computing Research, U.S. Department of Energy under contract number DE-AC05-00OR22725 with UT-Battelle, LLC.

References

[1] B. L. Smith, T. E. Schaffer, M. Viani, J. B. Thompson, N. A. Frederick, J. Kindt, A. Belcher, G. D. Stucky, D. E. Morse, and P. K. Hansma, Nature, **399**, 761 (1999).
[2] S. Kamat, X. Su, R. Ballarini, and A. H. Heuer, Nature, **405**, 1036 (2000).
[3] A. G. Evans, Z. Suo, R. Z. Wang, I. A. Aksay, M. Y. He, and J. W. Hutchinson, J. Mater. Res., **16**(9), 2475 (2001).
[4] H. Gao, B. Ji, I. L. Jager, E. Arzt, and P. Fratzl, Proceedings of the National Academy of Sciences (PNAS), **100**(10), 5597 (2003).
[5] de Arcangelis L, Redner S, and Herrmann HJ, J. Phys. (Paris) Lett. **46,** 585 (1985); Sahimi M and Goddard JD, Phys. Rev. B, **33**, 7848 (1986).
[6] Herrmann HJ and Roux S (eds.), *Statistical Models for the Fracture of Disordered Media*, (North-Holland, Amsterdam, 1990). Bardhan KK, Chakrabarti BK and Hansen A (eds.), *Non-linearity and breakdown in soft condensed matter*, (Springer Verlag, Berlin, 1994). Chakrabarti BK and Benguigui LG, *Statistical physics of fracture and breakdown in disordered systems* (Oxford Univ. Press, Oxford, 1997). Krajcinovic D and van Mier, *Damage and fracture of disordered materials*, (Springer Verlag, New York, 2000).
[7] Nukala PKVV, and Simunovic S, J. Phys. A: Math. Gen. **36**, 11403 (2003)
[8] F. Kun, S. Zapperi, and H. J. Herrmann, Eur. Phys. J. B **17**, 269 (2000).

Coarse-Graining DNA Energy Landscapes

Jonathan A. Othmer*, Justin S. Bois† and Niles A. Pierce*‡
***Applied & Computational Mathematics, †Chemical Engineering, ‡Bioengineering**
Caltech, Mail Code 114-96, Pasadena, CA 91125, niles@caltech.edu

ABSTRACT

Given a DNA energy landscape defined in terms of secondary structure microstates, we describe a coarse-graining approach for performing kinetic simulations that accurately captures the temporal evolution of physically-meaningful macrostates. The approach is based on the solution of local eigenvalue problems to identify the dominant local relaxations between interacting macrostates.

1. Introduction. Single-stranded DNA is a versatile construction material [1] that can be programmed to self-assemble into nanoscale structures and devices driven by the free energy of base pair formation. Conceptually, the equilibrium and kinetic properties of a DNA strand can be elucidated by characterizing its energy landscape, including the partition function, minimum energy structure, metastable structures, transition structures and folding pathways. An energy landscape based on nucleic acid secondary structure [2] may be represented as a graph, with each vertex corresponding to a secondary structure and each edge corresponding to an elementary step between structures (*e.g.,* formation or breakage of a single base pair [3]). The number of vertices in the landscape scales exponentially with the length of the strand, so efficient algorithms are required to examine landscapes of practical interest.

For a molecule with M_s secondary structures, the probability $p_i(t)$ of finding the molecule in structure i may be modeled by the master equation

$$\frac{dp_i(t)}{dt} = \sum_{\substack{j=1,\,M_s \\ j \neq i}} \left[k_{j\to i}p_j(t) - k_{i\to j}p_i(t)\right], \quad (1)$$

where $k_{j\to i}$ and $k_{i\to j}$ are non-negative constants describing the rates at which transitions $j \to i$ and $i \to j$ proceed, respectively. These equations can be assembled into a coupled system of linear ODEs, $\frac{dP}{dt} = WP$, with solution* $P(t) \equiv (p_1(t), \ldots, p_{M_s}(t))^T = Te^{\Lambda t}c$, where Λ is a diagonal matrix of eigenvalues of W (that may by ordered by magnitude $|\lambda_0| < |\lambda_1| < \ldots < |\lambda_{M_s-1}|$), the columns of T are the eigenvectors of W, and c is a constant vector determined by the initial conditions $P(0)$.

It is desirable to develop a method for constructing a coarse-grained landscape that retains the essential thermodynamic and kinetic features of the full landscape, includ-

*For an irreducible landscape (*i.e.,* one in which every state can be reached by a series of elementary steps from every other state) with rate definitions for $k_{j\to i}$ and $k_{i\to j}$ that satisfy detailed balance (*i.e.,* $k_{j\to i}p_j(t_\infty) = k_{i\to j}p_i(t_\infty)$, ensuring compatibility with equilibrium), the matrix W is symmetrizable, possessing a complete set of eigenvectors, a single zero eigenvalue (corresponding to the unique equilibrium eigenvector), and $M_s - 1$ negative real eigenvalues [4]. In practice, the system of ODEs can be solved deterministically using standard numerical solvers or stochastically as a continuous-time Markov process [3]. The stochastic procedure has the advantage that only a single (sparse) column of W is needed at any step in the algorithm; constructing and discarding columns on the fly permits the examination of increased strand lengths.

ing important local minima (basins) and the transition structures that connect them (saddles). Flamm *et al.* [5] developed compact energy landscape descriptions by representing basins and the energy barrier between any two basins as a tree. However, for kinetic simulations it is desirable to account for the connectivity of the basins in the landscape. Here, we adopt an alternative *basin graph* approach with nodes that represent either basins surrounding local minima or saddles that connect two or more basins [6] (see, *e.g.*, Figure 1a). Physically, the basin macrostates cluster microstates with qualitatively similar secondary structures. The objective is to define a macrostate analog to the microstate master equation (1).

2. Two-Basin Analysis. Widom [7] insightfully examined the issue of defining rate constants between macrostates for the case of generic microstates divided into two basins (say A and B) separated by a saddle (defined by microstates in A or B that are high in energy and have nonzero transition rates to microstates in the other basin). At equilibrium, each microstate has probability $p_i^{eq} = f_i/Q$, where f_i is the Boltzmann factor for state i and $Q \equiv \sum_i f_i$ is the partition function. The microstate kinetics are described by (1), with transients that decay exponentially as characterized by the $M_s - 1$ nonzero relaxation rates $|\lambda_i|$. After an initial transient period corresponding to $t \gg (\lambda_1 - \lambda_2)^{-1}$, the fluctuation in the probability of each microstate is dominated by the λ_1 relaxation mode $p_i(t) = p_i^{eq} + c_1 T_{i,1} e^{\lambda_1 t}$. Differentiating and substituting into the result yields the microstate rate equation $dp_i(t)/dt = \lambda_1[p_i(t) - p_i^{eq}]$, where the dependence on the microstate transition rates is implicit in the definition of λ_1.

At equilibrium, the basin probabilities are $p_A^{eq} = Q_A/Q$ and $p_B^{eq} = Q_B/Q$ expressed in terms of the basin partition functions $Q_A = \sum_{i\in A} f_i$ and $Q_B = \sum_{i\in B} f_i$. The time varying basin probabilities are sums of the microstate probabilities $p_A(t) = \sum_{i\in A} p_i(t)$ and $p_B(t) = \sum_{i\in B} p_i(t)$. For $t \gg (\lambda_1 - \lambda_2)^{-1}$, the basin kinetics are described by $\frac{dp_A(t)}{dt} = \lambda_1[p_A(t) - p_A^{eq}]$, $\frac{dp_B(t)}{dt} = \lambda_1[p_B(t) - p_B^{eq}]$. Noting that $p_A(t) + p_B(t) = 1$, these rate equations can be recast in the form of a first-order phenomenological rate law

$$-\tfrac{dp(t)_A}{dt} = \tfrac{dp(t)_B}{dt} = k_f p_A(t) - k_r p_B(t),$$

with forward and reverse rate constants $k_f = \lambda_1 p_B^{eq}$ and $k_r = \lambda_1 p_A^{eq}$. Hence, if the initial transient is rapid (*i.e.*, $|\lambda_1| \ll |\lambda_2|$), k_f and k_r can be interpreted as the phenomenological rate constants that would be observed by experimentally measuring $p_A(t)$ and $p_B(t)$.

By contrast, the rate at which probability flows from basin A to basin B at equilibrium is

$$k_{A\to B}^{eq} = \sum_{i\in A}\sum_{j\in B} k_{i\to j} f_i/Q_A,$$

where f_i/Q_A represents the conditional probability of sampling microstate i at equilibrium in basin A. Defining $k_{B\to A}^{eq}$ analogously, we have at equilibrium $k_{A\to B}^{eq} p_A^{eq} = k_{B\to A}^{eq} p_B^{eq}$, expressing the balance of probability fluxes between basins A and B.†

3. Local Equilibrium Approximation. In defining the rate constants for transitions

†Note that these equilibrium basin transition rate constants are not equal to the phenomenological rate constants k_f and k_r (although ratios of both sets of rate constants correspond to the same equilibrium constant $K \equiv p_B^{eq}/p_A^{eq} = k_f/k_r = k_{A\to B}^{eq}/k_{B\to A}^{eq}$). This can be seen, for example, by observing that $k_{A\to B}^{eq}$ depends only on microstate rates involving $A \to B$ events, but k_f is a scaling of λ_1 which contains an implicit dependence on intrabasin and interbasin transition events of all types.

between basins in a coarse-grained energy landscape with M_b basins, Zhang and Chen [6] and Wolfinger *et al.* [8] adopt a local equilibrium approximation for each pair of connected basins and calculate $k^{eq}_{A\to B}$ and $k^{eq}_{B\to A}$ to define a coarse-grained master equation

$$\frac{dp_A(t)}{dt} = \sum_{\substack{B=1,M_b \\ B\neq A}} \left[k^{eq}_{B\to A}p_B(t) - k^{eq}_{A\to B}p_A(t)\right].$$

This approach makes the approximation of using equilibrium basin transition rate constants $k^{eq}_{A\to B}$ to simulate nonequilibrium conditions.

4. Dominant Local Relaxation. We now suggest a different approximate master equation by defining coarse-grained phenomenological rate constants. The microstate rate matrix W consists of M_b diagonal blocks describing intrabasin transitions and sparse off-diagonal blocks describing interbasin transitions. Calculating the phenomenological rate constants k_f and k_r for each pair of connected basins by solving a local eigenvalue problem (defined by the two diagonal and two off-diagonal blocks relating the two basins) yields the coarse-grained master equation

$$\frac{dp_A(t)}{dt} = \sum_{\substack{B=1,M_b \\ B\neq A}} \left[k_r p_B(t) - k_f p_A(t)\right].$$

This approach attempts to capture the dominant local relaxation behavior (embodied by λ_1 when $t \gg (\lambda_1 - \lambda_2)^{-1}$) for each pair of connected basins in the landscape. Figure 1 demonstrates that the method holds promise for reproducing the basin kinetics predicted by the microstate master equation without solving the global microstate system.

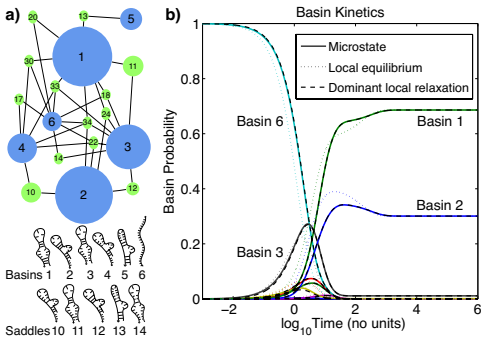

Figure 1. a) Basin graph showing the six lowest-energy basins (blue) and their connecting saddles (green) for a 21-base sequence with 250 secondary structures. Node size increases with decreasing free energy; node number corresponds to a rank ordering in free energy. Depicted structures represent the minima of each basin or saddle. b) Comparison of basin kinetics when solving the microstate master equation and coarse-grained master equations based on either the local equilibrium approximation or dominant local relaxation.

References

[1] N.C. Seeman. DNA in a material world. *Nature*, 421:427–431, 2003.

[2] S.-J. Chen and K.A. Dill. RNA folding energy landscapes. *Proc Natl Acad Sci USA*, 97(2):646–651, 2000.

[3] C. Flamm, W. Fontana, I.L. Hofacker, and P. Schuster. RNA folding at elementary step resolution. *RNA*, 6:325–338, 2000.

[4] N.G. van Kampen. *Stochastic Processes in Physics and Chemistry*. North-Holland, 1992.

[5] C. Flamm, I.L. Hofacker, P.F. Stadler, and T. Wolfinger. Barrier trees of degenerate landscapes. *Z Phys Chem (Munich)*, 216:155–173, 2002.

[6] W. Zhang and S.-J. Chen. Analyzing the biopolymer folding rates and pathways using kinetic cluster method. *J Chem Phys*, 119(16):8716–8729, 2003.

[7] B. Widom. Molecular transitions and chemical reaction rates. *Science*, 148:1555–1560, 1965.

[8] M.T. Wolfinger, W.A. Svrcek-Seiler, C. Flamm, I.L. Hofacker, and P.F. Stadler. Efficient computation of RNA folding dynamics. *J Phys A: Math Gen*, 37:4731–4741, 2004.

Symposium – 6

Mathematical & Computational Foundations of Multiscale Modeling

Multiscale Modeling of Defected Carbon Nanotubes

Ted Belytschko and **Sulin Zhang**

Department of Mechanical Engineering, Northwestern University, 2145 Sheridan Road, Evanston, IL 60208-3111, USA
Email: tedbelytschko@northwestern.edu; s-zhang6@northwestern.edu.

ABSTRACT

Molecular mechanics (MM) calculations and coupling methods bridging MM and finite crystal elasticity (FCE) are employed to simulate the fracture of defected carbon nanotubes (CNTs) and to compare with the available experimental results. Our MM calculations show that one- and two-atom vacancies reduce the fracture strength of CNTs by 20% to 33%, but these fracture strengths are still much higher than the experimental data. We then demonstrate that this experimental/theoretical discrepancy can be attributed to the presence of large-scale defects, such as those that may arise from oxidative purification processes. Our simulations also show that the presence of inner shells, twisting prior to tensile loading, and misalignments of tube ends have negligible effects on the fracture strength, which indicates that these are not the causes of low experimental values.

1. Introduction

Extensive research has been done in predicting the strength of CNTs. So far, Comparisons of experimental data and theoretical calculations have manifested large discrepancies. According to the experimental measurements of Yu et al. [1], the fracture strengths of 19 multi-walled CNTs (MWCNTs) range from 11 to 63 GPa with a mean value of 27.8 GPa. However, the fracture stresses predicted by QM calculations fall in the range of 75—135 GPa. In this article, we use molecular mechanics (MM) calculations and a coupling method to examine potential sources of theoretical/experimental discrepancies.

2. Model formulation

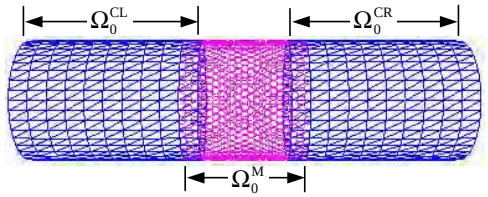

Fig. 1. Domain composition in the coupling method.

In our calculations, CNTs are stretched incrementally to fracture. At a given strain, the configuration is optimized using a conjugate-gradient method. The modified second-generation Tersoff-Brenner (MTB-G2) potential [2] is adopted to describe the many-body

interactions in the MM calculations. For increased computational affordability, a coupling method is employed to simulate large-diameter and MWCNTs. In this method, the entire domain is decomposed to three subregions (Fig. 1): an atomistic region local to defects (Ω_0^{M}); a continuum region undergoing homogeneous deformation ($\Omega_0^{\mathrm{C}} = \Omega_0^{\mathrm{CL}} \bigcup \Omega_0^{\mathrm{CR}}$); and an overlapping region in which atomistic and continuum representations overlap ($\Omega_0^{\mathrm{O}} = \Omega_0^{\mathrm{C}} \bigcup \Omega_0^{\mathrm{M}}$). The strain-energy density in the continuum region is obtained by homogenization of the atomistic binding energy through the exponential Cauchy-Born rule [3]. Compatibility conditions are imposed in the overlapping region such that the interpolation of continuum deformation at atomic positions conforms to the atomistic deformation. For given end displacements, atomic positions and continuum nodal positions are optimized simultaneously.

3. Results and discussions

We first consider single- and double vacancy defects (Fig.2), each of which has two possible stable configurations, symmetric and asymmetric. MM (QM) calculations showed that the one- and two-atom vacancy defects weaken the CNTs by 20~33% (14~27%) on average, as summarized in Table I.

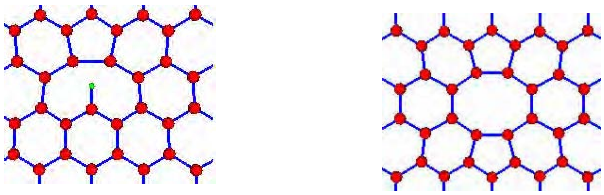

(a) (b)

Fig. 2. Vacancy defects. (a) Single vacancy; (b) Double vacancy. Dangling bond in the single vacancy is terminated by a hydrogen (red: carbon; green: hydrogen). Depending on the tube axial direction of the tube, the vacancies can be symmetric or asymmetric to the axial direction.

Table I. Fracture strengths of CNTs with single and double vacancies.

Defects	[10,0], MM	[10,0], QM	[5,5], MM	[5,5], QM
Pristine	87.9	124	105.5	135
Single vac.	64.8	101	70.4	100
Single vac., sym., +H	68.2	-	84.7	106
Single vac., asym., +H	64.7	-	70.9	99
Double vac., sym.	64.8	107	71.3	105
Double vac., asym	64.4	101	73.2	111

The fracture strengths of CNTs with single and double vacancies are still much higher than the experimental failure stresses. One explanation [4] is that significantly larger defects may have been introduced in the CNTs used in the experiments. Therefore we explore the fracture of CNTs containing large defects of two types — holes and slits

(Fig.3a). Figure 3b shows the fracture stresses decrease monotonically with increasing defect sizes. The computed fracture strengths for CNTs with large defects fall in the range of the experimental observations.

Using the coupling method, we further demonstrate that the presence of inner shells, twisting prior to tensile loading, and misalignment of tube ends insignificantly affect the fracture strength of the tubes.

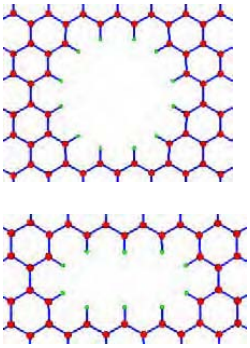

(a)

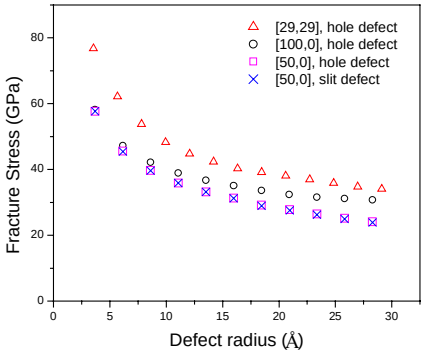

(b)

Fig. 3. Fracture of CNTs with large defects. (a) Hole (top) and slit (bottom) defects. Dangling bonds are terminated by hydrogens (red: carbon; green: hydrogen). (b) Fracture strength versus defect size.

4. Conclusions

The MM calculations show that single and double vacancy defects weaken CNTs by ~30%, while large holes and slits lower the fracture strength more significantly, falling in the range of the experimental observations. We have demonstrated using coupled MM/FCE calculations that reduction in CNT strength that was observed in the experiments of Yu et al. [1] cannot be attributed to shortcomings in the experimental apparatus. Instead, they are most likely due to large holes in the outer CNTs that are introduced from the oxidative purification processes.

References

[1] Yu, M.-F., Lourie, O., Dyer, M. J., Moloni, K., Kelly, T. F., Ruoff, R. S., 2000. Strength and breaking mechanisms of multiwalled carbon nanotubes under tensile load. Science 287, 637–640.

[2] Shenderova, O. A., Brenner, D. W., 2000. Atomistic modeling of the fracture of polycrystalline diamond. Phys. Rev. B 61 (6), 3877–3888.

[3] Arroyo, M., Belytschko, T., 2001. An atomistic-based finite deformation membrane for single layer crystalline films. J. Mech. Phys. Solids 50 (9), 1941–1977.

[4] Mielke, S. L., Troya, D., Zhang, S., Li, J.-L., Xiao, S. P., Car, R., Ruoff, R. S., Schatz, G. C., Belytschko, T., 2004. The role of vacancy defects and holes in the fracture of carbon nanotubes. Chem. Phys. Lett. 390 (4–6), 413–420.

Systematic Multiscaling in Materials Science Computations

A. Brandt

Department of Mathematics
University of California, Los Angeles, CA 90095
email: abrandt@math.ucla.edu

ABSTRACT

The multiscale computational methodology is a systematic approach to achieve efficient calculations of systems that inclue very many degrees of freedom (particle locations, discrete-function values, etc.). It includes fast multigrid solvers for discretized partial-differential equations (PDEs) and for other large systems of local equations; fast summation of long-range (e.g. electrostatic) interactions and fast solvers of integral and inverse PDE problems; collective computation of many eigenfunctions; slowdown-free Monte Carlo simulators; multilevel methods of global optimization; and general systematic upscaling procedures, which start at a microscopic scale where first-principle laws are known and lead scale-by-scale to processing rules of collective variables at increasingly larger scales.

1. The Scale Gap

Most difficulties in computing materials are primarily due to *the scale gap*, which exists between the microscopic scale at which physical laws are given and the much larger scale of phenomena we wish to understand.

This gap implies, first of all, a huge number of *variables* (e.g., atoms or grid-points), and possibly even a much larger number of *interactions* (e.g., one force between every pair of atoms). Moreover, computers simulate physical systems by moving *one variable at a time*; as a result, each such move must be extremely small, since a larger move would have to take into account all the motions that should in parallel be performed by all other variables. Such a computer simulation is particularly incapable of moving the system across large-scale *energy barriers*, which can each be crossed only by a large, and unknown, *coherent* motion of very many variables.

A general current approach to overcome the scale gap is by *multiscale modeling* (MSM; also called "multiscale simulation"). It studies a physical system by employing several different ad-hoc models, each describing a very different scale of the system. They are usually linked by *fine-to-coarse parameter passing*, in which data obtained from simulating a finer scale model, often coupled with experimental observations, are used to determine certain parameters of a larger scale model, regarding the latter as a coarse graining of the former.

Successful as MSM is in various special cases, its applicability and accuracy are generally severely limited, especially when the different simulated scales are not well separated, or when they interact with (possibly many) intermediate scales that introduce their own characteristics. Also, the calculation of the large-scale parameters usually still requires the full simulation of very large systems with painfully small steps.

2. Multiscale Algorithms

Past studies have demonstrated that the slowness associated with the necessarily small steps of moving one variable at a time can be overcome by multiscale algorithms. Such algorithms have first been developed in the form of fast **multigrid solvers** for discretized PDEs [1]. These solvers are based on two processes: (1) classical *relaxation* schemes, which are generally slow to converge but fast to *smooth* the error function; (2) approximating the smooth error on a *coarser grid* (typically having twice the meshsize), by solving there equations which are derived from the PDE and from the fine-grid residuals; the solution of these coarse-grid equations is obtained by using recursively the same two processes. As a result, large scale changes are effectively calculated on correspondingly coarse grids, based on residual information gathered from finer grids. In many years of research, the range of applicability of these methods has steadily grown, to cover most major types of linear and nonlinear large systems of equations appearing in sciences and engineering. This has been accomplished by diversifying the types of coarse representations, to include for instance grid-free solvers, called *algebraic multigrid* [2], non-deterministic problems ([3], [4]) and multiple coarse-level representations for wave equations [5].

Structural mechanics PDEs, discretized on well-structured grids, can be solved by multigrid in just several dozen operations per discrete unknown. For *unstructured* discretizations (e.g., by finite-element or finite-volume or mesh-free methods) algebraic multigrid solvers come close to achieving similar efficiency.

Nonlinear problems are solved as fast, with no need for global linearization, by a multigrid version called FAS. In this version, the relaxed solution at each fine level supplies corrections to the *equations* of the next coarser level. These *fine-to-coarse defect corrections* (DCs) can be calculated *locally*, just on a small patch of the fine level at a time, and they rarely need updating upon re-solving the problem. Thus, solving a problem many times (as part of some **evolution in time**, or in **optimizing design or control**) can usually be made mostly on very coarse grids with fixed DCs, rarely updating the DCs by visits to finer levels. Moreover, the finer the level the smaller the subdomain on which its DCs will usually need updating (e.g., a smaller neighborhood of the changes being introduced for optimizing the design).

In case of a **singularity (e.g., a material defect)**, increasingly finer patches introduced over progressively smaller neighborhoods of the singularity restore the *regular efficiency* (i.e., the same order of accuracy per unit work obtained in the absence of singularities). Such local-refinement patches can use their own *coordinates* (providing grids fitted to local boundaries, local solution characteristics, etc.) and their own *PDEs* (e.g., adding singular-perturbation terms at boundary layers). In particular, while the global description is in terms of continuum-mechanics PDEs, the local patches description can be *atomistic*. (This **quasi-continuum** method, as it is called today, was already described in §1.1 of [4].)

3. Upscaling

Such methods, that employ finer resolutions very sparingly, depend of course on having coarser-level (larger-scale) models. In some cases such models are readily available (e.g., a coarser discretization of the same PDE, or a continuum-mechanics description corresponding to the given fine-level atomistic model), but generally they need to be *derived*, one coarsening level at a time, starting from the known fine-level model. Since there is no reason to assume that accurate coarse-level descriptions will have nice analytic form (like simple PDEs), a general approach should derive them in the form of numerical tables.

Systematic Upscaling (SU) is a recent methodology for doing just that. It offers systematic procedures to iterate back and forth between all the scales of the physical problem, with a general criterion for choosing appropriate variables that operate at increasingly coarser levels (larger scales), and general techniques to derive their operational rules. Indefinitely large systems can in this way be simulated, with computation at each level being needed only within certain windows containing only a limited number (typically several thousands) of variables. Each level derives its operational rules (e.g., a Hamiltonian-like functional implying transition probabilities) from the next finer level, while the windows where it operates, and their boundary conditions, are provided by the next coarser level.

Unlike conventional ad-hoc multiscale modelling, SU is in principle generally applicable, free of slowdowns and bears fully-controlled accuracy.

First examples of SU, for simple polymers and fluids in equilibrium are described in the general review paper [6] and references therein. Other examples are currently under development, including solids and non-equilibrium examples. Variables at increasingly coarser levels have been identified, suitable for a variety of situations, indirectly describing features such as local crystal dimensions and directions, defects, dislocation, grains, etc.

Acknowledgement. The research is supported by the US Air Force Office of Scientific Research, Contract No. F33615-03-D5408.

References

[1] Brandt, A., Multi-level adaptive solutions to boundary value problems, *Math. Comp.* **31** (1977) 333–390. Brandt, A., Guide to multigrid development, in *Multigrid Methods* (Hackbusch, W. and Trottenberg, U., eds.), Springer-Verlag, 1982, pp. 220–312. Briggs, W.L., Henson, V.E., and McCormick, S.F., *A Multigrid Tutorial*, 2nd Ed., SIAM, 2000. Trottenberg, U, Oosterlee, C.W., and Schüller, A., *Multigrid*, Academic Press, London, 2000.

[2] Brandt, A., McCormick, S. and Ruge, J., Algebraic multigrid (AMG) for sparse matrix equations, in *Sparsity and its Applications* (Evans, D.J., ed.), Cambridge University Press, Cambridge, 1984, pp. 257–284. Ruge, J. and Stüben, K., Algebraic multigrid. In *Multigrid Methods* (McCormick, S. F., ed.), SIAM, Philadelphia, 1987, pp. 73–130.

[3] Brandt, A., Ron, D. and Amit, D.J., Multi-level approaches to discrete-state and stochastic problems, in *Multigrid Methods, II* (Hackbusch, W. and Trottenberg, U., eds.), Springer-Verlag, 1986, pp. 66–99. Brandt, A., Galun, M. and Ron, D., Optimal multigrid algorithms for calculating thermodynamic limits, *J. Stat. Phys.* **74** (1994) 313–348.

[4] Brandt, A., Multigrid methods in lattice field computations, *Nucl. Phys. B* (Proc. Suppl.) **26** (1992) 137–180.

[5] Brandt, A. and Livshits, I., Wave-ray multigrid method for standing wave equations, *Electronic Trans. Num. An.* **6** (1997), 162–181.

[6] Brandt, A., Multiscale scientific computation: review 2001. In Barth, T.J., Chan, T.F. and Haimes, R. (eds.): *Multiscale and Multiresolution Methods: Theory and Applications*, Springer Verlag, Heidelberg, 2001, pp. 1–96. Available at www.wisdom.weizmann.ac.il/∼achi.

Multiscale modeling of epitaxial growth processes: level sets and atomistic models

Russel E. Caflisch
Christian Ratsch

Mathematics Department, UCLA
Los Angeles, CA 90095-1555
USA
caflisch@math.ucla.edu cratsch@math.ucla.edu

ABSTRACT

Epitaxy is the growth of a thin film by attachment to an existing substrate in which the crystalline properties of the film are determined by those of the substrate. No single model is able to address the wide range of length and time scales involved in epitaxial growth, so that a wide range of different models and simulation methods have been developed. This talk will review several of these models - kinetic Monte Carlo (KMC), island dynamics and continuum equations.

1. The Level Set Method

The level set method, first introduced by [4], represents the interface as a level set of a *smooth* function, $\phi(x)$—for example the set of points where $\phi = 0$. For numerical purposes, the interface velocity is smoothly extended to all points x of the domain, as $v(x)$. Then, the interface motion is captured by solving the convection equation

$$\frac{\partial \phi}{\partial t} + v \cdot \nabla \phi = 0 \tag{1}$$

on a fixed, regular spatial grid.

2. Epitaxial Growth

The models that are typically used to describe epitaxial growth include the following: *Molecular dynamics* (MD) consists of Newton's equations for the motion of atoms on an energy landscape. A typical *Kinetic Monte Carlo* (KMC) method simulates the dynamics of the epitaxial surface through the hopping of adatoms along the surface. The hopping rate comes from an Arrhenius rate of the form $e^{-E/kT}$ in which E is the energy barrier for going from the initial to the final position of the hopping atom. *Island dynamics and level set methods* describe the surface through continuum scaling in the lateral directions but atomistic discreteness in the growth direction. *Continuum equations* approximate the surface using a smooth height function $h = h(x, y, t)$, obtained by coarse graining in all directions. *Rate equations* describe the surface through a set of bulk variables without spatial dependence.

Within the level set approach, the union of all boundaries of islands of height $k+1$, can be represented by the level set $\varphi = k$, for each k. For example, the boundaries of

islands in the submonolayer regime then correspond to the set of curves $\varphi = 0$.

3. Island Dynamics

Burton, Cabrera and Frank [2] developed the first detailed theoretical description for epitaxial growth. In this "BCF" model, the adatom density solves a diffusion equation with an equilibrium boundary condition ($\rho = \rho_{eq}$), and step edges (or island boundaries) move at a velocity determined from the diffusive flux to the boundary. Modifications of this theory were made, for example in [3], to include line tension, edge diffusion and nonequilibrium effects. These are "island dynamics" models, since they describe an epitaxial surface by the location and evolution of the island boundaries and step edges. They employ a mixture of coarse graining and atomistic discreteness, since island boundaries are represented as smooth curves that signify an atomistic change in crystal height.

Adatom diffusion on the epitaxial surface is described by

$$\partial_t \rho - D\nabla^2 \rho = F - 2dN_{\rm nuc}/dt \tag{2}$$

in which the last term represents loss of adatoms due to nucleation. Desorption from the epitaxial surface has been neglected.

For the boundary conditions at a step edge (or island boundary) and velocity v of a step edge (or island boundary), the simplest model is

$$\begin{aligned} \rho &= \rho_* \\ v &= D[\partial\rho/\partial n] \end{aligned} \tag{3}$$

in which the brackets indicate the difference between the value on the upper side of the boundary and the lower side. Two choices for ρ_* are $\rho_* = 0$, which corresponds to irreversible aggregation in which all adatoms that hit the boundary stick to it irreversibly, and $\rho_* = \rho_{eq}$ for reversible aggregation, in which ρ_{eq} is the adatom density for which there is local equilibrium between the step and the terrace [2].

4. Nucleation and Submonolayer Growth

For the case of irreversible aggregation, a dimer (consisting of two atoms) is the smallest stable island, and the nucleation rate is

$$\frac{dN_{\rm nuc}}{dt} = D\sigma_1 \langle \rho^2 \rangle \quad , \tag{4}$$

where $\langle \cdot \rangle$ denotes the spatial average of $\rho(\mathbf{x}, t)^2$ and σ_1 is the adatom capture number as derived in [1]. Expression (4) for the nucleation rate implies that the time of a nucleation event is chosen deterministically. Whenever $N_{\rm nuc}L^2$ passes the next integer value (L is the system size), a new island is nucleated. Numerically, this is realized by raising the level-set function to the next level at a number of grid points chosen to represent a dimer.

The choice of the location of the new island is determined by probabilistic choice with spatial density proportional to the nucleation rate ρ^2. This probabilistic choice constitutes an atomistic fluctuation that must be retained for faithful simulation of the epitaxial morphology. For growth with compact islands, computational tests have shown that additional atomistic fluctuations can be omitted [6].

5. Conclusions

Computational results have established the validity of the level set method for simulation of epitaxial growth. This method can now be used with confidence in many applications that include epitaxy along with additional phenomena and physics, such as strain, faceting and surface chemistry. For example, the coexistence of regions with different facets or different surface reconstructions could be represented in a level set formulation using two level set functions, one for crystal height and the second to mark the boundaries between adjacent facets [5].

6. Acknowledgements

This research supported in part by an NSF grant DMS-0402276.

References

[1] G.S. Bales and D.C. Chrzan. Dynamics of irreversible island growth during submonolayer epitaxy. *Phys. Rev. B*, 50:6057–6067, 1994.

[2] W.K. Burton, N. Cabrera, and F.C. Frank. The growth of crystals and the equilibrium structure of their surfaces. *Phil. Trans. Roy. Soc. London Ser. A*, 243:299–358, 1951.

[3] B. Li and R.E. Caflisch. Analysis of island dynamics in epitaxial growth. *Multiscale Model. Sim.*, 1:150–171, 2002.

[4] S. Osher and J.A. Sethian. Front propagation with curvature dependent speed: Algorithms based on Hamilton-Jacobi formulations. *J. Comp. Phys.*, 79:12–49, 1988.

[5] C. Ratsch, C. Anderson, R.E. Caflisch, L. Feigenbaum, D. Shaevitz, M. Sheffler, and C. Tiee. Multiple domain dynamics simulated with coupled level sets. *Appl. Math. Lett.*, 16:1165–1170, 2003.

[6] C. Ratsch, M.F. Gyure, S. Chen, M. Kang, and D.D. Vvedensky. Fluctuations and scaling in aggregation phenomena. *Phys. Rev. B*, 61:10598–10601, 2000.

A Coupled Meso-Macro Scale Formulation for Modeling of Microstructure Evolution and Wrinkling Formation in Polycrystalline Materials

J. S. Chen and S. Mehraeen

Civil & Environmental Engineering Department, 5731G Boelter Hall
University of California, Los Angeles,
Los Angeles, CA 90095, USA, email: jschen@seas.ucla.edu

ABSTRACT

This work aims to develop multi-scale mathematical formulation and computational algorithm for modeling microstructure evolution and wrinkling formation in polycrystalline materials. In this development, a multi-scale variational formulation based on asymptotic expansion and principle of virtual power [1], in conjunction with a double-grid numerical method [2], is proposed for modeling stressed grain growth. The expanded variational equation gives rise to multi-scale Euler equations describing evolution processes at different scales, the scale coupling relation, as well as the homogenized material properties. A multi-scale formulation for obtaining fine-scale eigenmodes corresponding to the wrinkling formation is also proposed.

1. Multi-scale Variational Formulation for Modeling of Stress Grain Growth

A unit cell with domain Ω and boundary Γ of a continuum in the physical domain measured by macro-scale coordinate $\boldsymbol{x}$ is mapped to referential domain Ω^y and boundary Γ^y measured by a meso-scale coordinate $\boldsymbol{y}$. A variational equation for stressed grain growth based on the principle of virtual power described in the $\boldsymbol{x}$-coordinate [2] is

$$d\prod(\boldsymbol{v},\bar{\boldsymbol{v}}) = \int_{\Gamma_{gb}} \gamma\left(\frac{\partial d\bar{v}_s}{\partial s} + \frac{d\bar{v}_n}{R}\right) d\Gamma + \int_{\Gamma_{gb}} \frac{d\bar{v}_n}{m}\bar{v}_n d\Gamma + \int_{\Gamma_{gb}} \frac{1}{2}\left(\boldsymbol{s}^+ : \boldsymbol{e}^+ - \boldsymbol{s}^- : \boldsymbol{e}^-\right) d\bar{v}_n \, \mathrm{d}\Gamma$$
$$+ \int_{\Omega} \frac{1}{2} d\left(\boldsymbol{s} : \dot{\boldsymbol{e}}\right) \, \mathrm{d}\Omega - \int_{\Gamma_h} d\boldsymbol{v}\cdot\boldsymbol{h} \, \mathrm{d}\Gamma - \int_{\Omega} d\boldsymbol{v}\cdot\boldsymbol{b} \, \mathrm{d}\Omega \tag{1}$$

where $\boldsymbol{v}$ is the grain material velocity, $\bar{\boldsymbol{v}}$ is the grain boundary migration velocity, $\bar{v}_n$ is the normal velocity pointing away from the center of curvature of the grain boundary, $\bar{v}_s$ is the tangential velocity along the grain boundary, γ is the surface tension (the boundary energy per unit area), R is the radius of curvature of the grain boundary, μ is the mobility representing the ease with which the grain boundary can migrate, $\boldsymbol{h}$ is the surface traction applied on the traction boundary Γ_h, $\boldsymbol{b}$ is body force, $\boldsymbol{\sigma}^+$ and $\boldsymbol{\varepsilon}^+$ respectively are the stress and strain in the grain that gains virtual area $\delta\bar{v}_n d\Gamma$, and $\boldsymbol{\sigma}^-$ and $\boldsymbol{\varepsilon}^-$ respectively are the stress and strain in the grain located on the other side of

the boundary. Introducing asymptotic expansion into $\boldsymbol{v}$ and $\bar{\boldsymbol{v}}$, the variational formulation can be split hierarchically into coarse and fine scale components

$$\delta\Pi\left(\boldsymbol{v}^{[0]}+\lambda\boldsymbol{v}^{[1]},\bar{\boldsymbol{v}}^{[0]}+\ \lambda\bar{\boldsymbol{v}}^{[1]}\right)=\lambda^{-2}\delta\Pi^{[-2]}+\lambda^{-1}\delta\Pi^{[-1]}+\delta\Pi^{[0]}+O(\lambda)=0. \tag{2}$$

From Eqn. (2), we obtain (1) coarse scale conditions, (2) scale-coupling equation, (3) homogenized grain deformation equation, and (4) grain boundary migration equations. Solving the scale-coupling equation by the conventional finite element method requires a continuous remeshing in the event of grain boundary topological changes and the evolution of grain structures. Alternatively, a moving least-square reproducing kernel (MLS/RK) approximation with grain boundary interface enrichment [3] is introduced for the approximation of grain material velocity, whereas $\bar{\boldsymbol{v}}$ on the grain boundaries is approximated by the finite element shape functions [1,2]. A multi-scale modeling of grain growth subjected to a uniaxial horizontal tensile load using the proposed multi-scale variational equation in conjunction with the double-grid method is shown in Fig. 1.

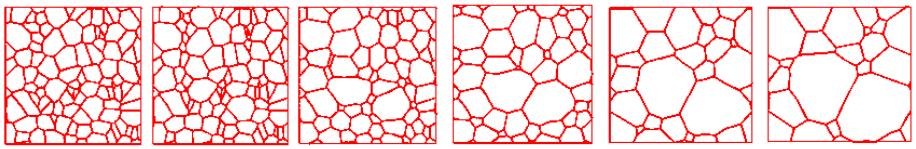

Figure 1. Meshfree modeling of grain growth in polycrystalline materials

2. Multi-scale Method for Prediction of Wrinkling Formation

For modeling of wrinkling formation, variational equation for total Lagrangian formulation in the rate form is adopted. The interrelation between coarse and fine scales of incremental deformation is

$$\Delta u_i^{\text{micro}}(Y)=\Delta F_{ij}^{[0]}y_j+\Delta F_{mn}^{[0]}\alpha_{imn}(Y) \tag{3}$$

where α_{imn} is the coupling function, Y and y are the material coordinates on the meso-scale, and $F_{ij}^{[0]}$ is macroscopic deformation gradient. The coupling function is obtained by

$$\int_Y \frac{\partial\delta u_i^{[1]}}{\partial Y_j}\left(D_{ijmn}+S_{ijmn}\right)\frac{\partial\alpha_{mkl}(Y)}{\partial Y_n}dY=-\int_Y \frac{\partial\delta u_i^{[1]}}{\partial Y_j}\left(D_{ijkl}+S_{ijkl}\right)dY,\ \ \forall du_i^{[1]}\in H_0^1 \tag{4}$$

where $D_{ijkl}=F_{im}C^2_{jmln}F_{kn}$, $S_{ijkl}=S_{jl}\delta_{ik}$, C^2_{ijkl} is the 2nd elasticity tensor. Upon employing the coupling function in the multi-scale Euler equations derived from total Lagrangian variational equation, a macroscopic governing equation can be obtained. The average strain energy density of the unit cell corresponding to an integration point of the continuum body can be evaluated from

$$W^{[0]}=\frac{1}{|Y|}\int_Y W(\boldsymbol{F})\,d\Omega,\ \ F_{ij}=\partial u_{\text{i}}^{\text{micro}}\big/\partial X_j \tag{5}$$

Consequently, the macroscopic total Lagrangian incremental equation is obtained as

$$\int_{\Omega_X} \frac{\partial \delta u_i^{[0]}}{\partial Y_j} A_{ijkl}^{[0]} \Delta u_{k,l}^{[0]} d\Omega = \int_{\Omega_X} \delta u_i^{[0]} \Delta b_i^{[0]} d\Omega + \int_{\Gamma_X^h} \delta u_i^{[0]} \Delta h_i^{[0]} d\Omega - \int_{\Omega_X} \frac{\partial \delta u_i^{[0]}}{\partial Y_j} P_{ij}^{[0]} d\Omega, \ \forall \delta u_i^{[0]} \in H_0^1 \quad (6)$$

$$A_{ijkl}^{[0]} = 1/|Y| \int_Y A_{pqrs} K_{pqij} K_{rskl} d\Omega, \quad K_{nmij} = \delta_{jm} \delta_{in} + \alpha_{mjin} \quad (7)$$

where $P^{[0]}$ is the coarse-scale 1st Piola Kirchoff stress. An example is demonstrated in which the wrinkling formation of a sheet metal is modeled as presented in Fig 2. It is shown that the proposed method captures the wrinkles induced by the microstructure upon its initiation. It is noted that unlike recent asymptotic expansion based methods [4], taking the advantage of coupling function, the tangent stiffness matrix possesses the major symmetry property.

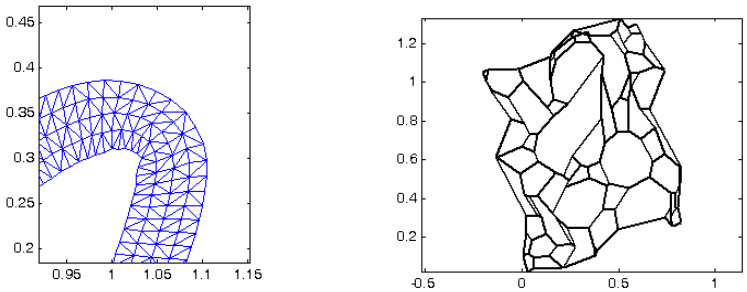

(a) **(b)**

Figure 2. (a) wrinkling formation in sheet metal forming, **(b)** microstructure deformation in elements adjacent to wrinkles

References

1. Chen, J. S. and Mehraeen, S., "Variationally Consistent Multi-scale Modeling and Homogenization of Stressed Grain Growth," Computer Methods in Applied mechanics and Engineering, Vol. 193, pp. 1825-1848, 2004.
2. Chen, J. S., Kotta, V. Lu, H., Wang, D., Moldovan, D., Wolf, D., "A Variational Formulation and a Double-grid Method for Meso-scale Modeling of Stressed Grain Growth in Polycrystalline Materials," Computer Methods in Applied Mechanics and Engineering, , Vol. 193, pp. 1277-1303, 2004.
3. D. Wang, J.S. Chen, Homogenization of magnetostrictive particle-filled elastomers using meshfree method with interface discontinuity, J. Finite Element Anal. Design, 39 (2002) 765-782 (Finalist of Robert Melosh student paper competition, 2002).
4. N. Takano, Y. Ohnishi, M. Zako, K. Nishiyabu, The formulation of homogenized method applied to large deformation problem for composite materials, Int. J. Solids Stru. 37 (2000) 6517-6535.

Multiscale modeling of ductile polycrystalline metals at high strain rate

S. Kuchnicki[a], R. Radovitzky[b], L. Stainier[c], A. Cuitiño[a], M. Ortiz[d]
[a]Department of Mechanical and Aerospace Engineering
Rutgers University, Piscataway, NJ 08854 USA
E-mail: *cuitino@jove.rutgers.edu*
[b]Department of Aeronautics and Astronautics
Massachusetts Institute of Technology, Cambridge, MA 02139 USA
[c]Laboratoire de Techniques Aéronautiques et Spatiales
University of Liège, 4000 Liège, Belgium
[d]Graduate Aeronautical Laboratories
California Institute of Technology, Pasadena, CA 91125 USA

Abstract

We formulate a fully explicit model for the behavior of bcc metals based in part on the variational model of Stainier, *et al* [5]. This model uses the average behavior of small-scale unit processes to inform the response at larger scales; specifically, we consider double-kink motion, the thermally-activated motion of kinks, close-range interactions between primary and forest dislocations, percolation motion of dislocations, dislocation multiplication via double cross-slip, and dislocation annihilation. Additionally, we take into account the effects of changing pressure on the elastic moduli via the equation of state, and on the dislocation core energies via atomistic calculations. The current model's plasticity solution is based on the implicit formulation of Cuitiño and Ortiz [1], modified to an explicit form. The explicit form is found to use considerably less computer time per integration step than both the implicit Cuitino and variational models, with little loss of accuracy. We validate our new model versus existing experimental data for single-crystal bcc Tantalum. We then apply our model to deformation of polycrystalline Tantalum through direct numerical simulation (DNS) and Taylor averaging. A large-scale finite-element solver utilizing both message passing and adaptive meshing is employed for these tests. The common Taylor anvil simulation is chosen as an appropriate test of our simulation capabilities. We find our deformed shape predictions to be acceptable.

1 Methodology

Modeling the deformation of body-centered cubic (bcc) metals takes on several degrees of complexity beyond face-centered cubic (fcc) metals. This is due both to the increase in the possible number of slip systems (defining the solution space for an implicit solver) and the addition of more mechanisms that affect the deformation, including the Peierls resistance and the motion of dislocation cores. Stainier, *et al* [5] presented a fully-implicit variational formulation for bcc metals, using atomistic data derived at the microscale to inform the material model at the macroscale. This model is quite effective for bcc Tantalum, but is also quite slow for use with the smaller time steps required by a dynamic simulation. In the interest of increasing computational speed, we combine the hardening laws of the variational model with the power-law slip-rate model of Cuitiño and Ortiz

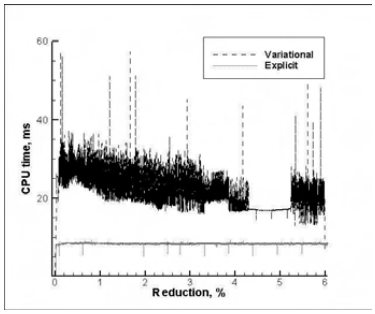

Figure 1: Time spent per integration step for the explicit and variational models.

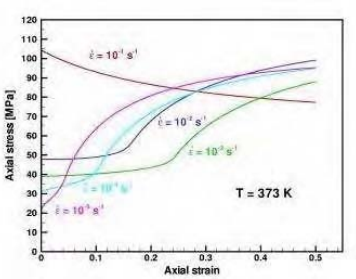

Figure 2: Predictions of the variational model. After Stainier, *et al* [5]

[1] to produce a hybrid model. This hybrid is cast in both implicit and explicit forms, with the addition of a subcycling algorithm to extend the maximal time step that the explicit model can evaluate. A similar implementation for fcc metals is described by Kuchnicki, *et al* [2]. Fig. 1 compares the evaluation time per step between the variational model of Stainier, *et al* and the current implementation in its explicit forms. Note that we gain a factor of about three to five in computational speed by using the explicit formulation. This gain of speed is not nearly as great as reported for the fcc case, a difference we attribute to the relative complexity of the bcc material model, even in its explicit form.

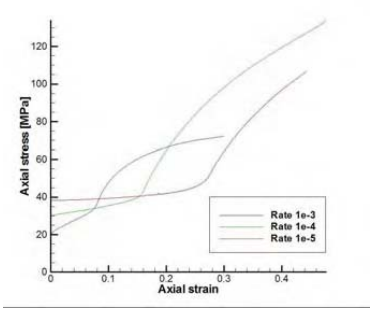

Figure 3: Predictions of the implicit form of the current model at 373K.

2 Results

We begin by presenting constitutive-level results on single-crystal tests to provide a basis for comparison with the variational model. Figs. 2 and 3 compare the variational and implicit model predictions for a [213] Tantalum crystal in uniaxial tension for several strain rates. The results are in agreement with each other and with the experimental data of Mitchell and Spitzig [4]. We also tested the explicit and implicit models in uniaxial extension at strain rate $10^{-1}/s$. We found that these models return similar stress-strain predictions, differing by 2.8% at 25% extension.

Finally, we extend our analysis to polycrystals via the Taylor anvil test. We model the Tantalum rod as a polycrystal via Taylor averaging, taking the stress response at each point in the mesh as the average of ten orientations, each given the same overall deformation gradient. This simulation is applied over a large-scale finite-element mesh, utilizing an adaptive meshing algorithm and message passing. Fig. 4 shows the deformed shape after most of the initial velocity of $100m/s$ has been dissipated. The predictions provide a qualitative match with this sort of experiment (see, for example, Maudlin, *et. al.* [3]).

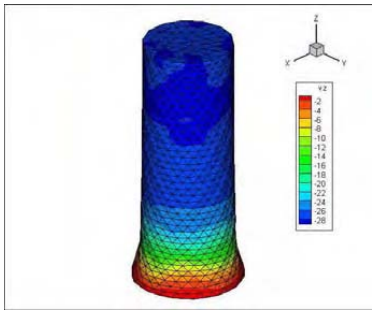

Figure 4: Predicted shape of the Taylor anvil test sample.

3 Conclusions

We have presented a material model for bcc metals that is a hybrid of two earlier algorithms. We borrow much of the physical description of the model from the variational model of Stainier, *et al* [5] and the mechanics of the update (including slip strain rates) from Cuitino and Ortiz [1]. The resulting model agrees qualitatively with the predictions of the variational model, while gaining an order of magnitude in computational speed. The resulting explicit formulation is well-suited to applications over large-scale finite-element simulations, as shown by our Taylor anvil test predictions.

Acknowledgements

This work was sponsored by the U.S. Department of Energy's Accelerated Strategic Computing Initiative (ASC) and the ASC Center at the California Institute of Technology.

References

[1] A. Cuitiño and M. Ortiz. Computational modeling of single crystals. *Modelling and Simulation in Materials Science and Engineering*, 1:255–263, 1993.

[2] S. Kuchnicki, A. Cuitiño, and R. Radovitzky. Toward increasing the computational efficiency of single-crystal plasticity algorithms. *Sumbitted for review*, 2004.

[3] P. Maudlin, J. Bingert, J. House, and S. Chen. On the modeling of the taylor cylinder impact test for orthotropic textured materials: Experiments and simulations. *International Journal of Plasticity*, 15:139–166, 1999.

[4] T. Mitchell and W. Spitzig. Three-stage hardening in tantalum single crystals. *Acta Metallurgica*, 13:1169–1179, 1965.

[5] L. Stainier, A. Cuitiño, and M. Ortiz. A micromechanical model of hardening, rate sensitivity, and thermal softening in bcc crystals. *Journal of the Mechanics and Physics of Solids*, 50(7):1511–1545, 2002.

Thermodynamic Field Estimators for Atomistic-Continuum Hybrid Simulations

Jacob Eapen[*], Ju Li[+] and Sidney Yip[*]

[*] *Department of Nuclear Engineering, Massachusetts Institute of Technology, Cambridge, MA 02139*
[+] *Department of Material Science, Ohio State University, Columbus, OH 43210*

ABSTRACT

A central issue in linking particle-continuum simulations is to efficiently couple two descriptions that involve very different sets of degrees of freedom, particle trajectory data on the one hand and spatial fields on the other. Currently, the field descriptions are commonly based on *ad-hoc* averaging using bins. In this paper, we present a systematic way to generate smooth and continuous fields from particle simulations using statistical inference. These techniques are applied to a molecular dynamics (MD) simulation of shear or lid-driven flow in a confined enclosure. For generating the spatial density field, we propose a non-parametric field estimator based on the maximum-entropy (ME) principle. For generating the velocity field we use a parametric estimator based on maximum likelihood technique. The field estimators indicate that for lid speeds smaller than the thermal speed, the flow in the nano-enclosure is essentially Newtonian.

1. INTRODUCTION

An accurate field description is an essential ingredient to multiscale modeling which in most cases involves coupling of microscopic simulators with the continuum field equations. A spatial buffer is typically prescribed for transferring data from the continuum to the molecular region and *vice versa*. The continuum supplies the mean field variables to the molecular simulator and in return, the interfacial or boundary conditions for the continuum are calculated from the molecular simulator. Equation-free multiscale methodology works in a different fashion. Rather than coupling the microscopic simulators with the continuum, the equation-free approach bypasses the continuum models such as the Navier-Stokes equation completely. Instead, it works exclusively with microscopic simulators and employs a series of numerical operations that are akin to the buffer transfers in coupled atomistic-continuum simulations [1]. This methodology is appropriate for phenomena where macroscopic equations are unavailable in the closed form such as in colloidal or melt flows.

Coarse grained averages in MD simulations often suffer from noisy fluctuations or poor resolution. This behavior arises primarily due to the *ad-hoc* bin averaging procedure that is commonly employed for extracting the field information. In this paper, we focus on a systematic way to construct smooth and continuous fields from fluctuating MD data using statistical inference techniques. Li, Liao and Yip [2] have formulated a parametric method based on maximum likelihood inference for generating smooth velocity and temperature fields. In this technique, the particles of interest are assumed to conform to a local Maxwellian distribution.

For the macroscopic variables such as density and stresses, the form of the distribution is not known *a priori*. Hence, any field estimator for these variables should be necessarily non-parametric. In this paper, we present a density estimator based on maximum entropy principle. As a model problem, we simulate a two-dimensional shear or lid-driven flow in a confined enclosure with both MD and continuum methods. The flow in a confined enclosure is a non-trivial fluid-dynamical problem and it exhibits a higher degree of complexity than that is observed in the regularly studied Coutte and Poiseuille flows.

2. ME DENSITY ESTIMATOR

The ME method identifies the least biased distribution that is consistent with the given constraints. The constraints are generally in the form of moments of the distribution. The ME principle states that the least biased distribution can be obtained by maximizing Shannon's information entropy which is given by:

$$H(\mathbf{x}) = -\int \rho(\mathbf{x}) \ln \rho(\mathbf{x}) d\mathbf{x} \tag{1}$$

The solution to this maximization problem is:

$$\rho(\mathbf{x}) = \exp\left(-\sum_{\mathbf{m}} \lambda_{\mathbf{m}} \varphi_{\mathbf{m}}(\mathbf{x}) \right) \tag{2}$$

where $\lambda_{\mathbf{m}}$ denote the Lagrange multipliers. They can be evaluated by solving the following set of non-linear equations [3]:

$$\int \varphi_{\mathbf{m}}(\mathbf{x}) \exp\left(-\sum_{\mathbf{m}} \lambda_{\mathbf{m}} \varphi_{\mathbf{m}}(\mathbf{x}) \right) dx = \mu_{\mathbf{m}} \tag{3}$$

The empirical moments μ are determined from the known particle positions $\mathbf{X}_n$ and are given by:

$$\mu_{\mathbf{m}} = \frac{1}{N} \sum_{n=1}^{N} \varphi_{\mathbf{m}}(\mathbf{X}_n) \tag{4}$$

where N is the total number of particles and φ stands for trial functions. **m** is a d dimensional vector which contains the empirical moments derived from the particle locations. d denotes the dimensionality of the physical system. The Lagrange parameters are determined by solving the set of non-linear equations in Eqn. (3) by Newton method.

3. RESULTS AND CONCLUSIONS

The field estimators are applied to a MD simulation of shear driven cavity flow. The cavity has a linear dimension of 100 with 4184 fluid atoms and 1952 solid atoms. The top lid moves in the

positive x-direction with a speed of 0.68. The density field generated by ME is delineated in Fig. 1 and the corresponding scatter plot is depicted in Fig. 2. It is not difficult to visualize that the bottom-left region is more thickly populated than the other regions especially near the top right corner. ME estimator captures this essential information. A bin average for the corresponding particle position is shown in Fig. 3. The field representation is jagged and additional interpolation is required to smoothen out the unevenness. Fig.4. shows the streamlines obtained with the maximum likelihood estimator. They show excellent conformity, in spite of noticeable density gradients, to those from Newtonian continuum simulations (results not shown).

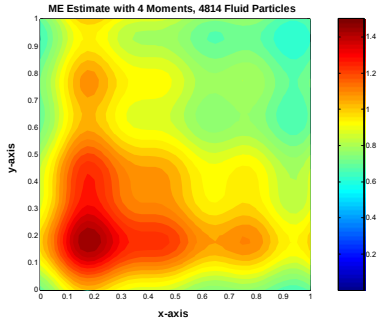

Figure 1. Maximum Entropy Density Field, $Re = 100$, $T = 1$ $\rho = 0.49$

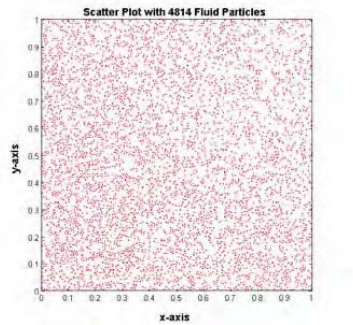

Figure 2. Scatter Plot of Fluid Atoms, $Re = 100$, $T = 1$ $\rho = 0.49$

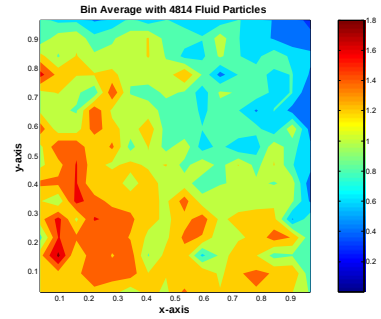

Figure 3. Density Field with Bin Average $Re = 100$, $T = 1$ $\rho = 0.49$

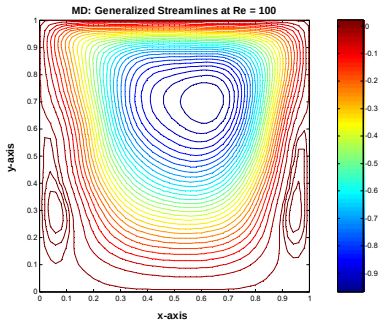

Figure 4. Streamlines with MD Simulation, $Re = 100$, $T = 1$ $\rho = 0.49$

4. REFERENCES

[1] I.G. Kevrekidis, C.W Gear, J.H. Hyman, P.G. Kevrekidis, O. Runborg and C. Theodoropoulos, Comm. Math. Sci. **1** (**4**): 715-762 (2003).

[2] J. Li, D. Liao and S. Yip, Phys. Rev. E, **57** (**6**)**:** 7259-7267 (1998).

[3] A. Mohammad-Djafari, *Proc. of the Eleventh International Workshop on Maximum Entropy Methods of Statistical Analysis*, ed. C. R. Smith, G. J. Erickson and P. O. Neudorfer, 131-139, 221-233, Kluwer Academic Publishers, Netherlands (1991).

Deformation Behavior Analysis in ECAP Using Arbitrary Lagrangian-Eulerian Formulation

Jun-Hyun Han[1], Hyung-Joon Chang[2], Jin-Kook Yoon[1], Kwang-Koo Jee[1] Jong-Woo Park[1], and Kyu Hwan Oh[2]

[1] Div. of Materials Science & Technology, Korea Institute of Science and Technology (KIST), Seoul, 136-791, Korea, jhhan@kist.re.kr,
[2] School of Materials Science and Engineering, Seoul National University, Shinrim-dong 56-1, Kwanak-ku, Seoul 151-742, Korea,

ABSTRACT

The deformation behavior during equal channel angular pressing (ECAP) was investigated using the arbitrary Lagrangian-Eulerian (ALE) formulation as an analysis tool of finite element method. Effects of the oblique angle (Φ) and the curvature angle (Ψ) of die on the deformation behavior were studied in terms of variation of the deformation rate (D). The deformation zone was divided into two regions showing the different deformation characteristics by the zero dilatation line.

1. Introduction

To analyze the deformation behavior during equal channel angular pressing (ECAP), several studies [1-2] have been in general conducted using the finite element method (FEM), in which Lagrangian analysis method has been used as a calculating tool. However, this calculating tool has some difficulty in calculating the deformation behavior in high strained region such as deformation zone in ECAP. If the Arbitrary Lagrangian-Eulerian (ALE) formulation [3] is adopted for deformation analysis within deformation zone of ECAP, the calculation can be easy and simple since mesh flow can be embodied by Eulerian analysis method. In this study, the deformation history within the deformation zone during ECAP was investigated using the ALE formulation. Effects of the oblique angle (Φ) and curvature angle (Ψ) of die [1-2] on the deformation behavior were studied from the variation of the deformation rate calculated from the deformation gradient, and then the characteristics of the deformation zone were defined.

2. Procedure

The deformation behavior of the workpiece during ECAP was simulated using the commercial finite element analysis software ABAQUS. The oblique angles of the die considered in this study were 105^{o}, 120^{o}, and 135^{o}, and the curvature angle was varied from 15^{o} to 90^{o}. A two dimensional problem was considered since the ECAP process satisfies the plane-strain condition. Friction between die and workpiece was neglected, and the material considered for the elasto-plastic analyses was regard as a perfectly

plastic one. From the coordinates of points of concern in material flow analyzed by FEM, the deformation gradient (**F**) [4] was calculated. The velocity gradient (**L**) was determined from the relationship with deformation gradient given as $\mathbf{L} = \dot{\mathrm{F}} \cdot \mathrm{F}^{-1}$ at several thickness positions of workpiece (S= 0.10~ 0.85, where S represents the distance from the bottom of workpiece normalized with respect to its thickness). The symmetric part of the velocity gradient **L** (or **D**) [4] given as $\mathbf{D} = 1/2(\mathbf{L} + \mathbf{L}^{\mathrm{T}})$ describes the deformation rate at any material point. Thus **D** is known as the deformation rate tensor or strain rate tensor. In this study, the deformation rate tensor (**D**) was considered in order to analyze the deformation history with only pure deformation without rigid body rotation inducing textural evolution during ECAP.

3. Results and Discussion

Fig. 1 represents the variations of the deformation rate components (D_{11}, D_{12}, D_{21}, and D_{22}) at S=0.85 of die with curvature angle (Ψ) of 0^{o} and oblique angle (Φ) of 120^{o}, where a special processing time was found during ECAP at which not only are two dilatation components (D_{11} and D_{22}) of the deformation rate equal to zero but the shear component (D_{12} or D_{21}) also has a maximum. In this study, therefore, it was called zero dilatation point or maximum shear point. Results similar to the variations of the deformation rate components as shown in Fig. 1 could be also obtained at the S=0.65, S=0.45, and S=0.25 of die. The zero dilatation points and the starting and finishing points of deformations obtained from a series of relative distances from the bottom of the workpiece (S=0.85, 0.65, 0.45, and 0.25) were put together in Fig. 2, from which it was observed that a line connecting the zero dilatation points, so called zero dilatation line, agrees well with the line of intersection of the two die channels. Such a result mentioned above could be also obtained in workpieces with both different oblique angles ($\Phi = 135^{o}$ and 105^{o}) and different curvature angles ($\Psi = 28^{o}$, 48^{o}, and 90^{o}) of die. Therefore, it can be concluded intersection of the two die channels regardless of die geometry such as curvature angle

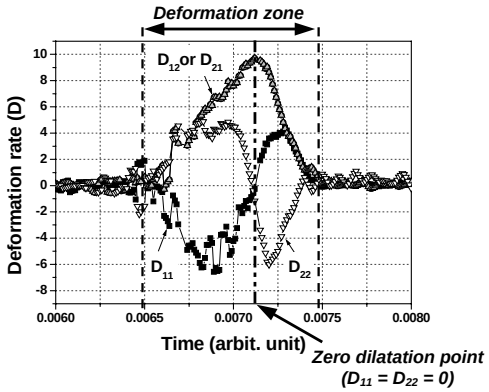

Fig. 1. Variations in the deformation rate components during ECAP analyzed by finite element method at S=0.85 of die with curvature angle (Ψ) of 0^{o} and oblique angle (Φ) of 120^{o}.

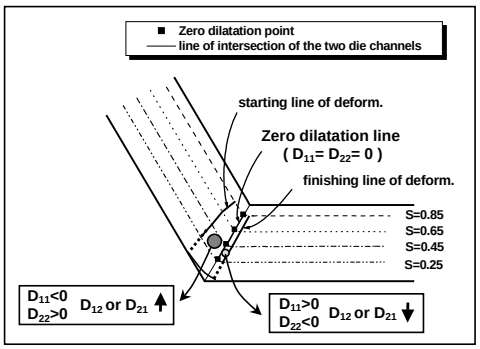

Fig. 2. Zero dilatation points and deformation zones at different relative distances, S=0.25, 0.45, 0.65, and 0.85 under curvature angle (Ψ) of 0^o and oblique angle (Φ) of 120^o. The deformation zone is divided into two regions by the zero dilatation line.

and oblique angle. The deformation zone consists of two regions showing different deformation characteristics as shown in Fig. 2; the first region prior to the zero dilatation line is characterized as $D_{11}<0$ and $D_{22}>0$, and the second region raging from the zero dilatation line to the finishing line of deformation is defined as $D_{11}>0$ and $D_{22}<0$. I.e., a significant change in the deformation characteristics takes place on the zero dilatation line. Therefore, the zero dilatation line in workpiece plays an important role in understanding the deformation behavior during ECAP.

4. Conclusions

There is a zero dilatation line, at which two dilatation components (D_{11} and D_{22}) of the deformation rate are equal to zero and the shear components (D_{12} or D_{21}) are maximum, within the deformation zone of a workpiece during ECAP. It is coincided with the line of intersection of the two die channels irrespective of die geometry such as curvature angle and oblique angle. The deformation zone is divided into two regions showing the different deformation characteristics by the zero dilatation line.

Acknowledgements

This work was financially supported by the Center for Nanostructured Materials Technology under the 21C Frontier R&D Programs of the Ministry of Science & Technology of Korea.

References

[1] A. Gholinia, P. Bate, and P.B. Prangnell, Acta Mater. **50**, 2121 (2002).
[2] J.Y. Suh, J.H. Han, K.H. Oh, J.C. Lee, Scripta Mater. **49**, 185 (2003).
[3] F. Martinet, P. Chabrand, Int J Solid Structures **37**, 4005 (2000).
[4] A.S. Khan, S. Huang, *Continuum Theory of Plasticity* (John Wiley & Sons, New York,1995), p. 20.

Multiscale Computation for Flow in Porous Media

Thomas Y. Hou

Applied and Computational Mathematics, 217-50, Caltech, Pasadena, CA 91125, USA. Email: hou@acm.caltech.edu.

ABSTRACT

Many problems of fundamental and practical importance contain multiple scale solutions. Direct numerical simulations of these multiscale problems are extremely difficult due to the range of length scales in the underlying physical problems. Here, we introduce a dynamic multiscale method for computing nonlinear partial differential equations with multiscale solutions. The main idea is to construct semi-analytic multiscale solutions local in time, and use them to approximate the multiscale solution for large times. It provides an effective multiscale numerical method for computing incompressible flow with multiscale solutions.

The flow and transport problems in porous media are considered in a hierarchical level of approximation. At the microscale, the solute transport is governed by the convection-diffusion equation in a homogeneous fluid. However, for porous media, it is very difficult to obtain full information about the pore structure. Certain averaging procedure has to be carried out, and the porous medium becomes a continuum with certain macroscopic properties, such as the porosity and permeability. Through the use of sophisticated geological and geostatistical modeling tools, engineers and geologists can now generate highly detailed, three dimensional representations of reservoir properties. Such models can be particularly important for reservoir management, as fine scale details in formation properties, such as thin, high permeability layers or thin shale barriers, can dominate reservoir behavior. The direct use of these highly resolved models for reservoir simulation is not generally feasible because their fine level of detail (tens of millions grid blocks) places prohibitive demands on computational resources. Therefore, the ability to coarsen these highly resolved geologic models to levels of detail appropriate for reservoir simulation (tens of thousands grid blocks), while maintaining the integrity of the model for purpose of flow simulation (i.e., avoiding the loss of important details), is clearly needed.

In recent years, we have introduced a multiscale finite element method (MsFEM) for solving partial differential equations with multiscale solutions [1, 2, 4]. The central goal of this approach is to obtain the large scale solutions accurately and efficiently without resolving the small scale details. The main idea is to construct finite element base functions which capture the small scale information within each element. The small scale information is then brought to the large scales through the coupling of the global stiffness matrix. Thus, the effect of small scales on the large scales is correctly

captured. In our method, the base functions are constructed from the leading order homogeneous elliptic equation in each element. As a consequence, the base functions are adapted to the local microstructure of the differential operator. In the case of two-scale periodic structures, we have proved that the multiscale method indeed converges to the correct solution independent of the small scale in the homogenization limit [2]. We remark that the idea of using base functions governed by the differential equations has been used in the finite element community, see e.g. [5, 6, 7].

The main idea of MsFEM is to construct finite element base functions which capture the small scale information within each element. This is accomplished by requiring that the base functions satisfy the leading order homogeneous differential equation within each coarse grid element with some appropriate boundary condition in the boundary of the local element. The choice of boundary conditions in defining the multiscale bases will play a crucial role in approximating the multiscale solution. The simplest choice of the boundary condition for the base function is a linear boundary condition. By performing a careful error analysis, we identify a resonance error and propose an *over-sampling* method to reduce this resonance error [1]. We remark that the multiscale finite element method has been recently extended to nonlinear problems by introducing a multiscale mapping instead of using multiscale bases [8].

To solve transport problems in the subsurface formations, as in oil reservoir simulations, one needs to compute the velocity field from the elliptic equation for pressure, i.e $\mathbf{v} = -a_\varepsilon \nabla p$, here p is pressure. For MsFEM, the fine scale velocity can be easily recovered from the multiscale base functions, noting that they provide interpolations from the coarse grid to the fine grid. To test the accuracy of the recovered velocity and effect of small-scale velocity on the transport problem, we have performed two sets of computations. In the first computation, we reconstruct the fine scale velocity field (1024 by 1024 grid) from a coarse grid (64 by 64 grid) pressure computation, and use the reconstructed fine scale velocity field to transport the saturation in the two-phase flow. In the second computation, we compute both the pressure and the saturation using a fine grid (1024 by 1024). To demonstrate that we can recover the fine grid velocity field from the coarse grid pressure calculation, we compare the velocity fields obtained by the two approaches. The agreement is excellent. The recovered velocity field captures very well the layer structure in the fine grid velocity field. Moreover, we observe that the agreement in the saturations obtained by the two approaches is striking.

References

[1] T. Y. Hou and X. H. Wu, *A Multiscale Finite Element Method for Elliptic Problems in Composite Materials and Porous Media,* J. Comput. Phys., **134** (1997), 169-189.

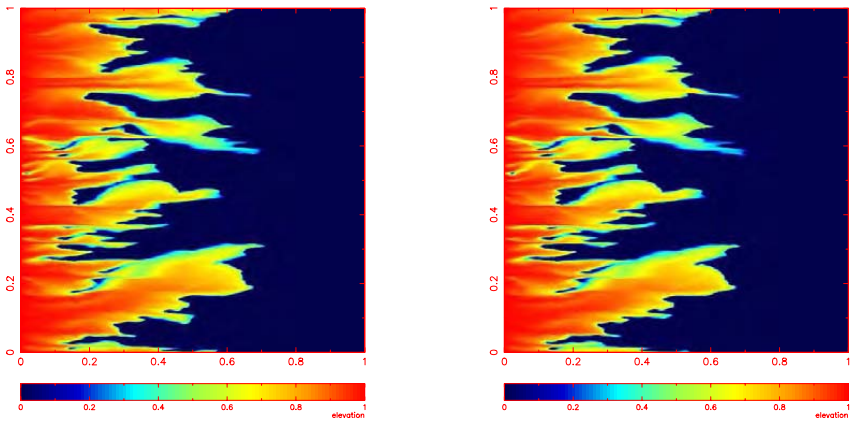

Figure 1: (a): Fine grid saturation at $t = 0.06$, $N = 1024$. (b): Saturation computed using the recovered velocity field from the coarse grid calculation ($N = 64$) using multiscale bases.

[2] T. Y. Hou, X. H. Wu, and Z. Cai, *Convergence of a Multiscale Finite Element Method for Elliptic Problems With Rapidly Oscillating Coefficients,* Math. Comput., **68** (1999), 913-943.

[3] Y. R. Efendiev, T. Y. Hou, and X. H. Wu, *Convergence of A Nonconforming Multiscale Finite Element Method,* SIAM J. Numer. Anal., **37** (2000), 888-910.

[4] Z. Chen and T. Y. Hou, *A Mixed Finite Element Method for Elliptic Problems with Rapidly Oscillating Coefficients,* Math. Comput., published electronically on June 28, 2002.

[5] I. Babuska, G. Caloz, and E. Osborn, *Special Finite Element Methods for a Class of Second Order Elliptic Problems with Rough Coefficients,* SIAM J. Numer. Anal., **31** (1994), 945-981.

[6] T. J. R. Hughes, *Multiscale Phenomena: Green's Functions, the Dirichlet-to-Neumann Formulation, Subgrid Scale Models, Bubbles and the Origins of Stabilized Methods,* Comput. Methods Appl. Mech Engrg., **127** (1995), 387-401.

[7] F. Brezzi, L. P. Franca, T. J. R. Hughes and A. Russo, $b = \int g$, Comput. Methods in Appl. Mech. and Engrg., **145** (1997), 329-339.

[8] Y. Efendiev, T. Y. Hou, and V. Ginting, *Multiscle Finite Element Methods for Nonlinear Problems and Their Applications,* to appear in Comm. Math. Sci..

Combining Coarse-Grained-Particles Dynamics and Molecular Dynamics for Multiscale Simulation of Materials

Takahiro Igarashi[a], Shuji Ogata[b], and Hiroshi Iyetomi[c]

[a]Japan Science and Technology Agency, 4-1-8 Honcho, Kawaguchi 332-0012, Japan; E-mail: t.igarashi@nitech.ac.jp
[b]Graduate School of Engineering, Nagoya Institute of Technology, Gokiso-cho, Showa-ku, Nagoya 466-8555, Japan; Email: ogata@nitech.ac.jp
[c]Department of Physics, Niigata University, 2-8050 Ikarashi, Niigata 950-2181, Japan; E-mail: hiyetomi@phys.sc.niigata-u.ac.jp

ABSTRACT

It is difficult to directly simulate realistic materials with an atomistic simulation method such as the molecular dynamics because of huge numbers of atoms involved in the system. One of the solutions to this problem is to use the idea of hybrid simulation, in which atomistic calculations are adopted for small but important regions, and continuum modeling is applied to the peripheral regions. Coarse-grained (CG) molecular dynamics method is one of such continuum models with many interesting features for large-scale simulations. However, original formulation of the CG method contains several problems that hinder its applications to real systems. In this paper, we improve CG method to overcome the problems. Applications of the improved CG method to interesting engineering problems are presented. We are planning to couple the improved CG method with the atomistic, molecular dynamics method.

1. Introduction

As characteristic scales of the materials become smaller, theoretical understating of materials properties such as fracture toughness requires coherent treatment of multiple scale processes. Various kinds of multiscale simulation method have been developed in recent years: hybrid molecular-dynamics/finite-element-method [1], hybrid quantum-mechanics/ molecular-dynamics/finite-element-method [2], and so on.

Recently, Rudd and Broughton [3] developed a new continuum approximation method for elastic materials; it is called the coarse-grained (CG) molecular dynamics method. In the method, CG particles are set into the system and interaction potentials between the CG particles are obtained by taking constrained thermal average of the atomic system. Through phonon spectra analyses and wave reflection analyses it is shown that the CG method gives accurate results than the finite-element-method does. We note that the

CG potential become equivalent to the atomic potential with the harmonic approximation when we set the CG particles on the atomic positions. Because of this feature, the CG region can be connected to the atomic region seamlessly by gradually changing degrees of coarsening near the region boundary. Therefore the CG method is expected to play a key role in developing a hybrid simulation code for large-scale realistic materials.

2. Improvement of the Original CG Formulation

Though CG method has many interesting features, its original formulation contains several problems. We improve the formulation to overcome the problems.

2.1 CG Potential As a Function of Positions

In the original formulation, the interaction potential between the CG particles is written as a function of their displacements not as a function of their absolute positions. This causes difficulty when the system deforms much. We have succeeded to reformulate the CG interaction potential as a function of CG positions.

2.2 Adaptation to Rotation

In the original formulation, the CG interaction potential is written with rotation angle of the total system fixed. In real applications, the simulation system often rotates or deforms as the simulation proceeds. In the present CG method, local rotation-angles are determined dynamically, which are used to calculate the CG interaction potentials. This procedure makes us possible to apply the present CG method to realistic systems.

2.3 Fast Calculation of Stiffness Matrix

When we calculate the stiffness matrix for the CG particles, we have to calculate inverse of dynamical matrix of the atomic system. As the cost of inverse matrix calculation is $O(N^3)$, it is difficult to directly handle a large system composed of billions of atoms by the original CG method. In the present formulation, we introduce the cut-off "distance" in the matrix space to reduce calculation costs. Stiffness matrix elements become zero when the distance is large enough. We can calculate stiffness matrix of a coarser grained system by renormalizing the stiffness matrix. By this way we can avoid huge number of calculations.

3. Stress Analyses of Two-Dimensional System with Notch

To confirm accuracy of our new CG method, we apply it to a two dimensional atomistic system in which atoms interact through the Lennard-Jones potential. System size is 1,400 x 1,200 Å with a notch at the center of the system. Number of atoms and CG

particles are 128,164 and 3,555, respectively. The system is 1% stretched along horizontal axis and both side-edge are fixed. Figure 1 shows the result of stress distribution. Clearly MD system and CG system behave in the same way.

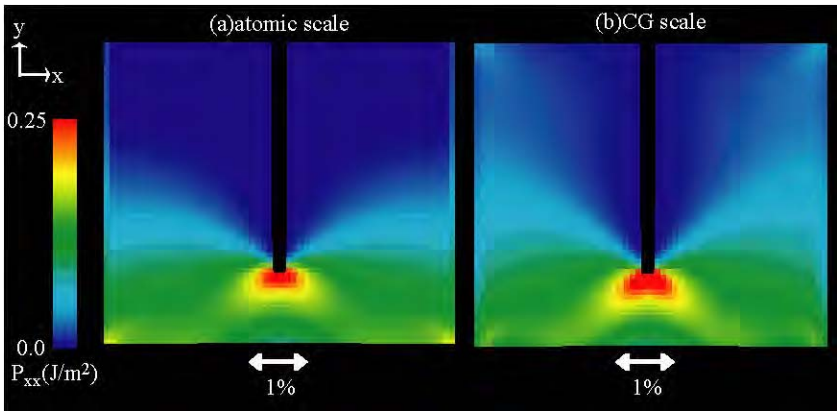

Figure 1. Stress analyses of two dimensional Lennard-Jones system with a notch.: (a) atomic scale analysis, (b)CG scale analysis.

Acknowledgements

Present work is supported by ACT-JST.

References

[1]S. Kohlhoff, P. Gumbsch, and H. F. Fischmeister, "Crack propagation in b.c.c. crystals studied with a combined finite-element and atomistic model", Philos. Mag. A64, 851 (1991).
[2]S. Ogata, E. Lidorikis, F. Shimojo, A. Nakano, P. Vashishta, and R. K. Kalia, "Hybrid Finite-Element/Molecular-Dynamics/Electronic-Density-Functional Approach to Materials Simulations on Parallel Computers", Comp. Phys. Comm. 138, 143 (2001).
[3]R. E. Rudd and J. Q. Broughton, "Coarse-grained molecular dynamics and the atomic limit of finite elements", Phys. Rev. B58, R5893 (1998).

Micromechanical Evolutionary Elastoplastic Damage Model for Fiber Reinforced Metal Matrix Composites with Fiber Debonding

J. W. Ju[*], H. N. Ruan[†], and Y. F. Ko[‡]

Department of Civil and Environmental Engineering
University of California, Los Angeles, CA 90095-1593
Tel: (310) 206-1751, juj@ucla.edu, Fax: (310) 206-2222

ABSTRACT

A micromechanical evolutionary damage model is proposed to predict the overall elastoplastic behavior and interfacial damage evolution of fiber-reinforced metal matrix composites. Progressive, fully debonded fibers are replaced by equivalent voids. The effective elastic moduli of three-phase composites, composed of a ductile matrix, randomly located yet unidirectionally aligned circular fibers, and voids, are derived by using a rigorous micromechanical formulation. In order to characterize the overall elastoplastic behavior, an effective yield criterion is derived based on the ensemble-area averaging process and the first-order effects of eigenstrains. The proposed effective yield criterion, together with the overall associative plastic flow rule and the hardening law, constitutes the equivalent three-dimensional analytical framework for the estimation of effective elastoplastic responses of metal matrix composites containing both perfectly bonded and completely debonded fibers. An evolutionary interfacial fiber debonding process, governed by the internal stresses of fibers and the interfacial strength is incorporated into the proposed framework. Further, the Weibull's statistical function is employed to describe the varying probability of complete fiber debonding. The proposed micromechanical elastoplastic-damage model is applied to the transverse uniaxial and varied stress ratio of transverse biaxial tensile loading to predict the various stress-strain responses under the plane-strain condition. Efficient step-by-step iterative computational algorithms are also presented to implement the proposed elastoplastic-damage model. Finally, comparison between the present predictions and available experimental data and other simulations are performed to illustrate the potential of the proposed formulation.

1. Introduction

Fiber-reinforced ductile matrix composites (FRDMCs) have been increasingly applied in engineering due to their improved mechanical properties. Matrix materials of FRDMCs are made of ductile metals or alloys with high strain capability, such as aluminum, steel or titanium. Fibers dispersed in matrix behave elastically, which are composed of carbon, boron or glass.

---

[*] Professor and corresponding author.
[†] Visiting Scholar; on leave from Hohai University, Nanjing, China.
[‡] Doctoral student and presenting author.

2. Procedure of inelastic micromechanical homogenization

First, we derive the effective elastic moduli of three-phase composites by neglecting pairwise interaction between fibers and voids, featuring both perfectly bonded and completely debonded fibers, emanating from the formulation by Ju and Chen [1]; i.e.,

$$\mathbf{C}_* = \mathbf{C}_o \bullet \{\mathbf{I} + \mathbf{B} \bullet (\mathbf{I} - \mathbf{S} \bullet \mathbf{B})^{-1}\} \tag{1}$$

Before any interfacial debonding occurs in a fiber-reinforced composite, it is simply a two-phase material. It has also been shown that the analytical formulation in Eqn. (1) recovers the variational lower bound of Hashin [2] for three-phase composites. Subsequently, an effective plastic yield criterion is micromechanically constructed based on the ensemble-area averaging procedure and the first-order effects of eigenstrains, on the basis of the ensemble-averaged stress norm in the matrix material:

$$< H >_m = H^\circ + \int_{\mathcal{B}_1} \left\{ H(\mathbf{x}|\boldsymbol{\beta}_1) - H^\circ \right\} P(\boldsymbol{\beta}_1)\, \mathrm{d}\boldsymbol{\beta} + \int_{\mathcal{B}_2} \left\{ H(\mathbf{x}|\boldsymbol{\beta}_2) - H^\circ \right\} P(\boldsymbol{\beta}_2)\, \mathrm{d}\boldsymbol{\beta} \tag{2}$$

Following the framework proposed by Zhao and Weng [3] and Ju and Lee [4], an evolutionary interfacial fiber debonding model is adopted here by using the Weibull's probabilistic function:

$$\phi_2 = \phi\, P_d[(\bar{\sigma}_{11})_1] = \phi \left(1 - \exp\left(-\left(\frac{(\bar{\sigma}_{11})_1}{S_o} \right)^M \right) \right) \tag{3}$$

The explicit relationship between the average internal stress inside a randomly located circular fiber and the macroscopic total strain is then derived. Under the plane-strain condition, the proposed elastoplastic-damage formulation is applied to the transverse uniaxial and various stress ratio of biaxial loading. Efficient step-by-step iterative computational algorithms are proposed to implement the new interfacial damage model.

3. Select predictions and comparisons

Finally, the present model predictions are compared with available experimental data reported by Adams [5] in Fig. 1. A number of numerical simulations are also carried out to illustrate the potential capability of the proposed framework to metal matrix composites with damage.

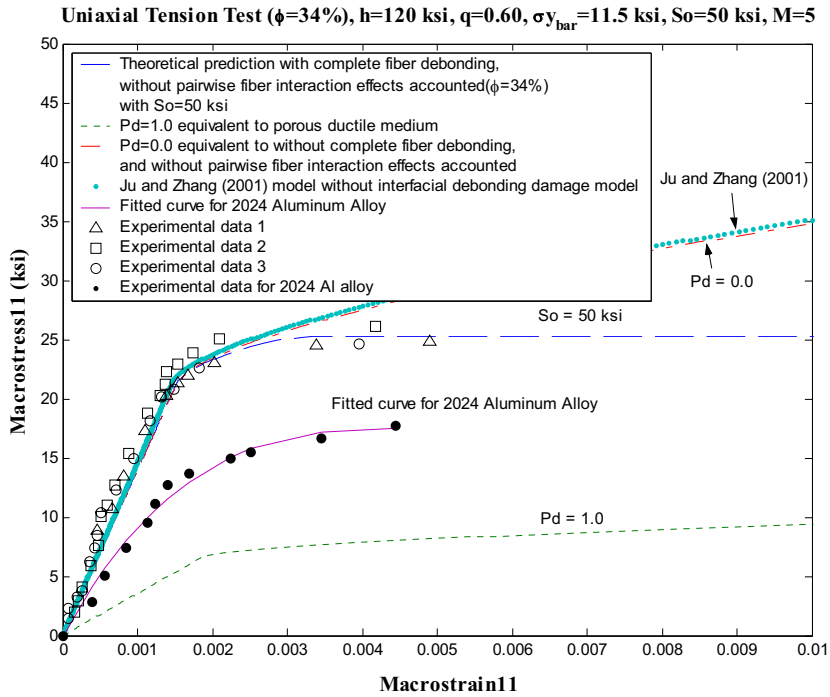

Fig. 1. The uniaxial tension test – the overall transverse stress-strain relationships $\bar{\sigma}_{11}$ vs. $\bar{\varepsilon}_{11}$ of the 2024 Al-Boron composites ($\phi = 34\%, \phi$ is initial fiber volume fractions) under the uniaxial tensile loading $\bar{\sigma}_{11}$. The comparison between the present predictions and experimental data is displayed using the Weibull interfacial strength of $S_o = 50$ ksi.

4. References

[1] Ju, J. W. and Chen, T. M., (1994a), "Micromechanics and effective moduli of elastic composites containing randomly dispersed ellipsoidal inhomogeneities", *Acta Mechanica*, **103**, 103-121.

[2] Hashin, Z., (1972), "Theory of fiber reinforced materials", NASA CR-1974.

[3] Zhao, Y. H., and Weng, G. J., (1995), "A theory of inclusion debonding and its influence on the stress-strain relations of a ductile matrix", *International Journal of Damage Mechanics*, **4**, 196-211.

[4] Ju, J. W. and Lee, H. K., (2000), "A micromechanical damage model for effective elastoplastic behavior of ductile matrix composites considering evolutionary complete particle debonding", *Comput. Methods Appl. Mech. Engrg.*, **183**, 201-222.

[5] Adams, D. F., (1970), "Inelastic analysis of a unidirectional composite subjected to transverse normal loading", *J. Comp. Mater.*, **4,** 310-328.

Study of 180 Degree Domain Wall in $PbTiO_3$ using Complex Lattice Quasicontinuum Theory

O. Kowalewsky and M. Ortiz

Graduate Aeronautical Laboratories
MC 105-50, California Institute of Technology
Pasadena CA 91125
olga@aero.caltech.edu and ortiz@aero.caltech.edu

ABSTRACT

Complex lattice Quasicontinuum theory is developed and applied to the description of ferroelectric phenomena. Quasicontinuum theory is a multiscale theory that provides a unified description of materials by combining atomistic and continuum approaches. Ferroelectrics are especially suited to the application of Quasicontinuum theory. The nature of defects in ferroelectric materials is atomistic, but their influence over the material is long ranged due to induced elastic fields. As an example we study a 180 degree domain wall in $PbTiO_3$. We obtain a very small thickness of the wall, in agreement with the recent experimental research. In contrast to molecular dynamics simulations, we are able to consider samples consisting of hundreds of thousands to millions of atoms with more realistic non-periodic boundary conditions.

1. Complex Lattice Quasicontinuum Theory

Quasicontinuum theory as introduced in [1] is a multiscale theory which bridges an atomistic and continuum description of materials. It provides a seamless transition between atomistics and continuum, but the description of the material is derived directly from the underlying atomic structure, using the computationally expensive atomistics only where they are needed - at the location of phenomena of atomistic origin. Thus, the constitutive relations for the continuum part of the theory are derived from ab initio quantum mechanics calculations.

The Quasicontinuum theory was originally designed for, and since then applied to, homogeneous crystals. We further develop the force-based non-local homogeneous crystal version of the Quasicontinuum theory proposed by Knap and Ortiz [2] for complex lattice crystals. We treat each component sub-lattice of the complex crystal as separately and independently as possible, providing separate sets of representative atoms (nodes), triangulations, shape functions and clusters around each node for the summation rule. Therefore, each sublattice becomes an instance of a Quasicontinuum by itself, with the component Quasicontinua coupled through the microscopic forces within nodal clusters, making the complex atomistic of the heterogeneous lattice the basis of the description. To find the equilibrium of the system we need to find the minimum of its potential energy. Due to the interpolation of the atom positions and summation rule, the

energy depends only on node positions. The energy minimum corresponds to the vanishing of the representative forces on the node atoms as in [2], with the microscopic forces depending on atoms of all Quasicontinua in this case. For example, with two Quasicontinua A and B the following system of equations needs to be solved:

$$\mathbf{f}_h(\mathbf{X}_a^A) \approx \sum_{all\ clusters\ s} n_s \left[\sum_{all\ atoms\ in\ cluster\ s} \mathbf{f}(\mathbf{x}_h^A) N_a(\mathbf{X}^A) \right] = 0 \quad (1)$$

$$\mathbf{f}_h(\mathbf{X}_b^B) \approx \sum_{all\ clusters\ p} n_p \left[\sum_{all\ atoms\ in\ cluster\ p} \mathbf{f}(\mathbf{x}_h^B) N_b(\mathbf{X}^B) \right] = 0 \quad (2)$$

2. Study of the 180 Degree Wall in $PbTiO_3$

Ferroelectrics attract a lot of research attention due to their excellent piezoelectric and dielectric properties and digital storage capabilities. Ferroelectrics are especially suited for the application of the complex lattice Quasicontinuum theory due to the long ranging effects resulting from atomistic defects in ferroelectrics. Quasicontinuum can track atomistic resolution near defects and continuum resolution far away from the defects, and is able to calculate samples of the order of hundreds of thousands to ten millions of atoms depending on the potential involved.

We investigate a specimen of $PbTiO_3$ in tetragonal phase. The specimen consists of more than 200,000 atoms with dimensions 25 by 25 unit cells at the wall and 65 unit cells perpendicular to the wall. The triangulation is shown in Fig.1. The resolution at the wall is atomistic.

The potential used is the shell model potential by Sepliarsky et al. [3]. Each atom core and shell are considered as separate entities. The $PbTiO_3$ lattice subdivides into five sub-lattices, one for each atom in the unit cell. Considering cores and shells for each atom, the simulation consists of ten separate Quasicontinuum instances coupled through actual microscopic forces. The Coulombic interaction of the ions which is a part of the potential is summed according to Wolf's summation rule [4] using a small damping constant. The accuracy of the summation is verified for the sample. The non-Coulombic part of the interaction is long ranged and requires a large cutoff radius for force and energy evaluation. Thus for a potential with a shorter range non-Coulombic interaction much larger samples can be simulated with complex lattice Quasicontinuum.

The results of the calculation show a very thin wall profile. The polarization of each unit cell, see Fig.1, changes very rapidly from up to down polarization. Most of the switching happens in 2-6 unit cells adjacent to the wall, corresponding to the wall thickness to be 1-2.5 nm. This is consistent with the recent ab initio calculations [5] and experimental measurements [6]. The largest supercell size used in calculations in [5] was 50 atoms with periodic boundary conditions. Our sample is much larger, more than 200,000 atoms and it includes only one domain wall with the end of the sample consisting of bulk

tetragonal domains of the opposite polarization. It is hard to say how wide the domain wall is exactly: the most polarization switching happens in the first unit cell adjacent to the wall, but the polarization is adjusting to the bulk value even 2-5 unit cells away from the wall. These results cannot be seen with quantum mechanics calculations, which have only few unit cells between the periodic walls and thus are missing long range effects.

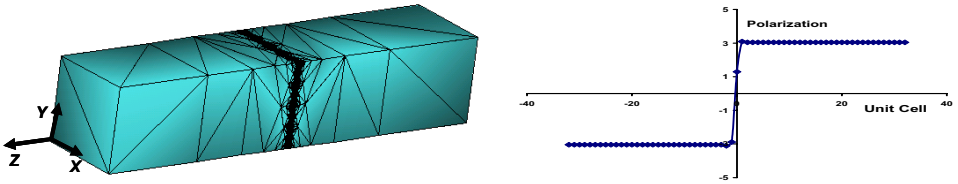

Figure 1. Triangulation and resulting polarization profile of the domain study.

The phenomenological continuum descriptions of the domain walls which can account for long ranging effects are questionable since the domain walls are so atomistically thin. The quantum mechanics calculations provide very detailed results but cannot capture the long ranging effects and also impose periodicity on the sample. The study presented here, of the domain wall using Quasicontinuum, is able to bridge atomistic resolution at the domain wall with incorporation of long range effects on a continuum scale.

3. Acknowledgements

We gratefully acknowledge the financial support of the Army Research Office (DAAD-19-99-1-0319) through a MURI. We would like to thank J. Knap and Arash Yavari for helpful discussions.

References

[1] E.B. Tadmor, R. Phillips, and M. Ortiz. Mixed atomistic and continuum models of deformation in solids. *Langmuir*, 12(19):4529-4534, 1996.
[2] J. Knap and M. Ortiz. An analysis of the quasicontinuum method. *Journal of the Mechanics and Physics of Solids*, 49:1899-1923, 2001.
[3] M. Sepliarsky, Z. Wu, A. Asthagiri, and R.E. Cohen. Atomistic model potential for $PbTiO_3$ and PMN by fitting first principles results. To be submitted to Conference Proceedings for EMF 2003, 2003.
[4] D. Wolf, P. Keblinski, S.R. Phillpot, and J. Eggebrecht. Exact method for the summation of coulombic systems by spherically truncated, pairwise r^{-1} summation. *Journal of Chemical Physics*, 110(17):8254-8282, 1999.
[5] B. Meyer and David Vanderbilt. Ab initio study of ferroelectric domain walls in $PbTiO_3$. *Physical Review B*, 65:104111, 2002.
[6] Y.G. Wang, J. Dec, and W. Kleemann. Surface and domain structures of $PbTiO_3$ crystals studied by atomic force microscopy. *Journal of Applied Physics*, 84:6795-9, 1998.

The Bridging Scale for Nano Mechanics and Materials

Harold S. Park, Eduard G. Karpov and Wing Kam Liu

Northwestern University, Department of Mechanical Engineering, 2145 Sheridan Road, Evanston, IL 60208-3111 USA
Email: w-liu@northwestern.edu

ABSTRACT

This paper focuses on the bridging scale, a concurrent multiple scale method that couples atomistic and continuum simulations. Major advantages of the proposed approach include a non-reflecting molecular dynamics (MD) boundary condition that is also coupled to the overlaying continuum, and the compact size of the resulting time history kernel. Numerical examples concentrate on the application of the method to predicting and capturing material failure in realistic two and three-dimensional atomic lattices.

1. Introduction and Overview of Bridging Scale

In this paper, we concentrate on the bridging scale, which was developed by Wagner and Liu [1], and extended to higher dimensions by Park et al [2][3]; a review of other multiple scale methods can be found in Liu et al [4]. The bridging scale couples an atomistic region that exists in a small portion of the domain to a continuum region that exists everywhere. The elimination of unwanted MD degrees of freedom is accomplished by using techniques introduced by Wagner, Karpov and Liu [5] and extended by Park, Karpov and Liu [6] for repetitive lattice structures. The same procedure can be utilized for quasistatic calculations as in Karpov et al [7]. In that case, the elimination of unwanted degrees of freedom can be done without including an explicit continuum model, and therefore a handshake region. The final coupled MD and FE equations of motion are

$$\begin{aligned} M_A\ddot{q}(t) &= f(t) + \int_0^t \theta(t-\tau)\big(q(\tau) - d(\tau)\big)d\tau + R(t) \\ M\ddot{d}(t) &= N^T f(t) \end{aligned} \tag{1}$$

The first equation is the modified MD equation of motion; the second equation is the FE equation of motion with internal forces directly obtained from the underlying MD forces $f(t)$. Advantages of the bridging scale formulation are that the matrix $\theta(t)$ has a compact size, corresponding to the minimum number of degrees of freedom in a unit cell, and that the MD equation of motion contains the FE displacements $d(\tau)$, which allows continuum boundary conditions to be transferred to the atomistic region. Furthermore, the random force $R(t)$ injects thermal energy into the system, and is the term that allows the bridging scale to be considered a finite temperature method. Finally, the time history kernel can be calculated for arbitrary lattice structures and interatomic potentials using an automated numerical procedure involving only Laplace and Fourier transforms [5][6][7].

2. Numerical Examples: Two and Three-Dimensional Dynamic Fracture

The bridging scale method has been utilized to study the dynamic fracture and failure of two and three-dimensional atomic lattices. As can be seen in Fig. (1), the boundary conditions applied to the continuum are transferred to the MD, causing fracture in the hexagonally arranged lattice interacting via a Lennard-Jones 6-12 potential. Comparisons to full MD simulations were also performed by Park et al [2]. In that work, it was demonstrated that the bridging scale simulations matched the crack initiation and propagation velocity of the full MD simulations.

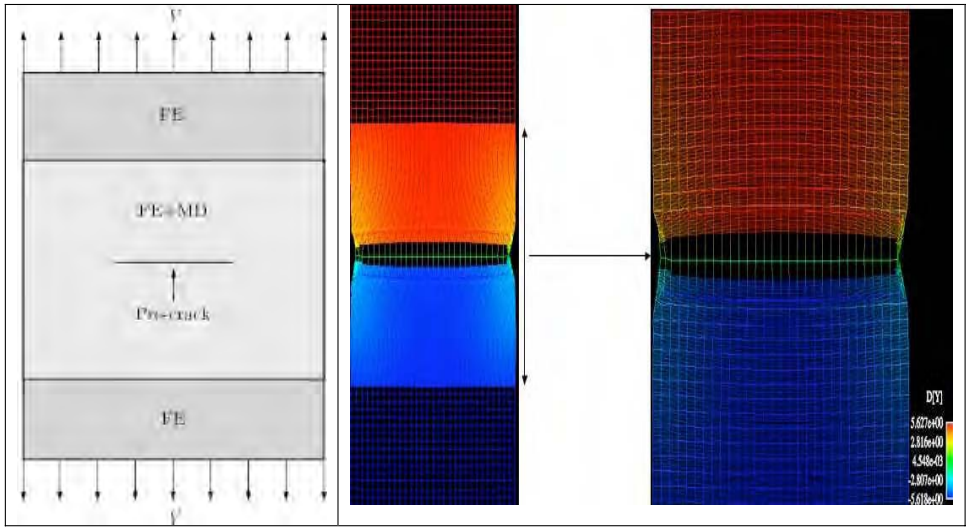

Figure 1. Left: 2D coupled MD/FEM crack propagation schematic. Right: propagation of crack in coupled MD/FEM bridging scale simulation.

In three-dimensions, fracture was analyzed in an FCC crystal interacting via a Lennard-Jones 6-12 potential. In the three-dimensional simulations, as shown in Park et al. [3] and seen in Fig. (2), interesting physics such as crack branching are seen; such physics are again accurately captured by the bridging scale simulations.

3. Conclusions and Future Research

We have briefly outlined the bridging scale concurrent method, and commented on the relative strengths of the approach. Numerical validation has been presented in two and three-dimensions on the failure modeling of realistic lattice structures. Current and future research will focus on the implementation of the random force $R(t)$ using the method of Karpov et al. [8] such that a fully thermo-mechanically coupled multiple scale methodology can be developed.

Acknowledgements

We would like to gratefully acknowledge the support of the NSF-IGERT program, the NSF Summer Institute on Nano Mechanics and Materials, and the Army Research Office (ARO).

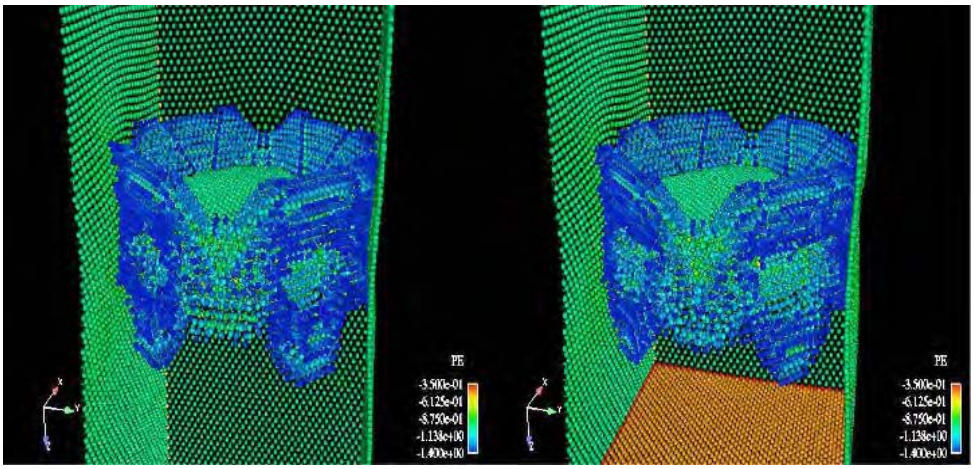

Figure 2. Left: crack branching in 3D full MD simulation. Right: crack branching in 3D coupled MD/FEM bridging scale simulation.

References

[1] G.J. Wagner, W.K. Liu, Coupling of atomistic and continuum simulations using a bridging scale decomposition, Journal of Computational Physics 190 (2003) 249-274.
[2] H.S. Park, E.G. Karpov, P.A. Klein, W.K. Liu, The bridging scale for two-dimensional atomistic/continuum coupling, accepted for publication in Philosophical Magazine (2004).
[3] H.S. Park, E.G. Karpov, P.A. Klein, W.K. Liu, Three-dimensional bridging scale analysis of dynamic fracture, submitted to Journal of Computational Physics (2004).
[4] W.K. Liu, E.G. Karpov, S. Zhang, H.S. Park, An introduction to computational nano mechanics and materials, Computer Methods in Applied Mechanics and Engineering 193 (2004) 1529-1578.
[5] G.J. Wagner, E.G. Karpov, W.K. Liu, Molecular dynamics boundary conditions for regular crystal lattices, Computer Methods in Applied Mechanics and Engineering 193 (2004) 1579-1601.
[6] H.S. Park, E.G. Karpov, W.K. Liu, Non-reflecting boundary conditions for atomistic, continuum and coupled atomistic/continuum simulations, submitted to International Journal for Numerical Methods in Engineering (2004).
[7] E.G. Karpov, H. Yu, H.S. Park, W.K. Liu, Q. Wang, D. Qian, Multiscale boundary conditions in crystalline solids: theory and application to nanoindentation, submitted to Physical Review B (2004).
[8] E.G. Karpov, H.S. Park, W.K. Liu, D.L. Dorofeev, On the modeling of chaotic thermal motion in solids, submitted to Applied Physics Letters (2004).

Multiscale Simulations Coupling Molecular Dynamics with Material Point Method

B. Wang, N. P. Daphalapurkar, H. Lu, S. Roy, and R. Komanduri*

School of Mechanical & Aerospace Engineering
Oklahoma State University, Stillwater, OK 74078, USA
***e-mail: ranga@ceat.okstate.edu**

ABSTRACT

A multiscale simulation approach is introduced that couples atomistic scale simulations using molecular dynamics (MD) with continuum scale simulations using material point method (MPM). In MPM, a hierarchical mesh refinement technique is used to scale down from the continuum level to the atomistic level, so that material points at the fine level in MPM are allowed to directly couple with the atoms in MD. A one-to-one correspondence of MD atoms and MPM points is used in the transition region, and non-local elastic theory is used to assure seamless coupling between MD and MPM regions. Uniaxial tension tests were conducted on a single crystal silicon to demonstrate the viability of the technique. A Tersoff-type, three-body potential was used in MD simulations. Coupled MD/MPM simulations show that silicon under nanometric tension experiences with increasing elongation, elastic deformation, dislocation generation and plasticity by slip, formation of voids and their growth, formation of an amorphous structure, necking, and final rupture. Results are presented in terms of stress - strain relationships at several strain rates, as well as strain rate dependence of uniaxial material properties.

1. Introduction

Coupled atomistic and continuum simulations have received increasing attention due to their potential linkage between structure-property relationships from nano- to macro-levels [1-3]. Most research focuses on simulations of coupled MD and finite element method (FEM), in which seamless coupling is a key issue. Kohlhoff *et al.* [3] introduced the transition region between atomic lattice and continuum. However, under large deformations, FEM elements get distorted and consequently it is difficult to run the entire computational process. Recently, a new computational method, namely, the material point method (MPM) was introduced [4]. Compared to FEM, MPM has some advantages, such as ability to handle large deformations in a more natural manner and easy coupling with MD simulations. As a result, MPM is a logical choice for coupling MD to continuum for multiscale simulations. However, the current MPM mesh is rather inefficient in dealing with stress concentration issues and cannot be refined to scale down the size to different levels. Consequently, a hierarchical mesh refinement technique in MPM simulations needs to be developed in coupling simulations, which is the subject of this investigation.

2. Computational Methodology

In MD, the atomistic potential for the interaction between Si-Si atoms used herein is a general form of Tersoff-type three-body potential [5]. In MPM [4], a material continuum is discretized into a finite collection of material points. Each material point is assigned with the material density and the volume of the point, and all other variables, such as position, acceleration, velocity, strain, and stress. The equations of motion are solved at the background grid nodes for each time step of the analysis. Information is transferred from the material points to grid nodes using finite element shape functions. In coupled MD/MPM simulations, there are essentially three regions, namely, MD, MPM, and their transition regions. In MD region, atoms are initially placed at lattice points. In MPM region, eight material points are equally positioned in each cubic cell. The coupling of the two descriptions of the media is brought about using a transition region where both MPM points and MD atoms are initially overlap and coincide with the atomic lattice. The width of the transition region is equal to the cutoff distance of the interaction potential used in the MD region. This provides a complete set of neighbors within the interaction range for all the atoms in the MD region. Atoms/points that belong to the transition region not only interact via the interaction potential with the MD region but also are part of the points in the MPM region. The positions and velocities of these atoms/points in the transition region (both on the MD side and on the MPM side) must be consistent with each other. The atom velocities in the transition region due to the interaction with the MD region furnish the loading boundary condition on overlapped points for the MPM simulation. To ensure complete compatibility of both strain and stress for seamless coupling between MD and MPM, the non-local elasticity theory is used in this study.

3. Numerical Results and Discussion

Fig. 1 shows 3D coupled MD/MPM model at the initial stage of tensile testing showing the MD region, MD/MPM transition regions, and MPM regions. There are three levels in the MPM region. The dimensions of this model are 32.6 Å × 32.6 Å × 222.8 Å. There are 2,901 atoms in the MD region and 9,280 material points in the MPM regions. In the transition regions, MD atoms and MPM points are initially overlapped in one-to-one correspondence and coincide with the atomic lattice. In the MD region, the crystal is set up with [001] orientation and the load is applied along the [001] direction under various velocities (see Fig.2 for details). The initial temperature

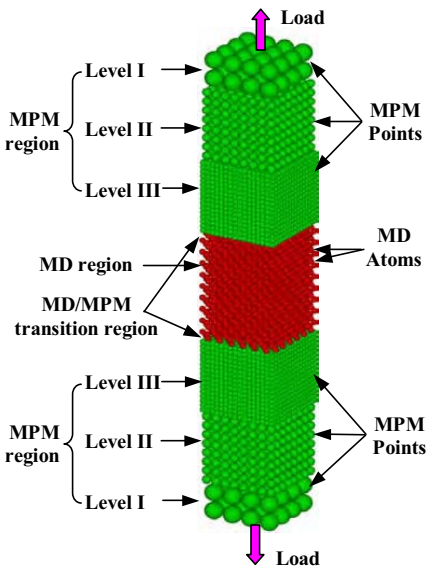

Figure 1. Coupled MD/MPM model

is 293 K for the MD simulations. The coupling simulations on the tension model are conducted for silicon at different strain rates. Animations of the coupled MD/MPM simulations show that the tensile specimen experiences with increasing elongation, elastic deformation, generation of dislocations and plasticity by slip, formation of voids and their growth, formation of amorphous structure, necking, and final fracture in the MD region. In Fig. 2, the engineering stress-strain curves at different strain rates show that material undergoes both elastic and plastic deformations as well as final rupture at different strain rates. As the strain rate increases from 44.88 to 89.76 ns^{-1}, the tensile strength increases from 15 to 18 GPa and the ultimate strain increases up to 0.54.

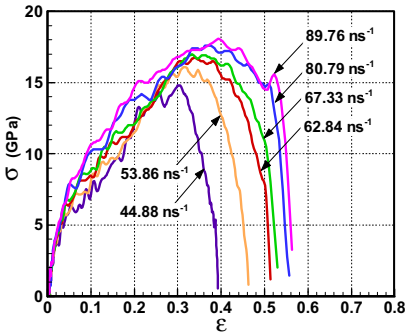

Figure 2. Stress-strain curves from coupling simulations for silicon

4. Conclusions

(1) A novel computational approach has been developed for coupling MD with MPM for multiscale simulations from atomistic to continuum; (2) The coupled MD/MPM simulations of uniaxial tension at multiscale were conducted on silicon at different strain rates; (3) All detailed deformation stages were shown in coupling simulations; and (4) Engineering stress and strain curves for silicon were determined at different strain rates, showing an increase in the tensile strength and the ultimate strain with strain rate.

Acknowledgements: The work was supported by a grant from the Air Force Office of Scientific Research (AFOSR) through a DEPSCoR grant (No. F49620-03-1-0281). The authors thank Dr. Craig S. Hartley, for his interest in and support of this work.

References

[1] Wang B., Daphalapurkar N. P., Lu H., Roy S., and Komanduri R., "Multiscale Simulation from Atomistic to Continuum - Coupling Molecular Dynamics (MD) with Material Point Method (MPM)," Phil. Mag. B, submitted (2004).

[2] Abraham, F. F., Broughton, J. Q., Bernstein, N., and Kaxiras, E., "Spanning the Length Scales in Dynamic Simulation," Comput. Phys. **12**, 538 (1998).

[3] Kohlhoff, S., Gumbsch, P., and Fischmeister, H., "Crack Propag. in BCC Crystals Studied with Combined a FE and Atomistic Model," Phil. Mag. A **64**, 851 (1991).

[4] Sulsky, D., Zhou, S., and Schreyer, H., "Application of a Particle-in-cell Method to Solid Mechanics," Comput. Phy. Commun. **87**, 236 (1995).

[5] Komanduri, R., Chandrasekaran, N., and Raff, L. M., "Molecular Dynamics (MD) Simulations of Uniaxial Tension at Nanoscale of Semiconductor Materials for MEMS Applications," J. Mater. Sci. and Eng. A **340**, 58 (2003).

Atomistic and Mesoscopic Simulations of Grain Boundary Migration and Grain Growth in Nanocrystalline Materials

D. Moldovan[a], V. Yamakov[b], A. J. Haslam[c], D. Wolf[d] and S.R. Phillpot[e]

[a] Department of Mechanical Engineering, Louisiana State University, Baton Rouge, LA, moldovan@me.lsu.edu
[b] National Institute of Aerospace, Hampton, VA
[c] Department of Chemical Engineering, Imperial College London, London, U.K.
[d] Materials Science Division, Argonne National Laboratory, Argonne, IL
[e] Department of Materials Science and Engineering, University of Florida, Gainesville, FL

ABSTRACT

We present a new methodology for measuring the mobility of curved grain boundaries using combined molecular-dynamics (MD) and mesoscopic simulation (MS) modeling of grain growth in a small, specifically tailored, Pd nanocrystalline structure. In the model system, the boundaries move under the forces provided by their curvature and the triple junctions. The mesoscopic model used is based on the Needleman-Rice variational formalism for dissipative processes, which can be readily extended to include a wide range of mechanisms contributing to the microstructural evolution. We incorporate the grain-boundary mobilities, energies and growth mechansisms, determined in the MD simulations, into the mesoscopic simulation model and investigate the grain growth in a system containing a large number of grains. The effect of a distribution in GB mobilities on the onset and development of abnormal grain growth is investigated.

1. Introduction

Grain growth is an important process which takes place during annealing of polycrystalline materials and is mediated by the migration of grain boundaries (GBs). In turn, the migration is driven by the presence of a gradient in the free energy across the GBs. There is currently great interest in developing simulation methodologies capable of giving not only qualitative but quantitative descriptions of microstructures evolution. Knowledge of the values of GB mobilities is a key issue for any simulation study. It is however difficult to measure the GB mobilities either in experiments or in atomistic simulations, mainly because one needs to measure simultaneously both the driving force and boundary velocity. Most of the atomistic simulation reported are based on a bicrystal geometry, focusing on either planar [1,2] or curved boundaries [3], and rely on driving the GB migration by either the anisotropic elastic properties of the material or by capillarity. In this study we present a novel methodology of measuring the GB mobility using a combined atomistic and mesoscopic simulation methodology. In a polycrystalline microstructure, due to relationship between GB migration and GB mobility, grains having GBs with larger mobilities grow or shrink faster than those containing lower mobility GBs, thereby promoting either normal or abnormal growth. The mechanism of abnormal grain growth in a microstructure with a distribution of GB mobilities is

investigated by a mesoscale simulation model.

2. Simulation Methodology

The simulation polycrystal model, presented in Fig. 1, consists of two square grains and two octagons. The time evolution of the model system is followed by both atomistic MD and MS simulations. By choosing the same orientation for the crystalline lattice of grains 1 and 4, based on the system symmetry, there are potentially only three different grain boundaries in this system. Moreover if the orientations with respect to x-axis are chosen as: $\theta_1 = \theta_4 = 22.5^o$, $\theta_2 = 0^o$ and $\theta_3 = 45^o$ this number is reduced further to two different GBs in the system, i.e $\gamma_{12} = \gamma_{13} = \gamma$ and $\gamma_{23} = \gamma' \neq \gamma$. As the basis for the mesoscale simulations we use the variational formalism for dissipated power of Needleman and Rice [4] adapted to grain-growth studies by Cocks and Gill [5, 6]. The atomistic system consists of a Pd nanocrytalline structure simulated by MD using the Parrinello-Rahman approach [7] at zero pressure and at 1200K.

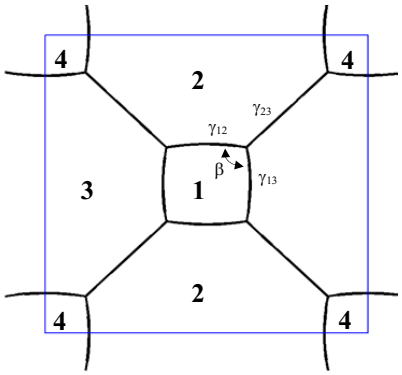

Fig1. The polycrystal simulation model

3. Simulation Results

According to the general derivation of von Neumann-Mullins law [8], one can write the relation for the rate of area change of the central four-sided grain:

$$\frac{dA_4}{dt} = m\gamma\left[2\pi - 4\beta\right] \qquad (1)$$

which may be derived by considering a general value for the dihedral angle β as given by:

$$\beta = \arccos\left(\frac{\gamma_{23}^2 - \gamma_{12}^2 - \gamma_{13}^2}{2\gamma_{12}\gamma_{13}}\right) \qquad (2)$$

The constant steady-state decrease of the area, A_4, of the central grain is followed in both MD and MS simulations as exemplified in the simulation snapshots of Fig. 2.

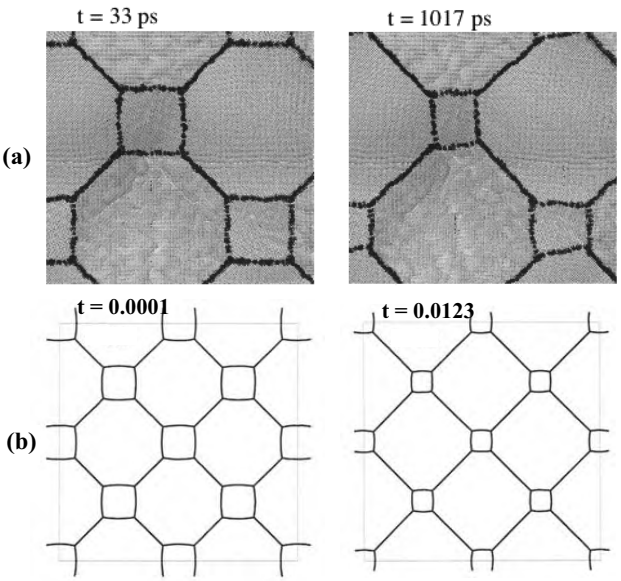

Fig. 2. Two snapshots of the evolving system described at the atomistic (a) and mesoscale (b) levels.

Following the rate of area change of the central grain by both MD and MS and knowing the GB energy from the MD simulation to be $\gamma = 0.86$ J/m^2 we can deconvolute the actual GB mobility, which at $T = 1200$ K is $m = 2.64 \times 10^{-8}\ m^4/Js$.

The effect of GB mobility anisotropy on abnormal grain growth was studied in a large mesoscale simulation. As shown in Fig. 3 a system in which about 5% of the initial grains have GBs with mobilities 7 times larger than the rest of the GBs develop in the early stage an abnormal growth characterized by a bimodal grain-size distribution. However as the microstructure coarsens a clustering of larger grains occurs which later percolates throughout the entire system. We find that the onset of this percolation coincides with the change in the growth character from abnormal back to normal growth. Moreover our studies indicate that the transition from abnormal growth stage back to normal growth occurs when the total area of abnormal grains reaches 50% of the system area.

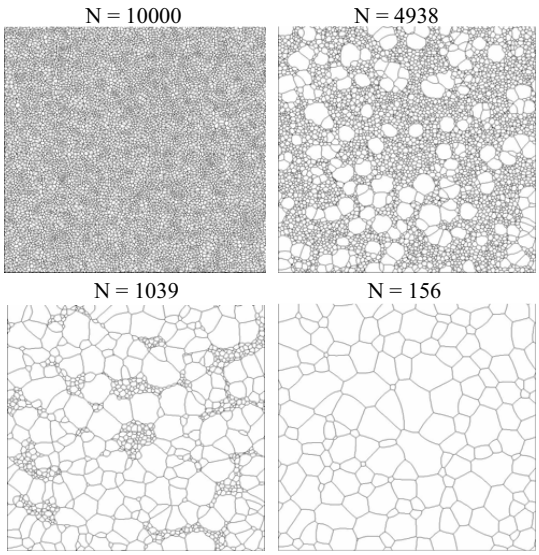

Fig 3. Four snapshots of the evolving microstructure in the presence of GB mobility inhomogeneities showing the successive transition from normal to abnormal and then back to normal grain growth.

4. Conclusions

In this study we briefly presented a new methodology for measuring the mobilities of curved GBs using a combined atomistic and mesoscopic methodology applied to a specifically tailored nanocrystalline Pd system. The effect of anisotropic GB mobilities on the transition from normal to abnormal and back to normal grain growth was investigated.

* DM acknowledges support from Louisiana Board of Regents. DW was supported by the US Department of Energy, BES-Materials Science under contract W-31-109-Eng-38.

References

[1] Schönfelder B, Wolf D, Phillpot SR, Furtkamp M, Interface Science, **5**, 245, (1997).
[2] Zhang H, Mendelev MI, Srolovitz DJ, Acta Mat., **52**, 2569 (2004)
[3] Upmanyu M, Srolovitz DJ, Shvindlerman LS, Gottstein G, Acta Mat., **4,**3901, (1999).
[4] Needleman A, Rice JR, Acta Metall., **28**,1315, (1980).
[5] Cocks ACF, Gill SPA, Acta Mater., **44**, 4765, (1996).
[6] Moldovan D, Wolf D, Phillpot SR, Haslam AJ, Phil. Mag. A, **82**, 1271, (2002).
[7] Yamakov V, Wolf D, Phillpot SR, Gleiter H. Acta Mater.; **50**, 61 (2002).
[8] Mullins WW, J. App. Phys., **27**, 900 (1956).

VIMES: A Graphical Interface for Multiscale Modeling

Richard P. Muller
Department of Computational Materials and Molecular Biology,
Sandia National Laboratories,
Albuquerque, NM, 87185-0196
rmuller@sandia.gov

ABSTRACT

We present a preview of the VIMES (Visual Interface to Material Simulation) program. VIMES is an open-source, extensible graphical interface to different types of atomistic simulation programs currently in development at Sandia National Laboratories. VIMES has been developed as an interface to many of the quantum mechanical and molecular mechanical programs at use at Sandia, and promises an easy method of integrating these methods in, for example, hybrid quantum mechanical/classical mechanical simulations of solvation. VIMES uses the Python programming language, OpenGL graphics, and the wxWindows widgets, and is being developed simultaneously on Windows, Macintosh, and Linux platforms. VIMES currently provides interfaces to the Quest and Socorro density functional theory programs, and the Towhee classical Monte Carlo program; interfaces to other programs such as MPQC, Grasp, LAMMPS, Jaguar, and GAMESS are currently either in development or under consideration. VIMES also includes builders for simple crystals, supercells, surfaces, nanotubes, and proteins.

1. Introduction

The scientist interested in multiscale modeling is presented with an array of different software choices. Each program typically uses its own input and output file formats, and each program contains a set of options that can be completely different from other programs. Substantial amounts of time are required to become fluent with each new program. The time investment is particularly costly for the multiscale modeler, as many different programs are required to bridge the length and time scales from the micro to the macroscale.

We are in the process of developing VIMES, the Visual Interface to Materials Simulation, to simplify the process of using different multiscale materials modeling software. Our current focus is on developing simple graphical front ends to different materials software, but our intention is also to use VIMES as an aid in bridging multiple length scales.

This paper will describe capabilities and technical details of the VIMES program, will describe where the program will be available, and will give an overview of areas of interest for future development.

2. VIMES Capabilities

We believe that very often a tight coupling between the interface and the underlying software is responsible for code brittleness and a short-lived interface. We have striven to design VIMES as a loosely-coupled interface: the program can read and generate input files, read output files, but does not directly execute the software.

VIMES is currently focused on simulation packages being developed at Sandia, including

- Quest density functional theory;
- Socorro density functional theory;
- Jaguar quantum chemistry suite;
- Towhee classical Monte Carlo simulation.

Additionally, several other packages are either currently in development, or are currently being considered, including

- MPQC quantum chemistry suite;
- PyQuante quantum chemistry suite;
- GAMESS quantum chemistry suite;
- LAMMPS classical molecular dynamics;
- GRASP classical molecular dynamics;
- Tinker classical molecular dynamics;
- Ab Init density functional theory suite;
- VASP density function theory suite.

Interested users should contact the author with feedback about which packages are high priorities for them.

VIMES contains simple builders for crystals, surfaces and slabs, supercells, nanotubes, and peptides.

Several other generic file formats are currently supported, including

- Biograf BGF format;
- Xmol XYZ format;
- PDB protein format.

Again, interested users should contact the author with feedback on additional file formats that are most important.

VIMES also contains the ability to do isosurfacing via a marching cubes approach, and has a preliminary ability to do atom-picking-based operations such as distance measurement.

3. VIMES Availability

Vimes is currently under license review by Sandia and the Department of Energy. When this is completed, the code will be available under the Gnu General Public License from the author's web page at http://www.cs.sandia.gov/~rmuller.

An Iterative Asymptotic Expansion Multi-scale Method for Elliptic Eigenvalue Problems

S. Mehraeen and J. S. Chen

Civil & Environmental Engineering Department, 5731G Boelter Hall
University of California, Los Angeles,
Los Angeles, CA 90095, USA, email: jschen@seas.ucla.edu

ABSTRACT

This work aims to develop an efficient multi-scale formulation with superlinear rate of convergence to obtain the eigenmodes and natural frequencies of the structure by solving the coarse scale problem. It has been shown that introducing asymptotic expansion to the eigenpairs of an eigenvalue problem leads to corresponding leading order equations. Based on the leading order equations, an iterative muli-scale eigenvalue formulation is then proposed which combines the inverse iteration and Rayleigh quotient iteration to yield a correction of asymptotic expansion solution. It has been shown that the solution given by the asymptotic expansion based predictor provides a good initial guess for the proposed iterative muli-scale eigenvalue formulation.

1. Multi-scale formulation in eigenvalue problems

The aim of this work is to study the two-scale behavior of elliptic differential operators. Utilizing the homogenization theorem, one can use same operators for homogenization of static problem to homogenize eigenvalue problems as well. Recently, first and second order homogenized operator in the periodic case has been studied [1,2]. However the abovementioned method [1] is not efficient and accurate enough in case of considering elliptic problems with highly oscillatory coefficients. To improve this method, an iterative predictor corrector eigenpair solver is proposed for problems solution of which can be fairly separated in two scales. Let the homogeneous Dirichlet eigenvalue problem be expressed by

$$A^{\varepsilon}u_{\varepsilon} = \lambda_{\varepsilon}u_{\varepsilon} \text{ in } \Omega,\ u_{\varepsilon} = 0 \text{ on } \Gamma,\ A^{\varepsilon} = -\partial/\partial x_i\left(a_{ij}^{\varepsilon}(x)\partial/\partial x_j\right) \tag{1}$$

where u_{ε} is the total solution, A^{ε} is the differential operator, and a_{ij}^{ε} is oscillatory coefficients. ε is scaling parameter which relates coarse and fine scale coordinates, x_i and y_i, respectively through

$$y_i = x_i/\varepsilon \tag{2}$$

The weak formulation of the boundary value problem in Eqn. (1) is given by

$$\forall v \in H_0^1(\Omega),\ a_{\varepsilon}(u_{\varepsilon}, v) = \lambda_{\varepsilon}(u_{\varepsilon}, v),\ a_{\varepsilon}(u_{\varepsilon}, v) = \int_{\Omega} a_{ij}^{\varepsilon}(x)\frac{\partial u_{\varepsilon}}{\partial x_i}\frac{\partial v}{\partial x_j}dx \tag{3}$$

Let $A=\left(a_{ij}\left(x\right)u_{,x_j}\right)_{,x_i}$ be the homogenized operator. Then, homogenized weak form reads

$$\forall v\in H_0^1\left(\Omega\right),\ a\left(u,v\right)=\lambda\left(u,v\right),\ a\left(u,v\right)=\int_{\Omega}a_{ij}\left(x\right)\frac{\partial u}{\partial x_j}\frac{\partial v}{\partial x_i}dx \tag{4}$$

in which we consider that if $u_\varepsilon\to u$ in $H^1\left(\Omega\right)$ weekly, then $\xi_i^e=a_{ij}^\varepsilon\left(x\right)\frac{\partial u_\varepsilon}{\partial x_j}\to\xi=a_{ij}\left(x\right)\frac{\partial u}{\partial x_j}$ in $L^2\left(\Omega\right)$ weakly for all $1\le i\le n$.

2. Eigenpair predictor equations

In order to capture eigenpairs of fine scale eigenvalue problem without solving Eqn. (3), we adopt the homogenized eigenpair as a predictor. The predictor can be obtained by introducing asymptotic expansion of eigenpairs

$$\lambda_\varepsilon=\lambda_0+\varepsilon\lambda_1+\varepsilon^2\lambda_2+\cdots,\ u_\varepsilon=u_0+\varepsilon u_1+\varepsilon^2u_2+\cdots \tag{5}$$

into the weak form in Eqn. (3). Further, the following auxiliary problem is constructed

$$\forall v,w_\varepsilon\in H_0^1\left(\Omega\right),\ a_\varepsilon\left(w_\varepsilon,v\right)=\lambda_0\left(u_0,v\right) \tag{6}$$

The symmetry of $a_\varepsilon\left(.,.\right)$ and making use of Eqns. (3) and (6) yields

$$\lambda_0\left(u_0,u_\varepsilon\right)=\lambda_\varepsilon\left(u_\varepsilon,w_\varepsilon\right) \tag{7}$$

Substituting Eqn. (5) into Eqn. (7) and introducing asymptotic expansion for w_ε gives rise to the eigenvalue predictor equation

$$\lambda_0=\lambda_0\ \text{ coeff. of }\varepsilon^0,\ \lambda_1=-\lambda_0\left(u_0,w_1\right)/\left(u_0,u_0\right)\ \text{ coeff. of }\varepsilon \tag{8}$$

Further, the homogenization theory for static problems states the following form of coarse-fine scale interrelationship of eigenpair components

$$u_1=\chi^j u_{0,x_j} \tag{9}$$

where χ^j is coupling function. In addition, utilizing asymptotic form of eigenvectors in Eqn. (5) in the general eigenvalue problem in Eqn. (3) leads to

$$A_1\chi^j=A_1y_j\ \text{ in }\ Y,\ A_1=-\partial/\partial y_i\left(a_{ij}\left(y\right)\partial/\partial y_j\right),\ \chi^j\left(y\right)\text{ is }Y-\text{periodic} \tag{10}$$

from which coupling function is obtained. Next, employing Eqn. (5) in the strong form Eqn. (1) leads to the following leading order equations used for eigenvector predictor

$$\begin{aligned}&u_0\left(x,y\right)=u_0\left(x\right)\\&Au_0=\lambda_0u_0\ \text{ in }\Omega,\ \ u_0=0\ \text{ on }\Gamma,\ u_1\left(x,y\right)=-\chi^j\left(y\right)\frac{\partial u_0}{\partial x_j}+\tilde{u}_1\left(x\right)\end{aligned} \tag{11}$$

3. Eigenpair corrector equations

The following two-step iterative corrector equation is proposed to obtain eigenpairs of Eqn. (3). First, using Eqns. (8) and (11), we correct eigenvectors $\overline{u}=u_0+\varepsilon u_1$ with few

steps of inverse iteration [3] using $\overline{u}$ as initial guess in Eqn. (12). Gram-Schmidt orthogonalization is employed to get eigenpairs in order. Mode shifting method is also utilized to remove the singularity of the system induced by the rigid body modes.

$$given \left\| \overline{u}_m \right\| = 1,\ \overline{u}_m = \sum_{i=1}^{n} a_i q_i,\ Aq_i = \lambda_i q_i,\ i = 1,...,n \tag{12}$$

Next, we correct the result of step 1 using Rayleigh quotient iteration [3] for faster convergence (cubic rate of convergence) along with Gram-Schmidt orthogonalization to remove the repetitive eigenmodes, i.e.

$$\begin{aligned} &\text{(a) } \mu_k = \left(\overline{u}_m^{\mathrm{T}} A \overline{u}_m\right) \Big/ \left(\overline{u}_m^{\mathrm{T}} \overline{u}_m\right), \text{(b)solve } \left(\boldsymbol{A} - \mu_k \boldsymbol{I}\right) \overline{u}_{m+1} = \overline{u}_m, \\ &\text{(c)GM orthogonalization, (d) } \overline{u}_{m+1} = \overline{u}_{m+1} \Big/ \left\| \overline{u}_{m+1} \right\|, \quad k = 0,1,...,n \end{aligned} \tag{13}$$

An example is demonstrated in which first 6 eigenpairs of an elliptic problem in Eqn. (14) with highly oscillatory coefficient E is analyzed.

$$\left(Eu_{,x}\right)_{,x} = \lambda u, \quad x \in]0,5[\tag{14}$$

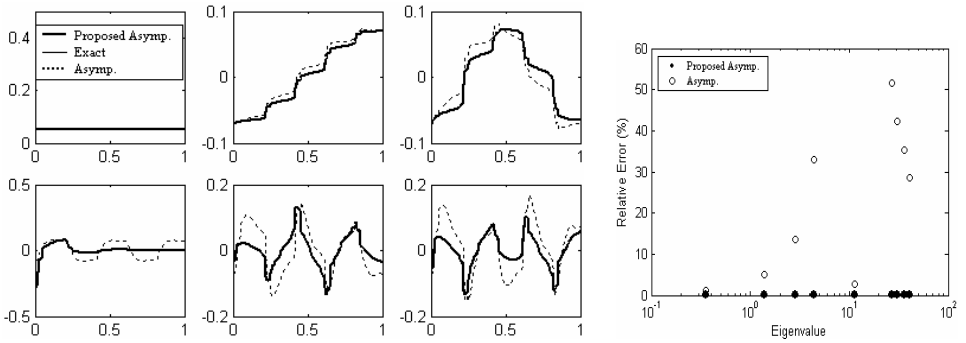

Figure 1. (a) Comparision of eigenvectors, (b) Comparision of eigenvalues

As shown in Fig 1 the proposed multi-scale asymptotic based method can capture fine details of eigenpairs of inhomogenous system. Unlike the asymptotic method [1], the proposed method leads to the exact solution with few numbers of iterations.

4. References

[1] Kesavan, Homogenizaiton of elliptic eigenvalue problems: part 2, Appl. Math. Opt. 5, (1979) 197-216.

[2] A. Benssousan, J.L. Lions and G. Papanicoulau, Asymptotic analysis for periodic structures, (North Holland, Amsterdam, 1978).

[3] G.H. Golub, C. F. val Loan, Matrix computation, (The John Hopkins University Press, 1996).

Multiscale Instability Analysis of Corrugated Fiberboard

Hirohisa Noguchi[a], Nobutada Ohno[b], and Dai Okumura[b]

[a] Department of System Design Engineering, Keio University,
Hiyoshi, Kohoku-ku, Yokohama 223-8522, Japan, noguchi@sd.keio.ac.jp
[b] Department of Mechanical Engineering, Nagoya University,
Furo-cho, Chikusa-ku, Nagoya 464-8603, Japan

ABSTRACT

In this study, multiscale micro-macro interaction analyses of corrugated fiberboard are conducted by the finite element method in conjunction with the homogenization theory. The updated Lagrangian method is adopted for the geometrically nonlinear analyses of microstructure and the scaled corrector method is adopted for detecting the buckling mode. By comparing with the experimental results, the validity of the proposed method is illustrated.

1. Introduction

Corrugated fiberboard is frequently used as packing material and, being piled together, it is also utilized as shock absorber because it can assimilate impact energy by large deformation of inner corrugating medium. The mechanical properties of corrugated fiberboard are sometimes unstable due to bifurcation buckling and very difficult to estimate because of the variety and the complexity of microscopic structure. Macroscopic behavior of corrugated fiberboard is also varied by the change of mechanical properties of microscopic structures undergoing large deformation. In this paper, firstly a focus is placed on the variation of the macroscopic property of corrugated fiberboard caused by the microscopic inner local buckling. Assuming that a piled corrugated fiberboard is composed of periodic structures, the macroscopic equivalent properties are calculated from the microscopic, properties and deformation by using the updated Lagrangian geometrically nonlinear finite element method combined with the homogenization theory. The scaled corrector method is adopted for detecting the bifurcation mode and the branch switching. Secondly, the micro-macro interaction analysis based on the homogenization theory is carried out from the viewpoint of localization. Numerical examples demonstrate the macroscopic instability induced by the microscopic buckling and show good agreement with the experimental results.

2. Micro/Macroscopic Virtual Work Principle Based On Homogenization [1]

The rate form of principle of virtual work is written at time t, as

$$\int_{t_V}^{t} \dot{S}_{ij}\,\delta_t E_{Lij}\,d^t v + \int_{t_V}^{t} T_{ij}\left(\delta_t E_{NLij}\right)'\,d^t v = \delta\dot{R} \tag{1}$$

$$\delta_t E_{Lij} = \frac{1}{2}\left(\delta u_{i,j} + \delta u_{j,i}\right) \tag{2}$$

$$\left(\delta\, {}_t E_{NLij}\right)^{\nabla} = \frac{1}{2}\left(\delta u_{k,i}\cdot \dot{u}_{k,j} + \dot{u}_{k,i}\cdot \delta u_{k,j}\right) \tag{3}$$

$\dot{S}_{ij}$ is the Truesdell rate, E_{ij} the Green-Lagrange strain tensor and T_{ij} is the Cauchy stress tensor. The rate of displacement can be divided into $\dot{u}_i^0$ and $\dot{u}_i^*$ as shown in Eqn.(4), which are macroscopic and microscopic components, respectively.

$$\dot{u}_i = \dot{u}_i^0 + \dot{u}_i^* \tag{4}$$

Substituting Eqn.(4) into Eqn.(1), Eqn.(2) and Eqn.(3), the following microscopic and macroscopic equations are finally obtained.

$$\int_Y \left({}_t^t C_{ijpq} + \delta_{pi}\, {}^t T_{qj}\right)\chi_{p,q}^{kl}\delta u_{i,j}^* dY = \int_Y \left({}_t^t C_{ijkl} + \delta_{ki}\, {}^t T_{lj}\right)\delta u_{i,j}^* dY \tag{5}$$

$$\int_{{}^t v} D_{ijkl}^{\mathrm{H}}\, {}^t\dot{u}_{k,l}^0 \delta u_{i,j}^0 d^t v + \int_{{}^t v} \delta_{ki}\, {}^t T_{lj}^{\mathrm{H}}\, {}^t\dot{u}_{k,l}^0 \delta u_{i,j}^0 d^t v = \delta \dot{R}^{\mathrm{H}} \tag{6}$$

where D_{ijkl}^{H} is the homogenized stiffness tensor. T_{lj}^{H} is the homogenized Cauchy stress tensor. ${}_t^t C_{ijkl}$ is the constitutive tensor. χ_i^{kl} is the characteristic displacement vector corresponding to ${}_t\dot{\varepsilon}_{kl}^0$ as shown in Eqn.(7).

$${}^t\dot{u}_i^* = -\chi_i^{kl}\, {}_t\dot{\varepsilon}_{kl}^0 \tag{7}$$

After finite element discretization, Eqn.(5) and Eqn.(6) are solved alternately by exchanging the macroscopic strain rates and the homogenized stiffness and the Cauchy stress tensor.

3. Numerical Examples

The multiscale micro-macro interaction analyses of corrugated fiberboard are conducted. Fig.1(a), (b) show an obtained homogenized stress-strain curve and bifurcation buckling mode of microscopic structure, respectively. It is noted that this macroscopic stress-strain curve shows strain-softening behavior and it might cause macroscopic instability. The macroscopic structure is illustrated in Fig.2(a) and each element in macroscopic structure has the same unit cell shown. In the analyses, the following three cases are considered. Case 1: Buckling (in unit cell) does not occur in all macroscopic elements. Case 2: Buckling occurs simultaneously in all macroscopic elements. Case 3: Buckling occurs only in the middle layer of macroscopic elements. The load-displacement curves are shown in Fig.2(b) In the experiment, only one layer buckles first, then other layers buckle subsequently one by one. Each local maximum point in Fig.2(b) corresponds to buckling of each layer. Which layer starts buckling depends on initial irregularity of corrugated fiberboard. On the contrary, in numerical analysis, load-displacement path can be controlled by path switching in bifurcation analysis. The load-displacement curve obtained in Case 1 is the primary path of this structure and no unit cells buckle. In Case 2 that unit cell is controlled to buckle simultaneously at every point of macroscopic structure, the secondary path varies linearly after bifurcation and goes between local maximum and minimum points. The total absorption energy seems equivalent to that by the experiment. In Case 3, only the middle layer is controlled to buckle. As shown in

Fig.2(b), the first buckling point is almost equal to that observed in the experiment, however, the recovery of stiffness is slower than the experimental result. This is due to the ignorance of contact condition inside the corrugated fiberboard. From these results, the validity of the present analyses is clarified.

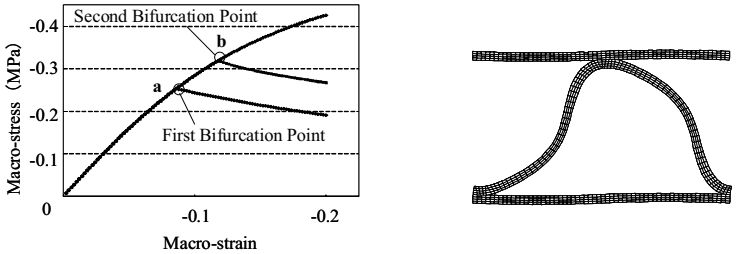

(a) Homogenized Stress-Strain Curve (b) Bifurcation mode at a

Figure 1. Microscopic response of Corrugated Fiberboard

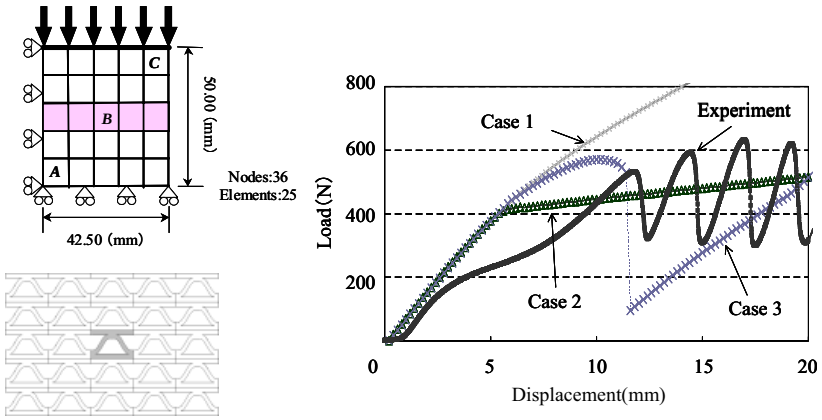

(a) Analysis model (b) Load-Displacement Curve

Figure 2 Macroscopic response of Corrugated Fiberboard

4. Conclusion

In this paper, the multiscale micro-macro interaction analysis of corrugated fiberboard based on the homogenization theory was conducted. Firstly, the microscopic bifurcation of unit cell was analyzed and the macroscopic mechanical properties of corrugated fiberboard were investigated. Secondly, the results of micro-macro interaction analysis are compared with the experimental results and the present analyses were validated.

References

[1] Ohno N, Okumura D, Noguchi H.: Microscopic symmetric bifurcation condition of cellular solids based on a homogenization theory of finite deformation. *J. Mech. Phys Solids* **50** (5), 1125-1153, 2002.

An Adaptive Hybridization of Electronic-Density-Functional-Theory and Molecular Dynamics for Multiscale Modeling of Nanostructured Devices on Computation Grid

Shuji Ogata[a] and Takahiro Igarashi[b]

[a]Graduate School of Engineering, Nagoya Institute of Technology, Gokiso-cho, Showa-ku, Nagoya 466-8555, Japan; E-mail: ogata@nitech.ac.jp
[b]Japan Science and Technology Agency, 4-1-8 Honcho, Kawaguchi 332-0012, Japan; E-mail: t.igarashi@nitech.ac.jp

ABSTRACT

We review recent development in our hybrid electronic-density-functional/molecular-dynamics scheme for dynamic simulation of semiconductor and ceramic materials. In the hybrid scheme, a quantum region composed of a relatively small a number of atoms and treated with the density-functional theory, is embedded in a large- scale classical system composed of particles interacting through an empirical inter-atomic potential. In the former scheme, the link-atom method was used to couple between the quantum and classical regions. Degrees of coupling between the two regions were, however, fairly sensitive to the shape and size of the quantum region. To overcome the difficulty we propose a novel hybridization scheme, which requires no link-atoms and is applicable to a wider range of settings. The present scheme is successfully applied to various important engineering problems such as stress-dependent water dissociation on nanostructured Si. During the simulation run, size and shape of the quantum region change adaptively by monitoring inter-particle distances. We also demonstrate that the present hybrid scheme runs efficiently on a computation grid composed of distributed PC clusters.

1. Introduction

Various engineering processes in materials, such as oxidation and fracture, involve chemical reactions between constituent atoms. Empirical inter-atomic potentials used in molecular dynamics (MD) simulations often fail to describe such processes. Inter-atomic interaction in the reactive region needs to be calculated by a quantum mechanical (QM) method that can describe breaking and formation of bonds. Furthermore heat produced in the QM region by reactions should be correctly transferred to surrounding regions. Large-scale atomistic simulations are therefore required, in which reacting atoms are described by a reliable QM method. There have been growing interests in developing hybrid QM-MD simulation schemes, in which a reactive

region treated by a QM method is embedded in a classical system of atoms interacting via an empirical inter-atomic potential.

Computationally efficient QM approaches based on the density-functional theory (DFT) have been advanced. Recently hybrid DFT-MD simulation schemes have been developed [1,2] using the link-atom to couple between the DFT atoms and the MD atoms. Successful applications are found, for example, in Ref. 3. However, we find that the hybrid DFT-MD results with the link-atom scheme are sensitive to selection of the QM atoms. To overcome the difficulty, we here propose a novel hybrid scheme, which requires no link-atoms.

2. Adaptive Hybrid Scheme

In the present scheme, dynamics of all atoms are determined by the following Hamiltonian [1,2]:

$$H = H_{\mathrm{MD}}^{\mathrm{system}}(\vec{R}_{\mathrm{all}}, d\vec{R}_{\mathrm{all}}/dt) + \sum_{\mathrm{cluster}} (E_{\mathrm{QM}}^{\mathrm{cluster}} - E_{\mathrm{MD}}^{\mathrm{cluster}}) . \qquad (1)$$

Here $\vec{R}_{\mathrm{all}}$ represents a set of all atoms. The $H_{\mathrm{MD}}^{\mathrm{system}}$ in Eq. (1) is the MD Hamiltonian of the total system. The last two terms on the right hand side of Eq. (1) represent the QM correction by the DFT to the MD potential energy for the cluster of atoms in the QM region. All the atoms in the total system are grouped into MD and QM atoms. Positions of the MD and QM atoms are denoted as $\{\vec{r}_{\mathrm{MD}}\}$ and $\{\vec{r}_{\mathrm{QM}}\}$, respectively. The cluster terms in the right hand side of Eq. (1) are functions of $\{\vec{r}_{\mathrm{QM}}\}$: $E_{\mathrm{QM}}^{\mathrm{cluster}} = E_{\mathrm{QM}}^{\mathrm{cluster}}(\{\vec{r}_{\mathrm{QM}}\})$ and $E_{\mathrm{MD}}^{\mathrm{cluster}} = E_{\mathrm{MD}}^{\mathrm{cluster}}(\{\vec{r}_{\mathrm{QM}}\})$. Additional atoms are put on surfaces of the QM and MD clusters to buffer possible boundary effects in the QM region. Positions of those buffer atoms in the MD cluster are determined dynamically to minimize the potential energy of the cluster in the MD calculations. In the DFT calculation, positions of the buffer atoms are determined using that of the buffer atoms obtained in the MD cluster calculations. Example of the selection of the QM region and corresponding QM and MD clusters are shown in Fig. 1.

3. Application to Water Dissociation Dynamics on Nanostructured Si

Present hybrid scheme is applied to reaction of a water molecule near the notch of a Si slab under stresses to understand its adsorption and dissociation dynamics. The bottom of the notch assumes Si(100) facet. Reaction region is treated by the DFT; surrounding region, by the MD method. During the simulation run, the QM region changes in size and shape dynamically to trace trajectories of the H and O atoms of the water molecule and large distortions in the Si structures. We find that the

reaction dynamics are fairly sensitive to the degrees of applied stress. For unstrained Si, the water molecule dissociates and connects to different Si-Si dimmers on Si(100), while for strained Si, the molecules to the same dimmer. Reasons of such stress dependence of the water reaction are explained through detailed analyses on the reaction paths. We also demonstrate that the present hybrid scheme runs efficiently on a computation grid composed of distributed PC clusters.

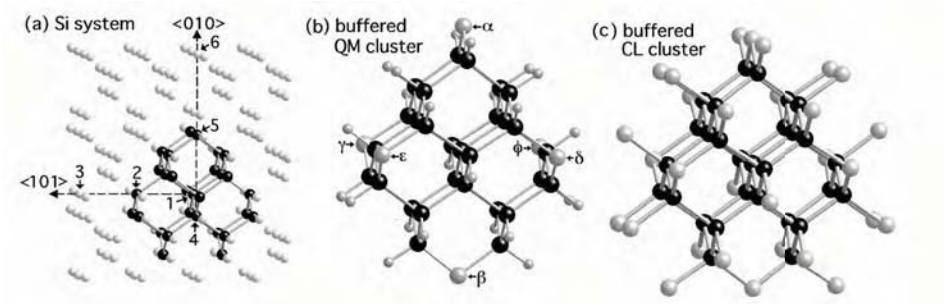

Figure 1. (a) A QM region (black spheres) in crystalline Si. (b) Corresponding QM cluster with buffer atoms. (c) Corresponding MD cluster with buffer atoms.

Acknowledgements

Present work is supported by ACT-JST.

References

[1] S. Ogata, F. Shimojo, R.K. Kalia, A. Nakano, and P. Vashishta, "Hybrid Quantum Mechanical/Molecular Dynamics Simulations for Parallel Computers: Density Functional Theory on Real-Space Multigrids,"Comp. Phys. Comm. 149, 30-38 (2004).

[2] S. Ogata, E. Lidorikis, F. Shimojo, A.Nakano, P. Vashishta, and R.K. Kalia, "Hybrid Finite-Element/Molecular-Dynamics/Electronic-Density-Functional Approach to Materials Simulations on Parallel Computers,"Comp. Phys. Comm. 138, 143 (2001).

[3] S. Ogata, F. Shimojo, A. Nakano, P. Vashishta, and R.K. Kalia, "Environment effects of H_2O on fracture initiation in Si: a hybrid electronic-density-functional/molecular-dynamics study," J. Appl. Phys. 95, 5316-5323 (2004).

Calibration of a Nonlinear Elastic Composite with Goal-Oriented Error Control Using a Sub-Scale Modeling Approach

Håkan Johansson, Fredrik Larsson and Kenneth Runesson

Chalmers University of Technology,
Dept of Structural Engineering and Mechanics, SE-41296 Göteborg, Sweden
e-mail: kenneh.runesson@sem.chalmers.se

ABSTRACT

A recently proposed technique for the calibration of constitutive models is based on the optimization problem expressed such that the state equation is incorporated via an additional costate field. A distinct advantage is that error control is formally straightforward. This technique is applied to calibration of a nonlinear elastic composite using a meso-macro-transition approach, whereby the RVE is analyzed using (in this case) Dirichlet boundary conditions. The numerical results show the effectivity of the error prediction.

1 Introduction

Among many important modeling issues is the need to devise efficient strategies for parameter identification based on experimental information. A strategy for calibration of macroscopic constitutive models with built-in error control was elaborated in some detail by Johansson and Runesson [1], and the developments were based essentially on the general setting for optimal control as put forward by Rannacher and coworkers in several publications, e.g. [2]. Key elements in the general framework is (a) the use of the adjoint system format with a costate variable field ensuring the simultaneous satisfaction of optimality and state equations, and (b) the possibility to freely choose error measures and to compute the error a posteriori using duality arguments.

2 Abstract formulation of calibration problem

The material parameters defining the constitutive behavior of the sub-scale constituents are collected in the column vector $\underline{p} \in \mathbb{R}^M$. The calibration problem thus boils down to the task of minimizing a suitably chosen function(al) $\mathcal{F}(\underline{p}, \boldsymbol{u}(\underline{p}))$ in terms of the difference between simulated and experimentally observed macroscopic stress $\bar{\boldsymbol{P}}$[1] as follows:

$$\mathcal{F}(\underline{p}, \boldsymbol{u}(\underline{p})) = \sum_{i=1}^{N^{\text{obs}}} \frac{c_i}{2} |\bar{\boldsymbol{P}}(\underline{p}, \boldsymbol{u}_i(\underline{p})) - \bar{\boldsymbol{P}}_i^{\text{obs}}|^2 \tag{1}$$

[1] Overbar denotes macroscopic quantity

where c_i are suitably chosen weights, $\sum_{i=1}^{N^{\text{obs}}} c_i = 1$, and where $|\boldsymbol{P}| \stackrel{\text{def}}{=} (\boldsymbol{P} : \boldsymbol{P})^{\frac{1}{2}}$ defines the Euclidean length.
The minimization of $\mathcal{F}$ is subjected to the constraint that the state variable $\boldsymbol{u}(\underline{p})$, sought in a solution space $\mathbb{U}(\bar{\boldsymbol{H}})$,[2] satisfies the appropriate state equation, whose variational format is of the form

$$a(\underline{p}, \boldsymbol{u}, \delta\boldsymbol{\lambda}) = \int_{\Omega_\square} \boldsymbol{P}(\underline{p}, \boldsymbol{H}[\boldsymbol{u}]) : \boldsymbol{H}[\delta\boldsymbol{\lambda}] \mathrm{d}\Omega = 0 \quad \forall \delta\boldsymbol{\lambda} \in \mathbb{U}^0 \tag{2}$$

where $\boldsymbol{H}$ is the displacement gradient. Next, we adopt the self-adjoint format of the optimization problem upon introducing the Lagrangian functional $\mathcal{L}(\underline{q}, \boldsymbol{v}, \boldsymbol{\mu})$ as follows

$$\mathcal{L}(\underline{q}, \boldsymbol{v}, \boldsymbol{\mu}) \stackrel{\text{def}}{=} \mathcal{F}(\underline{q}, \boldsymbol{v}) + a(\underline{q}, \boldsymbol{v}, \boldsymbol{\mu}) \tag{3}$$

where all the arguments of $\mathcal{L}$ are treated as *independent*. It can be shown that the solution $z = (\underline{p}, \boldsymbol{u}, \boldsymbol{\lambda})$ to the optimization defines a stationary point of $\mathcal{L}$, whereby $\boldsymbol{\lambda}$ is the costate corresponding to the state variable $\boldsymbol{u}$. We are thus faced with the problem of finding $z \in \mathbb{Z} \stackrel{\text{def}}{=} \mathbb{R}^M \times \mathbb{U}(\bar{\boldsymbol{H}}) \times \mathbb{U}^0$ that solves

$$\mathcal{L}'_z(z; \delta z) = 0 \quad \forall \delta z \in \mathbb{Z}^0 \stackrel{\text{def}}{=} \mathbb{R}^M \times \mathbb{U}^0 \times \mathbb{U}^0 \tag{4}$$

The corresponding FE-discretized problem is: Find $z_h \in \mathbb{Z}_h \subset \mathbb{Z}$ such that

$$\mathcal{L}'_z(z_h; \delta z_h) = 0 \quad \forall \delta z_h \in \mathbb{Z}_h^0 \subset \mathbb{Z}^0 \tag{5}$$

which is solved using Newton's method. We then resort to a strategy, that utilizes the FE-topology of the state problem, cf. Johansson and Runesson [1].
Next, we select a suitable goal function $Q(z)$ for the error analysis such that the error measure $E(z, z_h)$ can be expressed as

$$E(z, z_h) \stackrel{\text{def}}{=} Q(z) - Q(z_h) = \int_0^1 Q'_z(z_h + se; e)\mathrm{d}s = \overline{Q}'_z(z_h; e) \simeq Q'_z(z_h; e) \tag{6}$$

In standard fashion we shall then establish the *dual* problem to find $z^* \in \mathbb{Z}$ with which the error can be computed. Because of the Galerkin orthogonality, an approximation of z^* must be sought in practice in a space $\tilde{\mathbb{Z}}_h$ that is richer than $\mathbb{Z}_h$. We thus seek $z_h^* \in \tilde{\mathbb{Z}}_h$ such that

$$\mathcal{L}''_{zz}(z_h^*, \delta z_h^*) = Q'_z(\delta z_h^*) \quad \forall \delta z_h^* \in \tilde{\mathbb{Z}}_h^0 \tag{7}$$

The dual solution z^* is used to obtain the "exact" error representation.

[2]For Dirichlet boundary conditions, the solution space varies with the (prescribed) macroscopic displacement gradient $\bar{\boldsymbol{H}}$.

3 Computational results

As a numerical example, we consider a two-phase Neo-Hooke elastic material with particles in a continuous matrix. We consider the matrix material as unknown, i.e. we seek to determine the values of $\underline{p} = [G_{\text{matr}}, K_{\text{matr}}]^{\text{T}}$ for given $[G_{\text{part}}, K_{\text{part}}] = [5, 10]$; thus $M = 2$. A single unit cell composite is randomly realized with a prescribed volume fraction $V_{\text{part}}/V_{\text{matr}} \approx 1$. The observed data set $\{\bar{\boldsymbol{P}}_i^{\text{obs}}\}_{i=1}^{N^{\text{obs}}}$ is constructed by randomly perturbing computed stresses for in-plane macro-scale simple shear and uniaxial stretch combined, $\bar{H}_{11} = \bar{H}_{12} \neq 0, \bar{H}_{21} = \bar{H}_{22} = 0$. We study the effectivity of the error estimators for $\underline{p}$ in the case of a prescribed displacement, $(\bar{H}_{11})_{\max} = (\bar{H}_{12})_{\max} = 0.25$. The effectivity index is defined as $\eta = \tilde{E}/E$, where $\tilde{E}$ and E are the estimated and the exact error, respectively. The "exact" optimal parameter values were $\underline{p} = [G_{\text{matr}}, K_{\text{matr}}]^{\text{T}} = [0.685, 4.57]^{\text{T}}$. The deformed meshes are shown in Fig. 1, while the effectivities for this case are given in Table 1.

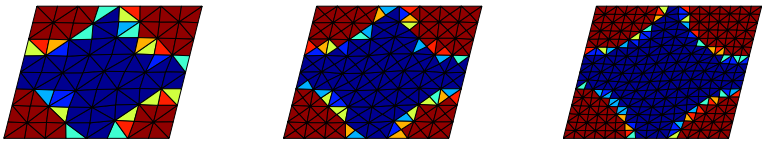

Figure 1: Deformed RVE:s with uniform mesh refinement

Table 1: Computational results with uniform mesh refinements

$\underline{p}_h =$	$[0.492, 4.40]^{\text{T}}$	$[0.588, 4.49]^{\text{T}}$	$[0.602, 4.51]^{\text{T}}$
$(\tilde{E}_1, \tilde{E}_2) =$	$(0.133, 0.133)$	$(0.0878, 0.0841)$	$(0.0796, 0.0669)$
$(\eta_1, \eta_2) =$	$(0.691, 0.785)$	$(0.903, 0.999)$	$(0.966, 1.02)$

4 References

[1] H. Johansson and K. Runesson. Parameter identification in constitutive models via optimization with a posteriori error control. Accepted for publication in International Journal for Numerical Methods in Engineering, 2004.

[2] R. Becker and R. Rannacher. An optimal control approach to a-posteriori error estimation in finite element methods. *Acta Numerica*, 10:1–102, 2001.

A Seamless Coupling of Atomistic and Continuum Fields in the Quasicontinuum Method

T. Shimokawa[a,b,1], J. Schiøtz[b,2], J. J. Mortensen[b,3], and K. W. Jacobsen[b,4]

[a]Department of Mechanical Systems Engineering, Faculty of Engineering, Kanazawa University, 2-40-20, Kodatsuno, Kanazawa, Ishikawa, 920-8667, Japan, [1]simokawa@t.kanazawa-u.ac.jp
[b]CAMP and Department of Physics, Technical University of Denmark, DK-2800 Lyngby, Denmark, [2]schiotz@fysik.dtu.dk, [3]jensj@fysik.dtu.dk, [4]kwj@fysik.dtu.dk

ABSTRACT

In the quasicontinuum method, due to the different ways the energies of the atoms are calculated in the coarse-grained (or local) regions and the fully atomistic (or non-local) regions, unphysical forces called "ghost forces" arise at the interfaces. We show that it is possible to formulate the quasicontinuum method without these problems by introducing a new type of atom, called quasi-non-local atoms, between the two regions of space. Quasi-non-local atoms behave like local atoms when they interact with atoms in the local region, and as non-local atoms when they interact with atoms in the non-local region. This ensures a consistent description, free of ghost forces.

1. Introduction

The basic idea of the quasicontinuum method [1] is conceptually simple. In order to perform an atomic simulation efficiently and save computational resources, a continuum approximation is adopted where atomic deformation-gradient fields are small, assuming that the continuum method provides almost the same result as a full atomistic simulation. However, it turns out to be very difficult to define the energy of the interface region in such a way that the coupling of the atomic description (non-local atoms) and the continuum description (local atoms) is completely seamless: unphysical forces (ghost forces) appear at interfaces due to the fact that the interaction range of a non-local atom is different from that of a local atom [2]. This leads, for example, to serious problems with energy conservation during molecular dynamics simulations. In this study, we show a seamless coupling of the two descriptions by introducing a buffer layer of a new kind of atoms, called quasi-non-local atoms.

2. Methodology

Figure 1(a) shows a usual QC model (model QC[1]) near a vacancy. Here, open circles near the vacancy are so-called non-local [2] because the energy depends on the positions of all atoms within a certain cutoff distance, R_c, from the atoms. Solid circles far from the vacancy indicate so-called local atoms making up the corners of a triangulation of the region with a slowly varying deformation gradient. When the force acting on atom α in the

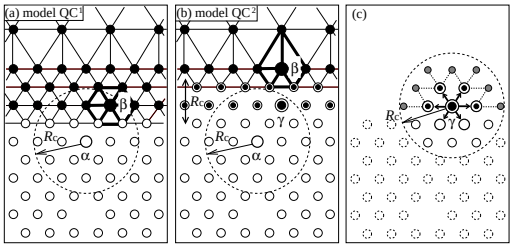

Figure 1: Coupling of atomic and continuum model with one vacancy. Open, closed and double circles show non-local, local and quasi-non-local atoms, respectively.

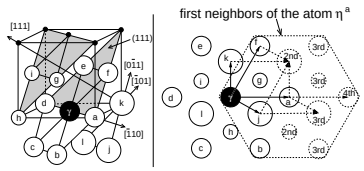

Figure 2: First nearest neighbors to the atom γ and superposed atomic configurations on (111) planes for f.c.c. structures.

model QC^1 is compared to the force acting on an atom in the full-atomistic model, we can confirm that these forces are not equivalent: a ghost force appears at the interface between non-local and local regions. To solve this problem, we introduce a new type of atom, named *quasi-non-local* atom, to be positioned between the non-local and local regions, so that no non-local atom interacts with any local atom [3]. The concept of a quasi-non-local atom is very simple: A quasi-non-local atom can feel first nearest neighbor atoms and all non-local atoms within the cutoff distance R_c. The idea of the improved QC model is shown in Fig. 1(b) (model QC^2). Double circles correspond to quasi-non-local atoms.

The potential energy of a quasi-non-local atom is calculated as if it was a non-local atom with one important difference: When calculating the energy of a quasi-non-local atom, only the positions of nearest neighbor atoms as well as the positions of non-local atoms within the cutoff distance are used. On the local side of the interface, the distance vectors to the nearest neighbor atoms are used to extrapolate the positions of second nearest neighbors, third nearest neighbors and so on. This is illustrated in Fig. 1(c). Big open circles and double circles around the quasi-non-local atom γ are the nearest neighbor atoms, gray circles are extrapolated neighbor atoms, and broken circles are non-local atoms not needed to calculate the potential energy of the quasi-non-local atom γ. If the position of an extrapolated neighbor atom and the positions of a non-local atom are almost the same, the non-local atom is used instead of the extrapolated position. By using these extrapolated neighbor atoms, we have enough information to calculate the potential energy of a quasi-non-local atom in the same way as for a non-local atom. Consequently, a quasi-non-local atom acts like a non-local atom on the non-local side of the interface, and it acts like a local atom on the local side of the interface.

To avoid ghost forces, the range of the potential must be limited to first neighbors of first neighbors. In this way, if atom 1 extrapolates the position of atom 2 using common nearest neighbors, atom 2 extrapolates the position of atom 1 using the same neighbors, and the situation is symmetric. The limit is fourth, fourth and third nearest neighbors for hcp, fcc and bcc lattices, respectively. If the range of the potential goes beyond this limit, ghost forces can no longer be avoided. As an example, let us look at the fcc structure shown

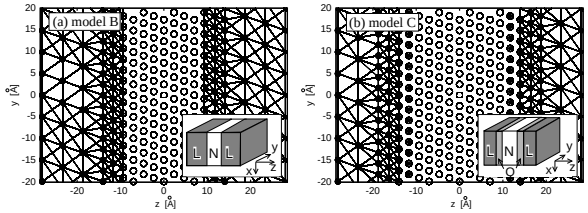

Figure 3: Atomic configuration of (a) old style QC model and (b) improved QC model with new buffer layers.

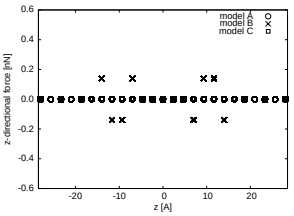

Figure 4: Atomic force in perfect f.c.c. structure of each model

in Fig. 2. Full circles express nearest neighbors to the black atom γ and middle, large and small circles mean atoms in the same plane, one plane above or below as the black atom γ. Dashed circles correspond to first neighbors to the first neighbor η^a of the atom γ. We can extrapolate neighbors by using the twelve difference vectors $\mathbf{d}_\eta = \mathbf{r}_\eta - \mathbf{r}_\gamma$ as follows: $\mathbf{r}_{2\mathrm{nd}} = \mathbf{r}_\gamma + \frac{1}{2}(\mathbf{d}_\mathrm{a} + \mathbf{d}_\mathrm{f} + \mathbf{d}_\mathrm{j} + \mathbf{d}_\mathrm{k})$, $\mathbf{r}_{3\mathrm{rd}} = \mathbf{r}_\gamma + \mathbf{d}_\mathrm{a} + \mathbf{d}_\mathrm{j}$, and $\mathbf{r}_{4\mathrm{th}} = \mathbf{r}_\gamma + 2\mathbf{d}_\mathrm{a}$.

3. Results

Figure 3 show atomic configurations of aluminum perfect fcc structure in a previous QC style (model B) and in an improved QC style (model C). Open circles, solid circles and double circles represent non-local, local and quasi-non-local atom, respectively. Periodic boundary conditions are adopted in all directions. An EAM potential [4] is adopted. The cutoff distance is 6.29 Å which includes fourth neighbor atoms. Figure 4 shows z components of the force of each model in its initial configurations. Ideally, no atomic forces should appear in the perfect f.c.c. structure. As expected, a full non-local simulation (model A) gives no forces. On the other hand, non-zero forces (ghost forces) appear near the interface between non-local and local atomic regions in model B. In the models C with quasi-non-local atoms no ghost forces are found.

References

[1] E. B. Tadmor, M. Ortiz, and R. Phillips. Quasicontinuum analysis of defects in solids. Phil. Mag. A, **73**, 1529(1996).

[2] V. B. Shenoy, R. Miller, E. B. Tadmor, D. Rodney, R. Phillips, and M. Ortiz. An adaptive finite element approach to atomic-scale mechanics - the quasicontinuum method. J. Mech. Phys. Solids, **47**, 611(1999).

[3] T. Shimokawa, J. J. Mortensen, J. Schiøtz, and K. W. Jacobsen. Matching conditions in the quasicontinuum method: Removal of the error introduced at the interface between the coarse-grained and fully atomistic region. Phys. Rev. B, **69**, 214104(2004).

[4] Y. Mishin, D. Farkas, M. J. Mehl, and D. A. Papaconstantopoulos. Interatomic potentials for monoatomic metals from experimental data and *ab initio* calculations. Phys. Rev. B, **59**, 3393(1999).

Parallel TBMD, Hybrid Classical/TB-MD, and their Application to Interfacial Phenomena in Nanostructured Semiconductors

Kenji Tsuruta[a], Chieko Totsuji[a], Hiroo Totsuji[a], and Shuji Ogata[b]

[a]Department of Electrical and Electronic Engineering, Okayama University
3-1-1 Tsushimanaka, Okayama 700-8530, Japan
[b]Shikumi College, Graduate School of Engineering, Nagoya Institute of Technology
Gokiso-cho, Showa-ku, Nagoya 466-8555, Japan
Email: tsuruta@elec.okayama-u.ac.jp

ABSTRACT

We present large-scale molecular-dynamics (MD) simulations, based on an order-*N* tight-binding (TB) method and on a hybrid classical/TB-MD method, to analyze interfacial phenomena in nanostructured semiconductors. The Fermi-operator expansion method for efficient calculations of the band-structure energy and the Hellman-Feynman forces has been employed and implemented on our PC-based parallel machines. We have also developed a hybrid classical/TB-MD algorithm based on the ONIOM scheme, in which the interatomic forces on atoms in "quantum regions" embedded in a "classical" total system are calculated accurately within the TB approximation. We apply these methods to analyses on the stability of high-energy grain boundary (GB) of Si and SiC. Also, the effect of the presence of hydrogen atom in a Si grain boundary on its structural and electronic properties is investigated using the hybrid MD method. Our hybrid code is modular and hence is suitable for GRID computation. Some preliminary tests on our GRID system will be reported.

1. Introduction

Nanostructured semiconductors have drawn much attention due to their unconventional characteristics in various aspects such as an enhanced luminescence, efficient catalytic reaction, strengthening against external load etc. It is believed that the gross feature of the mechanisms in these unique properties can be captured by understanding and controlling their interfacial phenomena. In this talk, we focus on structural and electronic properties of a high-angle ((001)Σ5 twist) grain boundary of

Si and SiC. Such a high-energy grain boundary is known to be rather unstable and hence be hardly found in nature. However, recent observations of nanostructured Si under large strain reveal that such a boundary may be accommodated through a local "solid-state amorphization"[1]. One of the purposes of this study is to clarify whether atomic rearrangement in high-energy grain boundaries can lead to local disordering, and how such a phenomenon is correlated with the change of electronic structure.

2. Model and Numerical Procedures

Our GB model consists of 2000 atoms. As depicted in Fig. 1, there are two boundaries between twins of crystal layers in a MD cell, and these layers are periodically repeated along <001> direction. We employ a linear-scaling algorithm called the Fermi-operator expansion method (FOEM) [2]. The time reversible integrator algorithm for *NPT* ensemble [3] has been used for MD simulation. The TB parameters for Si and for SiC are taken from Ref. [4] and Ref [5], respectively.

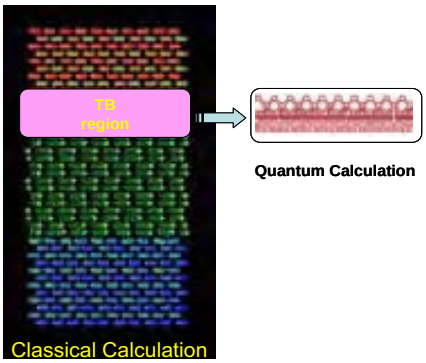

Fig. 1: Atomic configuration of (001)Σ5 twist GB (left) and schematic view of the hybrid classical/TB system.

We have also developed a hybrid classical MD/ TB-MD method, similar to what is called ONIOM method [6], i.e. a quantum region is embedded in the total system, described by a classical interatomic potential, via "handshake" atoms. We have examined the stability and accuracy for several cases of the handshaking schemes using hydrogen atoms, Si atoms, and H-terminated Si atoms. The hybrid method is useful especially for the case that more accurate calculation of interatomic forces on atoms near the grain boundary is required, such as impurity segregation and diffusion.

These algorithms have been implemented on parallel PC clusters. Also, the hybrid algorithm designed for a GRID computation and its performance on our PC-cluster-based GRID system will be outlined briefly in the talk.

3. Results

We first obtained a relaxed structure of the twist GB of Si and SiC at zero temperature. The results show that the local rearrangement occurs only within a few atomic layers, indicating no incipience toward disordering. On the other hand, the electronic density-of-states (DOS) of the system with the Si GB, depicted in Fig. 2, reveals that a large peak appears in bandgap of the system, implying that many defects or dangling bonds still exist in the Si GB after local atomic rearrangement.

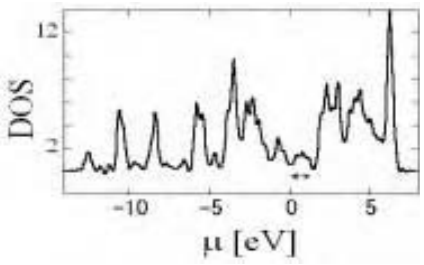

Fig. 2: Electronic density of states for the relaxed system with (001)Σ5 GB of Si. The arrow indicates energy range of bulk bandgap.

Figure 3 shows atomic configuration of the "TB region" after relaxation by the hybrid classical/TB calculation. It also shows that the local atomic rearrangement occurs only within a few atomic layers.

Fig.3: Atomic configuration of "TB region" near (001)Σ5 GB of Si after relaxation by hybrid classical/TB-MD method.

The results for the system with a hydrogen atom and the effects of temperature on the stability and the electronic structure of these GB will also be reported in the talk.

Acknowledgements

This work was supported partially by "Research and Development for Applying Advanced Computational Science and Technology" of Japan Science and Technology Corporation (ACT-JST) and by the Grant-in-Aid for Young Scientists (B) 14750554 from the MEXT of Japan.

References

[1] J.Y. Huang, H. Yasuda, and H. Mori, *Phil. Mag. Lett.* **79**, 305 (1999).

[2] S. Goedecker, *Rev. Mod. Phys.* **71**, 1085 (1999).

[3] J. Martyna, M.E. Tuckerman, D. J. Tobias, and M. Klein, *Mol. Phys.* **87**, 1177 (1996).

[4] I. Kwon *et al.*, *Phys. Rev. B* **49**, 7242 (1994).

[5] K. Tsuruta, H. Totsuji, and C. Totsuji, *Phil. Mag. Lett.* **81**, 357 (2001).

[6] F. Mareras and K. Morokuma, *J. Comput. Chem.* **16**, 1170 (1995).

Symposium – 7

Multiscale Modeling of Irradiated & Aging Materials

Long-term behaviour of irradiated hcp Zr coupling molecular dynamics and Monte Carlo simulations

C. Arévalo[1], M. J. Caturla[2,3] and J. M. Perlado[1]

[1] Instituto de Fusión Nuclear, ETSII/ J. G. Abascal 2, 28006 Madrid, Spain, cristina@denim.upm.es
[2] Universidad de Alicante, Dep. Física Aplicada, Alicante, Spain
[3] Lawrence Livermore National Laboratory, Livermore CA, USA

ABSTRACT

Using the input data obtained from molecular dynamics (MD) simulations on defect energetics and cascade damage, we have studied irradiation of Zr under different conditions with a kinetic Monte Carlo model. The initial cascade damage produced by recoils from 10 to 25 keV energies from MD simulations have been followed for times of hours and at 600K which is the operation temperature of the reactor. Results from MD simulations show that for the same recoil energy the size of vacancy and interstitial clusters can vary significantly. Therefore we have studied in detail the evolution of those defects produced in cascades with large initial clustering and compared to those where most of the defects are isolated. The evolution of the microstructure under fission irradiation conditions has been studied.

1. Introduction

The first barrier of the radioactive material is proposed to be build of ZrNb alloys in an advanced light water reactor. The understanding of the effect of irradiation on its mechanical properties is crucial for safe operation of the reactor. However, knowledge of irradiation effects in ZrNb is very scarce, both in basic microscopic and macroscopic experimental results. We have focused our work on the description of microscopic effects of irradiation using computer simulations in a multi-scale approach.

MD is a powerful tool to obtain atomic-scale information and it can provide data about the initial damage production during the collisional cascade produced by high energy recoils from energetic neutrons. However, the time scales affordable by this method are only up to a few nanoseconds. In order to understand the evolution of the accumulated damage for long times at a microscopic scale, it is necessary to use other simulation techniques such as rate theory or kinetic Monte Carlo (kMC). In this paper we present a study of the evolution of the microscopic damage in hcp Zr with a kMC approach using cascade data from MD simulations.

2. Cascade Ageing

D.J. Bacon et al. have generated, using MD, a database of displacement cascades for hcp alpha-Zirconium. Cascades were produced by recoils from 10 to 25 keV in steps of 5 keV at 600K [1]. Information about migration and binding energies of different cluster types and sizes has also been obtained using MD [2,3] and introduced in our simulations.

We initially focused on the evolution of single cascades, and studied the diffusion and stability of clusters for long times (hours), as well as the possibility of formation of clusters. We have obtained the number of defects escaping recombination as a fraction of those produced in the cascade, and therefore the number of defects that would interact with the microstructure. These cascade ageing simulations follow the same methodoly than previous for Fe [4].

The size of the computational box used was 1000x1000x1000 nm^3 with boundaries as perfect sinks. The starting defect microstructure from MD was introduced in the centre of the kMC computational box. Then the system was annealed during 1000 s at 600K. In order to have a good statistics, we performed 100 annealing runs for each cascade and calculated the average escape ratio, recombination ratio between vacancies and interstitials, defects surviving the bulk, and average clusters size for those remaining defects. The effect of the recoil energy on the final number of freely migrating defects has been studied using four different energies, 10, 15, 20 and 25 keV.

We conclude that recombination between vacancies and interstitials occurring in the bulk does not change with PKA energy. Between 10 and 15 keV, the number of vacancies remaining in the bulk changes; the reason is that displacement cascades with PKA energy higher than 15 keV present clusters of vacancies with larger size, which are very stable and remain in the bulk. However, only small vacancy clusters, that dissolve and move to the surface, appear for 10 keV. The percentage of interstitials that remain in the bulk does not change, and it is always a small value. This is explained by the one dimensional (1D) migration of these defects. This 1D migration is also responsible for the low recombination in the bulk. The average cluster size increases with increasing PKA energy for both vacancies and interstitials.

3. Damage accumulation

Using 25 keV cascades we have studied the evolution of the microstructure during irradiation under fission environment conditions: dose rate of 10^{-6} dpa/s, 600K and final dose of 0.1 dpa. Periodic boundary conditions were used in this case. These preliminary results show that the total concentration of vacancies in the bulk is larger than the concentration of interstitials when clusters of all sizes are accounted for. The average cluster size of interstitials is independent of dose, due to their stability. However, an increase in the average cluster size for vacancies with dose has been observed, because of small vacancy clusters dissolve and migrate effectively at that temperature, joining to those of largest size. This effect is shown in Fig.1.

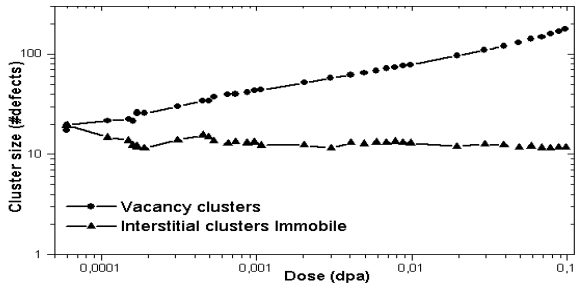

Fig.1 *Defect cluster size in number of defects versus total dose*

4. Conclusions

Our simulations show that dissolution of small vacancy clusters at 600K is expected as well as migration of single vacancies. 1D migration of interstitials causes an small recombination between interstitials and vacancies. The number of vacancies that move to the surface increases when PKA energy decreases because of vacancy clusters are small at low energy and dissolve. However, the number of interstitials that diffuse to the surface is constant with PKA energy. The percentage of vacancies remaining in the bulk is larger than the percentage of interstitials. Calculations show that final number of defects escaping intracascade recombination as well as the final average cluster sizes is very dependent on the initial damage structure obtained from MD simulations.

Accumulation damage in Zr predicts an increase in the average cluster size with dose for vacancies while the average cluster size of interstitials remains practically constant. The presence of both vacancies and interstitials at 600K has been observed experimentally [5].

5. Acknoledgements

This work has been performed under funding of EURATOM-project FIKS-CT-2001-00137 (SIRENA).

6. References

[1] R. Voskoboinikov and D.J Bacon, “MD simulation of displacement cascades in pure Zirconium”, SIRENA meeting report (March, 2003)
[2] C. Arevalo and J.M. Perlado, “State of the art of diffusion parameters for Zr: Preparing kMC simulations”, SIRENA meeting report (March, 2003)
[3] Y.N. Osetsky, D.J. Bacon, N. de Diego, Metall. and Mater. Trans. A 33(2002) 777
[4] N. Soneda and T. Diaz de la Rubia, Phil. Mag. **78** (1998) 995
[5] M. Griffiths, Jour. Of Nuclear Materials **159** (1988) 190

Simulation of Point Defect, Interstitial Cluster and Copper Atom Diffusion in Fe-Cu Alloys

A.C. Arokiam, A.V. Barashev and D.J. Bacon

Materials Science and Engineering, Department of Engineering, The University of Liverpool, Brownlow Hill, Liverpool L69 3GH, UK (e-mail: alanca@liv.ac.uk)

ABSTRACT

Molecular dynamics (MD) simulations of the vacancy and interstitial migration in a bcc Fe-1at.%Cu alloy using the many-body potential set by Ackland *et al*. [1] and Monte Carlo (MC) calculations of the transport coefficients for the fluxes of vacancies and Cu atoms are presented. The MC simulations were performed using data from the MD studies and *ab initio* calculations [2] on the activation energy of different atomic jumps.

1. Introduction

Precipitation of Cu atoms is one of the reasons for the hardening increase observed in pressure vessel steels of nuclear reactors. Development of predictive models of this phenomenon requires knowledge of the diffusion and interaction properties of solute atoms, point defects and their clusters. In this paper we study the diffusion of copper atoms via the vacancy mechanism and interstitial cluster migration in Fe-Cu alloys and discuss possible implication of the results in the copper precipitation phenomenon.

2. MD Calculations

Calculations were carried out at temperatures of 1000 to 1800K for up to 250 ns, to accumulate statistics for the vacancy jumps. The results are summarised below.

1) The static and dynamic values of the migration energy are in close agreement, and the diffusion coefficients agree well with predictions of the model of Barbu and Lidiard for solute diffusion in dilute bcc alloys [3].

2) The vacancy-Cu atom cross-diffusion coefficient (see the definition in [4]) was estimated. Despite large statistical errors, a conclusion was made that it is negative at all temperatures studied, indicating that Cu atoms migrate in the direction opposite to the vacancy flux, thus away from sinks of point defects, such as dislocation loops.

3) At temperatures above 1500K, about 1% of the vacancy jumps are double jumps result from synchronised movement of two atoms towards the vacancy. The static value of the activation energy of such jumps has been found to be a little smaller than twice the value of a single jump.

3. MC Calculations

The methodology of these simulations is described in ref [4]. The calculations show (see Fig.1) that the vacancy-copper atom cross diffusion coefficient is

1. negative over the entire temperature range studied, if the activation energies of atomic jumps are calculated using the potential set of Ackland *et al*. [1]; and

2. positive below and negative above 900K, if the activation energies are taken from *ab initio* calculations of Becquart and Domain [2].

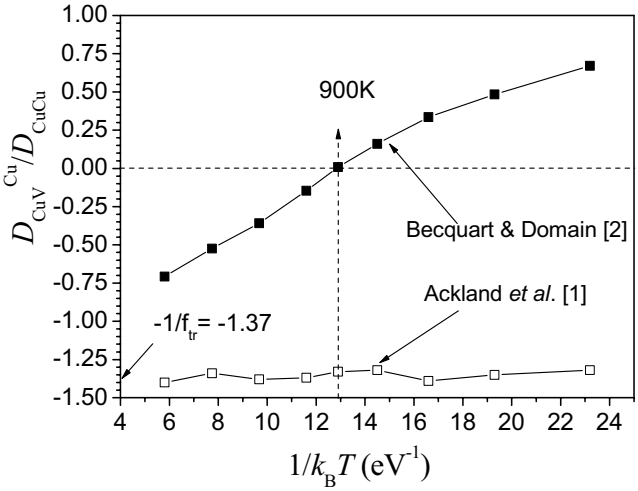

Fig.1. Temperature dependence of the ratio of vacancy-Cu atom cross-diffusion coefficient and Cu atom diffusion coefficient calculated by the MC method.

We note that the vacancy migration energy in pure Fe given by the potential set of Ackland *et al*. [1] is 0.87 eV, and thus much higher than 0.55 eV found experimentally [5]; while the uncertainty of the *ab initio* calculations is ~0.1 eV. Hence, the crossover temperature for change of sign of the vacancy-Cu atom cross-diffusion coefficient, i.e. for changing the direction of Cu atom flux with respect to the vacancy flux, may be well below 900 K obtained for the *ab initio* dataset as input.

4. Concluding Remarks

The results obtained may have an important implication for explanation of features of copper precipitation in ferritic steels under neutron irradiation, namely: the absence of precipitate growth below ~600K [3] and loose structure of precipitates, i.e. Cu concentration <100% [6]. Indeed, if vacancies drag Cu atoms to sinks, such as interstitial clusters produced in displacement cascades, this can be an effective mechanism for removal of Cu atoms from matrix, and hence suppression of precipitate growth. This is important above some dose of irradiation, when interstitial clusters become an efficient sink for vacancies. The loose precipitates are explained as those formed near interstitial clusters, where vacancy jumps are governed by the vacancy-interstitial cluster interaction rather than that between Cu atoms, and hence the free energy of these precipitates is not minimised. The growth of precipitates at high temperature can be explained by either changing the direction of Cu atom diffusion with respect to the vacancy flux or less efficient accumulation of interstitial clusters.

Acknowledgments

This work was performed under a grant from the UK Engineering and Physical Sciences Research Council. ACA would also like to thank the University of Liverpool for providing a studentship grant.

References

[1] G.J. Ackland, D.J. Bacon, A.F. Calder and T. Harry, Computer simulation of point defect properties in dilute Fe-Cu alloy using a many-body interatomic potential, Philos. Mag. A **75**, 713 (1997).
[2] C.S. Becquart and C. Domain, Ab initio contribution to the study of complexes formed during dilute FeCu alloys radiation, Nucl. Inst. Meth. B **202**, 44 (2003).
[3] A. Barbu and A.B. Lidiard, Solute segregation in dilute bcc alloys under irradiation, Philos. Mag. A **74**, 709 (1996).
[4] A.V. Barashev, Simulation of phosphorus diffusion in α-iron under irradiation conditions, these proceedings (2004).
[5] A. Vehanen, P. Hautojärvi, J. Johansson, J. Yli-Kauppila and P. Moser, Vacancies and carbon impurities in α-iron: Electron irradiation, Phys. Rev. B **25**, 762 (1982).
[6] P. Auger, P. Pareige, S. Welzel and J.C.Van Duysen, Synthesis of atom probe experiments on irradiation-induced solute segregation in French ferritic pressure vessel steels, J. Nucl. Mater. **280**, 331 (2000).

Simulation of Phosphorus Diffusion in α-Iron Under Irradiation Conditions

A.V. Barashev

Materials Science and Engineering, Department of Engineering, The University of Liverpool, Brownlow Hill, Liverpool L69 3GH, UK (e-mail: a.barashev@liv.ac.uk)

ABSTRACT

Molecular dynamics and Monte Carlo studies of vacancy and interstitial diffusion in bcc Fe-P alloy in the dilute limit are presented. An EAM-type potential set developed recently for this system is used. The MC simulations show that vacancies drag P atoms towards sinks of point defects, which is opposite to the situation described by existing models of P segregation. Rate theory calculations of P segregation in a Fe-P-C alloy under irradiation conditions are presented.

1. Introduction

Quantitative analysis of experimental data on P segregation to grain boundaries (GBs) requires knowledge of the diffusion coefficients and, hence, of the activation energies of atomic jumps. It is usually assumed that there is no significant interaction between a vacancy and a P atom and the P-interstitial binding energy is relatively small [1,2]. As a consequence, the mean-free paths of P-vacancy and P-interstitial complexes during their lifetimes from formation until thermally-activated dissociation are both small; the flux of P atoms via vacancies is always away from sinks of point defects, such as GBs, and the diffusion of P atoms is predominantly via interstitials.

Recently a new EAM type potential set for a dilute Fe-P system has been developed based on *ab initio* data [3]. Molecular static calculations show high ~0.37eV binding energy of a vacancy-P atom complex when the vacancy is in the first or second nearest neighbour (nn) sites from the P atom. Such an interaction makes it possible for P atoms to co-migrate with vacancies to sinks and this has to be clarified for the temperature range of practical importance. Furthermore, the binding energy a P-interstitial complex is found to be of ~1 eV, hence a P-interstitial complex should migrate over long distances without dissociation.

In this paper we present Monte Carlo (MC) calculations of the diffusion coefficients of vacancies and P atoms in a Fe-P alloy using the new data on solute-vacancy interaction [3] and rate theory calculations of P segregation in a Fe-P-C alloy under irradiation.

2. The Model and Calculation Results

In a dilute AB alloy, the vacancy (V) and solute atom (B) fluxes are expressed in terms of the gradients of concentrations of unpaired species, c'_{V} and c'_{B} [4]. These expressions contain three independent coefficients:

$$D_{\mathrm{VV}} = D_{\mathrm{V}}^{\mathrm{A}} + c'_{\mathrm{B}}\, D_{\mathrm{BV}}^{\mathrm{V}} = \frac{k_{\mathrm{B}}TL_{\mathrm{VV}}}{nc'_{\mathrm{V}}};\; D_{\mathrm{VB}}^{\mathrm{B}} = \frac{k_{\mathrm{B}}TL_{\mathrm{BB}}}{nc'_{\mathrm{B}}\, c'_{\mathrm{V}}};\; D_{\mathrm{BV}}^{\mathrm{B}} = \frac{k_{\mathrm{B}}TL_{\mathrm{VB}}}{nc'_{\mathrm{B}}\, c'_{\mathrm{V}}}, \qquad (1)$$

where n is the lattice site density and $D_{\mathrm{V}}^{\mathrm{A}}$ is the vacancy diffusion coefficient in pure matrix. The D coefficients are calculated here by the MC method [5] using the generalised Einstein form for the L coefficients [6] ($i, j = \mathrm{B}, \mathrm{V}$)

$$L_{ij} = \frac{1}{Vk_{\mathrm{B}}T}\frac{\langle \mathbf{R}_i \mathbf{R}_j \rangle}{6t}, \qquad (2)$$

where V is the system volume, and $\mathbf{R}_{\mathrm{V}}$ and $\mathbf{R}_{\mathrm{B}}$ are the total displacement vectors of vacancies and solute atoms, respectively, during time t.

The calculated temperature dependence of the D coefficients normalised by $D_{\mathrm{V}}^{\mathrm{A}}$ is presented in Fig.1. As can be seen, over the entire temperature range studied, $D_{\mathrm{BV}}^{\mathrm{B}}$ and $D_{\mathrm{VB}}^{\mathrm{B}}$ are close to each other and the cross-coefficient $D_{\mathrm{BV}}^{\mathrm{B}}$ is positive, indicating that vacancies drag P atoms towards sinks. It has also been found that the temperature dependence of D_{VV} is described accurately assuming that $D_{\mathrm{BV}}^{\mathrm{V}} \approx D_{\mathrm{VB}}^{\mathrm{B}}$.

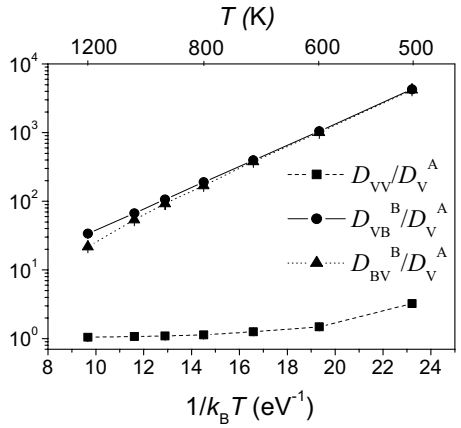

Fig.1. Temperature dependence of the D coefficients in a dilute Fe-P alloy.

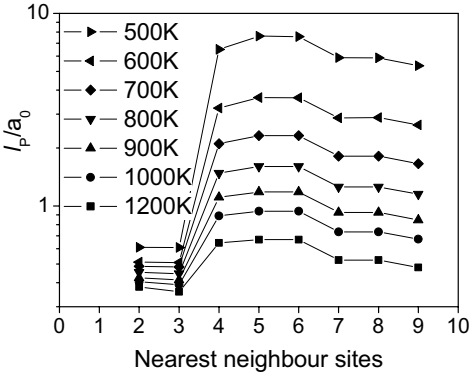

Fig.2. The mean-free path of a vacancy-P atom complex during its lifetime.

The mean-free path of a V-P atom complex, l_P, during its lifetime from creation until thermally-activated dissociation is presented in Fig.2 as a function of the nn sites included in the V-P range used for definition of the creation/dissociation events. As can be seen, the maximum l_P is for a complex that includes up to 5th nn sites, and is $> 8a_0$ (i.e. >2 nm) at low temperature. We suppose, that the assumption of local equilibrium used in diffusion equations is preserved, however, since l_P is much smaller than the mean distance between sinks of point defects in materials (typically 30 to 100 nm).

3. Conclusions

1. Under irradiation conditions vacancies drag P atoms towards sinks of point defects.
2. Description of this process may be performed using equations defined locally.
3. The theory of P atom segregation to GBs under neutron irradiation [2] has been modified to account for the new diffusion mechanisms and to include influence of C atoms (not described here due to the limited space available).

Acknowledgments

This work was performed under the contract FIKS-CT-2000-00080 ("PISA") from the European Commission. The author thanks Prof D.J. Bacon and Prof A.B. Lidiard for valuable discussions.

References

[1] A.B. Lidiard, The migration of phosphorus in ferritic iron alloys under irradiation, Philos. Mag. A **79**, 1493 (1999).
[2] A.V. Barashev, Segregation of phosphorus atoms to grain boundaries in ferritic steels under neutron irradiation, Philos. Mag. Lett. **82**, 323 (2002).
[3] G.J. Ackland, M.I. Mendelev, D.J. Srolovitz, S. Han and A.V. Barashev, Development of an interatomic potential for phosphorus impurities in α-iron, J. Phys.: Condens. Matter **16**, S2629 (2004).
[4] A. Barbu and A.B. Lidiard, Solute segregation in dilute bcc alloys under irradiation, Philos. Mag. A **74**, 709 (1996).
[5] A.R. Allnatt and E.L. Allnatt, Computer simulation of phenomenological coefficients for atom transport in a random alloy, Philos. Mag. A **49**, 625 (1984).
[6] A.R. Allnatt, Einstein and linear response formulas for the phenomenological coefficients for isothermal matter transport in solids, J. Phys.: C **15**, 5605 (1982).

Kinetic Monte Carlo Simulations Of Microstructural Evolution in α-Fe Under Irradiation

C. Domain[1], C. S. Becquart[2] and L. Malerba[3]

[1]EDF-R&D, Dept MMC, Les Renardières, F-77818 Moret-sur-Loing, France – christophe.domain@edf.fr
[2]LMPGM, UMR 8517, Université de Lille 1, F-59655 Villeneuve d'Ascq, France - Charlotte.Becquart@univ-lille1.fr
[3]SCK•CEN, Department RMO, Boeretang 200, B-2400 Mol, Belgium – lmalerba@sckcen.be

ABSTRACT

An object kinetic Monte Carlo (OKMC) method is used to study the influence of the description of the migration of self-interstitial atoms (SIA) clusters, as well as the boundary conditions, on the prediction of neutron irradiation damage production in α-Fe, through comparison with a model experiment.

1. Introduction

The microstructural changes produced in materials by radiation damage accumulation can be modelled using kinetic Monte Carlo (KMC) and rate theory (RT) methods. Both ignore partially or totally the crystal lattice and rely on the same set of parameters: defect diffusivity coefficients, binding energies and reaction radii. Many unknowns remain about these parameters and one way of assessing the sensitivity of the models to their choice is to try to reproduce model experiments using different sets. A first set of OKMC studies performed using our code was presented and discussed in [1]. In this work the same OKMC code is used to test different descriptions of, particularly, the behaviour of self-interstitial atom (SIA) clusters and the influence of the boundary conditions, through comparison with a reference neutron irradiation experiment performed on α-Fe [2]. Indeed, the advantage of KMC versus RT approaches is that the former takes naturally into account spatial inhomogeneities. The associated drawback as compared to RT is that the size of the simulation box (compromise between computing time and realistic conditions) and the choice of the boundary conditions may influence the results, especially for high dose-rates.

2. The model

OKMC methods treat defects as objects with specific positions in a simulation volume. Probabilities for physical transition mechanisms are calculated as Boltzmann factor

frequencies. After a certain event is chosen, time is increased according to a residence time algorithm [3]. The basic aspects of the parameterisation used in our code are described in [1]. In the present work the influence of the description of SIA cluster migration is explored. In set I, all SIA clusters (size $m \geq 2$) migrate in 1D, with a migration energy E_m=0.04 eV (as in [1]) and a prefactor decreasing with size according to the law: $\nu_0 \cdot m^{-s}$ (ν_0=6·10^{12} s^{-1}, s=0.51, following Osetsky et al. [4]). Thus, set I embodies the picture of SIA cluster migration widely accepted till recently based on molecular dynamics results. In set II, small clusters (m<5) migrate in 3D with E_m=0.4 eV, as broadly suggested by recent *ab initio* calculations [5], while larger clusters keep 1D motion with E_m=0.04 eV; for all clusters the prefactor decreases with s=0.51. Set III treats small clusters (m<5) in the same way as set II, but assumes that larger clusters are completely immobile (see Table 1). For vacancy clusters, the same mobility has been used for the three sets: a migration energy of 0.69 eV and a prefactor decreasing with size according to the law $\nu_0 \cdot p^{-m}$ with p=100 (as in [1]).

SIA clus. size	**Set I**			**Set II**			**Set III**		
(E_m in eV)	***s***	***E_m***	***D***	***s***	***E_m***	***D***	***s***	***E_m***	***D***
m=1	-	0.3	3D	-	0.3	3D	-	0.3	3D
2<m<5	0.51	0.04	1D	0.51	0.4	3D	0.51	0.4	3D
$m \geq 5$	0.51	0.04	1D	0.51	0.04	1D	Immobile		

Table 1: Summary of parameter sets for the description of SIA clusters.

In the simulation, the HFIR [2] neutron spectrum was decomposed into 3·10^{16} Frenkel-pairs·cm^{-3}·s^{-1}, 4·10^{14} 10 keV cascade-debris·cm^{-3}·s^{-1} and 2·10^{14} 20 keV cascade-debris·cm^{-3}·s^{-1}, as was done in [1]. The simulations were performed in a $200a_0 \times 200a_0 \times 200a_0$ volume, using both periodic and absorbing boundary conditions (denoted respectively as PBC and ABC). With all sets, 100 ppm traps for SIA clusters (binding energy 0.65 eV, capture radius 5 Å) were included. The irradiation temperature was 70°C [2].

3. Results

Figs. 1 and 2 show the comparison between the density of vacancy clusters (of any size) at different doses after neutron irradiation in the experiment [2] and in the simulation with the three proposed sets. Fig. 1 refers to the case of PBC, fig. 2 to the case of ABC. With PBC, both set I and II reproduce the experimentally observed saturation of the density with dose. Set III yields almost linear damage accumulation. As already suggested [6], the SIA cluster high mobility and dimensionality of motion (1D/3D) appear to be the most important factor to reproduce experimental data concerning void accumulation. The use of ABC (which somehow correspond to a case of extremely strong extended sinks) worsens the results, indicating that a correct description of the strength of

extended sinks is important, particularly in the case of highly mobile defects. Note, however, that PBC are not necessarily more physical than ABC, particularly in the case of reasonably low dose-rates, as under neutron irradiation.

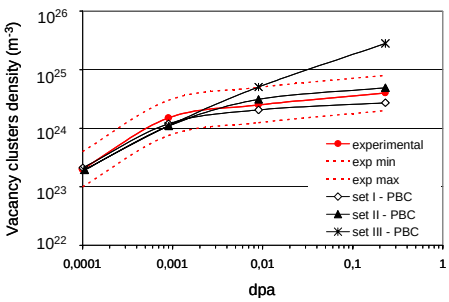

Fig. 1 Vacancy cluster density vs neutron dose: experimental data and uncertainty compared to simulations with PBC.

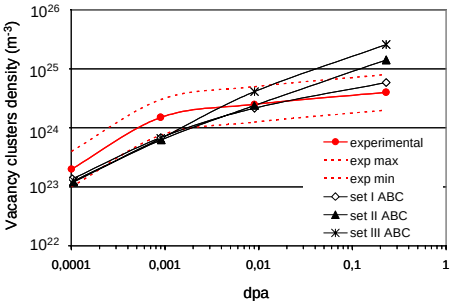

Fig. 2 Vacancy cluster density vs neutron dose: experimental data and uncertainty compared to simulations with ABC.

4. Conclusion

The assumption of immobile clusters above a certain size fails to reproduce experimental irradiation results in terms of vacancy cluster density, while the combined use of *ab initio* data, high mobility of larger clusters and traps succeeds in reaching the objective. The choice of the boundary conditions and, in general, the sink description, is also important. While the latter clearly still need to be improved, the description of SIA cluster mobility used here should be tested against other experimental results, before being fully accepted.

References

[1] C. Domain, C. S. Becquart and L. Malerba, J. Nucl. Mater. (in press).
[2] M. Eldrup, B.N. Singh, S.J. Zinkle, T.S. Byun, K. Farrell, J. Nucl. Mater. **307-311** (2002) 912-917; M. Eldrup and B.N. Singh, J. Nucl. Mater. **323** (2003) 346-353.
[3] W. M. Young and E. W. Elcock, Proc. Phys. Soc. **89** (1966) 735-746.
[4] Yu. N. Osetsky, D. J. Bacon, A. Serra, B. N. Singh and S. I. Golubov, J. Nucl. Mater. **276** (2000) 65-77.
[5] F. Willaime, C.C. Fu, M.C. Marinica and J. Dalla Torre, NIMB (in press).
[6] H.L. Heinisch, B.N. Singh and S.I. Golubov, Jour. Nucl. Mater. **283-287** (2000) 737-740.

Modeling Helium Effects in Irradiated Materials

M. Victoria [1,2], M. J. Caturla [2,3], J. M. Perlado [1], T. Diaz de la Rubia [2]

[1] Instituto de Fusión Nuclear, Universidad Politécnica(ETSII), Madrid, Spain

[2] Lawrence Livermore National Laboratory, Livermore CA

[3] Dept. Física Aplicada, Universidad de Alicante, Alicante, Spain (mj.caturla@ua.es)

ABSTRACT

Kinetic Monte Carlo simulations are compared to experimental results on void swelling as well as helium desorption. The influence of different input parameters in the final results of the calculations is studied in order to identify the key mechanisms that control void swelling. In particular, our simulations show that the initial stage of the damage after the cascade collapse influences significantly the results regarding the dependence with temperature. Finally, we use kinetic Monte Carlo calculations to fit the experimental results on He desorption existing in the literature in order to obtain information about the binding energies and migration energies of He and He-vacancy complexes.

1. Introduction

It is known since several decades that the presence of impurities such as He or H enhances the formation of voids during irradiation that results in volume changes, therefore deteriorating the properties and reducing the lifetime of structural materials [1]. However, despite years of research, there is not yet a complete model for the formation of such voids that predicts the dependence on He content, dose, dose rate, irradiation energy and temperature. The large number of parameters and mechanisms involved in void swelling under irradiation makes the task of finding a unified model a very difficult one. Our approach has been to use as much information as possible from first principle calculations and molecular dynamics simulations on the nature of those defects created under irradiation and the interaction of these defects with impurities (He in particular), and transfer this information to a kinetic Monte Carlo (kMC) model of defect diffusion to study the evolution of the microstructure under irradiation.

2. Modeling Approach

There is extensive data in the literature about the initial stage of the damage produced by energetic recoils in different metals from molecular dynamics simulations [2]. Lately kMC simulations using input data obtained from molecular dynamics simulations, ab initio calculations and /or experimental data are being routinely used to model the long-term behavior of those defects produced during irradiation [3]. In order to model the evolution of the microstructure under irradiation in the presence of impurities such as He it is necessary to have information about the migration mechanisms of such impurity as

well as the interaction with the defects produced during irradiation. Recent calculations by F. Williame and C. C. Fu using first principle calculations [4] are starting to provide some insight to the migration mechanisms of He in Fe and the interaction of He with vacancies. In our kMC calculations we make use of all significant data available in order to model the formation of voids.

3. **Results**

We have used kMC models to study first qualitatively the formation of voids during irradiation and the influence of the initial conditions of the simulation in the void swelling dependence with temperature. We have focused on the role of the initial structure of the damage produced after the cascade collapse. Using the same information regarding migration and binding energies of defects and He-vacancy complexes we have varied the form of the initial distribution of defects produced during irradiation. In one case we have used the damage produced in an f.c.c. material, gold, where all vacancies are forming large clusters. In a second case we have used the damage produced in a b.c.c. material, iron, where most of the vacancies are isolated. Results of such calculations are presented in fig. 1. The solid line is the percentage of swelling, obtained from the number of vacancies forming voids as a function of temperature for the case of the f.c.c. type of damage. The discontinuous lines are the results for the case when the initial vacancies are isolated. Clearly, the dependence with temperature is very different in both cases, even though all other parameters in the simulation are kept constant.

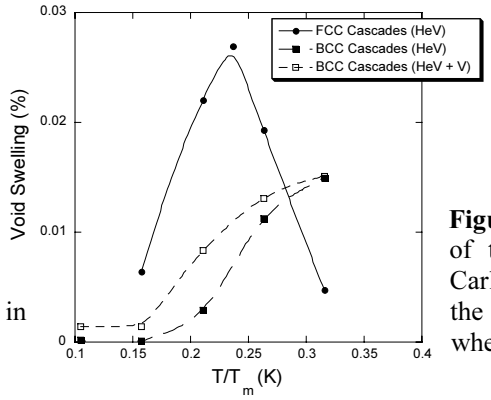

Figure 1: Values of void swelling as a function of temperature obtained from kinetic Monte Carlo calculations when the vacancies produced the cascade are forming clusters (circles) and when they are isolated (squares).

in

However the calculations presented above are only qualitative since no realistic values of the migration energies of He-vacancy complexes or its migration mechanism have been used to be able to represent any relevant material. Partly this is due to the lack of information on these parameters as already pointed out above. In order to obtain some information about these parameters we are using kMC simulations to fit experimental results already available in the literature. In particular we have focused our work in studying desorption of He from Fe samples since a large database is already available, compiled by Vassen, Trinkaus and Jung in reference [5]. Moreover, an analytical model was also used in this case to fit the experimental data and therefore the results can also be used to compare with the kMC calculations. Fig. 2 shows the initial results of our

calculations for the case of three experimental conditions where the impurity concentration, the depth of the sample and the temperature differ on each case. A dissociative mechanism is assumed for the migration of He with dissociation energy of 1.09 eV.

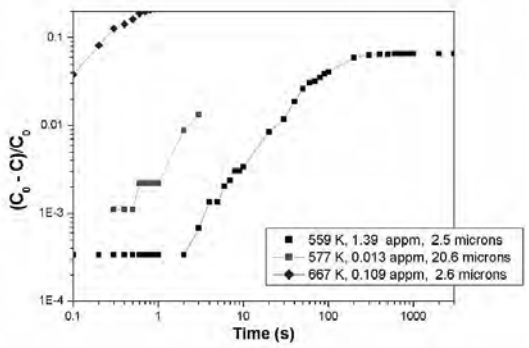

Figure 2: Concentration of He desorbed as a function of time as obtained from kinetic Monte Carlo simulations for three different experimental conditions.

4. Conclusions

KMC simulations used systematically show that one of the key parameters to understand the dependence of void swelling with temperature is the initial stage of the defects produced during the cascade collapse. If these defects are forming clusters the dependence with temperature resembles that of the dependence measured in f.c.c. metals while if the initial distribution of vacancies is such that they are isolated the temperature dependence resembles that of b.c.c. metals, keeping all other parameters the same. Quantitative information about void swelling, however, requires of accurate values of the binding energies and migration energies of defects and their interactions with impurities. In order to obtain these values we use the kMC model to fit experimental data on He desorption existing in the literature. We are in the process of extracting information about binding energies of small He-vacancy clusters using this procedure.

Acknowledgements

This work was carried out under the auspices of the US Department of Energy by LLNL under contract W-7405-Eng-48. One of the authors (MJC) wants to thank the Spanish MEC for support under the Ramon y Cajal program.

References

[1] W. G. Wolfer, F. A. Garner, *Radiation Effects*, **78**, (1983) 275
[2] D. J. Bacon, T. Diaz De La Rubia, *J. Nucl. Mater.,* **216**, (1994) 275
[3] See review on kinetic Monte Carlo simulations to be presented in this
[4] F. Willaime, C.C. Fu, CEA-Saclay internal report (2004)
[5] R. Vassen, H. Trinkaus, P. Jung, Phys. Rev. B **44**, (1991) 4206

Multi-scale modeling of the evolution of defect populations in electron-irradiated α-Fe

J. Dalla Torre, Chu-Chun Fu, F. Willaime , J.-L. Bocquet and A. Barbu

Service de Recherches de Métallurgie Physique, Centre d'Etudes de Saclay, 91191 Gif-sur-Yvette, France - fwillaime@cea.fr

We have performed a multi-scale modeling of the evolution under isochronal annealing of the defects produced by electron irradiation in α-Fe. The stability and mobility of the relevant point defects and defect clusters (vacancies, self-interstitials, and small clusters of vacancies or interstitials) have been determined by ab initio calculations performed using the SIESTA method [1,2]. These results are used as input data for an event-based kinetic Monte Carlo model (JERK) [3] to simulate the defect-population evolution: defects may migrate, aggregate, dissociate or annihilate. We followed closely the conditions of existing experiments by Takaki et al., where evolutions in the defect population are evidenced by abrupt changes in the resistivity of the sample (so-called recovery stages) [4]. We successfully reproduce all the recovery stages and we clearly attribute them to the migration or dissociation of specific defects. Dose effects, i.e. shifts of the recovery stages when the irradiation dose is increased, are also properly reproduced.

Acknowledgements
This work was supported by the PERFECT European Integrated Project under Contract No. FI6O-CT-2003-508840.

References

1. J. Soler, E. Artacho, J.D. Gale, A. García, J. Junquera, P. Ordejón and D. Sánchez-Portal. *The SIESTA Method for ab initio order-N materials simulation*. J. Phys.: Condens. Matter **14**, 2745 (2002).
2. C.C. Fu, F. Willaime and P. Ordejón. *Stability and mobility of mono- and di-interstitials in α-Fe*. Phys. Rev. Lett. **92**, 175503 (2004).
3. J. Dalla Torre, J.-L. Bocquet, N.V. Doan E. Adam, and A. Barbu. *Jerk, an event-based kinetic Monte Carlo model to predict microstructure evolution of materials under irradiation*. Philos. Mag. (in press).
4. S. Takaki, J. Fuss, H. Kugler, U. Dedek and H. Schultz. *The resistivity recovery of high purity and carbon doped iron following low temperature electron irradiation.* Rad. Effects, **79**, 87 (1983).

A Fast Quantum-Mechanical Model for Molecular Dynamics Simulations of Interstitial Defects in Transition Metals

S. L. Dudarev

EURATOM/UKAEA Fusion Associaton, Culham Science Centre, Oxfordshire OX14 3DB, United Kingdom
sergei.dudarev@ukaea.org.uk

ABSTRACT

We develop a quantum-mechanical approach to the treatment of directional interatomic interactions occurring in the region of strong local deformations associated with the core of an interstitial atom defect. Using analytical expressions for the elements of the $\hat{H}^2$ matrix evaluated using the second-order matrix recursion formalism, we derive an efficient method for computing forces acting on atoms in a molecular dynamics simulation of cascade damage and radiation defects in materials. Preliminary tests show that a code based on the new approach runs at approximately one third of the speed of a code based on the Finnis-Sinclair potential model.

A significant but not yet sufficiently well understood issue associated with molecular dynamics (MD) concerns the range of validity of the many-body empirical potentials used in simulations of interstitial atom defects produced in materials by high-energy collision cascades. Recent density functional calculations [1,2] showed that practically all the available models of interatomic forces developed before the new density functional results became available were unreliable in the large deformation limit, and were generally inaccurate on the ~ 0.1 eV energy scale. This scale is of particular significance for the investigation of radiation effects since it characterizes the difference between energies of formation of various configurations of defects in metals and alloys, and it also describes thermally activated diffusion of interstitial defects in materials. To improve the accuracy of MD simulations one needs to investigate the limits of validity of the functional representation of interatomic interactions within the framework of a chosen (e. g. the Finnis-Sinclair) model, as well as to address the conceptual accuracy of the model itself or, in other words, the extent to which processes described by a particular model adequately match predictions made on the basis of density functional theory.

The scalar second-moment approximation representing the basis of the Finnis-Sinclair model is known to be insufficient for predicting the difference between energies of various crystal structures. These energy differences are determined by the higher-order terms in the moment expansion for the relevant Green's functions. There is also a further issue related to the degeneracy of multiplets of atomic d-states giving rise to the formation of directional interatomic bonds. The treatment of an initially degenerate multiplet of states requires using the matrix rather than the scalar recursion formalism, where the former involves the diagonalisation of a circular matrix, i.e. an operation that highlights the difference between the classical and the quantum-mechanical pictures of interatomic interactions.

In this study we show that the use of a quantum-mechanical, i.e. based on matrix diagonalisation, approach to the evaluation of interatomic forces does not have a significant detrimental effect on the speed of MD simulations. In the matrix recursion approach the energy of a system of interacting atoms is given

by

$$E_{tot} = \sum_{\alpha} \left[-\sum_{n=1}^{5} \Theta_{n\alpha} \sqrt{H_n^2(\alpha)} + \sum_{n=6}^{10} \Theta_{n\alpha} \sqrt{H_n^2(\alpha)} \right] + \frac{1}{2} \sum_{\alpha} \sum_{\beta \neq \alpha} V(R_{\alpha\beta}), \quad (1)$$

where $H_n^2(\alpha)$ is the n-th eigenvalue of the matrix $(0,\alpha|\hat{H}^2|0,\alpha)$ entering the second-moment matrix recursion expression for the on-site Green's function

$$(0,\alpha|\hat{G}(E)|0,\alpha) = \frac{1}{(E+i0)\hat{I} - \frac{1}{E+i0}(0,\alpha|\hat{H}^2|0,\alpha)} \quad (2)$$

and $\Theta_{n\alpha}$ is the occupation number of a collective many-body bonding (i.e. corresponding to energy $-\sqrt{H_n^2(\alpha)}$) or an antibonding (corresponding to energy $+\sqrt{H_n^2(\alpha)}$) state formed as a result of the overlap between d-states centred on atom α and d-states localised on the neighbouring atoms. Occupation numbers $\Theta_{n\alpha}$ satisfy the sum rule $\sum_n \Theta_{n\alpha} = N_d(\alpha)$, where $N_d(\alpha)$ is the total number of d-electrons on site α. Forces acting on atoms are found by the differentiation of (1) using analytical expressions [3] derived for the matrix elements of $(0,\alpha|\hat{H}^2|0,\alpha)$.

To take a full advantage of the ability of the Finnis-Sinclair potential to correctly reproduce the elastic response of the material to small atomic displacements we included the directional quantum terms in the form of a quantum 'core', i.e. in the form of an operator correction that becomes significant only if the distance between the interacting atoms becomes smaller than a certain critical value [3]. The parameters of the 'quantum core' term were determined through fitting of the predicted interstitial defect formation energies to the values found from density functional calculations.

To test if the new method can be used for carrying out realistic MD simulations we investigated the formation of a small collision cascade in body-centred cubic vanadium. Simulations were performed for systems containing up to 10^5 atoms. We found that the introduction of the quantum-mechanical matrix-recursion treatment of interatomic interactions did not have a substantial detrimental effect on the speed of the MD code. On average, MD simulations were running at approximately 35% of the speed of the corresponding Finnis-Sinclair model. A sequence of MD snapshots illustrating the process of development of a 380 eV cascade is shown in Fig. 1. The cascade produces five single interstitial defects of the $\langle 111 \rangle$ type that, according to density functional calculations [1], represent the lowest energy state of a single interstitial atom in bcc vanadium.

Simulations have also been performed of thermally activated diffusion of single interstitial atoms at several elevated temperatures. We found that the $\langle 111 \rangle$ interstitial configurations retained their stability up to relatively high temperatures of the order of 200°C and were able to diffuse one-dimensionally over distances of the order of ~ 50 Å on the ~ 60 ps time scale.

The example given in Fig. 1 shows that MD simulations of relatively large systems containing about a hundred thousand atoms can now be readily performed on the quantum-mechanical level of approximation, i.e. on the level where an explicit form of a function describing many-body interactions between atoms remains unknown. In the quantum-mechanical molecular dynamics the evolving system chooses the energy surface in the space of atomic coordinates $\{\mathbf{R}_1, \mathbf{R}_2, ..., \mathbf{R}_N\}$ locally by diagonalising matrices $\langle i,\alpha|\hat{H}^2|j,\alpha\rangle$ for every atom

in the system. The fact that the introduction of the diagonalisation step does not have a significant detrimental effect on the speed of MD simulations suggests that a similar method could be developed to accelerate molecular dynamics simulations based on the fourth- and sixth-moment bond-order potentials.

This work was funded by the UK Engineering and Physical Sciences Research Council and by EURATOM.

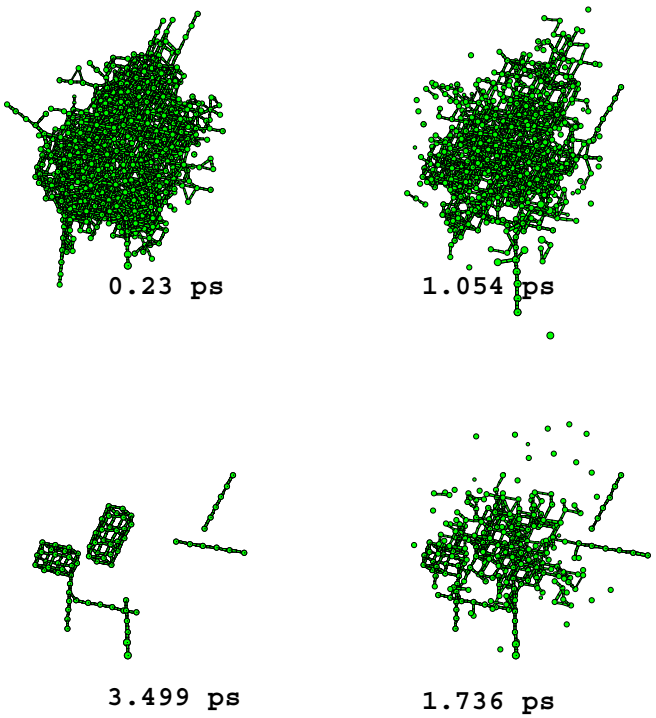

Figure 1: A small 380 eV collision cascade in body-centred cubic vanadium simulated using the quantum-mechanical approach described in the text using a cell containing 59582 atoms. The cascade produces five ⟨111⟩ single interstitial atom crowdion-type defects, as well as one double vacancy and one triple vacancy cluster.

References

[1]. S. Han, L. A. Zepeda-Ruiz, G. J. Ackland, R. Car and D. J. Srolovitz, *Interatomic potential for vanadium suitable for radiation damage simulations*, Journ. Appl. Phys. **93** (2003) 3328–3335

[2] C.-C. Fu, F. Willaime and P. Ordejon, *Stability and mobility of mono- and di-interstitials in α-Fe*, Phys. Rev. Lett. **92** (2004) art. no. 175503

[3]. S. L. Dudarev, *'Quantum core' interatomic potentials for transition metals*, Journ. Nucl. Mater. **329/333** (2004) 1151–1155

Interaction of He with Self Interstitial Atoms and Small Vacancy Cluster in α-Fe Studied by the Dimer Method

F. Gao, H. L. Heinisch and R. J. Kurtz

Pacific Northwest National Laboratory, Richland, Washington, 99352, USA. E-mail: fei.gao@pnl.gov

ABSTRACT

The dimer method is employed to study the migration of He interstitials and small He-vacancy cluster complexes. As expected, interstitial He atoms can diffuse at low temperatures. The migration mechanism for He-divacancy complexes is found to be somewhat more complicated. Within the divacancy the He atom can jump to a nearest neighbor vacancy or to a second nearest neighbor vacancy. The dimer method is also used to study the interactions of migrating self-interstitial atom (SIA) crowdions with substitutional He atoms. The energy paths for kicking out the He atom and the preferential kick-out region around a substitutional He atom are determined, as well as the effects of the He atoms on directional change of the SIA.

1. Introduction

In fission and fusion reactor environments, the creation of helium atoms in metals due to nuclear (n, α)–reaction during neutron irradiation is considered with particular concern because their precipitation into bubbles can substantially deteriorate mechanical properties [1]. The understanding of helium behavior and helium accumulation in metals represents one of the most important issues in the field of nuclear fusion technology, which requires multi-length and multi-time scale approaches. In the present study, the dimer method [2] is employed to study the diffusion of He interstitials, and the interaction of helium with self interstitial atoms and small vacancy clusters in α-Fe. The Ackland potential [3], the Wilson-Johson potential [4] and the Beck potential [5] are employed to describe interactions of Fe-Fe, Fe-He and He-He, respectively.

2. Results

Starting with an initial configuration of a He substitutional atom, 50 dimer searches result in two significant saddle points, one representing the He atom moving directly into an interstitial position with the energy of 3.74 eV and another one corresponding to the energy barrier of the second nearest neighbor atom kicking out the He from the substitutional position (4.53eV). This suggests that the substitutional He atom is very stable, and may not become mobile at very high temperature. In the case of a He atom with a di-vacancy, the He atom can easily jump from one vacancy position to the first-nearest neighbor vacancy position, with an energy barrier of 0.02 eV, but the energy required for the He atom jumps to the second-nearest neighbor vacancy position is 0.66 eV. In general, the vacancy can also jump, but the energy for vacancy jump is higher than that for a mono vacancy in pure Fe (0.78 eV), which may be due to the strong binding between He atom and vacancies. A tri-vacancy-He-complex has been studied, and it is found that the stable position of the He atom is at the middle of three vacancies, and forms a very stable configuration. There is no jump observed for the He atom, and all possible saddle points associate with vacancy jumps.

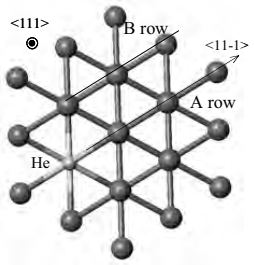

Fig. 1 Atomic plot showing a <111> plane, and A and B rows.

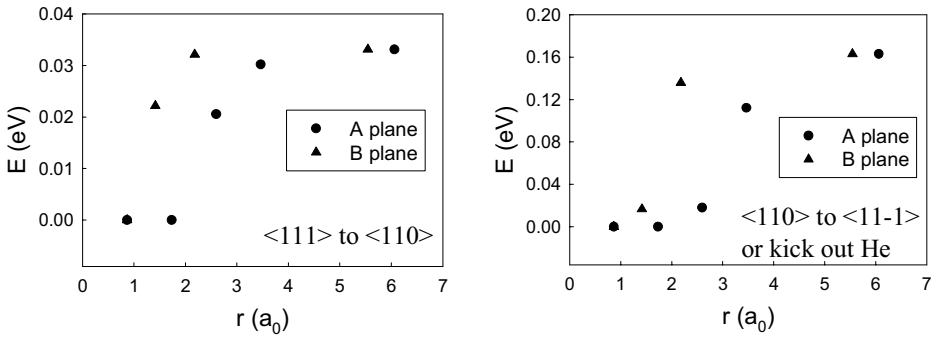

Fig. 2 Energy barriers for the SIA to change orientation from the <111> to <110> direction (a) and from the <110> to kicking out the substitutional He atom, as a function of distance.

The dimer method has been employed to explore the interaction of a SIA with a substitutional He atom. The initial SIA is set as a <111> crowdion configuration at the different positions near the He atom, and the center of the crowdion is either on the plane containing the He atom or out of the plane along the <111> direction. Fig. 1 shows a <111> plane containing the He atom, where there are two nonequivalent rows, namely A and B rows. The results suggest that the SIA located at the distance from the He atom less than 4.0 a_0 along A row and 3.0 a_0 along B row can kick out the He atom preferentially, and the energy barrier is very small. The mechanism for kicking out the He atom consists

of the SIA changing its orientation from the <111> to the <110> configuration, and then from the <110> to kicking out the He atom. Fig. 2 shows the energy barriers for the SIA to change its orientation from the <111> to <110> direction (a) and <110> to kicking out the He atom (b). The energy barriers for rotation when the SIA is located within the preferential region are generally smaller than the corresponding energy barriers in a perfect crystal of Fe. The preferential positions for kicking out the He atom out the <111> plane containing the substitutional He atom have been also studied. However, the present study suggests that the preferential reaction region is very anisotropic.

3. Summary

Helium diffusion in α-Fe has been studied using the dimer method, and the preferential position and the dominant migration mechanism of He atoms has been determined for He interstitial, He-vacancies-complex, and the interaction of the SIA with a substitutional He atom. Interstitial He atoms can diffuse at low temperatures (0.084 eV). In the case of di-vacancy-He-complex, the He atom can jump to a nearest neighbor vacancy or to a second nearest neighbor vacancy. A substitutional He atom can easily be displaced to an interstitial position by an incoming SIA. The energy paths for kicking out the He atom and the preferential kick-out region around a substitutional He atom, as well as the effects of the He atoms on directional changes of the <111> crowdions, are determined. Some new insights into the atomic-level simulations and long-time dynamics are discussed.

Acknowledgements

This work was supported by the US Department of Energy, Office of Fusion Energy Science under contract DE-AC06-76RLO 1830.

References

[1] E. E. Bloom, J. Nucl. Mater. **258-263**, 7 (1998).
[2] G. Henkelman and H. Jónsson, J. Chem. Phys. **111**, 7010 (1999).
[3] G. J. Ackland, D. J. Bacon, A. F. Calder and T. Harry, Philos. Mag. **A75**, 713 (1997).
[4] W. D. Wilson and R. D. Johnson: Interatomic Potential and Simulation of Lattice Defects, Plenum, 1972, p. 375.
[5] D. E. Beck, Mol. Phys. **14**, 311 (1968).

Investigations of Cavity Evolution in BCC Iron Implanted with Helium and Subsequently Irradiated with Neutrons

S.I. Golubov[1)], B.N. Singh[2)], M. Eldrup[2)], A.M. Ovcharenko[3)], R.E. Stoller[1)],

[1)]Metals and Ceramics Division, Oak Ridge National Laboratory, P.O. Box 2008, Oak Ridge, TN 37831-6376, USA, golubovsi@ornl.gov
[2)]Material Research Department, Risø National Laboratory, DK-4000, Denmark
[3)]Department of Mechanical Engineering, The Hong Kong Polytechnic University, Hong Kong

Abstract

The expected high helium generation rate in metals and alloys under fusion irradiation conditions gives rise to a serious concern regarding the performance and lifetime of materials used in the structural components of a commercial fusion reactor. In order to establish a proper understanding of the effect of helium on the evolution of cavity microstructure under cascade damage conditions, detail numerical calculations based on solution of two-dimensional kinetic equation for size distribution function of helium-vacancy clusters have been carried out for pure iron implanted with helium or irradiated with neutrons. In addition the case neutron irradiation helium implantation has also been studied. A new grouping method [1,2] has been used to integrate the kinetic equation. The evolution of cavity microstructure has been calculated within the framework of production bias model (PBM) [3]. The calculated results are compared with the recent experimental results.

1. Introduction

The concurrent generation of helium and displacement damage may enhance volumetric swelling in the grain interior and may induce grain boundary embrittlement. This is the reason that starting from the middle of sixties effects of He in metals have been modeled by using different approaches. It has been shown (see e.g. [4]) that the He- vacancy cluster evolution under irradiation is driven by several mechanisms responsible for transport of He atoms in crystal, such as interstitial replacement, diffusion of He-divacancy clusters, Brownian motion of the clusters and thermal/radiation resolution of He from the clusters. The basic method to describe the He- vacancy cluster evolution taking into account all the transport mechanisms is the discrete kinetic equation, which in the past has not been explored properly due to computing problems. A new grouping method developed for two-dimensional kinetic equation [1,2] which allows to drastically reduce the number of equations needed to be solved. This method is used in the present work to study He-vacancy cluster evolution in pure iron irradiated with neutrons and high energy helium ions. The case helium implantation followed by neutron irradiation is also studied. The calculations are capable of demonstrative the role of different mechanisms that may be involved in the cluster evolution.

2. Experiments

He implantations were carried out at temperatures below and above the recovery stage V to different concentration levels. Subsequently, both unimplanted and implanted specimens were neutron irradiated at the implantation temperatures to different dose levels. Cavity parameters were determined in the as-implanted as well implanted and neutron irradiated conditions using Positron annihilation spectroscopy (PAS) technique. Whenever possible transmission electron microscopy (TEM) has also used to determine cavity size and density. Fig. 1 illustrates some of the results for He implantation and for neutron irradiation with and without pre-implantation of He at 350°C. For all cases of He implantation and/or neutron irradiation, long-lived components in the positron lifetime spectra provide evidence for the presence of small cavities. The analysis of the life time spectra suggests that the presence of He atoms in the cavities are like to shorten the positron

lifetime. Preliminary estimates of the sizes and densities of the cavities and He density in cavities based on an analysis of the spectra shown in Fig. 1 are quated in Table1.

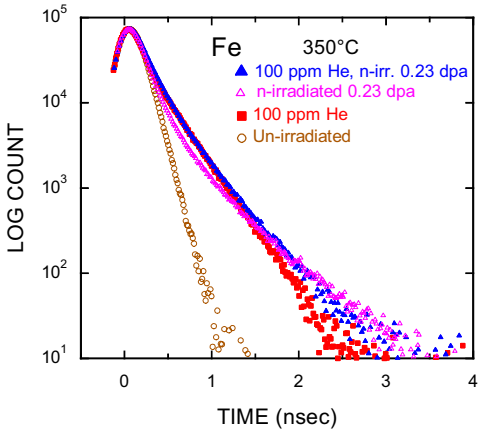

Figure 1. Positron lifetime spectra for iron (○) un-irradiated, after He-implantation (100 ppm He) (■), neutron irradiation (0.23 dpa) (△) and neutron irradiation after He implantation (▲) at 350°C.

Table.1. Cavity parameters determined by PAS .

	Diameter (nm)	Density (10^{21} m^{-3})	He density, $<n_{He}>$, (10^{28} m^{-3})
He-implantation	1.5 – 2.3	30 – 90	6.0
n- irradiation	~3.5*	2	0
He-impl.+n-irr.	4 – 6	2 – 7	3.3

* based on TEM results

3. Calculations

The evolution of cavity microstructure under irradiation has been calculated within the framework of PBM, which takes into account continuous production of clusters of self-interstitial atoms in collision cascades and 1D diffusion of glissile SIA clusters. Cascade parameters such as damage efficiency, ε_r, and the fraction of SIAs stored in mobile clusters, ε_i, are varied in a certain range depending on the average PKA energy. Dislocation bias is taken to be 4%. An example of the calculations is presented in Fig. 2 for the case of He-vacancy cluster evolution during helium implantation at 350°C (ε_r=0.5, ε_i=0.05) together with the experimental data from Table 1. The calculated results are obtained using the replacement mechanism of He transport only. As can be seen from Fig. 2a the calculated results are in a reasonable agreement with experimental observations. Similar calculations for neutron irradiation with and without He implantation have been also carried out and the results agree well with experimental observations. Calculations using deferent mechanisms of He transport are still in progress.

It should be pointed out that detail description of cavity parameters such as He density in the cavities and cavity size distribution is a complicated problem. Effort is in progress to improve determination of these parameters by PAS using the present calculation technique to solve the two-dimensional kinetic equation.

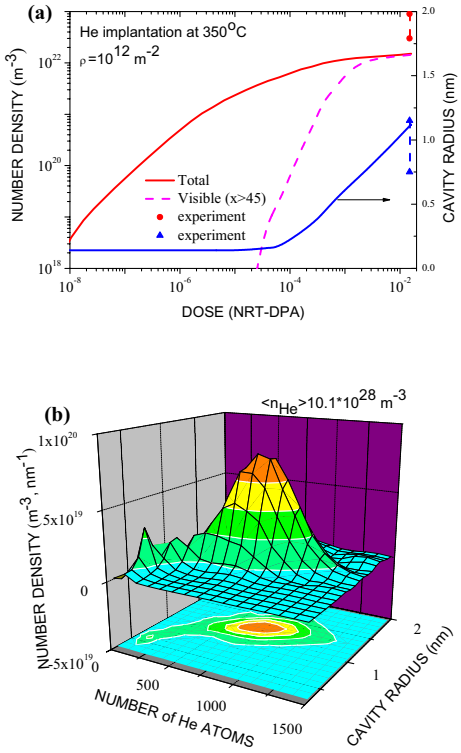

Figure 2. The calculated results for He-vacancy cluster evolution during helium implantation at 350°C: (a) dose dependence of density and average radius of cavities and (b) size distribution function at terminal dose corresponding to the implantation level of 100 appm He.

References

1. S.I. Golubov, R.E. Stoller, S.J. Zinkle, Nucleation and growth of helium-vacancy clusters in irradiated metals. Part. I. A group method for an approximate solution of two dimensional kinetic equations describing evolution of point defect clusters, Fusion Materials Semiannual Progress Report for Period Ending December 31, 2002, DOE/ER-0313/33, US Department of Energy, 155.
2. S.I. Golubov, R.E. Stoller, S.J. Zinkle, Nucleation and growth of helium-vacancy clusters in irradiated metals. Part II. A grouping method for an approximate solution of two dimensional kinetic equations describing evolution of point defect clusters taking into account Brownian motion of the clusters, Fusion Materials Semiannual Progress Report for Period Ending December 31, 2003, DOE/ER-0313/35, US Department of Energy, 214.
3. S.I. Golubov, B.N. Singh, H. Trinkaus, Defect accumulation in FCC and BCC metals and alloys under cascade damage conditions- towards a generalization of the production bias model, J. Nucl. Mater. 276 (2000) 78.
4. H. Trinkaus, B.N. Singh, Helium accumulation in metals during irradiation-where do we stand?, J. Nucl. Mater. 323 (2003) 229.

The Interaction of Helium Atoms with Edge Dislocations in α-Fe

H. L. Heinisch, F. Gao, and R. J. Kurtz

Materials Science Division, Pacific Northwest National Laboratory
P.O. Box 999, Richland WA 99352 USA hl.heinisch@pnl.gov

ABSTRACT

Formation energies, binding energies, and the migration of interstitial He atoms in and near the core of an a/2<111>{110} edge dislocation in α-Fe are determined using molecular dynamics and conjugate gradient relaxation methods. Results are compared as a function of the proximity of the He to the dislocation core and the excess volume around the dislocation. Interstitial He atoms have negative binding energy on the compression side of the dislocation and strong positive binding energy on the tension side. Even at low temperatures, interstitial He atoms in the vicinity of the dislocation easily migrate to the dislocation core, where they form crowdion interstitials with binding energies in excess of 2 eV. The binding is stronger in the vicinity of a jog corner. He-divacancy complexes are more weakly bound to the dislocation.

1. Introduction

An important first step in mitigating helium effects in fusion reactor materials is to understand the fate of helium with respect to the microstructural features with which it can interact. Molecular statics, molecular dynamics and the dimer method of potential surface mapping are being used to study the fate of helium in the vicinity of dislocations in alpha-iron. We report here on results of conjugate gradient relaxation calculations of formation energies of He atoms in interstitial positions about the dislocation, which are used to map the locations of the most stable configurations of the He atom-dislocation interaction. In addition, some molecular dynamics simulations at 100 K have been performed to study the migration of interstitial He atoms within about 1 nm from the dislocation core. The correlation of this information with the spatial distribution of excess volume around the dislocation is also discussed.

2. Procedure

An a/2<111>{110} edge dislocation was created along the axis of a cylindrical cell of body-centered cubic Fe atoms by displacing the atoms according to the elastic displacement field of the dislocation, then relaxing the entire model. He defects were placed within the cell and further relaxation or molecular dynamics (MD) were performed. Interstitial formation energies were calculated for He atoms initially at both octahedral and tetrahedral sites at various locations about the dislocation. He-divacancy

complexes were similarly studied. Relaxation calculations were also performed for an interstitial He atom near the corner of a jog on the dislocation. Molecular dynamics (MD) simulations were performed at a lattice temperature of 100 K for individual interstitial He atoms starting from several different positions about the dislocation for simulated times as long as 8.4 ps. Excess volume associated with interstitial sites in the vicinity of the dislocation was determined using a "Voronoi volume" approach to determine the volumes associated with various interstitial sites, where the volume is centered at the interstitial site.

Figure 1 shows the orientation of the computational cell. Calculations were performed for He atoms placed at crystallographically equivalent interstitial positions along lines normal to the dislocation slip plane.

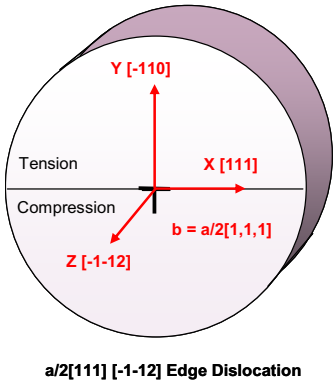

Figure 1. Cylindrical cell for an a/2 [111] [-1-12] dislocation in α-Fe.

3. Results

In these simulations a He atom in an octahedral interstitial position is slightly more stable than in the tetrahedral interstitial position both in the perfect Fe lattice and in the vicinity of the edge dislocation. However, octahedral interstitial He atoms placed within about 2 Burgers vectors of the dislocation core relax into crowdion interstitial sites along the direction of the Burgers vector, [111], resulting in significant displacements of Fe atoms along the close-packed row. The binding energies of interstitial He atoms to the dislocation are shown in Fig. 2, plotted as a function of their initial unrelaxed positions. He atoms near the core relax to crowdion interstitial positions and have binding energies in excess of about 1-2 eV, depending on their location, while the He atoms placed farther from the dislocation core relax to positions near their original octahedral interstitial sites and have significantly smaller binding

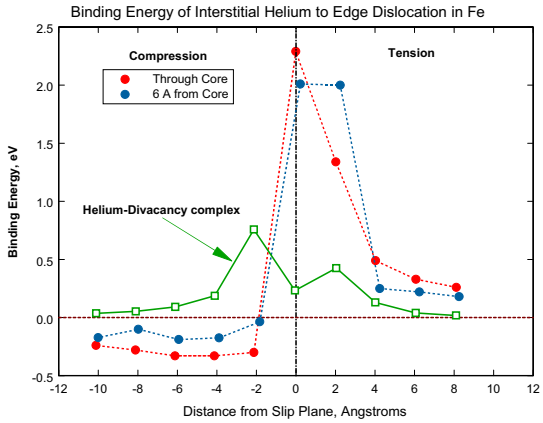

Figure 2. Binding energies of interstitial He atoms at various positions near the edge dislocation. The green points (boxes) are binding energies for He-divacancy complexes.

energies.

MD simulations at a lattice temperature of 100 K were performed for individual interstitial He atoms starting at various distances from the dislocation. In Fig. 3 a composite of their individual trajectories is shown. In these cases, interstitial He atoms beginning well away from the dislocation core migrate to the layer of atoms nearest the slip plane, and become crowdion interstitial defects.

Relaxation calculations have also been performed to determine formation and binding energies of He-divacancy complexes near the dislocation. Figure 2 also contains the binding energies for He-divacancy complexes, which are significantly smaller than for the He interstitials.

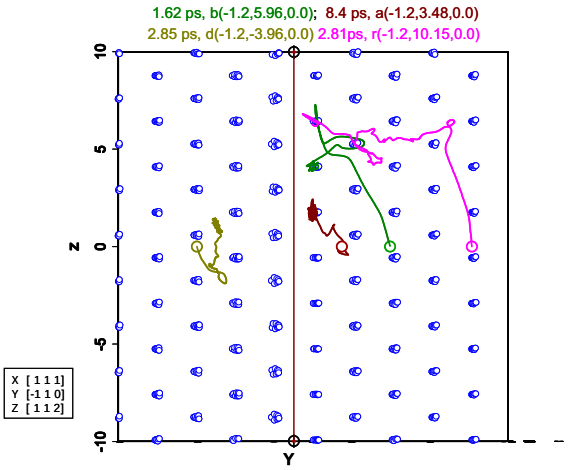

Figure 3. Trajectories of interstitial He atoms in α-Fe migrating at a temperature of 100 K. The figure is a composite of 4 individual migration simulations. The large circles are starting positions of He atoms and the small blue circles are initial positions of Fe atoms. The vertical line lies along the center of the dislocation core.

4. Conclusions

As expected, interstitial He atoms are attracted to the tension side of the dislocation and repelled from the compression side. Within about 2 Burgers vectors of the core on the tension side of the dislocation He atoms relax to crowdion configurations. The formation of stable He crowdions can be correlated with excess volume, but the correlation depends on position relative to the dislocation. These results indicate that interstitial He atoms are either repelled from or trapped at edge dislocations in α-Fe, depending on the direction of approach. He is strongly trapped as a crowdion with 1-2 eV greater binding energy than as an octahedral interstitial. He-divacancy complex defects have much weaker binding to the dislocation than do interstitial He atoms.

5. Acknowledgements

This work was supported by the US Department of Energy, Office of Fusion Energy Science under contract DE-AC06-76RLO 1830.

Basic Aspects of Bias Mechanism under Irradiation in Fe

Eiichi Kuramoto, Kazuhito Ohsawa, Junichi Imai+, Kiyokazu Obata+
and Tetsuo Tsutsumi
Research Institute for Applied Mechanics, Kyushu University
+Interdisciplinary Graduate School of Engineering Sciences, Kyushu University
6 – 1 Kasuga-koen, Kasuga, Fukuoka 816-8580 Japan
kuramoto@riam.kyushu-u.ac.jp

ABSTRACT

Bias effects usually play important roles in the damage structure evolution in materials under irradiadion, and two types of bias mechanisms such as dislocation bias and production bias are widely recognized. Dislocation bias is usually a problem of sink strength, that is, the interaction between an edge dislocation and a self-interstitial atom (SIA) and a vacancy, but here the view from the total energy of a crystal, that is, nucleation and growth problem of defect cluslters is presented, resulting in the same conclusion as the conventional dislocation bias mechanism. In production bias mechanism the one dimensional motion of interstitial clusters, that is, bundles of crowdions plays the most important roles and relation between a bundle of crowdions and a straight edge dislocation is studied on the viewpoint of the change of each crowdion on the periphery of a loop on the path to a straight edge dislocation. Thermally activated motion of dislocation loops is also an important subject to be studied and MD simulations are made for small interstitial loops.

1. Introduction

In materials under irradiation various phenomena such as cascade formation, one dimensional motion of small interstitial clusters, interaction between a dislocation and interstitial clusters, three dimensional motion of radiation induced defects, dislocation bias [1], production bias [2] occur and finally complicated damage structures are formed, resulting in the degradation of materials. In the present paper the fundamental process of bias mechanisms will be studied.

2. Dislocation bias

It is well recognized that the so-called dislocation bias mechanism is the result of the preferential absorption of SIAs prior to vacancies to an edge dislocation line due to the difference in the interaction with the stress field of a dislocation between these two kinds of point defects, resulting in the presence of excess vacancies in a matrix which contributes to the void formation.

The simulation on the interaction between a straight edge dislocation and a SIA or a vacancy placed at various surrounding positions of an edge dislocation was already made for Fe and Ni and much higher interaction (larger capture radius) for a SIA than a

vacancy was obtained, finally giving rise to excess vacancies in a matrix which contribute to void formation, that is, dislocation bias effect. It is well recognized that a larger capture radius comes from a larger relaxation volume of a SIA which gives a stronger interaction with the stress field of an edge dislocation. This is the conventional view for the dislocation bias from the standpoint of sink strength problem, i.e., the interaction between an edge dislocation and radiation-induced point defects.

Extending this viewpoint to the free energy consideration of a whole crystal which contains oversaturated point defects induced by the irradiation, in other word, nucleation and growth problem of defect clusters, the situation can be considered to be similar to the precipitation problem, because SIAs and vacancies left after recombination process form their own clusters, that is, SIA clusters and vacancy clusters.

In order to decrease the total energy of a crystal it is highly desired to form planar defects because crystal periodicity will be recovered by this process and defects involved into planar defects will be brought back to a perfect lattice. SIAs form only planar defects due to its large strain, i.e., dislocation loops. During irradiation both SIAs and vacancies arrive at a periphery of a dislocation loop, but more SIAs are absorpted into a loop than vacancies, resulting in the conventional view of the dislocation bias.

This is again an expected situation even if viewpoint is slightly changed, that is, SIAs arrive at a dislocation loop, but vacancies arrive at a vacancy planar defect extending outside. A dislocation loop can be seen in two ways, that is, an interstitial type dislocation loop or a vacancy type planar defect extending outside of this region. Then the actual situation occurring here is the competition of the formation of a SIA planar cluster and a vacancy planar cluster, in other word, the competition of the precipitate formation of SIAs and that of vacancies to decrease the total energy of a crystal. A driving force of this precipitation mainly comes from the formation energy of these defects in a matrix, and SIAs usually have two or three times larger formation energy than vacancies in metals. This means that the driving force for SIA precipitation is much larger than vacancy precipitation, resulting in the preferential absorption of SIAs prior to vacancies at a dislocation loop. This is a view from the energy consideration and comes to the same conclusion as the conventional dislocation bias mechanism.

3. Production bias

It has been known that the interstitial clusters which can make one dimensional motion and arrive at sinks such as dislocations significantly contribute to the production bias, resulting in the formation of voids in materials under irradiation. This type of interstitial cluster is a bundle of crowdions, i.e., dislocation loop of Burgers vector (a/2)<111> in bcc crystals and (a/2)<110> in fcc crystals. A bundle of crowdions I_n (n = 7,19,37,61,91---) is of a hexagonal shape consisting of six edge dislocation segments all of which lie on {110} slip planes in bcc metals and makes slip motion under the shear stress applied symmetrically on each slip plane. Increasing the size of bundles of crowdions tends dislocation loops finally to a straight edge dislocation [3].

In this process several interesting and important features appear, e.g., 1) each crowdion in a bundle (dislocation loop), especially on the periphery of a loop changes its property as the increase of a loop size, 2) each segment of a hexagonal loop has a character of an edge dislocation and the relationship between a crowdion and the dislocation core structure is unknown, 3) inherent lattice resistance (Peierls stress) to the slip motion of a hexagonal loop must be connected to that for a straight edge dislocation. 4) at finite temperatures motion of dislocation loops are controlled by kink formation or

To make these fundamental features clear will be useful to understand the final production bias mechanism in materials under irradiation. Detailed investigations are made in model Fe lattice and new results are obtained. One of the results is as follows; a single crowdion has two types depending upon the strain distribution on the crowdion axis (type 1 and type 2), but a crowdion on the periphery of a dislocation loop and a straight edge dislocation (in this case on the atomic plane just upon the slip plane) has three types (type1 and type 2+ and type 2-). These three types of crowdions correspond to three types of core structures existing just below the position of the crowdion. On a straight edge dislocation these three types of crowdions make a regular periodic array along a dislocation line and on the forward slip motion of a dislocation line this periodic array is shifted one atomic distance sideway at every b/3 (b is the magnitude of the Burgers vector) step and has a stable configuration of a total edge dislocation line at every b/3 step not b step as shown in Fig. 1. Decreasing the loop size this regular feature gradually becomes irregular because of the end effect of the segment of a hexagonal loop and this causes the gradual increase of the inherent lattice resistance (Peierls stress) to the loop motion. Another problem is the thermally activated motion of small dislocation loops and kink formation on a dislocation loop was studied by MD simulation, but no clear kink was observed in a small loop of 19 crowdions at 100K.

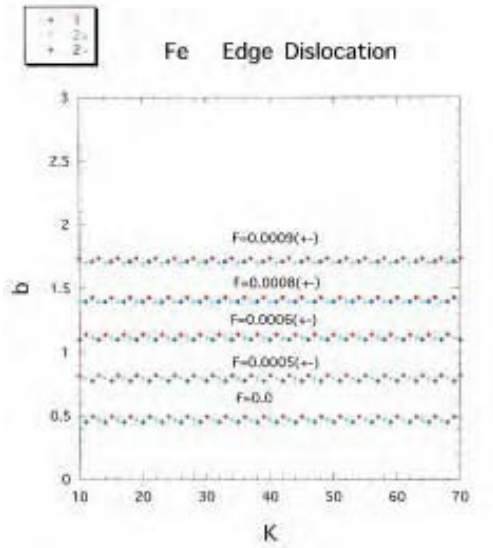

Fig. 1 Stable configuration of an edge dislocation in Fe figured by three types of crowdions

References

[1] R. Bullough, B. L. Eyre and K. Krishan, Proc. Roy. Soc. London A346 (1975) 81-102.
[2] C. H. Woo and B. N. Singh, Phil. Mag. A65 (1992) 889-912.
[3] E. Kuramoto, J. Nucl. Mat. 276 (2000) 143-153.

On The Binding Energies And Configurations Of Vacancy And Copper-Vacancy Clusters In Bcc Iron: A Computational Study

D. Kulikov[1,2,3], L. Malerba[2], M. Hou[1]

[1] Physique des Solides Irradiés et des Nanostructures CP234, Université Libre de Bruxelles, Bd du Triomphe, B-1050 Brussels (Belgium), dmitri.koulikov@ulb.ac.be and mhou@ulb.ac.be
[2] SCK•CEN, Department RMO, Boeretang 200, B-2400 Mol (Belgium), lmalerba@sckcen.be
[3] A.F. Ioffe Physico-Technical Institute of RAS, Polytechnicheskaya Str. 26, 194021 St.Petersburg (Russia)

ABSTRACT

Copper-vacancy clusters (CuVC) in bcc Fe alloys have been studied using a combination of Monte Carlo (MC) and molecular dynamics (MD) techniques, to investigate their lowest energy configurations and corresponding binding energies, for sizes up to ~2 nm diameter, using two different many-body interatomic potentials. Copper atoms, when present, tend to coat an inner vacancy cluster. The binding energy appears to be a monotonously growing function of the ratio between number of vacancies and number of copper atoms. Slight differences in the predictions of the two potentials are found, particularly in the dependence on the number of Cu atoms of the binding energies. A comparison with available ab initio calculations was also performed.

1. Introduction

Copper precipitation under irradiation via formation of CuVC is an important phenomenon related with the embrittlement of reactor pressure vessel steels. Thus, CuVC in bcc Fe-Cu alloys have been studied using a combination of MC and MD techniques to investigate their lowest energy configurations and corresponding binding energies, up to a few hundreds of elements (~2 nm). Two different many-body interatomic potentials were used to perform the calculations, namely Ludwig-Farkas's, LF [1], and Ackland-Bacon's, AB [2]. The objectives of the work were: (1) to provide reliable formulae for the binding energies of V, Cu and Cu-V pairs to CuVC, of immediate use for kinetic MC (kMC) or rate theory (RT) models; (2) to get more insight into the actual atomic-level configurations of these microstructural features, with a view to study how they will appear to specific experimental techniques (e.g. positron annihilation); (3) to compare the performance of the two most widespread interatomic potential for the Fe-Cu system, by contrasting the results also with available ab initio calculations.

2. Computational method

The procedure for the energy calculation consists of three steps:

1) Search for the lowest energy configuration. All the different possible atomic distributions for the selected CuVC (defined by number of Cu atoms, N_{Cu}, and number of vacancies, N_V) on a rigid lattice are sampled using a conventional Metropolis MC algorithm, based on the exchange of atomic co-ordinates and inherently biased to decrease the total energy of the system, evaluated according to an empirical interatomic potential, till the lowest energy configuration is found.
2) Relaxation and determination of the formation energy. The lowest unrelaxed energy configuration from the previous step is inserted into a MD code, where the same interatomic potential is used for force calculation. The system is relaxed and quenched so as to find its energy at 0 K. The following formula expresses the formation energy of CuVC (N_0=number of atomic sites):

$$E_f(N_V+N_{Cu}) = (N_0-N_V)\times E^{NV+NCu\ in\ bcc\ FeCu} - [(N_0-N_{Cu}-N_V)\times E^{bcc\text{-}Fe} + N_{Cu}E^{fcc\text{-}Cu}] \qquad (1)$$

3) Determination of the binding energy of a vacancy, a Cu atom or a Cu-V pair to the complex, as difference of corresponding formation energies; the global binding energy was determined as formation energy divided by number of elements in the complex.

3. Main results

- Analytical formulae to evaluate the binding energy of a vacancy, a Cu atom or a Cu-V pair to a CuVC in kMC or RT models have been obtained. For example,

$$E_b^V(N_V+N_{Cu}) = 1.63 - 1.72[N_V^{1/3}-(N_V+1)^{1/3}] + 2.69[N_V^{2/3}-(N_V+1)^{2/3}] - 0.0004N_{Cu}[N_V^{1/3}-(N_V+1)^{1/3}+N_V^{2/3}-(N_V+1)^{2/3}] \qquad (2)$$

  gives the binding energy of a vacancy to a CuVC.

- Similar formation energy surfaces are obtained with both potentials: the difference remains below 3% for clusters below 100 elements. The main disparity is that, while LF predicts a monotonous increase of the formation energy versus N_{Cu}, AB produces less regular dependences, with constant or even decreasing formation energies versus size. The latter behaviour has been reported also by other authors [3].
- For both potentials the global binding energy of Cu-V clusters is a monotonously growing function of the N_V/N_{Cu} ratio: the addition of vacancies, therefore, always increases the strength of the binding between cluster elements and Cu atoms contribute only very weakly (Fig.1).
- A criterion of maximisation of the number of 1nn and 2nn pairs, consistent with early suggestions by Beeler and Johnson [4], governs the geometry of pure vacancy clusters and the overall binding energy can be obtained as a summation of the contribution of

each 1nn and 2nn pair. A similar criterion seems to hold also for pure Cu precipitates, but limited to 1nn Cu-Cu pairs.

- In mixed complexes, no clear pair number maximisation criterion was observed. Cu atoms tend to distribute so as to separate the vacancies from the Fe matrix. When the N_V/N_{Cu} ratio is small enough, *coated voids*, or *hollow precipitates*, are formed. The inner vacancy core is never concentric with the outer Cu shell and vacancies tend to gather close to the surface. Depending on the potential used, the vacancies may (LF) or may not (AB) be also partially in contact with the Fe matrix (Fig.2). Positron annihilation results from neutron-irradiated Fe-Cu alloys have been interpreted in such a way that the fully coated void should be the most likely configuration [5]. However, in irradiated materials also *partially* coated voids (with high N_V/N_{Cu} ratio) should be expected. Extensive positron response calculations on the configurations obtained in this work should reveal up to what extent positrons are sensitive to small differences in the configuration of Cu-V complexes.
- A comparison with available ab initio results [6] shows that in most of the cases where the comparison is possible, the binding energies found with the two interatomic potentials are in fair agreement with first principle predictions.

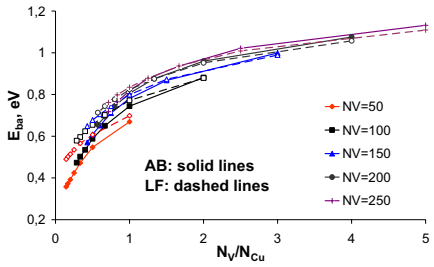

Fig.1 Global CuVC binding energy vs N_V/N_{Cu} ratio.

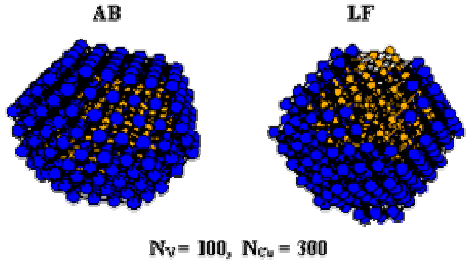

Fig.2 Example of CuVC configuration with the two potentials used.

References

[1] M. Ludwig, D. Farkas, D. Pedraza and S.Schmauder, Modelling Simul. Mater. Sci. Eng. 6 (1998) 19-28.
[2] G.J. Ackland, D.J. Bacon, A.F. Calder and T. Harry, Phil. Mag. A75 (1997) 713-732.
[3] A. Takahashi, N. Soneda, S. Ishino and G. Yagawa, Phys. Rev. B 67 (2003) 024104.
[4] J.R. Beeler and R.A. Johnson, Phys. Rev. 156 (1967) 677.
[5] Y. Nagai, Z. Tang, M. Hasegawa, T. Kanai and M. Saneyasu, Phys. Rev. B **63** (2001) 134110.
[6] C. S. Becquart and C. Domain, Nucl. Instr. Meth. In Phys.Res.B **202** (2003) 44-50.

DUPAIR: a line tension model for a first assessment and interpretation of radiation-induced hardening experiments.

C. Domain[a], L. Malerba[b], G. Monnet[a], K. Verheyen[b], S. Jumel[a] and J.C. van Duysen[a]

[a] EDF – R&D, Les Renardières, Dpt MMC, F-77250 Moret sur Loing, France
christophe.domain@edf.fr, ghiath.monnet@edf.fr, stephanie.jumel@edf.fr, jean-claude.van-duysen@edf.fr
[b] SCK•CEN, Belgian Nuclear Energy Research Centre, Reactor Materials Research Unit, Boeretang 200, B-2400 Mol, Belgium
lmalerba@sckcen.be, kverheye@sckcen.be

ABSTRACT

A line-tension computational model suitable to treat dislocation-defect interaction is presented. The line-tension depends on the dislocation curvature between two defects, characterised by their pinning forces. The suitability of superposition laws to predict yield strength increase due to different defect populations is thereby assessed.

1. Introduction

Dislocation-defect interactions are the link between microstructural features and macroscopic mechanical properties of a material. The problem of realistically describing the interaction of dislocations *between themselves* is currently being solved using computationally intensive dislocation dynamics (DD) methods, where the effect of defects can also be introduced [1, 2]. The interaction between a dislocation and a given type of defect is a complicated phenomenon presently addressed using molecular dynamics (MD) to clarify the interaction mechanisms [3, 4], but limitations (accuracy of the interatomic potential, boundary conditions, simulation box size, ...) still exist. Between sophisticated MD and DD simulations, it seems reasonable to make the best use possible of simple algorithms, such as the scheme proposed, back in 1966, by Foreman and Makin [5]. These can help give an estimate of how the yield strength of a material increases due to the presence of an array of obstacles to the free glide of a dislocation. With their low computational burden, they are useful tools for a first examination of experimental results, with deeper physical insight than the simple Orowan formula ($\Delta\sigma = \alpha G b\sqrt{ND}$).
In this work a model of this type (DUPAIR) is presented, where the line tension depends on the dislocation curvature between two pinned defects and each defect is characterised by its pinning force. The general features are described and the model is applied to support existing engineering analytical approaches for the prediction of yield strength increase versus dose in, e.g., reactor pressure vessel steels.

2. Model description

The 2D quasi-static code DUPAIR, we developed, upgrades the algorithm of [5] by considering defect pinning forces as input parameters and by removing the constant line tension approximation. All kinds of defect distributions, with different types and sizes, can be easily introduced, randomly distributed on a plane array (dislocation

glide plane). An applied shear stress τ causes the segments of the single dislocation line to bow into a sequence of arcs of circles, each delimited by two pinning defects. The applied stress is increased until depinning occurs at some defect. The shape of the dislocation line is then accordingly reconfigured and the process of increasing the shear stress restarted, till the following depinning occurs. Periodic boundary conditions are used. The highest shear stress applied to allow the dislocation to move is taken as yield stress increase due to the array of obstacles.
The equilibrium shape of the dislocation line pinned between two defects is obtained setting the force balance at the pinning point between the two line tensions $\mathbf{T_1}$ and $\mathbf{T_2}$ vectors and the pinning force $\mathbf{F_p}$ (Fig.1). The main breakaway criterion is $|\mathbf{T_1} + \mathbf{T_2}| > |\mathbf{F_p}|$. If the angle θ between the two dislocation branches becomes smaller than a critical value θ_c, the Orowan breakaway mechanism is assumed to intervene [5] and the dislocation line depins independently of the value of line tensions and pinning force. A third breakaway criterion activates whenever the curvature radius of the dislocation line pinned at two defects becomes larger than half the size of the box.

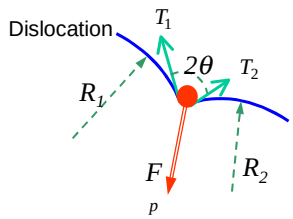

Fig.1: dislocation – defect interactions

The main physical input is the model used for the calculation of the line tension. The following formula is used [6]:

$$T = \frac{\mu b^2}{4\pi} \frac{1+\nu-3\nu\sin^2\alpha}{1-\nu} \ln\frac{R}{r_0} \qquad (1)$$

where μ is the shear modulus, b is the Burgers vector, ν is the Poisson coefficient, α is the angle between Burgers vector and dislocation segment and r_0 is the dislocation core radius. R is a parameter related to the distance between pinning defects. It can be calculated to account for the actual size of the defects, as proposed by Bacon [7]:

$$R = \frac{1}{\frac{1}{\max(r_A, r_B)} + \frac{1}{L - r_A - r_B}} \qquad (2)$$

where r_A and r_B are the radii of the two pinning defects and L the distance between their centres. A single simulation with DUPAIR takes only minutes. Thermal activation effects can be accounted for. The main unavoidable shortcoming is that cross-slip cannot be allowed for.

3. Applications

DUPAIR allows parametric studies of the effect on hardening of different defect populations, defined by different pinning forces, concentrations and sizes, to be

performed fastly and easily. The model provides spontaneously the square root dependence of the yield strength increase on concentration, in accordance with the Orowan formula. The superposition of the effects of two different defect populations on the total yield strength increase has been studied in particular. Two laws are typically used to address analytically this problem: linear summation ($\Delta\sigma_{tot}^{L} = \Delta\sigma_1+\Delta\sigma_2+\ldots$) or quadratic summation ($\Delta\sigma_{tot}^{Q} = \sqrt{\Delta\sigma_1^2+\Delta\sigma_2^2+\ldots}$). Neither is a priori supported by any clear justification. The error relative to the linear or quadratic summation versus ratio between the pinning forces associated to the two defect populations (F_s/F_w) and concentration is presented in Fig.2. The quadratic summation is the most suitable (except for low concentration and large force ratio).

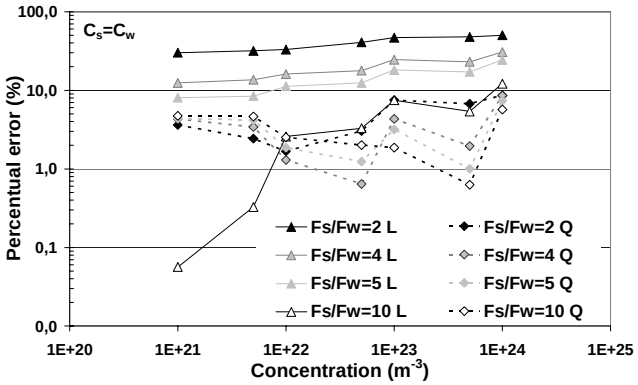

Fig. 2: Quadratic (Q) vs linear (L) summations to assess total shear stress increase vs concentration and F_s/F_w ratio: error committed. W stands for "weak", S for "strong".

4. Conclusion and perspectives

- DUPAIR allows the hardening of any obstacle distribution (knowing their pinning forces) to be evaluated without any specific superposition hypothesis.
- Work is in progress to improve the dislocation arc description, using parameter sets calculated by accurate DD simulations.

References

[1] H.M. Zbib, T. Diaz de la Rubia, M. Rhee, J.P. Hirth, J. Nucl. Mater. 276 (2000) 154; M. Hiritani, H.M. Zbib, J. Nucl. Mater. 323 (2003) 290.
[2] G. Monnet, to be published.
[3] D. Rodney, Acta. Mater. 52 (2004) 607.
[4] Y. N. Osetsky, D.J. Bacon, V. Mohles, Phil. Mag. 83 (2003) 3623.
[5] A.J.E. Foreman and M.J. Makin, Phil. Mag. 13 (1966) 911.
[6] J.P. Hirth, J. Lothe, Theory of dislocations, 1968.
[7] D.J. Bacon, U.F. Kocks, and R.O. Scattergood, Phil. Mag. 28 (1973) 1241.

Defect accumulation and diffusion in Fe using kinetic MonteCarlo

E. Martínez[1], J.M. Perlado[1], M.J. Caturla[2], M Hernández[3], D. Gómez Briceño[3]

[1] Instituto de Fusión Nuclear / E.T.S.I.I./ Universidad Politécnica Madrid (Spain), 2, José Gutierrez Abascal; enrique@denim.upm.es
[2] Departamento de Física Aplicada, Universidad Alicante (Spain),
[3]CIEMAT

ABSTRACT

Diffusion of defects in Fe generated by irradiation has been simulated using kinetic Monte Carlo. The effects of impurity concentration and the thickness of the sample have been studied. In particular we have focused our work in studying the possibility of formation of <100> loops during irradiation through the reaction of <111> mobile loops formed in the cascade, mechanism proposed by J. Marian et al. and based on molecular dynamics simulations. Our calculations show two critical parameters in the formation of these loops: the minimum size of the <111> loops to induce the transformation and the interaction between mobile loops and impurities present in the matrix. Results are compared to experiments of Fe implantation at 150 keV in Fe performed at CIEMAT.

1. Introduction

Despite years of research in the field of radiation effects in metals and alloys there are still several fundamental parameters that are not well understood in a material as important as iron [1]. In particular the interaction of impurities with defects produced by the irradiation, surface effects on defect formation and migration, the interaction between self-interstitials and their reactions and the influence of the sample's thickness among others, are features that are not well known even for ultra high purity α-Fe.

One of the intriguing features of irradiated Fe is the presence of loops with Burgers vector b = <100> together with others with b = ½ <111>, while in other b.c.c. materials all the observed loops are of the second type [2]. Recently Marian and Wirth [3] have proposed a mechanism for the formation of these <100> loops based on molecular dynamics results. This mechanism consists in the reaction of two 1/2<111> loops in order to create a <100> loop. We have included such mechanism into a kinetic Monte Carlo model of defect production, accumulation and diffusion in Fe. The purpose of this work is to study if the <100> loops formed with this mechanism reach those sizes observed experimentally. The results of the simulations were compared to experiments performed at CIEMAT. Samples were observed using TEM and the defects found were characterized in concentration, size and Burgers vector.

Another interesting feature observed experimentally is the dependence on the loop concentration as well as loop distribution, size and type on the thickness of the sample [7]. We will use our kinetic Monte Carlo model to study this dependence.

2. Results

Ultra High Purity (UHP) α-Fe with less than 5 ppm of impurities and pure α-Fe with 75 ppm of impurities were irradiated with 150 keV self ions. The damage produced by the 150 keV Fe in Fe was obtained from a database of cascade simulations in Fe by Stoller [4] and distributed according to calculations with SRIM [5]. The migration energies and binding energies used in the calculation have been reported in earlier works [6]. As mentioned above the BIGMAC code was implemented with the mechanism that makes possible the reaction between ½<111> interstitial clusters to obtain <100> interstitial cluster. This kind of reaction will take place when the sum of the Burgers vectors of the clusters reacting results in a <100> Burgers vector**.** The minimum size of the ½<111> clusters to induce the transformation to <100> loops is not clear and it will be taken as a parameter with minimum size equal 5 self-interstitial clusters and 15 self-interstitial clusters.

Fig 1 shows the effect of the minimum size of <111> loops for the formation of <100> loops for the case of (a) 5 defects on each <111> loop and (b) 15 defects. Clearly when using a minimum size of 15 defects the concentration of <100> loops is much lower than when the minimum size is 5 defects. The impurity content in this case was only 5 ppm, that is UHP-Fe. The total concentration of <100> and <111> loops of any cluster size is included in the figures.

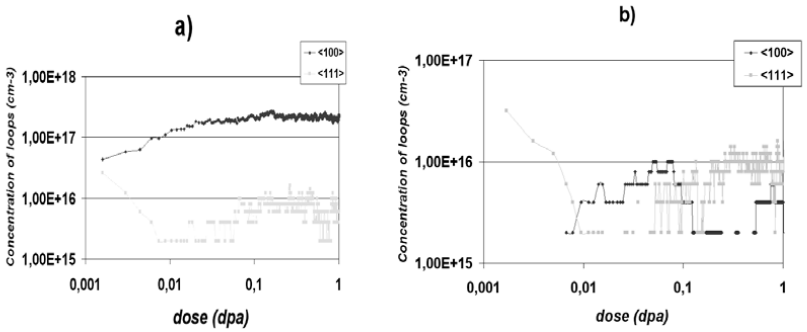

Figure 1. a) Concentration of loops <100> and <111> when the minimum size for transition is 5 defects. b) Concentration of loops <100> and <111> when the minimum size for transition is 15 defects.

As mentioned in the introduction there are many differences observed experimentally regarding defect type, concentration and size depending on the thickness of the irradiated sample. These surface effects are not completely understood. The way in which defects are created on the surface and their features are not well known. For that reason, simulations with 50 nm depth samples and 100 nm depth samples were performed keeping all other parameters of the calculation the same. Fig 2 shows results for the concentration of defects as a function of dose in displacement per atom (dpa) for the same case as in Fig 1 but with double thickness of the sample, in this case 100nm. Clearly, now the number of loops increases.

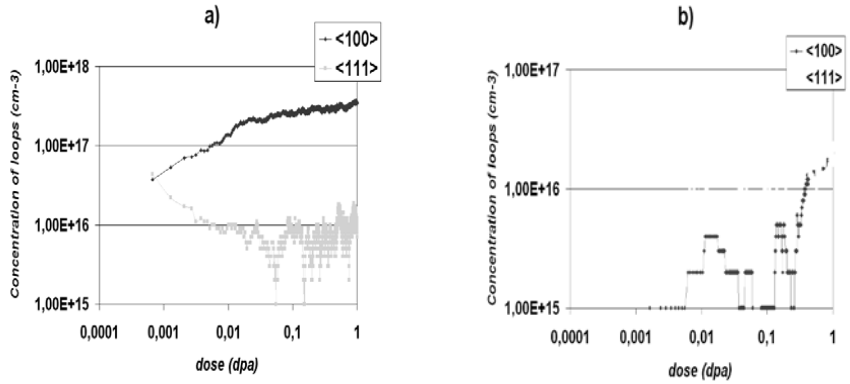

Figure 2. a) Concentration of <100> loops in a 100 nm depth sample when the transition size is 5 defects. b) Concentration of <100> loops in a 100 nm depth sample when the transition size is 15 defects.

3. Conclusions

These calculations show that the formation of <100> loops from interaction between <111> loops is feasible if the minimum size for this reaction is small (lower than 15 defects). However, the concentration of loops as well as the size of the loops obtained from these calculations are different from those measured experimentally. The reason for this discrepancy could be the small sizes of the simulation boxes used or possible surface effects not taken into account in the calculation. Simulations with larger box sizes are currently on the way.

4. Acknowledgements

This work has been performed at DENIM within the REVE Research Project framework under contract P030531762 (CNS/UNESA Coordinated Research Programme). This work has also been developed in the frame of the EURATOM/FUSION Keep in Touch Programme on Inertial Confinement Fusion.

5. References

[1] N.Soneda, S.Ishino et al., J. Nucl. Mater. 323 (2003) 169-180.
[2] A.E.Ward, S.B.Fisher, J. Nucl. Mater. 166 (1989) 227.
[3] J.Marian, B.Wirth, R.Schäublin, G.R.Odette, J.M.Perlado, J.N.M 323 (2003) 181-191.
[4] E.E.Stoller, G.R.Odette, B.D.Wirth. J. Nucl. Mater. 251 (1997) 49
[5] J.F.Ziegler, Stopping and Ranges of Ions in Matter, Pergamon, New York, 1977, vol. 1
[6] M.J.Caturla, N.Soneda, E.Alonso, B.D.Wirth, T.Díaz de la Rubia, J.M.Perlado, J.N.M. 276 (2000) 13-21.
[7] M. Hernandez, D.Gomez, F.J.Perosanz, G.de Diego. Internal Report on Venus-II, October 2003.

Atomistic Modeling of Helium Bubble Formation in Fe during Irradiation

K. Morishita and R. Sugano

Institute of Advanced Energy, Kyoto University
Uji, Kyoto 611-0011, Japan
morishita@iae.kyoto-u.ac.jp

ABSTRACT

Atomistic calculation was performed to evaluate a cavity bias factor (capture efficiency) for a small helium-vacancy cluster in Fe as a function of the number of helium atoms and cluster size. The results were compared with those obtained from continuum theory in the literature, which will provide a deep insight into the multiple lengthscale modeling of reactions between a helium cavity and a migrating point defect.

1. Introduction

The interactions of point defects and their clusters in materials during irradiation are described by multiple lengthscale models ranging from the atomistic to the continuum. When defect size is small and therefore one cannot ignore the fact that materials are composed of the crystal lattices of discretely-distributed atoms, the interaction is described by such atomistic analysis as lattice theory and molecular dynamics simulation. In the case of the other situation, on the other hand, continuum theory can provide a good approximation. Based on understanding of the limitations of models that one employs, establishing a methodology to connect the different scale models is significant for better modeling of the interactions, which leads to better understanding of material's response to irradiation.

In the nuclear fusion reactor environment, high rates of insoluble helium are generated in materials by direct helium implantation and by nuclear (n, α)-reactions during neutron irradiation. High helium concentrations and the formation of helium cavities (bubbles) in materials are known to enhance void swelling and produce surface roughening and high temperature intergranular embrittlement. Cavity growth is not only determined by the thermal stability of the cavity but also by reactions between helium cavities and migrating point defects (interstitial atoms and vacancies). Moreover, the reactions are controlled by the drift motion of migrating point defects caused by internal stress fields from the cavity. An efficiency of the reaction is usually represented by a bias factor (capture efficiency) that is one of the parameters employed frequently by such computational modeling of irradiated materials as a reaction rate theory equation analysis. Evaluation of the bias factor of a spherical helium cavity has successfully been done [1-3] using continuum theory on the assumption that a helium cavity is regarded as a dilatation center. However, when the cavity becomes too small to be regarded as a spherical, the

uncertainty of such evaluation may become innegligible. In the present study, molecular dynamics calculation was performed to evaluate the bias factor of relatively small helium cavities. Comparison is made between our results and those obtained by continuum theory.

2. Procedure

Molecular dynamics (MD) and molecular static (MS) calculations were performed to evaluate displacement fields from helium-vacancy clusters in Fe, which are denoted by He_nV_m, where n is the number of helium atoms in a void of m vacancies. In the present calculations, n and m ranged from 0 to 20 and from 1 to 20, respectively. A calculation method to make a cluster was almost the same as reported previously [7]. Using the displacement fields obtained here, interaction energies were evaluated between a helium-vacancy cluster and the point defect of stable and saddle point configurations at various positions from the cluster. Subsequently, by considering the existing probabilities of the point defect around the cluster during steady state diffusion, the radial distribution of the interaction energies was obtained as a function of separation distance from the cluster. Finally, a cavity bias factor was evaluated as a function of n and m, following the Wolfer's evaluation of a void bias factor [1]:

$$Z = \left[\int_0^a d\left(\frac{a}{r}\right) \exp\left(E_s(r)/kT\right) \right]^{-1}, \qquad (1)$$

where r is separation distance between a helium-vacancy cluster and a point defect, E_s is interaction energy for the saddle point configuration of the point defect, kT has a usual meaning, and a is a spontaneous capture radius. The evaluation method of the bias factor will be published in detail elsewhere [8].

3. Results & Discussion

Fig. 1 is a plot of the dependence of a cavity bias factor for self-interstitial atoms (SIAs) on the number of helium atoms, n, as a function of the number of vacancies in a helium-vacancy cluster, m. The figure roughly indicates that the cavity bias factor shows a first slight decrease, followed by a great increase with increasing n. It approximately takes the minimum value when $n/m \approx 1$, for a given cluster size, m. Since cavity equilibrium pressure, $p_{eq}=2\gamma/R$, corresponds to $n/m \approx 1$ for the size ranges investigated here, where γ is surface energy and R is a cavity radius, it qualitatively agrees with the cavity bias factor evaluated by continuum theory [1-3].

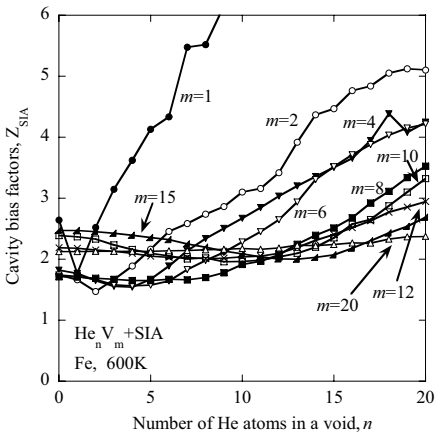

Fig. 1 Cavity bias factors for SIAs at 600K

Fig. 2 shows the dependence of a cavity bias factor for SIAs on a cavity radius, R, in units of interatomic spacing, b. The cavity bias factors provided by continuum theory [1, 2] are also indicated in the figure for comparison. It is noted in this figure that our bias factor was modified to be comparable with those evaluated by continuum theory, because, within the continuum theory evaluation, a cavity radius is usually given by the number of vacancies with the following relationship;

$$m\Omega = 4\pi R^3/3, \qquad (2)$$

where Ω is atomic volume, and additionally a of eq. (1) usually employs R of eq. (2). In this modification, our bias factor was recalculated so as not to change a capture radius, R_c. As shown in the figure, our present results indicate that the bias factor decreases with increasing the cavity radius, which is also qualitatively consistent with those evaluated by continuum theory. However, they are quantitatively different. The quantitative difference of those obtained by continuum theory from our results may be caused by the fact that the helium-vacancy cluster of such small size investigated here is no longer regarded as a spherical cavity, and therefore, continuum theory cannot be applicable in this size range.

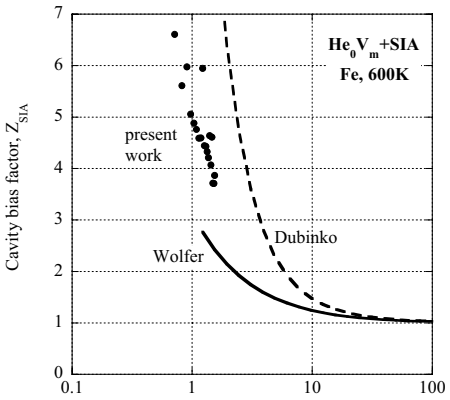

Fig. 2 Comparison between our bias factors for SIAs in Fe at 600K and those evaluated by continuum theory.

Acknowledgements

One of the authors (KM) wishes to express his thanks to Drs. W. G. Wolfer, T. Okita and A. Kubota for fruitful discussion during his visit to LLNL.

References

[1] W.G. Wolfer, in Proc. of Int. Conf. on Fundamental Aspects of Radiation Damage in Metals, (Ed. by M.T. Robinson and F.W. Young, Jr.), Gatlinburg, US ERDA Conf. 751006-P2, p. 812 (1975).
[2] V.I. Dubinko, J. Nucl. Mater. **206**, 1, (1993).
[3] V.A. Borodin, A.I. Ryazanov, C. Abromeit, J. Nucl. Mater. **207**, 242 (1993).
[4] G.J. Ackland, D.J. Bacon, A.F. Calder, T. Harry, Philos. Mag., A **75**, 713 (1997).
[5] W.D. Wilson, R.D. Johnson, in Interatomic potentials and simulation of lattice defects, (Ed. by P.C. Gehlen, J.R. Beeler, Jr., and R.I. Jaffee), Plenum p. 375 (1972).
[6] D.E. Beck, Mol. Phys., **14**, 311 (1968); J.P. Biersack and J.F. Ziegler, Nucl. Instrum. Meth., 194, **93** (1982).
[7] K. Morishita, R. Sugano, B.D. Wirth, J. Nucl. Mater. **323**, 243 (2003).
[8] K. Morishita *et al*., in preparation.

Molecular dynamics simulations of the formation of oxygen vacancies in SiO_2 by atomic collisions

F.Mota[1)], M.-J.Caturla[2,3)], J.M.Perlado[1)], E.Dominguez[1)] , A. Kubota[3)]

1 Instituto de Fusión Nuclear, Universidad Politécnica(ETSII), Madrid, Spain (mota@denim.upm.es)
2 Universidad de Alicante, Dep. Física Aplicada, Alicante, Spain
3 Lawrence Livermore National Laboratory, Livermore, CA, USA.

ABSTRACT

The interest of neutron radiation effects upon vitreous silica has increased recently due to its possible application as optical transmission component in fusion reactors. This radiation can change not only its mechanical properties but also its optical properties through the creation of color centers. Identifying and understanding the type of defects created during irradiation is a complicated experimental task that could benefit from some insight obtained from atomistic simulations. In this paper we present molecular dynamic simulations of defect production in amorphous silica glass. In particular we study the minimum energy required to generate a stable oxygen vacancy by atomic collisions. Different ranges of Primary Knock-on Atom (PKA) energy have been found depending on the initial displaced atom being silicon or oxygen. We show that oxygen recoil is able to easily generate stable oxygen vacancies while silicon recoil requires much higher energies to produce stable oxygen vacancies.

1. Introduction

Fused silica is a candidate material for optical and radio-frequency diagnostics systems in magnetic confinement fusion reactors [1] and as final optics in inertial confinement fusion reactors [2]. In both cases this material will be exposed to high energy neutron (14 MeV) and gamma irradiation. Radiation induces optical absorption, creating point defects that can act as color centers [3]. One of the defects observed experimentally after neutron irradiation is the oxygen deficient center (ODC) [5] and its conversion to E' centers after gamma irradiation [3]. However, a process of diffusion and recovery of the damage of the irradiated sample is also observed after high temperature annealing (>350 ºC) [3].

In this work we will study the production of point defects due to atomic displacements, such as those produced by neutron irradiation. We will center the study in one particular defect, the oxygen vacancy, since this is the most important defect observed in fused silica under neutron irradiation. This defect has been identified experimentally as a color center in the 248 nm wavelength (ODC), which appears under neutron irradiation and makes the material opaque [1, 2] and under gamma irradiation this defects is converted in almost totally in E' centers with a 214 nm wavelength [3]. We present calculations of the minimum energy to produce stable 3-fold and 2-fold coordinated silicon that is an oxygen vacancy or ODC that, as mentioned above, can be observed experimentally. We present results for the case

when the initially displaced atom is an oxygen (see also [4]) as well as for the case of a silicon atom being initially displaced.

2. Simulation modeling

We use molecular dynamics simulations to study the defects produced in fused silica. Fused silica is an amorphous system, formed by silicon atoms tetrahedrally bonded to oxygen atoms. The interatomic potential used for our calculations is the one developed by Feuston and Garofalini [5], potential that was fitted to reproduce the structure factor of this amorphous system as obtained experimentally through neutron diffraction. In order to generate the amorphous system of the fused silica, we start with a crystal lattice of beta-cristobalite for SiO_2 and this structure is melted and quenched through a series of steps until a final temperature of 300 K is achieved.

Once the initial amorphous structure is constructed, we performed calculations of those defects produced by energetic atoms. Periodic boundary conditions are used with a bath control to keep the final temperature at 300 K through scaling of velocities of those atoms close to the border of the simulation box. The energetic atom, either silicon or oxygen, is chose from the center of the simulation box.

3. Results

We have analyzed a rage of energies studying in detail the spectrum of energy between 13 to 70 eV for oxygen(extending our earlier result [4]) and between 40 to 700 eV for silicon. Identification of defects in an amorphous system is quite complex and unlike in perfect crystals is not unique, therefore, a definition of point defect must be described. For each atom in our lattice, we determine its coordination, considering a cut-off between first and second nearest neighbors distance of 2.35 Å to account for vibrations due to the finite temperature of the simulations (1,6 Å is the bond length in silica glass [5,6] indicated by the first peak in the calculated pair correlation function). We have focused on the identification of 3-fold and 2-fold coordinated Si atoms. An attempt to identify oxygen with coordination one, related to the defect called Non-Bridging Oxygen Hole Center (HBOHC) has been made. Some experimental observations point to a ratio of 0.8 between the number of ODCs and NBOHC produced after irradiation [3].

The production of a defect in an amorphous material will depend on the location of the energetic atom chosen, since not all positions are equivalent. Therefore the calculations have been repeated for a large number of cases, at least 24 for each energy, changing both the incidence direction and the initial atom. Figure 1 shows the results of the percentage of cases producing an oxygen vacancy as a function of the initial energy of the atom, in grey colour when the energetic atom is an oxygen and in black colour when the energetic atom is a silicon. The simulation is followed for a total time of 2 ps, using a time step of 0.1 fs.

Clearly the probability of creating a stable ODC increases with the initial energy of the recoil for both Si and O atoms. The probability of creating a stable oxygen vacancy when the initial energetic atom is an oxygen is, as expected much higher than for the case when the initial energetic atom is a Si, but interestingly, the efficiency of production of such a defect in the second case is quite low, and it never reaches 100%, increasing very slowly with energy with an efficiency of only 58% for the highest energy studied here, 700 eV.

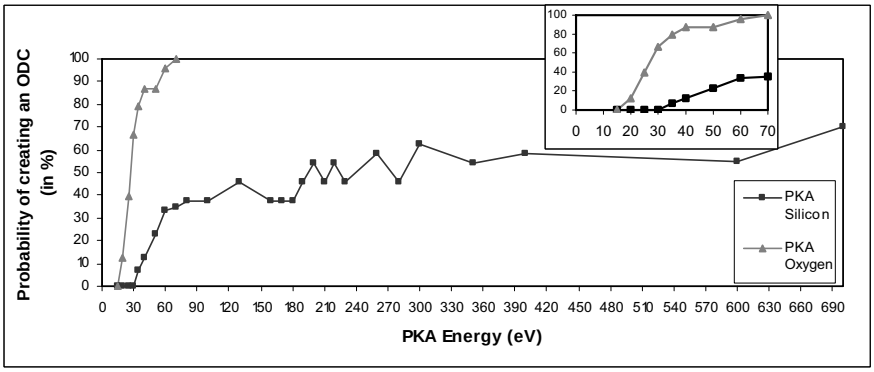

Figure 1.- Probability (%) of creating stable ODC as a function of energy (eV) when the energetic atom is an oxygen (gray line) or a silicon (black line).

4. Conclusions

Our initial calculations of the minimum energy to produce a stable oxygen vacancy in fused silica show that the probability to produce such defect when the initially displace atom is silicon is very low. For energies up to 600eV only a 50 % probability of forming such a defect is obtained from our calculations. Higher energies, up to 5 keV are being studied, as well as the identification of the types of defects formed that are not oxygen vacancies and their implications to he optical performance of this of this material.

4. Acknowledgments

This work has been performed under partial funding of Spanish national Project FNT2001-3886-C02-01 and European Union keep in touch Program on Inertial confinement Fusion, and IAEACRP on element of power plants design for Inertial Fusion Energy.

5. Reference

[1] E. R. Hogdson, "Challenges for insulating materials in fusion applications", Nucl. Instrum. & Methods B 191 (2002) 744

[2] Jeffery F. Latkowski,* Alison Kubota, Maria J. Caturla, Sham N. Dixit, Joel A. Speth, And Stephen A. Payne, "Fused Silica Final Optics For Inertial Fusion Energy: Radiation Studies and System-Level Analysis, Fusion Science and Technology", V43 N4 (2003) 540-558

[3] C. D. Marshall, J. A. Speth, S. A. Payne, "Induced optical absortion in gamma, neutron and ultaviolet irradiated fused quartz and silica", J. Non-Crist. Solids **212**, 59 (1997)

[4] F.Mota, M.-J.Caturla, J.M.Perlado, E. Dominguez, A. Kubota, "Atomistic simulations of threshold displacement energies in SiO_2", J. Nucl. Mater. 329-333 (2004) 1190-1193

[5] B.P.Feuston,S.H.Garofalini,"Empirical three-body potential for vitreous silica", J. Chem. Phy., Vol.89,No.9.1 1988

[6]P.Vashista,Rajiv K.Kalia, José P. Rino,"Interaction potential for SiO_2: A molecular-dynamics study of structural correlations", Phys. Rev. B V41 N17 (1990) 12197

Tight-Binding Models for Fusion Reactor Materials Based on Non-Magnetic and Magnetic BCC Transition Metals

D. Nguyen-Manh[1], S.L. Dudarev[1], D.G. Pettifor[2], R Gröger[3] and V. Vitek[3]

[1] UKAEA Culham Division, Culham Science Centre, Abingdon, OX14 3BD, UK,
duc.nguyen@ukaea.org.uk, sergei.dudarev@ukaea.org.uk
[2] University of Oxford, Department of Materials, Oxford, OX1 3PH, UK,
david.pettifor@materials.ox.ac.uk
[3] University of Pennsylvania, Department of Materials Science and Engineering, Philadelphia, PA 19014-6267, USA
groger@seas.upenn.edu, vitek@seas.upenn.edu

ABSTRACT

Body-centred cubic (BCC) transition metal based alloys are the prime candidate materials for structural components of future fusion power plants. The development of reliable hierarchy of models describing materials under neutron irradiation is an significant issue for the international fusion programme. We formulate a generic model bridging density functional theory and the real-space tight-binding description of interatomic interaction that enables construction of many-body angularly dependent potentials for atomistic simulation as well as incorporation of magnetic effects via the Stoner model. Application to point defects and dislocation core structure is presented.

1. Introduction

BCC transition metals (TM) and their alloys including a wide range of ferritic/martensitic steels are prime candidates for future power fusion plants. At the same time, experimental data on mechanical properties and effects of irradiation in these materials are very limited. Multi-scale modelling offers the opportunity to interpret such incomplete data with a broader outlook and utilise this understanding in the selection of materials that will form the first wall of fusion power plants. The precursor of simulations involved in multiscale modelling is reliable interatomic potentials. The embedded atom method or Finnis-Sinclair potentials are not adequate since they include electronic structure only indirectly and comprise neither the covalent character of d-bonds that determine the stability of non-magnetic BCC TM, nor the magnetic effect that control the structure of BCC iron based materials. To overcome these deficiencies we propose to bridge the gap between electronic and atomistic modelling using a tight-binding (TB) approach combined with density functional theory (DFT) studies when developing interatomic potentials. In this paper we first present such DFT study of point defects, then demonstrate application of TB based bond-order potentials (BOPs) to the study of dislocation in BCC TM, and finally suggest the development of interatomic potentials for ferromagnetic materials using the Stoner model.

2. Efficient Ab-initio Tight-Binding Calculations of Point Defects

The ab-inito calculations were performed using an efficient DFT package of linear

combination of atomic type orbitals (PLATO) [1]. It has been used to produce a theoretical database of defect properties for both non-magnetic and magnetic bcc TM within local density and generalised gradient approximations. Explicit inclusion of semi-core electrons into the relativistic Gaussian pseudo-potentials has been utilised in our calculations. The relative stabilities of six configurations of self-interstitial atoms (SIAs) for V, Mo and W are given in Table 1. We found that the crowdion

Table 1. Relative SIAs formation energy differences predicted by the PLATO calculations

(in eV)	<111>-crowdion	<111>-dumbbell	<110>-dumbbell	tetrahedral	<100>-dumbbell	octahedral
V	0.00	0.00	0.31	0.48	0.54	0.58
Mo	0.00	0.00	0.18	0.98	1.59	1.64
W	0.00	0.00	0.29	1.46	2.11	2.20

is the most stable in agreement with a recent DFT calculations for V and Mo using plane wave basis set [2]. Our calculations suggest that in non-magnetic BCC TM, SIAs have a systematic stability trend from <111> to <110> to tetrahedral to <100> and finally to the octahedral configuration. The electron charge density plots (Fig.1)

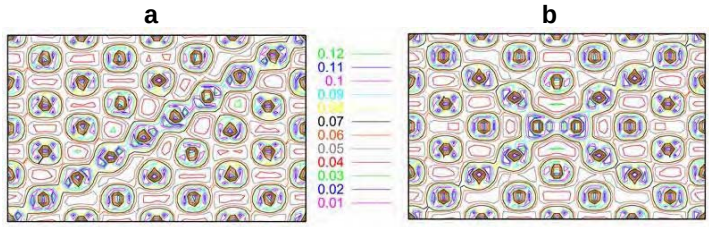

Figure 1. Electron charge density (in $(a.u.)^3$) on (110) plane for crowdion (a) and <110> dumbbell (b) SIAs configurations for bcc-W.

show a striking contrast between the crowdion and the <110> dumbbell configurations: the former has a strong one-dimensional character being extended along the <111> direction while the latter appears to be rather localised defect.

3. BOPs for BCC-TM: Application to Dislocations

Recently, the BOPs for BCC-TM have been successfully constructed taking into account the environmental dependence of bond integrals due to non-orthogonalility of TB orbitals [3,4]. The calculated γ surface for {110} planes and the core structure of ½<111> screw dislocation in BCC-Mo agree excellently with those found in ab-initio calculation (Fig.2a). The glide behaviour using the BOPs not only agrees with available DFT data but also with many experimental observations and explains some of the reasons for the breakdown of the Schmid law in BCC TM. Figs. 2b and 2c show the effect of non-glide shear stress component τ_2 acting in the direction perpendicular to the Burgers vector. For negative τ_2 (compression in uniaxial tests), the core structure shrinks in the $(\bar{1}01)$ plane (2b) and extends into the $(0\bar{1}1)$ and $(\bar{1}10)$ planes while the opposite occurs for positive τ_2 (tension). Since the glide takes along the $(\bar{1}01)$ plane, it is more difficult in the former and easier in the latter case.

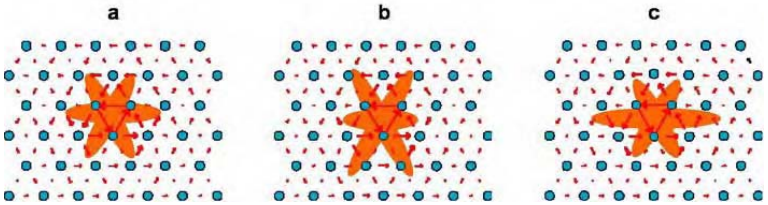

Figure 2. Motion of the ½<111> screw dislocation in BCC-Mo under applied shear stress τ_2, perpendicular to the Burgers vector: a) no applied stress; b) τ_2/C_{44}=-0.04; c) τ_2/C_{44}=+0.04.

4. Tight-Binding Bond Formalism for Magnetic BCC-TM within Stoner Model

Within the tight-binding bond model formalism, the cohesive energy can be written as

$$U = \sum_{\sigma} \sum_{i\alpha \neq j\beta} \rho^{\sigma}_{j\beta,i\alpha} H^{\sigma}_{i\alpha,j\beta} - U^{dc}_{exchange} + U_{rep} + (\sum_{\sigma} \sum_{i\alpha} \rho^{\sigma}_{i\alpha,i\alpha} H^{\sigma}_{i\alpha,i\alpha} - U_{atom}) \qquad (1)$$

when the spin-polarisation is taken into account. With the on-site energy given by $H^{\sigma}_{i\alpha,i\alpha} = E_{i\alpha} \mp I_{\alpha} m_{i\alpha}$, eqn. (1) can be rewritten as

$$U^{spin} = \sum_{\sigma} \sum_{i\alpha \neq j\beta} \rho^{\sigma}_{j\beta,i\alpha} H_{i\alpha,j\beta} - \frac{1}{4} \sum_{i} I_d (m_i^2 - m^2_{free-atom}) + U^{LCN}_{prom} + U_{rep} \qquad (2).$$

The Hellmann-Feynman theorem allow us to evaluate forces on the atom k as

$$-F^{spin}_k = \frac{\partial U^{spin}}{\partial r_k} = \sum_{\sigma} \sum_{i\alpha \neq j\beta} \rho^{\sigma}_{j\beta,i\alpha} \frac{\partial H_{i\alpha,j\beta}}{\partial r_k} + \frac{1}{2} \sum_{i \neq j} \frac{\partial \Phi_{rep}(r_{ij})}{\partial r_k} \qquad (3)$$

where $\Phi_{rep}(r_{ij})$ is the pair-wise repulsive potential and $r_{ij} = | r_i - r_j |$. Eqns. (1-3) have been recently used to study both structural stabilities and point defects in magnetic iron. Preliminary results show that the <110> dumbbell is indeed predicted to be the most stable magnetic configuration and the SIAs formation energy increases from <110> to <111> to <100> is found in good agreement with the DFT calculations [5].

This work was funded by the UK EPSRC and by EURATOM (DNM, SLD) and in part by the NSF Grant no. DMR02-19243 (RG, VV)

References

[1] D. Nguyen-Manh, et.al., *Electronic structure, bonding and magnetic properties of transition metals in carbon nanotubes* , Bull. Am. Phys. Soc., Vol. 48, 187, (2003).
[2] S. Han, et.al., *Self-interstitials in V and Mo*, Phys. Rev. B, vol. 66, 220101,(2002).
[3] D. Nguyen-Manh, et.al., *Analytic environment-dependent tight-binding bond integrals: Application to $MoSi_2$*, Phys. Rev. Lett., vol. 85, 4136, (2000).
[4] M. Mrovec, et.al., *Bond-order potentials for molybdenum: Application to dislocation behaviour*, Phys. Rev. B, vol. 69, 094155, (2004).
[5] C. Domain and C.S. Becquart, *Ab-initio calculations of defects in Fe and dilute Fe-Cu alloys*, Phys. Rev. B, vol. 65, 024103 (2002).

Edge Dislocation – Copper Precipitate Interaction Process in BCC Iron

A.Nomoto[a] , N.Soneda[a], A.Takahashi[b] and S.Ishino[a,c]

[a] Central Research Institute of Electric Power Industry, 2-11-1 Iwado-kita, Komae, Tokyo 201-8511, Japan, E-mail a-nomoto@criepi.denken.or.jp
[b] Department of Mechanical Engineering, Tokyo University of Science, 2641 Yamasaki, Noda, Chiba 278-8510, Japan, E-mail takahash@me.noda.tus.ac.jp
[c] Department of Applied Science, Tokai University, 1117, Kitakaname, Hiratsuka-shi, Kanagawa 259-1292, Japan, E-mail koishino@criepi.denken.or.jp

ABSTRACT

The interaction process between an edge dislocation and a coherent copper precipitate in BCC iron is studied using molecular dynamics (MD). A model bcc iron containing one edge dislocation and one copper precipitate, whose diameter ranges from 1nm to 5nm and copper concentration ranges from 50 at.% to 100 at.%, is deformed at a constant shear stress, so that the edge dislocation runs over the copper precipitate located on the slip plane of the edge dislocation. Small pure copper precipitates with 1~2nm diameters are simply cut by the edge dislocation and are weak obstacles to the dislocation motion. On the other hand, large pure copper precipitates with 3~5nm diameters transform from bcc to fcc like structures as interacting with the dislocation, resulting in strong obstacles to the dislocation motion. This structure transformation does not occur if the half of the copper atoms of the precipitate are randomly replaced by iron atoms (50% copper precipitate), and such 50% copper precipitates are not strong obstacles any more.

1. Introduction

In irradiated bcc Fe-Cu alloys, irradiation induced microstructure such as coherent copper precipitates are known to causes hardening of the materials. Osetsky et al. reported their MD simulations showing that copper precipitates inhibit dislocation motion and the crystal structure of precipitates transform from bcc to fcc during the interaction[1]. In this study, we show MD simulation results on the interaction between a copper precipitate and an edge dislocation with specific interests on the effect of precipitate size on their

interaction mechanisms as well as the effect of copper concentration in the precipitates. The latter concern arises from the 3D atom probe observations where the copper precipitates are not necessarily pure copper precipitates, rather copper enriched clusters especially when they are formed by irradiation.

2. Calculation Methods

A model bcc iron crystal was constructed so that crystallographic orientation of <1-11>, <110> and <-2-11> corresponding to x, y and z directions, respectively, where extra-half plane is located on in the y-z plane, and the x-y plane is the slip plane, (110), of the dislocation. The center of the dislocation is located in slip plane. Constant shear stress is applied on the top and bottom of x-y planes. The motion of the atoms is simulated by molecular dynamics assuming the inter atomic potential developed by Ackland et al. Precipitate diameter is ranged from 1nm to 5nm to look at the change of interaction mechanisms. 50% copper precipitate with diameter of 5nm is also investigated. The calculation box size is 50x36x56nm and the temperature of the crystal was set to 300K.

3. Results and Discussions

Conventionally, cosine of the critical angle, θ_c, of the bowing dislocation line is need as a measure of the obstacle strength. However it is very difficult to obtain a unique value of the angle from MD results. In this study, we define a critical bowing distance, Lc, instead of θc. Fig.1 shows Lc dependence on the precipitate diameter. Lc increases with size, but it is clearly shown that there is a threshold diameter, ~2.5nm, beyond which the obstacle strength increase drastically. This mode change is well described by the change of the interaction

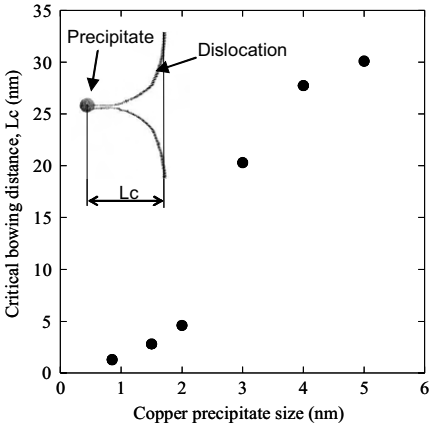

Fig.1 Critical dislocation shape in slip plan (100 at.% copper)

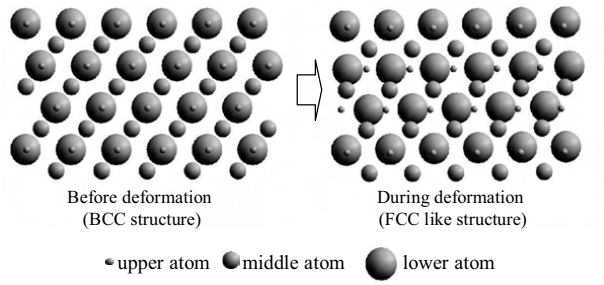

Fig.2 Atomic arrangement of (011) in the copper precipitate

mechanism. The interaction between the edge dislocation and the copper precipitate is a simple shear when the precipitate size is smaller than the threshold diameter. The precipitates always have coherent bcc structure before, during and after the interaction. On the other hand, when the precipitate size is beyond the threshold size, the crystal structure of the precipitate transforms from bcc to fcc-like structure as shown in Fig.2 once the dislocation contacts the precipitate. This transformation occurs on the limited atoms within the volume including slip plane. The precipitate is no more coherent, thus can be a strong obstacle to dislocation motion. The fcc-like structure can recover back to the original bcc structure after the cut by the dislocation. However if the precipitate size is sufficiently large, the fcc-like structure remains in the precipitate even after the completion of the interaction. In such cases, we observed that the straight parallel dislocation lines ahead of the precipitate, whose character is pure screw, glide on different slip planes to meat to annihilate. A super jog is formed in the dislocation line as a result of this interaction. Fig.3 shows the critical dislocation line shape interacting with the precipitate containing 50 at.% and 100 at.% copper. Dislocation bow-out of the precipitate containing 50 at.% copper is obviously smaller than that containing 100 at.% copper. No structure transformation in observed in the 50% precipitate.

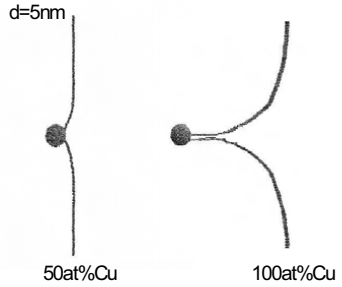

Fig.3 Critical dislocation shape in slip plan (d=5nm)

Activation Energy for One-Dimensional Slip Motion of a Dislocation Loop

Kazuhito Ohsawa and Eiichi Kuramoto

Research Institute for Applied Mechanics, Kyushu University,
Kasuga-Koen 6-1 , Kasuga-shi, Fukuoka 816-8580, Japan
ohsawa@riam.kyushu-u.ac.jp

ABSTRACT

We report activation energies and saddle point configurations of dislocation loops for thermally activated transport in terms of a line model. Peierls potential, resistance for the dislocations, is a double sine-Gordon type in the present model. Plural saddle point configurations exist in general and a new bifurcation branch is found for a somewhat flattened Peierls potential. However, the lowest energy configuration is realized among them in the thermal activation. The activation processes qualitatively change depending on the length of the dislocation loop and Peierls potential. For example, if the dislocation loops are longer than a critical length, the saddle point configurations are a conventional double-kink type. While, if the loops are shorter than the critical length, a non-deformation type is realized.

1. Introduction

Prismatic dislocation loops are observed in materials irradiated with high-energy particles. In particular, perfect dislocation loops with $a/2\langle 111\rangle$ Burgers vector in BCC metals are regarded as a bundle of crowdions accumulated on a habit plane. Therefore, the dislocation loops are expected to have quite high mobility and play an important role in formation of radiation damage. The thermal activation and mobility of defects in crystals have been investigated by various methods. In molecular dynamics simulations, the dislocation loops are treated as peripheries of self interstitial atom clusters and the motion of each atom is simulated using appropriate interatomic potentials [1, 2]. The activation energies are numerically estimated from Arrhenius plots for the jump frequency of the clusters. On the other hand, a static method has been used as well [3]; the activation energies are estimated from the saddle point configurations. In fact, the activation (kink-pair formation) energies of straight dislocations are analytically evaluated by this method [4, 5]. We also analytically estimate the activation energies and saddle point configurations of dislocation loops in terms of a line tension model where the dislocations are assumed to be a flexible string. Though this model is, of course, a drastic simplification for prismatic dislocation loops in actual metals, it is available for qualitative analysis. In fact, we obtain new properties which straight dislocations do not have. The Peierls potential in the present model is a double sine-Gordon type; the shape is adjustable in some degree with one parameter. If the Peierls potential is somewhat flattened, even if it is not camel-hump, a new bifurcation appears as the saddle point configuration.

2. Line Tension Model

We assume that a dislocation loop surrounds a circular cylinder as shown in Fig. 1. The Peierls potential $V(z)$ takes minimum at $z = \pm b/2$ and maximum at $z = 0$, where b is Burgers vector. Therefore, the dislocation is located at $z = \pm b/2$ in stable condition. A schematic saddle point configuration is represented on a flattened lateral surface of the cylinder as shown in Fig. 2. At first, we suppose the saddle point configuration is a double-kink type. The parameter z_0, bow-out of the dislocation line, is specially introduced for analysis. The total energy E_t is

$$E_t = \int_{-L/2}^{L/2} \left\{ \frac{1}{2}\gamma_0 \left(\frac{dz}{dr} \right)^2 + V(z) \right\} dr, \tag{1}$$

where γ_0 is energy per unit length of the dislocation and L is the length of the dislocation loop. The equilibrium condition of the dislocation line is

$$\gamma_0 \frac{d^2 z}{dr^2} = \frac{dV}{dz}. \tag{2}$$

One easily obtains a trivial solution $z \equiv 0$ for the saddle point configuration. Then, we look for nontrivial solutions of the double-kink type likely shown in Fig. 2. By integration of Eq. (2), we obtain exact representation of the nontrivial solution. The length of the dislocation loop L and activation energy E_a are expressed, as follows, where $C_0 = V(z_0)$.

$$L = 2\sqrt{2\gamma_0} \int_0^{z_0} \frac{1}{\sqrt{V(z) - C_0}} dz, \tag{3}$$

$$E_a = C_0 L + 4\sqrt{2\gamma_0} \int_0^{z_0} \sqrt{V(z) - C_0}\, dz, \tag{4}$$

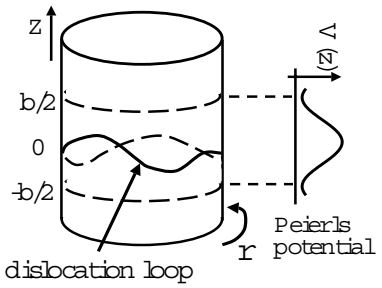

Figure 1: Flexible dislocation loop surrounding a circular cylinder.

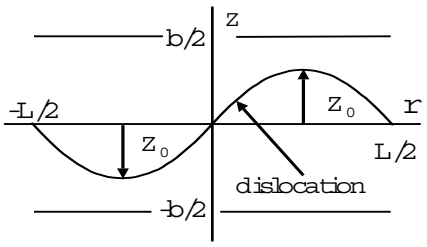

Figure 2: Saddle point configuration of double-kink type. Parameter z_0 is bow-out at the saddle point.

Peierls potential is assumed to be a double sine-Gordon type in the present work.

$$V(z) = V_0 \left\{ 1 + \cos \frac{2\pi z}{b} + \mathrm{g}(1 - \cos \frac{4\pi z}{b}) \right\}, \tag{5}$$

where $|\mathrm{g}| < 1/4$. Equations (3) and (4) are represented with a linear combination of elliptic integrals of first, second and third kinds by inserting Eq. (5). Figure 3 shows the dependence of the normalized activation energy E_a/E_0 on the loop length L/L_c for various values of $\mathrm{g} = 0, \pm 0.2$. If the dislocation loops are shorter than a critical length, the saddle point configuration is only the trivial solution ($z \equiv 0$) and activation energy is proportional to the length (dashed line). On the other hand, for longer dislocation loops the saddle point configuration is the double-kink type [4]. The activation energy then monotonously increases with the length but almost constant (solid line). When $1/16 < \mathrm{g}$, a new bifurcation appears and the number of the possible saddle points is three at most, as shown in Fig. 4.

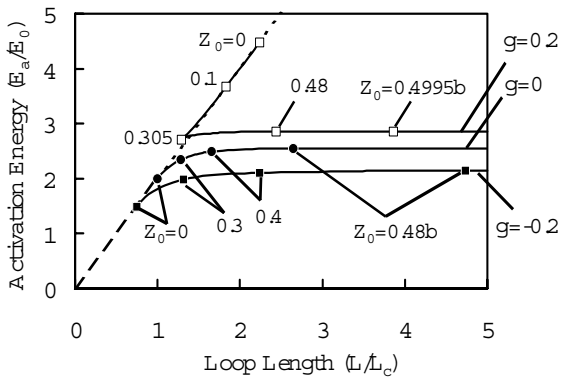

Figure 3: Activation energy versus dislocation loop length: $E_0 = \sqrt{\gamma_0 V_0}b$, $L_c = \sqrt{\gamma_0/V_0}b$. Some values of z_0 are exhibited

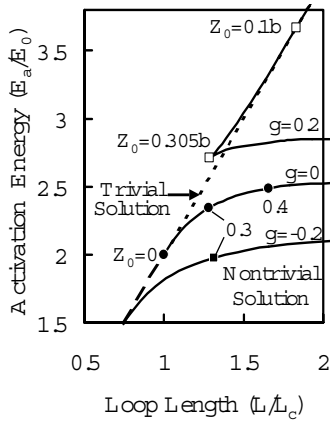

Figure 4: Acute line (g=0.2) corresponds to the new bifurcation.

References

[1] B. D. Wirth, G. R. Odette, D. Maroudas, and G. E. Lucas, J. Nucl. Mater. **276,** 33 (2000).

[2] Y. N. Osetsky, D. J. Bacon, A. Serra, B. N. Singh, and S. I. Golubov, Philos. Mag. **83,** 61 (2003).

[3] G. H. Vineyard, J. Phys. Chem. Solids, **3,** 121 (1957).

[4] A. Seeger, Philos. Mag. **1,** 651 (1956).

[5] V. Celli, M. Kabler, T. Ninomiya, and R. Thomson, Phys. Rev. **131,** 58 (1963).

Atomic-scale modeling of dislocation dynamics in radiation defect environments

D. Rodney[1],B.D. Wirth[2], Yu.N. Osetsky[3]

[1]GPM2-INPG, 101 rue de la physique BP46 F38402 Saint Martin d'Hères France, david.rodney@gpm2.inpg.fr

[2]UCB Department of Nuclear Engineering, 4165 Etcheverry Hall, MC 1730, Berkeley, CA 94720-1730, bdwirth@nuc.berkeley.edu

[3]ORNL, Computational Materials Science Group, Computer Sciences and Mathematics Division, One Bethel Valley Road, P.O.Box 2008, MS-6138, Oak Ridge, TN 37831-6138, osetskiyyn@ornl.gov

Irradiation defects induce a degradation of the mechanical properties with a hardening and, above low doses, a localization of the deformation in shear bands which are cleared of all irradiation defects by the moving dislocations. This process requires short-range interactions between the dislocations and the irradiation defects, the latter being either *transformed* (*unfaulted*), *sheared* or *absorbed* and *dragged*. Modeling the dynamics of dislocations in such an environment has therefore to start from the atomic scale.

With the rapid increase in computing speed and in simulation techniques at the level of both interatomic potentials and boundary conditions, it is now possible to simulate, from the atomic scale, with realistic time and space scales, edge and screw dislocations interacting with crystalline defects of various natures.

We review recent molecular dynamics simulations involving the most common irradiation defects encountered in FCC crystals: vacancy-type Stacking Fault Tetrahedra [1,2] and interstitial Frank loop [3]. The different interatomic potentials and boundary conditions employed are presented and compared.

Our aim is (1) to study from the atomic scale the interaction mechanisms between dislocations and irradiation defects, showing for example, the role of athermal cross-slip events on the unfaulting of Frank loops and (2) to evaluate directly from the simulations critical unpinning stresses that can be used in a multi-scale approach in larger scale Discrete Dislocation Dynamics simulations.

One of the main findings of the present simulations is that *simple shear of irradiation defects is more common than usually assumed*. For example, in the case of Frank loops the classical unfaulting process is observed, but is not the general rule, defect shearing being frequently observed, depending of the morphology of the loops. Consequences of this observation on the mechanisms of clear band formation will be discussed. The talk will end with a discussion on current challenges and directions for future works.

References

1- B. Wirth, V. Bulatov, T. Diaz de la Rubia, J. Eng. Mat. Technol. 124 (2002) 329.
2- Y. Osetsky, D. Bacon, in: H. Kitagawa, Y. Shibutani (Eds.), IUTAM Symposium on Mesoscopic Dynamics of Fracture Process and Materials Strength, Kluwer Academic Publishers, Dordrecht, The Netherlands, p. 173.
3- D. Rodney, Acta Mater. 52 (2004) 607.

Deduction of an He-Fe interaction potential from first-principle calculations

Tatiana Seletskaia, Yu. N Osetskiy, R. E. Stoller, G. M. Stocks

Metals and Ceramics Division, Oak Ridge National Laboratory, Oak Ridge, TN 37831-6138, USA; seletskaiat@ornl.gov

ABSTRACT

Helium is produced in neutron-irradiated metals as the result of (n, α) reactions, and experiments show that it has a strong tendency to cluster and form bubbles. The goal of the present computational research is to develop an equation of state for He in α-iron for application in multiscale modeling. Results are presented from the initial stage of this research, first-principle calculations of He defect properties in iron, in which an unexpected influence of He on iron magnetism was observed. In contrast with previous work that neglected such effects, the calculations show that the tetrahedral position is energetically more favorable for the He interstitial than the octahedral. The calculated He defect formation and relaxation energies in iron will be used to fit an empirical He-Fe interaction potential. The results indicate that the He-Fe interaction cannot be approximated by a pair potential.

1. Introduction

Helium is produced in neutron-irradiated metals as the result of (n, α) transmutation reactions and plays a significant role in the microstructure evolution and mechanical properties degradation [1]. Simulation of this microstructural evolution requires a significant multiscale computational effort. Primary damage formation and defect/cluster properties, such as stability, mechanisms of motion and interactions, are typically studied using molecular dynamics (MD) with the results strongly dependent on the interatomic potential. The only He-Fe potential found in the literature is the He-Fe^0 dimer potential obtained by Wilson [2] using the Thomas-Fermi-Dirac formalism. Development of a more realistic potential requires detailed atomic scale information that cannot be obtained directly from experiments. Therefore, first-principle calculations based density functional theory must play an important role here. The properties of He defects in iron, such as their formation and relaxation energies and He-Fe interatomic forces, can be studied by first-principle methods and then used to parameterize an empirical potential. Results from the first step of this process are presented in this paper, namely, the first-principle calculation of He defect properties in iron.

2. Method

The calculations have been performed using the Vienna *ab initio* simulation package VASP [3, 4]. The self-consistent energy minimization was carried out with a plane-wave basis set using PAW pseudopotentials [5]. Exchange and correlation functionals were taken in a form proposed by Perdew and Wang (PW91) [6] within the generalized gradient approximation (GGA). The cutoff energy for the plane-wave basis set providing energy convergence was found to be 300 eV. The summation of the energy eigenvalues was carried over 75 k-points in the irreducible wedge for a 54 atom supercell and with 18 k-points for a 128 atom supercell.

3. Results

As will be published elsewhere [7], electronic structure calculations have shown an unexpected influence of He on iron magnetism. The change of the magnetic moment produced by He on its first iron neighbors is not large, but sufficient to change the site-preference of the He defect. In contrast with the previous calculations, the tetrahedral interstitial site is found to be energetically more favorable than the octahedral site. The difference between the formation energies of the interstitial and substitutional He defects is found to be 0.29 eV, substantially smaller than that obtained in previous work [2].

The easiest way to obtain a He-Fe interatomic potential is by integrating their interaction force calculated from first principles. Suppose that He and Fe atoms interact through a pair-potential and Fe-Fe interaction does not change in the presence of the He defect. An iron *bcc* supercell is evaluated with the He atom placed in an interstitial position. In the unrelaxed configuration, Fe-Fe interaction forces are canceled due to the crystal symmetry and the only force experienced by the Fe atoms is the interaction force with the He defect. The forces acting on different Fe atoms can be calculated using an *ab initio* method and they can be determined as a function of He-Fe interatomic distance. Integration of the force with respect to the distance will yield the potential. This potential can be used in MD simulations in combination with any other Fe empirical potential, such as the Finnis-Sinclair potential [8]. However, the approach of the direct force integration is valid only under assumption that He does not change the Fe-Fe interaction. In fact, an interstitial defect disturbs the electrons of the host atoms and the interaction between them changes.

The distance dependence obtained for the He-Fe interaction force is shown in Figure 1. It can be well approximated by an exponential function of the distance. When the force is integrated with respect to the distance and the potential obtained is used to calculate He defect formation energies, the results strongly differ from the first principles calculations. The relaxation and formation energies of He in Fe obtained from the pair-potential and VASP calculations are given in Table 1. Since the forces were directly calculated by the same *ab initio* method, the relaxation energies obtained with the pair-potential match the ones obtained from VASP. For the formation energies, the pair-potential and VASP give very different results. This indicates that the pair-potential approximation is not applicable for the He-Fe interaction and Fe is strongly polarized by the He interstitial. The latter observation is confirmed by electronic structure calculations [7].

Figure 1. He-Fe interaction force: circles show the results of 54 atom supercell calculations and triangles indicate 128 atom supercell results. The solid line is an interpolated function: $V(R)=3.6854\, e^{-3.0039(R/1.5683-1)}$.

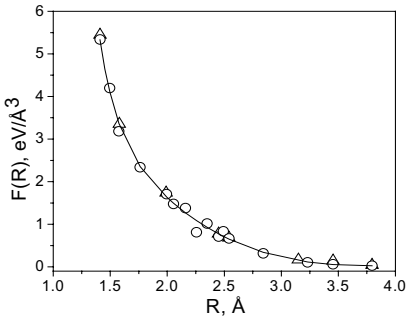

Table 1. He defect formation and relaxation energies in iron.

		octahedral	tetrahedral	substitutional
E^{rel} (eV)	pair potential	1.49	1.22	0.21
	VASP	1.58	1.29	0.09
E^{f} (eV)	pair potential	6.99	6.93	4.90
	VASP	4.60	4.37	4.08

Conclusions

Since magnetism plays a crucial role in He defect behavior, it is impossible to describe the He-Fe interaction by a simple pair-potential. The self-consistent set of He defect calculations in Fe partially presented here will be used for construction of new He-Fe interatomic potential. It will include a many-body interaction term to account for the iron polarization induced by the He defect.

References

[1] R. E. Stoller and G. R. Odette, J. Nucl. Mater., 154, 286-304, (1988).
[2] W. D. Wilson in Fundamental Aspects of Radiation Damage in Metals, F. W.Young and M. T. Robinson, Eds., USERDA-CONF-751006-P2, p.1025, (1975).
[3] G. Kresse and J.Hafner, Phys. Rev. B **47**, 558 (1993); **49**, 14 251 (1994).
[4] G. Kresse and J. Furthmüller, Phys. Rev. B **54**, 11 1698 (1996).
[5] G. Kresse and J. Joubert, Phys. Rev. B **59**, 1758 (1999).
[6] J. P. Perdew, *et al.*, Phys. Rev. B **46**, 6671 (1992); **48**, 4979(E) (1993).
[7] T. Seletskaia, Yu. N. Osetskiy, R. E. Stoller, and G. M. Stocks, submitted to Phys. Rev. Lett.
[8] M. W. Finnis and J. E.Sinclair, Phil.Mag. A, 50 1, 45-55 (1984) .

Vacancy-related Changes on the Structure and Mobility of Interstitial Clusters in Cubic Metals.

M. A. Puigví[1], A. Serra[1] and Yu. N Osetsky[2]

[1)] Departament de Matemàtica Aplicada III, Universitat Politècnica de Catalunya, Jordi Girona 1-3 modul C-2, 08034 Barcelona, Spain; a.serra@upc.es
[2)] Oak Ridge National Laboratory, One Bethel Valley Road, P.O.Box 2008, Oak Ridge, TN 37831, USA; osetskiyyn@ornl.gov

ABSTRACT

We present results on the atomistic study of interactions between glissile clusters of self-interstitial atoms (SIAs) and a vacancy in bcc and fcc metals. We demonstrate that the interaction depends strongly on the structure of clusters. Thus, clusters in iron are perfect dislocation loops and a vacancy recombines only on its perimeter. Clusters in copper dissociate into partial dislocation loops and recombination occurs only with the interstitial at the acute vertices where dissociation is weak. When a vacancy is positioned inside the loop perimeter there is no recombination but the vacancy affects cluster mobility suppressing its glide.

1. Introduction

The reaction between defect clusters and mobile point defects is the main mechanism of cluster's growth and shrinkage. Such interaction can be rather complicated and in some cases point defects may qualitatively change cluster's properties. Knowledge of these reactions, which can be studied only at atomic scale, is a necessary part of any model predicting the microstructure evolution during irradiation. We present here results of the atomistic study of interactions of clusters of self-interstitial atoms (SIAs) with a vacancy in bcc Fe (perfect glissile ½<111> loops) and fcc Cu (glissile ½<110> and sessile Frank 1/3<111> loops). We show that vacancies recombine only with the SIAs on the non-dissociated edges of the cluster. Vacancies located on the habit plane within the cluster glide prism may suppress its mobility.

2. Computational procedure

Crystals containing up to ~400,000 mobile atoms were simulated with fixed boundaries using interatomic many-body potentials parameterized by Ackland et al. [1, 2]. We have simulated glissile clusters of 127 and 469 SIAs in Fe and of 49 and 225 SIAs in Cu and sessile Frank loops of 37 and 397 SIAs in Cu. Initially, an isolated cluster was created in the centre of a crystal and relaxed to the minimum of the potential energy. A vacancy was then inserted at a chosen position and the system was relaxed again using a combination of conjugate gradients and quasi-

dynamic relaxation until the final mean gradient per atom was reduced to ~10^{-8}eV/a_o (a_o is the lattice parameter). After the final relaxation the cluster-vacancy binding energy was estimated and the configuration was investigated.

3. Results

Detailed description of SIA clusters in bcc and fcc metals was presented by Osetsky *et al* [3]. Here we provide a short description of features relevant to cluster-vacancy interactions.

3.1 bcc Fe

The most stable clusters are hexagonal formed by <111> crowdions in {111} planes with sides along <112> directions. In terms of dislocations, these are edge loops with **b** = ½<111>. Clusters exhibit a thermally-activated one-dimensional glide in the direction of crowdions. Vacancy-SIA recombination occurs only with interstitials at the perimeter by the cluster gliding athermally to the vacancy site. Both, the recombination distance and interaction energy (E_{int}) depend on the cluster size and vacancy location. For clusters of 127 and 469SIAs, the maximum recombination distance of a vacancy positioned in front of the middle of the cluster edge along the **b** direction is 4.5 and 3.7a_0 with E_{int} equal to 1.21 and 0.95 eV respectively. Vacancies interacting with SIAs within the cluster/loop perimeter do not recombine and have significantly weaker E_{int} with a minimum near the cluster centre. Fig.1 shows E_{int} of a vacancy located in the habit plane of a 469 SIAs cluster (x=0 is the cluster centre; x=8.5 is the edge of the cluster). Triangles represent the results of the simulation. For comparison we have included the interaction energy calculated using the isotropic elasticity: $E_{el}=P\delta V_V$, where P is the pressure created by the cluster at the vacancy site and $\delta V_V = 0.18\Omega_0$ is the vacancy dilatation volume simulated in the bulk of a perfect crystallite (Ω_0 is the atomic volume). Open circles correspond to P calculated using the linear elasticity theory and stars correspond to P estimated in the simulation. We conclude that for large loops the theory gives a reasonable approximation out of the dislocation core. This is not the case for smaller sizes as shown in [4]. When a vacancy is inside the glide cylinder the cluster moves towards it and a complex cluster-vacancy is formed since the vacancy does not recombine. The main effect is a significant decrease of clusters mobility. Fig.1 shows that the interaction energy increases towards the edge of the cluster indicating a preferential path for the vacancy migration. When the vacancy reaches the edge of the cluster the recombination occurs and the clusters mobility is restored.

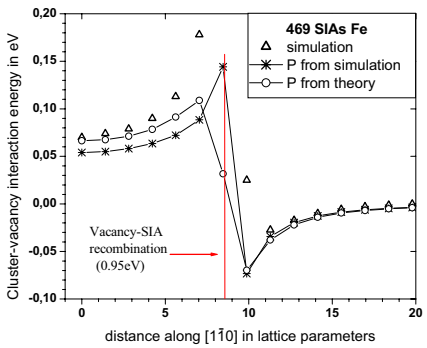

Figure 1. Interaction energy of a vacancy and a 469 SIAs cluster calculated by simulation (Δ) and using E=PδV: P from simulation (*) and P from elasticity theory (o).

3.2 fcc Cu

3.2.1. Glissile clusters

The most stable clusters are rhombic with sides along <112> directions and these are glissile edge loops with **b** = ½<110>. They are formed by <110> crowdions and their structure and properties depend on cluster size. Clusters over 25 SIAs dissociate on the {111} planes that form their glide prism, creating Shockley partials and stair-rod dislocations. The width of the stacking-fault ribbon on the <112> loop edges is not constant; it varies from zero in the acute vertex to the maximum width (~8a for clusters containing more than 100 SIAs) in the obtuse vertex. Only interstitials in the acute vertex can recombine with the vacancy. The recombination distances and E_{int} are $4.3a_0$ and $3.7a_0$ and 1.20eV and 1.14eV for the 49 and 225SIA clusters respectively. Once this first SIA has recombined the two adjacent interstitials can recombine and the resulting cluster has the fifth side along a non dissociated <110> direction. All interstitials in this side can recombine resulting in the shrinkage of the cluster. A vacancy located within the glide cylinder at any other site does not recombine but cause the cluster glide towards it. In a static simulation (T=0K) the maximum distance at which the cluster glides towards the vacancy is about $6a_0$. A vacancy located on the partial dislocation core prevents the cluster mobility.

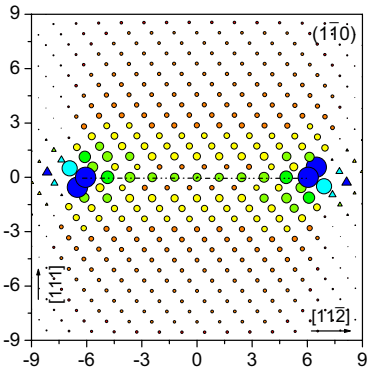

Figure 2. Pressure map of the (1$\underline{1}$0) cross section containnig a Frank loop. Compression (O); tension (Δ). P_{max}=113kbar

3.2.2. Sessile Frank loops

Hexagons with sides along <110> directions are the most stable Frank loops with **b**= ⅓<111>. Fig.2 shows the pressure map of a cross section through the centre of a 397 SIAs loop (dashed line). The sizes of the symbols are proportional to the pressure. Vacancies recombine only when they are at the first neighbor sites of the interstitials of the cluster edge. E_{int} is equal to 1.75eV and 1.2eV for the interstitials at the vertexes and edges respectively.

References

[1] G.J.Ackland, G.Tichy, V.Vitek, M.W.Finnis, 'Simple N-body potentials for noble metals and nickel', *Philos. Mag., A*, **56** (1987) 735.
[2] G.J.Ackland, D.J.Bacon, A.F.Calder, T.Harry, 'Computer simulation of point defects in dilute Fe-Cu alloys using many-body interatomic potentials', *Philos. Mag., A* **71** (1997) 553.
[3] Yu.N. Osetsky, A. Serra, B.N.Singh and S.I. Golubov, 'Structure and properties of clusters of self-interstitials in bcc and fcc metals'; *Phiosl. Mag. A*, **80**, (2000) 2131.
[4] M. Pelfort, Yu.N. Osetsky and A. Serra,'Vacancy interaction with glissile interstitial clusters in bcc metals'; *Phil Mag, Letters*, **81** (2001) 803

Modeling of Temperature Effect on the Formation of Matrix Damage in bcc-Fe: Combined MD and KMC Study

N. Soneda [a*], A. Takahashi [c], K. Dohi [a] and S. Ishino [a,b]

[a] **Materials Science Research Laboratory, Central Research Institute of Electric Power Industry, 2-11-1 Iwado-kita, Komae, Tokyo 201-8511, Japan**
E-mail: soneda@criepi.denken.or.jp

[b] **Department of Applied Science, Tokai University, 1117, Kitakaname, Hiratsuka -shi, Kanagawa 259-1292, Japan**

[c] **Department of Mechanical Engineering, Tokyo University of Science, 2641 Yamasaki, Noda, Chiba 278-8510, Japan**

ABSTRACT

Understanding the effect of temperature on the formation of matrix damage, such as vacancy clusters and self-interstitial atom (SIA) clusters, in bcc Fe is important for the accurate prediction of irradiation embrittlement of reactor pressure vessel materials of nuclear power plants. Two models are available at present time to describe the irradiation temperature effect on matrix damage formation: Jones' F_T model and USNRC/ASTM model. This paper describes our effort to characterize the effect of irradiation temperature on the formation of matrix damage, and to compare the results with the two models. We use kinetic Monte Carlo (KMC) technique to simulate the time evolution of radiation damage. We also use the molecular dynamics (MD) to obtain the information at smaller space and shorter time scales such as defect formation in displacement cascades and defect kinetics, which can be input data to KMC simulations. Both forms of the Jones' F_T model and the USNRC/ASTM model look describing the temperature dependence, but the Jones' F_T model provides consistent basis for the temperature effect on vacancy and SIA clusters.

1. Introduction

The effect of irradiation temperature on the formation of radiation damage, especially matrix damage, in reactor pressure vessel materials of light water reactors needs to be well understood in order to develop a reliable embrittlement correlation method. Jones

and Williams have proposed F_T model based on the embrittlement database irradiated at wide range of temperature [1], where the effect of temperature on the contribution of matrix damage to the transition temperature shift is described as a linear function of temperature, $F_T = 1.9\text{-}4.6\text{x}10^{-3}T$. On the other hand, US NRC [2], and later ASTM, have proposed another type of temperature dependence of matrix damage contribution, where an exponential function of irradiation temperature, exp(10,728/T) in US NRC, is assumed. In this paper, we study the effect of irradiation temperature on the formation of vacancy and SIA clusters during neutron irradiation in pure iron using our multi-scale radiation damage simulation tool, and then try to apply the above two temperature effect models to see how they describe the simulation results.

2. Computer Simulation of Radiation Damage Accumulation

We use a multi-scale computer simulation approach with the combination of MD and KMC techniques for the damage accumulation calculations during irradiation. Formation of point defects in displacement cascades due to irradiation was calculated using MD. In order to consider the effect of the primary knock-on atom (PKA) energy spectrum, we performed extensive MD simulations for different PKA energies ranging from 100eV to 50keV. Formation and binding energies of point defect clusters were calculated using MD to describe the thermal stability of the defect clusters. We also calculated the diffusivities of the defects. All the above information is passed as input data to the KMC simulations at longer time and larger space scales, where the fates of all the defects are tracked during simulation time. Effects of sinks such as pre-existing dislocations and grain boundaries are effectively considered in the KMC simulations [3].

3. Results

Calculations are done at a dose rate of $1\text{x}10^{-8}$dpa/s to a dose of 0.1dpa. Fig. 1 (a) and (b) show square root of the number densities of vacancy and SIA clusters at 0.1 dpa plotted against (a) T and (b) 1/T, respectively. Broken lines were obtained by regression analyses to fit (a) a linear function of temperature, and (b) an exponential function of temperature. In Fig.1 (a) and (b), broken lines well describe the data, demonstrating that both a linear function of temperature and an exponential function of temperature work for the data

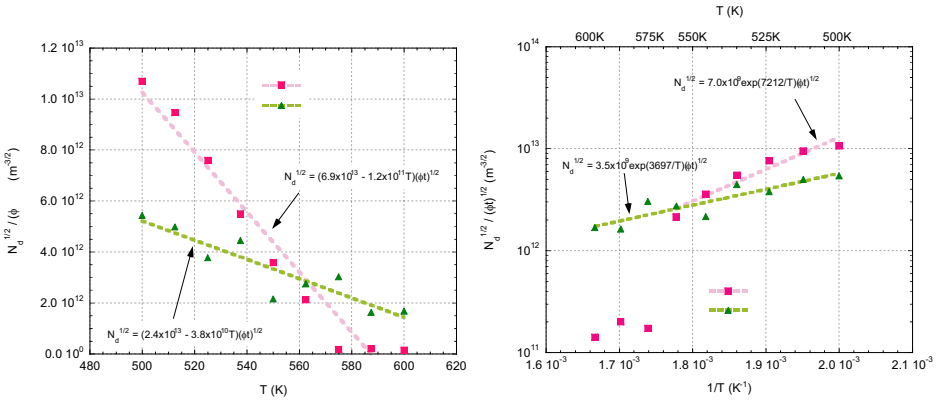

(a) Nd is plotted against T (b) Nd is plotted against 1/T

Fig. 1 Temperature dependence of the number density (Nd) of defect clusters at a dose of 0.1dpa.

Table 1 Fitting function to the simulation results

	F_T Model	USNRC/ASTM Model
Original	$1.9 - 4.6x10^{-3}T$	exp(10,728/T)
Vacancy cluster	$(1.9 - 3.0x10^{-3}T) \times 3.63x10^{13}$	exp(7,212/T)
SIA cluster	$(1.9 - 3.3x10^{-3}T) \times 1.26x10^{13}$	exp(3,697/T)

in this temperature range. However, when we investigate the fitted function shown in Table 1 in detail, one can see that the temperature dependences of vacancy and SIA clusters of F_T model are very similar while the activation energies of vacancy and SIA clusters of USNRC/ASTM model are very different. This temperature range between 500 and 600°C corresponds to stage V of the vacancy clusters, where vacancy clusters are unstable while SIA clusters are very stable. This means that temperature dependences should be primarily determined by the stability of vacancy clusters, thus the temperature dependences of vacancy and SIA clusters should be similar. In this sense, F_T model is rather rational and consistent than the USNRC/ASTM exponential model.

References

[1] R.B. Jones, T.J. Williams, ASTM-STP 1270 (1996) 569.

[2] E.D. Eason, J.D. Wright , G.R. Odette, NUREG/CR-6551 (1997).

[3] N. Soneda, S. Ishino, A. Takahashi, K. Dohi, J. of Nuclear Materials 323 (2003) 169.

Self-Interstitial Cluster Diffusion In BCC Fe-Cr Alloys: A Molecular Dynamics Study

D. Terentyev[1], L. Malerba[1], Yu.N. Osetsky[2], A.V. Barashev[3]

[1] SCK•CEN, Department RMO, Boeretang 200, B-2400 Mol, Belgium, (e-mail: dterenty@sckcen.be, lmalerba@sckcen.be)
[2] Oak Ridge National Laboratory, Computational Materials Science Group, Computer Sciences and Mathematics Division, USA (email: osetskiyyn@ornl.gov)
[3] Material Science and Engineering, Department of Engineering, The University of Liverpool, Brownlow Hill, Liverpool L69 3GH, UK (e-mail: a.barashev@liv.ac.uk)

ABSTRACT

Molecular dynamics (MD) simulations of the migration of self-interstitial atom (SIA) clusters in pure Fe, Fe-7at.%Cr and Fe-12at.%Cr alloys are presented. It is shown that chromium atoms reduce the diffusivity of SIA clusters and the effect becomes stronger with increasing cluster size.

1. Introduction

The formation of SIA clusters in metals under irradiation with energetic particles is observed in experiments and confirmed in MD studies of displacement cascades. The thermally-activated migration of these clusters and their interaction with each other and other defects lead to the accumulation of the so-called 'matrix damage', which causes significant changes in the mechanical properties of irradiated materials. The migration of these clusters is an essential part of the accumulation process and its knowledge is required to develop predictive models of the long-term microstructural evolution under different irradiation conditions. The migration of SIA clusters in pure iron has already been studied using MD [1-4], but the effect of alloying elements is not well understood yet. Experimental observations and theoretical studies suggest that solute atoms can significantly reduce the diffusivity of interstitial loops [5]. In particular, recent experiments on irradiated Fe-Cr alloys show that high concentrations (~9at%) of Cr atoms reduce the mobility of loops, due to trapping at Cr atoms segregated at the periphery of the loops [6]. In this paper MD is used to study the effect of Cr solute atoms on the SIA cluster migration in bcc Fe-Cr alloys.

2. Simulation technique

MD studies of the migration of clusters containing from 4 to 37 SIA in pure Fe, Fe-7at.%Cr and Fe-12at.%Cr alloys, in the temperature range from 300 to 1200 K, were

performed applying the same method as in [1-4]. Cr atoms were distributed randomly in the bcc-Fe matrix. An embedded atom type potential developed for this system [7,8] was used to describe the atomic interactions. The calculations were performed in the microcanonical NVE ensemble, using cubic simulation boxes containing up to 120,000 atoms, with periodic boundary conditions at zero pressure. The migration process was followed for ~10 ns. During the simulations detailed information on the configuration of the cluster, i.e. the positions of the centres of each interstitial atom, was recorded every 5 fs. The jump frequency of each crowdion in the cluster and the centre of mass of the cluster, the corresponding correlation factors and the diffusion coefficients were thereby calculated. The chemical composition of the loops and other features were also analysed.

3. Results

The results show that the presence of chromium atoms reduces the mobility of SIA loops. Arrhenius plots of the diffusion coefficients of loops of different size in pure Fe and Fe-12%Cr alloy are shown in Figs.1 and 2, respectively. In pure Fe the pre-exponential factor of the diffusion coefficient decreases with cluster size, while the migration energy is about 0.02 eV and almost independent of the loop size (Fig.1). This is consistent with the results of previous work on pure Fe [3,8]. The presence of 7at.% of Cr atoms (results not shown here) increases the migration energy of the clusters: to 0.05 eV for a four-SIA cluster and to 0.14 eV for a 37-SIA cluster. Thus, this effect is more significant for bigger clusters. At even higher chromium concentration (~12at.%), the dependence of the migration energy on the loop size is not so strong (Fig.2), with an average migration energy value of ~0.09 eV, almost five times higher than that in pure Fe.
An analysis of correlation effects reveals that the migration of the loops in pure iron and in the alloy displays an opposite response to a rising temperature. In pure iron, a rise in the temperature increases the probability of backward jumps and the effective migration energy value, perhaps due to defocusing of crowdions. In the alloy, at low temperature the loops are trapped and their motion is confined, while a rise in the temperature reduces the trapping effect and allows the clusters to migrate more freely.

4. Conclusions

1. Cr atoms reduce the diffusivity of SIA clusters in bcc iron, decreasing the pre-exponential factor and increasing the effective migration energy.
2. This effect is stronger for larger clusters.
3. At high Cr concentrations (~12at.%), the migration energy is still much higher than in pure iron, but the cluster size dependence becomes weaker.

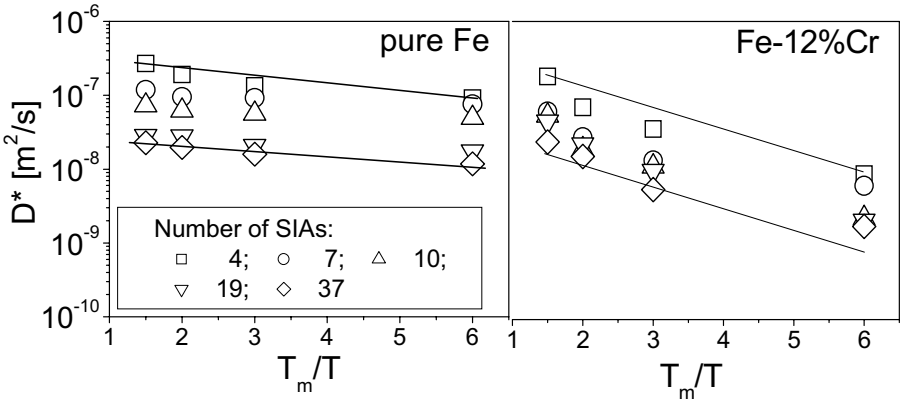

Fig.1. Diffusion coefficients of different size SIA loops in pure Fe.

Fig.2. Diffusion coefficients of different size SIA loops in Fe-12%Cr alloy.

References

[1] Y. Osetsky, D.J. Bacon, A. Serra, B. Singh and S. Golubov, "One-dimentional atomic transport by clusters of self-interstitial atoms in iron and copper", Phil. Mag A, Vol. 83, pp. 61 (2003)

[2] N. Soneda and T. D. De la Rubia, "Migration Kinetics of the self-interstitial atom and its clusters in bcc Fe", Phil. Mag. A, Vol. 81, 331 (2001).

[3] A.V. Barashev, Y. N. Osetsky and D.J. Bacon, "Mechanism of one-dimentional glide of self intertitial atom clusters in α-iron", Philos. Mag. A Vol. 80, 2709 (2000).

[4] J. Marian, B. Wirth, A. Caro, B. Sadigh, G. Odette, J. Perlado and T. Diaz de la Rubia, "Dynamics of self-interstitial cluster migration in pure Fe and Fe-Cu alloys", Phys. Rev. B **65**, 144102 (2002).

[5] G.A. Cottrel, S.L. Dudarev and R.A. Forrest, "Immobilization of interstitial loops by substitutional alloy and transmutation atoms in irradiated metals", J. Nucl. Mater. 325, 195 (2004).

[6] K. Arakawa, M. Hatanka, H. Mori and K. One, "Effect of chromium on the one-dimentional motion of interstitial-type dislocation loops in iron", J. Nucl. Mater. **329-333**, 1194 (2004).

[7] L. Malerba and D. Terentyev, P. Olsson, R. Chakarova and J. Wallenius, "Molecular dynamics simulation of displacement cascades in Fe-Cr alloys", J. Nucl. Mater. **329-333**, 1156 (2004).

[8] D. Terentyev and L. Malerba, "Diffusivity of solute atoms, matrix atoms and interstitial atoms in Fe-Cr alloys: molecular dynamics study", J. Nucl. Mater. **329-333**, 1161 (2004).

Reaction Kinetics of SIA Clusters and Damage Accumulation in Metals under Cascade Irradiation: Impact of Impurities

H. Trinkaus[a], B.N. Singh[b], and S.I. Golubov[c]

[a] Institut für Festkörperforschung, Forschungszentrum Jülich, D-52425 Jülich, Germany, h.trinkaus@fz-juelich.de
[b] Materials Res. Department, Risø National Laboratory, DK-4000 Roskilde, Denmark,
[c] Met. & Cer. Div., Oak Ridge National Laboratory, Oak Ridge, TN-37831-6138, USA

ABSTRACT

In the present contribution, the one-dimensional (1D) diffusion of clusters of self-interstitial atoms (SIAs) produced in displacement cascades is considered to be disturbed by direction changes and transversal diffusion resulting in diffusion reaction kinetics (RK) between the 1D and 3D limiting cases. An analytical single-variable function ("master curve") describing the increase of the sink strength for the absorption of SIA clusters with increasing 1D disturbance from very low values for pure 1D to high values for 3D diffusion is presented. The interaction of SIA clusters (small dislocation loops) with impurities, which is estimated on the basis of elastic continuum theory, is shown to result in a shift of the RK towards 3D. Implications for the evolution of voids, particularly for the saturation of void growth at high doses are discussed.

1. Introduction

In pure metals exposed to cascade producing irradiation, the damage accumulation at low doses (<1dpa) and at temperatures around $0.4T_m$ (T_m: melting temperature) occurs in a spatially highly segregated fashion: self-interstitial atoms (SIAs) segregate in the form of dislocation loops near dislocations while vacancies accumulate in the form of voids in between and, intensified, near grain boundaries. During the last decade, these phenomena have been rationalized in terms of intra-cascade clustering of vacancies and SIAs, and 1D diffusion of SIA clusters [1]. However, various aspects in damage accumulation are difficult to be understood in terms of undisturbed 1D diffusion of SIA clusters: its tendency to change with increasing alloying from highly heterogeneous towards more homogeneous, the dependence of void growth at high doses on crystal structure and the stability of once formed void super-lattices. Extending the previous work [2-4], we present a general treatment of the 1D to 3D RK of SIA clusters and discuss the role of impurities in it.

2. 1D to 3D Diffusion Reaction Kinetics

In order to derive expressions for the partial sink strengths, k_s, for the absorption of SIA clusters (performing disturbed 1D diffusion) by randomly distributed sinks of type s (voids, dislocations etc) we have employed a self-consistent sink embedding procedure

assuming steady-state under constant defect production [4]. The form of the resulting expressions suggests an interpolation between the 1D and 3D limits, $k_{(1)s}$ and $k_{(3)s}$, of k_s which may be written as a single-variable function ("master curve")

$$y = k_s^2 / k_{(1)s}^2 = 0.5\left\{1+\sqrt{1+4x^2}\right\} \quad \text{with}$$
$$x^2 = \frac{\delta f^2(\delta) l_{ch}^2 k_{(3)s}^4 /(12k_{(1)s}^2)+1}{l_{ch}^2 k_{(3)s}^4 /(12k_{(1)}^2)+1}(k_{(3)s}^2/k_{(1)s}^2)(k_{(3)s}^2/k_{(1)s}^2-1) \qquad (1)$$

where $\delta = D_{tr}/D_{lo}$ is the ratio of the transversal (2D) to longitudinal diffusion (1D) diffusion coefficient ($f^2(\delta) \sim 1$) and $l_{ch} = \sqrt{2D_{lo}\tau_{ch}}$ is the mean 1D diffusion length covered during the time τ_{ch} between two direction changes. Equation (1) comprises the whole RK of SIA clusters between its 1D and 3D limits defined by $k_s \to k_{(1)s}$ for $\delta \to 0$ and $l_{ch} \to \infty$, and $k_s \to k_{(3)s}$ for $\delta f^2(\delta) \to 1$ or $l_{ch} \to 0$, respectively.

3. Effects of Impurities

Both parameters, l_{ch} and δ, controlling, according to Eqn. (1), the RK are affected by the interaction of the SIA clusters (SIA-type dislocation loops, l) with impurities (i), mainly by a reduction of D_{lo}, changing the RK more towards 3D. We have estimated the loop-impurity interaction energy $E_{l,i}(\underline{r})$ on the basis of elastic continuum theory using

$$E_{l,i}(\underline{r}) = p(\underline{r})\Delta V\,, \qquad (2)$$

where $p(\underline{r})$ is the hydrostatic pressure induced by the loop and ΔV is the volume misfit of the impurity. $E_{l,i}(\underline{r})$ assumes positive and negative values depending on the position vector $\underline{r}$ of the impurity relative to the loop. Accordingly, impurities act as both temporary traps and barriers. On the basis of Eqn. (2), we have estimated the impurity induced changes in D_{lo} and, via this, in l_{ch} and δ, as a function of the loop size, the relative volume misfit, $e = \Delta V/\Omega$ (Ω: matrix atom volume), and the concentration, c_i, of impurities, and the temperature. An example is shown in Fig. 1a.

Combining the analysis of impurity induced changes in l_{ch} and δ with Eqn (1), the effects of impurities on the RK of SIA clusters and its consequences for damage accumulation can be treated. An example is the saturation of void growth at high doses. For pure 1D RK of SIAs, the void size (radius R) converges to a constant saturation size $R_s^{(1D)} = \pi d$, determined solely by the diameter of the dislocations for the absorption of SIA clusters, d, independent of the sink densities. Any disturbance of the pure 1D RK such as the additional production of 3D diffusing single SIAs, 1D direction changes and transversal diffusion of SIA clusters results, however, in an increase of the saturation size compared to that for pure 1D RK, depending on the sink densities.

We have studied the change in the void saturation size, R_s, as a function of various conditions using Eqn. (1) for the sink strength of SIA clusters. For 1D diffusion disturbed by transversal diffusion, Fig.1b shows a significant increase of R_s with decreasing void density, particularly for low dislocation densities. Differences in the void evolution in BCC and FCC metals may be considered in the light of this dependence. The effect of impurities on the RK and the resulting damage accumulation can be discussed in terms of impurity induced changes in l_{ch} and δ.

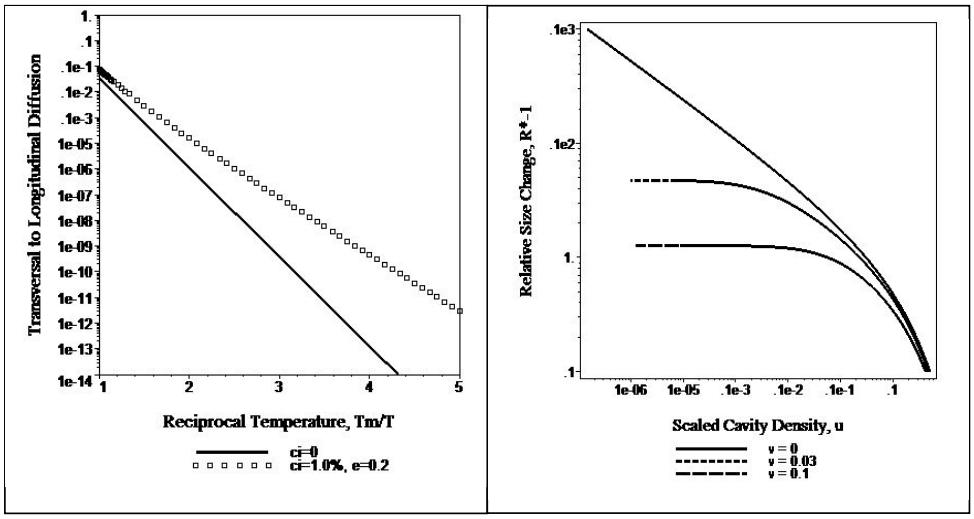

Fig.1. (a) Diffusion ratio, $\delta = D_{tr}/ D_{lo}$, vs reciprocal homologous temperature, T_m/T, for pure a metal (c_i=0) and a metal containing c_i = 1% impurities with relative volume misfit e = 0.2; (b) Relative change of saturated void size, $R^* - 1 = R_s/(\pi d) - 1$, vs scaled void density, $u = (\pi d)^3 N/\sqrt{\delta}$ for various values of the scaled dislocation density, $v = \pi d^2 \rho/4\sqrt{\delta}$. The dependence of the saturated void size on temperature and impurity parameters can be studied by using in the scaled densities for the δ the dependences shown in Fig.1(a).

References

1. B.N. Singh, H. Trinkaus and S.I. Golubov, Radiation Damage Theory, Encycl. of Mater.: Science and Techn. ISBN: 0-08-0431526 (2001) 7957.
2. U. Gösele, Reaction Kinetics and Diffusion in Condensed Matter, Prog. Reaction Kinetics 13/2 (1984) 63.
3. A.V. Barashev, S.I. Golubov and H. Trinkaus, Reaction Kinetics of Glissile Interstitial Clusters in a Crystal Containing Voids and Dislocations, Philos. Mag. **A81** (2001) 2515.
4. H. Trinkaus, H.L. Heinisch, A.V. Barashev, S.I. Golubov and B.N. Singh, 1D to 3D Diffusion Reaction Kinetics of Defects in Crystals, Phys. Rev. B66 (2002) 060105(R).

Ab Initio Study of the Stability and Mobility of Self-Interstitials and Small Interstitial Clusters in α-Fe

F. Willaime and Chu-Chun Fu

Service de Recherches de Métallurgie Physique, Centre d'Etudes de Saclay, 91191 Gif-sur-Yvette, France - fwillaime@cea.fr

ABSTRACT

The stability and mobility of self interstitials and small interstitial clusters, I_n, in α-Fe is investigated by means of Density Functional Theory calculations performed on 128 atom supercells at constant pressure using the SIESTA code. The stable configuration of mono-interstitials, *I*, is found to be the <110> dumbbell in agreement with experiments. Di- and tri-interstitials, I_2 and I_3, are made of parallel <110> dumbbells. These three defects, *I*, I_2 and I_3, are shown to migrate by nearest-neighbour translation-rotation jumps, according to the Johnson mechanism. The calculated migration barriers are in excellent agreement with experiments: 0.34 eV for *I* and 0.42 eV for I_2. The <111> orientation of the dumbbells becomes more favourable for I_5 and larger clusters. These results are at variance with the picture suggested by most empirical potentials, i.e. a fast <111> migration of all these defects. The EAM potential recently developed by Mendelev et al. for Fe, including ab initio self-interstitial formation energies in the fitted properties, is shown to perform much better than previous potentials for interstitial-type defects.

1. Introduction

Interstitial-type defects have two specificities in α-Fe with respect to other body-centred cubic metals: self-interstitials have an unusually large migration energy – 0.3 eV instead of at most 0.1 eV in other metals – and the Burgers vector of interstitial loops are observed to be either ½<111> or <100> instead of predominantly ½<111>. Pioneer predictions were made by Johnson on the basis of a pair wise potential: (i) the stable configuration of self-interstitials is the <110> dumbbell ; (ii) the di-interstitial consists of two parallel <110> dumbbells at nearest-neighbor lattice sites with their axes perpendicular to the line joining their centers ; and (iii) these defects migrate both by a nearest-neighbor translation-rotation mechanism [1]. These predictions are consistent with experiments in particular concerning the configuration of self-interstitials and they led Eyre and Bullough to suggest a mechanism for the formation of interstitial loops, based on two possible shears of small ½<110> nuclei towards more stable ½<111> or <100> loops [2].

The use of many-body potentials, of the Finnis-Sinclair or EAM type, then yielded a quite different picture. First, the <110> dumbbell was found to migrate by a two step mechanism: a rotation to the <111> orientation followed by a fast one dimensional migration [3]. Second, all interstitial clusters, $I_{n\geq 2}$, are stabilized in the <111> orientation [4,5]. The absence of <110> nuclei for interstitial loops led Marian et al. to suggest an alternative mechanism for the formation of <100> loops, based on the interaction between rapidly migrating ½<111> loops [5]. However these potentials had some discrepancies with experiments, in particular a too low migration energy (~0.16 eV instead of ~0.3 eV) and some difficulties to account for stage II in resistivity recovery experiments, attributed originally to di-interstitials.

A more accurate description of the interatomic interactions was clearly needed to elucidate the open questions on equilibrium structures and migration mechanisms of self-interstitials and small interstitial clusters. This is the reason why we resorted to ab initio electronic calculation techniques [6,7]. This work was performed using a particular implementation of Density Functional Theory electronic structure calculations, namely the SIESTA code [6]. We have developed and tested a pseudopotential and a basis set with ten localized functions for Fe [7]. The results presented here were obtained on 128(+n) atom supercells with a complete relaxation of the atomic positions and the of the cell geometry. The migration paths are calculated using the drag method.

Meanwhile improved empirical potentials for Fe have been developed by Mendelev et al., including formation energies of various self-interstitial configurations in the fitted properties [8]. The performance of version 2 of these new potentials is investigated here.

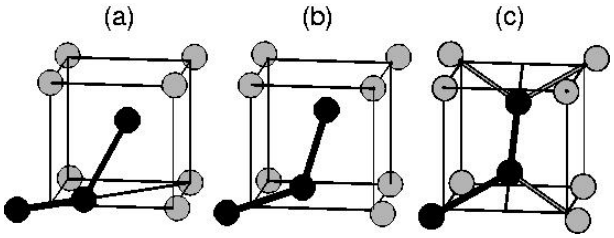

FIG 1. Schematic representation of the Johnson mechanism for the migration of <110> dumbbells in bcc metals: (a) initial ; (b) intermediate and (c) final configurations. The atoms are represented at the relaxed positions obtained by ab initio calculations in Fe.

2. Results and discussion

The formation energies of six high symmetry configurations of the self-interstitial were calculated. The most stable one is found to be the <110> dumbbell in agreement with experiments, but the main characteristics is the large energy difference between the <110> and <111> configurations, namely 0.7 eV, which excludes the migration via <111> configurations. The migration mechanism proposed by Johnson, schematized in Fig. 1, is found to the most favourable energetically, with a migration energy of 0.34 eV,

in very good agreement with the experimental value of 0.3 eV. The second-nearest neighbour jump is only slightly above with a barrier of 0.5 eV. The on-site rotations are higher in energy showing that the rotation activation energies measured experimentally indeed correspond to interstitial migration.
Di and tri-interstitials are formed by parallel and aligned <110> dumbbells, and they also migrate by the Johnson mechanism. The migration energy for I_2, 0.42 eV, is in excellent agreement with the experimental value deduced from the activation energy at stage II. These results support the existence of small nuclei with <110> orientation in the nucleation and growth process of interstitial loops. The <111> orientation of the dumbbells becomes more favourable for I_5 and larger clusters.
Unlike previous potentials, these characteristics are qualitatively well reproduced with the Mendelev potential. The main quantitative discrepancies with ab initio calculations are: the energy difference between the <110> and <111> dumbbells (0.5 eV instead of 0.7 eV) , the migration energy of di-interstitials (0.31 eV as for self-interstitials) ; the transition to <111> orientation occurs at slightly larger size (I_6 instead of I_5).

Acknowledgements
This work was supported by the PERFECT European Integrated Project under Contract No. FI6O-CT-2003-508840.

References

1. R.A. Johnson. *Interstitials and vacancies in α iron.* Phys. Rev. **134**, A1329-A1336 (1964).
2. B.L. Eyre and R. Bullough. *On the formation mechanism of interstitial loops in BCC metals*. Philos. Mag. 12, 31 (1965).
3. B.D. Wirth, G.R. Odette, D. Maroudas and G.E. Lucas. *Energetics of formation and migration of self-interstitials and self-interstitial clusters in α-iron*. J. Nucl. Mater. **244**, 185 (1997).
4. Y.N. Osetsky, A. Serra, B.N. Singh and S.I. Golubov. *Structure and properties of clusters of self-interstitial atoms in fcc copper and bcc iron.* Philos. Mag. A **80**, 2131 (2002).
5. J. Marian, B. Wirth and J.M. Perlado. *Mechanism of formation and growth of <100> interstitial loops in ferritic materials*. Phys. Rev. Lett. **88**, 255507 (2002).
6. J. Soler, E. Artacho, J.D. Gale, A. García, J. Junquera, P. Ordejón and D. Sánchez-Portal. *The SIESTA Method for ab initio order-N materials simulation*. J. Phys.: Condens. Matter **14**, 2745 (2002).
7. C.C. Fu, F. Willaime and P. Ordejón. *Stability and mobility of mono- and di-interstitials in α-Fe*. Phys. Rev. Lett. **92**, 175503 (2004).
8. M.I. Mendelev, S. Han, D.J. Srolovitz, G. Ackland, D.Y. Sun and M. Asta. *Development of new interatomic potentials for crystalline and liquid iron.* Philos. Mag. **83**, 3977 (2003).

Symposium – 8

Thin Film Processing

Structural and Mechanical Properties of Amorphous Silicon Surfaces: A Combination Study of *ab-initio* and Classical Molecular Dynamics

S. Hara, T. Kumagai, S. Izumi and S. Sakai

Department of Mechanical Engineering, The University of Tokyo, 7-3-1 Hongo, Bunkyo-ku, Tokyo, 113-8656 JAPAN, E-mail: harasho@fml.t.u-tokyo.ac.jp

ABSTRACT

Despite amorphous silicon (a-Si) being one of the most fundamental thin film materials, little is known about the microscopic details of a-Si surfaces. Several theoretical works using *ab-initio* approach have been performed to investigate this subject. However, creating an a-Si surface model that provides results comparable to experimental results is still a matter of debate. The origin of this difficulty arises from the insufficient thermal annealing for structural relaxation due to its heavy computational burden. To overcome this problem, we use a combined method of a classical molecular dynamics (CMD) and an *ab-initio* calculation based on density functional theory (DFT). The main role of the CMD method is the full relaxation of a-Si. Subsequently, the results of the CMD calculations are used as starting points for *ab-initio* calculations. This combination method (CMD-DFT) can provide quantitative evaluation of the surface energy and surface stress of well-relaxed amorphous silicon in addition to its structure. This calculation also led to a new discovery of the microscopic characteristic of a-Si surface, which was not revealed through the use of an empirical potential. It was shown that there are two types of threefold coordinated atoms at the surface region; one with p^3-like bonding and the other with sp^2-like bonding.

1. Methodology

The outline of the combination method is as follows. The first step is to prepare well-relaxed amorphous structures by CMD calculations with the Tersoff potential. In the next step, DFT calculations are carried out to relax the atomic geometries obtained from CMD simulations. The present calculations are performed using Vienna *ab-initio* simulation package [1] based on pseudopotential and plane-wave techniques. We

employed the ultra-soft Vanderbilt pseudopotential and the generalized-gradient approximation. In order to find the minimum-energy structure, the system is first allowed to dynamically relax at a finite temperature for several picoseconds and is then cooled down to 0 K. After quenching, the structural optimization was performed.

To create a surface model, a bulk model containing 128 atoms is first prepared. The detailed procedure to create the bulk model was discussed in Ref. 2. We found that the structural properties of the bulk model are excellent agreement with experimental results [2]. Following this, two surfaces are produced by removing the periodic boundary condition in one direction. This surface model is annealed at 1200 K for 2 ns within the framework of a CMD to relax the surface atoms. The subsequent DFT calculations are performed using a supercell system; a slab (2.18 nm) and a vacuum layer (0.68 nm) are periodically repeated toward the z direction. The whole system is dynamically annealed at 840 K for 1 ps, and then is optimized by using a plane-wave cutoff energy of 225 eV and (2×2×1) k-grids. In the present work, we performed a total of 15 simulations.

2. Surface Energy and Surface Stress of a-Si

Using a CMD-DFT method, the surface energy γ of 1.05±0.14 J/m^2, and the surface stress f of 1.5±0.2 N/m, of a-Si are obtained. These results are averaged over 30 surfaces whose each surface area is equal to 1.21 nm^2. For comparison, the DFT results of s(001) 2×1 (γ =1.40 J/m^2, f_{xx}=0.7, f_{yy}=-1.1 N/m) and p(001) 2×2 (γ =1.28 J/m^2,f_{xx}=1.2, f_{yy}= 0.6 N/m) crystal surface are also provided. The f_{xx} and f_{yy} values for surface stress correspond to the component of the dimer bond and the dimer row direction, respectively. We find that the surface energy of a-Si is lower than those of (001) surfaces. It is noted that the surface stress of a-Si is positive and the scatter of surface stress is a factor of one higher than that of the surface energy.

3. Coordination Defects of a-Si Surface

In this section, we characterize the local structure of an individual threefold coordinated atom, which is the predominant coordination defect located in the surface region, by using the averaged value θ_{ave} of three bond angles around the atom. This parameter quantifies the sharpness of the vertical angle formed by the three back bonds. Interestingly, we find a distinct difference of the distribution of θ_{ave} between the CMD-DFT model and the CMD model. In the CMD-DFT model, two main peaks at approximately 100º and 120º are observed, while in the CMD model only one peak, at approximately 113º, is observed. The threefold coordinated atom of 100º will be referred to as a P1 type atom, and 120º as a P2 type atom. Fig. 1 provides a typical snapshot of the

a-Si surface containing both types of atom. The atomic geometries and contour plots of the valence electronic charge density are also presented in Fig. 1.

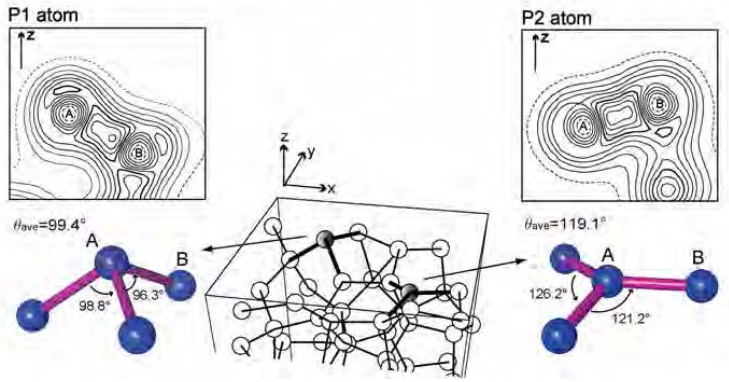

Fig. 1: Detailed diagram of two characteristic threefold-coordinated atoms (P1) with p^3-like bonding and (P2) with sp^2-like bonding. The corresponding contour plots of the valence electronic charge density on a plane, which is perpendicular to the surface and contains both A and B atoms, are also shown.

Clearly, it is shown that the P1 type atom has back bonds forming a sharp pyramidal geometry, while the P2 type atom has those lying on a plane. The respective atomic geometries deviate from the sp^3 tetrahedral bond angle (θ_{ave} = 109.5º). From an evaluation of the atomic geometries, it is proposed that the back bonding of the P1 atom is p^3-like bonding and that of the P2 atom is sp^2-like bonding. The difference in these bonding characteristics can be deduced from the electronic structure. Fig. 1 shows that, in the case of P1 atom, more charge is localized on the dangling bond site, as compared with the case of P2 atom. On the other hand, the CMD calculation cannot distinguish between these two types of atom. Brenner [3] pointed out that the Tersoff potential has a disadvantage in the intermediate bonding situation. Specifically, when the threefold coordinated atoms is bonded to the fourfold coordinated atoms, this potential yields the unphysical bond characteristics which is intermediate between sp^2 and sp^3 bonding. The appearance of only one peak would result from this disadvantage. As a result, the CMD-DFT method provides new findings of the microscopic features of a-Si surface.

References

[1] Kresse, G., and Hafner, J., "Ab initio molecular dynamics for liquid metals", Phys. Rev. B 47, 558-561 (1993).

[2] Izumi, S., Hara, S., Kumagai, T., and Sakai, S., "Classification of amorphous silicon microstructures by structural parameters: Molecular dynamics study", Comput. Mater. Sci. 39, (in press) (2004).

[3] Brenner, D. W., "Empirical potential for hydrocarbons for use in simulating the chemical vapor deposition of diamond films", Phys. Rev. B 42, 9458-9471 (1990)

Elastic Properties of Nanoplates: Electronic and Atomic Factors

L. G. Zhou [1], H. W. Shim [1], Hanchen Huang [1], and Timothy S. Cale [2]

[1] Department of Mechanical, Aerospace and Nuclear Engineering, [2] Department of Chemical and Biological Engineering, Rensselaer Polytechnic Institute, Troy, NY 12180 (e-mail: hanchen@rpi.edu)

ABSTRACT

The mechanical properties of nanostructures are very different from their macroscopic counterparts. Nanoplates deform elastically like regular crystalline solids. However, their elastic "constants" vary with thickness. Using Cu, W, Ti, and Si as prototypes, we have studied the elastic properties of face-center-cubic, body-center-cubic, hexagonal-close-packed, and diamond-cubic nanoplates. The study relies on classical molecular statics, based on either the embedded atom method potential or the bond order potential. Several calculations based on density functional theory serve to validate the classical calculations and to reveal the electron redistribution. Our calculations show that Young's modulus of nanoplates may increase or decrease with thickness. Decreases result from loss of bonds by surface atoms, and increases result from bond saturation. The competition of bond loss and bond competition dictates the magnitude of the Young's modulus. In diamond-cubic nanoplates, a third factor – surface reconstruction – may also result in increases or decreases in Young's modulus. Beyond the quantitative results, this study indicates that the mechanical properties of nanostructures are intimately related to the electronic nature and atomic restructuring of surfaces. A successful macroscopic description must take this electronic and atomic information into account when used to study nanostructures.

1. Introduction

The mechanical properties of nanostructures depend on electronic and atomic details at interfaces, in addition to geometry and bulk materials properties. Nanoplates and nanobeams, like nanotubes, will be key elements of the emerging nanotechnology. A single nanoplate is one of the simplest elements, and its mechanical response to static and dynamic loading is of both scientific and technological relevance. Under small static loading, the nanoplate deforms elastically. The Young's modulus along an in-plane direction is characteristic of the elastic deformation. The modulus is generally referred to as an elastic "constant", since it is a materials constant for macro or micro crystalline structures. This is not the case anymore for nanoplates.

A nanoplate consists of particles, each bonded to its nearest neighbors in a classical discrete representation. Near surfaces, each particle has several bonds missing. These missing bonds would have participated in resisting mechanical deformation. Effectively, surfaces are less stiff to mechanical deformation and thereby elastically softer. The surface to volume ratio of nanoplates is so large that surface effects dominate. Based on this observation, the elastic constants of nanoplates are not expected to be

constant, but depend on their thickness. More precisely, the elastic constants are expected to decrease with decreasing thickness. Indeed, experimental [1] and simulation [2] results do exist to support this reasoning. However, two important factors were left out of the above argument; electronic redistribution and atomic reconstruction on surfaces. These factors affect and even dictate the elastic properties of nanoplates. This paper summarizes our recent ab initio and classical molecular statics studies of nanoplate elasticity.

2. Calculation Method

For a nanoplate with two surfaces perpendicular to z axis of a Cartesian coordinate system, its potential energy as functions of strains along the x and y axes, $E(\varepsilon_x, \varepsilon_y)$, constitutes the energy surface. Because of the small thickness along z axis, stress is freely relaxed. For each strain ε_x, the strain energy has a minimum corresponding to a definite ε_y. Young's modulus is given by the curvature along the minimum energy path, viz $Y = \frac{1}{V}\frac{dE^2(\varepsilon_x)}{d\varepsilon_x^2}$. Here, V is the volume of the nanoplates; with the convention that each atomic layer occupies equal space on its two sides. The two strains are imposed on the atomic or nuclei positions, and the corresponding strain energy is determined by either classical molecular statics or ab initio calculations [3].

In a molecular statics calculation, the total energy is a function of atomic or nuclei positions. The electrons are assumed to distribute in accordance with the nuclei positions. This distribution reflects itself in the form of many-body interactions; the embedded atom method potential [4] for metals and the bond order potential [5] for diamond-cubic covalent silicon. At each strain set, ε_x and ε_y, the atomic configuration is relaxed to minimize the potential energy according the prescribed potential function. The molecular statics calculations are fast, but may suffer from inaccuracy and deserve validation. Ab initio calculations, based on density functional theory [6], are more accurate and serve to validate the molecular statics calculations. Based on density functional theory, the minimum energy corresponding to each configuration of nuclei is a unique functional of the electron density. This density is in turn determined by a single-electron Schrödinger equation in an effective potential field, which includes columbic, external, exchange, and correlation potentials. The self-consistent solution of the electron density leads to the minimum energy for a given nuclei configuration. Under an imposed strain, the energy will be minimized with respect to the nuclei positions as well. The relaxation of nuclei positions follows the classical Newtonian equation as in the molecular statics calculations. In addition to validating the molecular statics results, the ab initio calculations reveal how electrons redistribute near surfaces of nanoplates.

3. Results

As shown in Fig 1, the Young's modulus of a metal nanoplate may increase or decrease as its thickness goes down. For close-packed FCC and HCP metals, bond saturation makes it possible for the Young's modulus of a nanoplate to be larger than its bulk counterpart. This effect is confirmed by ab initio calculations. The higher electron

density that is responsible for the bond saturation is shown in the inset of Fig 1. For BCC metals, the bond saturation is insufficient to compensate the bond loss, leading to the Young's modulus of a nanoplate being smaller than its bulk counterpart. Similar effects of bond saturation and bond loss are seen in silicon nanoplates (Fig 2). Further, the surface reconstruction leads to substantial reduction of the Young's modulus of the silicon nanoplate.

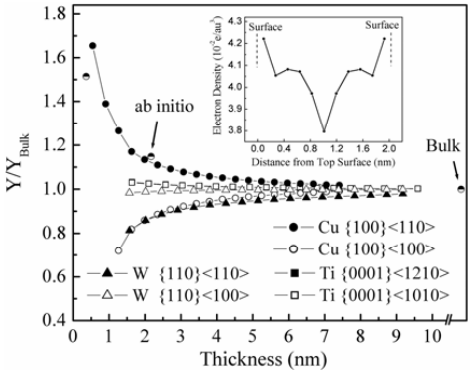

Fig 1: Young's modulus, normalized with respect to the bulk value; the inset shows the electron density perpendicular to the {100} surface of a Cu nanoplate.

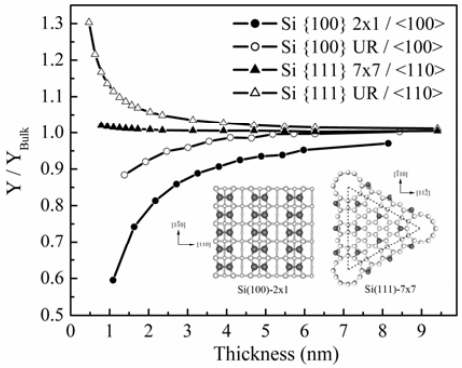

Fig 2: Young's modulus, normalized with respect to the bulk value, for reconstructed (2x1 and 7x7) and unreconstructed (UR) surfaces; the inset shows reconstructed surfaces.

4. Conclusions

Using a combination of molecular statics and ab initio calculations, we have shown that the Young's modulus of nanoplates depends on their thickness. The Young modulus may increase or decrease with the thickness, depending on the competition of bond loss and bond saturation at surfaces, and depending on the surface reconstruction.

Acknowledgements

The authors gratefully acknowledge financial support from Focus Center—New York, Rensselaer: Interconnections for Hyperintegration.

References:

[1] P. O. Renault, E. Le Bourhis, P. Villain, P. Goudeau, K. F. Badawi, and D. Faurie, Appl. Phys. Lett. 83, 473 (2003).
[2] R. E. Miller and V. B. Shenoy, Nanotechnology 11, 139 (2000).
[3] L. G. Zhou and H. C. Huang, Appl. Phys. Lett. 84, 1940 (2004).
[4] M. S. Daw and M. I. Baskes, Phys. Rev. Lett. 50, 1285 (1983).
[5] J. Tersoff, Phys. Rev. B 37, 6991 (1988).
[6] P. Hohenberg and W. Kohn, Phys. Rev. B 136, 864 (1964).

Analytic Solution of Particle Kinetics in Magnetron Sputtering

Moayyed Hussain, Mark Johnson, and Paul Cote

Benet Laboratories, 1 Buffington Street, Watervliet, NY 12189-4000
hussain@pica.army.mil, majohn@pica.army.mil, pcote@pica.army.mil

ABSTRACT

An analytic solution is developed for the particle kinetics in a magnetized DC discharge and compared to particle-in-cell simulation results. The solution provides guidance to engineers in the design of new experimental sputtering systems and in the selection of process control parameters that produce coatings with the desired properties.

1. Introduction

Adherent, erosion, and corrosion resistant coatings are critical to the performance of many systems. The U.S. Army Armament Research, Development, and Engineering Center's (ARDEC's) Benet Laboratories is currently developing a cylindrical magnetron sputtering (CMS) process to coat the bore of large caliber cannons in order to extend service life. A sputtered coating is generated by material that has been dislodged from a cathode target by an ionized gas species accelerated across a voltage gradient. The production of the ionized gas species is maintained by the emission of electrons upon impact by the ions, resulting in a self-sustaining DC discharge. Sputtering efficiency is greatly enhanced when these electrons are confined using magnetic fields [1]. The configuration of magnets required to produce coatings with the desired properties is determined by the magnetic fields that confine the electrons along the flux lines.

2. Approach

An analytic solution has been developed for the particle kinetics and compared to particle-in-cell (PIC) simulation results [2]. Velocity profiles of the particles were used to validate the proposed continuum solution. A simple geometry with three equally spaced magnets was simulated using typical parameters for a low pressure glow discharge.

3. Results

The analytic solution approximates the magnetic field as a set of Maxwell or Helmholtz coil pairs with current I. The magnetic field components, Br and Bz, at r and z, for a single coil located at z0 with radius, ρ using Biot-Savart law were employed [3]. The optimum Helmholtz coil consists of two coils of radii ρ placed at distance of ρ coaxially with current running in the same direction. The Maxwell pair consists of two coils of radii ρ placed at a distance of $\sqrt{3}\rho$ coaxially with current running in the opposite directions. Lieberman [1] explains magnetic mirroring, curvature drift, gradient drift using perturbation analysis. The complexity of the magnetic field in this work suggests that the plasma also exhibit these phenomena, however, unperturbed Lorentz equations were employed. E and B were coupled through Maxwell's equations and with $B_\theta = 0$ simplify in cylindrical coordinates to:

$$m\frac{\partial v_r}{\partial t} = qE_r + q(v_\theta B_z),\ m\frac{\partial v_\theta}{\partial t} = qE_\theta - q(v_r B_z - v_z B_r),\ m\frac{\partial v_z}{\partial t} = qE_z + q(-v_\theta B_r) \quad (1)$$

Eqs. (1) are coupled partial differential equations that can be solved with the method of lines. Particles in a DC discharge are subjected to a pressure field as well as various collisions. Low pressure was assumed where collisions in the continuum analysis could be neglected and ambipolar diffusion [1] was assumed in the plasma region. The solution of the diffusion equation for the particle density is given in terms of Bessel functions and trigonometric functions. The velocity field for the initial boundary conditions was taken as inversely proportional to particle density, assuming finite flux. A simple trigonometric function with a proper constant corresponding to initial kinetic energy was also assumed. Note that the magnetic field does no work on any particle; it only shifts the energy from one component to another. Eqs. (1) are non-dimensionalized with respect to the gyration frequency of particles, defined as $\omega_c = \frac{qB_0}{m}$. B_0 is taken at some representative plasma region. Assuming the E field has attained a constant steady state outside the sheath region, and non-dimensional time $\tau = \omega_c t$ is used, the non-homogeneous set of equations becomes:

$$\frac{\partial}{\partial \tau}\begin{bmatrix} v_r \\ v_\theta \\ v_z \end{bmatrix} = \begin{bmatrix} 0 & \frac{B_z}{B_0} & 0 \\ -\frac{B_z}{B_0} & & \frac{B_r}{B_0} \\ 0 & -\frac{B_r}{B_0} & 0 \end{bmatrix}\begin{bmatrix} v_r \\ v_\theta \\ v_z \end{bmatrix}, \quad \textit{or in vector form } \frac{\partial \overline{U}}{\partial t} = A\overline{U} \quad (2)$$

The form of eqs. (2) allows for the use of method of lines by discretizing along the spatial coordinates and using high order Runge_Kutta method along the time scale. Fig. 1 shows velocity profiles of the charged particles obtained from the integration in time. The results shown are typical and are comparable to particle-in-cell results to within a multiplicative constant depending upon the initial conditions taken for the method of lines solution for the Lorentz equations.

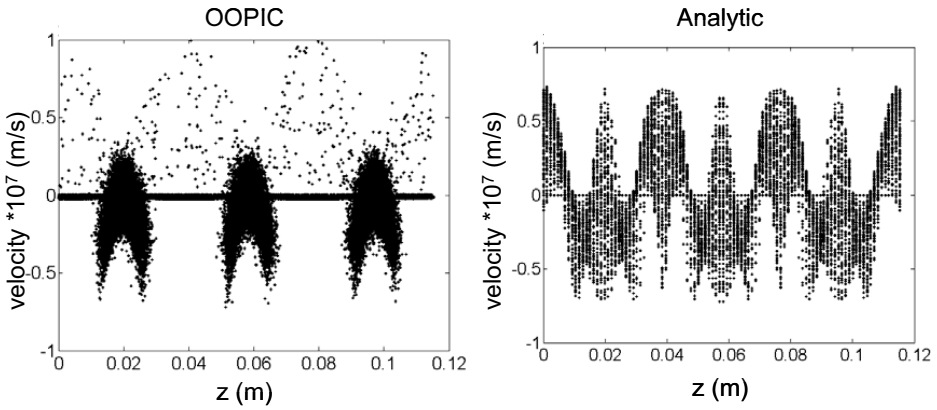

Figure 1. Velocity v_r vs. z for OOPIC and as obtained by the method of lines.

4. Conclusions

- The analysis of a magnetic field model using a Maxwell coil pair and method of lines solution of Lorentz equation produces results that are consistent with particle-in-cell simulations.

- An analytic magnetic field model is a useful tool for optimizing the magnetic configuration in a sputtering magnetron to produce coatings with the desired properties.

5. References

1. M.A. Lieberman and A.J. Lichtenberg, *Principles of Plasma Discharges and Materials Processing* (John Wiley & Sons, Inc. 1994)

2. J.P Verboncoeur, A.B. Langdon, and N.T. Gladd, *Comp. Phys. Comm.*, **87**, 199 (1995)

3. J.A. Stratton, *Electromagnetic Theory* (McGraw-Hill Book Company, Inc. 1941)

464 A uniform methodology for the implementation of large-scale scientific simulations based on the ψ-calculus *

James E. Raynolds†
School of NanoSciences and NanoEngineering, University at Albany, State University of New York, Albany, NY 12203

Lenore R. Mullin
Department of Computer Science, University at Albany, State University of New York, Albany, NY 12203
(Dated: September 1, 2004)

The complexity inherent in software for large-scale scientific computational problems poses significant challenges and often demands the concerted effort of collaborative groups over multi-year development times. A new discipline is emerging to handle the complexity of large computational problems through the use of a systematic design protocol based on the rigorous mathematical formalism of the ψ-calculus and Mathematics of Arrays. Success has been achieved through the application of these techniques to a number of algorithms that are ubiquitous across science and engineering disciplines, such as the Fast Fourier Transform (FFT), LU decomposition, matrix multiplication, time domain convolution, etc. In this paper the FFT serves as an example.

Large-scale scientific computational codes are generally developed by collaborative groups over multi-year development times. Traditionally the fruits of such efforts, large computational programs (e.g. electronic structure codes based on the Density Functional Theory), were treated as trade secrets accessible only to a select group of researchers closely involved with the development efforts. In recent years, however, the culture has been changing. A number of groups have made their software (executable and source code) freely available to the world via the internet, the philosophy being that the benefits of sharing the codes (every one has access to the development efforts of everyone else) outweigh the professional advantage that any one group can maintain by keeping their codes secret.

The developers of such large codes must understand both the application (the science, the mathematics, the realization of the mathematics in software) and the architectural platforms to which the application software is mapped. Mapped in this context implies the exploitation of computer resources, i.e. processor and memory hierarchies in a general, uniform algebraic way. Such exploitation must guarantee the highest performance, and the largest problem sizes given processor/memory constraints. Furthermore, for device applications such as in the field of digital signal processing and embedded systems, the computation should consume the least amount of energy and produce the least amount of heat.

As advances in engineering physics continues to miniaturize circuitry, larger processor memory configurations will emerge. Consequently, the need to deterministically, accurately predict performance will grow. Determinism is difficult given that today's compilers lack operational equivalence, i.e. two semantically and syntactically equivalent programs will not likely have the same executable codes on the same machine and operating system when compiled by two different compilers. Also, they remove the *intent* of the mathematics through *scalarization* of monolithic structures in the software, i.e. matrix, array, tensor, operations in languages such as F90 or Matlab. For example, in radar we might say: $QR(FFT(TD(X)))$, i.e. beamforming, filtering, then QR decomposition. If each operation is scalarized and done separately, loops and scalars are produced, distributions are done separately, and communications must redistribute data for the next operation. That is, $FFT(temp)$ is performed after $temp = TD(X)$. When multiple processors are available a pipeline of these functions is kept full, while such communications are going on. Our methods compose the entire expression without the creation of temporary arrays. Distributions are minimized as determined by the normal form produced from ψ-reduction (to be discussed below).

Operating systems have similar operational anomalies even when there is a semantic (or even worse semantic and syntactic) equivalence in terms of ANSI written software using existing computer science and software engineering methods. Initially, operating systems were written in the language of the machine. Today, they are written in languages such as C, thus relying on a compiler for optimizations and the reliable use of machine instructions. Unfortunately, it is quite possible that in certain cases a computer architecture's finest hardware components are not even used by a compiler.

A new discipline, which the authors have named Conformal Computing, is emerging to handle the complexity of large computational problems through the use of a systematic design protocol based on the rigorous mathematical formalism of the ψ-calculus and Mathematics of Arrays (MoA) [1]. MoA is based on Joseph Sylvester's Universal Algebra [2], reintroduced by Iverson. So powerful was the notation that it was the basis for a popu-

lar programming language (APL)[3] and subsequent machine design[4] which introduced indexing using shapes, the beginnings of the ψ-calculus. Unfortunately, the language had too many anomalies [5] to use as a formal mathematical tool. Similarly, closure was not obtained for Abram's indexing rules despite 10+ years of research [6–10].

Mullin's introduction of MoA and ψ-calculus removed all anomalies in both and put closure on Abrams's indexing ideas using the indexing function, ψ. She also combined MoA and ψ-calculus with the λ-calculus [11] to achieve full reasoning capabilities computationally building upon recommendations from Perlis [12], Berkling [13], and Budd [14]. Together these theories are used to describe a patent for sparse array caching [15].

Using our algebraic approach together with an index calculus, an analysis is done globally so that intent (data flow, access patterns, distributions) is know prior to scalarization. That is, an expression is algebraically reformulated to include processor/memory hierarchies, and distributions. Then, expressions are ψ-reduced (to be discussed below) to reveal loop nests. Note that the dimension of the new abstracted array is increased by the number of processor/memories. The new shape of the abstracted array is created by partitioning the shape of the original array.

During ψ-reduction, indices are composed to a *normal form* using shapes to define all functions and operations: e.g. transpose, shift, reverse, rotate, and higher order operations such as inner and outer product, as well as any user defined functions (or operations); all compose. This *normal form* details how to index the original array arguments without the need for intermediate (temporary) arrays, commonly produced in today's programming languages. A nice side effect of ψ-reduction is that when two expressions yield the same *normal form* they are equivalent.

Success has been achieved through the application of Conformal Computing (CC) techniques to a number of algorithms that are ubiquitous across science and engineering disciplines, such as the Fast Fourier Transform (FFT) [16], LU decomposition [17], matrix multiplication, Time Domain convolution, QR decomposition [18, 19], etc. That is to say, these and other algorithms were first expressed algebraically using MoA. Then through ψ-reduction to a normal form, all expressions defining the algorithms were optimized to eliminate all intermediate arrays. These designs were realized in both hardware and software [20–27].

Intermediate or temporary arrays cause an enormous amount of overhead especially when parallel/distributed computing is desired. Current compilers do not know how to remove them in a general way. For example, in an expression such as $(A + B^T)^T$, all known languages create a temporary after the B^T, then another after $A + B^T$, then another after $(A + B^T)^T$. When loop nests are revealed to a compiler, the compiler is more likely to be able to exploit the hardware it targets. That is, it can simply translate.

We now use the above example to illustrate the process of ψ-reduction. The function ψ is the indexing function and its use lies at the heart of the ψ calculus. For an abstract array: A, ψ is used to extract the components of the array. For example we write $< i\ j > \psi A \equiv A[i, j]$, where for the purpose of illustration, we use C++ notation for the array element $A[i, j]$ on the right hand side of the equivalence. As another example, consider the transpose of A: A^T. The components of A^T are given by $< i\ j > \psi A^T \equiv A[j, i]$.

Now we continue with the example introduced two paragraphs ago with emphasis on consideration of the shapes of the arrays. Suppose the shape of A is $< m\ n >$ (i.e. A is an m by n matrix) and the shape of B is $< n\ m >$ (i.e. we say that the shape of B is the *reversal* of the shape of A). Thus the shape of $(A + B^T)^T$ is the reversal of the shape of $A + B^T$. This is determined from the reversal of the shape of A or the reversal of the shape of B^T since their shapes must be conformable for binary scalar operations: $< n\ m >$. Then by ψ-reduction:
$\forall\ i, j \quad < i\ j > \psi(A + B^T)^T \equiv (< j\ i > \psi A) + (< j\ i > \psi B^T)$ which is $(< j\ i > \psi A) + (< i\ j > \psi B)$. Then using the Psi Correspondence Theorem (PCT) [28], we can turn this denotational normal form (DNF) to its operational normal form (ONF) based on layout, i.e. starts, stops, and strides, independent of dimension.

We can then use the MoA algebra to characterize processor memory hierarchies, i.e. mapping functions. That is, we algebraically restructure the array expressions by lifting the dimension to as many processor memory levels as we like. In this simple example, if A and B are 2-dimensional arrays, adding processors and a cache would lift the dimension (algebraically) to 4 and we would know the strides between components prior to compilation and execution.

We now turn our attention to a study of the one-dimensional FFT, an important algorithm used throughout scientific and engineering disciplines, using the techniques of Conformal Computing. Furthermore, knowing we can *compose* this algorithm algebraically with others (e.g. with LU Decomposition, Gauss Seidel, etc.) and also knowing that we can algebraically describe how to map this and other algorithms to multiple processor memory hierarchies, enables our theory to transcend numerous vital scientific disciplines to achieve high performance, correctness, scalability, and portability using *a uniform* framework. Our results for the one-dimensional FFT in comparison with several well-tested routines on NCSA's Origin 2000 are summarized in Table I.

Ongoing research is focused on the development of a generalized platform-independent, multi-dimensional FFT that utilizes the most-efficient mapping to the underlying hardware (cache, processors, etc.) through the

466 use of Conformal Computing techniques. Presently, our 1-d design supports any radix. Experiments and theory indicate that based on a cache's associativity, a radix other than 2 may be more appropriate, i.e. a power of 2 assuming that the 1-d string is a power of 2. A processor loop has also been designed and built. A cache loop design is complete. When used with an n-dimensional fft, each of these parameters may be analyzed and fine-tuned.

---

† Electronic address: jraynolds@uamail.albany.edu

[1] L. M. R. Mullin, A Mathematics of Arrays, Ph.D. Thesis, Syracuse University, December 1988.

[2] J. Sylvester, in *American Journal of Mathematics: VI* (reprinted in Mathematical Papers, 1884), vol. 4.

[3] K. E. Iverson, *A Programming Language* (Wiley, New York, 1962).

[4] P. S. Abrams, Ph.D. thesis, Stanford University (1970).

[5] S. Gerhart, Ph.D. thesis, CMU (1972).

[6] A. Hassitt and L. E. Lyon, IBM Journal of Research and Development **16**, 45 (1972).

[7] L. J. Guibas and D. K. Wyatt, in *Conference Record of the Fifth Annual ACM Symposium o n Principles of Programming Languages* (1978), pp. 1–8.

[8] T. Miller, Tech. Rep. 133, Yale University (1979).

[9] A. Perlis, Tech. Rep. 24, Yale University (1975).

[10] T. A. Budd, ACM Transactions on Programming Languages and Systems **6**, 297 (1984), ISSN 0164-0925.

[11] L. R. Mullin, in *Arrays, Functional Languages, and Parallel Systems* (Kluwer Academic Publishers, 1991).

[12] H.-C. Tu and A. J. Perlis, IEEE Software **3**, 36 (1986).

[13] K. Berkling, Tech. Rep., CASE Center and School of CIS, Syracuse University (1990).

[14] T. Budd, Arrays, Functional Languages and Parallel Systems (1991).

[15] L. Mullin, D. Moran, and D. Dooling, *Method and apparatus for indexing patterned sparse arrays for microprocessor data cache*, US Patent No. 5878424 (1999).

[16] L. R. Mullin and S. G. Small, Journal of Mathematical Modelling and Algorithms **1**, 193 (2002).

[17] D. Dooling and L. Mullin, Proceedings of the Workshop on Solving Irregular Problems on Distributed Memory Machines (1995).

[18] L. Mullin, Digital Signal Processing (to appear).

[19] L. R. Mullin, D. J. Rosenkrantz, H. B. Hunt III, and X. Luo, in *Proceedings First Workshop on Optimizations for DSP and Embedded Systems (ODES)* (San Francisco, CA, 2003), pp. 1–12.

[20] N. Belanger, L. Mullin, and Y. Savaria, in *ATABLE92* (Universite d'Montreal, 1992).

[21] H. Pottinger, W. Eatherton, J. Kelly, L. Mullin, and R. Ziegler, in *Proceedings of the IEEE Circuits and Systems Sympos ium ISCAS95* (1995).

[22] H. Pottinger, W. Eatherton, J. Kelly, L. Mullin, and T. Schifelbein, in *Proceedings of INEL94* (1994).

[23] L. Mullin, E. Rutledge, and R. Bond, in *Proceedings of the High Performance Embedded Computing Workshop HPEC 2002* (MIT Lincoln Laboratory, Lexington, MA, 2002).

[24] T. McMahon, *Mathematical formulation of general partitioning of multi-dimensional arrays to multi-dimensional architectures using the Psi calculus* (1995), undergraduate Honors Thesis.

[25] M. A. Helal, Master's thesis, The American University in Cairo, Department of Computer Science (2001).

[26] L. Mullin and T. McMahon, Tech. Rep. CSC 94-05, University of Missouri-Rolla (1994).

[27] L. Mullin, W. Kluge, and S. Scholtz, in *Proceedings of the 8th International Workshop on Implementation of Functional Languages, Bonn, Germany* (1996).

[28] L. Mullin and M. Jenkins, Concurrency – Practice and Experience (1996).

Tables

Origin 2000					
Size	CC routine	IMSL	NAG	SCSL	FFTW
2^3	0.190	0.064	0.010	0.065	0.013
2^4	0.018	0.061	0.010	0.047	0.013
2^5	0.018	0.062	0.010	0.065	0.014
2^6	0.017	0.116	0.011	0.073	0.013
2^7	0.019	0.063	0.010	0.068	0.015
2^8	0.018	0.062	0.011	0.105	0.014
2^9	0.017	0.122	0.011	0.069	0.014
2^{10}	0.021	0.065	0.013	0.056	0.015
2^{11}	0.021	0.064	0.016	0.058	0.017
2^{12}	0.021	0.067	0.023	0.067	0.023
2^{13}	0.022	0.075	0.036	0.065	0.030
2^{14}	0.024	0.144	0.065	0.066	0.051
2^{15}	0.030	0.120	0.135	0.110	0.082
2^{16}	0.040	0.209	0.296	0.080	0.189
2^{17}	0.065	0.335	0.696	0.072	0.395
2^{18}	0.126	0.829	3.205	0.075	0.774
2^{19}	0.238	3.007	9.538	0.096	2.186
2^{20}	0.442	9.673	18.40	0.143	4.611
2^{21}	0.884	23.36	38.93	0.260	9.191
2^{22}	1.910	46.70	92.75	0.396	19.19
2^{23}	4.014	109.4	187.7	0.671	48.69
2^{24}	7.550	221.1	442.7	1.396	99.10

TABLE I: Real Execution Times(seconds) of the CC routine, comparative libraries and FFTW on NCSA's SGI/CRAY Origin 2000.

"Non-vacancy" Self-diffusion in Two-dimensional Metals

G.M. Poletaev[a] , M.D. Starostenkov[a], J.V. Patzeva [a]

[a]General Physics Deptartment, Altai State Technical University, Lenin st. 46, 656038, Barnaul, Russia, genphys@agtu.secna.ru;

ABSTRACT

The paper is concerned with the research of leading "non-vacancy" mechanisms of self-diffusion in two-dimensional metals. "Non-vacancy" mechanisms of self-diffusion are understood as mechanisms, which are not connected with vacancies, formed by Shottki method. It is found that self-diffusion mechanisms in ideal two-dimensional crystal are interchange cyclic mechanisms. They contain from three to several dozens of atoms in their cycle. It is concluded that main "non-vacancy" mechanism is formation and annihilation of Frenkel pairs. Frenkel pair forms in the result of crossing of two crawdion displacements.

1. Introduction

It is known that the most wide-spread mechanism of self-diffusion in metals is vacancy mechanism. But there are also "non-vacancy" mechanisms, which have higher activation energy than vacancy mechanism and take part in a general process of diffusion. In this work, "non-vacancy" mechanisms are mechanisms, which are not connected with vacancies, formed by Shottki method. Among these are: exchange two-atomic, exchange cyclic, crawdion, migration of atoms at interstitials [1].

The research of the contribution of every mechanism into the general process of diffusion by direct experiments is a difficult task. In this case, the most useful are the methods of computer simulation, in particular, the method of molecular dynamics. The present paper is devoted to the study of the fundamental "non-vacancy" mechanisms of self-diffusion in two-dimensional metals and their contribution into the general process of diffusion by the method of molecular dynamics.

The researches were made for metals Ni, Al and Cu. The packing of two-dimensional metals under study was corresponded to the plane (111) of FCC lattice. To describe interatomic interactions, pair Morse potentials were used. The interactions of atoms were limited by the distance 8 A°. Periodical boundary conditions were applied at the boundaries of the calculated block. The number of atoms in the calculated block did not exceed 10^4. The temperature was given by the initial velocities of atoms: every atom of the calculated block had the initial velocity equal to root-mean-square velocity in correspondence with Maxwell distribution multiplied by $\sqrt{2}$. The directions of the velocities were given as accidental ones, but on condition that total impulse of atoms in the calculated block was to be equal to zero. The temporal step of recalculation of movement equations in the method of molecular dynamics was equal to 10^{-14} seconds.

2. The Fundamental "Non-vacancy" Mechanism of Self-diffusion in 2D Metals

To clarify the fundamental "non-vacancy" mechanism of diffusion in two-dimensional metals, the calculated blocks with the structure of ideal crystals were

heated to pre-melting temperatures. Then, the dynamical relaxation was made at the given temperature during some time. The calculated block was cooled to 0 K after the relaxation. The displacements and trajectories of diffusion jumps of atoms relatively the initial positions were studied.

It was found that the fundamental "non-vacancy" mechanism of self-diffusion is cyclic mechanism, which can contain from three to several dozens of atoms in its cycle. Similar displacements of atoms are possible as a result of the formation and the subsequent annihilation of Frenkel pairs. However, it is worth to note that the probability of discovering a Frenkel pairs in the cooled metal under study is very small. The vacancy and the interstitial atom form at small distance from each other. To discover Frenkel pair, long-term experiments and heating of the metals to high temperatures (higher than melting temperatures) are required. To know the mechanism of Frenkel pair formation, it is necessary to take into consideration the nature of crawdions.

The atoms oscillate not randomly in the heated metals – they take part in so-called thermal collective atomic displacements (TCAD) [2]. TCADs are oriented advantageously along closely packed directions and it is the cause of crawdion displacements of atoms. Fig.1 depicts the picture of atomic displacements in a two-dimensional Cu in the moment of time 1.22 ps at the temperature 1300 K. The arrow shows the direction of the displacement of one atom in crawdion, provoked by TCAD, to the position of neighbouring site (the area of the site is given conditionally). But it does not mean that it is the formation of Frenkel pair. The point is that, the positions of equilibrium of atoms also displace in TCAD. The atom in the centre of TCAD has the biggest displacement and in this case, the displacement nearly reaches the value of interatomic distance. The atom returns to the former place when "recoil" of TCAD (and also the crawdion) takes place.

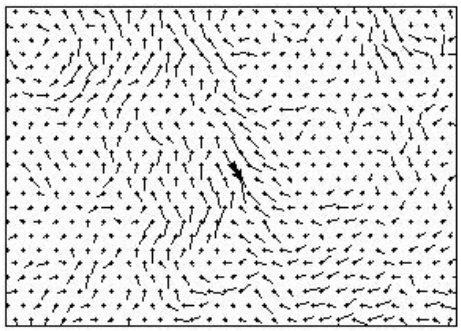

Fig.1. The displacement of the atom in TCAD to the position of the neighbouring site (the direction of the displacement is shown by the arrow) in two-dimensional Cu in the moment of time 1.22 ps at the temperature 1300 K. The displacements of atoms, increased in 3 times, are shown by the segments.

The formation of Frenkel pair, provoking multiatomic cyclic mechanisms, can be seen from Fig.2. Fig.2 shows the trajectories of diffusion jumps of atoms. It can be clearly seen that cyclic displacements of atoms have "tails", representing crawdion "recoils".

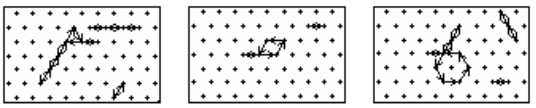

Fig.2. The trajectories of diffusion jumps of atoms: a) the formation of three-atomic cyclic mechanism; b) four-atomic; c) six-atomic.

Frenkel pair, provoking cyclic mechanisms of diffusion, is formed by two crawdions at the least. Fig.3 shows the process of the formation of such pair and the subsequent annihilation schematically.

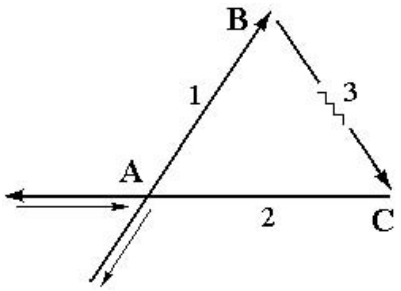

Fig.3. Schematic view of the process of the formation and annihilation of Frenkel pair, provoking a cyclic mechanism of diffusion. Thick arrows mark crawdions, thin arrows mark "recoils". The zigzag line shows that displacements of atoms on the way 3 can change direction.

First, crawdion displacement (TCAD) occurs; it is marked by the figure 1 in Fig.5. The first crawdion is not able to form Frenkel pair independently, it is important that it forms a free volume in the area, marked by the letter *A*. Then, the crawdion 2 (another TCAD) crosses the first crawdion in the area *A*. In other words, the intersection of TCADs take place. If surplus free volume in the area *A* and the power of the second crawdion are sufficient, "the blocking" of the first crawdion occurs. The crystal lattice near the area *A* restores, but "the cut off" parts of crawdions suffer reverse "recoils". Thus, an interstitial atom appears in the region of the area *B*, the vacancy in the area *C*. The distance between the areas *B* and *C* is small, that is why the annihilation of Frenkel pair takes place rapidly in the way 3. Besides, the trajectory 3 can have broken view because thermal movements of atoms can be constantly observed and Frenkel pair can take place not only in one closely packed atomic row.

Rarely, Frenkel pair can spread at big distance at high temperatures (near melting temperature) and annihilation does not occur. The diffusion mechanism is open-ended, and the vacancy and interstitial atom contribute in self-diffusion separately.

References

[1] Bokshtein B.S. *Diffusion in metals*, Moscow: Metallurgiya, 1978, 248 p.
[2] Poletaev G.M., Starostenkov M.D., Patzeva J.V., *Fundamental'nye problemy sovremennogo materialovedenia*, 2004, ¹1, pp.147 -151.

Relaxation of Two-dimensional Al and Ni_3Al Crystal Structures at the Impulsive Heating

M.D. Starostenkov[a], G.M. Poletaev[a], M.S. Aksenov[a], I.A. Dyomina[b]

[a]General Physics Deptartment, Altai State Technical University, Lenin st. 46, 656038, Barnaul, Russia, genphys@agtu.secna.ru;
[b]East-Kazakhstan State University, Serikbaeva st. 19, 492010, Ust-Kamenogorsk, Kazakhstan, pr1@bipek.kz

ABSTRACT

The consequences of an impulsive thermal initiation of separate atoms in the crystal lattice of two-dimensional Al and Ni_3Al systems are studied by the method of molecular dynamics. Thermal impulse of the definite energy is given to the separate atom. It is found that relaxation of the crystal of pure Al occurs with the appearance of concentric elastic acoustic waves with longitudinal and cross components. The velocities of dynamical displacements of atoms are close to the velocity of sound in Al. The interactions of elastic waves in two-dimensional crystal of Ni_3Al intermetallide with point defects (vacancies and interstitial atoms) are studied. It is obtained that the additional cross waves appear in this case.

1. Introduction

The present paper deals with the study of the distribution of locally initiated elastic waves in two-dimensional crystals Al and Ni_3Al by the method of molecular dynamics. The purpose of the research is in the development of the presentations on the dynamics of the elastic waves in the crystals of metals. The molecular dynamics method allows studying a general picture of the atomic displacements in a crystal by special visualizators. It takes place at different stages of the distribution of elastic waves after small time intervals of 10^{-14} seconds order. In this connection, the method of molecular dynamics is more preferable in comparison with the other methods.

The study of the dynamics of the elastic wave distribution in three-dimensional crystals is connected with the difficulty of the visualization of atomic displacements. That is why two-dimensional model is selected as the subject for study.

The packing of atoms of the calculated crystal block was corresponded to the plane (111) of the FCC lattice. The interactions between atoms were given by the sets of pair Morse potentials. The parameters of the potentials of the interactions Al-Al, Ni-Ni and Ni-Al were taken from the paper [1]. The given potential was approved to know if it was corresponded with the value of volume module of elasticity, lattice parameter and temperature coefficient of linear expansion.

The relaxation of the investigating systems was held by the method of molecular dynamics. The displacements of atoms in the calculated block were obtained by the solving of ordinary differential equations of Newton's movement. The interactions of atoms were limited by the distance 8 A°. The temporal step of recalculation of movement equations system was equal to 10^{-14} seconds. The calculated block in the

experiments contained about 4000 atoms. Strict conditions were applied to the boundaries of the calculated block.

Local impulsive heating was produced by the impulse, which was applied to one or several atoms in the centre of the calculated block (by given some initial velocity to this atoms). The value of the initial velocity was varied from 1000 m/s to 8000 m/s (the impulse was weak enough and could not initiate the jump of the atom into the interstice).

The dynamics of the elastic waves distribution was studied by the displacements of atoms relatively to their initial positions. The computer experiment was stopped, when the elastic waves began to reflect from the boundaries of the calculated block. The dynamics of the elastic waves distribution was investigated by the visualizator of the atomic displacements at different moments of time.

2. Results and Discussion

Fig.1 shows the atomic displacements in two-dimensional Al, observed at the moment of time 1.5 ps relatively to the beginning of the experiment. The impulse is given to one of the atoms along the closely packed direction. As shown in Fig.1, cross waves spread perpendicular to the direction of the impulse. The atomic displacements caused by the movement of the longitudinal waves can be seen around the front of the cross waves. It is worth to note that cross waves serve as the sources of the appearing of longitudinal waves, distributing perpendicular to the impulse direction.

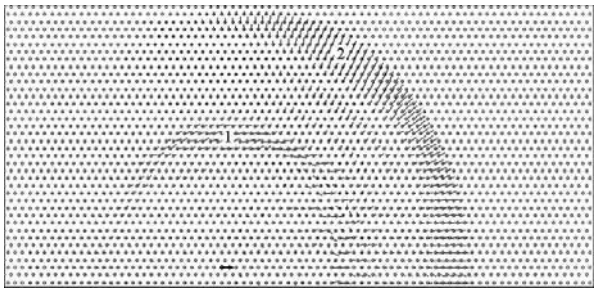

Fig.1. The picture of the atomic displacements in two-dimensional Al at the moment of time 1.5 ps relatively to the beginning of the experiment (the scale 30:1). The value of the initial velocity is equal to 3000 m/s. The cross waves – 1, the longitudinal waves – 2. The place and the direction of the initial impulse are marked by the arrow. The picture of atomic displacements is symmetric relatively the direction of the initial impulse.

The velocities of the distribution of cross and longitudinal waves in the crystal are measured. In this molecular-dynamics model, they are equal to ~6000 m/s and ~3000 m/s correspondingly independent on the direction of the initial impulse and the direction of the wave distribution. These values are well agreed with the reference sources for the real Al [2]: 6260 m/s and 3080 m/s.

The distribution of longitudinal and cross acoustic waves in two-dimensional Ni_3Al intermetallide at similar initiation has an analogous picture. It is difficult to

determine an optical mode by the visualizator of atomic displacements because of weak expression in comparison with acoustic mode.

Studying the interaction of the acoustic waves with point defects in two-dimensional Ni_3Al, the vacancy and interstitial atom were introduced. The defects were put on the way of the distribution of elastic waves at some distance from the atom, to which the initial impulse was given. It was determined that the additional cross waves appeared in the calculated block in both cases because of the interaction of elastic waves with the defect. Fig.2 show typical pictures of the atomic displacements in the cases of interaction of the waves with the vacancies (Fig.2a) and interstitial atom (Fig.2b).

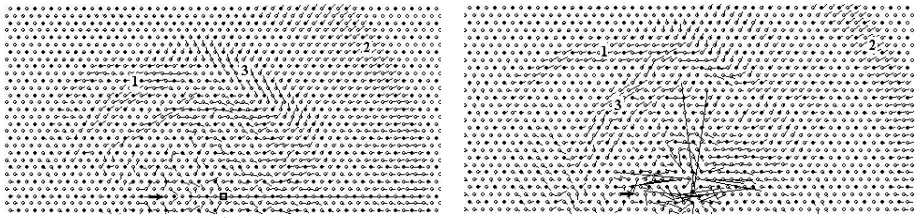

a) b)

Fig.2. The picture of the atomic displacements in two-dimensional Ni_3Al in the case of interaction of elastic waves with: a) vacancy (it is shown by square) at the moment of time 1.42 ps; the value of the initial velocity of the pushed atom 5500 m/s; b) interstitial Al atom at the moment of time 1.5 ps; the value of the initial velocity 4000 m/s. The initial cross waves – 1; initial longitudinal waves – 2; cross waves, formed in the result of interaction of the initial wave with the defect – 3.

As it can be seen from Fig.2, the orientations of additional cross waves are different at the interaction with vacancy and interstitial atom. When waves interact with a vacancy, additional cross waves are formed mainly before the defect; when the waves interact with an interstitial atom – mainly after the defect. However, the directions of the distribution of the initial cross wave and the wave formed as the result of the interaction with the defect differ by the angle 60° in both cases.

Thus, the transport of energy in two-dimensional metals and alloys at an impulsive heating takes place by elastic longitudinal and cross waves. The additional cross waves appear at the interaction of waves with point defects. In this connection, the initial longitudinal waves are not nearly changed.

References

[1] A.I. Tzaregorodtsev, N.V. Gorlov, B.F. Demyanov, M.D. Starostenkov, *Fizika Metallov i Metallovedeniye* (Russia), Vol. 58, 2 (1984), pp.336-343.

[2] *Ultrasound. Small encyclopedia*: under the edition of I.P. Golyamin, Moscow: "Sovetskaya encyclopedia", Russia, 1979, 400 p.

The Research of the Combustion Synthesis Process in Two-dimensional Crystals of Ni-Al System

M.D. Starostenkov[a], G.M. Poletaev[a], G.V. Popova[b]

[a]General Physics Deptartment, Altai State Technical University, Lenin st. 46, 656038, Barnaul, Russia, genphys@agtu.secna.ru;
[b]East-Kazakhstan State University, 30-Gvardejskoi Divizii, 492010, Ust-Kamenogorsk, Kazakhstan, pr1@bipek.kz

ABSTRACT

The peculiarities of the combustion synthesis reaction in two-dimensional crystals Ni-Al were studied by the method of molecular dynamics. The interactions between different pairs of atoms were given by the sets of empirical pair potentials. The particles of Ni and Al metals had different forms and structures. It was held the heating of the bimetal to the temperatures 400-600 K in the dependence on the presence of a free volume. The computer experiment determined the number of new diffusion mechanisms, taking place at microscopic atomic level, at high temperatures and velocities, corresponding to the combustion reaction.

1. Introduction

The present paper deals with the reaction of combustion synthesis, taking place in a two-dimensional crystal of Ni-Al system. The investigation is concerned with a thin film of Ni two-dimensional matrix crystal, Al particle of different forms and sizes is inserted in the crystal. The stages of combustion synthesis in the dependence on the presence of a free volume are studied in the paper. Free volume is introduced by the definite amount of vacancies situated near the boundary of the division of phases. Earlier, similar researches were made under conditions of the introduction of Ni particle in Al two-dimensional crystal [1].

2. The method of the experiment

The calculated block of bicrystal was presented by the packing of 10^4 atoms corresponding to the plane (111) of FCC lattice. The interactions between different pairs of atoms were given by Morse interatomic potentials, taking into account the bonds in the first six coordination spheres. The crystal was repeated by the introduction of periodical boundary conditions outside the calculated block. Al particle inserted in Ni matrix was given in a form of parallelogram, square and hexagon. Pure metals of Ni and Al had different temperature coefficient of a linear expansion and effective sizes of atoms (effective size of Al atom is bigger on 12% than size of Ni atom). That is why the system was heated impulsively to the temperature 10 K after the end of the procedure of a bicrystal relaxation. The system was subjected to the impulsive heating during the definite time of a computer experiment. Then, it was rapidly cooled to 0 K. The dynamical reconstruction of the system was carried out by the method of molecular dynamics. The velocities of the

displacements of atoms at the definite temperature were given by Boltzman distribution [2].

3. The results of the experiments

First of all, Al particles were introduced in the block of Ni crystal matrix. The packing of the crystal matrix and Al particle was ideal. Point defects and free volume were absent. In such conditions, the beginning of the structural reconstruction at the impulsive heating depended on the form and size of Al particle. For example, structural reconstruction for Al particle of hexagon form, consisting of 7 atoms began at the temperature 1750 K. Diffusion displacements of atoms were found only in Ni matrix. Main mechanisms of diffusion are the following: crawdion, ring and the formation of Frenckel pair, representing vacancy and interstitial atom. The beginning of the diffusion by ring and crawdion mechanisms in the case of Al particle of hexagonal form, consisting of 19 atoms was found at the temperature 1650 K. Point defects were not formed in the process of diffusion. When the sizes of the particles were big, the temperature of the beginning of structural reconstruction decreased (as for example, the beginning of reconstruction of the particle, consisting of 217 atoms took place at the temperature 450 K). In this connection, dislocations of discrepancy appeared inside the particle. The collective thermal displacements of Ni atoms in the matrix took place along closely-packed directions. When the sizes of Al particle were small (7 atoms), elastic field connected with different effective sizes of Ni and Al atoms led to the appearance of the pair of point defects (vacancy and interstitial atom). Structural reconstruction of bicrystal, stipulated by the presence of elastic fields at the phase boundaries with the increasing of the size of Al particle, led to a plastic deformation of Al particle and the appearance of dislocations of discrepancy. For all particles independent of their sizes, a diffusion process of interaction developed by different mechanisms in the limits of temperature 1500-1700 K. As a result, the germs and clusters of intermetallic phases $NiAl_3$, $NiAl_2$, NiAl, Ni_2Al and Ni_3Al were appeared. The release of energy and the increase of the temperature of the calculated block, typical for CS reaction, took place.

The introduction of one vacancy in the bicrystal led to sharp decrease of temperature of the beginning of diffusion processes. For hexagonal Al particle, consisting of 7 atoms, the temperature of the beginning of diffusion process was equal to 1000 K at the introduction of a vacancy in Al particle. In this connection, the vacancy displaced to the center of the particle. The introduction of a vacancy in interphase boundary of Ni matrix caused the beginning of diffusion process at the temperature 900 K. The vacancy displaced to the center of Al particle once again. The presence of a vacancy in Ni matrix in the second-fourth neighborhood from interphase boundary led to the beginning of diffusion process at the temperature 950-1300 K, and the vacancy displaced to the center of Al particle once again. When a vacancy was situated in more distant neighborhood in the limits of the given time interval of a computer experiment, the displacement of the vacancy was not sensible to the presence of Al particle. The vacancy displaced to more remote neighborhood from interphase boundary. In all the cases, the diffusion was observed only in Ni matrix. Main diffusion mechanisms were crawdion and ring. With the increase of the size of

Al particle, in particular, the realization of the initial stage of structure reconstruction, two factors began to compete: the presence of the vacancy and dislocation of discrepancy, connected with the difference of lattice's parameters of Al and Ni phases. The experiment showed that vacancies could introduce an independent factor in diffusion reconstruction of the bicrystal. It was realized in the case, when the vacancy was situated in Ni matrix and took part in a structural reconstruction of the system at the expense of the interaction with dislocation cores. In such situations, it was discovered a plastic deformation of Al particle, developing at the expense of climb of dislocations by vacancy mechanisms. In similar processes, dislocations were deepened in Al particle. Sometimes dislocations appeared in Ni matrix. Structural reconstruction of the bicrystal took place at an impulsive heating at the expense of the processes. In this connection, the temperature of the beginning of the bicrystal reconstruction decreased in the dependence on the position of the vacancy. When vacancies were introduced in Al particle, they displaced inside Al particle independent on their amount. The increasing of a free volume by the introduction of bigger amount of vacancies near interphase boundary of the bicrystal sharply decreased the temperature of the beginning of diffusion reconstruction of the system.

Then, the experiments were continued to a full reconstruction of the calculated block at thermoactivation and change of the length of the experiment. The experiment was made to a full solution of the particle at the initial temperature 1500 K. Full solution of Al particle took place to the moment of time 0.6 ns. The temperature of the calculated block increased to 2000 K to the final stage of solution. The gradient of the concentration of components appeared in diffusion zone of Ni matrix at the solution of Al particle. Phases Ni_2Al and Ni_3Al formed mainly near the surface of the particle. Phases $NiAl_2$ and $NiAl_3$ prevailed with the removing from the particle. In a real CS reaction, the gradient of concentration and the distribution of phases corresponding to it take place at the initial stages of solution of Ni in Al matrix.

References

1. M.D. Starostenkov, G.M. Poletaev. Structure-energetical transformations in Ni-Al system at SHS-reaction, *Proceeding of X Russian Conference "Construction and properties of metallic and melts"*, V.1, Ekaterinburg (2001), pp.152-155.
2. G.M. Poletaev, M.D. Starostenkov, Mutual Diffusion at the Interface in a Two-Dimensional Ni–Al System, *Technical Physics Letters*, Vol.29, №6 (2003), pp. 454–455.
3. G.M. Poletaev, The research of the processes of interdiffusion in a two-dimensional Ni-Al system. Dissertation of the scientific degree of candidate of physics-mathematical sciences, Barnaul, ASTU (2002), 186 p.

Deformation Instabilities in Heteroepitaxial Growth

Daniel Walgraef

Center for Nonlinear Phenomena and Complex Systems,
Université Libre de Bruxelles, CP 231,
B - 1050 Brussels, Belgium.
e-mail: dwaelgr@ulb.ac.be

ABSTRACT

The combination of atomic deposition and nonlinear diffusion leads, below a critical temperature, to the instability of uniform atomic layers deposited on a substrate. This instability triggers the formation of self-assembled nanostructures which correspond to regular spatial variations of substrate coverage. Since film-substrate lattice misfits and coverage inhomogeneities generate internal stresses, the coupling between deposition dynamics and film elasticity has to be considered. It is shown that this coupling is destabilizing and may generate different types of deformation patterns on the film surface.

1. Introduction.

Self-organized nanophases have been observed in binary and monoatomic epilayers (e.g. [1, 2, 3, 4]). Various atomistic computer simulation methods have been developed to describe this phenomenon. However, since the size of the films described by these methods remains small, continuous approaches remain of interest to describe mesoscopic scales. Up to now, these models had limited predictive capability, because of a rough description of kinetic processes. Nevertheless, they may provide a qualitative understanding of self-assembling phenomena and link microscopic and macroscopic scales in the framework of Multiscale Materials Modeling [5]. Continuous models have already been proposed to describe the spontaneous ordering of nanostructures or quantum dots in multicomponent epilayers on a substrate (e.g. [6]). It has also been shown that the competition between atomic deposition and adsorbed atomic layer instability may generate nanoscale spatial patterns, even in monoatomic films [7]. However, the formation of low or high coverage domains or islands generates internal stresses in the adsorbed layers, which have to be taken into account in the dynamics. Hence, the aim of the present paper is to incorporate elasticity effects in our previous model of nanostructure formation [7]. In this framework, it is shown that stress effects are destabilizing and generate deformation modes which may affect the morphology and stability of selected nanostructures.

2. The Dynamics of a Deposited Layer on a Substrate.

The deformation dynamics of a thin film on a substrate, in the presence of defects, has been analyzed in [8]. In the present case, vacant sites, deposited atoms and adatoms, islands,

grains, etc. also induce lattice dilatation in the adsorbed layer, and the evolution of the film bending coordinate may be described by a von Karman model, coupled with surface atomic coverage evolution:

$$\begin{aligned} \partial_t^2 \xi &+ \eta \partial_t \xi = -\frac{Eh^2}{12\rho(1-\nu^2)} \triangle^2 \xi + \frac{1}{2\rho} \sigma_{\alpha\beta} \xi_{,\alpha\beta} - \frac{\kappa}{\rho h} \xi + \frac{\theta c_0}{b^3 \rho h} (\phi_+ - 1) \\ \partial_t \phi_+ &= \frac{1}{\tau}(1-\phi_+)\phi_+ + D_h \nabla^2 [\frac{1}{c_0} \ln \frac{\phi_+}{1-c_0\phi_+} - \frac{\epsilon_0}{k_B T}\phi_+ - \frac{\xi_0^2}{k_B T}\nabla^2 \phi_+ + \frac{mh\theta}{2c_0 k_B T} \nabla^2 \xi] \quad (1) \end{aligned}$$

where atomic coverage at the bottom and upper surfaces are c_0, while $c_+ = c_0 \phi_+(\vec{r}, t)$, respectively. $c_0 = \frac{\alpha - \beta}{\alpha}$, where α and β are the adsorption and desorption rates. Other coefficients have been defined in [7, 8].

2.1. Deformation Instabilities in a Monoatomic Layer.

The system (1) admits a uniform steady state, $\phi_+ = 1$, $\xi = 0$, which corresponds to a uniform, undeformed deposited layer. At sufficiently high and low temperatures, the coefficient $\frac{D_h(T)}{k_B T}$ tends to zero and uniform atomic coverage is stable [7]. Furthermore, the coupling between film bending and coverage becomes vanishingly small in these limits, where the linear stability analysis may be performed through the linear evolution of the Fourier transform of small inhomogeneous perturbations, ξ, only. For compressive misfit strains ($\epsilon_m \propto \frac{a_s - a_f}{a_f} < 0$), it is found that uniform undeformed layers are unstable for:

$$|\epsilon_m|^2 > |\epsilon_c|^2 = \frac{16h\kappa}{3E} (\frac{1-\nu}{1+\nu}) \ , \ q_c^4 = \frac{12\kappa(1-\nu^2)}{Eh^3} \quad (2)$$

Furthermore, weakly nonlinear analysis show that deformation patterns should correspond to square lattices.

2.2. The effect of coverage dynamics on deformation patterns.

For temperatures such that the coupling between the evolution of coverage perturbations and film bending is relevant, the evolution equation for coverage perturbations in the upper film surface may be expanded in a power series, which yields a Cahn-Hilliard type of dynamics. Above the adsorbed layer critical temperature, $\mu < 1$, uniform coverage is stable, and nonuniform perturbations may be adiabatically eliminated. This results in the lowering of the instability threshold is and the increase of the most unstable wavenumber. Furthermore, it introduces quadratic nonlinearities in the resulting dynamics, which may lead to the formation of hexagonal deformation patterns instead of square ones.

3. Conclusion.

The evolution of a monoatomic layer, deposited on a substrate, has been described by a dynamical model, where coverage evolution is coupled with deformation fields. In this

description, this coupling is destabilizing. Below the critical thickness for nucleation of misfit dislocations, it may induce regular deformation patterns. For high and low temperatures, pattern formation may be induced by compressive misfit stresses only. Preferred structures should correspond in this case to square lattices in isotropic systems. For lower temperatures, but still above the adsorbed layer instability temperature, the coupling between coverage inhomogeneities and film deformation is twofold. On the one hand, it enlarges the linear instability domain. On the other hand, it adds new contributions to the nonlinear terms of the dynamics, and in particular quadratic ones. When coverage nonlinearities dominate, stable patterns should correspond to hexagons, or wrinkles. When elastic nonlinearities dominate, stable patterns should correspond to squares or hexagons.

Acknowledgments.

D.W. is supported by the Belgian National Fund for Scientific Research. This work has been supported in part by the European Community's Human Potential Programme under contract HPRN-CT-2002-00198, [DEFINO].

References.

[1] K. Kern, H. Niebus, A. Schatz, P. Zeppenfeld, J. George, and G. Comsa. Long-range spatial self-organization in the adsorbate-induced restructuring of surfaces: Cu110-(2x1)O. *Phys. Rev. Lett.*, 67:855–858, 1991.

[2] K. Pohl, M.C. Bartelt, J. de la Figuera, N.C. Bartelt, J. Hrbek, and R.Q. Hwang. Identifying the forces responsible for self-organization of nanostructures at crystal surfaces. *Nature*, 397:238–241, 1999.

[3] A.A. Baski, S.C. Erwin, and J.L. Whitman. The structure of Si(112):Ga-(n1) reconstructions. *Surf. Sci.*, 423:L265–L270, 1999.

[4] H.J. Ernst. Helium atom beam scattering as a probe for the kinetics on singular and vicinal surfaces: Fundamental aspects of ordering, growth and ablation. *Journal de Physique IV*, 7:C6–55, 1997.

[5] N.M. Ghoniem, H. Heinisch, H. Huang, S. Yip, and J. Yu. *Journal of Computer Aided Materials Design*. Kluwer Academic Publishers, Dordrecht, 1999.

[6] Z. Suo and W. Lu. Forces that drive nanoscale self-assembly on solid surfaces. *Journal of Nanoparticle Research*, 2:333–344, 2000.

[7] D. Walgraef. Nanostructure evolution during thin film deposition. *Physica E*, 18:393–401, 2003.

[8] D. Walgraef, N.M. Ghoniem, and J. Lauzeral. Deformation patterns in thin films under uniform laser irradiation. *Phys.Rev.*, B 56:15361–15377, 1997.

Multiscale Simulation of Static and Dynamic Grain Growth in Polycrystalline Thin Films*

A. Haslam [a], V. Yamakov [b], D. Moldovan [c], R. Ding [d], D. Wolf [d] and S.R. Phillpot [e]

[a] Dept. of Chem. Engrg., Imperial College London, London, U.K.,
[b] National Institute of Aerospace, Hampton, VA 23666
[c] Mechanical Engineering Dept., Louisiana State University, Baton Rouge, LA 70803
[d] Materials Science Division, Argonne National Laboratory, Argonne, IL 60439,
[e] Materials Science and Engineering Dept., University of Florida, Gainesville, FL 32611

ABSTRACT

Molecular-dynamics simulations have been used to elucidate the intricate, highly non-linear coupling between grain growth and grain-boundary diffusion creep in nanocrystalline thin films. We demonstrate how the materials-physics based insights into the underlying growth and deformation mechanisms extracted from these simulations can be rigorously incorporated into a mesoscopic simulation model, thus overcoming the length and time-scale limitations inherent to the MD approach. The objects evolving in space and time in the mesoscale simulations are the discretized grain boundaries and grain junctions rather than the atoms. This then enables analysis of the coupling between grain growth and grain-boundary diffusion creep for a system containing a large number of grains with arbitrary sizes.

1. Introduction

High-temperature deformation of fine-grained materials generally enhances the rate of grain growth compared to that due to thermal annealing alone [1–4]. In fact, this stress-induced phenomenon, called dynamic grain growth, can be responsible for most of the grain growth occurring during superplastic deformation of both metallic and ceramic materials. In spite of rich experimental evidence for the existence of dynamic grain growth and a variety of models proposed to explain the underlying correlation between dynamic grain growth and superplastic deformability, the mechanisms by which stress enhances grain growth are still not well understood. Here we use a combination of molecular-dynamics (MD) and mesoscale simulations to elucidate the coupling between high-temperature deformation and grain growth.

2. MD simulations

Building on our recent MD study of thermally driven grain growth [1], in the MD

simulations we consider a columnar nanocrystalline-Pd microstructure containing 25 grains with a grain size of 14 nm in the three-dimensional (3d), periodically repeated simulation cell. The grain boundaries (GBs) are identified by tracking the miscoordinated atoms, i.e., those with nearest-neighbor coordination differing from the fcc perfect-crystal value of 12. Figures 1(b) and (c) demonstrate that the grain growth in the initial microstructure shown in (a) is accelerated significantly by the presence of the GB diffusion creep (also known as Coble creep [2]) induced by the stress applied in the horizontal direction. [3] In the absence of the stress (Fig. 1(b)), little grain growth has occurred during the 5.49 ns of simulation time at 1200 K (the melting point for the Pd potential used here being about 1500 K [1]). In our previous simulations, at T = 1400 K the same microstructure had shown significant grain growth after 4.5 ns [1], by a mechanism involving both curvature-driven GB migration and grain-rotation coalescence events of neighboring grains. Fig. 1(c) reveals that in the presence of the stress considerable grain growth has taken place even at T=1200 K, in dramatic contrast to (b).

To investigate the deformation mechanism we have tracked the diffusion of all the atoms in the system. The position of each atom may be compared at any time t with its position at a previous time, $t - \Delta t$. Using this information, the deformation mechanism was identified as GB diffusion creep. Moreover, the value of the GB diffusion coefficient thus obtained is in quantitative agreement with that reported in Pd bicrystal simulations of high-energy GBs of Keblinski et al. [4].

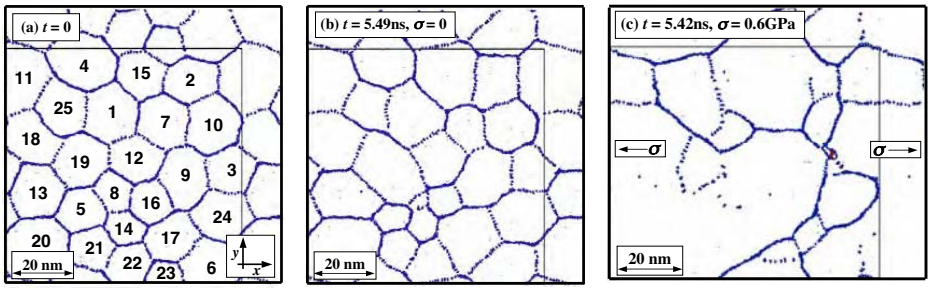

Fig. 1. In (a), the initial, fully 3d microstructure is seen as lines of miscoordinated atoms; the inset, thin lines delineate the periodically repeated simulation cell. In (b), after simulation at 1200K with no stress, little grain growth has taken place. In (c), applying stress in the horizontal direction has induced GB diffusion creep and caused a strong enhancement of the grain growth. [3]

2. Mesoscale simulations

Building on our recent, extensive simulations of grain growth [5], the model used for our mesoscale simulations is based on the variational principle of dissipated power [6]. Two dissipative processes are considered: GB diffusion and GB migration. During GB diffusion creep, atoms diffuse from boundary regions in compression to those in tension,

leading to homogeneous grain elongation. The diffusion is driven by the gradient of the chemical potential, which is induced by the gradient of the stress acting along each boundary. By contrast, GB migration is driven by the GB curvature. A finite-element formulation of coupled GB migration and diffusion within the variational approach was presented by Cocks et al. [7]; the relevant equations were incorporated into our mesoscale code. The microstructure is updated at each time step according to the velocity fields obtained from the finite-element equations, including the velocities of the grain centers, their rates of rotation and the migration velocities of GB junctions. In order to better handle the topological discontinuities associated with grain switches and the disappearance of small, three-sided grains, a new topological transformation rule was developed.

Mesoscopic simulations using this code were used to elucidate the fundamental effects of microstructural inhomogeneity in polycrystalline materials on the interplay between GB diffusion creep and GB migration. [8] Considering two-dimensional model microstructures with a distribution in the grain sizes and grain-boundary diffusivities, we were able to quantitatively capture the two distinct grain-growth processes that occur during Coble creep: the static grain growth driven by GB migration, and the dynamic grain growth induced by the grain switching and the disappearance of small, three-sided grains in the topological inhomogeneous microstructure. Our simulations also revealed the manner in which the grain growth affects, and accommodates, the GB diffusion creep. At relatively low stresses, the creep rate *decreases* with the plastic strain because of the rapid increase in the grain size during the dominating, static grain growth. On the other hand, at elevated stresses the creep rate *increases* with the plastic strain; the reason for this increase lies in the accelerated grain switching that takes place during dynamic grain growth. Moreover, our simulations show that the grains remain almost equiaxed during the Coble creep due to its accommodation by GB migration. By contrast, when GB migration is suppressed in the simulation, a highly elongated grain shape is obtained.

* This work was supported by the US Department of Energy, Basic Enery Sciences-Materials Sciences, under Contract W-31-109-Eng-38.

References

[1] A.J. Haslam, S.R. Phillpot, D. Wolf, D. Moldovan and H. Gleiter, Mater. Sci. Eng. A **318**, 293 (2001).
[2] R.L. Coble, J. Appl Phys. **34**, 1679 (1963).
[3] A.J. Haslam, D. Moldovan, V. Yamakov, D. Wolf, S.R. Phillpot and H. Gleiter, Acta Mater. **51**, 2097 (2003); ibid. **52**, 1971 (2004).
[4] P. Keblinski, D. Wolf, S.R. Phillpot and H. Gleiter, Phil. Mag. A **79**, 2735 (1999).
[5] D. Moldovan, D. Wolf and S.R. Phillpot, Phil. Mag. **83**, 3643 (2003).
[6] A. Needleman and J.R. Rice, Acta metall. **28**, 1315 (1980).
[7] J. Pan, A. C. F. Cocks and S. Kucherenko, Proc. R. Soc. Lond. **A453**, 2161 (1997).
[8] R. Ding, D. Moldovan, V. Yamakov, D. Wolf and S.R. Phillpot (in these proceedings)

Phase transition in thin films

C.H. Woo[1], B. Wang[1], Z. Man[1], W.C Liu[1], Hanchen Huang[2]

[1]Department of Electronic and Information Engineering, Hong Kong Polytechnic University, Hung Hom, Hong Kong
[2]Department of Mechanical, Aerospace and Nuclear Engineering, Rensselaer Polytechnic Institute, Troy, NY 12180, USA

ABSTRACT

Via a linear stability analysis of the Ginsberg-Landau evolution equation of the system, analytic expressions relating various critical parameters for a thin film subjected to various electro/mechanical surface conditions are derived. Using the para/ferro-electric transformation in thin films as an example, the Curie temperature and the critical thickness for ferroelectricity in thin films are calculated. The results are consistent and compare well with the experimental data.

1. Introduction

To successfully incorporate thin films into a working device, it is important to understand the change of thin-film properties as a function of environmental variables and film thickness. This is particularly relevant to functional materials in the thin film form, such as ferromagnetics, ferroelectrics, piezoelectrics, shape-memory alloys, liquid crystals, etc., in which drastic property changes due to phase transitions may seriously affect their performance.

The phase transition problem is complex, due to the interplaying relationships among the film thickness, ambient temperature, constraint of the substrate, surface relaxation, order and direction of the transition, etc. Except for the simplest cases, phase-transition models are mostly based on first-principle [1] or thermodynamic approaches [2]. In the latter case, the nonlinear Ginzburg-Landau equations or similar equations are solved numerically to take into account the through-thickness variation of the order parameter in thin films. However, the numerical work involved in the comprehensive investigation of a multi-parameter, multi-mechanism, system can become overwhelming.

Phase transitions from a stable state of a dynamical system do not occur without the state becoming unstable. The evolution equation of the order parameter in a thin film, when perturbed from equilibrium, can be derived from its free energy, in terms of control parameters such as the ambient temperature, boundary conditions, surface characteristics, sample dimensions, and misfit epitaxial stresses, etc. Then important characteristics of the film, such as the phase transition temperatures, critical thicknesses, domain morphology, substrate nature, etc., are related through the instabilities of the initial state,

which is accessible via a stability analysis, the linear nature of which opens the system to easy examination. This constitutes our approach in the present paper.

Without loss of generality, we consider the specific case of the para/ferro-electric transition in thin films. We establish the conditions of the stability of the paraelectric versus ferroelectric phases in a thin film. Expressions for the para/ferroelectric transition temperatures as a function of film thickness, and the corresponding critical thickness, is derived, and the complex relation of the critical thickness with the various parameters discussed. Both first-order and second-order transitions are considered.

2. The Evolution Equation and Stability of the Stationary States

We consider a thin film of ferroelectric material of dimensions $\infty \times \infty \times h$, h being the film thickness. The origin of the coordinate system is at the center of the cell. We suppose the spontaneous polarization P is orthogonal to the surface of the film. For rigid substrates, the transformation strain $\varepsilon^T = \varepsilon_{xx}^T = \varepsilon_{yy}^T = QP^2$ is fully constrained, causing an elastic contribution to the total free energy $F_e = GQ^2 \iiint_V P^4 dV$, where $G = (C_{11} + C_{12} - 2C_{12}^2/C_{11})$, C_{11} and C_{12} being components of the elastic modulus of the film, and V the volume of the film. We note that due to the free upper surface of the films, the component ε_{zz}^T of the transformation neither contributes to the elastic energy nor to the misfit energy. Including the effects of the depolarization field $\vec{E}_d = (0,0,E_d)$ and the epitaxial stresses $\sigma_{xx} = \sigma_{yy} = \sigma_r$, the time evolution of the order parameter of the system, the polarization field P, is governed by the time-dependent Ginzburg-Landau equation (GLE). The stability of the initial state can be probed by applying a small perturbation Δ to the system at equilibrium. The evolution equation of Δ follows straightly from the GLE, and is linear. System instability occurs at points where one or more of the eigen values of the evolution equation of Δ becomes positive. Analytic expressions of the transition temperatures (both supercooling and superheating) are derived using this procedure, from which the critical thicknesses for ferroelectricity in thin films, for which the Curie temperature is at zero, are obtained.

3. Results

Streiffer et. al. [3], who measured the Curie temperatures as a function of film thickness up to 50 nm of epitaxial films of $PbTiO_3$, grown on $SrTiO_3$ (001) substrate (i.e., $\phi = 0$), found that the Curie temperature decreased with decreasing film thickness. Our calculated results are shown in the following figure, together with the experimental points.

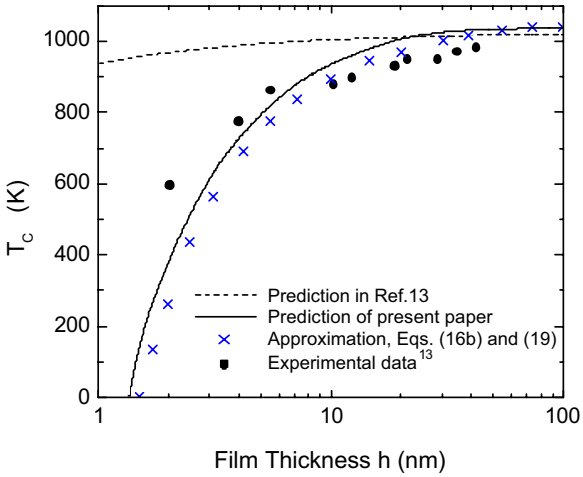

The transition temperature can be calculated analytically for large and small values of h, respectively. For $PbTiO_3$ these equations can be put into the simple forms $T_c = 1041 - 36000/h^2$ for $h > 20$ nm, and $T_c = 1041 - 1440/h$ for $h < 20$ nm, h being in units of nm, using the input parameters. It can be seen that this simple relationship describes the experimental data very well. Plotted together in the dotted line is the theoretical prediction used for comparison by Streiffer *et al.*[12]. The difference between the two theoretical results in the small film thickness regime is obvious. The calculated Curie temperature versus thickness for $PbTiO_3$ thin films under the two contact conditions, is obtained. For films with the same thickness, those on the dielectric substrates have Curie temperatures slightly lower than on short-circuit electrodes, due to the screened depolarization effect in the latter case.

3. Conclusions

By analyzing the conditions of dynamic instability of the time-dependent Ginzburg-Landau equation, we obtain analytic expressions for both first-order and second-order transitions, for the relationship among the epitaxial stresses, the surface-charge induced depolarization, the electro-mechanical contact conditions, the film thickness, and the Curie temperature. From this relation, analytic expressions for the critical thickness are also derived. Despite the simple form of these expressions, they give very good description of the system, as shown by comparing with the numerical solutions.

Acknowledgment:

This project was supported by grants from the Research Grants Council of the Hong Kong Special Administrative Region (PolyU 5173/01E, 5309/03E, 5312/03E).

References

[1] Ph. Ghosez and K. M. Rabe, Appl. Phys. Lett., **76**, 2767 (2000).
[2] D.R. Tilley, in *Ferroelectric Thin Films: Synthesis and Basic Properties*, p.11, Edited by Carlos Paz de Araujo, J. F. Scott and G.W. Taylor (1996).
[3] S. K. Streiffer, J. A. Eastman, D. D. Fong, C. Thompson, A. Munkholm, M. V. Ramana Murty, O. Auciello, G. R. Bai, and G. B. Stephson, Phys. Rev. Lett., **89**, 067601 (2002).